QUANTITATIVE WELL-LOG ANALYSIS OF

IN-SITU NATURAL GAS HYDRATES

VOLUME 1

by

Timothy S. Collett

A thesis submitted to the Faculty and Board of Trustees of the Colorado School of Mines in partial fulfillment of the requirements for the degree of Doctor of Philosophy (Geology).

Golden, Colorado

Date: _10/9/2000_

Signed: _____
Timothy S. Collett

Approved: _____
Dr. R.F. Wendlandt
Thesis Co-Advisor

Approved: _____
Dr. E.D. Sloan
Thesis Co-Advisor

Golden, Colorado

Date: _10/9/00_

_____
Dr. Murray W. Hitzman
Professor and Head,
Department of Geology
and Geological Engineering

ii

ABSTRACT

Gas-hydrate accumulations in onshore arctic and outer continental shelf marine environments are known to contain large volumes of natural gas. The amount of gas sequestered in gas hydrates is probably enormous, but estimates are highly speculative due to the lack of previous quantitative studies. Gas volumes that may be attributed to a gas-hydrate accumulation within a given geologic setting are dependent on a number of reservoir parameters, two of which, sediment porosity and gas-hydrate saturation, can be assessed with data obtained from downhole well-logging devices.
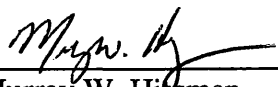
The primary objective of this study was to develop quantitative well-log evaluation techniques, which would permit the calculation of sediment porosities and gas-hydrate saturations in gas-hydrate-bearing reservoirs. Within this study, the well-logging devices that yielded the most accurate gas hydrate reservoir porosities included the gamma-gamma density and neutron porosity logs. The electrical resistivity, acoustic transit-time, and neutron spectroscopic logs also yielded accurate gas-hydrate saturations. The research conducted with these devices in this study can be generally divided into three categories: (1) gas hydrate well-log response modeling, (2) laboratory quantification of gas hydrate well-log responses, and (3) field data investigation and verification. During the gas hydrate well-log response modeling phase of this study, the known and modeled well-log responses attributed to the presence of gas hydrate were reviewed and assessed. The well-log response modeling phase of this study also included

the assessment of existing and the development of new gas hydrate well-log evaluation techniques used to characterize sediment porosities and gas-hydrate saturations in gas-hydrate-bearing reservoirs. The laboratory phase of this study focused on evaluating the acoustic well-log properties of gas hydrates. Laboratory measurements of the acoustic properties of laboratory-grown pure tetrahydrofuran hydrate samples and tetrahydrofuran-hydrate-bearing rock cores further demonstrated that compressional-wave acoustic velocities can be used to calculate accurate gas-hydrate saturations. In the field verification phase of this study, the gas hydrate well-log evaluation techniques developed in the response modeling phase of this study were tested and used to calculate reservoir porosities and gas-hydrate saturations with the downhole-log data from five known gas-hydrate accumulations: (1) Blake Ridge along the southeastern continental margin of the United States, (2) along the Cascadia continental margin off the Pacific coast of Canada, (3) near the Middle-America Trench off the Pacific coast of Guatemala, (4) on the North Slope of Alaska, and (5) in the Mackenzie River Delta of northern Canada.

The field investigation portion of this thesis also contains detailed estimates of the volume of gas associated with several of the regionally mapped gas-hydrate accumulations assessed in this study. It was determined that the Blake Ridge gas-hydrate accumulation may contain as much as 37.7 trillion cubic meters of gas trapped as hydrates and the gas-hydrate accumulation on the Cascadia continental margin may contain about 2.8 trillion cubic meters of gas. The three gas-hydrate-bearing stratigraphic units analyzed in northern Alaska may contain about 562 billion cubic meters of gas. The gas hydrate volumetric calculations in this thesis confirm that gas hydrates are a vast storehouse of natural gas.

In the field verification portion of this study, it was demonstrated that the quality of the available downhole-log data was the most significant factor controlling the accurate assessment of sediment porosities and gas-hydrate saturations. Within relatively high quality (in-gauge) boreholes, conventional downhole-density logs, with appropriate corrections for the presence of gas hydrates and shales, yielded the most accurate downhole-measured porosities in gas-hydrate-bearing sediments. It was also determined that the "standard" Archie (electrical-resistivity-log data) and the Lee (compressional-wave acoustic-log data) relations yielded the most accurate gas-hydrate saturations in the assessed gas-hydrate accumulations.

Sensitivity analysis in the field verification portion of this thesis also demonstrated the relative importance of selecting appropriate values for the "reservoir" constants in the porosity and gas-hydrate saturation equations developed and tested within this study. The field verification portion of this thesis includes case studies from a series of very diverse geologic environments, which in most cases can be applied as analogs to almost any gas-hydrate accumulation that might be discovered in the future.

The downhole-log-derived sediment porosities, calculated in the field verification phase of this study, were relatively high ranging from about 52 to 58 percent in most of the assessed marine gas-hydrate accumulations and from about 29 to 39 percent in the permafrost-associated gas-hydrate accumulations. Average gas-hydrate saturations within most of the clay-rich marine gas-hydrate accumulations assessed in this study were very low, ranging from about 3 to 6 percent. The clastic dominated permafrost-associated gas-hydrate accumulations, however, were characterized by relatively high gas-hydrate saturations, having average values that ranged from about 33 to 61 percent. The gas-hydrate saturations calculated in this thesis have provided the first direct field

evidence that the occurrence of gas hydrate is partially controlled by the mineralogy and lithology of the host sediments.

This thesis documents the fact that downhole-well-log data can yield critical information about the in-situ nature of gas hydrates. In this thesis it is also recognized that in order to advance our understanding of gas hydrates, there is a fundamental need to obtain additional high-quality downhole well logs from various geologic environments with known gas-hydrate accumulations. It is also acknowledged that more extensive integrated field and laboratory physical property studies are required to advance our basic understanding of gas hydrates in nature.

TABLE OF CONTENTS

viii

LIST OF FIGURES

LIST OF TABLES

ACKNOWLEDGMENTS

CHAPTER 1

INTRODUCTION

1.1 Background Information

With growing interest in natural gas hydrates, it is becoming increasingly important to be able to determine the volume of gas hydrates and included natural gas within a gas-hydrate accumulation. The primary objective of this study was to develop quantitative well-log evaluation techniques, which will permit the calculation of porosities and gas-hydrate saturations in gas-hydrate-bearing sedimentary units. To attain this objective, this study was subdivided into three general sections: (1) gas hydrate well-log response modeling, (2) laboratory quantification of gas hydrate well-log responses, and (3) field data investigation. During the response modeling and laboratory phases of this study, new gas hydrate well-log evaluation techniques were developed and tested. These newly developed gas hydrate well-log evaluation techniques were further tested and applied in the field data investigation portion of the study.

The introduction (Chapter 1) of this thesis begins with a discussion of the purpose of this study, followed by a technical overview of gas hydrate physical properties and a review of the known and inferred gas-hydrate occurrences in the world. The introduction concludes with a comprehensive review of previous gas hydrate well-log studies and an outline of the research approach that guided this study. Chapter 2 contains descriptions

of recovered gas hydrate samples along with reviews of proposed gas-hydrate-reservoir models. The well-log response modeling and application section of this thesis (Chapter 3) contains systematic descriptions of all the newly developed quantitative gas hydrate well-log evaluation techniques. Chapter 4 contains the results of the laboratory study of gas hydrate well-log responses. The quantitative gas hydrate well-log evaluation techniques developed in the response modeling and laboratory portion of this study have been used in Chapter 5 to assess gas hydrate reservoir properties within five known gas-hydrate accumulations. Chapter 6 includes a summary of the newly developed quantitative gas hydrate well-log evaluation techniques and a review of the utility of these newly developed techniques in the field. Chapter 6 also includes a section dealing with recommendations for future research along with an evaluation of the relative impact of this study on previously published gas hydrate volumetric estimates. This thesis ends (Chapter 7) with a comprehensive listing of the major achievements and conclusions of this study.

1.2 Purpose of Study

Gas hydrates are crystalline substances composed of water and gas, in which solid lattices of water molecules trap gas molecules in a cage-like structure, or clathrate. Gas hydrates are widespread in permafrost regions and beneath the sea in sediment of outer continental margins. While methane, propane, and other gases can be included in the clathrate structure, methane hydrates appear to be the most common in nature (Kvenvolden, 1988). The amount of methane sequestered in gas hydrates is probably

enormous, but estimates of the amounts are speculative and range over three orders-of-magnitude from about 3,114 to 7,634,000 trillion cubic meters (reviewed by Kvenvolden, 1993). The amount of gas in the gas hydrate reservoirs of the world greatly exceeds the volume of known conventional gas reserves, estimated to be about 250 trillion cubic meters (Masters et al., 1991). The production history of the Russian Messoyakha gas hydrate field demonstrates that gas hydrates are an immediate source of natural gas that can be produced by conventional methods (Collett 1993a; Collett and Ginsburg, 1998).

Gas hydrates also represent a significant drilling and production hazard. Russian, Canadian, and American researchers have described numerous problems associated with gas hydrates, including blowouts and casing failures (reviewed by Yakushev and Collett, 1992). As exploration and development activity moves into deeper water (>300 m) and high latitude arctic environments, the frequency of gas hydrate induced problems will likely increase. Recent studies indicate that atmospheric methane, a greenhouse gas, is increasing at a rate such that the current concentration will probably double in the next 50 years. Because methane is 21 times more radiatively active than carbon dioxide, it is predicted that methane will surpass carbon dioxide as the predominant atmospheric greenhouse gas in the second half of the next century. The source of this atmospheric methane is uncertain; however, numerous researchers have suggested that destabilized natural-gas hydrates may be contributing to the build-up of atmospheric methane (reviewed by Kvenvolden, 1988).

One of the fundamental problems that links the gas hydrate resource, hazard, and climate issues is the need for accurate assessments of the amount of gas stored within

gas-hydrate accumulations. Most of the published gas hydrate resource estimates have of necessity been made by broad extrapolation of only general knowledge of local geologic conditions. The amount of gas that might be stored in a gas-hydrate accumulation is dependent on a number of reservoir parameters, including the areal extent of the gas-hydrate occurrence, reservoir thickness, reservoir porosity, and the degree of gas-hydrate saturation (Collett, 1993b). Two of the most difficult reservoir parameters to determine are porosity and the degree of gas-hydrate saturation. Well logs often serve as a source of porosity and hydrocarbon saturation data; however, well-log calculations within gas-hydrate-bearing intervals are subject to error. The primary reason for this difficulty is the lack of previous quantitative laboratory and field calibration studies.

Most of the existing gas hydrate well-log evaluation techniques are qualitative in nature and have been developed by the extrapolation of untested petroleum industry log evaluation procedures (Collett et al., 1984; Mathews, 1986; Collett, 1993b). To adequately test the utility of standard petroleum log evaluation techniques in gas-hydrate-bearing reservoirs would require numerous laboratory and field measurements. Prior to this study, however, only two gas-hydrate occurrences had been sampled and surveyed with open-hole well-logging devices.

1.3 Gas Hydrate Technical Review

Under appropriate conditions of temperature and pressure (Figure 1.1), gas hydrates usually form one of two basic crystal structures known as Structure-I and Structure-II (Figure 1.2). Each unit cell of Structure-I gas hydrate consists of 46 water
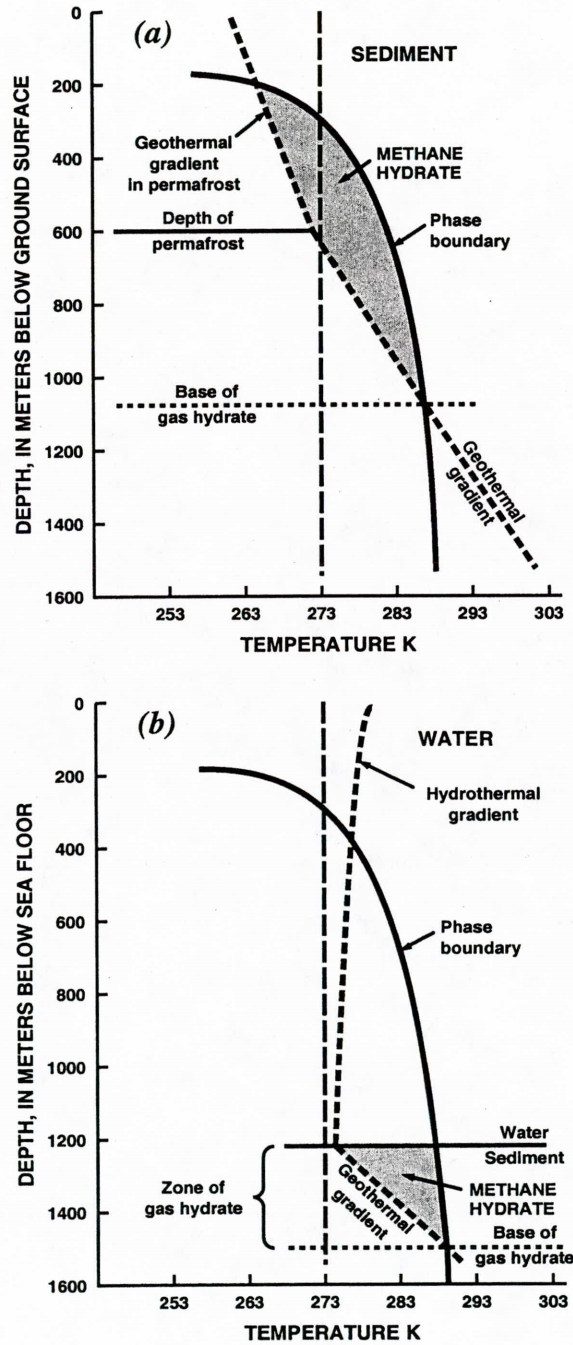
Figure 1.1 Graphs showing the depth-temperature zone in which methane hydrates are stable in (a) a permafrost region and (b) an outer continental margin marine setting (modified from Collett, 1995).
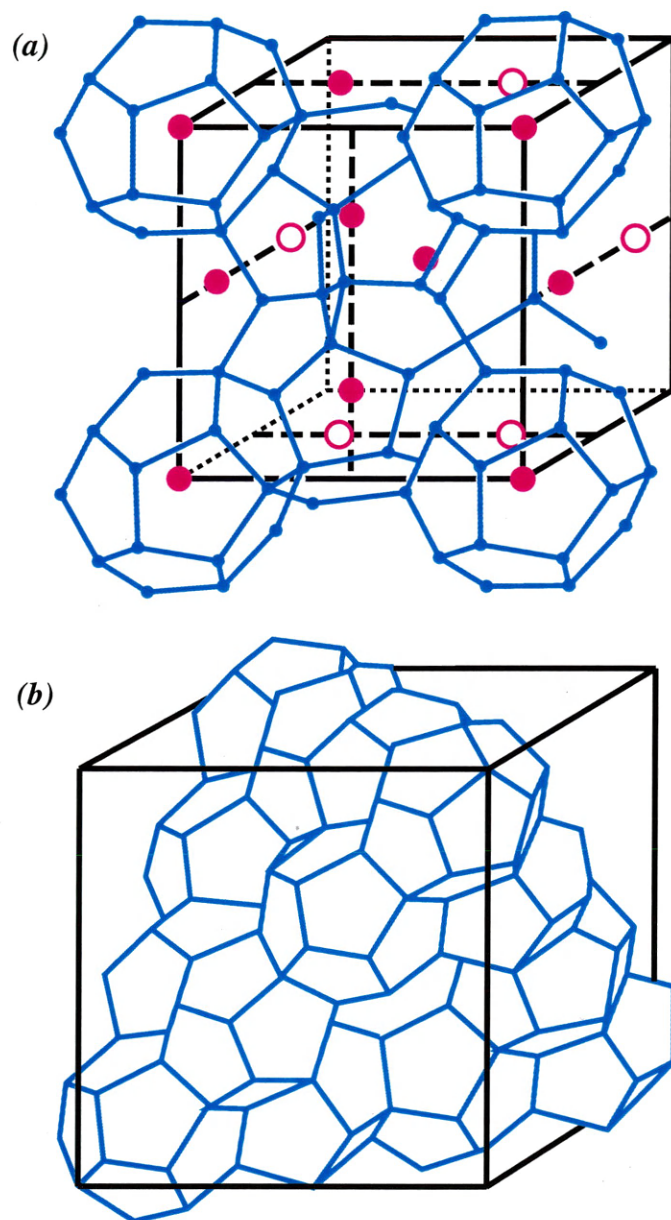
Figure 1.2 Two gas hydrate crystal structures: (a) Structure I; and (b) Structure II (modified from Sloan, 1998).

molecules that form two small dodecahedral voids and six large tetradecahedral voids.

Structure-I gas hydrates can only hold small gas molecules such as methane and ethane,

with molecular diameters not exceeding 5.2 angstroms. The chemical composition of a

Structure-I gas hydrate can be expressed as $8(Ar,CH_4,H_2S,CO_2)46H_2O$ or

$(Ar,CH_4,H_2S,CO_2)5.7H_2O$ (Makogon, 1981). The unit cell of Structure-II gas hydrate

consists of 16 small dodecahedral and 8 large hexakaidecahedral voids formed by 136

water molecules. Structure-II gas hydrates may contain gases with molecular dimensions

in the range of 5.9 to 6.9 angstroms, such as propane and isobutane. The chemical

composition of a Structure-II gas hydrate can be expressed as

$8(C_3H_8,C_4H_{10},CH_2Cl_2,CHCl_3)136H_2O$ or $(C_3H_8,C_4H_{10},CH_2Cl_2,CHCl_3)17H_2O$

(Makogon, 1981). At conditions of standard temperature and pressure (STP), one

volume of saturated methane hydrate (Structure-I) will contain as much as 164 volumes

of methane gas -- because of this large gas-storage capacity, gas hydrates are thought to

represent an important source of natural gas.

An overview of gas hydrate structures would not be complete without mentioning

the newly discovered hydrate structure, Structure H. The existence of this structure was

determined by laboratory nuclear magnetic resonance studies of Ripmeester et al. (1987),

and is characterized by three types of cages. Structure H hydrates have been shown to be

unique, with a number of large molecules able to fit into the largest cage of these newly

discovered gas hydrates. Structure H guest molecules include numerous natural

occurring substances, including adamantane, gasoline range hydrocarbons, and

napthalene ingredients. Structure H hydrates, however, will be neglected in this study since they have not been conclusively found outside of the laboratory.

On a macroscopic level, many of the gas hydrate mechanical properties resemble those of ice (Table 1.1), because hydrates contain a minimum of 85 percent water on a molecular basis. Among the exceptions to this heuristic is thermal conductivity, which is relatively low in gas hydrates; this can be attributed to the molecular structural differences between ice and gas hydrates. Of interest are the phase equilibrium properties of gas hydrates, which are mostly controlled by the fit of the guest gas molecules within the hydrate water cages. For example, the addition of propane to a pure methane hydrate changes the gas hydrate structure from a Structure-I to a Structure-II gas hydrate and broadens the temperature and pressure conditions in which the hydrates can occur. For a complete description of the structure and properties of gas hydrates see the summary by Sloan (1998).

Onshore gas hydrates (Figure 1.3) are known to be present in the West Siberian Basin (Makogon et al., 1972) and are believed to occur in other permafrost areas of northern Russia, including the Timan-Pechora province, the eastern Siberian Craton, and the northeastern Siberia and Kamchatka areas (Cherskiy et al., 1985). Permafrost-associated gas hydrates are also present in the North American Arctic. Direct evidence for gas hydrates on the North Slope of Alaska comes from a core-test, and indirect evidence comes from drilling and open-hole industry well logs which suggest the presence of numerous gas hydrate layers in the area of the Prudhoe Bay and Kuparuk River oil fields (Collett, 1983; Collett, 1993b). Well-log responses attributed to the

Table 1.1 Comparison of ice and gas hydrate physical properties (modified from Sloan, 1998).

Property	Ice	Gas hydrate structure	
		I	II
Dielectric constant at 273 K	94	≈58	58
NMR rigid lattice second moment of H_2O protons (G^2)	32	33	33
Water molecule reorientation time at 273 K (μsec)	21	≈10	10
Diffusional jump time of water molecules at 273 K (μsec)	2.7	>200	>200
Isothermal Young's modulus at 268 K (10^9Pa)	9.5	≈8.4	≈8.4
Speed of longitudinal sound at 273 K Velocity (km/sec)	3.8	3.3	3.6
Velocity ratio (V_p/V_s) (272 K)	1.88	1.95	1.97
Poisson's ratio (268 K)	0.33	≈0.33	≈0.33
Bulk modulus (272 K)	8.8	≈5.6	≈8.27
Shear modulus (272 K)	3.9	≈2.4	-
Bulk-density (g/cm^3)	0.92	0.90	0.94
Adiabatic bulk compressibility at 273 K (10^{-11} Pa)	12	≈14	≈14
Thermal conductivity at 263 K (W/m-K)	2.23	0.49	0.51
Linear thermal expansion at 273 K (K^{-1})	56×10^{-6}	104×10^{-6}	64×10^{-6}
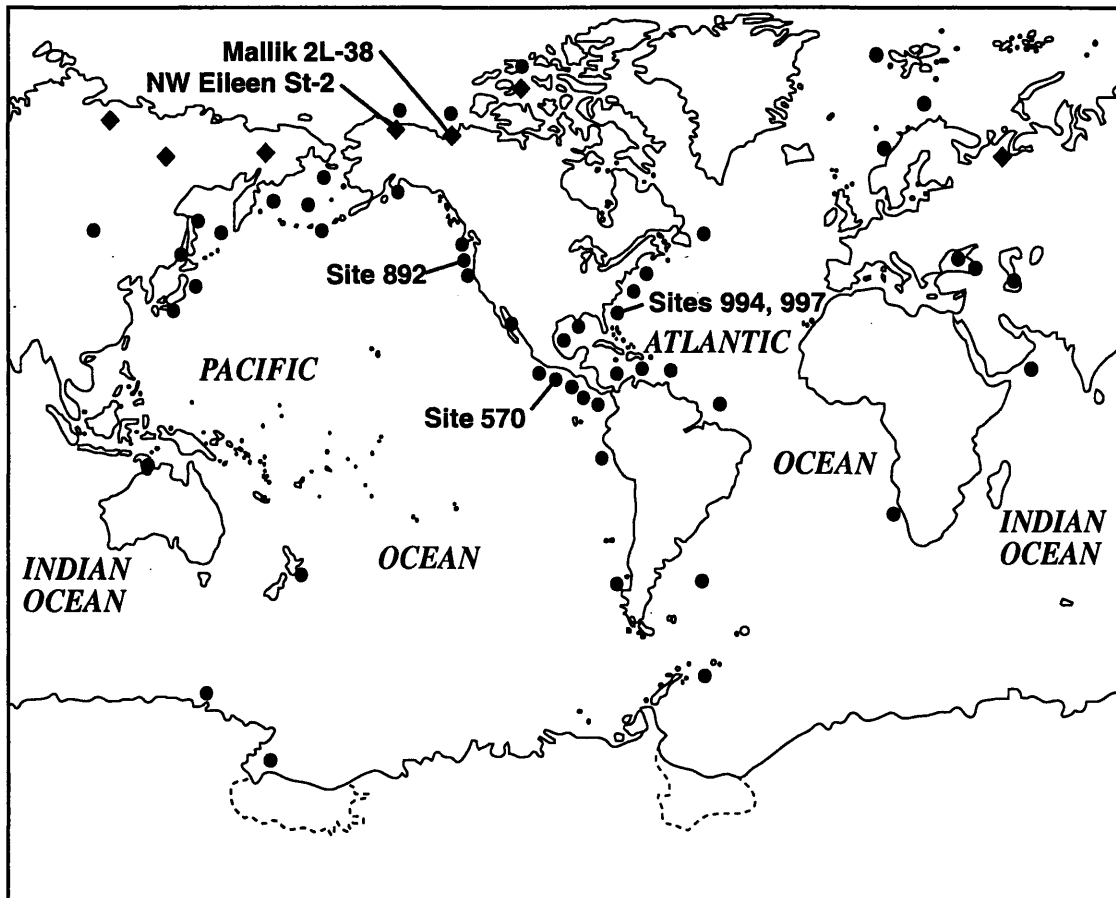
Figure 1.3 Locations of known and inferred gas-hydrate occurrences in oceanic sediment of outer continental margins (●), and permafrost regions (◆) (modified from Kvenvolden, 1988). Also shown are the locations of the drill-sites at which gas hydrates have been sampled and surveyed with open-hole logs (Table 1.3).

presence of gas hydrates have been obtained in about one-fifth of the wells drilled in the

Mackenzie Delta, and more than half of the wells in the Arctic Islands are inferred to

contain gas hydrates (Judge, 1988; Judge and Majorowicz, 1992). The combined

information from Arctic gas-hydrate studies shows that, in permafrost regions, gas

hydrates may exist at subsurface depths ranging from about 130 to 2,000 m (Kvenvolden,

1988).

The presence of gas hydrates in offshore continental margins (Figure 1.3) has

been inferred mainly from anomalous seismic reflectors that coincide with the predicted

phase boundary at the base of the gas-hydrate stability zone. This reflector is commonly

called a bottom-simulating reflector or BSR. BSR's have been mapped at depths below

the sea floor ranging from about 100 to 1,100 m (Kvenvolden, 1988). Gas hydrates have

been recovered in gravity cores within 10 m of the sea floor in sediment of the Gulf of

Mexico (Brooks et al., 1986), the offshore portion of the Eel River Basin of California

(Brooks et al., 1991), the Black Sea (Yefremova and Zhizhchenko, 1974), the Caspian

Sea (Ginsburg et al., 1992), and the Sea of Okhotsk (Ginsburg et al., 1993). Also, gas

hydrates have been recovered at greater sub-bottom depths during research coring along

the southeastern coast of the United States on the Blake Ridge (Kvenvolden and Barnard,

1983; Shipboard Scientific Party, 1996), in the Gulf of Mexico (Shipboard Scientific

Party, 1986), in the Cascadia Basin near Oregon (Shipboard Scientific Party, 1994), the

Middle America Trench (Kvenvolden and McDonald, 1985; Shipley and Didyk, 1982),

offshore Peru (Kvenvolden and Kastner, 1990), and on both the eastern and western

margins of Japan (Shipboard Scientific Party, 1990, 1991).

Because gas hydrates are widespread in permafrost regions and in offshore marine sediments, they may be a potential energy resource. World estimates for the amount of natural gas in gas hydrate deposits range from 14 to 34,000 trillion cubic meters for permafrost areas and from 3,100 to 7,600,000 trillion cubic meters for oceanic sediments (adapted from Kvenvolden, 1993). The estimates in Table 1.2 show considerable variation, but oceanic sediments seem to be a much greater resource of natural gas than continental sediments. Current estimates of the amount of methane in the world gas-hydrate accumulations are in rough accord at about 20,000 trillion cubic meters (reviewed by Kvenvolden, 1993). If these estimates are valid, then the amount of methane in gas hydrates is almost two orders-of-magnitude larger than the estimated total remaining recoverable conventional methane resources (Masters et al., 1991).

The recently completed 1995 National Assessment of United States Oil and Gas Resources, conducted by the U.S. Geological Survey, focused on assessing the undiscovered conventional and unconventional resources of crude oil and natural gas in the United States (Gautier et al., 1995). This assessment included for the first time a systematic resource appraisal of the in-place natural gas hydrate resources of the United States onshore and offshore regions (Collett, 1995). In this assessment, 11 gas-hydrate plays were identified within four offshore and one onshore gas hydrate provinces. The offshore gas hydrate provinces assessed lie within the U.S. Exclusive Economic Zone adjacent to the lower 48 States and Alaska. The only onshore province assessed was the North Slope of Alaska. In-place gas resources within the gas hydrates of the United States are estimated to range from about 3,200 to 19,000 trillion cubic meters of gas, at

Table 1.2 World estimates of the amount of methane in gas hydrates of terrestrial and oceanic settings (modified from Kvenvolden, 1993).

Terrestrial Gas Hydrates

Estimated in-place natural gas resources		Reference
(trillion cubic feet)	(cubic meters)	
5.0×10^2	1.4×10^{13}	Meyer (1981)
1.1×10^3	3.1×10^{13}	McIver (1981)
2.0×10^3	5.7×10^{13}	Trofimuk et al. (1977)
2.6×10^4	7.4×10^{14}	MacDonald (1990)
1.2×10^6	3.4×10^{16}	Dobrynin et al. (1981)

Oceanic Gas Hydrates

Estimated in-place natural gas resources		Reference
(trillion cubic feet)	(cubic meters)	
1.1×10^5	3.1×10^{15}	McIver (1981)
1.8 to 8.8×10^5	5 to 25×10^{15}	Trofimuk et al. (1977)
7×10^5	2×10^{16}	Kvenvolden (1988)
7.4×10^5	2.1×10^{16}	MacDonald (1990)
1.4×10^6	4×10^{16}	Kvenvolden and Claypool (1988)
2.7×10^8	7.6×10^{18}	Dobrynin et al. (1981)

the 0.95 and 0.05 probability levels, respectively. Although this range of values shows a high degree of uncertainty, it does indicate the potential for enormous quantities of gas stored as gas hydrates. The mean in-place value for the entire United States is calculated to be about 9,000 trillion cubic meters of gas.

1.4 Review of Previous Gas Hydrate Well-Log Studies

Gas hydrates have been inferred to occur at about 50 locations throughout the world (reviewed by Kvenvolden, 1988). Gas hydrates have only been sampled and surveyed with open-hole well-logging devices at five locations (Table 1.3, Figure 1.3): (1) North Slope of Alaska, (2) Middle-America Trench off the Pacific coast of Guatemala, (3) Cascadia continental margin off the Pacific coast of Canada, (4) Blake Ridge on the southeastern continental margin of the United States, and (5) the Mackenzie River Delta in northern Canada. The well-log data from the North Slope of Alaska and Middle-America trench have been the focus of several published studies (Collett et al., 1984; Mathews, 1986; Collett, 1993b), however, the available well-log data from the Cascadia continental margin, the Blake Ridge, and the Mackenzie Delta have not been examined in detail. The next several sections of this thesis review the results of the completed gas hydrate well-log studies in northern Alaska and offshore Guatemala. Discussions pertaining to well-log data from Cascadia, the Blake Ridge, and the Mackenzie Delta can be found in the field application section (Chapter 5) of this thesis, along with a more detailed assessment of the Alaska and offshore Guatemala well-log data sets.

Table 1.3 Drill-sites at which gas hydrates have been sampled and surveyed with open-hole well logs. Location of drill-sites are shown in Figure 1.3.

Well/Site identification	Operator	Location	Reference
NW Eileen State-2	ARCO/Exxon	North Slope of Alaska, USA	Collett (1993b)
Mallik 2L-38	JAPEX/JNOC/GSC	Mackenzie River Delta, Canada	Dallimore et al. (1999)
Leg 84 Site 570	Deep Sea Drilling Project	Middle-America Trench, Pacific Ocean	Shipboard Scientific Party (1985)
Leg 146 Sites 892 & 889*	Ocean Drilling Program	Cascadia Margin, Pacific Ocean	Shipboard Scientific Party (1994)
Leg 164 Sites 994, 995* & 997	Ocean Drilling Program	Blake Ridge, Atlantic Ocean	Shipboard Scientific Party (1996)

*Drill-site with only inferred gas hydrate occurrence, no gas hydrates recovered

1.4.1 North Slope of Alaska Gas-Hydrate Occurrence

The only confirmed natural gas-hydrate occurrence on the North Slope of Alaska

was obtained in 1972, when ARCO and EXXON successfully recovered a core

containing this substance (reviewed by Collett, 1993b). This sample was from a depth of

≈657 m in the Northwest Eileen State-2 well, located within the Prudhoe Bay Oil Field

(cored interval 656-659 m). The well was drilled with cool drilling muds in an attempt to

reduce thawing of the permafrost and decomposition of the in-situ gas hydrates. The core

containing the sample of gas hydrate was recovered in a pressurized core barrel. The

presence of gas in an hydrated state was confirmed by a pressure test (Figure 1.4) while

the core was maintained in the core barrel at a temperature of about 1.0 °C. As the gas

was withdrawn from the core barrel, the pressure dropped, but it subsequently rose

toward the theoretical gas-hydrate equilibrium pressure when the system was closed. If

the core had contained only free-gas, the pressure in the barrel would have decreased

linearly as gas was withdrawn and the pressure would not have increased when the

system was closed. This gas hydrate pressure response has been further discussed by

Hunt (1979, p. 167).

The confirmed gas-hydrate occurrence in the Northwest Eileen State-2 well

provides an ideal starting point for the development of gas hydrate well-log evaluation

techniques. The responses of the commonly available well logs within the confirmed

gas-hydrate interval (Unit C; which is further discussed in Section 5.5 of this thesis) of
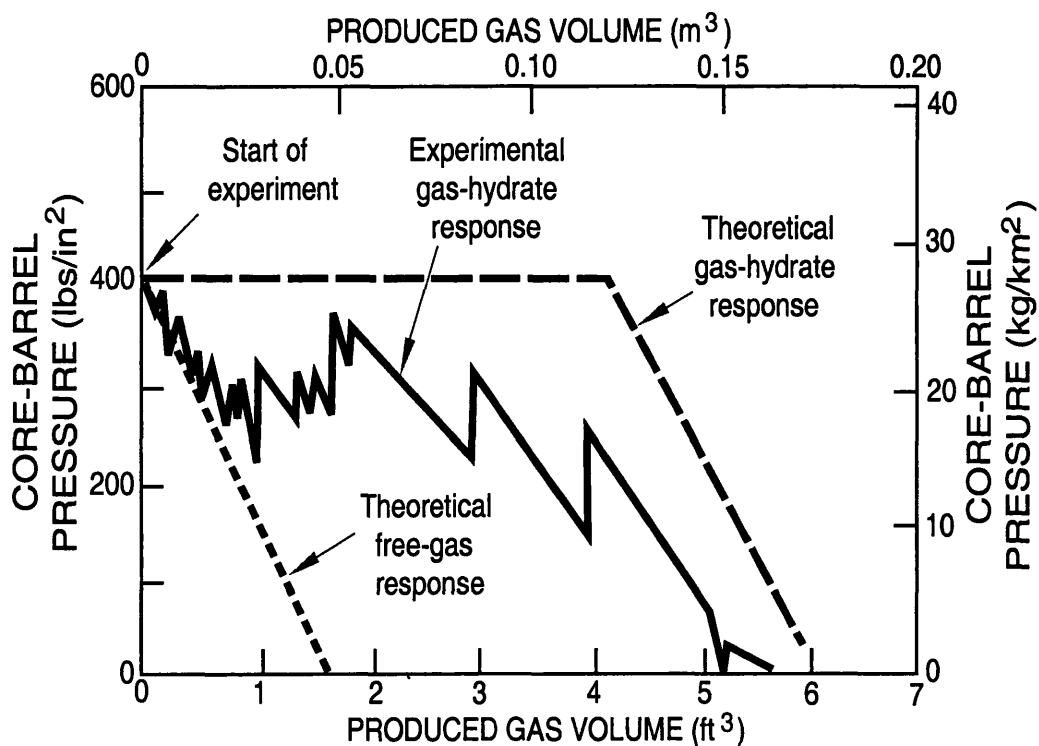
Figure 1.4 Graph of theoretical response and experimental results of the pressure-core experiment on a core (Core-4) from the Northwest Eileen State-2 well that proved the presence of gas hydrate (modified from Collett, 1993b).

the Northwest Eileen State-2 well (Figure 1.5) are summarized below (modified from Collett, 1983).

1. Mud Log: On a mud log there is a pronounced gas kick or gas flow associated with a gas hydrate due to hydrate decomposition during drilling.

2. Electrical Resistivity (Dual Induction) Log: There is a relatively high electrical-resistivity deflection on this log in a gas-hydrate zone, in comparison to that in a water-saturated horizon. If a rock were gas-hydrate saturated within the ice-bearing permafrost sequence, the resistivity response on the electrical log for the gas hydrate would not be significantly different from that in the surrounding ice-bearing permafrost. Below the base of the ice-bearing permafrost, however, the high-resistivity deflection associated with gas hydrate is distinct from the surrounding non-ice-bearing zones.

3. Spontaneous Potential (SP): There is a relatively lower (less negative) spontaneous-potential deflection in a gas-hydrate-bearing zone when compared to that associated with a free-gas zone. The spontaneous-potential log-curve for a gas-hydrate would be similar to that of a ice-bearing sequence.

4. Caliper Log: The caliper log in a hydrate usually indicates an oversized well bore due to spalling associated with hydrate decomposition. The caliper also indicates an enlarged borehole within an ice-bearing sequence.

5. Acoustic Transit-Time Log: Within a gas hydrate there is a decrease in acoustic transit-time in comparison to a unit saturated with either water or free-gas. Because the acoustic transit-time of ice is similar to that of gas hydrate, the
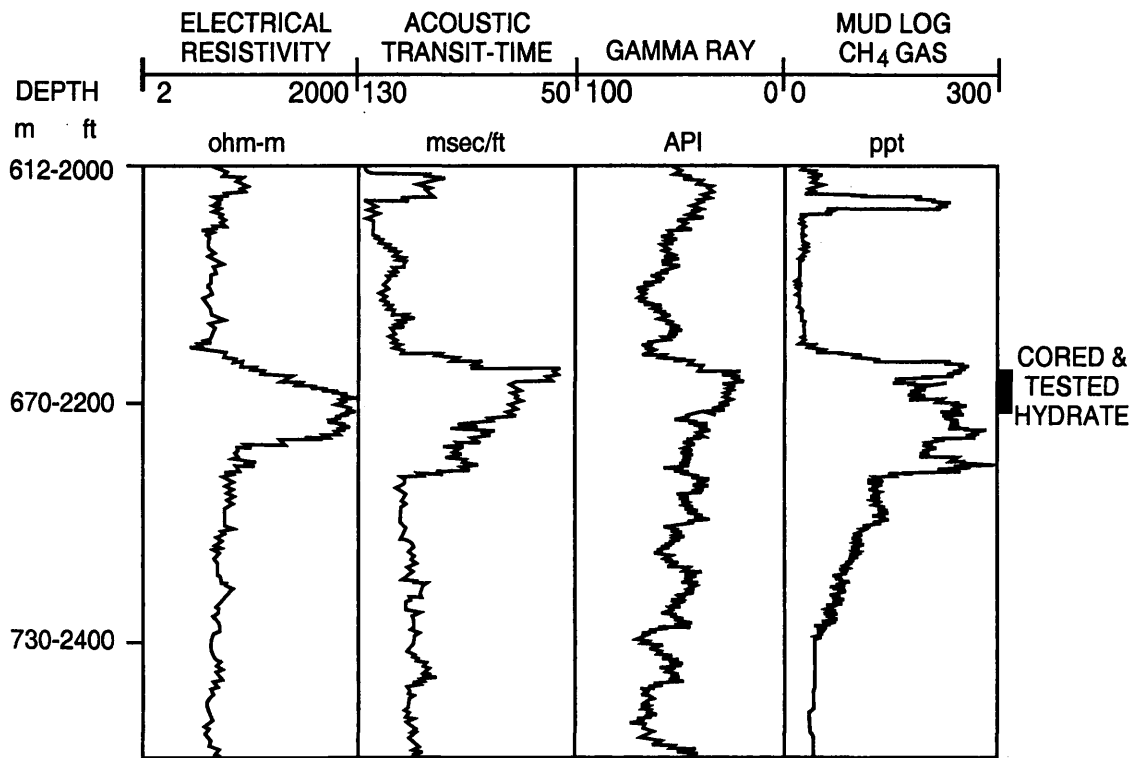
Figure 1.5 Open-hole well logs and methane (CH4) mud-log from the cored and production tested gas hydrate interval (Unit C) in the Northwest Eileen State-2 well (modified from Collett, 1993b).

acoustic log cannot be used to identify gas hydrates within the ice-bearing permafrost sequence.

6. Neutron Porosity: In a gas hydrate there is a slight increase in the neutron porosity; this response contrasts with the apparent reduction in neutron porosity in a free-gas zone.

7. Density Log: Within a gas hydrate there is a slight decrease in density in comparison to a unit saturated with water. Because the density of ice is similar to that of gas hydrate, the density log cannot be used to identify a gas hydrate within ice-bearing permafrost.

8. Drilling Rate: In a gas hydrate the relative drilling rate decreases, due to the solid nature of the gas hydrate. There is a similar drilling rate response within ice-bearing horizons.

In most gas hydrate studies only two well-logging devices are consistently used to identify potential gas hydrates: they are the electrical resistivity and acoustic transit-time logs. The electrical resistivity and acoustic logs behave similarly within an unit either saturated with gas hydrate or ice. Hence, the occurrence of gas shows on the mud log produced from decomposing hydrate often provides the only means of conclusively differentiating a gas hydrate from ice.

1.4.2 DSDP Site 570 Gas-Hydrate Occurrence

In 1982, while conducting research coring operations on Leg 84 of the Deep Sea Drilling Project (DSDP) a 1.05-m-long core of massive gas hydrate was recovered at Site

570 in the Middle-America Trench off the Pacific coast of Guatemala. The cored gas

hydrate sample was determined to be from the interval between 247.4 and 251.4 m sub-

bottom depth. Well-log surveys indicated that the actual thickness of the massive gas-

hydrate occurrence was about 3 to 4 m (Kvenvolden and McDonald, 1985). Site 570 was

drilled in 1,718 m of water and the well was completed at a sub-bottom depth of 402 m,

which is 300 m above the predicted lower boundary of the gas hydrate stability field.

Other cores from above and below the massive gas hydrate also showed evidence of gas

hydrates. Summarized in Table 1.4 are the shipboard scientists' descriptions of the Site

570 gas-hydrate occurrences (Kvenvolden and McDonald, 1985).

A suite of ten downhole logs were obtained at Site 570 which define the massive

gas hydrate interval (Figure 1.6) (Mathews, 1986). The massive gas hydrate was

characterized by high electrical resistivities ($\approx$155 ohm-m), rapid acoustic transit-time

velocities ($\approx$3.6 km/s), high neutron porosities ($\approx$67%), and low apparent densities ($\approx$1.05

g/cm^3). Among the available suite of logs, the responses of the electrical resistivity and

acoustic transit-time logs are most useful in identifying the in-situ gas hydrates

(Mathews, 1986). Table 1.5 lists the log data from Site 570 and whether or not it defines

any of the gas hydrates encountered (modified from Mathews, 1986).

1.4.3 Existing Quantitative Gas Hydrate Well-log Evaluation Techniques

The neutron porosity log measures the attenuation in the passage of neutrons as

emitted by the logging tool into the rock sequence. This response is a measure of mostly

the hydrogen content of the formation. As discussed in Collett et al. (1984), it is possible

Table 1.4 Description of the gas-hydrate occurrences in the DSDP Leg 84, Site 570 corehole (modified from Kvenvolden and McDonald, 1985).

Site and core number	Subbottom depth (mbsf)	Description
570-21-1	192	Ash lamina with gas hydrate at top of core
570-26-5	246	Gas hydrate in fractures of mudstone
570-27-1	249	Massive gas hydrate, 1.05-m-thick
570-28-1	259-268	Gas hydrate in fractures of mudstone
570-29-3	273	Gas hydrate in fractures of mudstone
570-32-4	303	Gas hydrate in a ash volcanic lamina
570-36-1	338	Gas hydrate in a sand lens
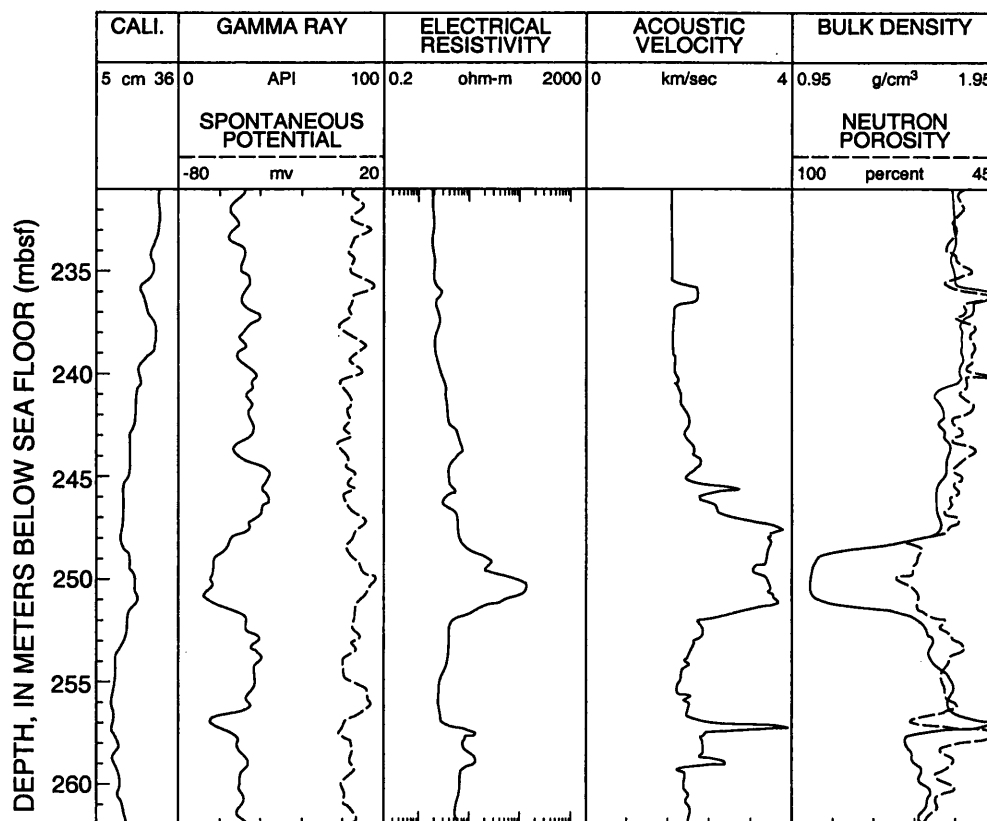
Figure 1.6 Downhole logs from the cored massive gas hydrate (247.4-251.4 mbsf) interval in the DSDP Site 570 corehole.

Table 1.5 Gas-hydrate well-log responses in the DSDP Leg 84, Site 570 corehole (modified from Mathews, 1986).

Well log	Massive gas-hydrate zone 247.4-251.4 (mbsf)
Acoustic transit-time (SVEL)	Responded to the gas hydrates
Density (RHOB)	Responded to the gas hydrates
Dual induction (LLS, shallow)	Responded to the gas hydrates
Dual induction (LLD, deep)	Responded to the gas hydrates
Neutron porosity (NPHI)	Responded to the gas hydrates
Spontaneous potential (SP)	Responded to the gas hydrates
Caliper (CALI)	Responded to the gas hydrates
Gamma ray (GR)	No response to gas hydrates

to calculate the amount of hydrogen present in a given pore-volume of the following

reservoir constituents: water, pure methane, ice, Structure-I and Structure-II gas hydrates

(Table 1.6). The neutron-porosity-log response to increasing hydrogen content is an

apparent increase in neutron porosity. Conversely a decrease in hydrogen content results

in an apparent reduction in the recorded neutron porosity. From this relation and by

utilizing the calculated hydrogen volumes in Table 1.6, it is possible to formulate the

following relation: assuming constant porosity, a rock saturated with a Structure-II gas

hydrate would more effectively slow the log-emitted neutron than a rock saturated with

only water or methane. Thus, a Structure-II gas hydrate would be characterized by

relatively high apparent neutron porosities, and a free-gas saturated unit would exhibit

low apparent porosities. By making several assumptions about borehole conditions and

taking into account the hydrogen pore-volume content for the different constituents listed

in Table 1.6, it is possible to correct the neutron porosity data within a gas-hydrate-

bearing interval. "Standard" neutron-porosity well-log evaluation procedures assume that

the pore-volume of a rock unit is occupied by only water. However, if hydrocarbon such

as free-methane-gas is present within the rock unit, the log-derived neutron porosities

require correction. These corrections are often accomplished by using empirically-

derived correction factors. It should be possible to develop a neutron porosity correction

factor for a gas-hydrate-bearing unit. By assuming constant porosity between two units,

one saturated with Structure-I gas hydrate and the second with water, it is possible to

determine the following ratio:

Table 1.6 Comparison of hydrogen content of
potential pore-filling constituents (modified from
Collett et al., 1984 and Serra, 1984).

Reservoir constituent	Amount of hydrogen (atoms of hydrogen/cm^3)
Methane gas, CH_4	0.01076×10^{22}
Natural gas, (mean)	0.011×10^{22}
Pure water, H_2O density = 1.00 g/cm^3	6.7×10^{22}
Ice, H_2O density = 0.72 g/cm^3	4.8×10^{22}
Gas hydrate - Structure I*	7.18×10^{22}
Gas hydrate - Structure II*	7.55×10^{22}

*Chemical formula and density from Makogon (1981)

$$\frac{\text{Amount of hydrogen in 1 cm}^3 \text{ of water}}{\text{Amount of hydrogen in 1 cm}^3 \text{ of gas hydrate}} =$$

$$\frac{6.7 \times 10^{22} \text{ (atoms of hydrogen/cm}^3)}{7.18 \times 10^{22} \text{ (atoms of hydrogen/cm}^3)} = 0.93$$

(1.1)

This ratio can be used as a neutron-porosity log correction factor within a gas-hydrate-saturated reservoir in order to obtain accurate porosities.

As noted earlier, acoustic transit-time is shorter within a gas hydrate than in either free-gas or water. The acoustic log measures the time required for an acoustic wave to travel through the formation adjacent to the wellbore. The travel-time can be related to porosity when the lithology is known. To accurately calculate porosities, however, the interval acoustic travel-time of the pore-fluids must be known. Compressional- and shear-wave velocities of a formation are not only properties of the matrix and pore-fluid velocities but are also affected by the temperature of the formation and the salinity of the pore-fluids (Pandit and King, 1979). In "standard" formation evaluation procedures, the empirical Wyllie equation is used to relate travel time and porosity. The Wyllie equation does not account for the effect of free-gas on the acoustic device, however, an empirical correction factor for the free-gas effect has been calculated. Similarly, the effect of gas hydrate on an acoustic velocity device can be determined, and an empirical correction factor can be calculated.

In order to develop a gas hydrate correction factor for acoustic measurements, it is necessary to calculate an acoustic transit-time relation between a rock saturated with

water and a second rock saturated with gas hydrate in which all other parameters are constant or controlled. In order to determine the acoustic velocity of a rock saturated with gas hydrate, the theoretical velocity constants for ice as determined by Pandit and King (1979) have been used in conjunction with the work of Whiffen et al. (1982). With the aid of Brillouin spectroscopy, Whiffen et al. (1982) were able to determine that the acoustic velocity of a gas hydrate (Structure-I) is approximately 0.88 that of ice. By taking this experimentally-derived relation between the acoustic velocity of gas hydrate and ice, along with the work of Pandit and King (1979), it is possible to calculate an acoustic velocity relation between a water-saturated unit and a gas-hydrate-saturated unit. In Collett et al. (1984), a series of acoustic velocities was calculated for a rock unit (Boise Sandstone) that was assumed to be saturated with each of the following pore-filling constituents: gas hydrate (Structure-I), water, and ice (Table 1.7). As in the case of the neutron porosity correction factor determined earlier, it is possible to calculate a correction factor for the acoustic transit-time measurements in a gas hydrate. If constant porosity is assumed, then the following relation can be written for the acoustic velocity characteristics of Structure-I gas hydrate and water within a given pore-volume:

$$\frac{\text{Velocity of Boise Sandstone saturated with gas hydrate}}{\text{Velocity of Boise Sandstone saturated with water}} =$$

$$\frac{3,400 \text{ m/sec}}{2,871 \text{ m/sec}} = 1.18$$

(1.2)

Table 1.7 Acoustic velocity of a Boise sandstone core
when occupied by different pore-filling constituents
(modified from Collett et al., 1984).

Reservoir constituent	Acoustic velocity of a Boise sandstone core (km/sec)
Gas hydrate -5°C, salinity 0.6M	3.400
Water salinity 0.6M	2.871
Ice (permafrost) -5°C, salinity 0.6M	3.864

In order to correct the porosity calculations made from the acoustic transit-time device in a gas hydrate, the ratio of 1.18 can be utilized as an correction factor. In Mathews (1986), the acoustic transit-time log was also used to calculate porosities within the gas-hydrate-bearing intervals in the Northwest Eileen State-2 well. Mathews (1986) obtained a gas hydrate acoustic transit-time correction factor of 1.49 by comparing the log values of a non-gas-hydrate-bearing interval to the log values in the cored gas hydrate interval.

In Collett et al. (1984), it was assumed that a Pickett crossplot, which is commonly used to determine oil saturations in oil-water systems, could be used to determine the degree of gas-hydrate saturation in a gas-hydrate- and water-bearing rock unit. A Pickett crossplot is based on the following logic: if the pore-space of a rock unit is 100% saturated with water, the deep resistivity device will record the resistivity of the 100% water-saturated rock unit (R_o). The water-saturated unit is considered a relative baseline from which hydrocarbon saturations can be determined. If the salinity of the pore-fluids is known to be constant within the units being examined, the recorded resistivity measurements can be plotted on a Pickett crossplot, and any deviation from the known 100% water-saturated resistivity measurement would indicate the presence of hydrocarbons. Similarly, the recorded resistivity values for a gas-hydrate-saturated unit would vary substantially from a known water-saturated unit, and this difference can be used to calculate gas-hydrate saturation.

A series of Pickett crossplots were used to calculate gas-hydrate saturations in four of the six delineated gas-hydrate occurrences overlying the Prudhoe Bay and Kuparuk River oil fields on the North Slope of Alaska (Collett et al., 1988). In the composite Pickett crossplot in Figure 1.7, the corrected neutron-porosity and deep-resistivity log values have been plotted for twenty-seven of the individual gas-hydrate occurrences. In Figure 1.7, the resistivity of the formation waters (R_w) was determined to be 0.4 ohm-m (pore-fluid salinity of about 9 to 15 ppt), and the gas-hydrate saturations (S_h) range from 70 to 95 percent [water saturation (S_w) is equal to (1.0-S_h)]. The accuracy of this procedure to determine gas-hydrate saturation is not known. No laboratory or core studies have been conducted to test the usefulness of Pickett crossplots relative to gas-hydrate research. The Pickett crossplot technique is susceptible to erroneous assumptions and interpretations. For example, the incorrect identification of a potential gas-hydrate occurrence or the wrong selection of a formation water resistivity (R_w) can alter the final saturation calculations. In addition, crossplot methods used to determine gas-hydrate saturation can only be used for a gas-hydrate interval below the base of the ice-bearing permafrost. Because of the relatively high electrical resistivity of ice within the permafrost sequence, the comparison of a gas-hydrate saturated unit to an ice-saturated unit will result in the calculation of erroneous gas-hydrate saturations. In using the crossplot-method to determine gas-hydrate saturation, it is assumed that the non-gas-hydrate saturated pore-space within a gas hydrate is occupied by free-water and not ice.
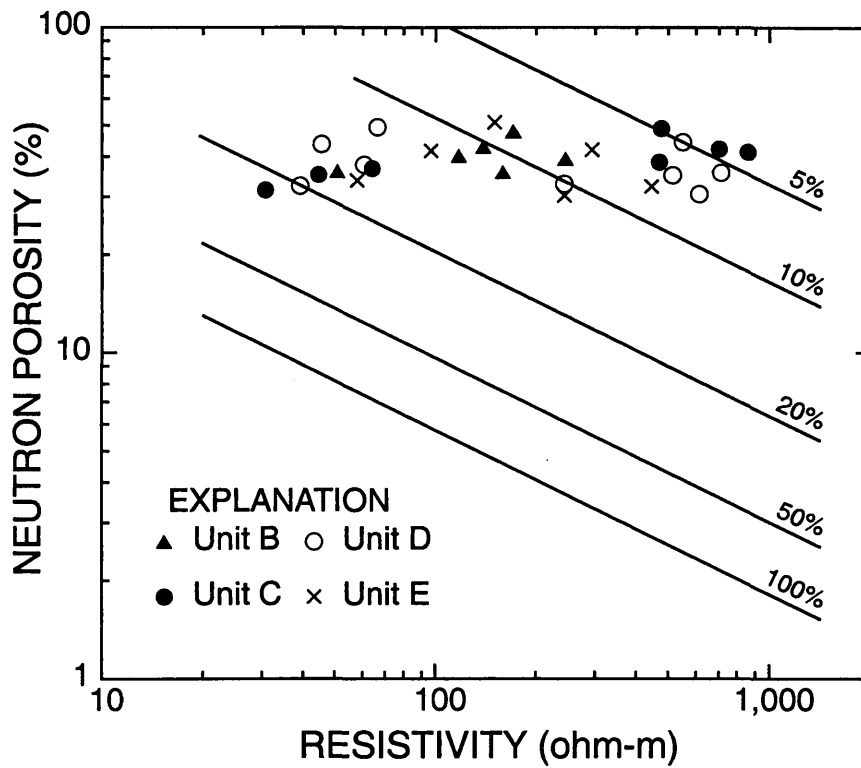
Figure 1.7 Composite Pickett crossplot used to calculate gas-hydrate saturations (shown as water saturations, S_W) in four gas-hydrate-bearing stratigraphic units (Units B, C, D, and E) in northern Alaska. This Pickett crossplot assumes a formation water resistivity (R_W) of 0.4 ohm-m (modified from Collett, 1993b).

Mathews (1986) also used the Pickett crossplot technique to estimate gas-hydrate saturations in the Northwest Eileen State-2 well. In Mathews (1986), the corrected acoustic transit-time data was used as the source of porosity data for the Pickett crossplot. In Collett et al. (1983), corrected neutron porosities were used to construct the Pickett crossplots. It appears, however, that both approaches yield similar gas-hydrate saturations.

Mathews (1986) also estimated the amount of methane gas within the gas-hydrate occurrences of the Northwest Eileen State-2 and Site 570 wells by using a well-log normalization technique. At Site 570, the resistivity well log plateaus in the massive gas hydrate zone, which was interpreted to indicate a 100% gas-hydrate saturated interval. Mathews (1986) normalized the resistivity data and assumed that a value of 1.0 indicates a 100% pure gas hydrate (Figure 1.8). Therefore, any deviation from 1.0 indicates that gas hydrate has been replaced by rock matrix material and formation water. In the Northwest Eileen State-2 well, Mathews (1986) normalized the deep-resistivity log in the cored gas hydrate interval (Figure 1.9). It was assumed that the 2,000 ohm-m limit indicates a reservoir rock sequence that is 100% saturated with gas hydrate. The value of 1.0 on the plot in Figure 1.9 represents 100% gas-hydrate saturation. As in Site 570, any deviation from 1.0 indicates that the gas hydrate has been replaced by rock material and/or formation water. Mathews (1986) used the calculated gas-hydrate saturations, derived from the normalization technique and the Pickett crossplot, to estimate the amount of methane gas in the cored gas hydrate interval (portion of Unit C as discussed in Section 5.5 of this thesis) of the Northwest Eileen State-2 well. Mathews' (1986)
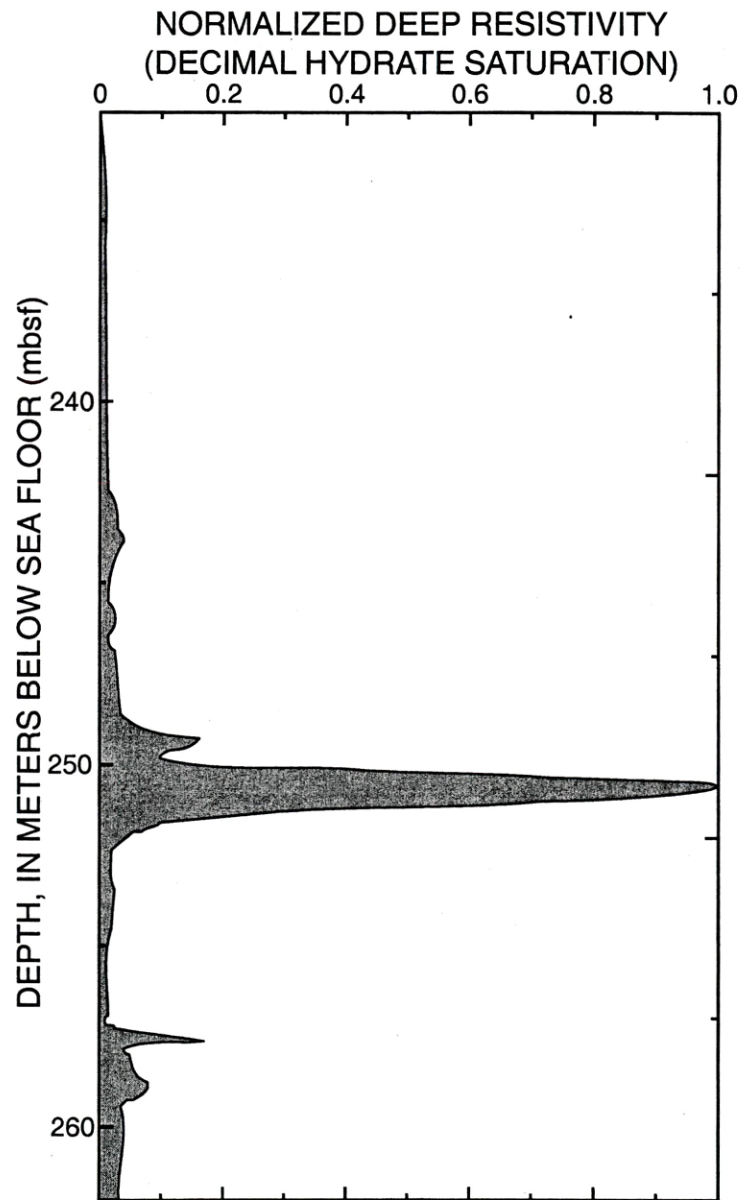
Figure 1.8 Normalized deep electrical resistivity data (dual induction log) from the cored massive gas hydrate interval (247.4-251.4 mbsf) in the DSDP Site 570 corehole (modified from Mathews, 1986).
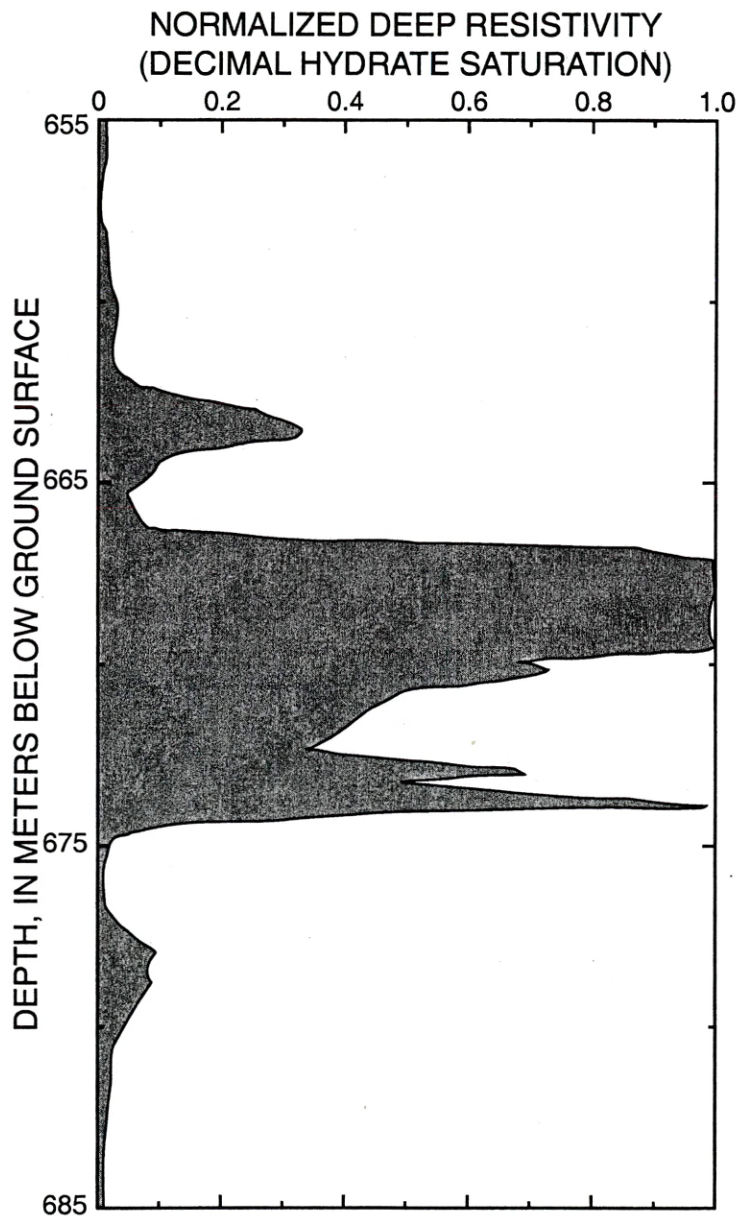
Figure 1.9 Normalized deep electrical resistivity data (dual induction log) from the cored and production tested gas hydrate interval (Unit C) in the Northwest Eileen State-2 well (modified from Mathews, 1986).

normalized resistivity technique yielded an estimate of 412,400,000 cubic meters of gas per square kilometer and the Pickett crossplot technique yielded an estimate of 191,600,000 cubic meters of gas per square kilometer. Mathews (1986), however, did not take into account that the induction-log measurements of electrical resistivity in the Northwest Eileen State-2 well probably underestimated the resistivity of the gas-hydrate-bearing units. It is likely the resistivity of the zones in which the induction log "plateaued" are actually much greater than the measured values. Thus, the resistivity-log normalization technique proposed by Mathews (1986) needs to be approached with caution. The limitations of induction-log measurements are further discussed in Chapter 3 of this thesis.

1.5 Research Approach

Most of the existing gas hydrate log evaluation techniques are qualitative in nature and have been developed by the extrapolation of "standard" oil industry procedures. Relatively little work has been done to check the usefulness of these "standard"-log evaluation techniques in gas hydrate systems. Most certainly more work is required to characterize the nature of well-log responses to the presence of gas hydrates.

In this study, the first comprehensive set of quantitative gas hydrate well-log evaluation techniques have been developed, tested, and used to ascertain critical gas hydrate reservoir data. Since gas hydrates are characterized by unique chemical compositions and distinct electrical resistivity and acoustic physical properties, it is

possible to obtain gas-hydrate reservoir porosity and hydrocarbon saturation data by characterizing the electrical resistivity and acoustic physical properties of gas hydrates and assessing the chemical composition of the pore-filling constituents within a gas-hydrate-bearing reservoir. The well-logging devices that show the greatest promise of yielding gas hydrate reservoir data, including porosity, are the density and neutron porosity logs (Table 1.8), which primarily respond to the chemical composition of the pore-filling constituents. The electrical resistivity, acoustic transit-time, and neutron spectroscopy well logs (Table 1.8) can yield highly accurate gas-hydrate saturation information. It is also possible that modern nuclear magnetic resonance well-logging tools may yield both reservoir porosity and gas-hydrate saturation data (Table 1.8). The research conducted with these devices in this study can be generally divided into three categories: (1) gas-hydrate well-log response modeling, (2) laboratory quantification of gas-hydrate well-log responses, and (3) field data interpretation.

As previously stated, the primary objective of this study was to develop quantitative gas hydrate well-log evaluation techniques, which will permit the calculation of reservoir porosities and the degree of gas-hydrate saturation in gas-hydrate-bearing rock units. Well logs can also be used to identify in-situ gas-hydrate occurrences and to distinguish gas hydrate from permafrost ice, and they can be used to characterize other critical gas hydrate reservoir parameters including determining the level of homogeneity in gas hydrate distribution and the mode of occurrence within the reservoir at the pore scale, and provide field calibration for improved seismic techniques used for resource

Table 1.8 Categories of well logs which yield gas hydrate reservoir data. The operational parameters controlling the well-log responses are given, along with potential gas hydrate applications.

Well log	Gas hydrate application	Well log measurement
Density	Reservoir porosity	Measures electron density of the formation
Neutron porosity	Reservoir porosity	Measures (mostly) the hydrogen content of the formation
Electrical resistivity	Gas hydrate saturation Reservoir porosity	Measures both the electrical resistivity and conductivity of the formation
Acoustic transit-time	Gas hydrate saturation	Measures the attenuation of sound in the formation
Neutron spectroscopy	Gas hydrate saturation	Measures the amount of carbon, oxygen, hydrogen, silica, calcium, and other reservoir matrix and pore-filling constituents
Nuclear magnetic resonance	Gas hydrate saturation Reservoir porosity	Analyzes the chemical bonding characteristics of hydrogen atoms

assessment purposes. Listed below are the primary research objectives for each part of this study.

1. Well-Log Response Modeling

- Use the results of published laboratory data and theoretical studies to assess the utility of the gamma-gamma density log as a porosity device in gas-hydrate-bearing reservoirs.

- Determine the chemical composition and calculate the neutron macroscopic cross section for various reservoir constituents including gas hydrate, ice, water, gas, and numerous rock matrixes.

- Adapt existing Monte Carlo neutron transport simulation computer programs and Discrete Ordinate Transport computer programs for use with gas hydrate. Utilize the modified neutron transport computer programs to calculate nuclear measurement parameters for gas hydrates.

- Use the results of the neutron transport computer modeling efforts to assess the utility of the neutron porosity log as a porosity device in gas-hydrate-bearing reservoirs.

- Use the results of published laboratory data and theoretical studies to assess the utility of the electrical resistivity log as a porosity device in gas-hydrate-bearing reservoirs.

- Combine results from "conventional" hydrocarbon well-log studies with information from studies of permafrost and gas hydrates to develop electrical resistivity methods of assessing gas-hydrate saturations.

• Evaluate and modify for the well-logging environment existing acoustic seismic techniques for assessing gas-hydrate saturations.

• Develop and test neutron spectroscopy methods for assessing gas-hydrate saturations.

• Use the results of published laboratory studies to mathematically model the nuclear magnetic resonance well-log response (T_1, T_2, FID, FFI) to gas hydrates.

2. Laboratory Quantification

• Construct a series of "synthetic" gas hydrate samples and gas-hydrate-bearing rock-cores to be used for well-log investigation studies.

• Conduct laboratory experiments on "synthetic" gas hydrate samples and gas-hydrate-bearing rock-cores to determine the compressional-wave acoustic properties of bulk gas hydrate samples and gas-hydrate-bearing cores.

• Combine the results of the laboratory and modeling efforts to develop and test acoustic well-log evaluation techniques with which to calculate gas-hydrate saturations.

3. Field Data Investigation

• Test and utilize the quantitative gas hydrate well-log evaluation techniques developed in the response modeling and laboratory testing phases of this study.

• Calculate reservoir porosities and the degree of gas-hydrate saturation within the known gas-hydrate occurrences (1) on the Blake Ridge along the southeastern continental margin of the United States, (2) along the Cascadia continental margin off the Pacific coast of Canada, (3) near the Middle-America Trench off the

Pacific coast of Guatemala, (4) on the North Slope of Alaska, and (5) in the

Mackenzie River Delta of northern Canada.

CHAPTER 2

NATURE OF GAS-HYDRATE OCCURRENCES --

RELATIVE TO WELL-LOGGING APPLICATIONS

2.1 Background Information

Most well-log calculations assume that simple mixing rules can be applied to evaluate reservoir conditions; however, little is know about the nature of gas hydrate reservoirs. Information about the nature and texture of gas-hydrate occurrences is needed to assess the response of well-logging devices to the presence of gas hydrate (Figure 2.1). The physical and chemical conditions that result in different forms (disseminated, nodular, layered, massive) and distributions (uniform or heterogeneous) of gas hydrates are not understood (reviewed by Sloan, 1998). The existing and proposed quantitative well-log evaluation techniques assume uniform distribution of gas hydrates as interstitial "deposits" or "cement". Under these conditions, gas-hydrate-bearing reservoirs can be evaluated using "standard" well-log evaluation techniques developed for a mixed multi-component rock-matrix, water, gas, ice, and/or gas hydrate systems. However, a massive gas hydrate such as that encountered at DSDP Site 570 (Mathews, 1986) would not be conducive to "standard" well-log interpretation procedures because of the non-pore-filling nature of the gas-hydrate occurrence. It is necessary, therefore, to systematically review descriptions of known gas-hydrate occurrences and evaluate existing gas hydrate

Disseminated Nodular Layered Massive Layered Nodular Disseminated
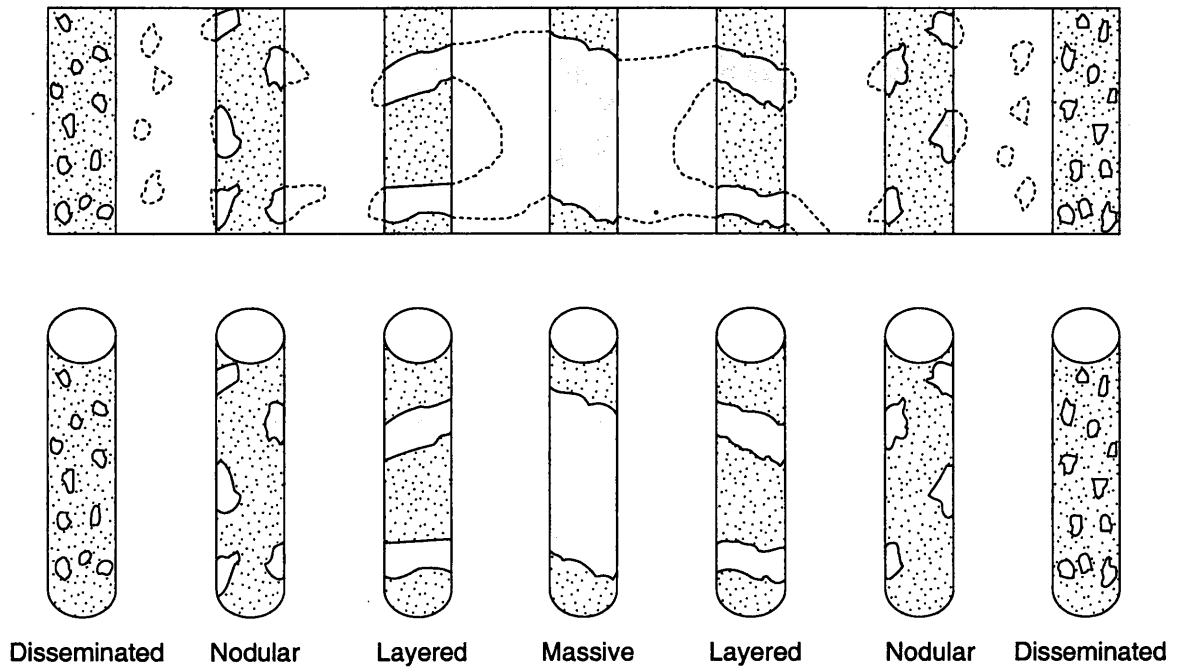
Figure 2.1 Various morphological forms of natural gas-hydrate occurrence (modified from Sloan, 1998).

reservoir models at both microscopic and macroscopic scales in order to assess the utility

of "standard" well-log evaluation techniques in gas-hydrate-bearing reservoirs. This

chapter begins with a review of published gas hydrate sample descriptions from both

marine and permafrost environments, which is followed by the first ever interpretive

discussion of the formation microscanner and microimager log data from coreholes on

the Blake Ridge and in the Mackenzie Delta. This chapter concludes with a review of

existing and proposed microscopic and macroscopic gas hydrate reservoir models.

2.2 Recovered Gas Hydrate Samples

This review of the nature of gas-hydrate occurrences has relied extensively on the

offshore gas hydrate sample database published by Booth et al. (1996). In this database,

Booth et al. (1996) systematically review and describe more than 90 recovered marine

gas hydrate samples from 15 different geologic regions. The individual descriptions of

the gas-hydrate occurrences include information on the number of recovered samples,

physiographic province, tectonic setting, geographic position, water depth, subbottom

depth of the recovered sample, geothermal gradient and temperature conditions, depth to

the base of the gas hydrate stability field, presence of a bottom simulating reflector,

thickness of the gas-hydrate-bearing sedimentary interval, thickness and size of pure gas

hydrate layers and grains, habit or mode of occurrence, host sediment lithologic

description, and the origin of the included gas. In general, most of the recovered gas

hydrate samples consist of individual grains or particles, which are often described as

inclusions or disseminated in the sedimentary section. Gas hydrates also occur as what

has been described as a cement, nodules, or as laminae and veins, which tend to be characterized by dimensions of a few centimeters or less. In several cases, thick pure gas hydrate layers measuring as much as 3- to 4-m-thick have been sampled (DSDP Site 570; Shipboard Scientific Party, 1985). In both marine and terrestrial permafrost environments, the thickness of identified gas-hydrate-bearing sedimentary sections varies from a few centimeters to as much as 30 m (Collett, 1993b; Booth et al., 1996). Most pure hydrate laminae and layers, however, are often characterized by thicknesses of millimeters to centimeters (Figure 2.2) (Booth et al., 1996; Dallimore and Collett, 1995). Booth et al. (1996) conclude that gas-hydrate-bearing sedimentary sections tend to be tens of centimeters to tens of meters thick, but thick zones of pure hydrate are relatively rare and only represent a minor constituent.

The Booth et al. (1996) data review, along with recently published gas hydrate sample descriptions from the Mackenzie Delta (Dallimore and Collett, 1995; Dallimore et al., 1999) and the Blake Ridge (ODP Leg 164, Shipboard Scientific Party, 1996), confirm that gas hydrates are usually disseminated within sediments and in most cases "standard" well-log evaluation techniques, with suitable gas-hydrate corrections, can be used to evaluate gas-hydrate-bearing reservoirs.

2.3 Well-Log Studies

A recent leg of the Ocean Drilling Program (ODP Leg 164; Shipboard Scientific Party, 1996) was designed to investigate the occurrence of gas hydrate in the sedimentary section beneath the Blake Ridge (ODP Leg 164 is further discussed in Chapter 5 of this
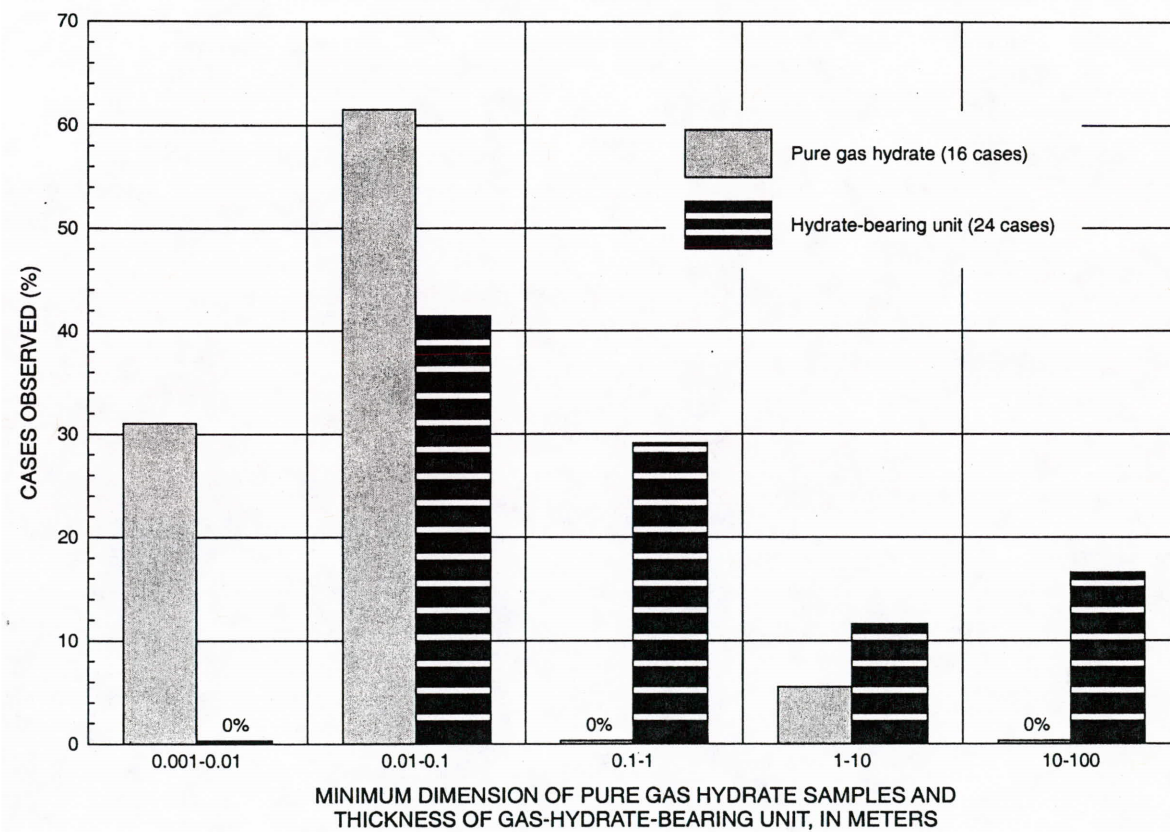
Figure 2.2 Dimensions of pure gas hydrate samples in comparison to the thickness of gas-hydrate-bearing sedimentary units (modified from Booth et al., 1996).

thesis). Sites 994, 995, and 997 were drilled on the Blake Ridge to refine our

understanding of the in-situ characteristics of natural gas hydrates. One of the logging

tools deployed on Leg 164 was Schlumberger's formation microscanner (FMS).

The FMS sonde produces high-resolution images of the microresistivity character

of the borehole wall that can be used for detailed sedimentological and structural

interpretations (Ekstrom et al., 1986). It is also possible that the FMS can be used to

make high-resolution electrical images of gas hydrates in the wellbore; thus yielding

information about the nature and texture of gas-hydrate occurrence in a rock interval.

The FMS has a deep depth of investigation (about 25 cm) which theoretically could allow

it to directly measure in-situ gas hydrates. The FMS makes continuous measurements of

detailed vertical and lateral variations, which allows the detection of very thin anomalous

features such as fractures, which have an opening on the order of a few to tens of microns

(Serra, 1989). The FMS tool comprises four orthogonal pads with 16 button electrodes

(6.7 mm in diameter) on each pad that are pressed against the borehole wall (Serra, 1989)

(Figure 2.3). The electrodes are arranged in two diagonally offset rows of eight

electrodes each. Each pad measures about 8 cm^2, and one pass of the tool covers

approximately 30 percent of a 25.72 cm borehole. Each individual electrode emits a

focused electrical current into the formation. The button electrode current intensity

measurements, which reflect microresistivity variations of the formation, are converted

into high resolution gray or color images of variable intensity. Black and white (darkest

or lightest color) indicate low and high microresistivity respectively. Processing corrects

the offset rows to one level, providing a vertical resolution of approximately 0.5 cm at a

**Formation
MicroScanner**

Natural gamma
spectrometry
tool (NGT)

• K, Th, U (%)

Formation Micro-
Scanner (FMS)

• Microresistivity
  images
• General purpose
  inclination
  tool (GPIT)

Lamont-Doherty
temperature logging
tool (LDEO-TLT)
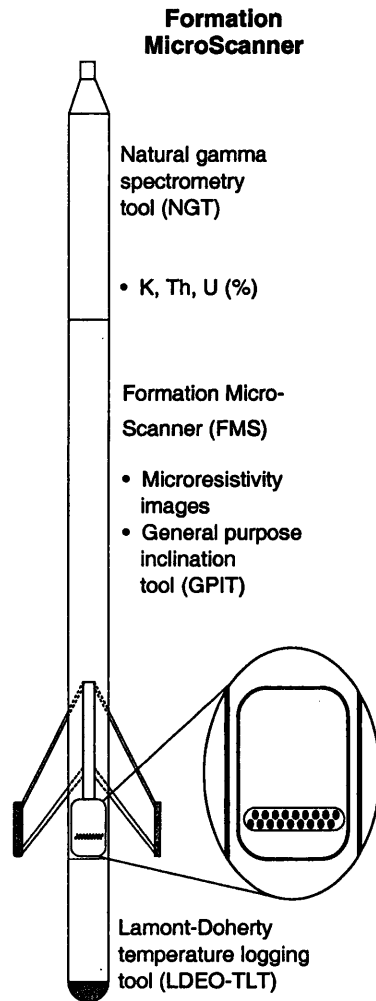
Figure 2.3 Schematic diagram of the Schlumberger formation microscanner
logging tool used during ODP Leg 164.

sampling interval of 0.25 cm (Serra, 1989). The FMS tool string contains a general

purpose inclinometry tool (GPIT) that orients the resistivity measurements through the

use of an accelerometer and magnetometer that respond to the declination and inclination

of the earth's magnetic field. The raw data are processed in real-time during logging to

transform individual microresistivity traces into oriented images. Detailed processing

and interpretation of the FMS resistivity images in combination with other log and core

data are usually carried out in post-field studies. The FMS has a number of limitations:

to produce high-quality images, the four pads of the FMS must be pressed firmly against

the borehole wall. Thus, in irregular or enlarged boreholes (>38 cm, maximum extension

of the FMS caliper arms), where pad contact is inconsistent, the FMS images can be

blurred. Another concern is related to the FMS depth of investigation (about 25 cm) into

the formation. Standard drilling practices often cause in-situ gas hydrates to disassociate

near the wellbore beyond a depth that the FMS can easily measure.

      To further assess the nature of in-situ gas-hydrate occurrences, FMS images from

a zone of inferred gas hydrates in ODP Hole 995B were reprocessed and examined. This

hole was selected because of the relatively high quality of the acquired FMS images and

because gas hydrates are inferred to occur in high concentrations at Site 995. Electrical

resistivity and acoustic transit-time well logs from Hole 995B indicate the presence of

gas hydrate in the depth interval between 193 and 450 mbsf on the Blake Ridge. The

deep measuring resistivity log also reveals two conspicuous high electrical resistivity

intervals between 218 and 242 mbsf (Figure 2.4), which have been interpreted to contain

about 10% bulk volume gas hydrate (gas hydrates at Site 995 are discussed in more detail
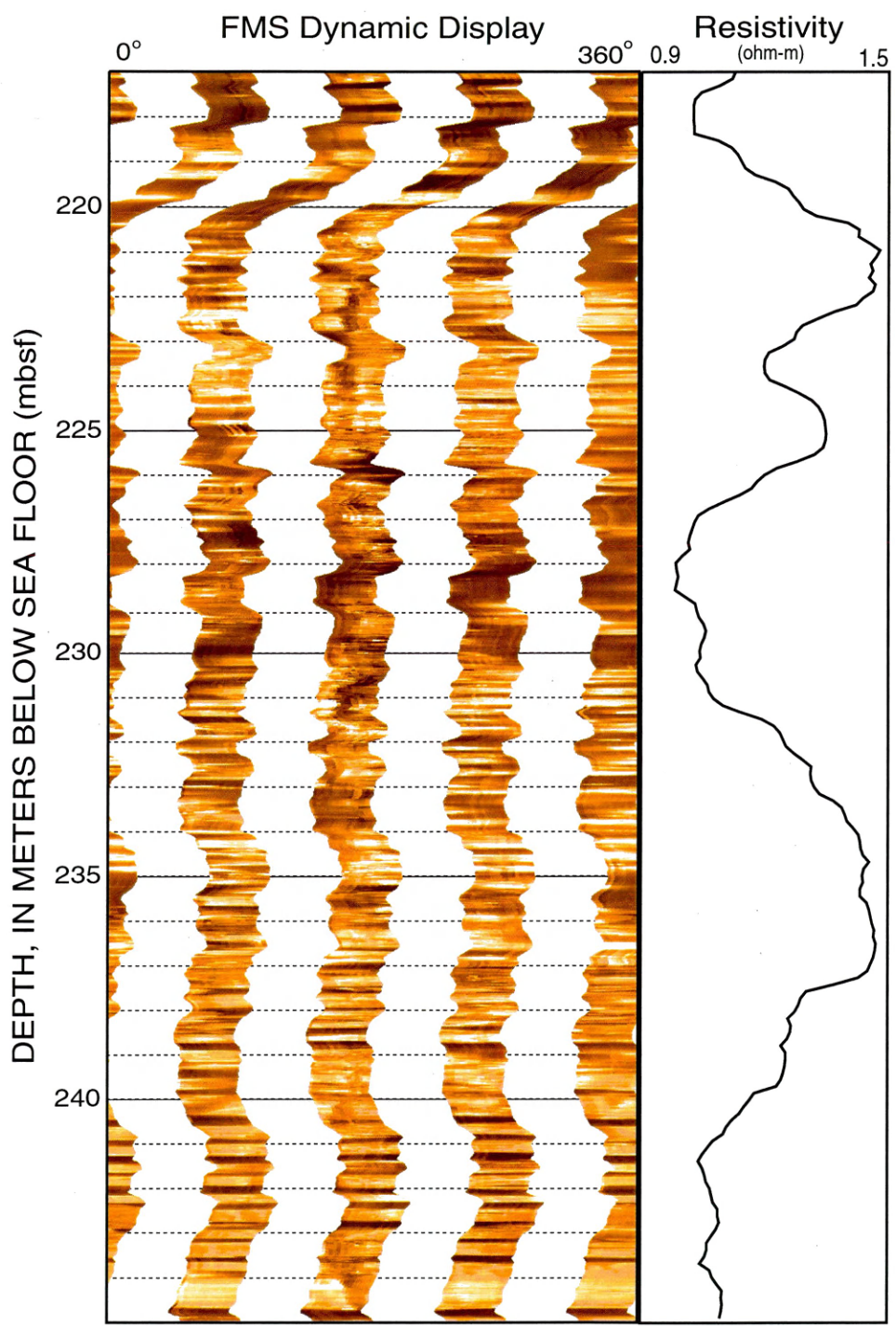
Figure 2.4 Formation microscanner log from the zone of downhole-log-inferred gas hydrate occurrence in ODP Hole 995B. Also shown is a log plot of the downhole electrical resistivity log in Hole 995B.

in Chapter 5 of this thesis). The FMS image in Figure 2.4 was generated with GeoFrame

software, which is a Schlumberger well-log data processing package. FMS log

processing followed "standard" ODP procedures as recommended by the Borehole

Research Group at the Lamont-Doherty Earth Observatory (Personnel Communication

Dr. Carlos Pirmez, Borehole Research Group, Lamont-Doherty Earth Observatory,

Palisades, New York), which included a series of special logging tool speed corrections.

The FMS image in Figure 2.4 was generated in "dynamic" mode, thus the measured

microresistivites within the depth interval displayed (217-245 mbsf) have been

normalized such that 64 individual shades of gray are depicted within a one-meter sliding

depth window. In Figure 2.4, the standard FMS four arm display is shown in the left-

hand-track, while the (deep) resistivity log from the dual-induction device ran in Hole

995B is plotted in the right-hand-track. The four arm FMS image is characterized by

light (high resistivity) to dark (low resistivity) bands, which in many cases can be traced

across the display in all four arms. These continuous bands likely represent distinct

stratigraphic units with thicknesses ranging between 10 and 50 cm. The fine-scale

bedding imaged in Figure 2.4, however, is not visually apparent in the recovered cores

(Shipboard Scientific Party, 1996). The apparent bedding in Figure 2.4 is likely caused

by small variations in sediment porosity (on the order of 1 and 2 %) and water content,

which could cause the small microresistivity variations detected by the FMS in Hole

995B. It is also possible that the light (high resistivity) stratigraphic beds may contain

gas hydrates, which are characterized by high electrical resistivities, that have been

directly measured by the FMS. It is also possible that the light stratigraphic beds contain

fresh water (which may exhibit high electrical resistivities) that was expelled from disassociating gas hydrates. Since the FMS does not yield calibrated data easily, there is no way to conclusively differentiate gas hydrates from other relatively high resistivity material. However, the FMS image in Figure 2.4 does suggest that the gas hydrate inferred to occur at Site 995 likely occur as disseminated pore-filling constituents throughout the zone depicted and that small porosity variations between relatively thin stratigraphic beds, measuring between 10-50 cm thick, have a direct affect on the amount of gas hydrate within the sedimentary section.

An additional observation that supports the interpretation that the FMS log has directly measured gas hydrates at Site 995 comes from the comparison of the four arm FMS image and deep resistivity log in Figure 2.4. In general, the FMS image within the two high (deep) resistivity zones (219-227 and 231-240 mbsf) are characterized by relatively lighter colors or higher FMS microresistivites which would collectively contribute to the high (deep) resistivity nature of the two anomalous zones that are interpreted to contain about 10% bulk volume gas hydrate.

Additional borehole microresistivity-log data from a gas hydrate research well drilled in the Mackenzie Delta of Canada was recently made publicly available (Dallimore et al., 1999). The JAPEX/JNOC/GSC Mallik 2L-38 gas hydrate research well was designed to investigate a known gas-hydrate occurrence in the Mallik area of the Mackenzie Delta of Canada. Downhole logs and the examination of recovered cores from the Mallik 2L-38 well confirm the occurrence of a thick gas-hydrate-bearing stratigraphic section at the Mallik drill-site within the subsurface depth interval between

889 and 1,101 m. The Schlumberger full-bore formation microimager (FMI) log ran in the Mallik 2L-38 well operates similar to the FMS device ran in ODP Hole 995B. The FMI, however, contains four additional electrode pads; thus in comparison, the FMI tool images more of the borehole (about 80% of a 20 cm diameter borehole).

To further assess the nature of in-situ gas-hydrate occurrences, the FMI log from the confirmed gas-hydrate-bearing interval in the Mallik well was also reprocessed and examined. The processing of the Mallik 2L-38 FMI data was conducted in a manner similar to the processing performed on the FMS log from Site 995. In addition to the normal "dynamic" processing, a "static" image was also generated (Figure 2.5). In a "static" FMI image the entire log is treated as one unit and the microresistivities are placed into 16 separate shades of gray. Therefore, intervals within the log that have the same shade of gray will have similar resistivity-log values, unlike the dynamic normalized presentation. In comparison to the "dynamic" processed FMI log display in Figure 2.5, the "static" processed FMI display is a less detailed image of the formation. Similar to the FMS image from Site 995, the FMI images from Mallik 2L-38 in Figure 2.5 are characterized by light (high resistivity) and dark (low resistivity) bands, which likely represent distinct stratigraphic units. When compared to the gas-hydrate saturation log (Mallik 2L-38 gas-hydrate saturation calculations are further discussed in Chapter 5 of this thesis) in the center track of the display in Figure 2.5, it is apparent that the light (high resistivity) stratigraphic intervals on the FMI displays correlate with stratigraphic units that are inferred to contain high concentrations (saturations) of gas hydrate. Analysis of cores from the high resistivity FMI-inferred gas-hydrate-bearing stratigraphic
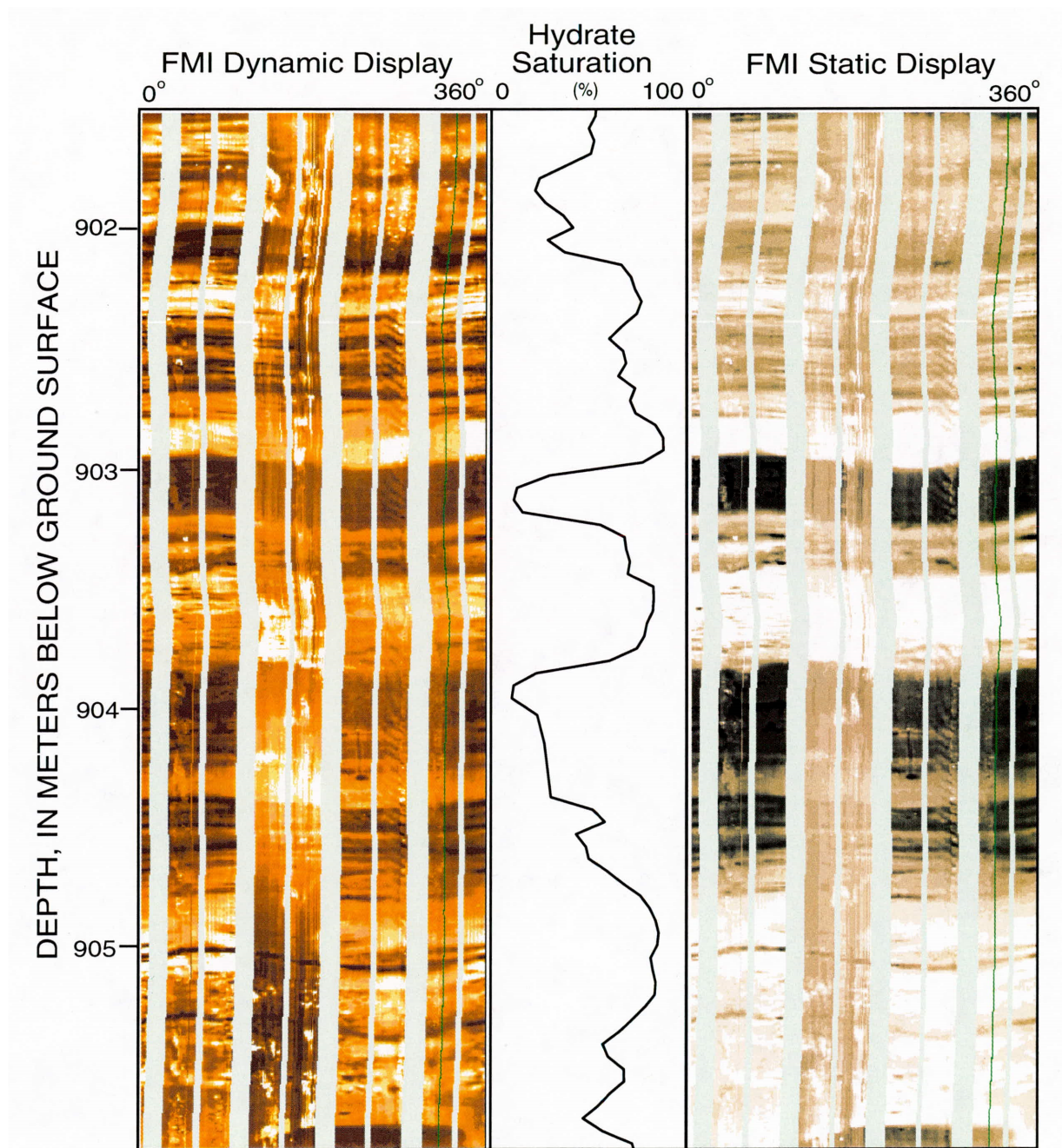
Figure 2.5 Formation microimager log from the zone of downhole-log-inferred gas-hydrate-bearing interval in the Mallik 2L-38 well. Also shown is a log plot of gas-hydrate saturations (percent of pore-space occupied by gas hydrate) calculated from the downhole electrical resistivity log in the Mallik 2L-38 well.

units in the Mallik 2L-38 well confirm the occurrence of disseminated pore-filling gas hydrate.

The FMS data in Figure 2.4 and the FMI data in Figure 2.5 indicate that the in-situ gas hydrates at these two drill-sites are mostly pore-filling constituents within thinly layered beds and that "standard" well-log evaluation techniques, with suitable gas hydrate corrections, can be used to assess the porosity and gas hydrate content of the sediments on the Blake Ridge and in the Mackenzie Delta.

2.4 Gas Hydrate Reservoir Models

Most discussions on the nature or texture of gas-hydrate occurrences deal with macroscopic issues (reviewed by Booth et al., 1996). However, information on the occurrence of gas hydrates at the pore-scale are needed since many gas hydrate reservoir physical properties are controlled by microscopic parameters (Dvorkin and Nur, 1993). Of particular concern is the acoustic nature of gas-hydrate-bearing sediments (Lee et al., 1993).

Dvorkin and Nur (1993) along with Ecker et al. (1996) have proposed and examined two "micromechanical" models that represent the two extreme cases of gas-hydrate occurrence at the pore-scale (Figure 2.6): (Model-1) gas hydrate cements grain contacts and increases the stiffness of the sediment; and (Model-2) gas hydrate is located away from grain contacts in the "bulk" pore-volume and it does not affect the stiffness of the sediment frame. Dvorkin and Nur (1993) experimentally demonstrated that even small amounts of intergranular cementation, such as proposed by gas hydrate Model-1,
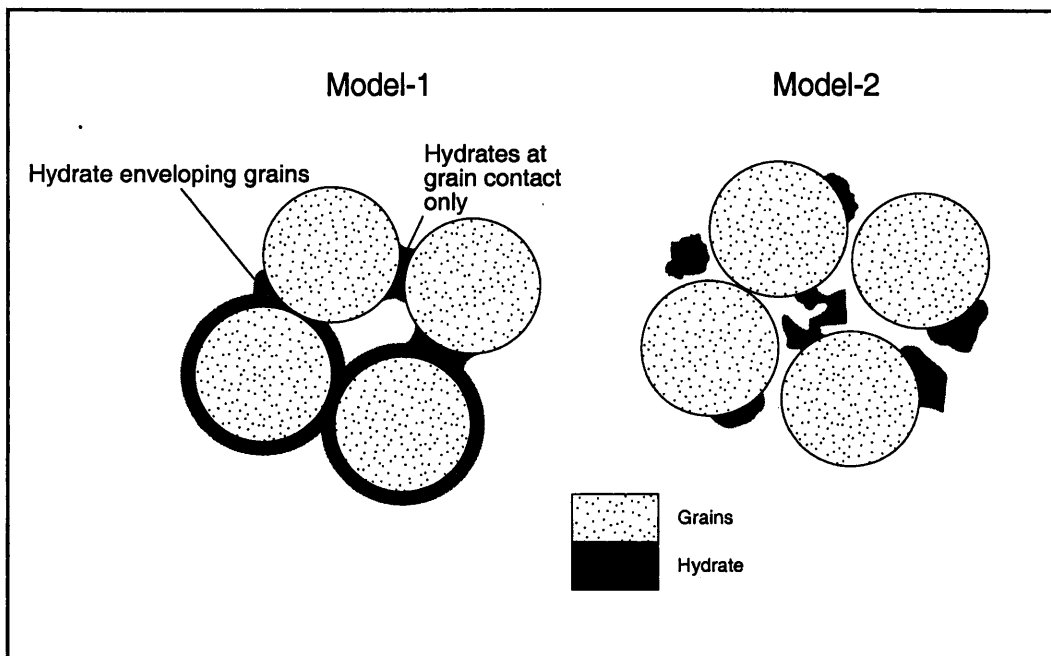
Figure 2.6 Two gas hydrate reservoir pore-models: (Model 1) gas hydrate cement grain contacts and envelops the grains; and (Model 2) gas hydrate is deposited away from grain contacts (modified from Ecker et al., 1996).

can dramatically increase the stiffness of granular material. Dvorkin and Nur (1993) used the intergranular gas hydrate cementation model (Model-1) to explain the occurrence of seismic bottom-simulating-reflectors (BSR's), which they attributed to a strong increase of the elastic moduli of the rock due to the occurrence of gas hydrates at the base of the gas hydrate stability zone. Ecker et al. (1996) used amplitude-versus-offset (AVO) analyses of the BSR on the Blake Ridge, however, to conclude that only reservoir Model-2 could qualitatively reproduce the observed BSR and that gas hydrates at the pore-scale are located away from the intergranular contacts, in large pores. Ecker et al. (1996) further concluded that the sediments above the BSR are uncemented and mechanically weak.

Recently reported analyses of downhole acoustic well-log data and vertical seismic profile data from the Mallik 2L-38 gas hydrate research well (Lee and Collett, 1999; Saki, 1999) support the micromechanical model of Ecker et al. (1996) with the occurrence of gas hydrate limited to the bulk pore-volume away from grain contacts (Model-2; Figure 2.6). For now, however, the micromechanical gas hydrate pore models of Dvorkin and Nur (1993) and Ecker et al. (1996) should be considered preliminary until additional laboratory and field observations are available. In Chapters 3, 4, and 5 of this thesis, the implications of various reservoir pore-models on the interpretation of well-log responses to gas hydrates will be discussed in greater detail.

As previously discussed at the beginning of this chapter, "standard" well-log evaluation techniques have been developed for relatively simple, mixed multi-component systems (Figure 2.7): rock matrix (consisting of quartz, calcite, and/or clay), water

$(1 - \phi)$ ϕ

| Solids (matrix) | Fluids | | |
| Quartz / Calcite | Clay | Bound water | Free water | Oil / Gas |

S_w S_h $(1\text{-}S_w)$
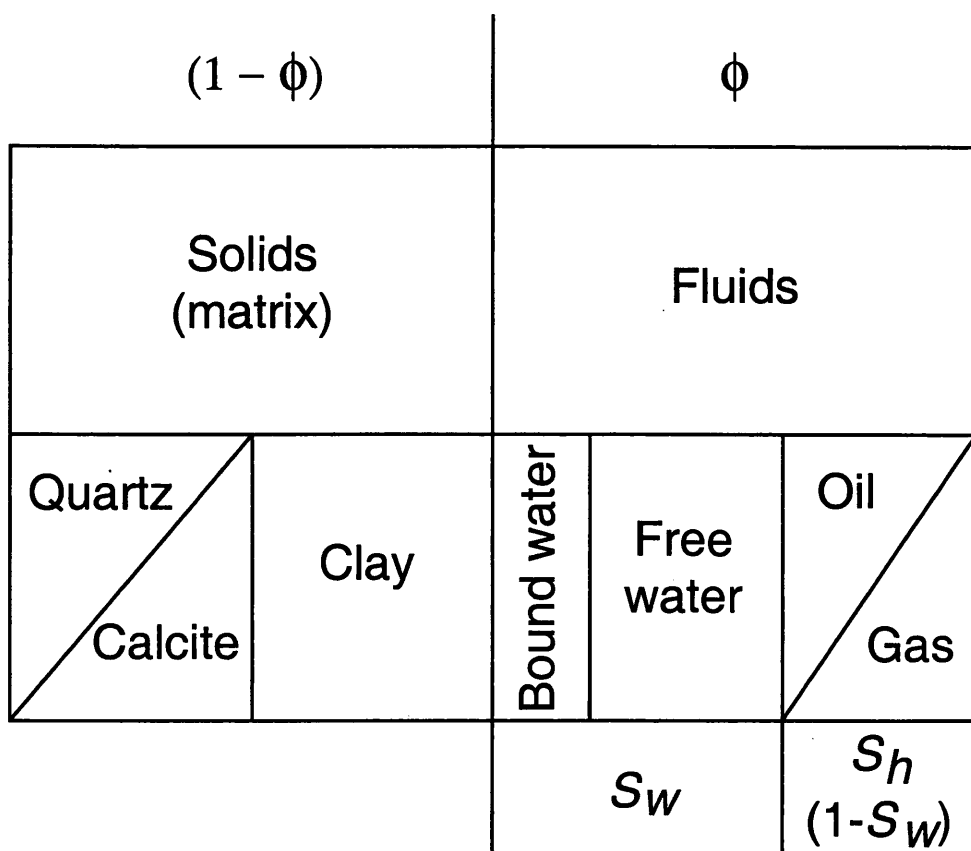
Figure 2.7 "Conventional" hydrocarbon reservoir model used in "standard" well-log evaluation studies.

(including clay-bound- and free-water), and hydrocarbons (gas and/or oil). In permafrost and relatively deep marine environments, however, other reservoir constituents can include gas hydrates and permafrost ice. Before evaluating well-log responses to gas hydrate in the next chapter (Chapter 3) of this thesis, it is necessary to develop and define a series of reservoir models for the occurrence of gas hydrates in nature. The first two reservoir models to be considered represent complex gas-hydrate-bearing reservoirs both below (Model A; Figure 2.8a) and above (Model B; Figure 2.8b) the base of ice-bearing permafrost in a terrestrial setting. In both of these models the sediment matrix consists of a simple mixture of quartz, calcite, and a relatively small amount of clay.

In all of the reservoir models presented in this discussion, the matrix minerals are considered electrically inert; the clay electrical conductivity is modeled as being derived from the conductivity of the bound-water. Gas hydrate reservoir Models A and B assume no free-gas phase (no excess gas): all of the available gas is in the gas hydrate. The only difference between Model A and B is that Model B assumes that all of the free-water and some of the clay-bound-water are frozen. Reservoir Model C (Figure 2.8c) has been designed to represent a clay-rich marine gas hydrate reservoir. Reservoir Models C and A are similar, but Model C assumes the clay content of the sediment and associated volume of bound-water are higher in most marine gas-hydrate reservoirs. The last complex gas hydrate reservoir model to be considered may not occur in nature. Reservoir Model D (Figure 2.8d) assumes that a free-gas phase exists and that all of the available water is included in the gas hydrate. Water, being relatively abundant in nature,
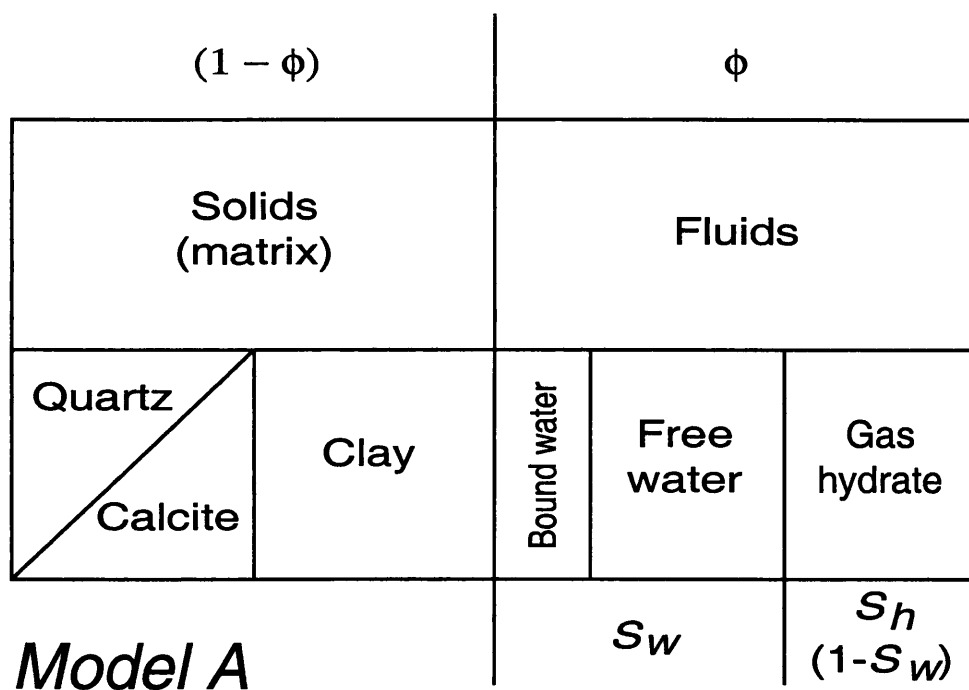
Figure 2.8a Complex permafrost associated gas-hydrate reservoir model for conditions below the base of ice-bearing permafrost (Model A).
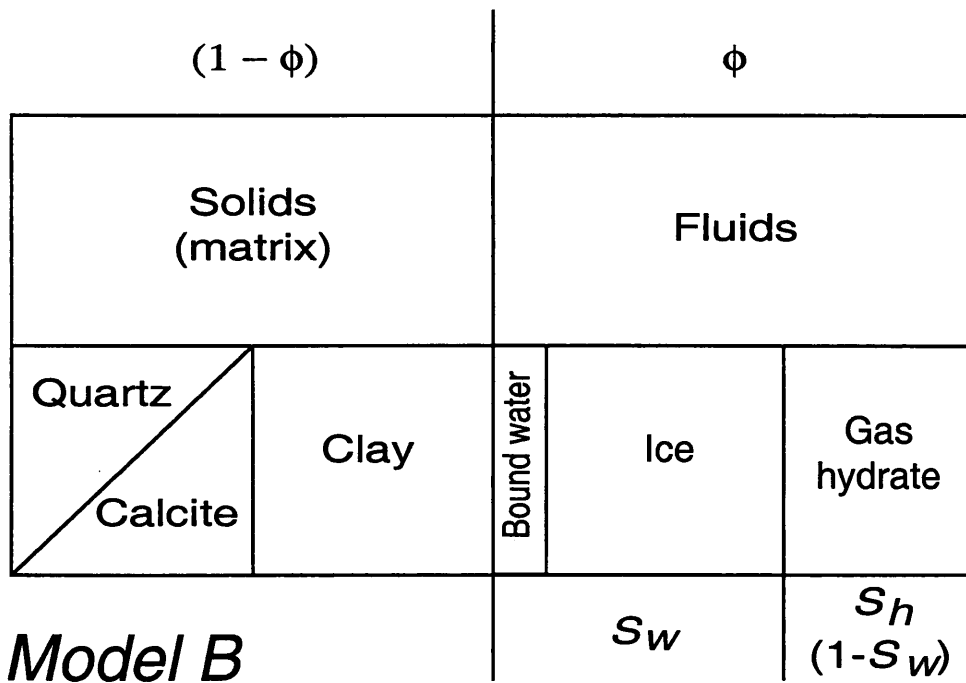
Figure 2.8b Complex permafrost associated gas-hydrate reservoir model for conditions above the base of ice-bearing permafrost (Model B).

$(1 - \phi)$ ϕ

Solids (matrix)	Fluids		
Qu. / Ca. Clay	Bound water	Free water	Gas hydrate

S_w S_h $(1\text{-}S_w)$
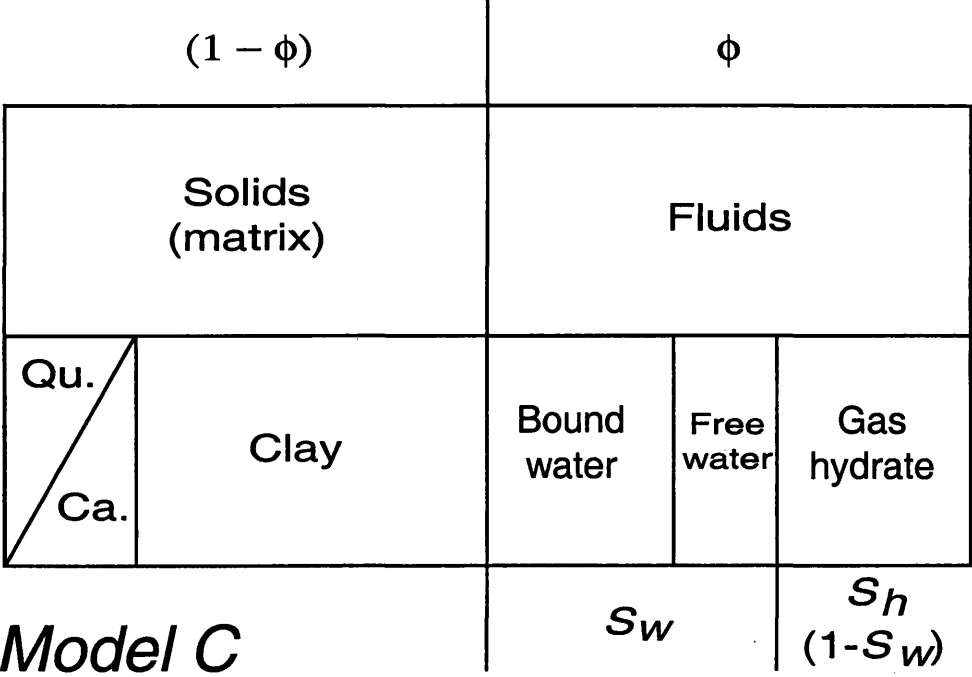
Model C

Figure 2.8c Complex marine (clay-rich) gas-hydrate reservoir model (Model C).

$(1 - \phi)$			ϕ		
Solids (matrix)			Fluids		
Quartz / Calcite	Clay	Bound water	Free Gas	Gas hydrate	

Model D

S_w S_g $\dfrac{S_h}{(1\text{-}S_w)}$
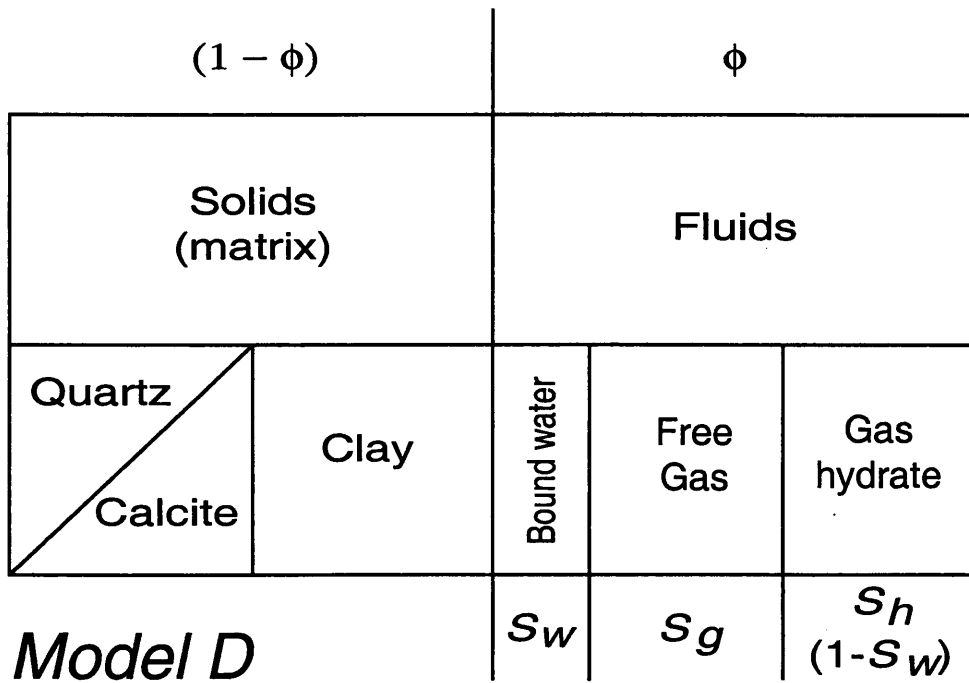
Figure 2.8d Complex free-gas- and gas-hydrate-bearing reservoir model (Model D).

$(1 - \phi)$ ϕ

Solids (matrix)	Fluids	
Quartz / Calcite	Free water	Gas hydrate

Model E

S_w S_h $(1\text{-}S_w)$
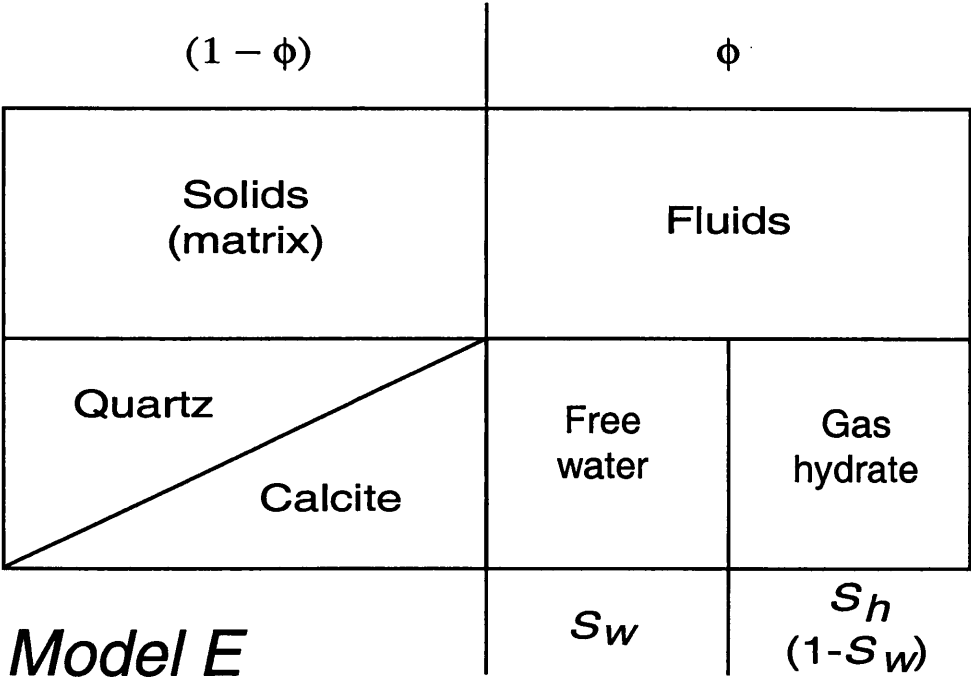
Figure 2.8e Simplified gas-hydrate reservoir model (Model E) with no matrix clay.

should not be a gas hydrate limiting factor in most reservoirs. Therefore, gas hydrate reservoir Model D will not be examined in detail.

The occurrence of various clays in sediments have numerous significant affects on well-log responses. Log responses to clays have been the focus of research studies since the first well log was acquired in the 1920's (see reviews by Serra, 1984; Hearst and Nelson, 1985; Timur and Toksöz, 1985; Schlumberger Educational Services, 1989). For most of the well-log response studies in Chapter 3, a simple gas-hydrate reservoir model, such as Model E (Figure 2.8e) with no matrix clay, is assumed (and no oil or free-gas). However, in situations where the well-log response to gas hydrates is also dependent on the clay content of the sediments, such as in neutron spectroscopy or electrical resistivity well logging, a complex reservoir model such as Model A (Figure 2.8a) has been considered.

For a more complete description of the gas-hydrate-bearing reservoir conditions considered in this study, see the detailed geologic descriptions in the field application section (Chapter 6) of this thesis.

CHAPTER 3

WELL-LOG RESPONSE MODELING AND APPLICATIONS

3.1 Background Information

The ephemeral nature of gas hydrate under surface conditions has placed a greater

emphasis on downhole measurements, which are needed to determine the in-situ physical

properties of gas hydrates. Numerous well-logging devices appear to respond to the

presence of gas hydrates. In most cases these responses are poorly understood or are only

hypothesized to occur. This section (Chapter 3) of the thesis reviews and assesses the

known and modeled well-log responses attributed to the presence of gas hydrates. The

well logs considered include gamma-gamma density, neutron porosity, electrical

resistivity, acoustic transit-time, neutron spectroscopy, and nuclear magnetic resonance

devices. Discussions pertaining to each of these devices include descriptions of existing

and newly developed well-log evaluation techniques used to characterize porosities and

water saturations (S_w) [gas-hydrate saturation (S_h) is equal to $(1.0-S_w)$] in gas-hydrate-

bearing reservoirs. Each section of this chapter begins with an overview of the original

contributions made during the course of this thesis research project. This chapter has

been written for a technical audience familiar with modern well-logging technology and

interpretation. Details of the operating principles of the various logging tools can be

found in Serra (1984), Hearst and Nelson, (1985), Timur and Toksöz (1985), and

Schlumberger Educational Services, (1989).

Three of the five sampled and well logged gas hydrate drill-sites (Table 1.3) are

within marine gas-hydrate occurrences, which were drilled by either the Deep Sea

Drilling Project (DSDP) or the Ocean Drilling Program (ODP). Therefore, most of the

following discussion will focus on the logging tools used in DSDP and ODP (Table 3.1).

With rare exceptions, downhole logging tools designed for use in hydrocarbon

exploration, have been adapted to meet DSDP/ODP requirements and hole conditions.

These modifications include the reduction of tool diameter to allow insertion into the 9.7-

cm (I.D.) drill-string. Logging sensors continuously monitor geophysical, geochemical,

and structural properties of the formation, which are recorded typically at 15-cm depth

increments. The depths of investigation into and vertical resolutions of the formation are

sensor-dependent, but are typically between 50 to 100 cm (Table 3.2).

Individual logging tools can be combined into numerous different strings or suites

of measurements. During ODP Leg 164 studies of the Blake Ridge (discussed in Chapter

5), four different logging strings were used: (1) seismic stratigraphic combination, (2)

lithoporosity combination, (3) formation microscanner tool (FMS), and (4) geochemical

logging tool (GLT). Schematic diagrams of these four tool strings are shown in Figure

3.1. The seismic stratigraphic and lithoporosity tool strings can be combined into a single

string termed the quad-combination. The quad-combination tool string reaches a total

length of 31 m (33 m with the Lamont-Doherty temperature tool [TLT]), making it

difficult or impractical to run in short holes or to obtain data from near the bottom of the

Table 3.1 Summary of logging tools used in the Ocean Drilling Program and a listing of their potential gas hydrate applications.

Tool	Acronym	Principle	Sediment porosity	Gas-hydrate saturation	Typical data
Acoustic	LSS-SDT	Travel-time	P	G	Velocity-Vp
	BHC	of sound	P	G	Velocity-Vp
	SDT-C		P	G	Velocity-Vp
Resistivity	DITE				
Shallow	SFL	Focused Current	G	VG	Resistivity
Medium	ILM	Induced Current	G	VG	Resistivity
Deep	ILD	Induced Current	G	VG	Resistivity
Dual laterolog	DLL				
Deep	LLd	Resistivity	G	VG	Resistivity
Shallow	LLs	Resistivity	G	VG	Resistivity
Gamma-ray	GR	Natural gamma-ray emissions	-	-	Gamma-ray counts
Caliper	MCD	Hole diameter	-	-	Hole size
Neutron porosity	CNT-G	Absorption of bombarding neutrons	VG	-	Porosity
Spectral gamma-ray	NGT NGT	Natural gamma-ray emissions	-	-	K,Th,U abundance
Litho-density	HLDT	Absorption of bombarding gamma-rays	VG	-	Bulk density
Neutron-spectroscopy	GST	Capture of bombarding neutrons	F	F	Elemental yields
Al activation clay tool	AACT	Absorption of bombarding neutrons	-	-	Aluminum abundance
Formation Mic-roScanner	FMS	Focused microcurrent	-	F	Resistivity images
Temperature	LDEO -TLT	Formation temperature	-	-	Temperature

Note: Usefulness of tool for application: VG=very good, G=good, F=fair, P=poor,
- = not applicable

Table 3.2 Approximate vertical resolution and depth of investigation of various logging tools used in the Ocean Drilling Program.

Tool	Vertical resolution	Depth of investigation*
Phasor induction tool (DITE)		
ILD Deep resistivity	200 cm, 88 cm, 59 cm	1.5 m
ILM Medium resistivity	150 cm, 88 cm, 59 cm	76 cm
SFL Shallow focused	59 cm	38 cm
Dual laterolog (DLL)	61 cm	Variable
Spectral gamma-ray tool (NGT)	46 cm	Variable
Litho-density tool (HLDT)	49 cm (6-in sampling)	Variable
	35 cm (2-in sampling)	15-60 cm
	20 cm Alpha processing (6-in)	
	30 cm Alpha processing (2-in)	
Sonic digital tool (SDT-C/array)	30 cm	Variable
	Special processing 15 cm	10-60 cm
Gamma-ray spectroscopy tool (GST)	75 cm	Variable
		12-20 cm
Aluminum activation tool (AACT)	25 cm	Variable
	Special processing 12-20 cm	12-20 cm
Dual porosity compensated	55 cm (6-in sample)	Variable
neutron tool (CNT-G)	33 cm Alpha processing (6-in)	5-15 cm
	25.4 cm Alpha processing (2-in)	
Formation MicroScanner (FMS)	6 mm	5-25 cm
Lamont temperature tool (LDEO-TLT)	Vertical resolution depends on logging speed	

Notes: Standard sampling is at 15-cm (6-in) intervals. High-resolution sampling is at 5.5-cm (2-in) intervals. Alpha processing is a special high-resolution processing routine.

*Depth of investigation is formation and environment specific; these depths are only rough estimates.

Seismic stratigraphic combination

Natural gamma
spectrometry
tool (NGT)

• K, Th, U (%)

Array sonic tool (SDT)

• Sonic traveltime
• Sonic waveforms

Centralizing
bowsprings

Phasor dual
induction
tool (DIT)

• Shallow
focused
resistivity

• Deep and
medium
resistivity

Lamont-Doherty
temperature logging
tool (LDEO-TLT)

Lithoporosity combination

Natural gamma
spectrometry
tool (NGT)

• K, Th, U (%)

Dual porosity
compensated
neutron tool
(CNT-G)

• Thermal and
epithermal
porosity

High-temperature
lithodensity tool
(HLDT)

• Bulk density

• Photoelectric
effect

(eccentralizing
bowspring)

Lamont-Doherty
temperature logging
tool (LDEO-TLT)

Geochemical logging tool

Natural gamma
spectrometry
tool (NGT)

• K, Th, U (%)

Aluminum
activation
clay tool (AACT)

• Al (%)

Gamma
spectroscopy
tool (GST)

• Si, Ca, Fe, Cl, H, S,
Ti, Gd, K, C, and O
(relative abundances)

Lamont-Doherty
temperature logging
tool (LDEO-TLT)

Formation MicroScanner

Natural gamma
spectrometry
tool (NGT)

• K, Th, U (%)

Formation Micro-
Scanner (FMS)

• Microresistivity
images
• General purpose
inclination
tool (GPIT)

Lamont-Doherty
temperature logging
tool (LDEO-TLT)

Figure 3.1 Schematic diagram of the Schlumberger downhole-logging tool strings used during ODP Leg 164.

hole. Splitting the quad-combination into two separate strings (1 and 2 above) also improves the quality of the acoustic and neutron porosity logs. The acoustic tool in the seismic stratigraphic tool string requires a centralizer for optimum performance, while the neutron porosity tool in the lithoporosity tool string performs best when in direct contact with the borehole wall. The Lamont-Doherty temperature tool (TLT) is usually attached to the bottom of all the tool strings. The natural gamma-ray tool (NGT) is placed at the top of all the tool strings to facilitate depth-correlating between logging runs at a single site. Logs from different tool strings may still, however, have depth mismatches caused either by cable stretch or ship heave during recording. Small errors in depth matching can impair the multilog analyses in zones of rapidly varying lithology. Ship heave is minimized by a hydraulic wireline heave compensator designed to adjust for rig motion during logging operations (Shipboard Scientific Party, 1996). Precise depth matching of logs with cores is difficult in zones where core recovery is low because of the inherent ambiguity of placing the recovered section within the cored interval.

Where incomplete core recovery has occurred, log data may serve as the only source of physical property and sedimentological data. Log measurements also complement the discrete measurements obtained from cores, and offer several advantages over core-based analyses in that they are rapidly collected and represent continuous, in-situ measurements of the formation. Integration of continuous and multivariate log data with core data can potentially ground-truth information provided by detailed core analyses, resulting in continuous and quantitative records of sediment lithological variability. Well-log data is also used to identify and quantify the pore-fluids within a

stratigraphic section. Log data quality may be seriously degraded by rapid changes in the

hole diameter and in sections where the borehole diameter is greatly increased or washed

out. The result of these effects is to impair logging by causing "bridging" or "tool

sticking" and to increase the fluid volume between the formation and the logging tool.

Deep investigation devices such as resistivity and acoustic tools are least sensitive to

borehole effects. Nuclear measurements (density, neutron porosity, and both natural and

induced spectral gamma ray) are more sensitive due to their shallower depth of

investigation. Corrections can be applied to the original data in order to reduce these

effects. The effects of very large washouts, however, cannot be corrected. See Appendix

1 for information on required well-log data processing.

3.2 Gamma-Gamma Density Logs

Density logs are primarily used to assess porosities. Other uses include

identification of minerals, detection of free-gas, determination of hydrocarbon density,

calculation of overburden pressure and rock mechanical properties. In this study the

utility of the density log as a porosity tool in gas-hydrate-bearing sediments has been

assessed. In this section of the thesis, two existing "conventional" density-porosity

relations (equations) have been introduced and reviewed. For the first time the sensitivity

of these density-porosity relations to the presence of gas hydrate have been assessed.

Within this study, a density-porosity nomograph has been developed to correct for the

effect of high gas-hydrate saturations. Also, for the first time, the downhole-log-

measured electron density of gas hydrate has been compared to the true density of gas hydrate.

The basic design of a density sonde consists of a gamma-ray source and detectors placed some distance apart. The emitted gamma-rays are scattered within the formation and some of these scattered gamma-rays return to the detector. The attenuation of the log emitted gamma-rays is controlled by the bulk density of the formation. The high temperature lithodensity tool (HLDT) used in ODP and DSDP, employs a 137-Cesium radioactive source and two detectors mounted on a shielded sidewall skid that is pressed against the formation by a hydraulically activated arm. The arm also provides a caliper measurement of borehole diameter. The medium energy (662 keV) gamma-rays emitted by the source lose energy by interaction with the electrons in the formation causing Compton scattering until absorbed through the photoelectric effect. The number of gamma-rays reaching the two vertically spaced detectors yields an energy spectrum for each detector that is directly related to the number of electrons in the formation, which in turn is related to bulk density. The resulting bulk-density is computed, assuming that most rock-forming elements have a ratio of atomic weight to atomic number of two.

As discussed above, photoelectric absorption occurs when the gamma-rays reach a low energy (<150 keV) after being continually scattered by the electrons in the formation. The photoelectric effect index (PEF) values, when used in combination with the NGT data, can provide an indication of the different types of clay minerals in the sediments, however no apparent information on gas-hydrate occurrence.

The density of natural gas hydrates has not been directly measured, however, it is possible to calculate gas hydrate density from the unit cell dimensions reviewed by Pearson et al. (1983) (Table 3.3). The density of a gas hydrate is calculated by adding the mass of the guest molecules to the lattice mass and dividing by the cell volume. Clearly, the density of gas hydrates will vary depending on the occupancy ratio and the guest species. This calculation also assumes that there is no free-gas in the gas hydrate crystal structure. The typical bulk-density of a Structure-I methane hydrate is about 0.9 g/cm^3 (Sloan, 1998).

In conventional formation density logging, porosities are derived from this standard relation:

$$\varnothing = \frac{\rho_m - \rho_b}{\rho_m - \rho_w} \tag{3.1}$$

where ρ_m is the known matrix density (g/cm^3), ρ_w is the fluid (water) density (g/cm^3), and ρ_b is the log-measured formation bulk-density (g/cm^3). To calculate porosities within a gas-hydrate-bearing rock unit a modified density equation has been developed for a three-component system (water, hydrate, matrix) (modified from Pearson et al., 1983):

Table 3.3 Bulk-density of various reservoir components (modified from Pearson et al., 1983).

Reservoir constituent	Density (g/cm^3)
Water, H_2O	1.00
Ice, H_2O	0.92
CH_4 hydrate - Structure-I	
100% cage occupancy	0.90
80% cage occupancy	0.88
C_2H_6 hydrate - Structure-I	
100% cage occupancy	1.01
80% cage occupancy	0.96
CO_2 hydrate - Structure-I	
100% cage occupancy	1.12
80% cage occupancy	1.05
C_3H_8 hydrate - Structure-II	
100% cage occupancy	0.94
80% cage occupancy	0.91
Quartz, SiO_2	2.65-2.70
Calcite, $CaCO_3$	2.71
Clay	2.12-2.77
Marine sediment	2.70

$$\rho_b = (1 - \varnothing)\rho_m + (1 - S_h)\varnothing\rho_w + S_h\varnothing\rho_h \qquad (3.2)$$

ρ_b = Bulk-density, g/cm^3

ρ_m = Matrix density, g/cm^3

ρ_w = Water density, g/cm^3

ρ_h = Hydrate density, g/cm^3

S_h = Hydrate saturation, fractional %

$\varnothing$ = Porosity, fractional %

Typical densities for marine and terrestrial sediments, gas hydrates, water, and ice are listed in Table 3.3. Figure 3.2 is a plot of the three-phase (water-hydrate-matrix; Reservoir Model C, Figure 2.8c) modified density equation for all possible porosity conditions in a marine sedimentary section. Figure 3.2 reveals that gas hydrate (Structure-I) can cause a small but measurable effect on density-derived porosities. At relatively high porosity (>40%) and high gas-hydrate saturation (>50%) the density-log-derived porosities need to be corrected for the presence of gas hydrate.

Before using density-log-derived gas-hydrate porosities or generating gas-hydrate porosity correction factors it is necessary to compare the electron density of gas hydrate with the true density of gas hydrate, because the density log actually responds to the electron density of the formation not the true density. For a molecular substance, consisting of numerous atoms, the electron density index (ρ_e) is related to the bulk-density (ρ_b) by the following equation (Schlumberger Educational Services, 1989):
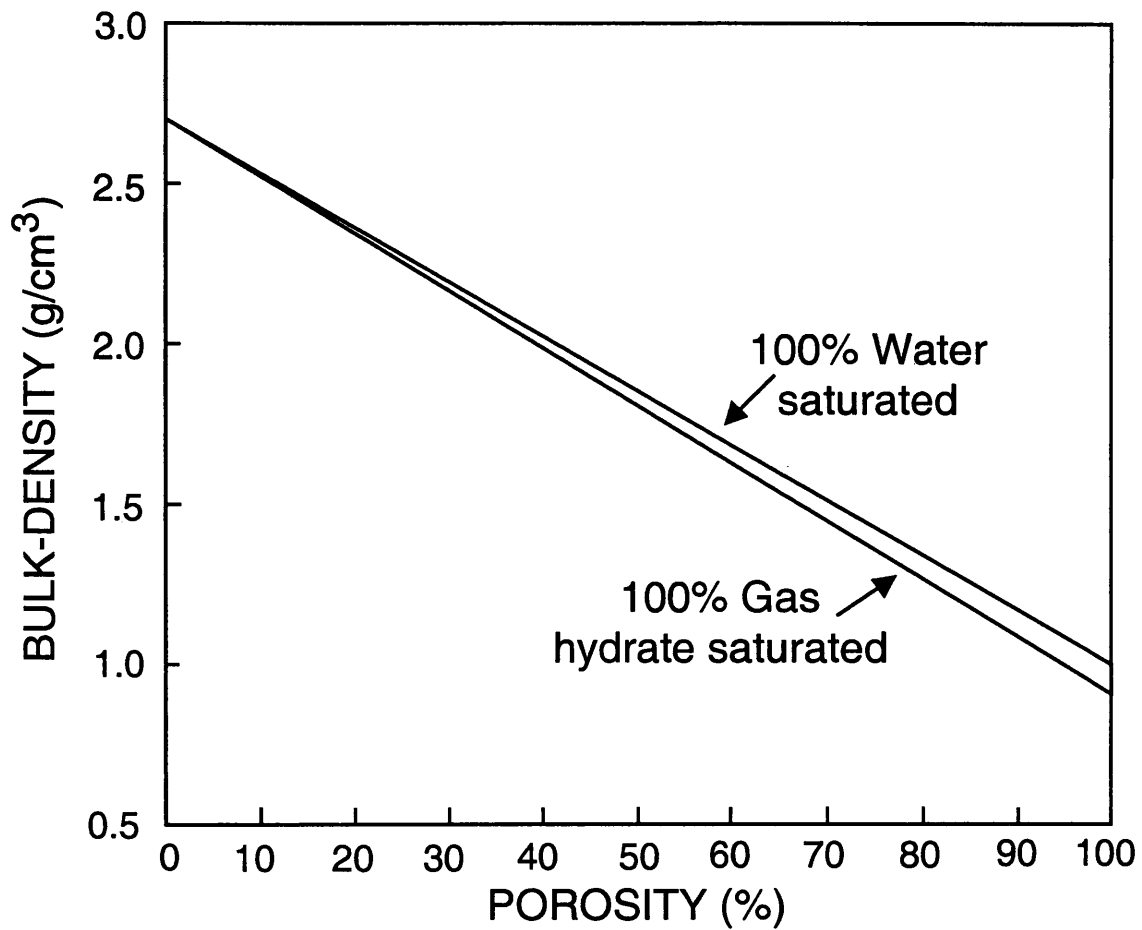
Figure 3.2 Plot of the modified three-component density equation (Equation 3.2) for all possible sediment porosity conditions and gas-hydrate saturations in a marine sedimentary section (Reservoir Model C, Figure 2.8c).

$$\rho_e = \rho_b \, 2(SUM\,Z's/Mol.\,Wt.) \tag{3.3}$$

where *SUM Z's* is the sum of the atomic numbers of the atoms making up the molecule

(equal to the number of electrons per molecule) and *Mol. Wt.* is the molecular weight.

Assuming the bulk-density (ρ_b) of a Structure-I methane hydrate is 0.9 g/cm^3, the

electron density index (ρ_e) would be 1.015 g/cm^3. When the density tool is calibrated in

freshwater-filled limestone formation, the apparent bulk-density (ρ_a) as measured by the

tool is related to the electron density index (ρ_e) by the following equation (Schlumberger

Educational Services, 1989):

$$\rho_a = 1.0704\,\rho_e - 0.1883 \tag{3.4}$$

For most cases, including gas hydrates, the true bulk-density (ρ_b) of a substance is almost

identical to the apparent bulk-density (ρ_a) measured by the logging tool (Table 3.4). It

can be assumed, therefore, that the density tool measures true bulk densities in a gas-

hydrate-bearing stratigraphic section.

Under most conditions, the bulk-density (ρ_b) of a water-bearing formation is

almost identical to the bulk-density (ρ_b) of a gas-hydrate-bearing formation as measured

by the density tool (Figure 3.2). At high porosities and high gas-hydrate saturations,

however, the density-derived porosities need to be corrected. Porosities calculated from

Table 3.4 True bulk-density (ρ_b) versus apparent bulk-density (ρ_a).

Substance	True bulk-density (ρ_b) (g/cm^3)	Apparent bulk-density (ρ_a) (g/cm^3)
Water	1.00	1.00
Methane hydrate Structure-I	0.9	0.898
Quartz (matrix)	2.65	2.65
Marine sediment (matrix)	2.70	2.71

density logs in hydrocarbon-bearing reservoirs are subject to error because most density

devices are calibrated to the density of the drilling fluids or water. However, if the

density of the hydrocarbon (gas hydrate) is known, it is possible to correct the density-

derived porosities. Figure 3.3 (which is an enlarged portion of Figure 3.2) can be used to

determine porosities from density-log measurements in gas-hydrate-bearing sediments.

To use this crossplot, enter the ordinate with the density-log-measured bulk-density (in

this example 1.75 g/cm^3), draw a horizontal line into the graph to the line that best

represents the degree of suspected gas-hydrate saturation ranging from 0-100% (in this

example 100% gas-hydrate saturation is assumed). From this intersection draw a vertical

line to the abscissa. At the intersection of the vertical line with the abscissa read the

corrected or "true" density porosity (which is about 52% in this example).

3.3 Neutron Porosity Logs

Neutron logs are used principally for delineation of porous formations and

determination of their porosity. In this section of the thesis, the ability of the neutron

porosity log to yield accurate rock porosity data from gas-hydrate-bearing reservoirs has

been assessed.

Neutron porosity devices emit fast neutrons from either radioactive sources or

particle accelerators. As the fast neutrons collide with the nuclei of atoms in the rock

medium the neutrons thermalize or slow. The slowed neutrons are eventually captured

by atoms and gamma-rays of capture are emitted. The slowing of fast neutrons emitted

by the logging tool is caused by collisions with mostly hydrogen nuclei, whose mass is
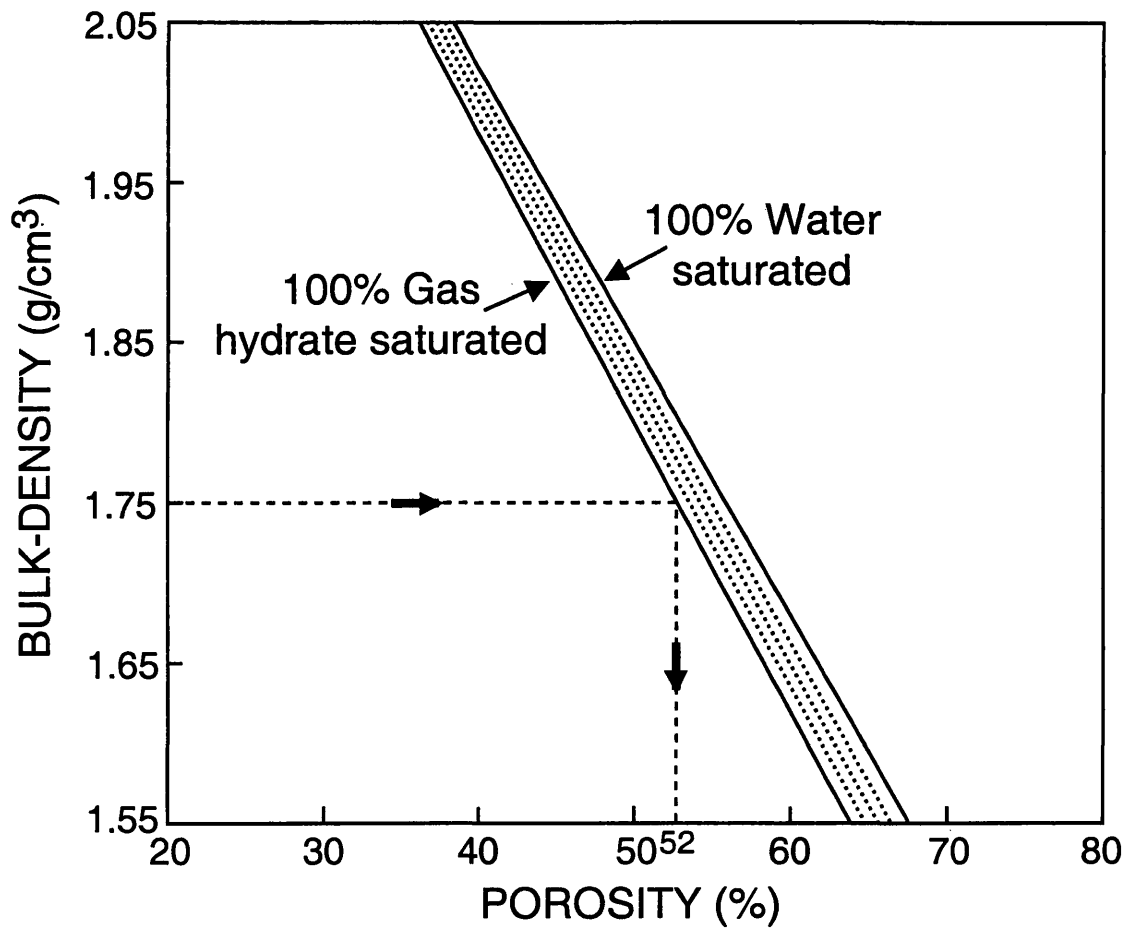
Figure 3.3 Plot of the three-component density porosity gas hydrate correction nomograph for a marine sedimentary section (Reservoir Model C, Figure 2.8c).

almost identical to that of a neutron. Thus, neutron logs that measure the number of

slowed neutrons are actually measuring the amount of hydrogen within the pore-space of

the rock sequence. The amount of hydrogen in a rock sequence is related to the amount

of water and hydrocarbons, including gas hydrates, that are present.

In this study, three approaches have been used to evaluate the effect of gas

hydrate on the neutron porosity log. In the first approach, the hydrogen index of a

Structure-I methane hydrate was calculated and compared to the hydrogen index of other

reservoir constituents. The next two approaches involve modeling expected neutron

porosity well-log response to gas hydrates with two mathematical response computer

simulators: a (1) numerical multigroup simulator [SNUPAR] and a (2) Monte Carlo

neutron transport simulator [MCNP-4].

The neutron modeling efforts reported in this thesis have for the first time

assessed the sensitivity of the neutron-porosity-log measurements to the presence of gas

hydrates. In addition, a series of neutron-porosity nomographs have been developed to

correct for the effect of high gas-hydrate saturations. It should also be noted that the

neutron modeling effort described in this thesis involved the complete assessment of the

chemical composition of gas-hydrate-bearing sedimentary rocks and the first ever

calculation of the neutron capture cross section (and other neutron transport parameters)

for a Structure-I methane hydrate.

As previously indicated, neutron porosity logs actually measure the amount of

hydrogen within the pore-space of the rock sequence; and the amount of hydrogen in a

rock sequence is related to the amount of water and hydrocarbons, including gas

hydrates, that are present. As described in Chapter 1 of this thesis, Collett et al. (1984)

developed a neutron porosity log gas hydrate correction factor based on assessing the

hydrogen content of a Structure-I methane hydrate and other potential pore-filling

constituents (Table 1.6). As discussed in Collett et al. (1984), an increase in the

hydrogen content would relate to an increase in the number of slowed neutrons and the

rate at which the neutrons slowed would be greater. Thus, assuming constant porosity, a

rock saturated with gas hydrate would more effectively slow (thermalize) the log emitted

neutrons than a rock saturated with only water, since gas hydrates contain more hydrogen

per unit volume (Collett et al., 1984). As part of this study, the amount of hydrogen and

other neutron slowing atoms (carbon, oxygen, silicon, calcium) that are present in a cubic

centimeter of pore-volume or matrix of the following substances were calculated: water,

methane gas, ice, Structure-I methane hydrate, quartz (sandstone) and calcite (limestone)

matrix (Table 3.5). These calculations assumed standard chemical formulas and bulk

densities for each of the reservoir constituents being considered (Table 3.5). For water,

ice, and the quartz and calcite matrix material these calculations are relatively

straightforward. In each case the chemical formula and bulk-density of the individual

reservoir constituents were used along with its atomic weight to calculate the moles per

cubic centimeter of each substance, which is then multiplied by Avogadro's number

$(6.022045 \times 10^{23})$ to determine the number of hydrogen and/or other atoms present in one

cubic centimeter of the pure substance. The elemental calculations for methane gas and

Structure-I methane hydrate are more complicated. Gas density data is needed to conduct

the methane gas elemental calculations, which requires assumed pressure and

Table 3.5 Elemental concentration of carbon, hydrogen, oxygen, silicon, and calcium in various reservoir constituents.

Reservoir constituent	Chemical formula	Bulk-density (g/cm^3)	Elemental concentrations (x10^{22} atoms/cm^3)				
			Carbon	Hydrogen	Oxygen	Silicon	Calcium
Gas hydrate Structure-I	7.598CH$_4$+ 46H$_2$O	0.9	0.439988	7.084028	2.662037	0	0
Methane gas	CH$_4$ 2.580 MPa 273.15 K	(1.209 mol/dm^3)	0.072807	0.291226	0	0	0
Pure water	H$_2$O	1.0	0	6.685516	3.342758	0	0
Ice	H$_2$O	0.92	0	6.016964	3.008482	0	0
Quartz	SiO$_2$	2.65	0	0	5.311965	2.655983	0
Calcite	CaCO$_3$	2.71	1.630520	0	4.891559	0	1.630520

temperature conditions. To simulate more closely natural conditions in deep marine or permafrost environments, a reservoir pressure and temperature of 2.580 MPa and 273.15 K were assumed, which yields a methane gas mole density of 1.209 mol/dm^3 (Friend et al., 1989). The resultant methane gas mole density of 1.209 mol/dm^3 is then converted to mole density per cubic centimeter and Avogadro's number is used to determine the number of hydrogen and carbon atoms present in one cubic centimeter of methane gas. The Structure-I methane hydrate elemental calculations were conducted using a unit cell approach. If the unit cell of a Structure-I methane hydrate is assumed to be 1.728×10^{-21} cm^3 in size (Kuustraa and Hammershaimb, 1983), it is possible to calculate that one cubic centimeter of Structure-I methane hydrate contains 5.787×10^{20} unit cells of Structure-I methane hydrate. Using standard methane hydrate cage occupancy relations (small cage 0.877%, large cage 0.974%; CSMHYD computer program; Sloan, 1998) and a Structure-I methane hydrate chemical formula of $8CH_4 + 46H_2O$, it was possible to calculate that each unit cell of a Structure-I methane hydrate contains 7.598 CH_4 and 46 H_2O molecules. Therefore, 5.787×10^{20} unit cells of Structure-I methane hydrate (i.e., one cubic centimeter of Structure-I methane hydrate) contains about 7.084×10^{22} hydrogen atoms, which is slightly lower then the value reported in Table 1.6 (modified from Collett et al., 1984). The small difference in reported hydrogen content calculations is because Collett et al. (1984) assumed a higher methane hydrate bulk-density of 0.92 g/cm^3.

Hydrogen indexes are often used to compare hydrogen concentrations in different reservoir constituents. The hydrogen index (HI) of a substance is defined as the ratio of the concentration of hydrogen atoms per cubic centimeter in the substance, to that of pure water at 24°C (6.686×10^{22} hydrogen atoms/cm^3). Pure water, therefore has a HI of 1.0. Since a Structure-I methane hydrate contains 7.084×10^{22} hydrogen atoms/cm^3 (Table 3.5), the HI of Structure-I methane hydrate is 1.059 which is near the HI of pure water. The HI of other hydrocarbons are highly variable from nearly zero for low pressure gas reservoirs to close to 1.0 for heavy oils. Most pure rock matrixes, such as quartz and calcite, have very low hydrogen concentrations, thus very low HI's. However, the HI for complex reservoirs with high clay content and associated bound water can be highly variable (complex reservoirs are discussed in more detail in Section 3.6 of this thesis). Since Structure-I methane hydrate and pure water have similar hydrogen concentrations and HI values it can be generally assumed that neutron porosity logs, which are calibrated to pure water, are not significantly affected by the presence of gas hydrates. It is possible, however, to further quantify the effect of gas hydrates on neutron porosity logs. The following equation has been proposed by Schlumberger Educational Services (1989) to determine the effect of hydrocarbons on measured neutron porosities:

$$\varnothing_N = \varnothing[HI_h S_h + HI_w S_w] \qquad (3.5)$$

$\varnothing_N$ = Measured neutron porosity, fractional %

$\varnothing$ = Actual porosity, fractional %

HI_h = Hydrocarbon hydrogen index

S_h = Hydrocarbon saturation, fractional %

HI_w = Water hydrogen index

S_w = Water saturation, fractional %

The above equation is plotted in Figure 3.4 for all possible porosity conditions and assuming the reservoired hydrocarbons are gas hydrates with a 1.059 *HI*. As shown in Figure 3.4, a Structure-I methane hydrate has relatively little affect on neutron porosity measurements within normal reservoir conditions (<40% porosity), however, at high reservoir porosities the neutron porosity log could overestimate porosities by as much as 6%. Similar to the density porosity corrections described in Figures 3.3, Figure 3.5 (which is an enlarged portion of Figure 3.4) may be used to correct the neutron-log porosities for the presence of in-situ gas hydrates. To use this crossplot, enter the ordinate with the "apparent" neutron-log-measured porosity (in this example 50%), draw an horizontal line into the graph to the line that best represents the degree of suspected gas-hydrate saturation ranging from 0-100% (in this example 100% gas-hydrate saturation is assumed). From the intersection of the horizontal line with the line of suspected gas-hydrate saturation, draw a vertical line to the abscissa and read the corrected neutron porosity (which is about 47% in this example).

As previously discussed, the slowing of neutrons in a rock sequence is primarily controlled by the presence of hydrogen in the pore-fluids. However, to predict the
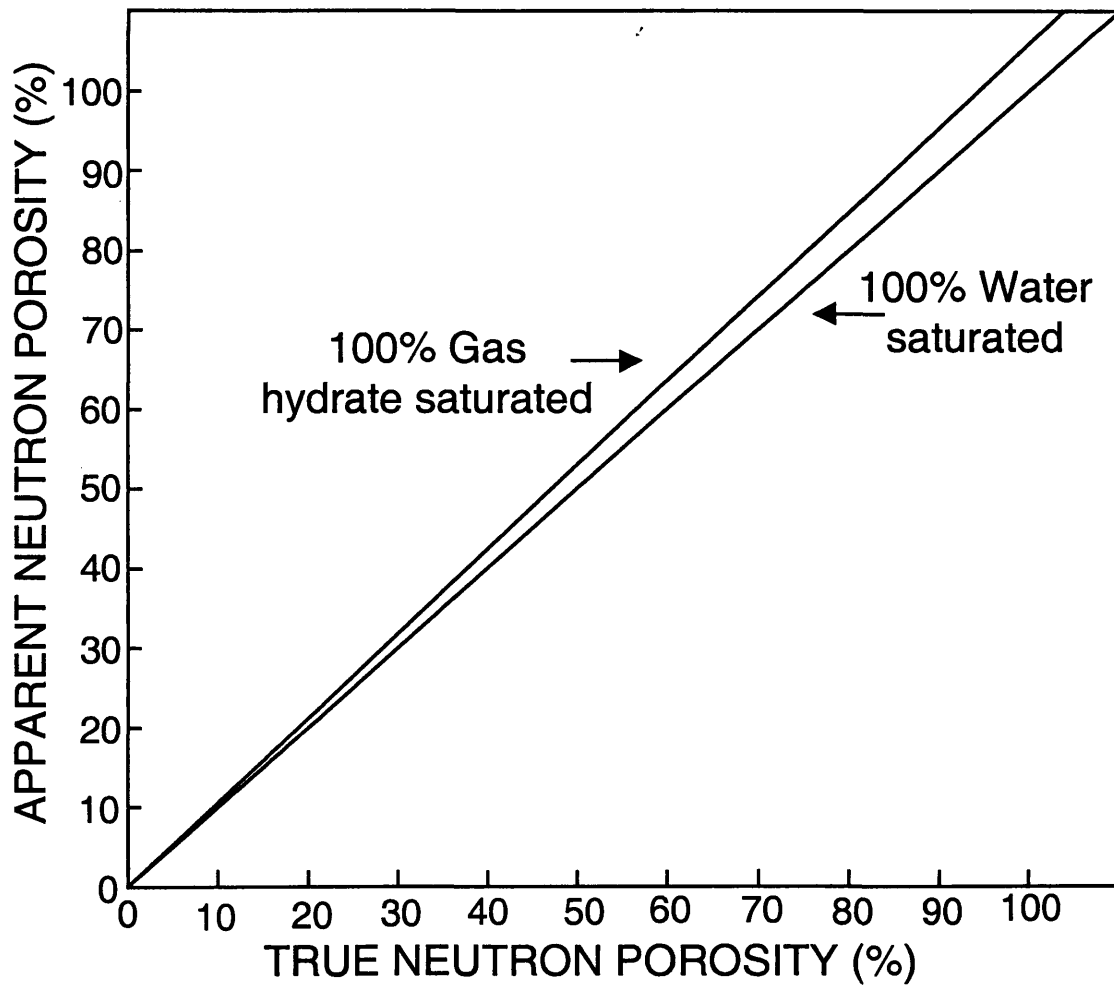
Figure 3.4 Plot of the hydrogen index (HI) neutron porosity equation (Equation 3.5) for all possible sediment porosity conditions and gas-hydrate saturations.
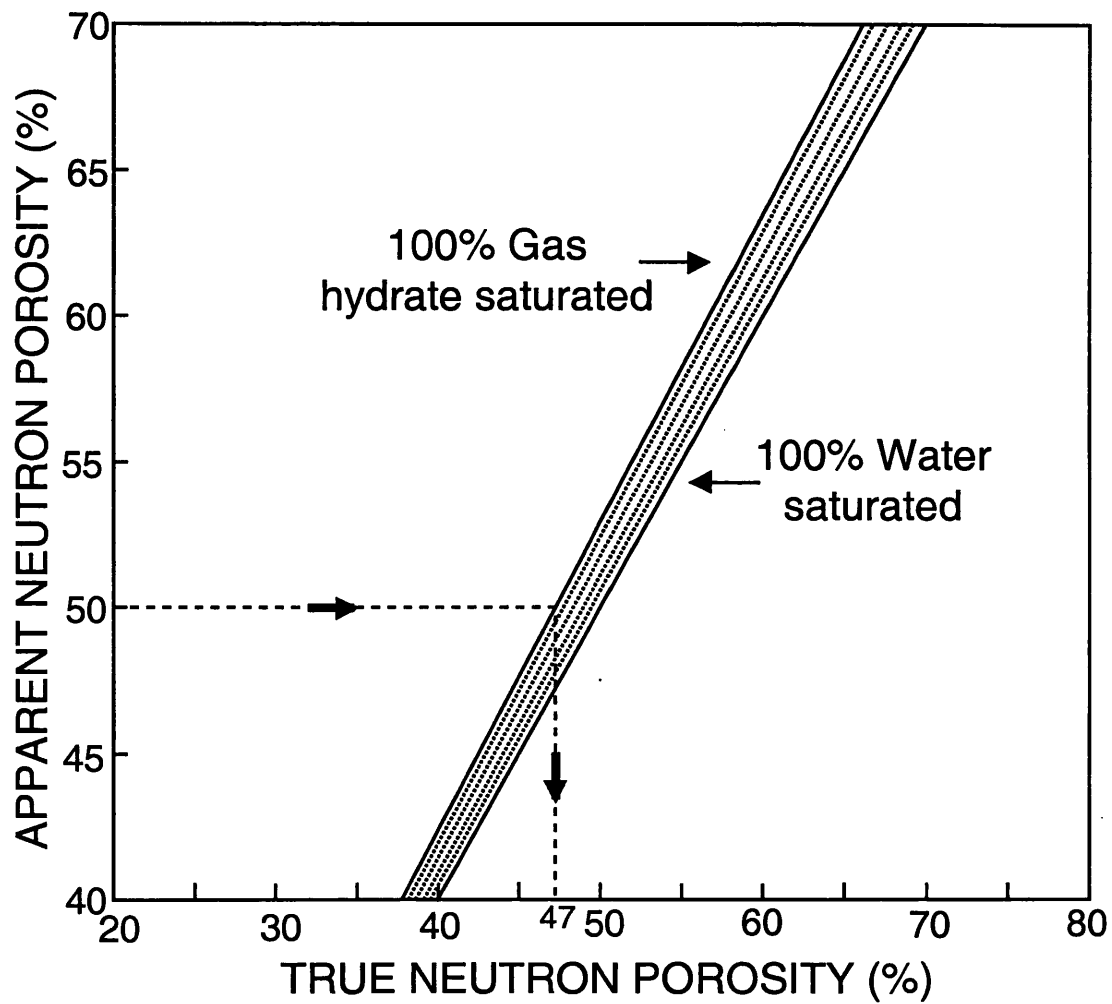
Figure 3.5 Plot of the hydrogen index (*HI*) neutron porosity gas hydrate correction nomograph.

neutron tool response to complex mixtures or rock minerals having various pore-filling

constituents, such as gas hydrates, it is necessary to conduct a more comprehensive

assessment of all the physical parameters affecting the neutron porosity measurements.

Careful mathematical response modeling has contributed greatly to the development of

existing neutron well-log evaluation techniques in complex reservoirs (Lichtenstein et al.,

1979; Ellis et al., 1981; Los Alamos Monte Carlo Group, 1991; Dupree and Noel, 1988;

McKeon and Scott, 1988; Smith et al., 1989; and Wiley and Patchett, 1990). These

modeling studies have been used to characterize the response functions of the individual

devices, to augment and check experimental measurements, and in many cases to model

conditions that are not possible to simulate in the laboratory. Neutron-log response

modeling efforts have generally followed two separate paths: (1) rigid numerical

characterization of predicted interactions, and (2) Monte Carlo simulation techniques. In

this study, the response of the neutron well logs to gas hydrates has been modeled with a

numerical multigroup simulator (SNUPAR) and a Monte Carlo neutron transport

simulator (MCNP-4).

The SNUPAR (Schlumberger Nuclear Parameters) program was developed to

calculate nuclear measurement parameters in complex mixtures of rock materials and

pore-fluids (McKeon and Scott, 1988). SNUPAR can yield numerous nuclear parameters

of interest, including information on neutron slowing, neutron capture cross sections,

hydrogen indexes, and both epithermal and thermal porosities. Table 3.6 contains a

complete list of nuclear parameters that can be calculated with SNUPAR Version 2.C.

Table 3.6 List of SNUPAR-calculated (Version 2.C)
nuclear parameters (modified from McKeon and Scott,
1988).

Measured parameters
Neutron slowing-down length (Ls) Thermal neutron diffusion length (Ld) Neutron migration length (Lm) Thermal neutron capture cross section (Σ) Thermal neutron diffusion coefficient (D) Thermal neutron decay time (tau) Density of the material (ρ) Electron density index (ρ_e) Effective atomic number (Z_{eff}) Photoelectric factor (PEF) Volumetric photoelectric absorption coeffienient (U_e) Hydrogen index (HI) Apparent thermal and epithermal porosities

To understand how SNUPAR calculates the nuclear parameters listed in Table 3.6 it is necessary to first review several important aspects of neutron transport theory.

The neutron sources used in most modern logging tools emit "fast" or epithermal neutrons with an average energy of about 4.5 million electronvolts (MeV). As fast neutrons collide with the nuclei of atoms in the rock medium the neutrons thermalize or slow. This process is called slowing down, which a neutron log measures to calculate the porosity of a rock sequence. The slowed neutrons are eventually captured by atoms and gamma-rays of capture are emitted. During the life of a neutron, which may last from less than a microsecond to over one millisecond, it may undergo three basic types of interactions: (1) inelastic scatter, (2) elastic scatter, and (3) radioactive capture; each of which are discussed in Appendix 2 of this thesis. One of the fixed variables required to accurately model neutron-gas hydrate interactions is the macroscopic cross section of gas hydrates. The probability of scattering from or reaction with a single nucleus is called the microscopic cross section (σ), which is expressed in square centimeters. A common unit for σ is barns; which is equal to 10^{-24} cm^2. When interactions with matter in bulk is considered it is necessary to express the interactions as macroscopic cross sections (Σ), where $\Sigma = n\sigma$, and n is the number of atoms per cubic centimeter. Listed in Table 3.7 are the macroscopic cross sections for several common earth materials.

Dual neutron porosity devices effectively measure both epithermal neutron slowing-down lengths (Ls) and thermal neutron diffusion lengths (Ld) of a rock formation. These two quantities are combined to provide the total migration length (Lm) of a neutron in a formation which is used to calculate reservoir porosities. SNUPAR uses

Table 3.7 Thermal neutron macroscopic capture
cross sections (Σ) of various reservoir components
(Schlumberger Educational Services, 1989).

Reservoir constituent	Neutron capture cross section (Σ, cm^{-1}x10^3)
Water solutions, H$_2$O	
0 ppm NaCl	22
150,000 ppm	71
Methane gas, CH$_4$	1-9
Quartz, SiO$_2$	4-12
Calcite, CaCO$_3$	7-10
Dolomite, CaMg(CO$_3$)$_2$	5-12
Clay/Shale	20-50
Halite, NaCl	760
Gypsum, CaSO$_4$+2H$_2$O	19

a numerical multigroup calculation method and an extensive library of neutron

microscopic and macroscopic cross sections (Table 3.7) of elements and substances

commonly found in oil and gas reservoirs to calculate nuclear measurement parameters

(Table 3.6), including total neutron migration lengths (Lm). Thus, SNUPAR can be used

to forward-model the neutron porosity well-log response to a complex mixture of

reservoir rocks or a substance such as gas hydrate. The numerical multigroup calculation

method employed by SNUPAR (Version 2.C) is a modified Kreft's method (Kreft, 1974),

which is based on multigroup diffusion theory. In numerical multigroup methods, the

complete neutron energy range (epithermal-thermal-capture; 14 MeV down to 0.414 eV)

is divided into a finite number of groups and transport equations are integrated over each

of the groups. SNUPAR uses an iterative process to solve the mutigroup transport

equations which yield the flux or slowing down length of particles throughout a given

system. For a complete description of the SNUPAR nuclear parameter code see the

summary by McKeon and Scott (1988).

The primary reason for conducting the SNUPAR modeling efforts was to

determine the total neutron migration length (Lm), macroscopic cross section (Σ), and

thermal decay time for a Structure-I methane hydrate, and to confirm the hydrogen index

(HI) for methane hydrate calculated earlier in this thesis. An additional goal of this

modeling effort was to determine the nuclear parameters for other reservoir constituents,

including water, ice, methane gas, quartz and calcite matrix. SNUPAR allows materials

with complex formulas to be entered into the program as either volume or weight

percents. Therefore the atomic elemental values of hydrogen, carbon, oxygen, silicon,

and calcium in Table 3.5 were converted to weight percents for the six substances being

considered (Structure-I methane hydrate, methane gas, water, ice, quartz, and calcite) and

placed into the SNUPAR program. SNUPAR also requires the bulk-density of the

material being modeled, which are also listed in Table 3.5. SNUPAR model results

(Table 3.8) indicate that the relative effect of gas hydrate on neutron porosity logs are

minimal, since all of the calculated nuclear parameters for Structure-I methane hydrate

are similar to those for pure water and because most neutron porosity logs are calibrated

to the response of pure water.

SNUPAR reveals that the total neutron migration length (Lm), macroscopic cross

section (Σ), and thermal decay time for a Structure-I methane hydrate and water are

almost identical (Table 3.8). Therefore, the compensated neutron log should yield

"accurate" total reservoir porosities in gas-hydrate-bearing rock units, assuming no free-

gas or other borehole effect. SNUPAR-calculated a hydrogen index (HI) for a Structure-I

methane hydrate of 1.05 which is slightly lower then the HI value for Structure-I methane

hydrate of 1.059 calculated earlier in this thesis. The difference in the two HI values is

possibly due to the number of significant digits SNUPAR uses to calculate HI values. To

further evaluate the effect of gas hydrates on the neutron porosity log, it is possible to

compare the SNUPAR-derived macroscopic cross sections (Σ) for gas hydrate and pure

water within the following thermal capture cross section equation (reviewed by Hill,

1990):

Table 3.8 SNUPAR-calculated nuclear parameters of various reservoir constituents assuming a 4.5 MeV (AmBe) neutron source.

Reservoir constituent	Chemical formula	Bulk-density (g/cm^3)	Neutron slowing-down length (Ls, cm)	Neutron migration length (Lm, cm)	Thermal neutron decay time $(tau, \mu sec)$	Hydrogen index (HI)	Thermal neutron capture cross section $(\Sigma, cm^{-1} \times 10^3)$
Gas hydrate Structure-I	$7.598CH_4+46H_2O$	0.9	7.12	7.3	195.7	1.05	23.226
Methane gas	CH_4 2.580 MPa 273.15 K	(1.209 mol/dm³)	194.33	288.99	4812.0	0.04	0.945
Pure water	H_2O	1.0	7.23	7.44	204.8	1.00	22.200
Ice	H_2O	0.92	8.04	8.35	227.5	0.90	19.980
Quartz	SiO_2	2.65	28.81	44.14	998.7	0.00	4.551
Calcite	$CaCO_3$	2.71	24.33	32.70	642.9	0.00	7.070

$$\Sigma_{log} = (1-\varnothing)\Sigma_{ma} + S_w \varnothing \Sigma_{wf} + (1-Sw)\varnothing\Sigma_{hc} \qquad (3.6)$$

Σ_{log} = "Bulk" capture cross section of the formation, $cm^{-1}x10^3$

Σ_{ma} = Capture cross section of the matrix, $cm^{-1}x10^3$

Σ_{wf} = Capture cross section of the formation water, $cm^{-1}x10^3$

Σ_{hc} = Capture cross section of the hydrocarbon, $cm^{-1}x10^3$

$\varnothing$ = True reservoir porosity, fractional %

S_w = Water saturation, fractional %

This standard three component (water-matrix-hydrocarbon; Reservoir Model E, Figure 2.7e) thermal capture cross section equation (3.6) can be used to assess the effect of various gas-hydrate saturations on the log-measured "bulk" macroscopic cross section (Σ_{log}). By substituting the SNUPAR-derived macroscopic cross sections for water, quartz (matrix), and Structure-I gas hydrate (Table 3.8) into this equation and assuming a range of gas-hydrate saturations (0-100% S_h) it is possible to generate a crossplot of reservoir porosity and "bulk" (log-measured) macroscopic cross sections for a complete range of gas-hydrate saturations. Figure 3.6 reveals that gas hydrates can cause a small but measurable effect on neutron-log-calculated porosities. At relatively high porosity (>40%) and high gas-hydrate saturation (>50%), neutron-log-calculated porosities need to be corrected for the presence of gas hydrates. Similar to the density and neutron porosity corrections described in Figures 3.3 and 3.5, Figure 3.7 (which is an enlarged
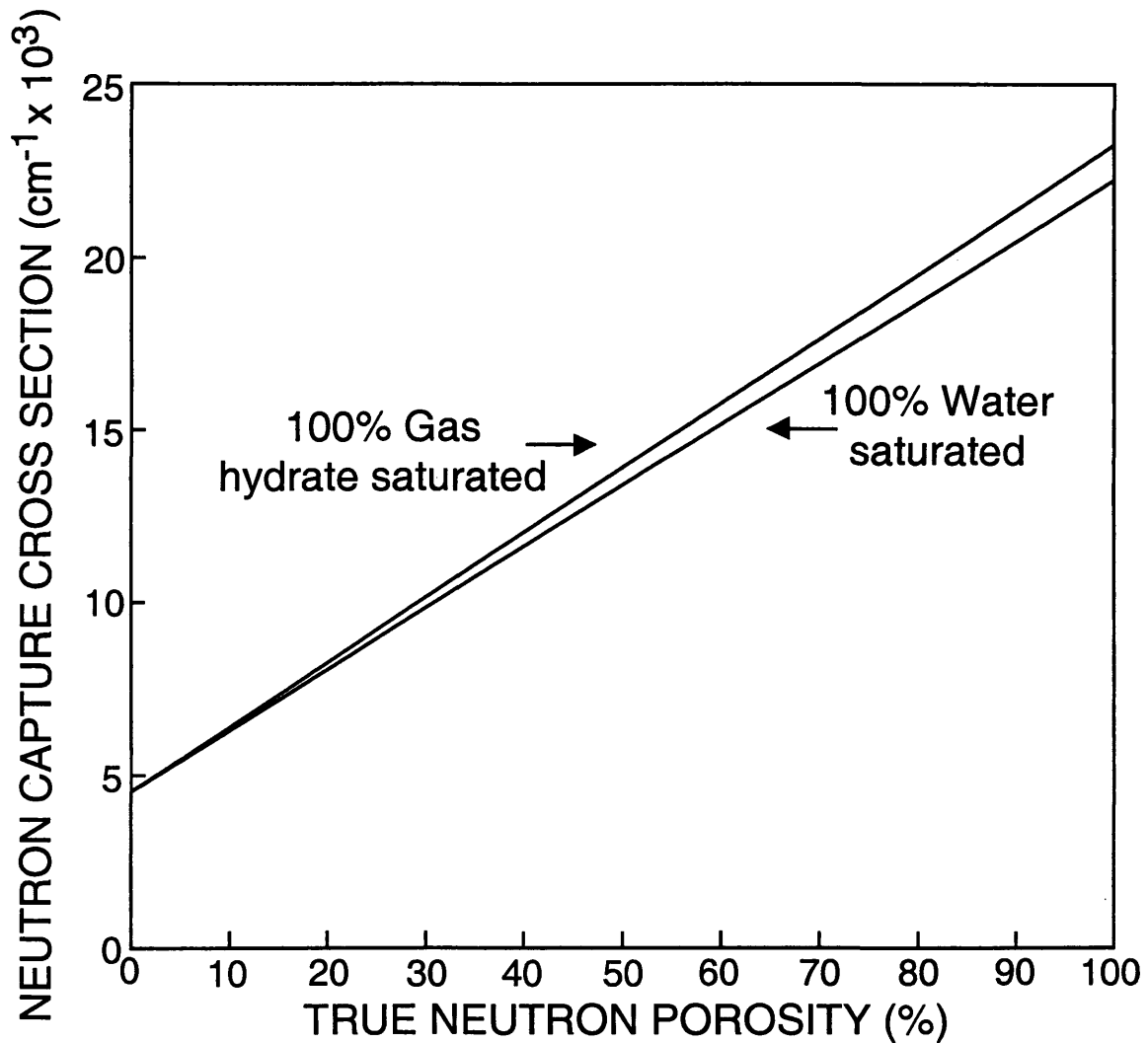
Figure 3.6 Plot of the three-component thermal neutron capture cross section (Σ) equation (Equation 3.6) for all possible sediment porosity conditions and gas-hydrate saturations in a simplified quartz matrix sediment (Reservoir Model E, Figure 2.8e).
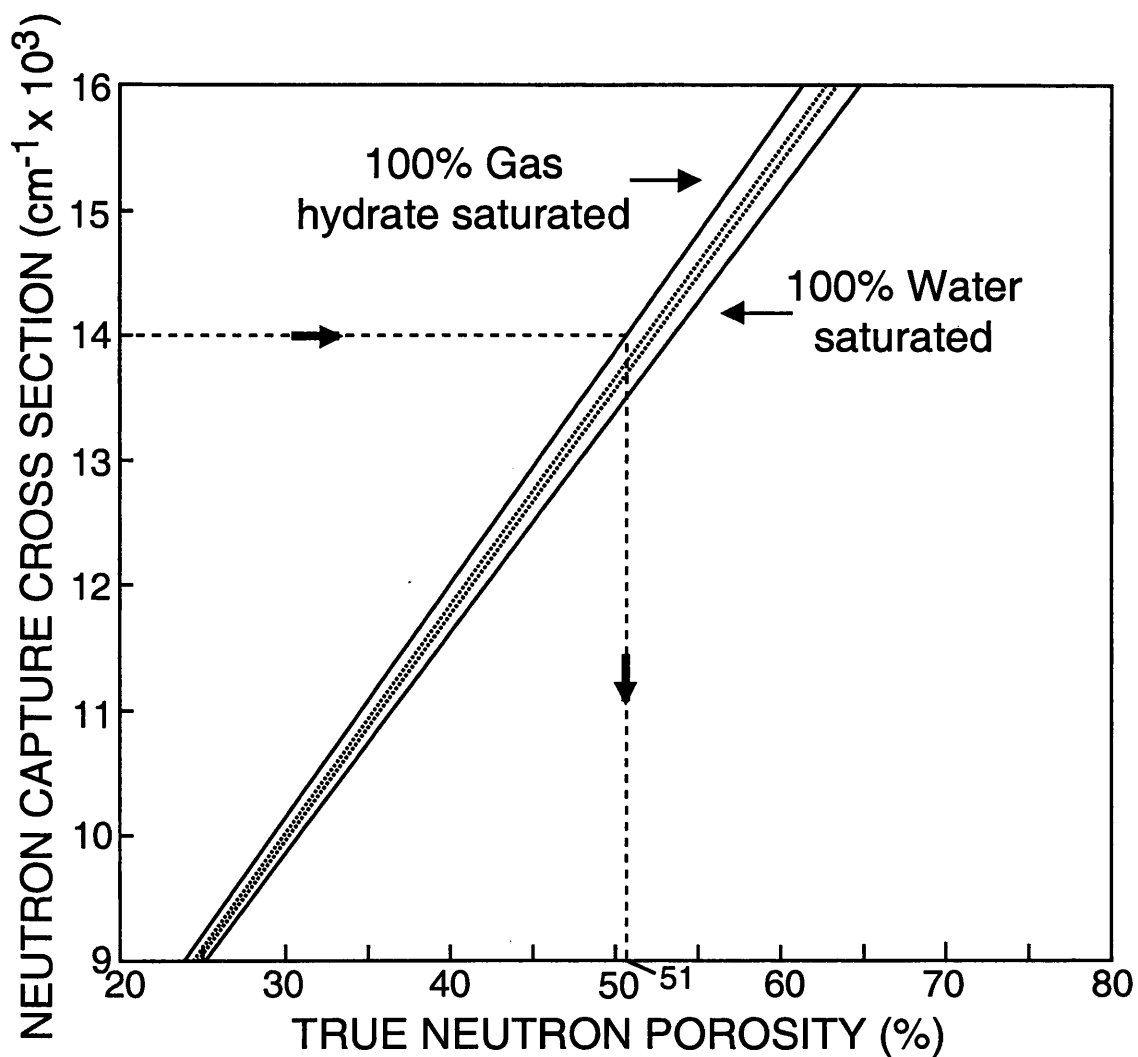
Figure 3.7 Plot of the three-component thermal neutron capture cross section (Σ) neutron porosity gas hydrate correction nomograph for a simplified quartz matrix sediment (Reservoir Model E, Figure 2.8e).

portion of Figure 3.6) may be used to calculate "true" neutron-log porosities from log-measured neutron capture cross sections (Σ_{log}). To use this crossplot, enter the ordinate

with the log-measured neutron capture cross section (in this example 14 cm^{-1}x10^3), draw

a horizontal line into the graph to the line that best represents the degree of suspected gas-hydrate saturation ranging from 0-100% (in this example 100% gas-hydrate saturation is

assumed). From the intersection of the horizontal line with the line of suspected gas-hydrate saturation, draw a vertical line to the abscissa and read the "true" neutron porosity

(which is about 51% in this example).

To further evaluate the validity of the quantitative results of the SNUPAR

modeling, a series of Monte Carlo computations using the MCNP-4 computer code were

conducted to simulate the neutron-porosity-log response to gas-hydrate- and water-

bearing reservoirs (quartz and calcite). MCNP-4 (Monte Carlo Neutron Photon) is a

public-domain, general purpose Monte Carlo transport computer code developed at the

Los Alamos National Laboratory (Los Alamos Monte Carlo Group, 1991). In Monte

Carlo transport simulators, such as MCNP-4, individual particle histories are simulated

on the computer without reference to transport equations. In these simulations, particles

(neutrons) are emitted from a source and the transport is a succession of straight line

flight paths which are interrupted by collision events. The length of the flight path to the

subsequent interaction is a random variable, as is the outcome of the interaction. The

neutrons are tracked until they pass through the detector, or are captured, or until they

escape from the model geometry. A more complete discussion of neutron transport

theory can be found in Appendix 2 of this thesis.

The Monte Carlo neutron transport theory method is often considered an improvement to rigid numerical mutigroup simulations, such as SNUPAR, because complicated three-dimensional geometries can be simulated (Los Alamos Monte Carlo Group, 1991). The MCNP-4 package contains several example problems, one of which was designed to simulate the response of a generic neutron porosity tool in a limestone formation (Figure 3.8). This generic neutron porosity log model consists of a solid iron sonde, with two detectors placed 19.1 (near) and 50.8 (far) centimeters from an AmBe (4 MeV) source. The sonde is in a 20.32 cm diameter, fresh-water-filled wellbore and the rock formation consists of a homogeneous 20% porosity limestone. The MCNP-4 code in this sample problem has been modified to calculate the slowing-down length (Ls), the thermal diffusion length (Ld), and the total migration length (Lm) of neutrons in a nearly infinite homogeneous substance. Each of these nuclear parameters can also be calculated with the SNUPAR computer code (Table 3.6). For the gas hydrate reservoir modeling effort in this thesis, the MCNP-4 generic sample problem was further modified in order to conduct a series of neutron calculations for different reservoir conditions. Comparable SNUPAR and MCNP-4 calculations have been made (assuming a 4 Mev AmBe neutron source) for both quartz (sandstone) and calcite (limestone) reservoirs modeled in this thesis, with porosities ranging from 0 to 100 percent (0, 5, 10, 15, 20, 40, 60, 80, and 100 percent), which are 100% saturated with either gas hydrate or water (Figure 3.9a-d). Both SNUPAR and MCNP-4 calculations require as input detailed information on the reservoir constituents, such as elemental weight percents and bulk densities. The atomic elemental values of hydrogen, carbon, oxygen, silicon, and calcium from Table 3.5 were
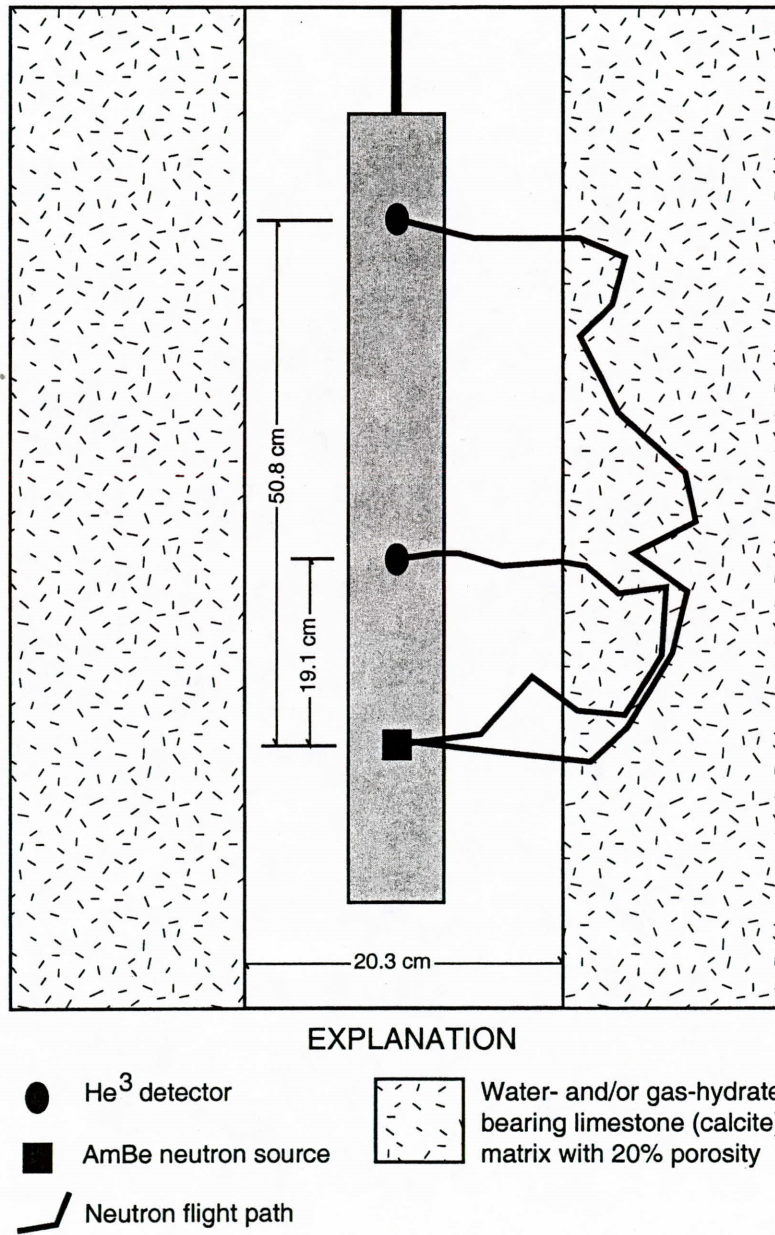
Figure 3.8 Schematic of the neutron porosity tool and borehole geometries used in the MCNP-4 neutron simulations.
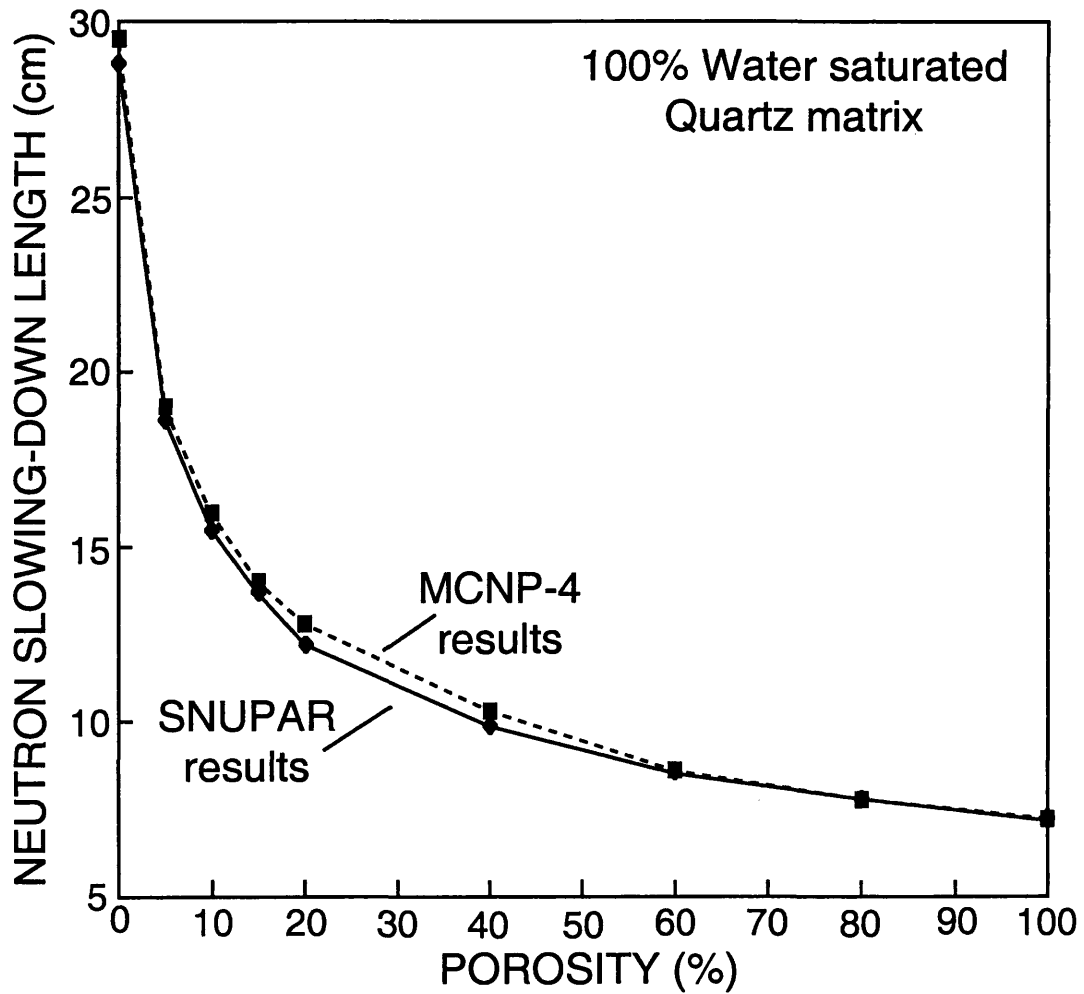
Figure 3.9a Comparison of MCNP-4- and SNUPAR-calculated neutron slowing-down lengths (L_S) in a water-saturated quartz sandstone.
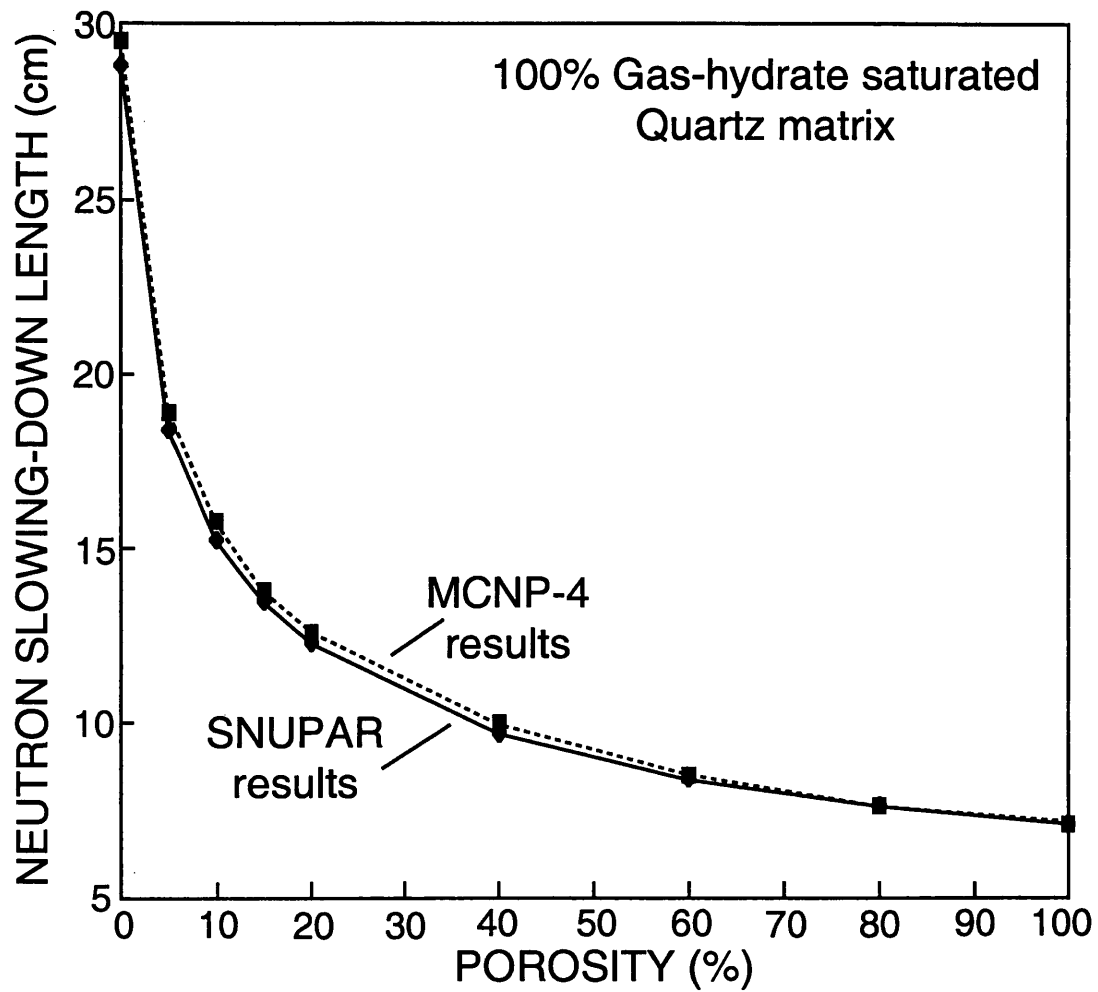
Figure 3.9b Comparison of MCNP-4- and SNUPAR-calculated neutron slowing-down lengths (L_S) in a gas-hydrate-saturated quartz sandstone.
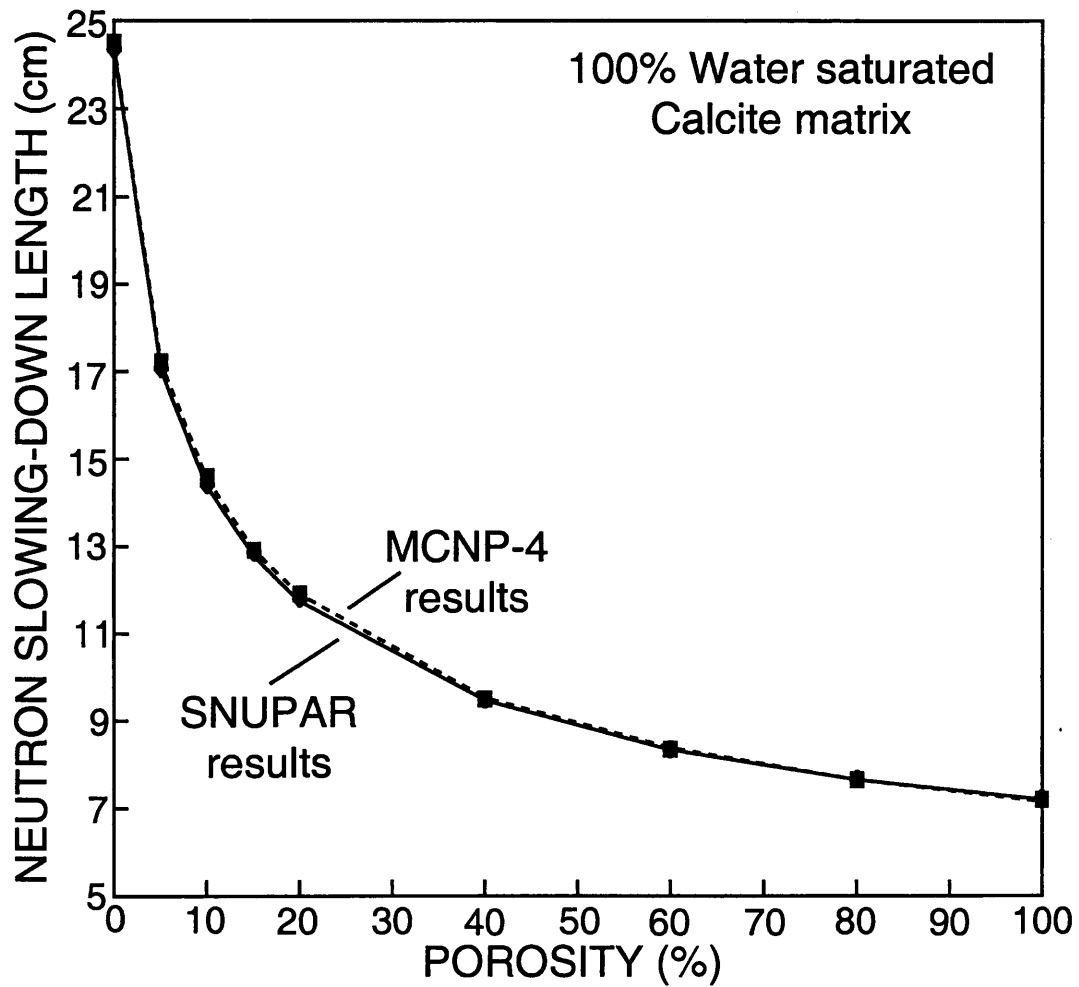
Figure 3.9c Comparison of MCNP-4- and SNUPAR-calculated neutron slowing-down lengths (L_S) in a water-saturated calcite limestone.
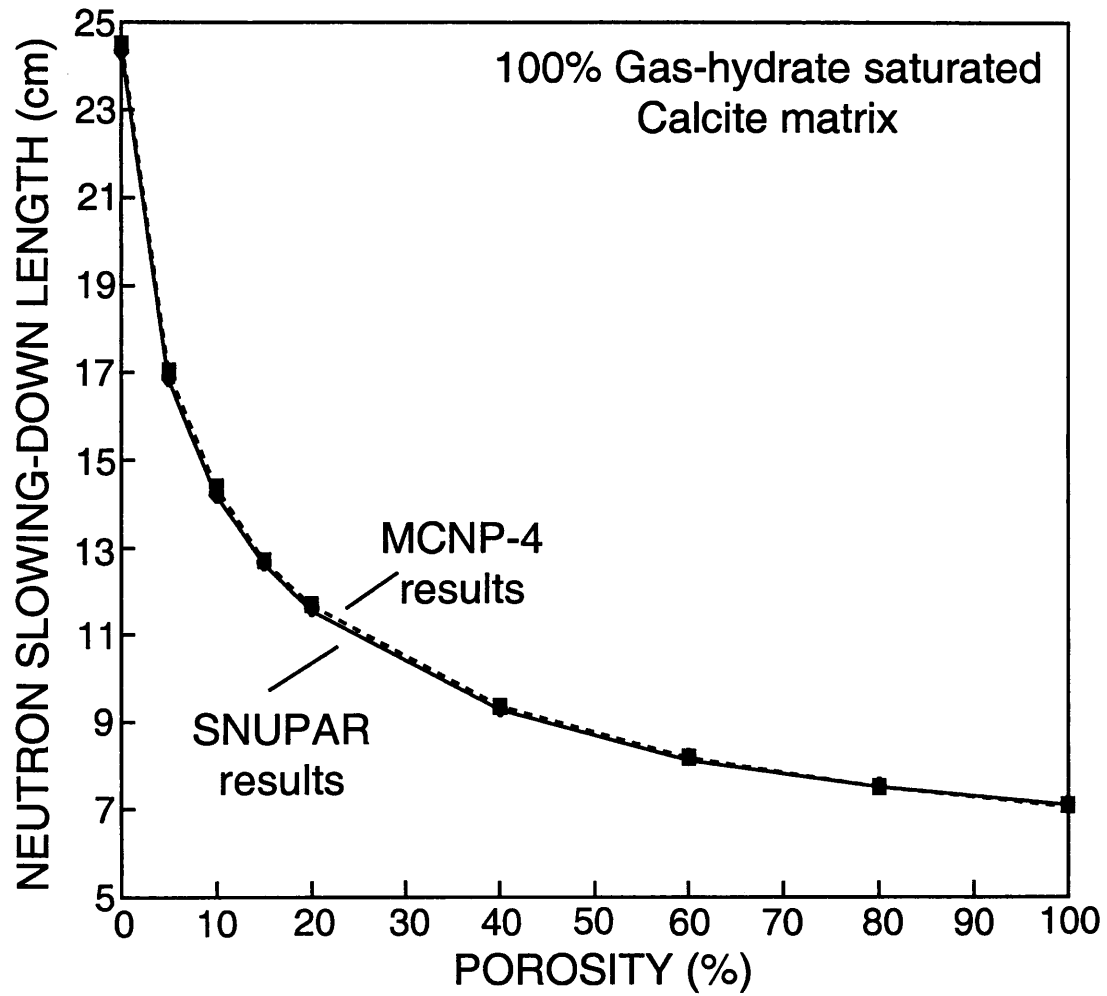
Figure 3.9d Comparison of MCNP-4- and SNUPAR-calculated neutron slowing-down lengths (L_S) in a gas-hydrate-saturated calcite limestone.

converted to weight percents for the four reservoir constituents (Structure-I methane

hydrate, water, quartz, and calcite) being considered in this SNUPAR and MCNP-4

comparison study. The required bulk-density data for Structure-I methane hydrate, water,

quartz, and calcite are also included in Table 3.5. Figure 3.9a-d, along with Table 3.9,

reveal that the calculated neutron parameters from the MCNP-4 code generally agree to

within a few percent with the SNUPAR results for most reservoir conditions studied. It

can be concluded that gas hydrates have relatively little effect on the neutron-porosity-log

response and the neutron correction crossplots in Figures 3.5 and 3.7, presented earlier in

this thesis, are valid.

3.4 Electrical Resistivity Logs

The electrical resistivity of most rock intervals is controlled by the pore-fluids.

The relation between rock and pore-fluid resistivity has been studied in numerous

laboratory and field experiments. From these studies, relations among porosity, pore-

fluid resistivity, and rock resistivity have been found, but the theoretical understanding of

these empirical findings is less than satisfactory. Among these findings is the empirical

relation established by Archie (Archie, 1942) which is used to estimate water saturations

in gas-oil-water-matrix systems (Figure 2.7). In comparison, gas-hydrate- and gas/oil-

bearing reservoirs appear to be characterized by relatively similar resistivities, which

suggest that the Archie relation may be used to calculate gas-hydrate saturations. In this

study, the usefulness of the Archie relation in gas-hydrate-bearing reservoirs has been

evaluated. Presented in this section and utilized in the field data application chapter

Table 3.9 Comparison of SNUPAR- and MCNP-4-calculated nuclear parameters for various reservoir constituents assuming a 4.5 MeV (AmBe) neutron source.

Reservoir constituent	Chemical formula	Bulk-density (g/cm^3)	SNUPAR calculated neutron slowing-down length (Ls, cm)	MCNP-4 calculated neutron slowing-down length (Ls, cm)
Pure water	H_2O	1.0	7.23	7.20±0.1
Quartz	SiO_2	2.65	28.81	29.5±0.8
Calcite	$CaCO_3$	2.71	24.33	24.5±0.4
Gas hydrate Structure-I	$7.598CH_4+$ $46H_2O$	0.9	7.12	7.1±0.5

(Chapter 5) of this thesis are three forms of the Archie relation which appear to yield useful gas-hydrate saturation data. Two additional electrical resistivity relations that deal with the effect of clay and clay-bound-water on the electrical properties of a clay-bearing reservoir rock are also examined in this section of the thesis. The equations and most of the concepts presented in this section are mostly from other previously published studies (Archie, 1942; Pearson et al., 1983). What is unique to this thesis is the application of conventional electrical resistivity relations to actual gas-hydrate-bearing reservoirs as described in Chapter 5.

Nearly all low to medium frequency (0 to 20,000 Hz) borehole electrical resistivity measurements are made with "focused" devices. Two types of tools exist: laterolog and induction tools. The induction log is generally recommended for holes drilled with moderate- to non-conductive drilling fluids. The laterolog, however, is generally recommended for holes drilled with very conductive drilling fluids (i.e., salt water) (Schlumberger Educational Services, 1989). The induction tool, being a conductivity-sensitive device, is most accurate in low- to medium-resistivity formations. The laterolog tool, being a resistivity device, is most accurate in medium- to high-resistivity formations. Since most gas-hydrate-bearing sediments exhibit very high electrical resistivities (Collett, 1983), a laterolog measurement would be preferred. However, four of the five sampled and logged gas-hydrate occurrences in the World (Table 1.3) have been logged with only dual induction devices. Therefore, the discussions in Chapter 5 pertaining to the actual field data resistivity logs should be

approached with caution because of the limited resolution of induction well-log data in high resistivity formations.

In the following discussion, the operational characteristics of both induction and laterolog devices will be discussed. The phasor dual induction - spherically focused resistivity tool (DITE-SFL) provides three different measurements of electrical resistivity (Table 3.2): deep induction (ILD), medium induction (ILM) and shallow spherically focused resistivity signals (SFL). The deep (ILD) and medium (ILM) induction devices transmit high-frequency alternating currents through transmitter coils, creating magnetic fields that induce secondary (foucault) currents in the formation. These ground-loop currents produce a new inductive signal, proportional to the conductivity of the formation, which is measured by the receiving coils. The measured conductivities are then converted to resistivities (in ohm-m). The SFL measures the current necessary to maintain a constant voltage drop across a fixed interval. The dual laterolog (DLL) provides two resistivity measurements with different depths of investigation into the formation: deep (LLd) and shallow (LLs). In both devices, a current beam is forced horizontally into the formation by using focusing currents, so no current flows into the borehole. The dual-laterolog response ranges from 0.2 to 40,000 ohm-m, thus permitting a good characterization of highly resistive rock formations such as gas-hydrate-bearing units.

The spontaneous potential (SP) log exhibits a relatively low (less negative) spontaneous-potential deflection in a gas-hydrate-bearing zone when compared to the

spontaneous-potential response in a free-gas zone. It is unlikely, however, that the spontaneous potential (SP) log can yield quantitative gas hydrate reservoir data.

Water content and pore-water salinity are the most significant factors controlling the electrical resistivity of a formation. Other factors influencing resistivity of a formation include the concentration of hydrous and metallic minerals, volume of hydrocarbons including gas hydrates, and pore structure geometry. As previously discussed, gas-hydrate-bearing sediments exhibit relatively high electrical-resistivities in comparison to water saturated units, which suggests that a resistivity log could be used to determine gas-hydrate saturations.

There is only one reported laboratory study of resistivities of (tetrahydrofuran) hydrate-bearing sediments (Figure 3.10, modified from Pearson et al., 1986); however, there is an extensive body of literature on the electrical properties of partially frozen sediments (reviewed by Hoyer et al., 1975). Because ice and gas hydrates are electrical insulators, the resistivities of gas hydrate and permafrost deposits are largely controlled by the salinity of the unfrozen pore-waters or brine inclusions. Archie's equation (Archie, 1942) is an empirical relationship between water content (saturation) and the resistivity of water-saturated sediments:

$$R_t = aR_w \varnothing^{-m} S_w^{-n} \qquad (3.7)$$

R_t = Formation resistivity (from log), ohm-m

a = Empirically-derived parameter
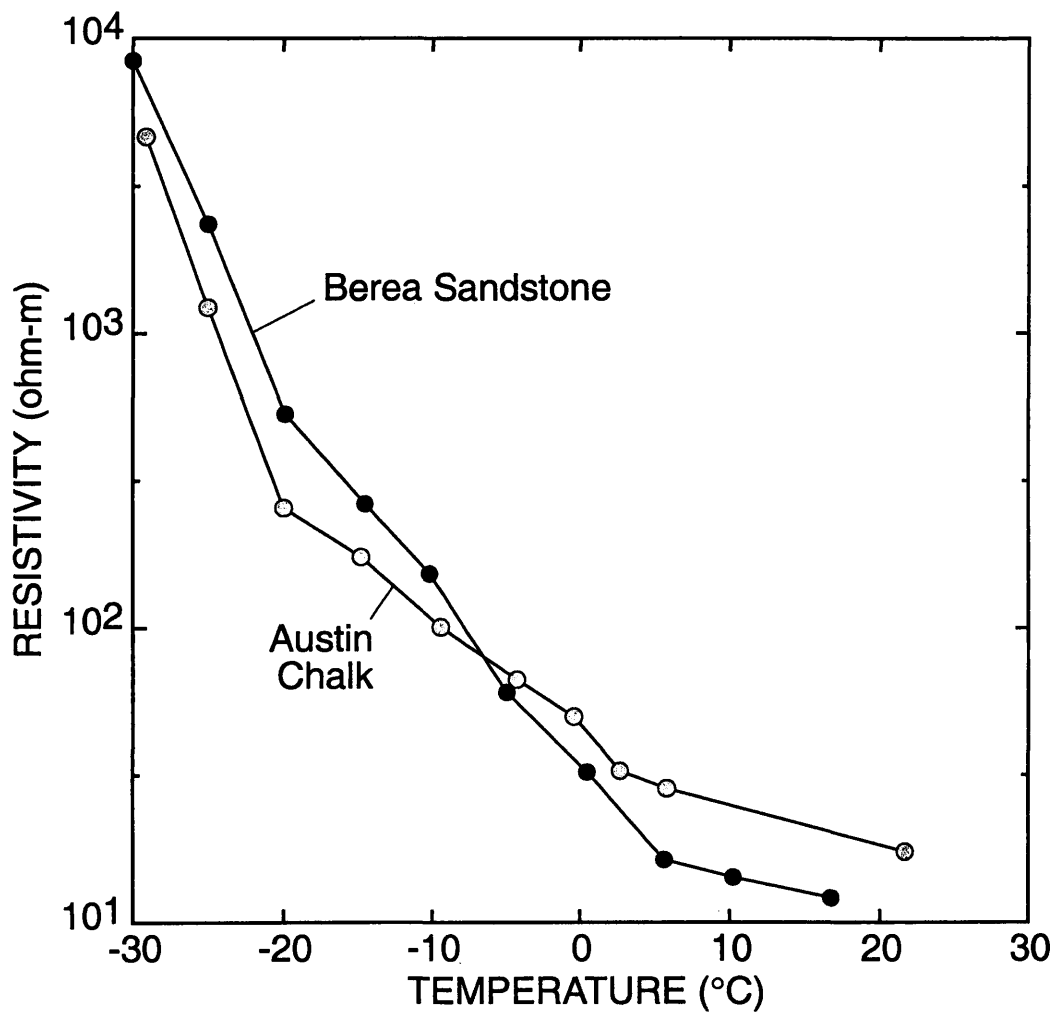
Figure 3.10 Laboratory-measured electrical resistivities of rock cores (Berea sandstone and Austin chalk) saturated with tetrahydrofuran hydrates (modified from Pearson et al., 1986).

R_W = Resistivity of formation water, ohm-m

$\varnothing$ = Porosity, fractional %

m = Empirically-derived parameter

S_W = Water saturation, fractional %

n = Empirically-derived parameter

To estimate water saturations (S_W) [gas-hydrate saturation (S_h) is equal to $(1.0\text{-}S_W)$] in

hydrocarbon-bearing sediments, the Archie equation is often rewritten as:

$$S_W = \left(\frac{aR_W}{\varnothing^m R_t} \right)^{\frac{1}{n}}$$ (3.8)

Pearson et al. (1983) have shown that as gas hydrates form in the laboratory or as

pore-waters freeze, the amount of bulk water decreases, S_W and R_W are reduced; S_W

because some of the available pore-space is now filled with a solid nonconductor, and R_W

because the dissolved salts are concentrated in the remaining unfrozen water. If the brine

is not near saturation, the effect of gas hydrate formation on R_W is relatively easy to

quantify because an increase in salt concentration causes a decrease in R_W. Including

both the temperature and salt concentration effects, the resistivity of a partially "frozen"

brine at temperature T is thus proportional to $(C)^{-T} S_W$ where C is a empirical parameter.

Substituting this relationship into Archie's equation (Equation 3.7) and dividing by the

resistivity at 0°C, the ratio of frozen (R_f) and thawed (R_O) resistivities becomes the

following relation (modified from Pearson et al., 1983):

$$\frac{R_f}{R_O} = C^{-T} S_W{}^{1-n} \qquad (3.9)$$

R_f = Frozen (gas-hydrate-bearing) formation resistivity

   (from log in the gas-hydrate-bearing interval),

   ohm-m

R_O = Thawed (non-gas-hydrate-bearing) formation

   resistivity (from log in a 100% water-saturated

   zone), ohm-m

C = Empirically-derived parameter (Table 3.10)

n = Empirically-derived parameter (Table 3.10)

S_W = Water saturation, fractional %

T = Formation temperature, °C

To use this relationship (Equation 3.9), one must know the empirical parameters C and n.

Fortunately, Pearson et al. (1983) have examined the relationship between formation

temperatures, pore-water resistivities, and formation resistivities. Values for the

empirical parameters (C, n) calculated by Pearson et al. (1983) are listed in Table 3.10. It

is now possible to use the above modified Archie equation to estimate water saturation in

a gas-hydrate-bearing stratigraphic unit. First the unfrozen (R_O: non-gas-hydrate-bearing)

Table 3.10 Empirical parameters for the modified Archie relation (modified from Pearson et al., 1983).

Reservoir lithology	n	C	a high salinity	low salinity
Sandstone (quartz)	2.1661	1.051	1.761	2.264
Limestone (calcite)	1.834	1.051	1.299	1.674
Unconsolidated material	1.715	1.051	0.551	0.710
Pooled estimate	1.9386	1.057	1.035	

resistivity must be known, which can be obtained from a water-saturated zone that has

reservoir properties similar to the gas-hydrate-bearing interval. It should also be noted

that the unfrozen resistivity (R_O: resistivity of non-gas-hydrate-bearing sediments) can be

calculated with the following relation: $R_O = R_W F$, if R_W (resistivity of the unfrozen pore-

water) and $\varnothing$ (porosity) are known and assuming the formation factor (F) can be

calculated by the relation: $F = a\varnothing^{-m}$. The variables a and m are empirical parameters

from the Archie relation (see discussion below). The "frozen" (gas hydrate) resistivity is

obtained from the (deep) resistivity log in the gas-hydrate-bearing portion of the reservoir

and the formation temperature is estimated from other sources. The utility of the Pearson

et al. (1983) modified Archie relation is assessed in Chapter 5 of this thesis.

Another resistivity approach for assessing gas-hydrate saturations is based on a

modification of the so-called "quick look" log analysis technique that compares the

resistivity of a water-saturated sediment (R_O) to the resistivity of a hydrocarbon-bearing

sediment (R_t). It is proposed here that the deep reading resistivity-log data can be used to

calculate water saturations (S_W) [gas-hydrate saturation (S_h) is equal to ($1-S_W$)] using the

following Archie relation:

$$S_W = \left(\frac{R_O}{R_t}\right)^{\frac{1}{n}} \tag{3.10}$$

where R_O is the resistivity of the sedimentary section if it contained only water (S_w=1.0), R_t is the resistivity of the hydrocarbon-bearing intervals (log value from gas-hydrate-bearing interval), and n is an empirically-derived Archie parameter (Table 3.10). This Archie relation is based on the following logic: if the pore-space of a sediment is 100% saturated with water, the deep-reading resistivity device will measure the resistivity of the 100% water-saturated section (R_O). This measured R_O value is considered to be a relative baseline from which hydrocarbon (gas hydrate) saturations can be determined within nearby hydrocarbon-bearing intervals.

The logic behind this R_O/R_t method is similar to the supporting logic behind the Pickett crossplot method. As discussed in Chapter 1 of this thesis (Figure 1.7) and in Collett (1993b), a Pickett crossplot method assumes that if the pore-space of a rock unit is 100% saturated with water, the deep resistivity device will record the resistivity of the 100% water-saturated rock unit (R_O). This water-saturated unit is considered a relative baseline from which hydrocarbon saturations can be determined. If the salinity of the pore-fluids is known to be constant within the units being studied, the recorded resistivity measurements can be plotted on a Pickett crossplot, and any deviation from the known 100% water-saturated resistivity measurement would indicate the presence of hydrocarbons. Figures 3.11 and 3.12 are plots of the three component (water-hydrate-matrix) modified "quick look" Archie relation for marine (Reservoir Model C, Figure 2.8c) and terrestrial (Reservoir Model A, Figure 2.8a) sediments, respectively. In both Figures 3.11 and 3.12 it is assumed that R_O (resistivity of the 100% water-saturated rock
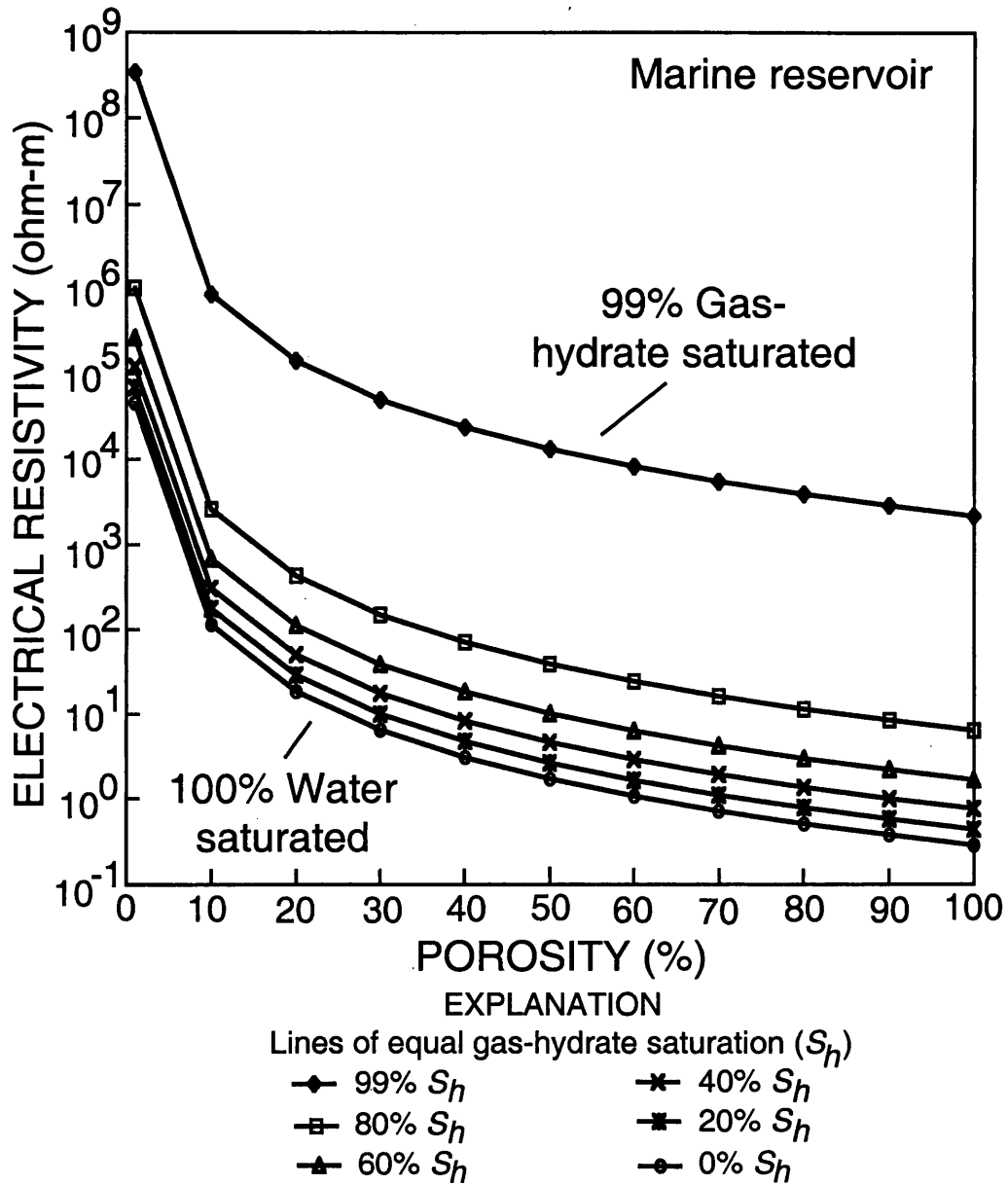
Figure 3.11 Plot of the modified "quick look" Archie relation (Equation 3.10) for a water- and gas-hydrate-bearing marine sediment (Reservoir Model C, Figure 2.8c).
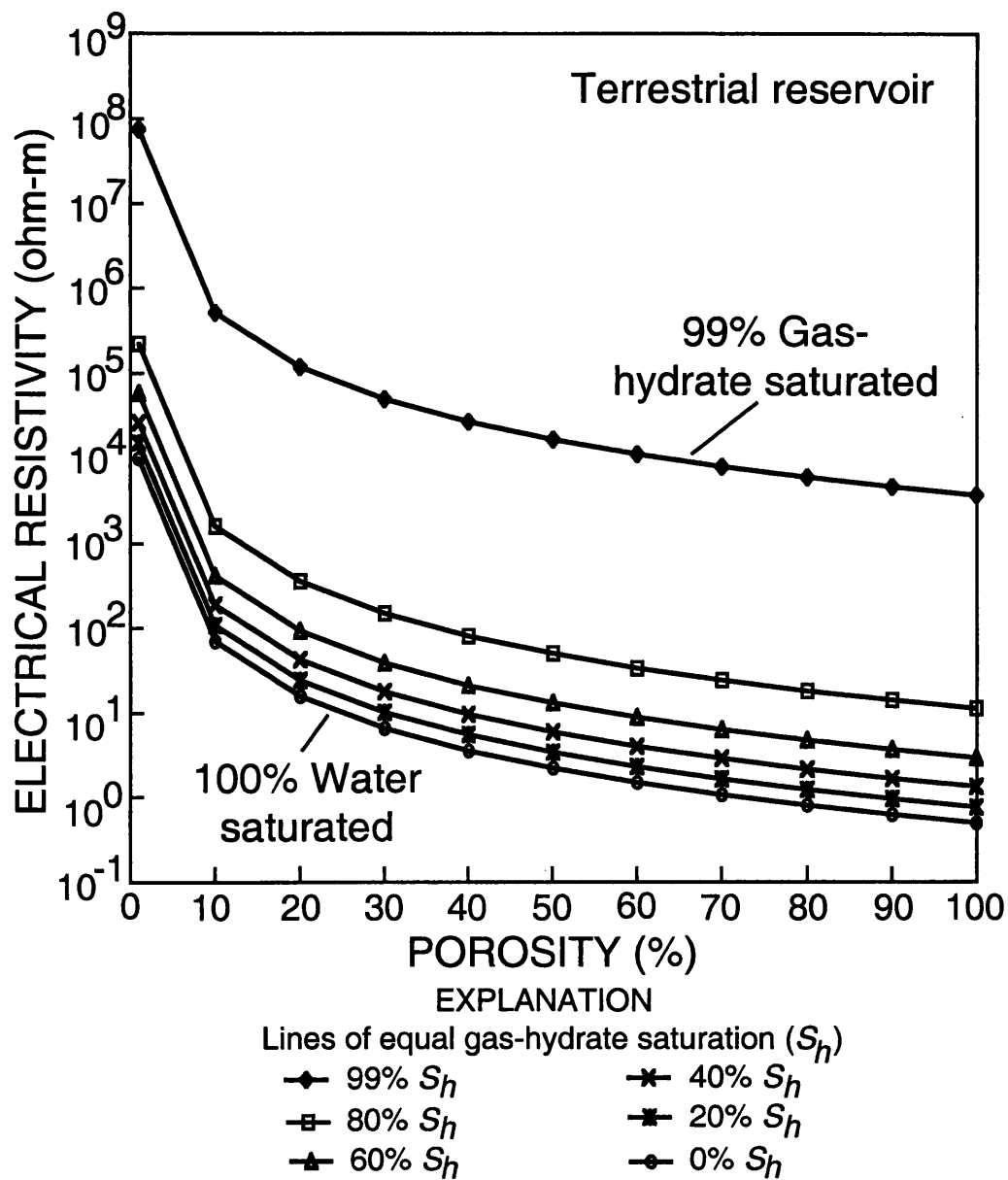
Figure 3.12 Plot of the modified "quick look" Archie relation (Equation 3.10) for a water- and gas-hydrate-bearing terrestrial (quartz sandstone) sediment (Reservoir Model A, Figure 2.8a).

unit) can be determined from the relation: $R_O = (R_W)\,(a\varnothing^{-m})$ and R_t is the log-measured

deep resistivity of the gas-hydrate-bearing rock interval. In the marine case (Figure

3.11), R_W is assumed to be 0.26 ohm-m (32 ppt pore-water salinity at 10°C), a and m are

equal to 1.1 and 2.6 respectively (calculated for sediments on the Blake Ridge; see

Chapter 5 of this thesis), and n is equal to 1.9386 (from Pearson et al., 1983). Figure 3.11

also assumes no corrections for the presence of clay/shale. In the terrestrial case (Figure

3.12), R_W is assumed to be 0.8 ohm-m (10 ppt pore-water salinity at 10°C), a and m are

equal to 0.62 and 2.15 respectively (from the Humble relation, reviewed by

Schlumberger Educational Services, 1989), and n is equal to 1.9386 (from Pearson et al.,

1983).

Most resistivity-log measurements and interpretations are concerned with

ascertaining hydrocarbon saturation information. However, resistivity-log data from

coreholes drilled in the Deep Sea Drilling Project (DSDP) and the Ocean Drilling

Program (ODP) are commonly used to calculate sediment porosities (Shipboard

Scientific Party, 1996). Sediment porosities can be determined from the resistivity logs

by using the Archie relation (Equation 3.7 discussed above) and assuming a water

saturation equal to 1.0 in the hydrocarbon-free sedimentary sections. The Archie

relationship between the resistivity of the hydrocarbon free formation (R_t) and porosity

($\varnothing$) can be written as $R_t/R_W = a\varnothing^{-m}$, where a and m are empirical parameters to be

determined and R_W is the resistivity of the pore-waters. The empirical parameters a and

m can be calculated by a crossplot method (described in Serra, 1984) where the ratio

R_O/R_W is plotted (log-log scales) against porosity ($\varnothing$) of a water-bearing zone in the reservoir. A line projected through the plotted data represents the "water-line" for the formation, and m can be derived from its slope, and a from its intercept with the porosity axis at $\varnothing = 1.0$. The porosity data needed for this crossplot method can be from core studies, or from density and/or neutron porosity logs.

It is well established that the occurrence of shale (clay) in reservoir rocks can result in erroneous values of water saturations as calculated from downhole-log data. All of the Archie related equations discussed previously in this section of the thesis apply to non-shaly formations that contain only non-conductive insulating matrix rocks. Shale contained in rocks, however, conduct electricity which affects the logging tool measurements. Many log analysis models have been developed to account for the affect of shales on resistivity-log measurements. Considered in this study are only two of the more widely used shaly-sand interpretive models: (1) the Indonesian and (2) the Waxman-Smits.

The Indonesian model (Poupon and Leveaux, 1971) was developed to account for over estimation of water saturations in Indonesian shaly-sand reservoirs. It was recognized that the volume of shale (clay) affects the true electrical resistivity of a formation. The empirical Indonesian model which relates downhole-log measured electrical resistivities to water saturations was developed by statistically evaluating frequency crossplots of matrix clay volumes (V_{cl}) estimates and computed water saturations (S_W). The best results were obtained with the follow equation:

$$C_t = \frac{C_w}{F} S_w^2 + \left[2\left(\frac{C_w V_{sh}^{2-V_{sh}} C_{sh}}{F} \right)^{\frac{1}{2}} S_w^2 + V_{sh}^{2-V_{sh}} C_{sh} S_w^2 \right]$$

(3.11)

C_t = Formation conductivity (from log), ohm-m

C_w = Conductivity of formation water, ohm-m

C_{sh} = Conductivity of shale (clay), ohm-m

F = Formation factor

S_w = Water saturation, fractional %

V_{sh} = Shale (clay) volume, fractional %

The accurate selection of the input values for the Indonesian model is discussed in the field application section of this thesis (Chapter 5).

In 1968, Waxman and Smits (1968) proposed a saturation-resistivity relationship for shaly formations that related the resistivity contribution of the shale to the cation exchange capacity (CEC) of the shale. Simply stated, the Waxman-Smits equation requires the pore-water resistivities to be corrected for the contribution of conductive clay which is the function of the CEC of the clays. In 1974 Waxman and Thomas (1974) extended the Waxman-Smits relation to hydrocarbon-bearing shaly-sand reservoirs. The Waxman-Smits relation compares the electrical conductivity (C_t) of the hydrocarbon-bearing shaly-sand reservoir (through the formation factor, F) to the reservoir water saturations (S_w), water conductivity (C_w), and the CEC per unit pore-volume (B, Q_v):

$$C_t = \frac{C_w}{F} S_w^n + \frac{BQ_v}{F} S_w^{n-1}$$

(3.12)

where F and S_w are values related to the total interconnected pore-space. Waxman and

Smits (1968) introduced the parameter B to fit experimental deviations found at low

electrical conductivities. The term Q_v, was introduced to represent the CEC per unit

pore-volume (meq/ml) within the reservoir rock:

$$Q_v = \frac{(1 - \varnothing)\rho_m CEC}{100\varnothing}$$

(3.13)

In Chapter 5 of this thesis the CEC values were measured from available core samples

and used to calculate shale-corrected gas-hydrate saturations in two of the gas-hydrate

accumulations assessed in this study.

3.5 Acoustic Transit-Time Logs

Acoustic transit-time logs measure the propagation of elastic vibrations through a

medium. There are two main types of elastic waves; compressional and shear. The

attenuation of compressional and shear sound waves in rocks depends on many properties

of the rock, including density, porosity, hydrocarbon saturations, and the amount of

fracturing. In most acoustic well-log studies, the Wyllie time-average equation relates

the compressional velocity of the bulk reservoir material to the velocity of the rock

matrix and fluid to determine porosity. However, studies of seismic data from the eastern continental margin of the United States have shown that the volume of gas hydrate in marine sediments can be estimated by measuring interval velocities (Lee et al., 1993). Presumably, acoustic transit-time well logs can also be used to measure the amount of gas hydrate within a drilled sedimentary unit.

Since Lee et al. (1993), acoustic modeling of gas-hydrate accumulations has followed two general paths dealing with either the development of empirical acoustic relations or the application of multiphase wave scattering theory and grain contact models to directly calculate gas-hydrate concentrations for various geologic conditions. Lee et al. (1996) generally pursued the development of a series of empirical acoustic equations that appear to accurately predict the acoustic velocity of gas-hydrate-bearing sediments. Lee et al. (1996) also reintroduced and applied the multiphase wave scattering theory developed by Kuster and Toksöz (1974), to assess the acoustic properties of gas-hydrate-bearing sediments. An alternative gas hydrate acoustic model has been proposed in Dvorkin et al. (1991) and Dvorkin and Nur (1993, 1996) which is based on estimating acoustic properties of cemented gas-hydrate-bearing sediments from grain contact theory.

In this section of the thesis, a series of empirically derived seismic acoustic relations, originally developed by Wood (1941), Timur (1968), and Lee et al. (1993), that can be used to estimate the volume of gas hydrate in a sedimentary section have been reviewed and modified for the borehole environment. In Chapter 5 of this thesis, gas-hydrate saturations calculated by various well-log and core analysis methods have been compared. The results of the field case studies presented in Chapter 5 indicate that the

multiphase wave scattering theory of Kuster and Toksöz (1974) and the cementation

theory of Dvorkin et al. (1991) significantly overestimate gas-hydrate saturations.

Therefore, the discussions in this section of the thesis pertaining to the multiphase wave

scattering and cementation modeling techniques are limited.

Most of the equations and concepts presented in this section of the thesis on the

acoustic properties of gas-hydrate-bearing sediments are adapted from other previously

published studies (Wood, 1941; Timur, 1968; Kuster and Toksöz, 1974; Zimmerman and

King, 1986; Lee et al., 1993, 1996). Unique to this thesis was (1) the modification and

application of seismic-derived acoustic relations to the borehole environment and (2) the

development of techniques used to derive the input parameters (described in Chapter 5)

for each of the acoustic equations considered in this study.

In general, acoustic travel-time logs measure the time required for a

compressional sound-wave to travel through the formation between a transmitter and a

receiver. Some of the more advanced acoustic transit-time tools, such as the

Schlumberger dipole shear sonic imager, yield shear-wave acoustic data. Acoustic tools

provide direct measurement of sound velocity through sediments from the interval transit

time measured, and are likely to yield measurements free from the effects of formation

damage and enlarged borehole from drilling processes. This interval transit time is a

function of the formation matrix, the amount of primary porosity, and the type of material

in the pore-space. The configuration of the LSS-SDT (digital sonic cartridge) used in the

Ocean Drilling Program (ODP) is arranged in the array-sonic mode (Shipboard Scientific

Party, 1996). Due to the longer spacing of the transmitters and receivers, the LSS

provides improved velocity measurement and greater depths of investigations than shorter spaced acoustic tools. Interval transit times are converted to compressional-wave velocities (km/sec) and full waveforms are recorded by the tool allowing post-field processing to estimate shear- and Stoneley-wave velocities.

As previously discussed in Chapter 1 of this thesis, gas hydrates exhibit high acoustic velocities and, unlike gas or water, gas hydrates support shear-waves. Table 3.11 summarizes the available data on the acoustic properties of pure gas hydrates. Whalley (1980) calculated (no laboratory confirmation of calculations) the compressional-wave velocity of a pure methane and pure propane hydrate to be 3.76 and 3.78 km/sec, respectively, assuming the speed of sound in ice is 4.0 km/sec. Laboratory studies of Whiffen et al. (1982) yielded a compressional velocity for methane hydrate of 3.4 km/sec. Kiefte et al. (1985) spectroscopic studies of pure methane and pure propane hydrates also yielded a 3.4 km/sec compressional velocity for methane hydrate and a 3.6 km/sec compressional velocity for propane hydrate. Pandit and King (1982) obtained laboratory-derived compressional- and shear-wave velocities for a propane hydrate of 3.25 and 1.65 km/sec, respectively. Most recently, Helgerud et al. (1999) obtained laboratory-derived compressional-wave velocities through six compacted methane hydrate samples ranging from 3.40 to 3.70 km/sec. Helgerud et al. (1999) also observed in the laboratory shear-wave velocities in four of the methane hydrate samples ranging from 1.80 to 1.90 km/sec. In this thesis, it was assumed that the compressional velocity of a pure methane hydrate is 3.35 km/sec and the shear-wave velocity is 1.68 km/sec (Table 3.12).

Table 3.11 Acoustic velocities of various gas hydrates.

Type of gas hydrate	Compressional-wave velocity (V_p, km/sec)	Shear-wave velocity (V_S, km/sec)	Reference
Methane hydrate Structure-I	3.756	-	Whalley (1980)
Methane hydrate Structure-I	3.4		Whiffen et al. (1982)
Methane hydrate Structure-I	3.3		Kiefte et al. (1985)
Methane hydrate Structure-I	3.40-3.70	1.80-1.90	Helgerud et al. (1999)
Hydrogen sulfide hydrate Structure-I	3.35		Kiefte et al. (1985)
Propane hydrate Structure-II	3.78		Whalley (1980)
Propane hydrate Structure-II	3.25	1.65	Pandit and King (1982)
Propane hydrate Structure-II	3.6		Kiefte et al. (1985)

Table 3.12 Acoustic velocity, elastic constants, and bulk-densities for various reservoir constituents.

Reservoir constituent	V_p (km/sec)	V_s (km/sec)	Bulk-density (g/cm^3)	Bulk moduli (K, MPa)	Shear moduli (G, MPa)	Reference
Methane hydrate Structure-I	3.35[†]	1.68[††]	0.9	6713[†††]	2540[†††]	[†]Estimated from Whiffen et al. (1982) and Kiefte et al. (1985) [††]Estimated from Pandit and King (1982) [†††]Calculated from V_p-V_s
Pure water	1.5	0.00	1.00	2250	0	Schlumberger Educational Services (1989)
Ice	3.8	2.00	0.92	8400	3700	King (1984)
Quartz	5.98	4.04	2.65	38000	44000	Toksöz et al. (1976)
Clay	3.40	1.60	2.60	21200	6666	Tosaya and Nur (1982)
Marine sediment	4.37	2.60	2.70	27200	18300	Lee et al. (1996)

Timur developed the first three component time-average equation (modified Wyllie time-average equation) that can be used to directly calculate the volume of gas hydrate within a rock interval (Timur, 1968). Since its development, the Timur equation has been modified for numerous geologic conditions. Pearson et al. (1983) were the first to apply the Timur equation to hydrate-bearing rocks, and they concluded that it adequately predicted the acoustic properties of gas hydrates in consolidated rock media. They used the following three component, Timur time-average equation:

$$\frac{1}{V_b} = \frac{\varnothing(1 - S_h)}{V_w} + \frac{\varnothing S_h}{V_h} + \frac{(1 - \varnothing)}{V_m} \qquad (3.14)$$

$\varnothing$ = Porosity, fractional %

S_h = Hydrate saturation, fractional %

V_b = Log-measured bulk compressional velocity, km/sec

V_w = Water compressional velocity, km/sec

V_h = Hydrate compressional velocity, km/sec

V_m = Matrix compressional velocity, km/sec

Several workers (reviewed by Lee et al., 1993) have shown that the observed velocity behavior of some sedimentary rocks is not always consistent with the predictions of the Timur time-average model. Four of the conditions causing discrepancies are (reviewed by Lee et al., 1993): (1) the degree of rock consolidation, (2) presence of organic matter in the sediments, (3) high clay content of the sediments, and (4) secondary porosity. The

first three conditions apply to sediments found on the Blake Ridge and in most deep marine environments: they are unconsolidated, contain about 50% clay minerals, and have an organic carbon content that ranges from 0.5 to 1.4%. Thus, the interval velocities computed from the time-average or modified time-average equations do not fit the observed interval velocities obtained from DSDP/ODP samples on the Blake Ridge (Shipboard Scientific Party, 1996). It has been proposed that a modified version of the Wood equation (Wood, 1941), which is approximately valid for particles in suspension, could be used to overcome the problems with the time-average equation. Like the three component time-average equation, the modified Wood equation for gas-hydrate-bearing sediments can be written as:

$$\frac{1}{\rho_b V_b^2} = \frac{\varnothing(1-S_h)}{\rho_w V_w^2} + \frac{\varnothing S_h}{\rho_h V_h^2} + \frac{(1-\varnothing)}{\rho_m V_m^2} \tag{3.15}$$

$\varnothing$ = Porosity, fractional %

S_h = Hydrate saturation, fractional %

V_b = Log-measured bulk compressional velocity, km/sec

V_w = Water compressional velocity, km/sec

V_h = Hydrate compressional velocity, km/sec

V_m = Matrix compressional velocity, km/sec

ρ_b = Bulk-density, g/cm^3 [ρ_b = (1-$\varnothing$)ρ_m + (1-S_h)$\varnothing\rho_w$ + $S_h\varnothing\rho_h$]

ρ_w = Water density, g/cm^3

ρ_h = Hydrate density, g/cm^3

ρ_m = Matrix density, g/cm^3

Similar to the Timur equation, the modified Wood equation does not always accurately predict observed velocity-porosity relations in marine sediments (reviewed by Nobes et al., 1986). Figures 3.13 and 3.14 are plots of the three component (water-hydrate-matrix) Timur equation for marine (Reservoir Model C, Figure 2.8c) and terrestrial/quartz (Reservoir Model A, Figure 2.8a) sediments, respectively. Figures 3.15 and 3.16 are plots of the three component (water-hydrate-matrix) Wood equation for marine (Reservoir Model C, Figure 2.8c) and terrestrial/quartz (Reservoir Model A, Figure 2.8a) sediments, respectively.

Lee et al. (1993) have proposed an acoustic equation for interval velocities within marine gas-hydrate-bearing sediments that uses weighted means of the Timur and modified Wood equations, that is:

$$\frac{1}{V_b} = \left[\frac{W\varnothing(1-S_h)^r}{V_{Wood}} \right] + \left[\frac{1-W\varnothing(1-S_h)^r}{V_{Timur}} \right] \tag{3.16}$$

$\varnothing$ = Porosity, fractional %

S_h = Hydrate saturation, fractional %

V_b = Log-measured bulk compressional velocity, km/sec

r = Gas hydrate cementation constant
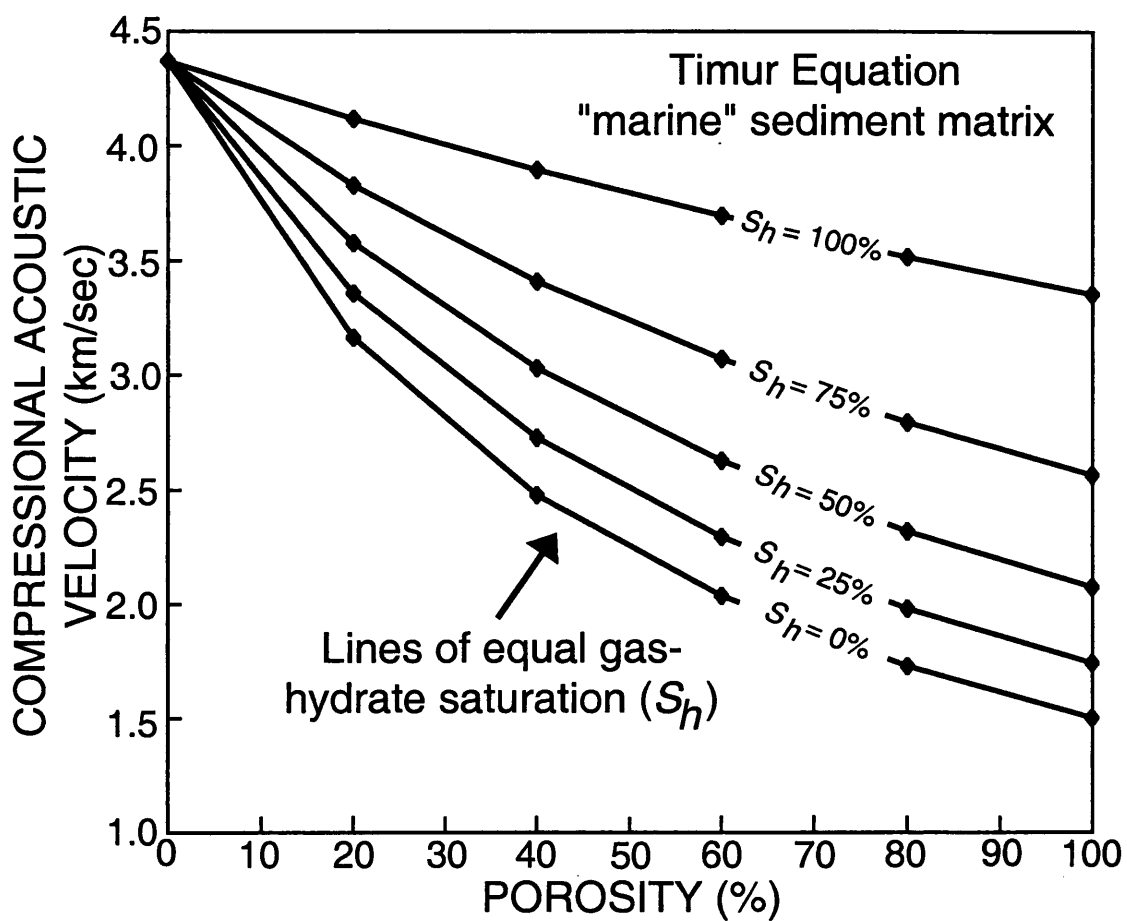
Figure 3.13 Plot of the three-component Timur compressional-wave (V_p) acoustic equation (Equation 3.14) for a water- and gas-hydrate-bearing marine sediment (Reservoir Model C, Figure 2.8c).

Figure 3.14 Plot of the three-component Timur compressional-wave (V_p) acoustic equation (Equation 3.14) for a water- and gas-hydrate-bearing terrestrial (quartz sandstone) sediment (Reservoir Model A, Figure 2.8a).
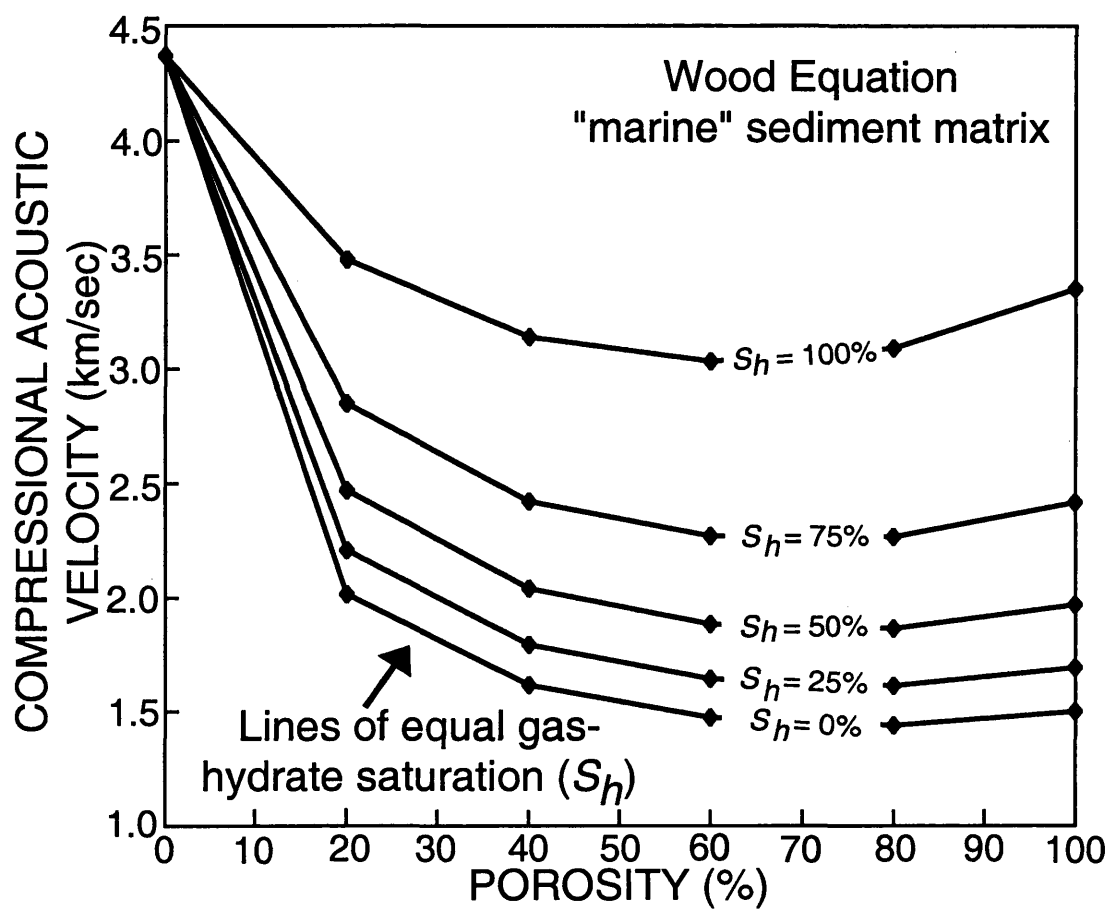
Figure 3.15 Plot of the three-component modified Wood compressional-wave (V_p) acoustic equation (Equation 3.15) for a water- and gas-hydrate-bearing marine sediment (Reservoir Model C, Figure 2.8c).

Figure 3.16 Plot of the three-component modified Wood compressional-wave
(V_p) acoustic equation (Equation 3.15) for a water- and gas-hydrate-bearing
terrestrial (quartz sandstone) sediment (Reservoir Model A, Figure 2.8a).

W = Weighting factor (most cases = 1)

V_{Wood} = Results of the Wood equation, km/sec

V_{Timur} = Results of the Timur equation, km/sec

In this proposed weighted average equation, a value of W>1 favors the Wood equation (particles in suspension) and W<1 favors the Timur equation (consolidated matrix). Figures 3.17 and 3.18 are plots of the three component (water-hydrate-matrix) Lee equation for marine (Reservoir Model C, Figure 2.8c) and terrestrial/quartz (Reservoir Model A, Figure 2.8a) sediments, respectively.

The relationship between compressional velocity and porosity for 100% water-saturated (no gas hydrate) unconsolidated sediments sampled during ODP Leg 164 (Sites 994 and 995; Shipboard Scientific Party, 1996) on the Blake Ridge is shown in Figure 3.19 together with theoretical 100% water-saturation curves of the Timur, Wood, and Lee (S_h=0, W=1, r=1) equations. In Figure 3.19, the matrix velocity in the Timur, Wood, and Lee equations is set equal to the value of the velocity for zero porosity and 65% clay content, 4.37 km/sec (Table 3.12). The Lee equation more accurately predicts the observed velocity-porosity relations on the Blake Ridge than either the Timur or Wood equations for the case where no gas hydrate is present (Figure 3.19).

The weight factor (W) and the gas hydrate cementation exponent (r) allow the Lee equation to be used for sediments with different consolidation characteristics and/or gas hydrate content. In order to use the proposed Lee equation, the W and r values that best fit the available velocity-porosity data must be selected. The weight factor variable, W,
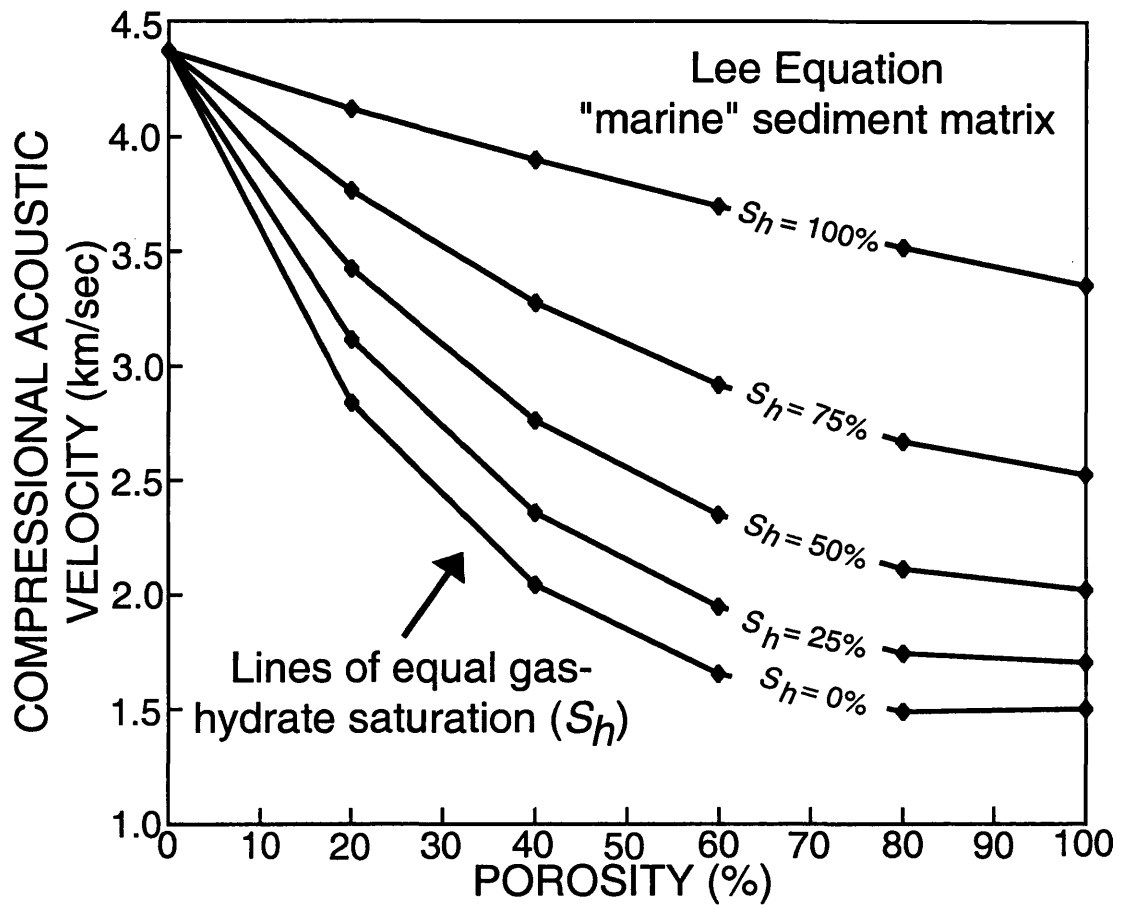
Figure 3.17 Plot of the three-component Lee compressional-wave (V_p) acoustic equation (Equation 3.16) for a water- and gas-hydrate-bearing marine sediment (Reservoir Model C, Figure 2.8c).
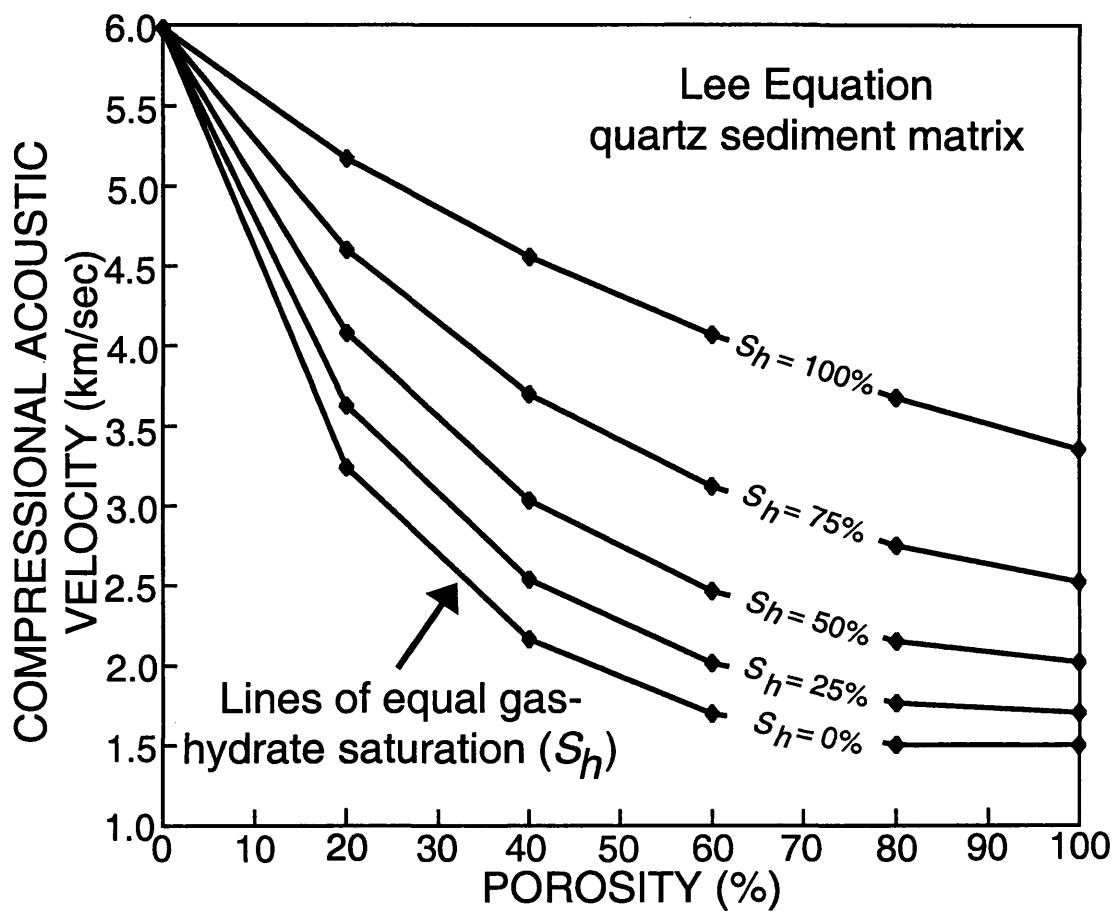
Figure 3.18 Plot of the three-component Lee compressional-wave (V_p) acoustic equation (Equation 3.16) for a water- and gas-hydrate-bearing terrestrial (quartz sandstone) sediment (Reservoir Model A, Figure 2.8a).
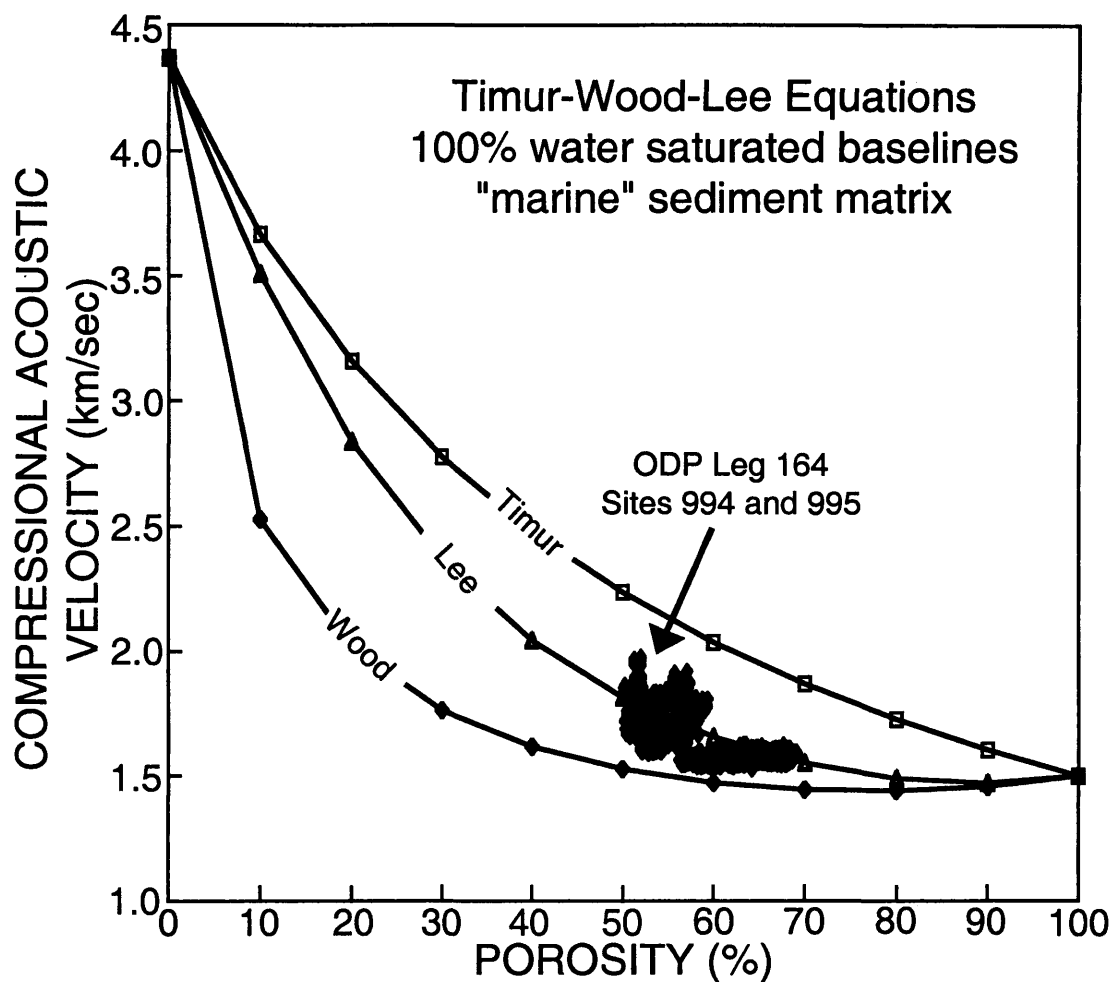
Figure 3.19 Graph showing downhole-log-derived compressional-wave velocities (V_p) and core-derived porosities for water-saturated sediments (no hydrocarbons) at ODP Sites 994 and 995 on the Blake Ridge. Also shown are the 100% water-saturated porosity-velocity curves predicted from the Timur (Equation 3.14), modified Wood (Equation 3.15), and Lee (Equation 3.16) compressional-wave (V_p) acoustic equations (marine sediment matrix, Reservoir Model C, Figure 2.8c).

can be estimated from field velocity-porosity data for sediments which contain no gas

hydrate. An example of the method used to determine the weight factor (W) is shown in

Figure 3.20, where the constant W is estimated by statistically fitting the field velocity-

porosity data with a series of theoretical (water saturation) curves calculated from the Lee

equation assuming different values for W. In this example (Figure 3.20), core-derived

porosity data and log-derived compressional velocity data from the water-saturated (no

hydrate or free-gas) portions of ODP Holes 994D and 995B on the Blake Ridge (ODP

Leg 164 drill-sites are discussed in more detail in Chapter 5 of this thesis) have been

plotted along with various curves calculated from the Lee equation (assumed W values of

0.7, 1.0, 1.1, and 1.3). In Figure 3.20, a W of 1.1 best fits the sediment porosity and

velocity conditions on the Blake Ridge. In this example, the best fit Lee equation derived

porosity-velocity model curve is selected such that the plotted porosities and velocities

from water-saturated zones in the Blake Ridge core holes fall on or below the best fit Lee

model curve for a specific W value.

The gas hydrate cementation exponent (r) simulates the amount of sediment

"cementation" that can be attributed to the occurrence of gas hydrates in sedimentary

section. As the cementation exponent (r) increases, the velocity predicted by the Lee

equation approaches that of the Timur equation at lower gas-hydrate saturations (Figure

3.21). When $r=1$, the Lee equation approaches the Timur equation at near 95% gas-

hydrate saturation; but when $r=32$, the Lee equation approaches the Timur equation near

10% gas-hydrate saturation. In general, a cementation exponent (r) of 32, best represents

sediments where gas hydrates occur at granular contacts and cement the grains together,
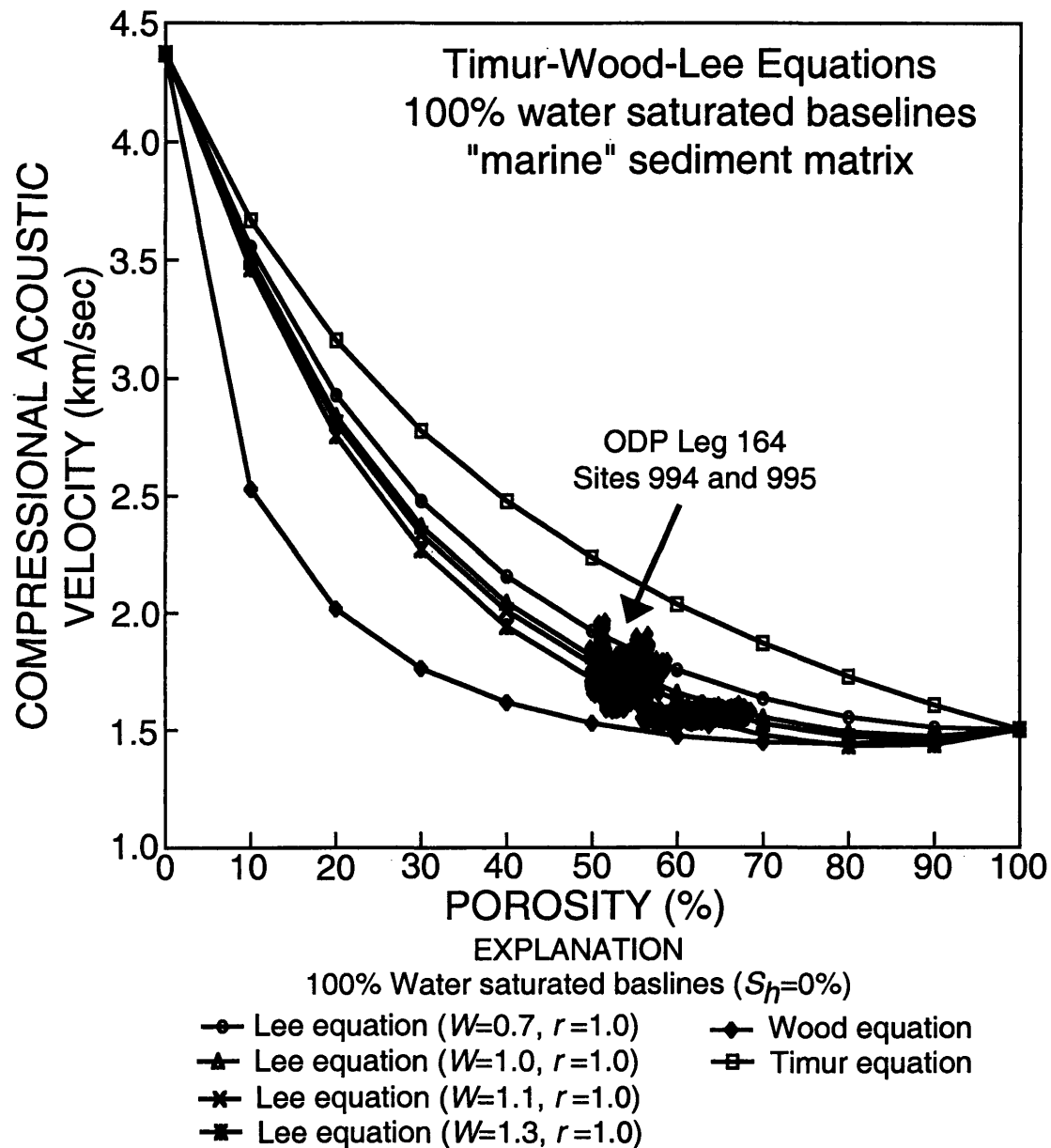
Figure 3.20 Graph showing downhole-log-derived compressional-wave velocities (V_p) and core-derived porosities for water-saturated sediments (no hydrocarbons) at ODP Sites 994 and 995 on the Blake Ridge. Also shown are the 100% water-saturated porosity-velocity curves predicted from the Timur (Equation 3.14), modified Wood (Equation 3.15), and a series of Lee (Equation 3.16) compressional-wave (V_p) acoustic equations that assume different Lee weight factors (W) (Reservoir Model C, Figure 2.8c).
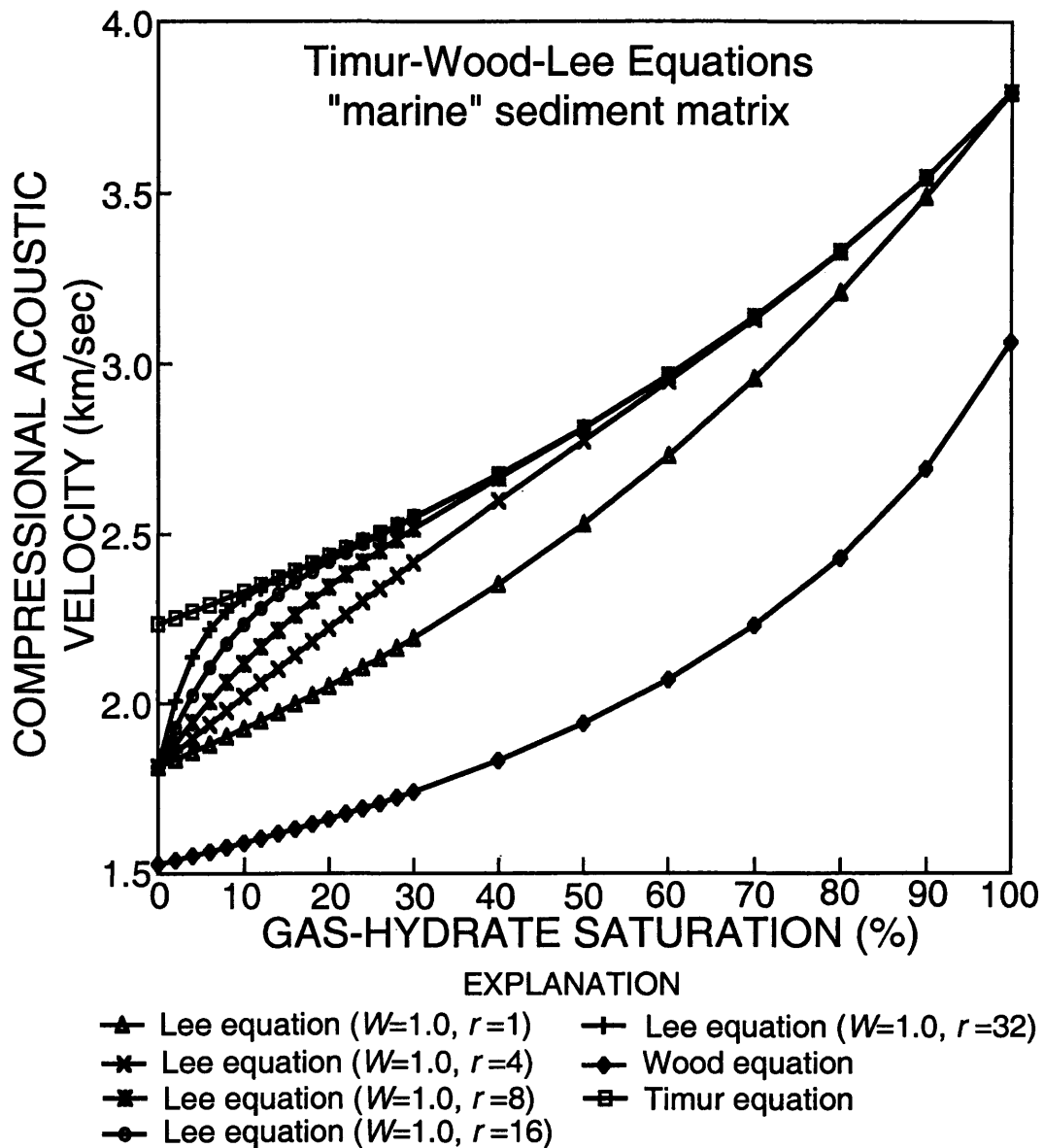
Figure 3.21 Graph showing predicted compressional velocities (V_p) for a marine sediment with respect to gas-hydrate saturation and the gas hydrate cementation exponent (r) using the Lee compressional-wave acoustic equation (Equation 3.16). The Timur (Equation 3.14) and modified Wood (Equation 3.15) predicted compressional-wave velocities (V_p) are also plotted for comparison (marine sediment matrix, Reservoir Model C, Figure 2.8c).

whereas a low cementation exponent (r) may best represent unconsolidated sediments where the gas hydrate is suspended in the pore-spaces between grains. Therefore, the two gas-hydrate pore-models (Model 1 and 2; Figure 2.6), discussed in Section 2.4 of this thesis, can be further evaluated by assessing the value of the cementation exponent (r) for various gas-hydrate-bearing reservoirs. In the pore-model (Model 1; Figure 2.6) where gas hydrate cements grain contacts the cementation exponent (r) will approach 32, and if gas hydrates are located away from the grain contacts (suspended in the pore-spaces) in the sediments (Model 2; Figure 2.6) the cementation exponent (r) will approach 1. However, the accuracy of estimating the gas hydrate cementation exponent (r) is not good.

All of the previous acoustic log-related discussions in this section of the thesis have dealt with the compressional-wave velocity of gas-hydrate-bearing sediments. Recently, however, Lee et al. (1996) have used an empirical relationship developed by Castagna et al. (1985) to calculate shear-wave velocities from compressional-wave velocities for various hypothetical gas-hydrate occurrences. Lee et al. (1996) proposed that the following three component equation can be used to evaluate the effect of gas hydrates on the compressional- and shear-wave velocity of a gas-hydrate- and water-bearing sediment. The shear-wave velocity for a three component system can be represented as:

$$V_s = V_p[\alpha(1-\varnothing) + \beta\varnothing S_h + \gamma\varnothing(1-S_h)],$$
(3.17)

where

$$\alpha = V_S / V_p \mid \text{matrix} \quad \beta = V_S / V_p \mid \text{hydrate} \quad \gamma = V_S / V_p \mid \text{water}$$

Since water cannot support shear-waves, the last term in the above equation can be dropped. In Figures 3.22 and 3.23, compressional velocity data from the Lee weighted average equation (Figures 3.17 and 3.18) have been converted to shear-wave velocities, by the method proposed by Lee et al. (1996), for various gas-hydrate reservoir conditions. Reservoir conditions depicted in Figures 3.22 and 3.23 include both marine (Reservoir Model C, Figure 2.8c) and terrestrial/quartz (Reservoir Model A, Figure 2.8a) systems.

An alternative approach to using the Timur, Wood, or Lee equations to evaluate gas-hydrate-bearing reservoirs is to use the three component acoustic model developed by Zimmerman and King (1986). The Zimmerman and King (1986) three component model was developed to predict compressional- and shear-wave velocities in permafrost and it is based on the two component wave scattering theory of Kuster and Toksöz (1974). Because the acoustic properties of ice are similar to those of gas hydrate (reviewed by Sloan, 1998), the Zimmerman and King (1986) approach should be applicable to the study of gas hydrates. Zimmerman and King (1986) showed that the theory worked well in predicting velocities in unconsolidated ice-bearing sediments. However, the Zimmerman and King (1986) three component model successfully predicts velocity-porosity-saturation relations for only a narrow range of porosities (30-50%) and for low water saturations (less than 60%). Hence its use in shallow marine sediments, which often have porosities ranging from 50 to 70 percent and high water saturations is
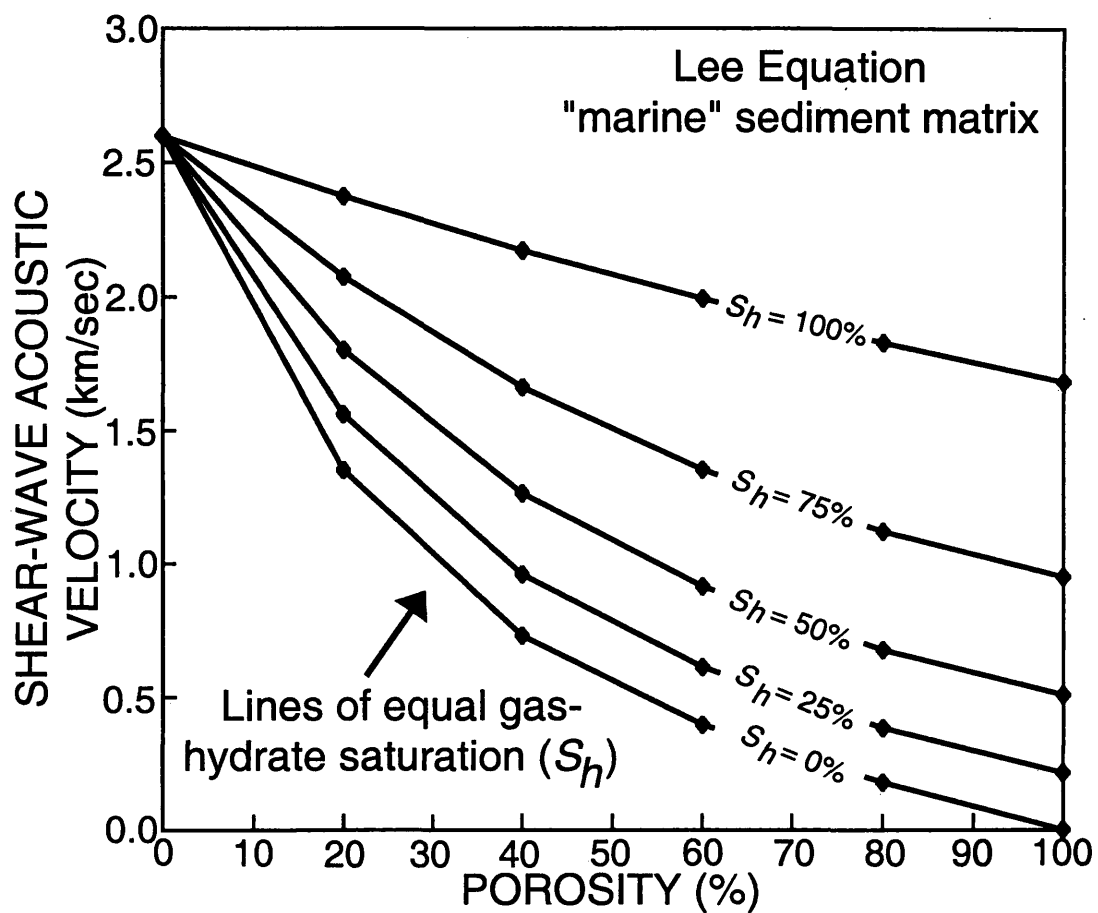
Figure 3.22 Plot of shear-wave velocities (V_S) of a marine gas-hydrate-bearing sediment (Reservoir Model C, Figure 2.8c) derived from the Lee compressional-wave acoustic equation (Equation 3.16) and converted to shear-wave velocities (V_S) with Equation 3.17.
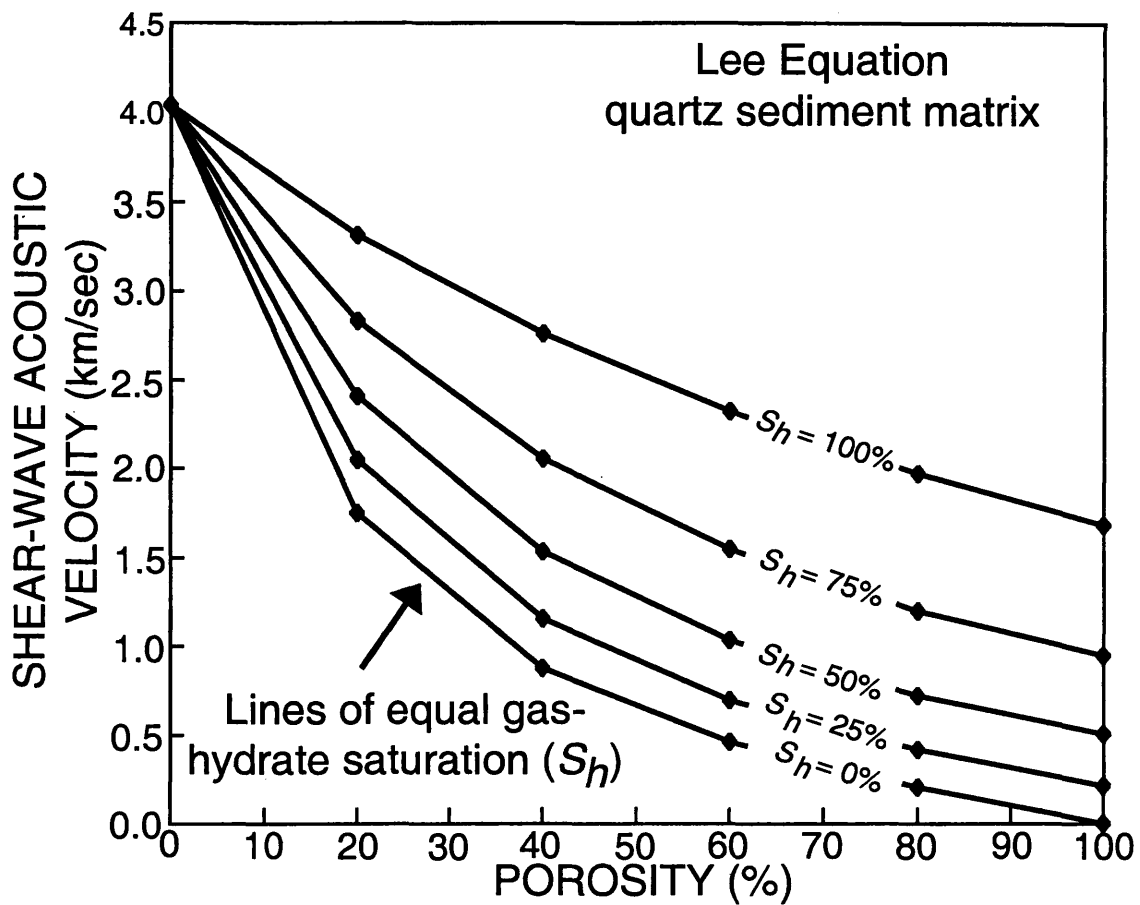
Figure 3.23 Plot of shear-wave velocities (V_S) of a terrestrial (quartz sandstone) gas-hydrate-bearing sediment (Reservoir Model A, Figure 2.8a) derived from the Lee compressional-wave acoustic equation (Equation 3.16) and converted to shear-wave velocities (V_S) with Equation 3.17.

limited. Following Zimmerman and King (1986), it was assumed in this study that the unconsolidated gas-hydrate-bearing sediments can be modeled as an assemblage of spherical quartz grains imbedded in a matrix of spherical inclusions of water and gas hydrate. The three component (hydrate-water-matrix) acoustic model is computed by first calculating the effective bulk (K) and shear (G) moduli of the gas hydrate (matrix component) and water (inclusion component) mixture with the two component Kuster-Toksöz equations. The Kuster-Toksöz equations for the effective bulk (K) and shear (G) moduli are:

$$\frac{K}{K_m} = \frac{1 + \left[4G_m(K_i - K_m)/(3K_i + 4G_m)K_m\right]c}{1 - \left[(K_i - K_m)/(3K_i + 4G_m)\right]c}$$

(3.18)

and,

$$\frac{G}{G_m} = \frac{(6K_m + 12G_m)G_i + (9K_m + 8G_m)\left[(1-c)G_m + cG_i\right]}{(9K_m + 8G_m)G_m + (6K_m + 12G_m)\left[(1-c)G_i + cG_m\right]}$$

(3.19)

where subscripts m and i indicate matrix and inclusion, and c is the fractional inclusion concentration. In the second part of this three component calculation, spherical quartz grains are modeled as imbedded particles in an homogeneous two component medium of gas hydrate and water for which the "mixed" elastic modulus was previously calculated. The Kuster-Toksöz equations are again used to calculate the required bulk (K) and shear

(*G*) moduli for the three component (hydrate-water-matrix) model. The computed bulk

(*K*) and shear (*G*) moduli for the three component system can be used to compute the

compressional (*Vp*) and shear (*Vs*) wave velocities of the three component mixture with

the following relations from Gassmann (1951):

$$V_p = \left[\frac{(K + \frac{4}{3}G)}{\rho_b} \right]^{\frac{1}{2}} \tag{3.20}$$

and,

$$V_s = \left[\frac{G}{\rho_b} \right]^{\frac{1}{2}} \tag{3.21}$$

where the bulk-density (ρ_b) of the three component mixtures is given by (discussed in

Section 3.2 of this thesis):

$$\rho_b = (1 - \varnothing)\rho_m + (1 - S_h)\varnothing\rho_w + S_h\varnothing\rho_h \tag{3.2}$$

ρ_b = Bulk-density, g/cm^3

ρ_m = Matrix density, g/cm^3

ρ_w = Water density, g/cm^3

ρ_h = Hydrate density, g/cm^3

S_h = Hydrate saturation, fractional %

$\emptyset$ = Porosity, fractional %

The results of this modified Kuster-Toksöz model for various reservoir porosity and gas-hydrate saturation conditions are plotted in Figures 3.24 and 3.25. Kuster-Toksöz predicted compressional-wave velocities for gas-hydrate-bearing sediments are much less than the velocities predicted by the Timur, Wood, or Lee equations and are closer to the results of the Wood equation. The results of the modified Kuster-Toksöz gas hydrate modeling efforts have been further compared in Figure 3.26 by plotting the ratio (V_p/V_s) of the calculated compression- and shear-wave velocities as a product of various reservoir porosities and gas-hydrate saturations. Figure 3.26 reveals that the V_p/V_s ratio in a gas-hydrate-bearing sediment is only moderately sensitive to porosity changes, and the V_p/V_s ratio decreases with increasing gas hydrate concentrations, which implies that V_p/V_s ratios can also be used to assess gas-hydrate reservoir saturations.

3.6 Neutron Spectroscopy Logs

Neutron-induced gamma ray spectroscopic well logging has been established as a means of evaluating the chemical composition of hydrocarbon reservoirs. The geochemical tool string (GLT; Figure 3.1) provides measurements of most of the elements present in rock-forming minerals, which can be used to construct detailed mineralogic models. In addition, GLT-derived data on the carbon and oxygen content of hydrocarbon reservoirs can be used to determine oil and gas saturation information. In
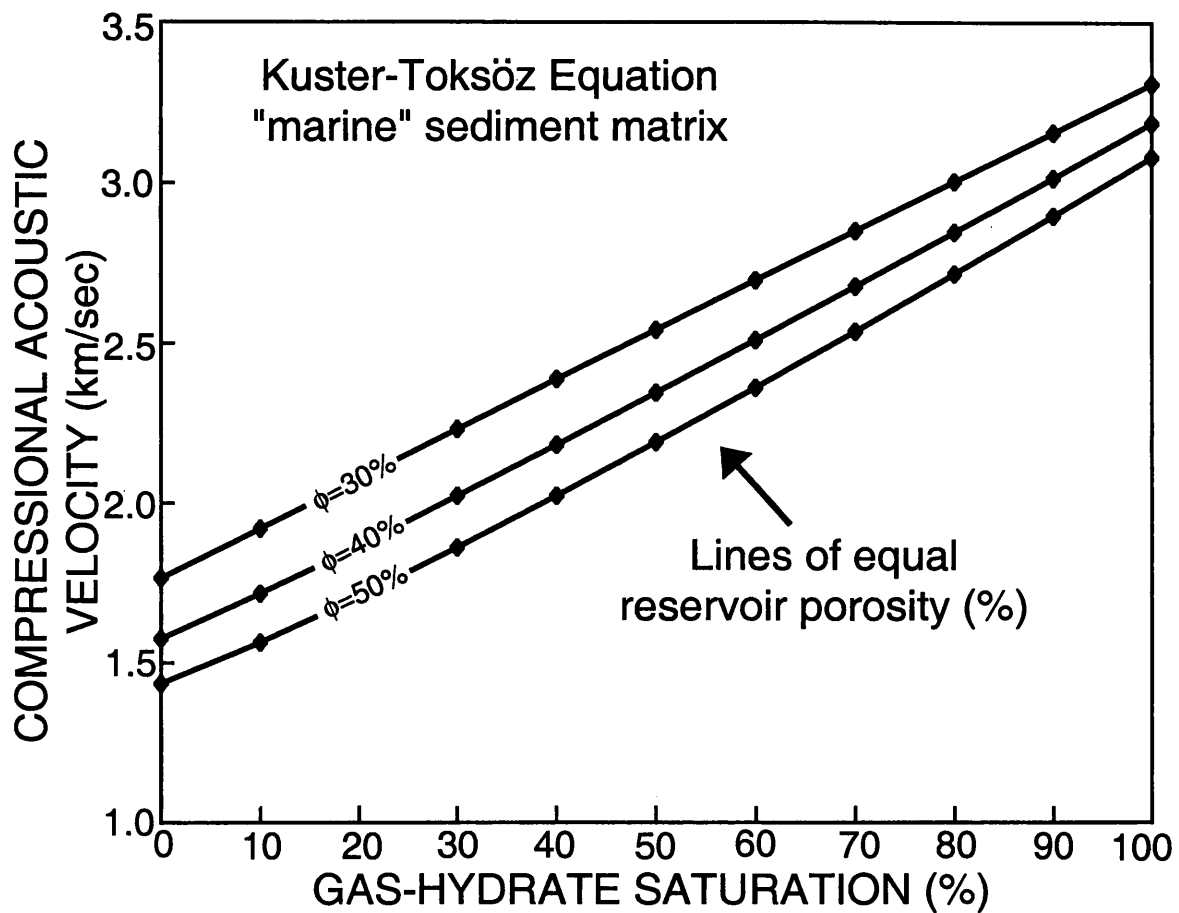
Figure 3.24 Plot of the three-component Kuster-Toksöz compressional-wave (Vp) acoustic model for a water- and gas-hydrate-bearing marine sediment (Reservoir Model C, Figure 2.8c).

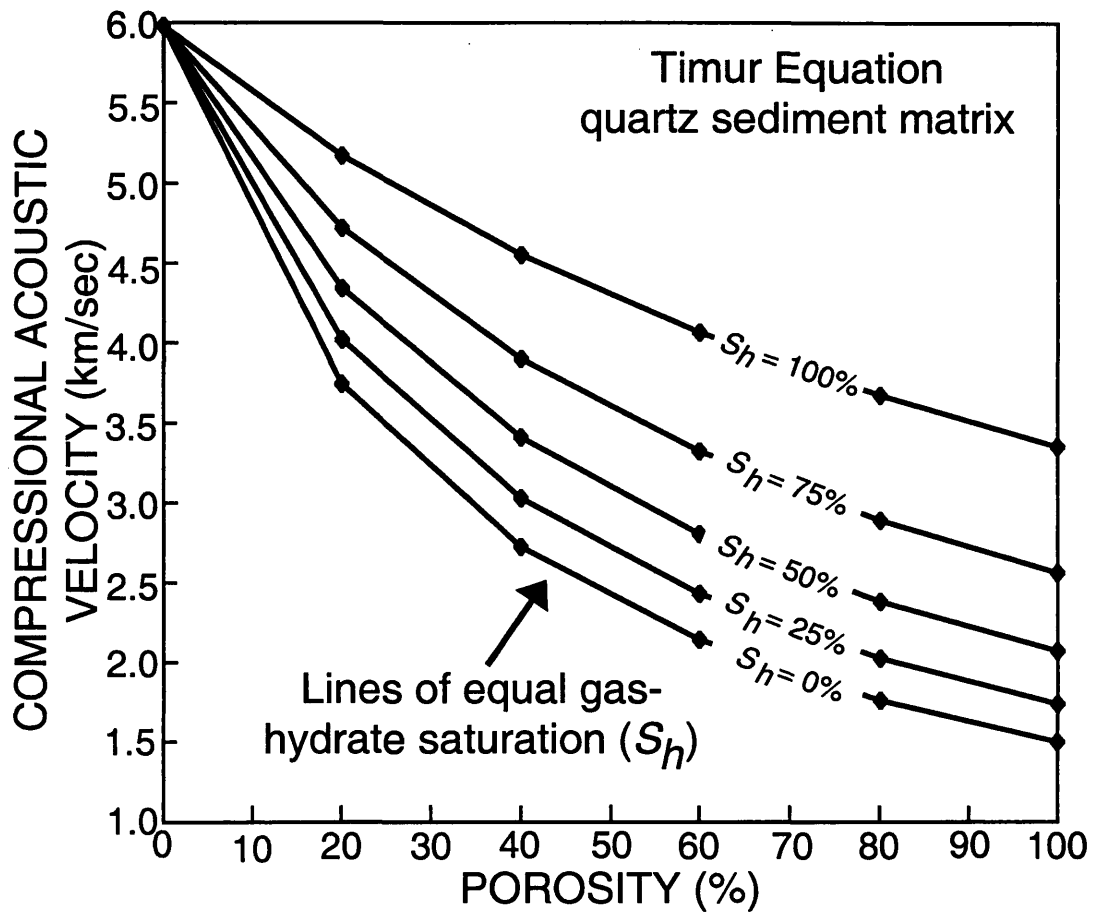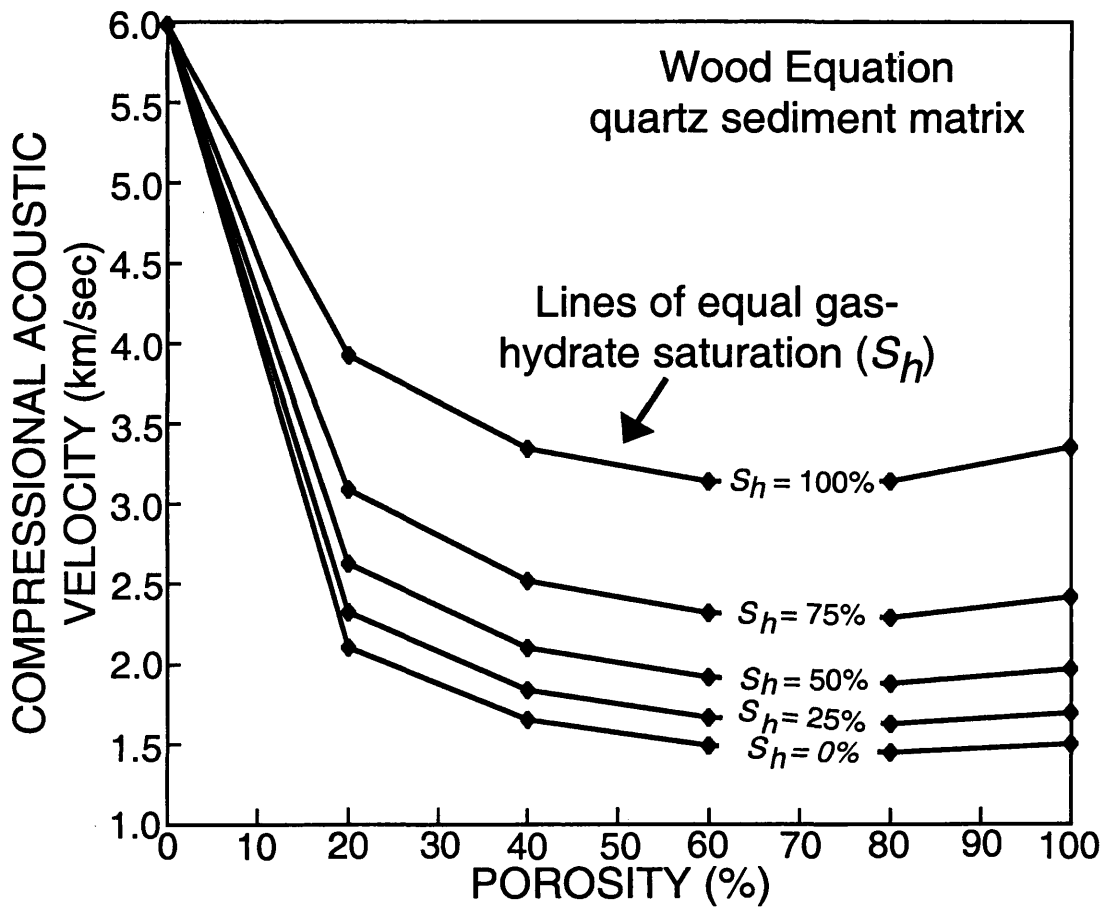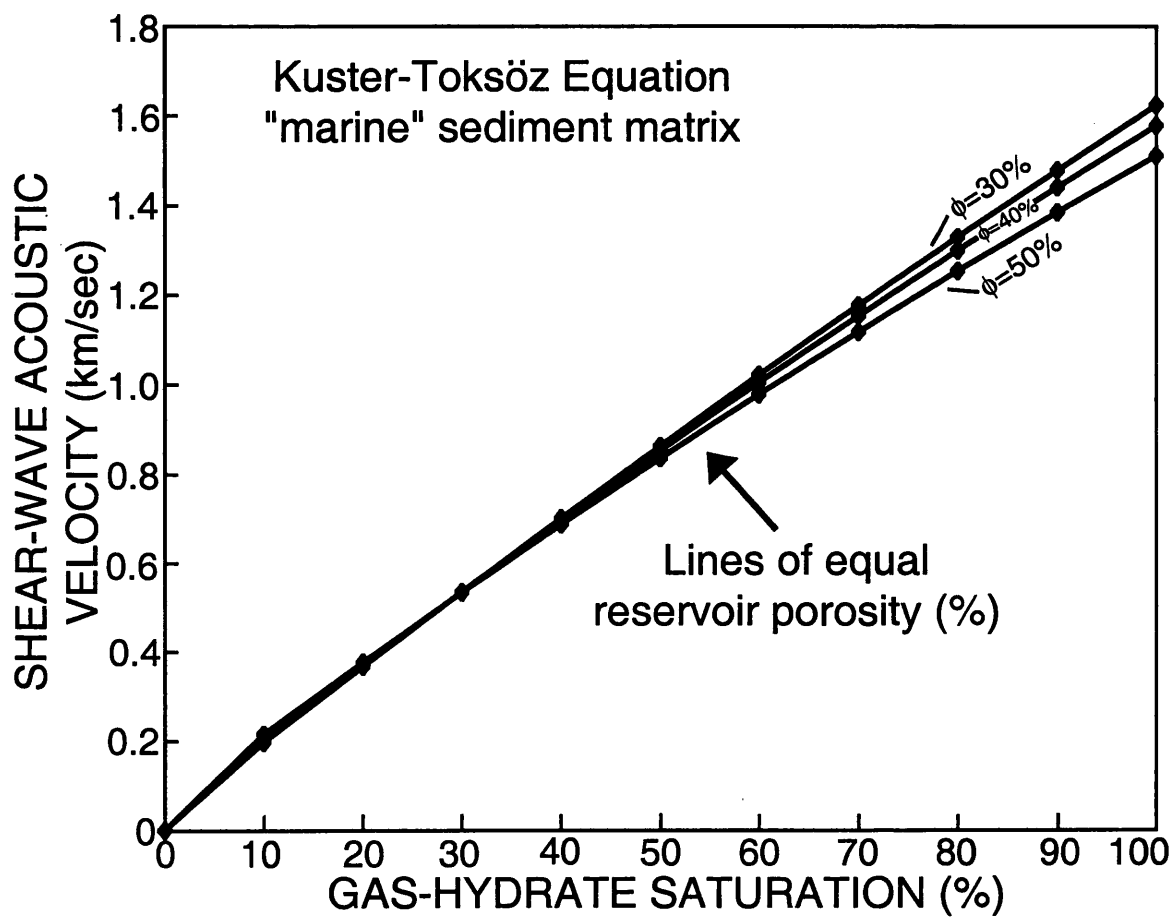Figure 3.25 Plot of the three-component Kuster-Toksöz shear-wave (V_S) acoustic model for a water- and gas-hydrate-bearing marine sediment (Reservoir Model C, Figure 2.8c).
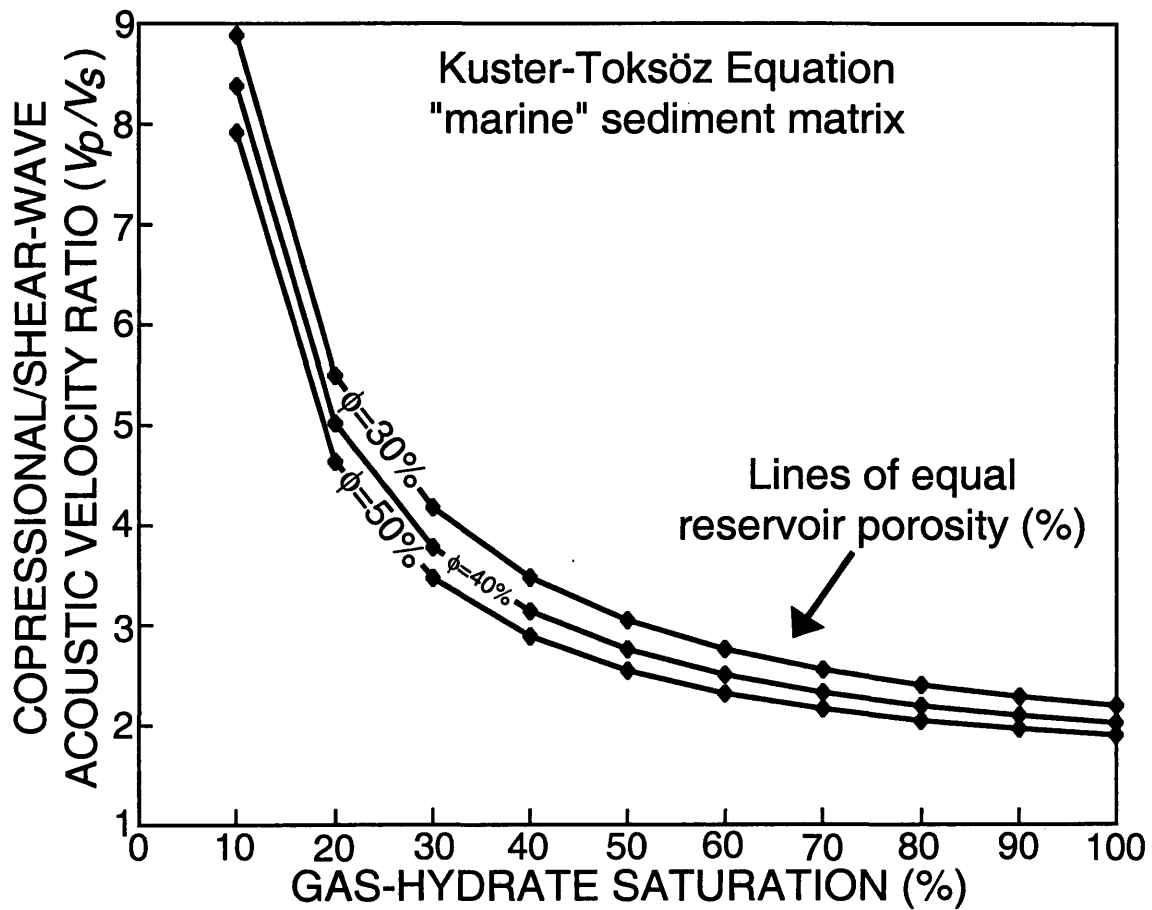
Figure 3.26 Plot of the three-component Kuster-Toksöz-derived ratio (Vp/V_s) of the calculated compressional-wave and shear-wave velocities for a water- and gas-hydrate-bearing marine sediment (Reservoir Model C, Figure 2.8c).

this section of the thesis, the theoretical carbon, oxygen, and hydrogen content of several

hypothetical gas-hydrate occurrences have been calculated for the first time and a series

of carbon/oxygen and hydrogen/carbon "fan charts" that can be used to calculate gas-

hydrate saturations have been constructed. The effect of complex reservoir conditions

(including the presence of clay and dispersed organic carbon) on the GLT gas-hydrate

saturation calculations have been assessed in this section of the thesis.

The geochemical logging tool (Figure 3.1) consists of four parts: a natural

gamma-ray spectrometry sensor (NGT), a neutron porosity tool (CNT-G) which carries a

^{252}Cf source of neutrons (2 MeV source) that is used in conjunction with the aluminum

activation clay tool (AACT) (Hertzog et al., 1989), and the gamma-ray spectroscopy tool

(GST). The NGT measures natural gamma ray emissions which are used to quantify the

potassium, thorium, and uranium content of the logged sediments. The AACT is similar

to the NGT, but the AACT measures the gamma-ray spectrum of the activated formation

in three additional windows. Comparing AACT measurements with those from the NGT,

results in a measure of the concentration of Al (in weight percent). The GST is located at

the base of the tool string (Figure 3.1) and consists of an high-energy pulsed neutron

accelerator (14 MeV) and a NaI scintillation crystal detector. In neutron spectroscopy

well logging (GST tool), each element has characteristic gamma-rays that are emitted

from neutron-element interactions. An element, therefore, can be identified by its

gamma-ray signature, with the intensity of emission related to the atomic elemental

concentration. See Appendix 2 for a more complete discussion on neutron transport

theory. By combining elemental yields from neutron spectroscopy well logs, reservoir

parameters including porosities, lithologies, formation fluid salinities, and hydrocarbon

saturations (including gas hydrates) can be calculated. The GST can be operated in two

timing modes: inelastic, which mainly measures the neutron reactions in the high energy

range (elements quantified: carbon, calcium, iron, oxygen, sulfur, silicon), and capture-

tau mode which measures the gamma rays emitted from neutron capture (elements

quantified: calcium, chlorine, iron, hydrogen, sulfur, silicon). In ODP boreholes, the

GST is usually ran in only capture-tau mode; however, on ODP Leg 164 a selected

number of inelastic measurements where made (ODP Leg 164 is discussed in more detail

in Chapter 5 of this thesis). Calculation of absolute concentrations (weight percent) of

elemental oxides requires additional post-field processing to estimate the contribution of

rare-earth elements (gadolinium and samarium in particular) and titanium. See Appendix

1 for additional information on required well-log data processing.

GLT elemental yields can be calibrated using XRD-XRF measurements and core

descriptions to infer downhole mineralogy variations. After post-field processing, the

GLT data may be used to make detailed assessments of mineralogical compositions.

As previously indicated, the GST measures the amount of carbon, calcium, iron,

oxygen, sulfur, silicon, chlorine, and hydrogen within a rock sequence. The amount of a

particular element in a rock is not only controlled by the matrix mineralogy but also by

the amount of water and hydrocarbons, including gas hydrates, that are present in the

rock. The elemental ratios that show promise of yielding gas-hydrate reservoir

saturations are carbon/oxygen and hydrogen/carbon. Through the aid of stoichiometric

calculations, it is possible to estimate the amount of carbon, oxygen, and hydrogen that

are present in a cubic centimeter of pore-volume or matrix for the following substances:
water, methane gas, ice, structure-I methane hydrate, sandstone matrix (quartz),
limestone (calcite) matrix, clay (smectite, illite, chlorite, and kaolinite) matrix, and
dispersed organic carbon (Tables 3.5 and 3.13). The process used to calculate the
elemental content of the various reservoir constituents listed in Table 3.13 was described
in Section 3.3 of this thesis. As previously discussed, the chemical formula and bulk-
density of the individual reservoir constituents were used to calculate the number of
carbon, oxygen, and hydrogen atoms present in one cubic centimeter of each substance.
The elemental calculations for the four clays being considered (Table 3.13: smectite,
illite, chlorite, and kaolinite) are complicated because of the variable chemical nature of
clays. In this example, standard "end-member" chemical formulas and bulk-densities
have been selected for the four clays being modeled.

By using simple mixing rules and the elemental concentrations in Table 3.13 it is
possible to develop elemental relations (ratios) that yield gas-hydrate reservoir
saturations. Depicted in Figures 3.27a-c, 3.28a-c, 3.29a-c, and 3.30a-c are the results of
the carbon/oxygen and hydrogen/carbon reservoir modeling efforts. All of the reservoir
conditions modeled assume the three component Reservoir Model E (Figure 2.8e) which
consists of either a quartz or calcite matrix (no clay), gas hydrate, and either water, ice, or
methane gas. Listed in Table 3.14 are the reservoir conditions modeled in Figures 3.27a-
c, 3.28a-c, 3.29a-c, and 3.30a-c. The carbon/oxygen and reservoir porosity (0-60 %)
crossplots in Figures 3.27a-c and 3.28a-c are similar to conventional oil and gas
carbon/oxygen "fan charts" (Woodhouse and Kerr, 1992). Of concern, however, is the

Table 3.13 Elemental concentration of carbon, hydrogen, and oxygen in various reservoir constituents.

Reservoir constituent	Chemical formula	Bulk-density (g/cm^3)	Elemental concentrations $(\times 10^{22}$ atoms/cm$^3)$		
			Carbon	Hydrogen	Oxygen
Gas hydrate Structure-I	$7.598CH_4 + 46H_2O$	0.9	0.439988	7.084028	2.662037
Methane gas	CH_4 2.580 MPa 273.15 K	$(1.209\ mol/dm^3)$	0.072807	0.291226	0
Pure water	H_2O	1.0	0	6.685516	3.342758
Ice	H_2O	0.92	0	6.016964	3.008482
Quartz	SiO_2	2.65	0	0	5.311965
Calcite	$CaCO_3$	2.71	1.630520	0	4.891559
Illite	$K_{1-1.5}Al_4(Si_{6.5-7}Al_{1-1.5})O_{20}(OH)_4$	2.53	0	0.823143*	4.938860*
Smectite	(Montmorillonite) $(Ca,Na)_7(Al,Mg,Fe,)_4(Si,Al)_8O_{20}(OH)_4$	2.12	0	0.772952*	4.637710*
Kaolinite	$Al_4(Si_4O_{10})(OH)_8$	2.42	0	2.248586	5.059320
Chlorite	$(Mg,Al,Fe)_6(Si,Al)_4O_{10}(OH)_8$	2.77	0	2.195048	4.938860
Pure carbon (organic)	C	1.2	6.016530	0	0

* Hydrogen and oxygen elemental concentrations do not include bound-water

Table 3.14 List of carbon/oxygen (C/O) and hydrogen/carbon (H/C) reservoir conditions that have been modeled and displayed in Figures 3.27a-c, 3.28a-c, 3.29a-c, and 3.30a-c.

Figure	Elemental ratio	Matrix	Pore-filling constituent	Reservoir porosity $(\emptyset, \%)$	Gas-hydrate saturation $(S_h, \%)$
3.27a	C/O	Quartz	Hydrate-Water	0-60	0-100
3.27b	C/O	Quartz	Hydrate-Ice	0-60	0-100
3.27c	C/O	Quartz	Hydrate-Gas	0-60	0-100
3.28a	C/O	Calcite	Hydrate-Water	0-60	0-100
3.28b	C/O	Calcite	Hydrate-Ice	0-60	0-100
3.28c	C/O	Calcite	Hydrate-Gas	0-60	0-100
3.29a	H/C	Quartz	Hydrate-Water	-	0-100
3.29b	H/C	Quartz	Hydrate-Ice	-	0-100
3.29c	H/C	Quartz	Hydrate-Gas	-	0-100
3.30a	H/C	Calcite	Hydrate-Water	0-60	0-100
3.30b	H/C	Calcite	Hydrate-Ice	0-60	0-100
3.30c	H/C	Calcite	Hydrate-Gas	0-60	0-100
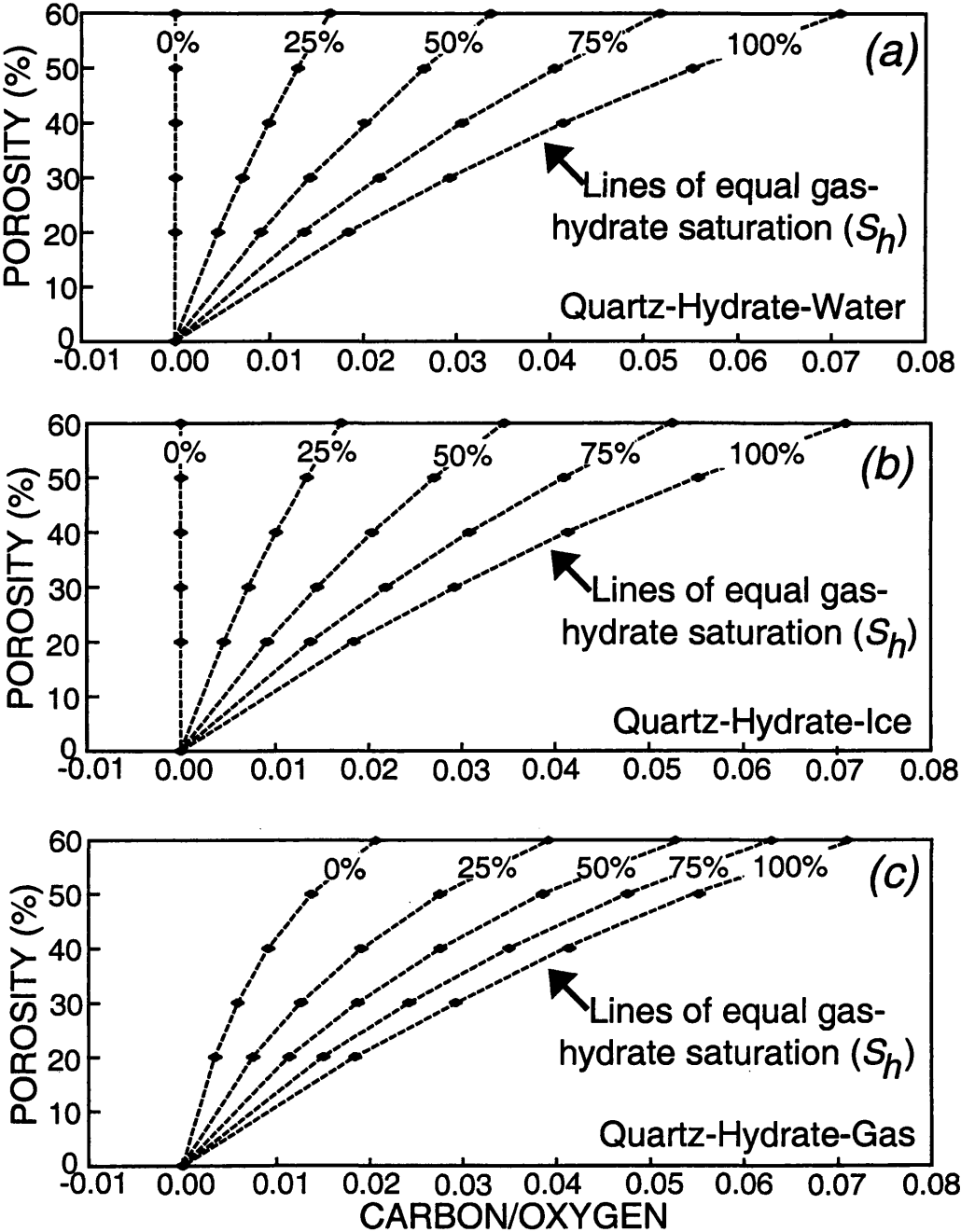
Figure 3.27a-c "Fan charts" for carbon/oxygen interpretation of gas-hydrate saturation in a quartz (sandstone) reservoir with various pore-filling constituents: (a) gas hydrate and water; (b) gas hydrate and ice; and (c) gas hydrate and free-gas (Table 3.14).
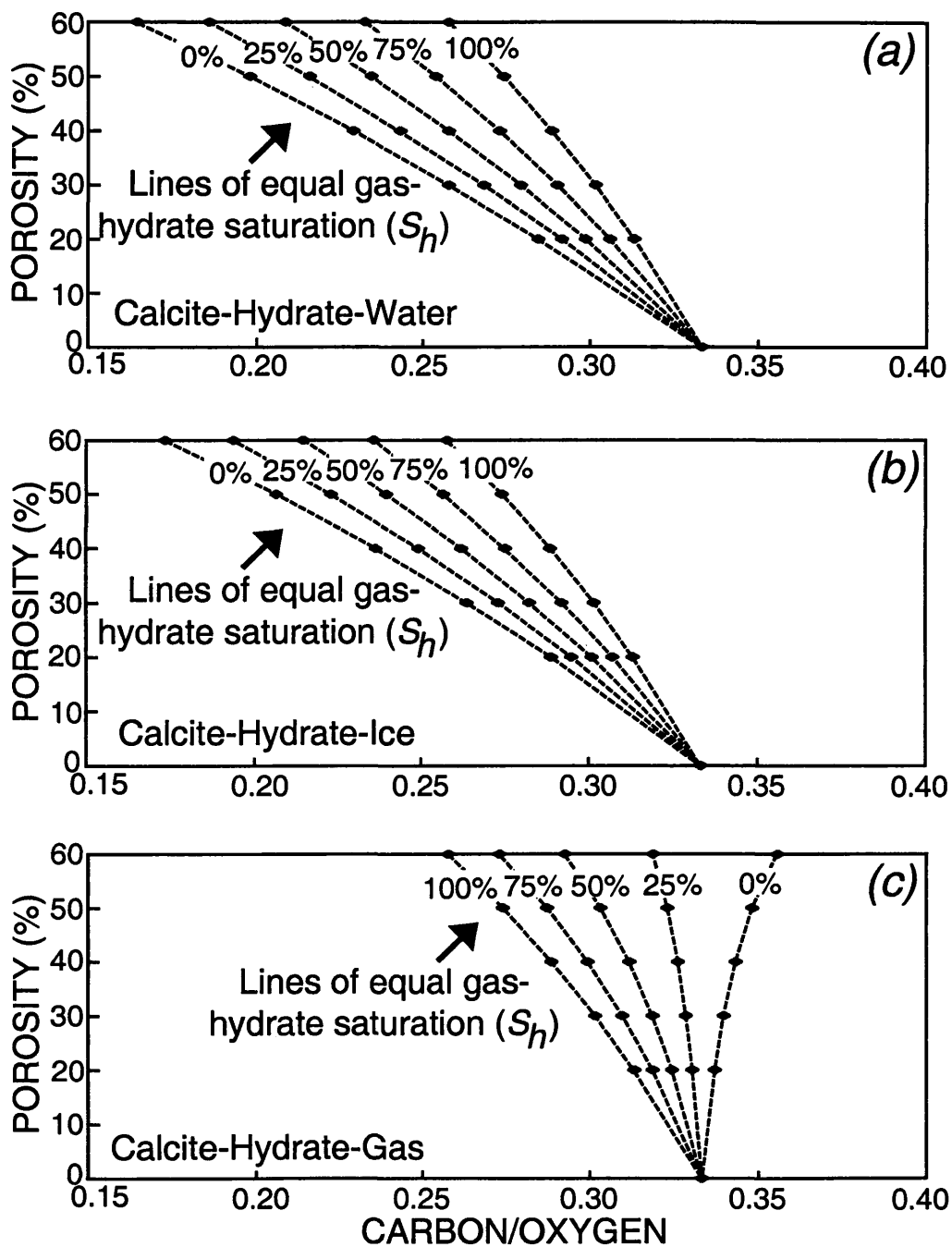
Figure 3.28a-c "Fan charts" for carbon/oxygen interpretation of gas-hydrate saturation in a calcite (limestone) reservoir with various pore-filling constituents: (a) gas hydrate and water; (b) gas hydrate and ice; and (c) gas hydrate and free-gas (Table 3.14).
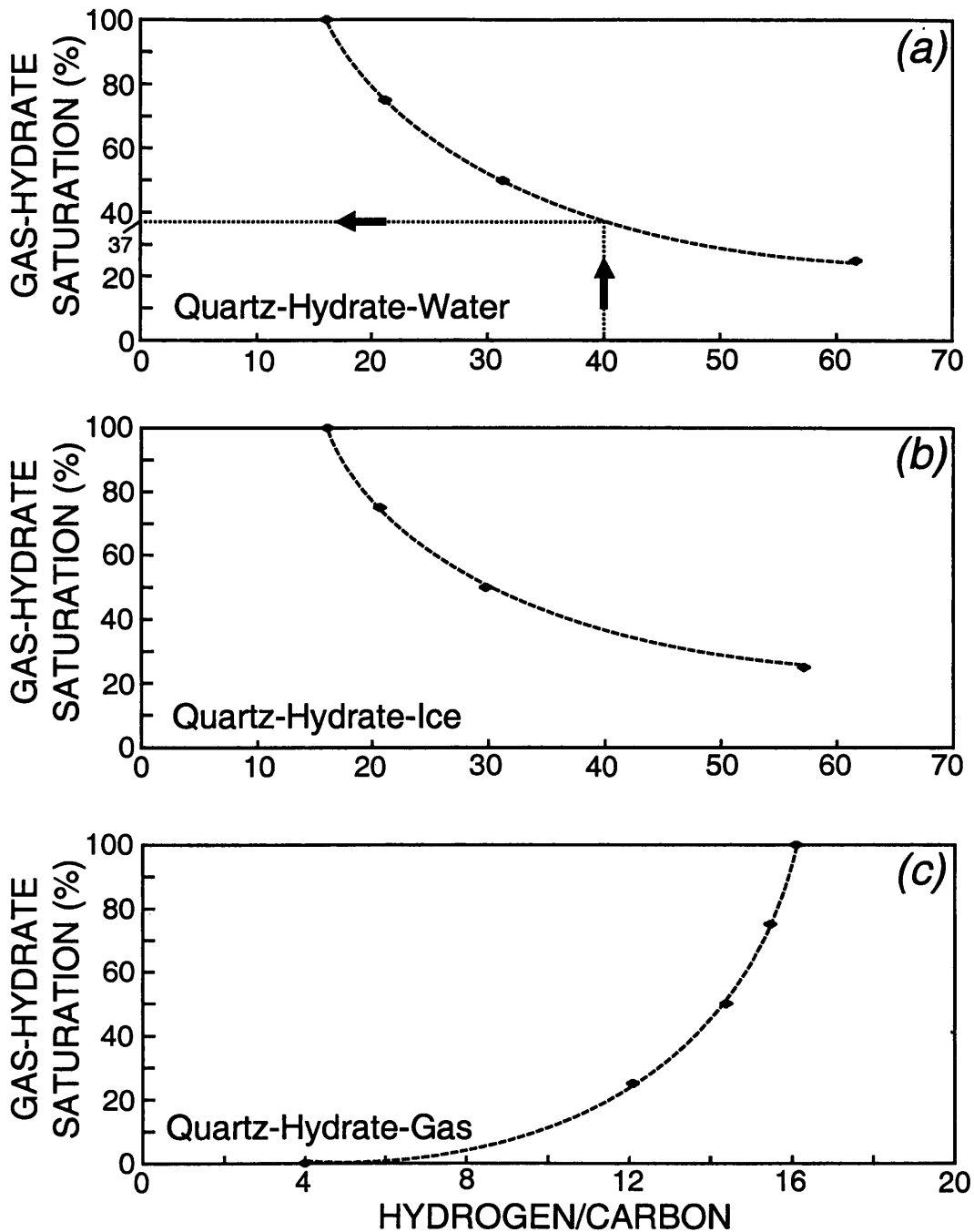
Figure 3.29a-c Charts for hydrogen/carbon interpretation of gas-hydrate saturation in a quartz (sandstone) reservoir with various pore-filling constituents: (a) gas hydrate and water; (b) gas hydrate and ice; and (c) gas hydrate and free-gas (Table 3.14).
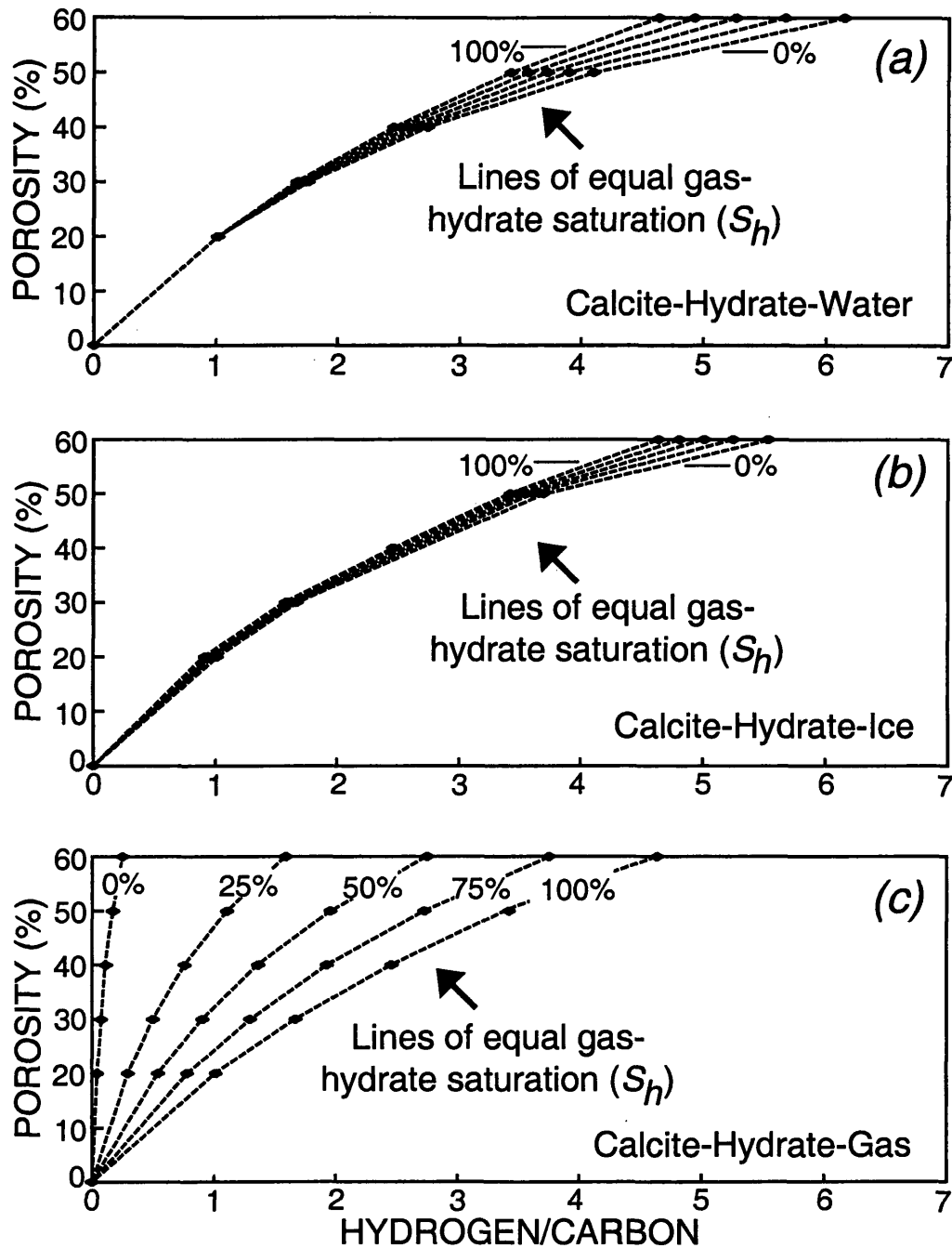
Figure 3.30a-c "Fan charts" for hydrogen/carbon interpretation of gas-hydrate saturation in a calcite (limestone) reservoir with various pore-filling constituents: (a) gas hydrate and water; (b) gas hydrate and ice; and (c) gas hydrate and free-gas (Table 3.14).

limited range of expected carbon/oxygen ratios in gas-hydrate-bearing sandstone (quartz) reservoirs (Figure 3.27a-c). For example, the maximum range of the carbon/oxygen ratio for a gas-hydrate- and water-bearing reservoir (Figure 3.27a) with 40% porosity would only be 0.04, which is near the likely uncertainty of the carbon/oxygen-log measurement (Woodhouse and Kerr, 1992). The uncertainty in carbon/oxygen-log measurements in gas-hydrate-bearing limestone (calcite) reservoirs should be less of a problem (Figure 3.28a-c). The uncertainty associated with standard carbon/oxygen-log measurements will be discussed in more detail later in this section of the thesis.

The hydrogen/carbon and gas-hydrate saturation (0-100%) crossplots in Figure 3.29a-c and the hydrogen/carbon and reservoir porosity (0-60 %) crossplots in Figure 3.30a-c are unique and don't exist for conventional oil and gas reservoirs. Of particular interest is the apparent direct relation between gas-hydrate saturation and hydrogen/carbon ratios in the simple quartz-matrix models depicted in Figure 3.29a-c. In the quartz-matrix reservoir model, all of the hydrogen and carbon in the system occur as pore-filling constituents; therefore gas-hydrate saturations can be calculated without knowing reservoir porosities. Figure 3.29a contains an example of a gas-hydrate saturation calculation, in which a hydrogen/carbon ratio of 40 yields a gas-hydrate saturation of 37% in a gas-hydrate- and water-bearing pure-quartz matrix reservoir. Hydrogen/carbon ratios within gas-hydrate-bearing quartz (Figure 3.29a-c) and calcite (Figure 3.30a-c) reservoirs are characterized by a wide-range of values, unlike the carbon/oxygen ratios discussed earlier; which suggests that hydrogen/carbon ratio measurements may be more useful. However, the neutron-capture measurement of

hydrogen in a rock formation with the GLT is more problematic than the inelastic neutron measurement of the carbon and oxygen content.

The uncertainty in the carbon/oxygen- or hydrogen/carbon-determined gas-hydrate saturations are dependent on the uncertainty in each measurement in the interpretation procedure. Woodhouse and Kerr (1992) have shown that the precision of the carbon/oxygen ratio measurement can be reduced to about 0.008. However, when the uncertainties in the other required measurements are considered, such as determining the carbon and oxygen content of the matrix and borehole fluids, the uncertainty in the log measured carbon/oxygen water saturations may be as great as 47%.

To further evaluate the likely uncertainty in the GLT-derived carbon/oxygen ratios and water saturations for various reservoir porosities, the approach described by Woodhouse and Kerr (1992) has been used in which the uncertainty of each measurement in the carbon/oxygen interpretation "chain" is assessed. The likely uncertainty in the GLT-derived carbon/oxygen water saturations for a wide range of reservoir porosities have been calculated in Table 3.15. The uncertainty in carbon/oxygen-derived water saturations decreases rapidly as porosity increases. At high porosities, such as in most known gas-hydrate occurrences, the quantities of formation-fluid carbon and oxygen are high and the accuracy of the GLT-derived gas-hydrate saturations could be relatively good. For example, in a gas-hydrate- and water-bearing reservoir (porosity of 60%), the uncertainty in the carbon/oxygen-calculated water saturations would be about 7%. Additional downhole calibration of the carbon/oxygen-interpreted water saturations in

Table 3.15 Most likely uncertainty in carbon/oxygen-calculated water saturations for various reservoir porosities (modified from Woodhouse and Kerr, 1992).

Reservoir porosity ($\emptyset$,%)	Uncertainty in C/O calculated water saturation (S_W, %)
10	47.0
20	22.9
30	15.0
40	11.2
50	8.8
60	7.3
70	6.2

known water-saturated zones (no hydrocarbon) allows the uncertainties in the

carbon/oxygen measurements to be reduced further (Woodhouse and Kerr, 1992).

Calculating potential uncertainties associated with the hydrogen/carbon-derived

gas-hydrate saturations is less clear due to the lack of previous quantitative

hydrogen/carbon ratio studies. It can be generally assumed that the uncertainty in the

hydrogen measurement will be relatively great, since neutron-capture measurements are

significantly affected by the presence of thermal-neutron absorbers in the formation, such

as boron and chlorine. The uncertainty in the hydrogen measurement is likely the

maximum uncertainty in the hydrogen/carbon gas-hydrate saturation interpretation

"chain". If it is assumed that a neutron logging tool can detect and measure a two percent

difference in the bulk-volume water content of a rock formation, which is equivalent to a

two percent porosity difference in a water-saturated rock, it can be assumed that the

neutron logging tool can resolve and measure hydrogen concentration differences of

about 1.3372×10^{21} hydrogen atoms per cubic centimeter of water-saturated rock. In

Figure 3.29a, a $1.3372 \times 10^{21}/cm^3$ change in the hydrogen content of the gas-hydrate- and

water-bearing quartz matrix reservoir would correlate to a hydrogen/carbon ratio change

of 0.3, which would have little affect on the hydrogen/carbon-derived gas-hydrate

saturations. Thus, it can be concluded that GLT-derived hydrogen/carbon and

carbon/oxygen ratios can yield highly accurate gas-hydrate saturation data. However,

unlike the carbon/oxygen-derived saturations, the absolute uncertainty of the

hydrogen/carbon-derived saturations cannot be determined without additional GLT

calibration studies.

As previously discussed, it is possible to generate a series of carbon/oxygen and hydrogen/carbon "fan charts" for relatively simple reservoir conditions; however, it is necessary to develop a more complete understanding of the chemistry of the entire borehole environment. The amount of carbon or oxygen measured by the GLT is not only controlled by the chemistry of the pore-fluids within the formation, but also by the chemistry of the rock matrix. An equation relating all of the carbon and oxygen sources associated with a borehole has been developed by Hertzog (1978):

$$\frac{\text{Carbon}}{\text{Oxygen}} \text{ ratio (COR)} = A \frac{[\text{Matrix Carbon}(C_m) + \text{Porosity Carbon}(C_p) + \text{Borehole Carbon}(C_b)]}{[\text{Matrix Oxygen}(O_m) + \text{Porosity Oxygen}(O_p) + \text{Borehole Oxygen}(O_b)]} \quad (3.22)$$

The coefficient "A" is determined by the relative inelastic neutron cross section of carbon and oxygen, and it is essentially constant over a variety of conditions. Direct calculations of the coefficient "A" and Monte Carlo simulations have yielded a value of 0.75 for the coefficient "A" in a wide range of formations (Roscoe and Grau, 1988). The matrix carbon (C_m) term is the sum of the various matrix volumes and their carbon concentrations. Carbonates, including limestone and dolomite, will normally be the only significant contributors of matrix carbon in conventional reservoirs. However, organic carbon can be relatively abundant in marine sediments. The porosity carbon (C_p) term is essentially due to the presence of hydrocarbons. The matrix oxygen (O_m) term is a more comprehensive sum than the matrix carbon (C_m) term because oxygen is present in most

all of the matrix constituents (Table 3.13). The porosity oxygen (O_p) term is mainly the

product of the water content of the formation in conventional hydrocarbon reservoirs.

The remaining two terms in Equation 3.22 are the borehole contribution to the carbon

(C_b) and oxygen (O_b) yields. Borehole carbon and oxygen content is a function of the

borehole size, the outside diameter of the tool and sleeve, and the chemical composition

of the borehole fluids. These factors need to be evaluated to account for potential

borehole effects on the GLT measurements. Equation 3.22 can be expanded to take into

account the carbon and oxygen content of various borehole constituents in conventional

hydrocarbon reservoirs:

$$COR = A \frac{[\alpha(1-\varnothing)+\beta\varnothing S_h + C_b]}{[\gamma(1-\varnothing)+\delta\varnothing(1-S_h)+O_b]}$$ (3.23)

COR = Log-measured carbon-oxygen ratio

A = Ratio of average carbon and oxygen fast neutron cross sections

$\varnothing$ = Porosity, fractional percent

S_h = Hydrocarbon (gas hydrate) saturation, fractional percent

C_b = Relative carbon concentration contribution from the borehole, variable units

O_b = Relative oxygen concentration contribution from the borehole, variable units

α = Atomic concentration of carbon in the matrix, variable units

β = Atomic concentration of carbon in the formation fluid (gas hydrate), variable units

γ = Atomic concentration of oxygen in the matrix, variable units

δ = Atomic concentration of oxygen in the formation fluid (water), variable units

In Equation 3.23, each constituent is weighted according to its bulk volume and the atomic concentration of carbon and oxygen atoms per cubic centimeter that it contains. The variables C_b and O_b account for the borehole background signal, which are typically O_b=0.05 and C_b=0.0 in water-filled holes (expressed in units of Avogadro's number) (Woodhouse and Kerr, 1992).

The borehole oxygen (O_b) and carbon (C_b) correction variables can also be directly calculated for a given borehole and tool configuration. Roscoe and Grau (1988) demonstrated that the borehole oxygen (O_b) and carbon (C_b) correction variables are calculated by first determining the volume of oxygen and carbon in the borehole. Each portion of the borehole (including casing, cements, and tool sleeves) that contributes to the carbon (C_b) and oxygen (O_b) borehole correction variables needs to be individually assessed. Therefore, O_b and C_b have been determined with volumetric parameters representing the borehole volume of carbon-bearing (V_C) and oxygen-bearing (V_O) material. These variables can be calculated from the relation $V_x = d_o^2 - d_i^2$, where d_o^2 and d_i^2 are the outside and inside diameters of the regions of interest, respectively. The borehole volumetric parameters V_O and V_C are obtained by summing the V_x values from all the regions of interest in the borehole. For example, in a 30 cm open (uncased) water-filled borehole the volume of water (V_O) measured by the GLT (3.475 cm diameter tool) would be 887.9 cm^2. The volume of carbon-bearing borehole fluids (V_C) in the same

borehole would be zero since the hole is filled with only water (no hydrocarbons). If a

sleeved tool is used, however, the V_C of the sleeve needs to be calculated in the same

manner as the example V_O calculation and included in the C_b correction variable. Roscoe

and Grau (1988) presented a series of comparison graphs that can be used to determine

values for O_b and C_b from the calculated V_O and V_C values for various borehole

conditions. Roscoe and Grau (1988) also demonstrated, however, that the actual value of

O_b and C_b are affected by changes in sediment porosities. This O_b and C_b porosity

dependence can be mathematically determined with the following relation: $O_b = O_b'$ [1-

$\ni(\varnothing-0.17)$], where O_b is the porosity-corrected value of O_b' and $\ni$ is the porosity

correction constant which has been determined to be 0.61 (Roscoe and Grau, 1988).

Since α, β, γ, and δ are constants for a specified mineralogy and fluid, and C_b

and O_b are constants for a particular borehole configuration, hydrocarbon saturations (S_h)

can be calculated directly from the carbon/oxygen ratio (COR) if the matrix porosity is

known. Equation 3.23 yields accurate hydrocarbon saturations in conventional oil and

gas reservoirs, where all of the porosity oxygen term (O_p) is the product of the water

content of the formation. In gas-hydrate-bearing sediments, however, the occurrence of

oxygen in the water molecules associated with the gas hydrate structure will also

contribute to the porosity oxygen (O_p) term. The effect of gas-hydrate-associated oxygen

content on the GLT-measured carbon/oxygen ratios can be explicitly explained by adding

a gas hydrate oxygen term to Equation 3.23:

$$COR = A \frac{[\alpha(1-\varnothing) + \beta\varnothing S_h + C_b]}{[\gamma(1-\varnothing) + \delta\varnothing(1-S_h) + \mu\varnothing S_h + O_b]} \qquad (3.24)$$

where μ is the atomic concentration of oxygen atoms in a Structure-I methane hydrate. The matrix mineralogy data necessary to assign values for the parameters α and γ may be obtained from the GLT-derived elemental lithologic indicator ratios or LIR (atomic elemental ratio of the amount of Si to Ca: Si/Ca), which is used to assess relative amounts of quartz and calcite in the matrix. For mixed quartz and calcite formations $\alpha = 0.027(1-LIR)$ and $\gamma = 0.081 + 0.007LIR$ (expressed in units of Avogadro's number) (Woodhouse and Kerr, 1992). The COR hydrocarbon saturation equation (3.24) can be modified to accommodate more complex mixtures of minerals, provided their atomic concentration coefficients are known. Accurate interpretation of COR data requires precise chemical analysis of all potential reservoir constituents. The atomic elemental concentrations of carbon and oxygen for most common reservoir constituents are listed in Table 3.13.

It is also possible to develop hydrogen/carbon saturation equations for complex reservoir systems similar to the carbon/oxygen saturation equation (3.24) discussed above. In a hydrogen/carbon saturation equation the rock matrix term for a mixed quartz and calcite reservoir can be removed. In clay-rich sediments, however, appropriate clay (or bound water) corrections would be required for the measured hydrocarbon saturations.

It is generally accepted that inelastic-scattering measurements of carbon and oxygen concentrations are largely insensitive to dissolved salts in the pore-waters or

shaliness (clay content) of the formation (Woodhouse and Kerr, 1992). However, little

work has been conducted to evaluate the affect of clay-rich marine sediments on

carbon/oxygen ratios. In some DSDP and ODP coreholes, the clay mineral content of the

formation sediments exceeds 60%. When considering the effect of clays on

carbon/oxygen-calculated gas-hydrate saturations, it was assumed that clays contain no

carbon. Carbon, however, is often concentrated in organic-rich marine sediments which

will be dealt with later in this section. In general, the oxygen content of quartz and most

clay minerals are similar (Table 3.13). Therefore, in conventional quartz matrix

reservoirs the effect of small amounts of clay (5-10% of matrix) on the GLT-derived

carbon/oxygen ratios are negligible. In clay-rich marine sediments, however, small

differences in the oxygen content between most clays and quartz may have significant

affects on the carbon/oxygen ratio of the sediment matrix. Figure 3.31 is a crossplot of

porosity (ranging from 0 to 40 percent) to the expected carbon/oxygen ratio in a quartz

and three pure clay (kaolinite, illite-chlorite, montmorillonite) matrix reservoirs with

various gas-hydrate saturations (S_h of 0, 25, 50, 75, and 100 percent). The pure illite and

chlorite matrix reservoirs are shown as a single clay type in Figure 3.31 since illite and

chlorite contain the same amount of oxygen per unit volume. At relatively high gas-

hydrate saturations and high reservoir porosities, the effect of clays on the GLT-derived

carbon/oxygen ratios are the greatest. As shown in Figure 3.31, a 100% gas-hydrate-

saturated pure montmorillonite "reservoir" with 40% porosity would be characterized by

a carbon/oxygen ratio of 0.045 which is about 0.005 higher than the carbon/oxygen ratio

for a pure quartz matrix reservoir under the same conditions. A 0.005 carbon/oxygen
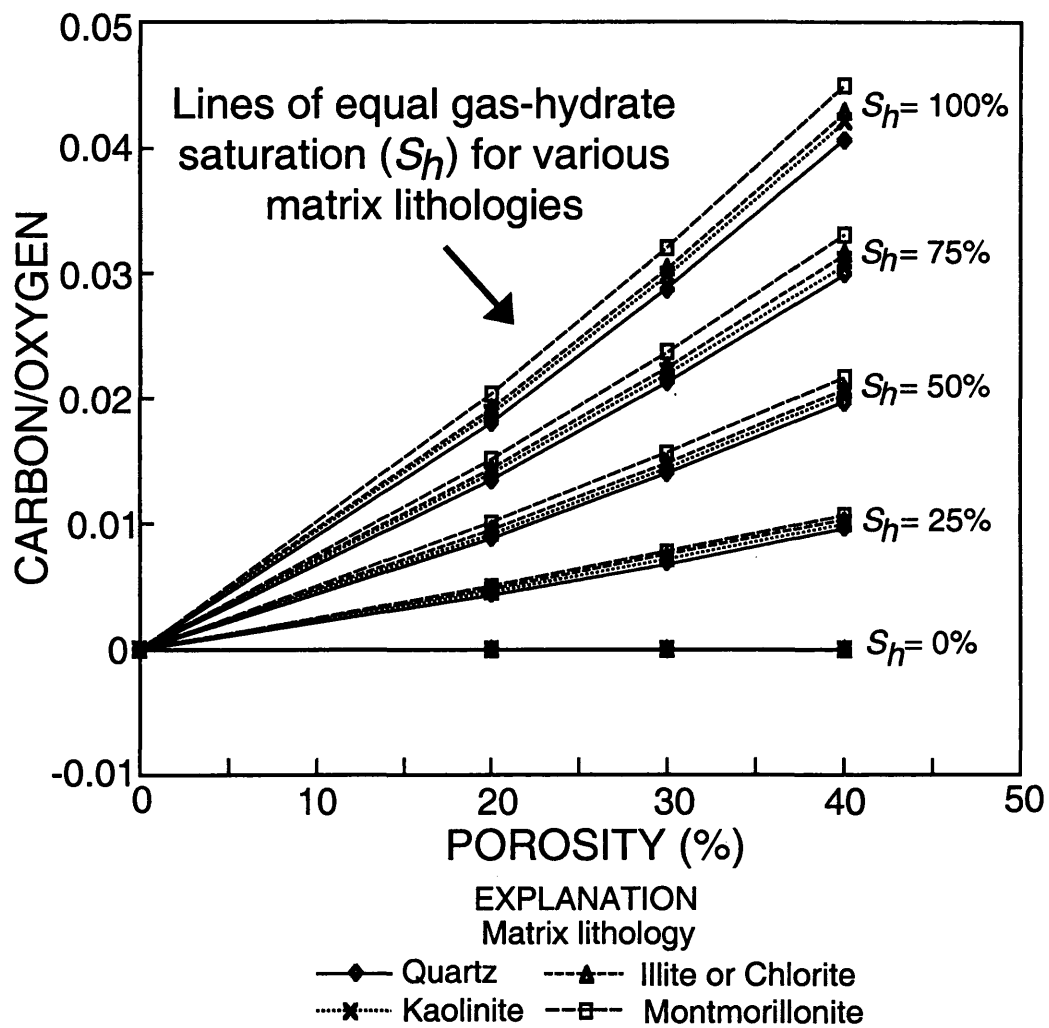
Figure 3.31 Crossplot of sediment porosities and carbon/oxygen ratios for gas-hydrate-bearing (S_h of 0, 25, 50, 75, and 100 percent) reservoirs with different lithologies (quartz, kaolinite, illite, chlorite, and montmorillonite).

difference, however, is below the resolution capability of the GLT (discussed earlier in this section). Figure 3.31 confirms that the occurrence of clay in most conventional reservoirs (porosity <30%, clay content <10%) and marine sediments have little to no effect on inelastic-neutron carbon/oxygen measurements.

Organic carbon can be concentrated in fine-grained marine sediments. For example, on the Blake Ridge the total organic carbon content (TOC) of the sediment ranges from 0.5 to 2.0 weight percent (Shipboard Scientific Party, 1996). The GLT will detect and measure the volume of organic carbon in marine sediments, which could have a significant effect on carbon/oxygen-calculated hydrocarbon saturations. To evaluate the potential effect of dispersed sedimentary organic carbon on neutron spectroscopy measurements, the atomic concentration of carbon atoms within a given volume of organic carbon was calculated. It was determined that there are about 6.0×10^{22} carbon atoms within a cubic centimeter of pure organic carbon (Table 3.13), assuming a grain density of 1.2 g/cm^3 (Schlumberger Educational Services, 1989). Crossplotted with porosity in Figures 3.32 and 3.33 are the expected carbon/oxygen ratio in pure quartz (Figure 3.32) and calcite (Figure 3.33) matrix reservoirs that are 100% saturated with either water or gas hydrate. Also shown in Figures 3.32 and 3.33 are plots of the same reservoir conditions, except two percent of the quartz and calcite matrix are replaced with organic carbon. As shown in Figures 3.32 and 3.33, the addition of organic carbon to the sediment matrix will significantly affect measured carbon/oxygen ratios. The addition of two percent organic carbon to a pure block of quartz or calcite (no porosity) results in a 0.023 and 0.025 increase in the carbon/oxygen ratio, respectively. The effect of organic
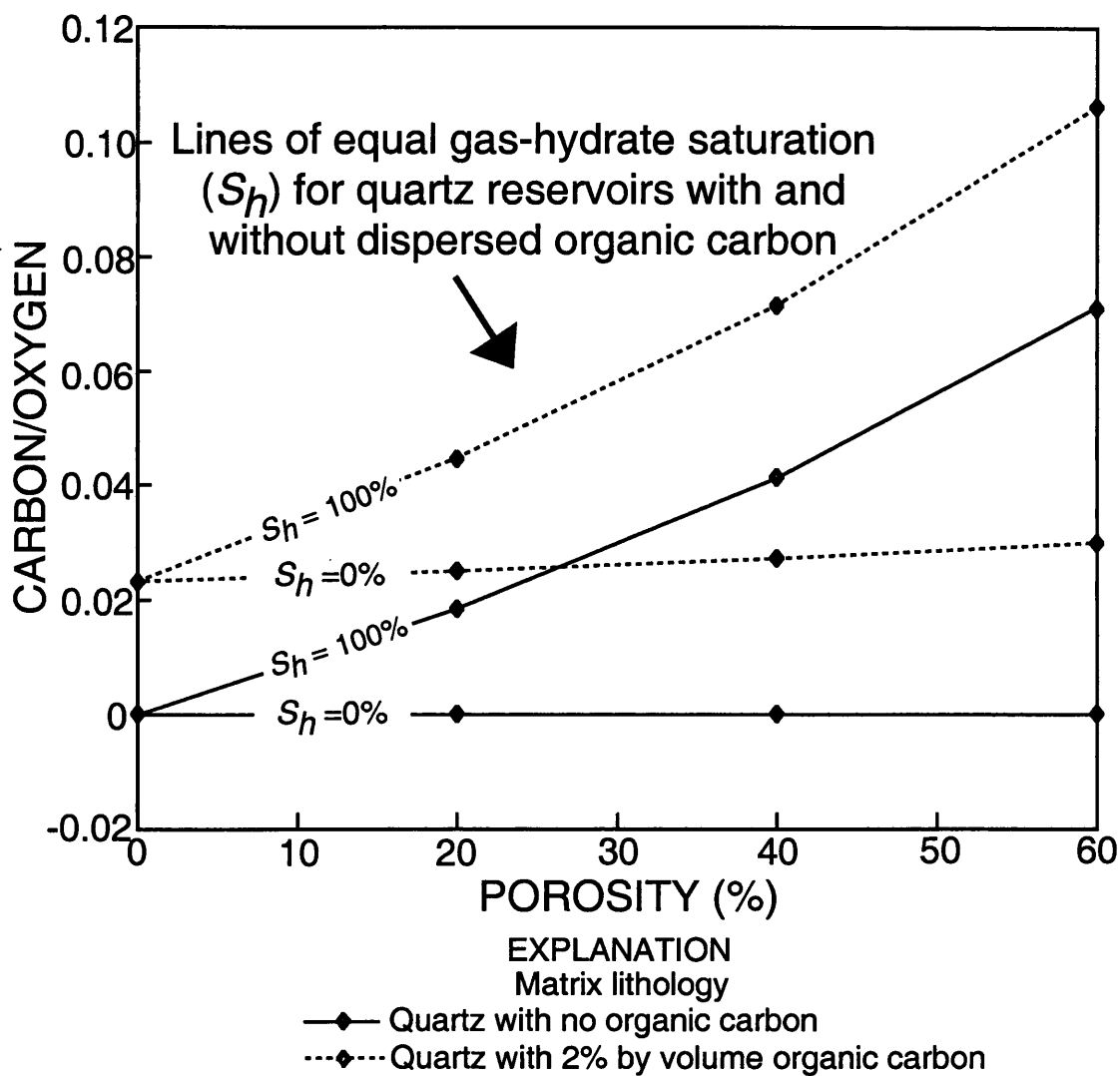
Figure 3.32 Crossplot of sediment porosities and carbon/oxygen ratios for a gas-hydrate-bearing (S_h of 0 and 100 percent) quartz (sandstone) reservoir with (2% by volume) and without dispersed organic carbon in the sediment matrix.
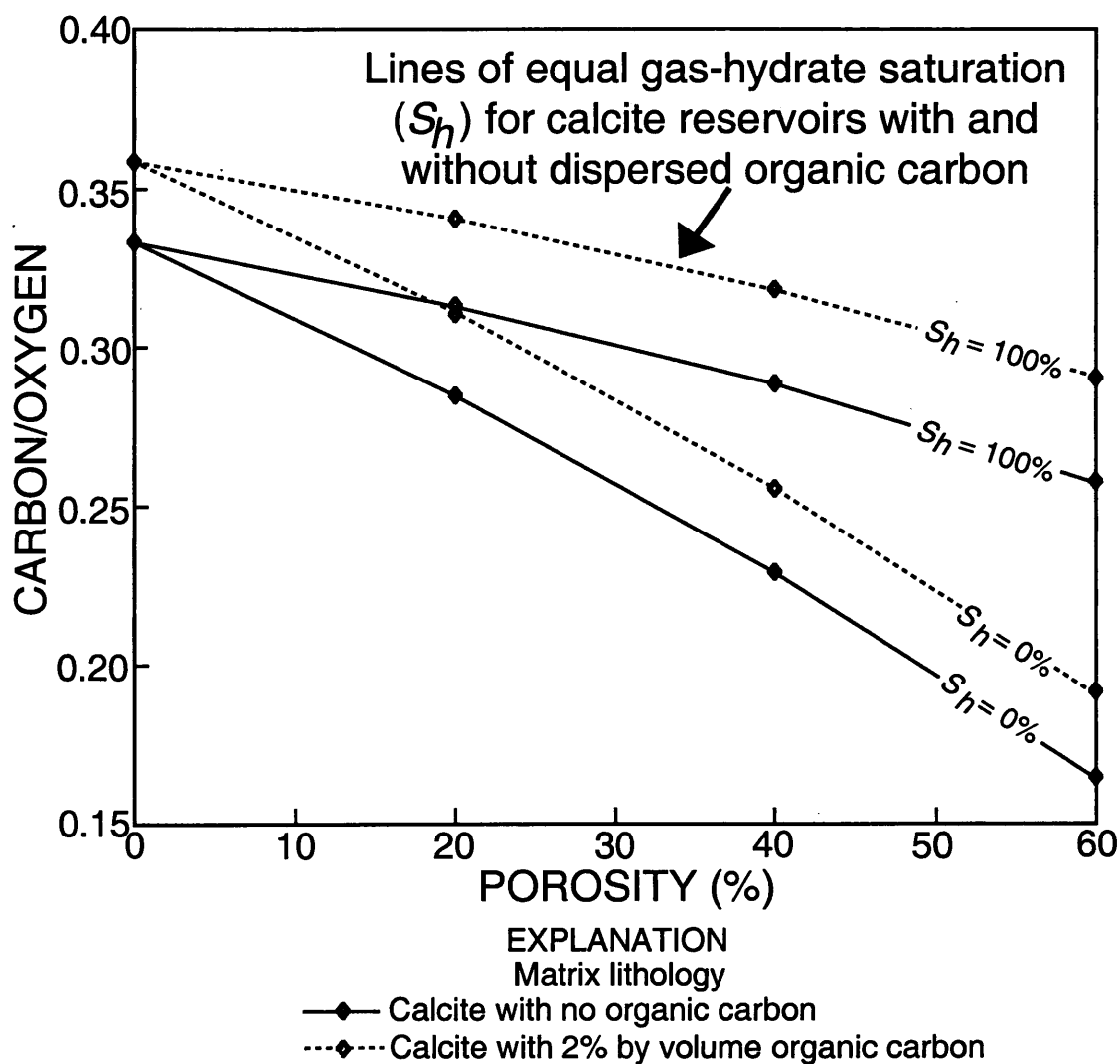
Figure 3.33 Crossplot of sediment porosities and carbon/oxygen ratios for a gas-hydrate-bearing (S_h of 0 and 100 percent) calcite (limestone) reservoir with (2% by volume) and without dispersed organic carbon in the sediment matrix.

carbon content on the GLT-measured carbon/oxygen ratios can be explicitly explained by the following four component COR equation, which is a modified version of the standard three-component equation (Equation 3.23):

$$COR = A \frac{[\alpha(1-C)(1-\varnothing) + \eta[C(1-\varnothing)] + \beta\varnothing S_h + C_b]}{[\gamma(1-C)(1-\varnothing) + \delta\varnothing(1-S_h) + \mu\varnothing S_h + O_b]} \qquad (3.25)$$

where C is the organic carbon content of the sediment as a volume fraction and η is the atomic concentration (variable units) of carbon atoms in natural occurring organic carbon. This four-component equation can be used to characterize a gas-hydrate- and water-bearing reservoir with a matrix consisting of a mixture of quartz, calcite, and organic carbon.

3.7 Nuclear Magnetic Resonance Logs

In recent years there have been significant developments in the field of nuclear magnetic resonance well logging (reviewed by Kleinberg, 1996). Similar to neutron porosity devices, nuclear magnetic resonance tools primarily respond to the presence of hydrogen molecules in the rock formation. Unlike neutron porosity logs, however, nuclear magnetic resonance logs use the electromagnetic properties of hydrogen molecules to analyze the nature of the chemical bonds within the pore-fluids. Relative to other pore-filling constituents, gas hydrates exhibit unique chemical structures and hydrogen concentrations. In theory, therefore, it should be possible to develop nuclear

magnetic resonance well-log evaluation techniques that would yield accurate reservoir

porosities and water saturations in gas-hydrate-bearing sediments.

Under the effect of a strong magnetic field, hydrogen nuclei will tend to align

with the induced magnetic field. A certain amount of time, called the longitudinal

magnetization decay time (T_1), is required for this alignment. When the magnetic field is

removed, the hydrogen nuclei returns to a disordered state with a characteristic relaxation

time, called the relaxation time of transverse magnetization (T_2). The actual oscillating

signal from the protons processing in the earth's magnetic field, used to calculate the

transverse relaxation time, is referred to as the fluid induction decay signal (FID). The

free fluid index (FFI), which represents the portion of pore-fluids free to flow, is

calculated from the amplitude of the fluid induction decay waveform (FID). In standard

nuclear magnetic resonance log evaluation techniques, the longitudinal magnetization

decay time (T_1) is used for permeability calculations, and the free fluid index (FFI) is

used to determine effective porosity and irreducible water saturations (S_{wirr}).

As discussed above, the transverse magnetization relaxation time (T_2) depends on

the relaxation characteristics of the hydrogen-bearing substances in the rock formation.

For example (Figure 3.34), the transverse magnetization relaxation time (T_2) for

hydrogen nuclei in solids is very short, however, the relaxation time (T_2) for hydrogen

nuclei in fluids can vary from tens to hundreds of milliseconds depending on fluid

viscosities and interactions with nearby surfaces (reviewed by Kleinberg, 1996).
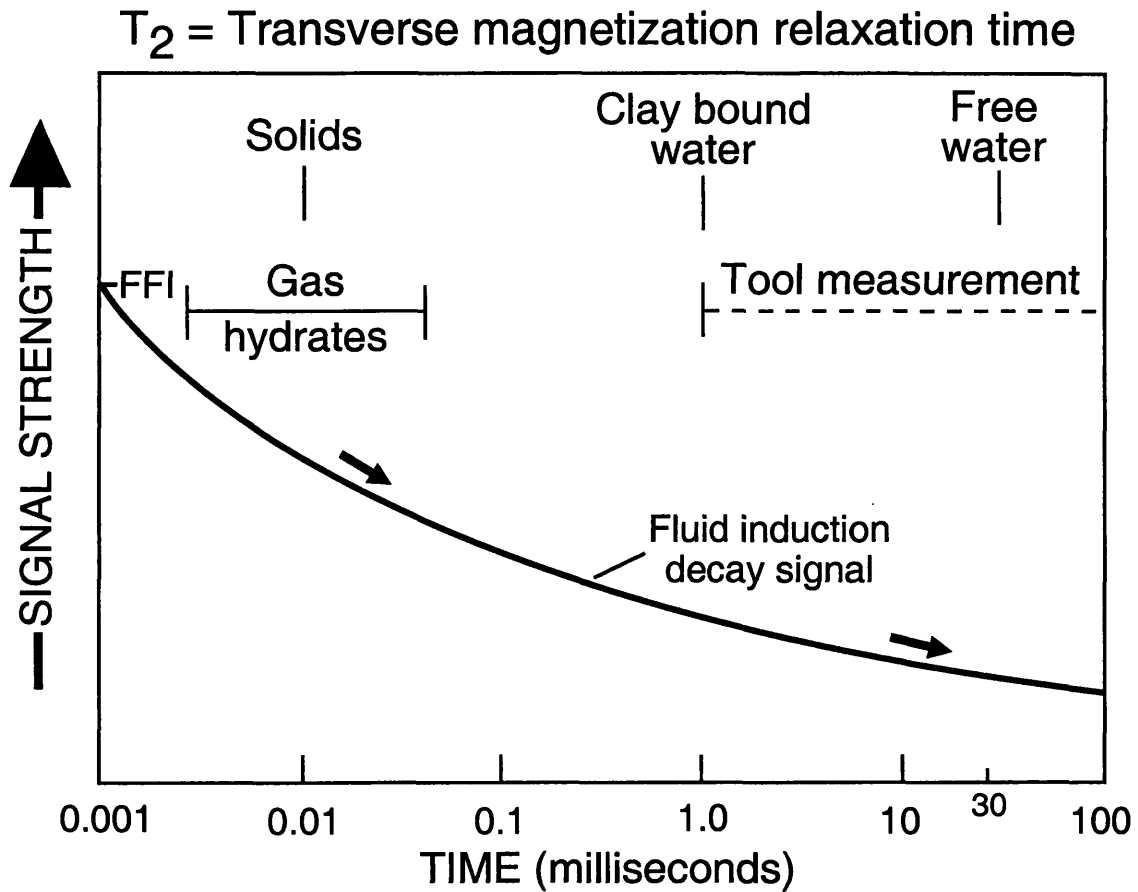
Figure 3.34 Nuclear magnetic resonance transverse magnetization relaxation times (T_2) for a typical rock containing gas hydrates and/or water (depicted as a fluid induction decay signal). FFI = free-fluid index

Since gas hydrates are solids consisting of weakly interacting host and guest molecules, nuclear magnetic resonance methods of analysis, which are sensitive to the mobility of the guest and host molecules, are useful in establishing the presence of gas hydrates in high resolution laboratory studies (Davidson and Ripmeester, 1984). Moreover, the high resolution capabilities of modern nuclear magnetic resonance laboratory devices can provide valuable information about clathrate structures. No laboratory experiments, however, have been conducted to analyze the response of wellbore nuclear magnetic resonance devices to the presence of gas hydrate.

There are numerous studies in which laboratory apparatuses have been used to characterize the nuclear magnetic properties of gas hydrates (Rodin et al., 1984; Davidson et al., 1986; Ratcliffe and Ripmeester, 1986; and Albayrak and Zeidler, 1987). Results of these laboratory nuclear magnetic resonance studies were summarized by Ripmeester and Ratcliffe (1989), from which most of the following discussion has been obtained. In Davidson et al. (1986), nuclear magnetic resonance lineshapes were obtained from a Gulf of Mexico gas hydrate sample. These laboratory experiments clearly showed that the sample contained substantial amounts of gas hydrate. Davidson et al. (1986) did not report any gas hydrate relaxation times or free fluid indexes; however, they did publish several gas hydrate nuclear magnetic resonance spectrums from which it is possible to obtain relaxation times.

If published nuclear magnetic resonance line shapes for Structure-I methane hydrates are assumed to be Gaussian in nature, it can also be assumed that the free induction decay is also Gaussian and the second moment (or mean square line width) is

then inversely related to the transverse magnetization measurement (T_2) (personal communication, J.A. Ripmeester, National Research Council Canada). Thus, if a nuclear magnetic resonance second moment of about 33 Gauss is assumed, the transverse magnetization relaxation time (T_2) of the water molecules in the Structure-I gas hydrate is about 0.01 milliseconds.

The example fluid induction decay signal (FID) plot in Figure 3.34 shows that the gas hydrate clathrate transverse magnetization relaxation time (T_2) of 0.01 milliseconds is very similar to the relaxation times of other solids such as the rock matrix. Transverse magnetization relaxation times (T_2) on the order of 0.01 milliseconds are sufficiently short enough to be lost in the "dead time" (below the detectable limit of the tool) of standard nuclear magnetic resonance borehole instruments. Gas hydrates, therefore, can not be directly detected with today's downhole nuclear magnetic resonance technology. It is possible, however, that existing nuclear magnetic resonance well logs could still yield very accurate gas-hydrate saturation data. In theory, due to the short transverse magnetization relaxation times (T_2) of the water molecules in the clathrate, gas hydrates would not be "seen" by the nuclear magnetic resonance tool and the in-situ gas hydrate would be assumed to be part of the solid matrix. Thus, the nuclear-magnetic-resonance-calculated free fluid index (FFI) and associated porosity estimate in a gas-hydrate-bearing sediment would be apparently lower than the actual porosity. With an independent source of accurate in-situ total porosities, such as density- or neutron-porosity-log measurements, it would be possible to accurately estimate gas-hydrate saturations by comparing the apparent nuclear-magnetic-resonance-derived porosities

with the actual total porosities. This theory, however, cannot be tested because a gas-hydrate accumulation has yet to be logged with a downhole nuclear magnetic resonance tool.

CHAPTER 4

LABORATORY INVESTIGATION OF

SYNTHETIC GAS HYDRATE

4.1 Background Information

The laboratory investigation portion of this study was designed to evaluate the

acoustic nature of gas hydrates in porous media, to evaluate the utility of acoustic well

logs as gas hydrate assessment tools, and to test the gas hydrate well-log analysis

procedures developed in the well-log modeling phase of this study (Chapter 3).

Chapter 3 introduced three acoustic velocity equations [the Timur (Equation

3.14), modified Wood (Equation 3.15), and Lee weighted average (Equation 3.16)

equations] that utilize compressional-wave acoustic data to calculate gas-hydrate

saturations. In this section of the thesis (Chapter 4), the results of laboratory acoustic

experiments on synthetic gas hydrate samples have been used to test the proposed

acoustic velocity gas-hydrate saturation equations and to verify the accuracy of the

acoustic velocity-derived gas-hydrate saturations.

The reservoir matrix and pore-filling constituents characterized within the

laboratory phase of this study included synthetic clean (clay-free) sedimentary rock, ice,

and tetrahydrofuran (THF) hydrates. Since the response of acoustic well logs is

dependent on the acoustic properties of the individual reservoir components as well as the

interaction of the various reservoir components, it is necessary to conduct laboratory

measurements on both the bulk end-member reservoir constituents (matrix material and

pore-filling constituents) and the actual mixed reservoir system. Therefore, both blocks

of pure THF hydrate and THF-hydrate-saturated rock cores have been individually

analyzed in the laboratory phase of this study.

Tetrahydrofuran (THF) was selected as the guest species in the laboratory hydrate

samples instead of a hydrocarbon gas, such as methane, because THF hydrate is stable at

atmospheric pressures and relatively high temperatures (up to about +4.4°C) (Figure 4.1).

It is also possible, depending on the composition of the initial THF-water solution, to

have a liquid phase of THF and water coexisting with THF hydrate at temperatures both

above and below 0°C (Figure 4.1). Tetrahydrofuran is also miscible in water which

eliminates the problem of mixing an immiscible guest molecule, such as methane, with

water. Pearson et al. (1986) concluded that because the crystal structure of hydrates is

mostly independent of the guest species' physical properties, the bulk physical properties

of THF hydrate are probably similar to those of natural gas hydrates. Tetrahydrofuran

forms a Structure-II hydrate, however, which in comparison to Structure-I methane

hydrate appears to be relatively rare in nature (Kvenvolden, 1988). Thus, applying the

analytical results of THF hydrate laboratory studies to natural gas hydrate systems needs

to be done with care and consideration of the mechanical property differences between

Structure-I and Structure-II gas hydrates (see Table 1.1 for comparisons of Structure-I

and Structure-II gas hydrate physical properties). However, it is assumed in this study

that the nature of Structure-I and Structure-II gas hydrate growth in porous media
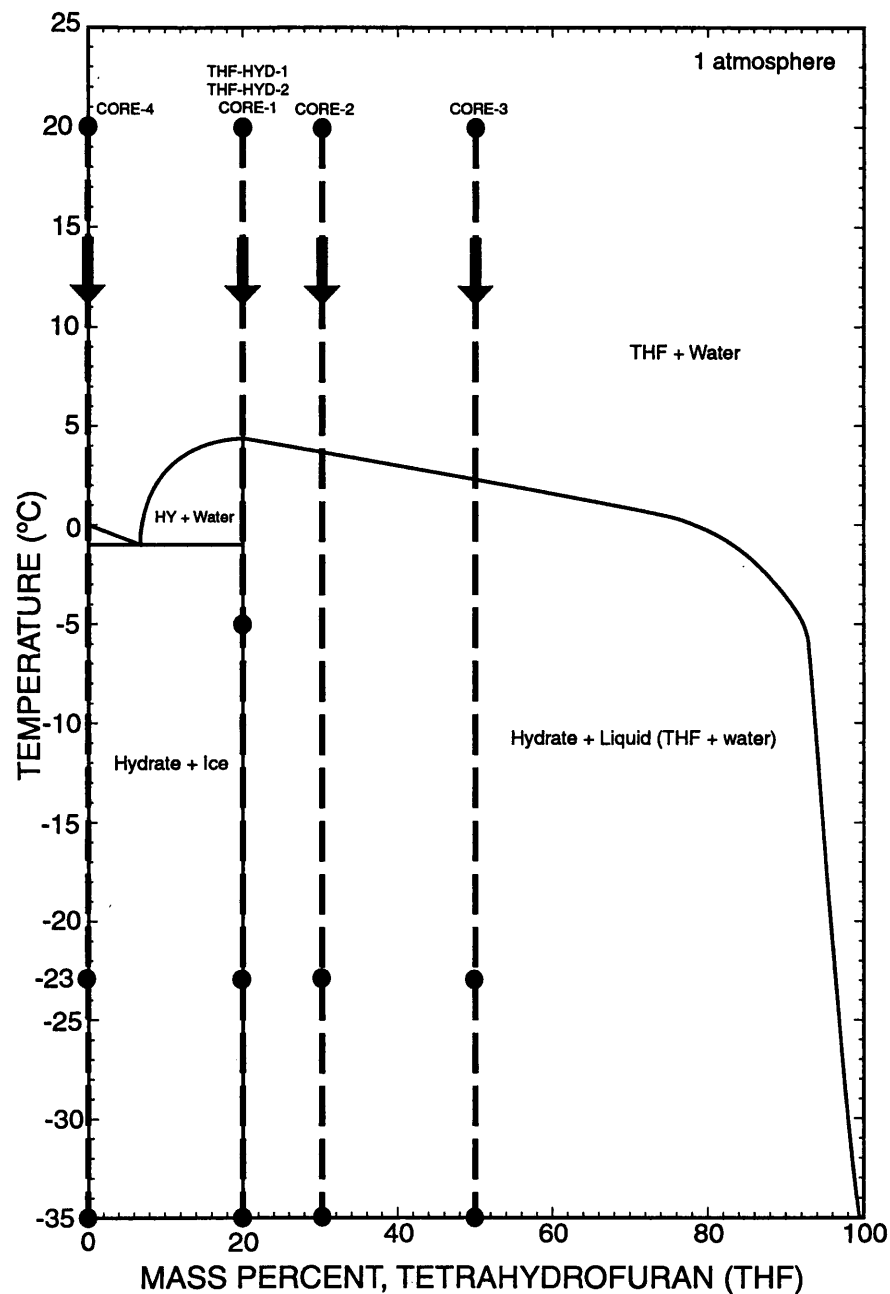
Figure 4.1 Tetrahydrofuran and water temperature-composition phase diagram (modified from Dyadin et al., 1973). Also shown are the experimental conditions (temperature conditions and chemical compositions of the fluids used to saturate the rock cores analyzed in this study) described in the methodology section of this chapter.

(sediments) are similar and that the relative affect of various gas hydrate types on the physical properties of the host sediments are also similar. THF hydrate has a long history of being used in the laboratory as an analog to gas hydrates (reviewed by Sloan, 1998), such as methane hydrate, which must be grown and stored in high pressure containment cells. The THF hydrate experiments presented in this thesis have been designed as an analog to more complex laboratory experiments yet to be conducted.

This chapter starts with a description of the laboratory methods used to construct and analyze the synthetic THF hydrate samples. The laboratory methods section is followed by discussions dealing with the laboratory acoustic properties of THF hydrate and acoustic properties of THF-hydrate-bearing rock cores. This chapter concludes with a review of the acoustic log analysis methods used to calculate gas-hydrate saturations.

4.2 Laboratory Methods

Laboratory procedures used to construct the synthetic THF hydrate samples were adapted from the published laboratory studies of Bathe et al. (1984) and Pearson et al. (1986). Two large blocks of pure THF hydrate were grown from a stoichiometric mixture of tetrahydrofuran (spectrophotometric grade) and distilled water (80 mass percent H_2O and 20 mass percent C_4H_8O) (Figure 4.1). The two blocks of THF hydrate are referred to in this thesis as THF-Hydrate-1 and THF-Hydrate-2. The blocks of THF hydrate were used for instrument calibrations as described later in this section of the thesis.

The blocks of THF hydrate were grown in a 15x15x20 cm Plexiglas box (Figure 4.2) under different cooling conditions. THF-Hydrate-1 was grown at a constant temperature of about -23°C and THF-Hydrate-2 was grown within a laboratory freezer that was slowly cooled from about +20°C to -5°C over a three day period. THF-Hydrate-1 fully crystallized in about 20 hours, while THF-Hydrate-2 took about 50 hours to fully crystallize. In each case, the stoichiometric mixture of tetrahydrofuran and distilled water filled about 80% of the Plexiglas box, which left a 4 cm headspace gap at the top of the box. The top of the box was sealed with a airtight lid and an electrical heat source was placed on top of the box. The Plexiglas box was insulated (5 cm thick ridged foam insulation) from the surrounding cold air in the freezers except for the bottom of the box which was in direct contact with the atmosphere. This configuration of insulation and a heat source at the top of the box created a temperature gradient from the bottom to the top of the box. THF hydrate crystal growth initiated along the bottom of the box with continued crystal growth up into the box.

After all of the tetrahydrofuran-water mixture was converted to THF hydrate, the blocks of THF hydrate were removed from the Plexiglas box and placed within the core storage area of the National Ice Core Laboratory at about -35°C for 48 hours. The individual blocks of THF hydrate (THF-Hydrate-1 and THF-Hydrate-2) were then cut into smaller working rectangular blocks (measuring about 15x10x10 cm) with flat parallel faces.

To evaluate the acoustic properties of gas-hydrate-bearing sediments, a series of acoustic measurements on synthetic rock cores saturated with stoichiometric and non-
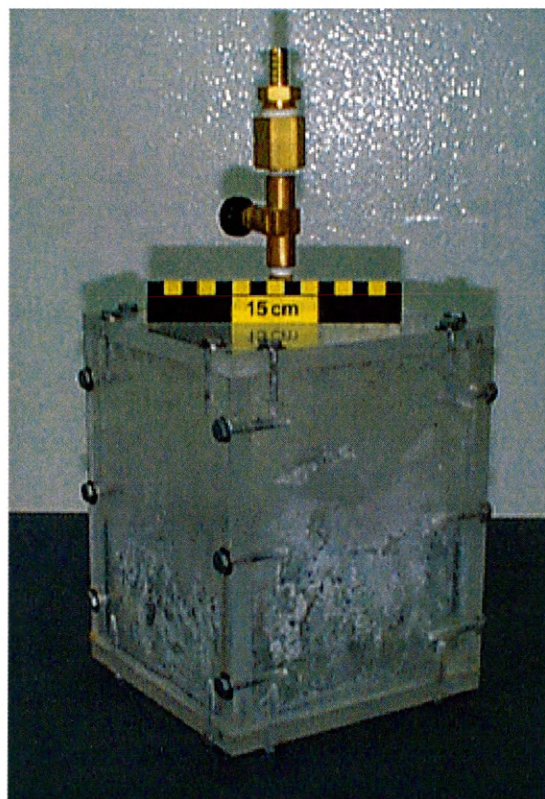
Figure 4.2 Photograph of the Plexiglas box in which the pure blocks of tetrahydrofuran hydrate were grown (THF-Hydrate-1 and THF-Hydrate-2).

stoichiometric THF hydrate mixtures of tetrahydrofuran and water were conducted. The synthetic rock core material (EP Brand Porous Structures) used in this study was purchased from Eaton Products International. "EP Brand Porous Structures" are constructed from nearly perfect spherical grains bonded together to form a highly uniform porous media. The grade designation of the EP Brand product selected for this study is identified as 175 which is described as very coarse. Standard industry core analyses of this synthetic material (Grade 175) reveal a highly uniform interstitial pore distribution and size with a void space ratio (porosity) of 26.4% (personal communication, R.F. Wendlandt, Colorado School of Mines). Additional analyses of the dry core weights relative to the volume and porosity of each core yields an average grain density for the synthetic rock core material of 3.03 g/cm^3. The four synthetic rock cores (Table 4.1, Figure 4.3) used in this study are about 3.2 to 3.6 cm in diameter and their lengths range from about 6.2 to 7.0 cm. The ends of the cores were cut parallel to ensure good contact between the mounted transducers.

Three of the rock cores (Table 4.1: Cores 1, 2, and 3) were saturated with different mixtures of tetrahydrofuran and distilled water. The fourth core (Table 4.1: Core 4) was saturated with only distilled water. One of the tetrahydrofuran-water mixtures was prepared to form a stoichiometric (80 mass percent H_2O and 20 mass percent C_4H_8O) THF hydrate (Core-1).

Core-1 contained only rock matrix material and THF hydrate (no fluid phase) (Figure 4.1). The other two non-stoichiometric mixtures of tetrahydrofuran and water were formulated to form a THF hydrate in the presence of an excess liquid

Table 4.1 Physical characteristics of the synthetic rock cores used in this study to assess the acoustic nature of THF hydrates in porous media (Figure 4.3). Also listed is the chemical composition of the fluid used to flood each core.

Rock core number	Core length (cm)	Core diameter (cm)	Core weight before flooding (g)	Composition of the fluid used to flood each core
1	6.530	3.209	253.61	80 mass % H_2O 20 mass % C_4H_8O
2	6.960	3.429	254.02	70 mass % H_2O 30 mass % C_4H_8O
3	6.950	3.556	254.15	50 mass % H_2O 50 mass % C_4H_8O
4	6.238	3.162	243.16	100 mass % H_2O

Figure 4.3 Photograph of two of the tetrahydrofuran-hydrate-bearing synthetic rock cores.

tetrahydrofuran-water phase. Therefore, Cores 2 and 3 (Figure 4.1) contained not only

rock matrix material and THF hydrate but also a liquid phase of tetrahydrofuran and

water. Relative to nature, Core 1 represented a 100% THF-hydrate-saturated rock, while

Core 2 represented an 88% THF-hydrate-saturated rock and Core 3 represented an 64%

THF-hydrate-saturated rock (Table 4.1). After freezing, Core 4 would represent a 100%

ice-saturated rock.

To ensure that the rock cores were completely saturated with the tetrahydrofuran-

water mixtures (Cores 1, 2, and 3) or water only (Core 4), the cores were first dried in a

vacuum oven for 24 hours at 100°C. The dried cores were individually placed in four

airtight containers with the appropriate mixtures of tetrahydrofuran and water (Cores 1, 2,

and 3) or just water (Core 4). After a period of eight days the cores were removed from

the tetrahydrofuran-water or water only solutions and immediately sealed within latex

condoms. The weight of the individual cores were compared to their pre-core-flood

weights and it was determined that all of the pore-spaces (assuming a rock porosity of

26%) were fully saturated with the tetrahydrofuran-water and water only mixtures. The

four rock cores were then placed within the core storage area of the National Ice Core

Laboratory at about -35°C for eight days. None of the rock cores exhibited evidence of

expansion or structural defects such as cracks.

The primary work space in the National Ice Core Laboratory is maintained at a

temperature of about -23°C. Therefore, all of the acoustic measurements made during

this study were at a temperature of -23°C. It should be noted, however, that all of the

known gas-hydrate accumulations in nature occur at temperatures considerably higher

than -23°C (reviewed by Collett, 1995). Therefore, the laboratory-measured velocities in this study cannot be directly compared to velocities measured in higher temperature gas-hydrate occurrences.

The acoustic apparatus used in this study consisted of two primary components (Figure 4.4), a specially designed jig in which the THF hydrate samples were mounted and a self-contained ultrasonic flaw detection system which generates, detects, and processes compressional-wave ultrasonic acoustic signals. The THF hydrate blocks and THF-hydrate-bearing rock cores were clamped between two 2.25 Mhz compressional-wave transducers within the specially designed acoustic jig. The transducers were coupled to the surface of the THF hydrate blocks and the THF-hydrate-bearing rock cores by placing a small amount of warm glycerin on the face of the sample and gently sliding the transducers together until the THF hydrate sample or core was held firmly in place between the two transducers. The commercial flaw-detector (Epoch 2000 manufactured by Panametrics Inc.) used in this study to measure compressional-wave acoustic velocities was operated in a reverse mode; where the measured travel time between the transducers is used to calculate the velocity of the samples over a pre-measured path length.

Two important features of the Epoch 2000 are the adjustable gain display and the automatic picking facility. The gain was adjusted such that the received signal pulse was exactly 75% of a predetermined reference level. The Epoch 2000 then automatically picks the time at which the pulse had achieved three-quarters of its peak height. Because of the consistency of pulse shape and rise time, the travel-time picks were unaffected by
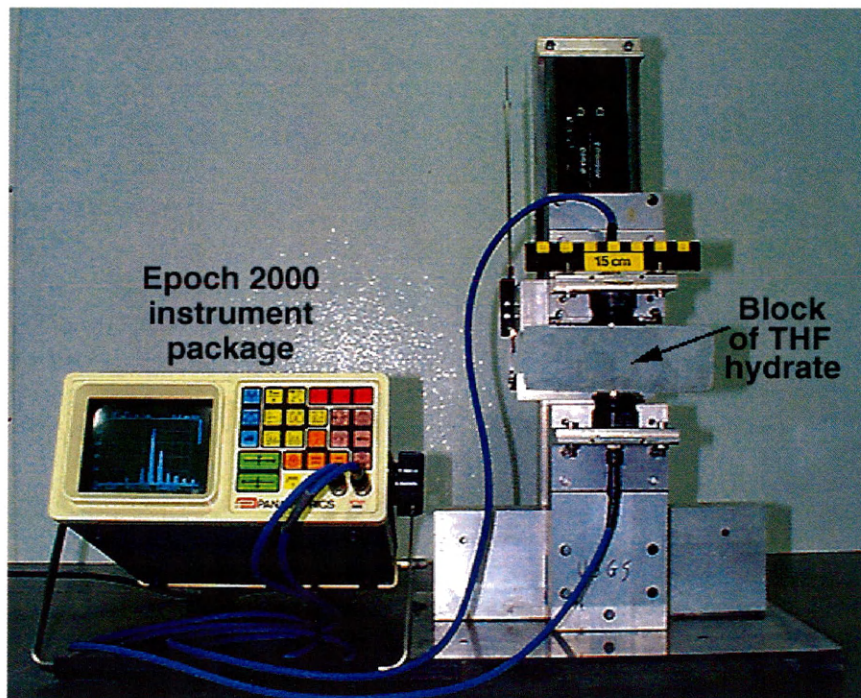
Figure 4.4 Photograph of the laboratory acoustic apparatus used to measure compressional-wave acoustic velocities of pure blocks of tetrahydrofuran hydrate (shown in this photograph) and compressional-wave acoustic velocities of tetrahydrofuran-hydrate-bearing and ice-bearing synthetic rock cores.

attenuation variations. The 75% signal pulse level was calibrated on an aluminum standard to determine the fixed delay introduced by the cables, transducers, and the rise time of the pulse to its pick level.

For calibration purposes, compressional-wave velocity measurements were made on the two blocks of pure THF hydrate (THF-Hydrate-1 and THF-Hydrate-2) (Table 4.2). The compressional-wave velocity measurements of the THF-hydrate-bearing rock cores (Cores 1, 2, and 3) and the ice-bearing core (Core 4) were conducted along the long axis of each core at a constant temperature of -23.0°C (Table 4.3). The compressional-wave velocity of an aliquot of pure tetrahydrofuran at -23°C was also measured in the laboratory phase of this study. The laboratory-measured pure tetrahydrofuran compressional-wave velocity of 1.54 km/sec was used for calibration purposes and as input for the required THF-water fluid velocities in a series of gas-hydrate saturation equations examined later in this chapter of the thesis.

4.3 Acoustic Properties of Tetrahydrofuran Hydrate

As previously discussed, two blocks of pure THF hydrate (THF-Hydrate-1 and THF-Hydrate-2) were grown and analyzed under laboratory conditions to assess the acoustic properties of THF hydrate as a potential reservoir component, to obtain the compressional-wave velocity of Structure-II THF hydrate, and to calibrate the laboratory measurements made in this study with those reported in previously published studies (Bathe et al., 1984; Pearson et al., 1986).

Table 4.2 Laboratory-measured compressional-wave acoustic velocities of THF hydrate samples (THF-Hydrate-1 and THF-Hydrate-2). All measurements were made at a constant temperature of about -23°C.

THF hydrate sample	Compressional-wave velocity (V_p, km/sec)
THF-Hydrate-1	3.50
	3.51
	3.51
	3.52
	3.52
	3.52
	3.53
	3.53
	3.53
	3.53
THF-Hydrate-2	3.51
	3.52
	3.52
	3.52
	3.52
	3.52
	3.53
	3.53
	3.53
	3.53

Table 4.3 Laboratory-measured compressional-wave acoustic velocities of synthetic rock cores containing stoichiometric and non-stoichiometric THF hydrate mixtures of tetrahydrofuran and water (Core 4 contained only ice). All measurements were made at a constant temperature of about -23°C.

Rock core number and composition of the fluid used to flood each core	Acoustic velocity of the synthetic rock cores (km/sec)
Core 1	3.669
80 mass % H_2O	3.690
20 mass % C_4H_8O	3.672
	3.675
	3.688
Core 2	3.598
70 mass % H_2O	3.585
30 mass % C_4H_8O	3.580
Core 3	3.260
50 mass % H_2O	3.265
50 mass % C_4H_8O	3.272
Core 4	3.772
100 mass % H_2O (ice)	3.751
	3.781
	3.783

A total of twenty compressional-wave velocity measurements were made of the two laboratory grown blocks of pure THF hydrate (THF-Hydrate-1 and THF-Hydrate-2) at a temperature of -23°C. Listed in Table 4.2 are the laboratory-measured compressional-wave velocities of THF-Hydrate-1 and THF-Hydrate-2. As shown in Table 4.2, the measured compressional-wave velocities in both THF-Hydrate-1 and THF-Hydrate-2 are similar, with measured velocities averaging about 3.522 km/sec. The range of the measured compressional-wave velocities varied by about ±0.02 km/sec to about ±0.03 km/sec. This range of measured values likely represents the potential uncertainty associated with each compressional-wave velocity measurement.

For comparison purposes, all of the compressional-wave velocities obtained from the two pure THF hydrate blocks (THF-Hydrate-1 and THF-Hydrate-2) have been displayed together in Figure 4.5. Compressional-wave velocities of THF hydrate reported by Bathe et al. (1984) for the temperature range from about -90°C to about -13°C have also been displayed in Figure 4.5. As shown in Figure 4.5, the compressional-wave velocities reported for THF hydrate by Bathe et al. (1984) compare favorably with the compressional-wave velocities measured in this study.

4.4 Acoustic Properties of Tetrahydrofuran-Hydrate-Bearing Rock Cores

As previously discussed, a series of compressional-wave acoustic velocity measurements have been made on three synthetic rock cores (Tables 4.1 and 4.3, Figure 4.3) containing stoichiometric (Core 1) and non-stoichiometric (Cores 2 and 3) THF hydrate mixtures of tetrahydrofuran and water. Compressional-wave velocity
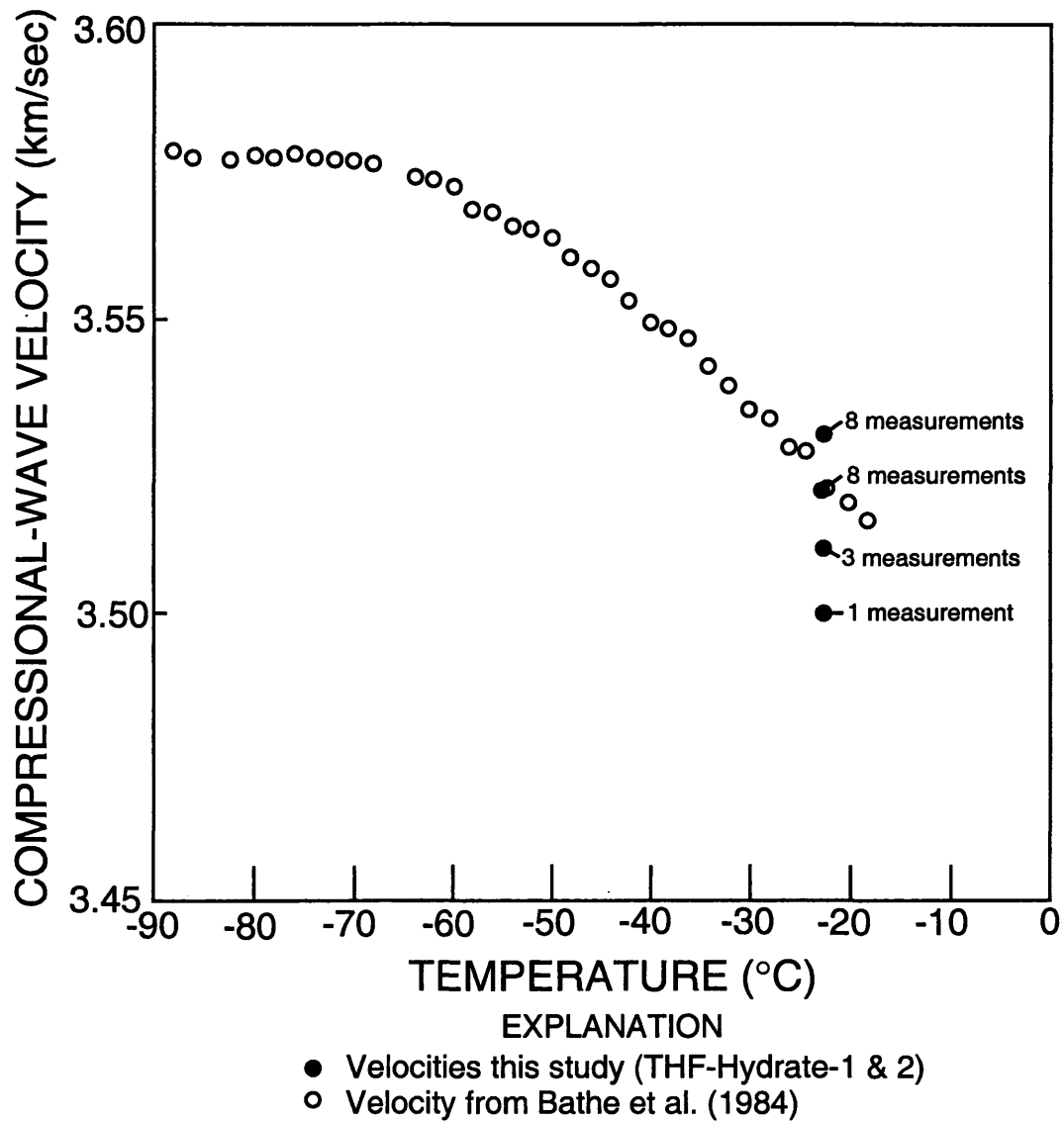
Figure 4.5 Comparison of laboratory-measured compressional-wave acoustic velocities of two pure blocks of tetrahydrofuran hydrate (both THF-Hydrate-1 and THF-Hydrate-2). Also shown are the compressional-wave acoustic velocities of tetrahydrofuran hydrate reported by Bathe et al. (1984).

measurements of a fourth synthetic rock core (Core 4) containing only ice were also

conducted (Tables 4.1 and 4.3, Figure 4.3). All of the velocity measurements of the

synthetic rock core material were made at a constant temperature of about -23°C.

The measured compressional-wave velocity of Core 1 ranged from 3.669 to 3.690

km/sec, and averaged 3.679 km/sec. The measured compressional-wave velocity of Core

2 ranged from 3.580 to 3.598 km/sec, and averaged 3.588 km/sec. The measured

compressional-wave velocity of Core 3 ranged from 3.260 to 3.272 km/sec, and averaged

3.266 km/sec. Acoustic velocity measurements of Core 4, which contained only ice

(100% ice-saturated), yielded an average compressional-wave velocity of 3.772 km/sec.

The uncertainty associated with the compressional-wave velocity measurements

(estimated at ±0.01 km/sec) of the THF-hydrate-bearing cores is lower than the

uncertainty associated with the compressional-wave velocity measurements of the pure

blocks of THF hydrate.

Before using the laboratory-derived rock core velocity data to assess THF-hydrate

saturations with the available acoustic velocity gas-hydrate saturation equations, it was

necessary to verify the "known" THF-hydrate saturations within the THF-hydrate-bearing

rock cores (Cores 1, 2, and 3). As previously discussed, the three THF-hydrate-bearing

cores were flooded with specially formulated mixtures of water and tetrahydrofuran that

should have yielded cores with three different predetermined THF-hydrate saturations

(S_h): Core 1 = 100% THF-hydrate saturation, Core 2 = 88% THF-hydrate saturation, and

Core 3 = 64% THF-hydrate saturation.

To verify the "known" THF-hydrate saturations within each core, aliquots of the specially formulated mixtures of water and tetrahydrofuran used to flood the cores were placed in three separate airtight containers and stored in a laboratory freezer at about -23°C for eight days. After complete or partial THF hydrate formation, the volume of solid THF hydrate and uncrystallized tetrahydrofuran and water were measured, with the relative volume of THF hydrate representing the percent of THF hydrate that should have formed within the pore-space of each rock core (Table 4.4).

This crystallization experiment confirmed that Core 1 should contain only THF hydrate (Core 1, S_h=100%). As shown in Table 4.4, however, Cores 2 and 3 may contain slightly more THF hydrate than predicted from the specially formulated mixtures of tetrahydrofuran and water. This apparent increase in THF hydrate content relative to the predicted compositional values may be due to the loss of volatile tetrahydrofuran to the atmosphere during mixing and subsequent handling.

To test the gas hydrate well-log analysis procedures developed in the well-log modeling phase of this study (Chapter 3), the laboratory-measured compressional-wave velocities of the THF-hydrate-bearing cores for "known" reservoir conditions have been used in a series of three acoustic velocity equations [the Timur (Equation 3.14), modified Wood (Equation 3.15), and Lee weighted average (Equation 3.16) equations] that utilize compressional-wave velocities to calculate gas-hydrate saturations.

Since the laboratory acquired velocity measurements have been made on rock cores with "known" THF-hydrate saturations, the accuracy of the THF-hydrate saturations calculated from the proposed acoustic velocity gas-hydrate saturation

Table 4.4 THF-hydrate saturations (S_h) of the synthetic rock cores as predicted from the predetermined chemical composition of the fluid used to flood each core and from the special crystallization experiment. THF-hydrate saturations (S_h) as calculated from the Timur (Figure 4.6) and Lee (Figure 4.8) acoustic equations are also listed.

Rock core number	THF-hydrate-saturation (S_h) predetermined from the chemical composition of the fluid used to flood each core (%)	THF-hydrate-saturation (S_h) determined from the crystallization experiment (%)	THF-hydrate-saturation (S_h) determined from the Timur equation (%)	THF-hydrate-saturation (S_h) determined from the Lee equation (%)
1	100	100	98.5	98.9
2	88	90	92.1	93.5
3	64	70	64.0	71.9

equations can be evaluated. Figures 4.6, 4.7, and 4.8 are plots of the three component

Timur (Figure 4.6, Equation 3.14), Wood (Figure 4.7, Equation 3.15), and Lee (Figure

4.8, Equation 3.16) acoustic equations for a rock matrix system containing THF hydrate

and a liquid phase of tetrahydrofuran and water. Also displayed in Figures 4.6, 4.7 and

4.8 are the laboratory-measured compressional-wave velocities (assuming a core porosity

of 26%) of the THF-hydrate-bearing cores (Tables 4.3 and 4.4) examined in the

laboratory phase of this study. In all three acoustic velocity gas-hydrate saturation

equations, the rock core porosity ($\emptyset$) was assumed to be 26% and the matrix density (ρ_m)

was assigned a value of 3.03 g/cm^3. Assuming an average mixture of 3 mass percent

water and 97 mass percent tetrahydrofuran (at -23°C, Figure 4.1), the liquid phase within

each of the partially THF-hydrate-saturated cores (Cores 2 and 3) should have a density

(ρ_w or ρ_f) of 0.892 g/cm^3 and a laboratory-measured compressional-wave velocity (V_w

or V_f) of 1.5 km/sec. Within all three equations, the density of the THF-hydrate (ρ_h) was

assumed to be 0.954 g/cm^3 (Bathe et al., 1984) and a THF-hydrate compressional-wave

velocity (V_h) of 3.52 km/sec was also assumed, which was obtained from the acoustic

velocity measurements of the pure blocks of THF hydrate discussed earlier in this section

of the thesis (Table 4.2). In order not to bias the Lee weighted average acoustic equation,

the weight factor, W, and the cementation exponent, r, were each assumed to be equal to

one in the laboratory phase of this study.

The final variable needed for the Timur and Wood acoustic equations is the

matrix velocity (V_m) of the synthetic rock cores. The laboratory-measured

compressional-wave velocities of the 100% ice-saturated core (Core 4; Table 4.3) and the

Timur acoustic equation (Equation 3.14) have been used to obtain the matrix velocity of

the synthetic rock cores. By assuming the compressional-wave velocity of ice at -23°C is

3.82 km/sec (measured within this study on a pure block of ice), a rock core porosity of

26%, and an ice-saturated rock core (100% ice-saturated) velocity of 3.772 km/sec (Table

4.3) it was possible to calculate a matrix velocity (V_m) of 3.76 km/sec for the synthetic

rock core material. As shown in Figures 4.6-4.8 and Table 4.4, the THF-hydrate

saturations predicted from the Timur and Lee ($W=1$) acoustic velocity equations compare

favorably with the "known" THF-hydrate saturations calculated for Core 1 ($S_h=100\%$),

Core 2 ($S_h=90\%$), and Core 3 ($S_h=70\%$). The Wood acoustic equation (Figure 4.7) failed

to yield reasonable results, with all of the predicted THF-hydrate saturations exceeding

100%.

4.5 Review of Acoustic Methods for Gas Hydrate Reservoir Evaluation

Laboratory analyses of THF-hydrate-bearing synthetic rock cores have shown that

for the most part the Lee weighted average equation (Equation 3.16), that utilizes

compressional-wave acoustic velocities, yielded THF-hydrate saturations that compare

favorably with "known" saturations. In addition, the Timur time-average equation

(Equation 3.14), which adequately predicts the acoustic properties of gas hydrates in

consolidated rock media, also yielded reasonable THF-hydrate saturations within the

laboratory phase of this study. The Wood equation (Equation 3.15) yielded unreasonable

THF-hydrate saturations from the laboratory-measured compressional-wave acoustic
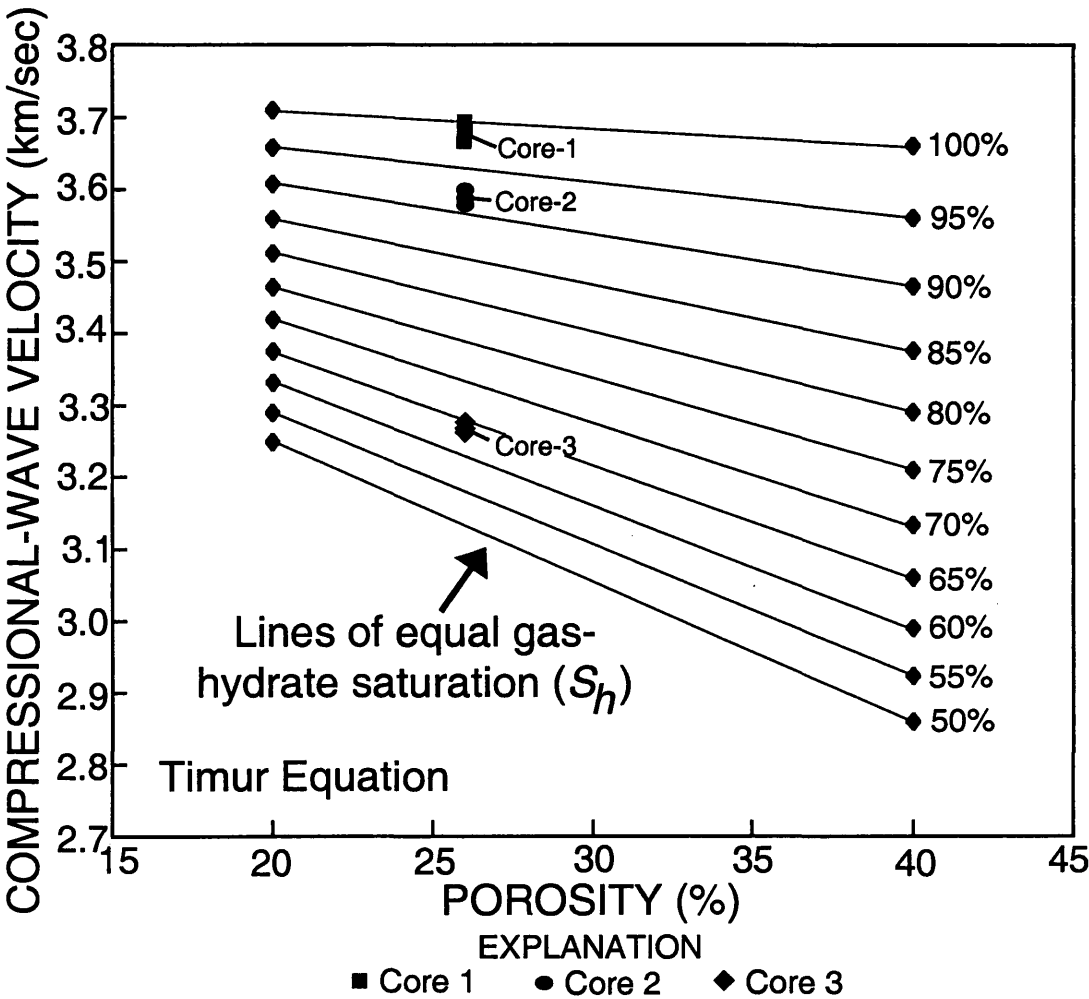
Figure 4.6 Plot of the three-component Timur compressional-wave (V_p) acoustic equation (Equation 3.14) for a tetrahydrofuran-hydrate-bearing reservoir with the same rock properties of the synthetic rock cores used in this study. Also shown are the laboratory-measured compressional-wave (V_p) acoustic velocities (assuming a rock core porosity of 26%) of the tetrahydrofuran-hydrate-bearing rock cores analyzed in this study (Table 4.3).
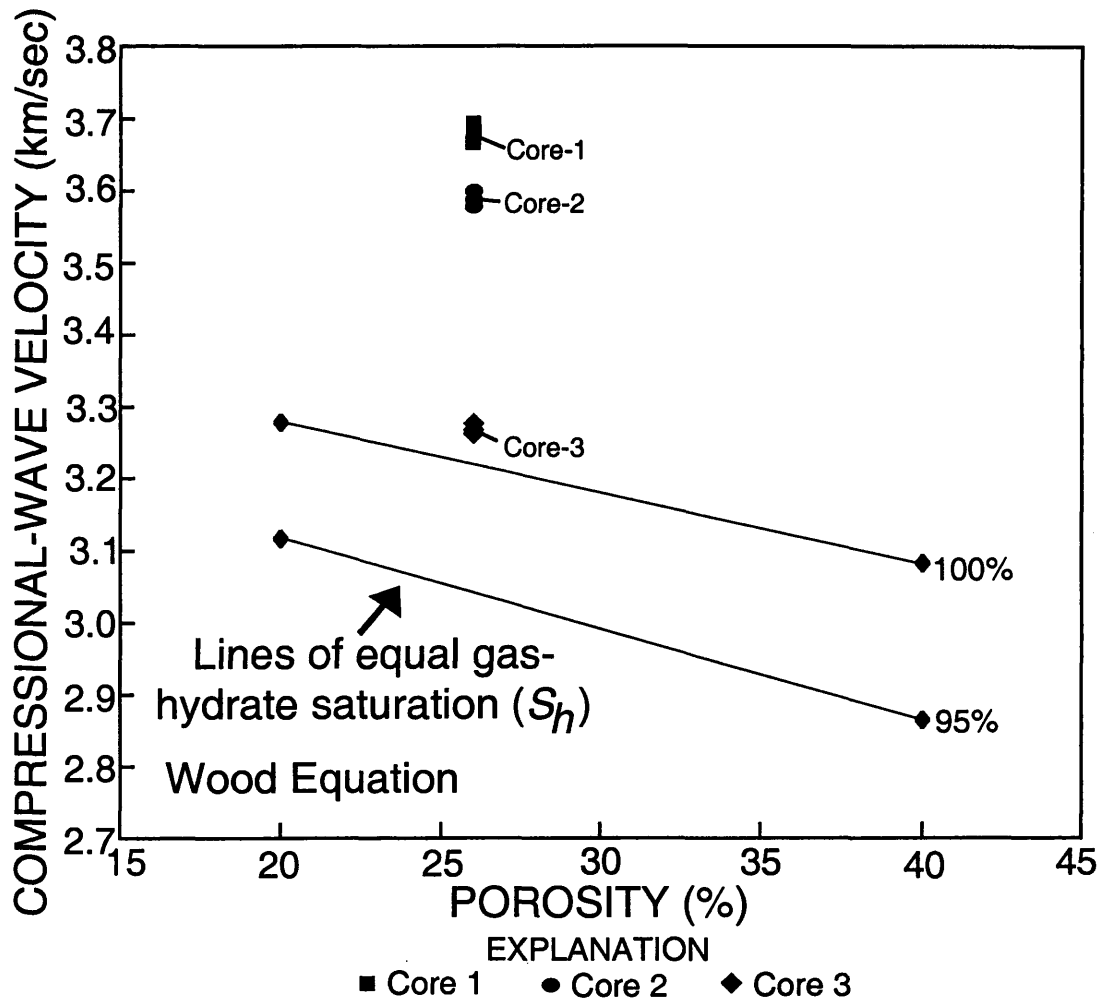
Figure 4.7 Plot of the three-component modified Wood compressional-wave (V_p) acoustic equation (Equation 3.15) for a tetrahydrofuran-hydrate-bearing reservoir with the same rock properties of the synthetic rock cores used in this study. Also shown are the laboratory-measured compressional-wave (V_p) acoustic velocities (assuming a rock core porosity of 26%) of the tetrahydrofuran-hydrate-bearing rock cores analyzed in this study (Table 4.3).
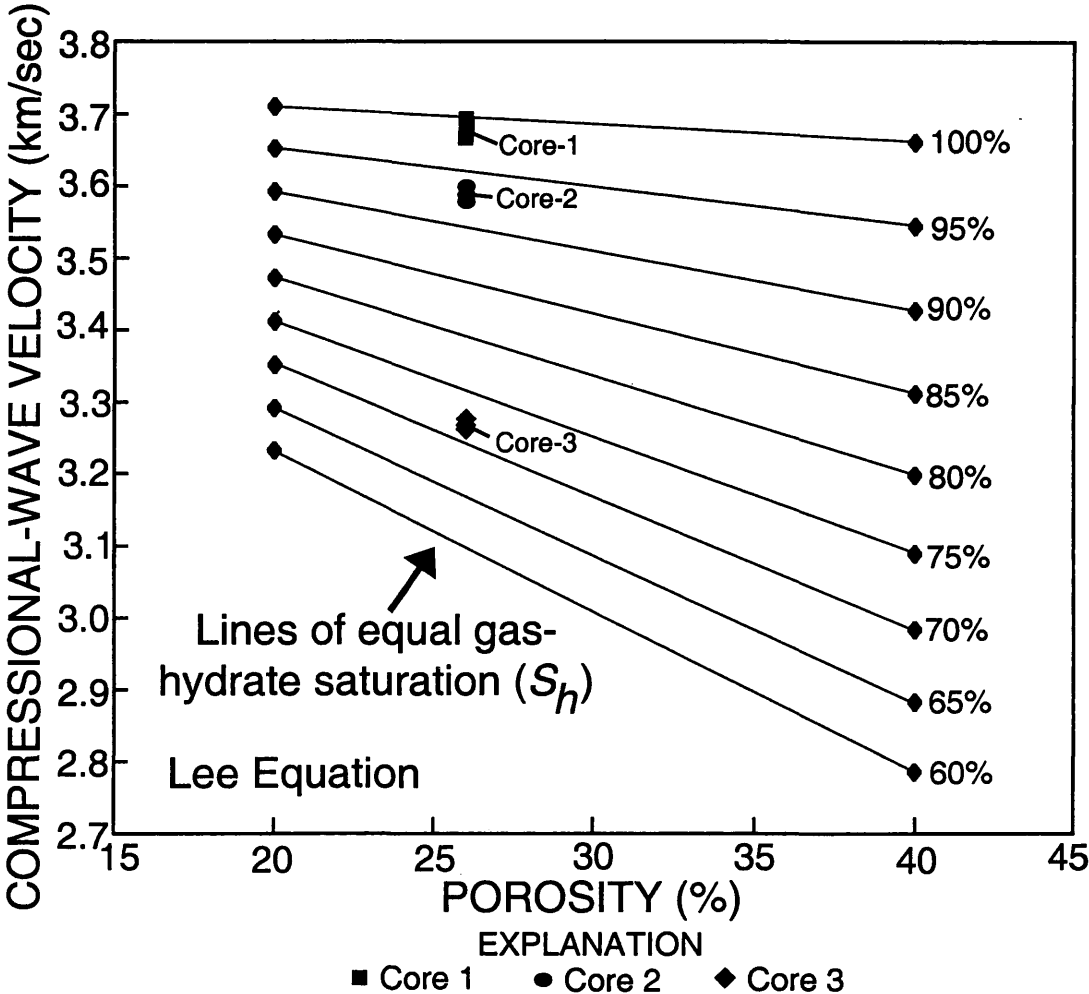
Figure 4.8 Plot of the three-component Lee compressional-wave (Vp) acoustic equation (Equation 3.16) for a tetrahydrofuran-hydrate-bearing reservoir with the same rock properties of the synthetic rock cores used in this study. Also shown are the laboratory-measured compressional-wave (Vp) acoustic velocities (assuming a rock core porosity of 26%) of the tetrahydrofuran-hydrate-bearing rock cores analyzed in this study (Table 4.3).

velocities. It is important to note that Pearson et al. (1986) also found that the Timur

time-average equation accurately predicted the velocity of THF-hydrate-saturated

(S_h=100%) rock cores composed of Berea sandstone, Austin chalk, and Solenhofen

limestone. The laboratory phase of this study revealed that at relatively high gas-hydrate

saturations (S_h>75%) the Timur time-average and Lee weighted average equations yield

similar results. However, at lower gas-hydrate saturations or within a less rigid rock

matrix the Lee equation should yield gas-hydrate saturations more compatible with the

gas-hydrate saturations calculated with the Wood equation.

QUANTITATIVE WELL-LOG ANALYSIS OF

IN-SITU NATURAL GAS HYDRATES

VOLUME 2

by

Timothy S. Collett

TABLE OF CONTENTS

CHAPTER 5

FIELD APPLICATION

5.1 Background Information

In this chapter, most of the quantitative gas hydrate well-log evaluation

techniques developed in the response modeling (Chapter 3) and laboratory testing

(Chapter 4) phases of this study have been tested and utilized to calculate reservoir

porosities and degree of gas-hydrate saturation within five known and logged gas-hydrate

occurrences: (1) Blake Ridge along the southeastern continental margin of the United

States, (2) Cascadia continental margin off the Pacific coast of Canada, (3) Middle-

America Trench off the Pacific coast of Guatemala, (4) North Slope of Alaska, and (5)

Mackenzie River Delta of northern Canada (Table 1.3 and Figure 1.3). Available well

logs from these known gas-hydrate occurrences include density and neutron porosity

logs, electrical resistivity and acoustic transit-time logs, and a limited number of neutron

spectroscopy surveys. The available well-log data have allowed the complete evaluation

of the proposed quantitative gas hydrate well-log evaluation techniques introduced in

Chapter 3 of this thesis.

Chapter 5 has been divided into five roughly parallel sections, with each section

dealing with one of the known and logged gas-hydrate occurrences discussed in Chapter

1 of this thesis. Each section in this chapter starts with a description of the known gas-

hydrate occurrences and associated geologic conditions. Each section contains descriptions of the downhole logging program and a complete listing of the available log data from each site. Relevant stratigraphic information along with descriptions of identified "Well Logging Units" are also included. The main body of each section includes the complete assessment of the reservoir porosities and gas-hydrate saturations within the known and logged gas-hydrate occurrences. Each section also contains estimates of the potential gas resources associated with the log-inferred gas-hydrate occurrences.

Shown in Figure 5.1a-f is a series of "Gas Hydrate Log Analysis Flow Charts" which graphically depict the procedures used to quantitatively evaluate a natural gas-hydrate accumulation. The log analysis flow charts in Figure 5.1a-f contain graphical descriptions of the log analysis procedures tested in the field portion (Chapter 5) of this study. These charts present a step-by-step approach to calculate, with downhole-log data, reservoir porosities and gas-hydrate saturations in gas-hydrate-bearing sedimentary units. The "Gas Hydrate Log Analysis Flow Charts" in Figure 5.1a-f have been used in this chapter as graphical guides to organize and explain the log analysis procedures used to quantitatively evaluate the known gas-hydrate accumulations assessed in this thesis.

5.2 Blake Ridge--Atlantic Ocean

5.2.1 Introduction and Regional Geology

The Atlantic continental margin of the United States is a classic "passive" margin and is generally used as an example of a geologic feature developed during continental

GAS HYDRATE LOG ANALYSIS FLOW CHART -- SEDIMENT POROSITY

Log bulk density (ρ_b)

$\dfrac{\rho_m - \rho_b}{\rho_m - \rho_f} = \phi$

ρ_m from core samples

$\rho_f = 1.00$
$\rho_f = 1.05$

Gas hydrate porosity correction $S_h > 50\%$

Density log porosity (ϕ)

Neutron log porosity (ϕ_n)

Gas hydrate porosity correction $S_h > 50\%$

Neutron log porosity (ϕ)

Deep resistivity log (R_t)

$R_t / R_w = a \, \phi^{-m}$
$S_w = 1.0$

$a \& m$
R_o / R_w vs. ϕ crossplot

R_w

Temp & PW salinity

Resistivity porosity (ϕ)
$S_w = 1.0$

Evaluate & compare, select best porosity
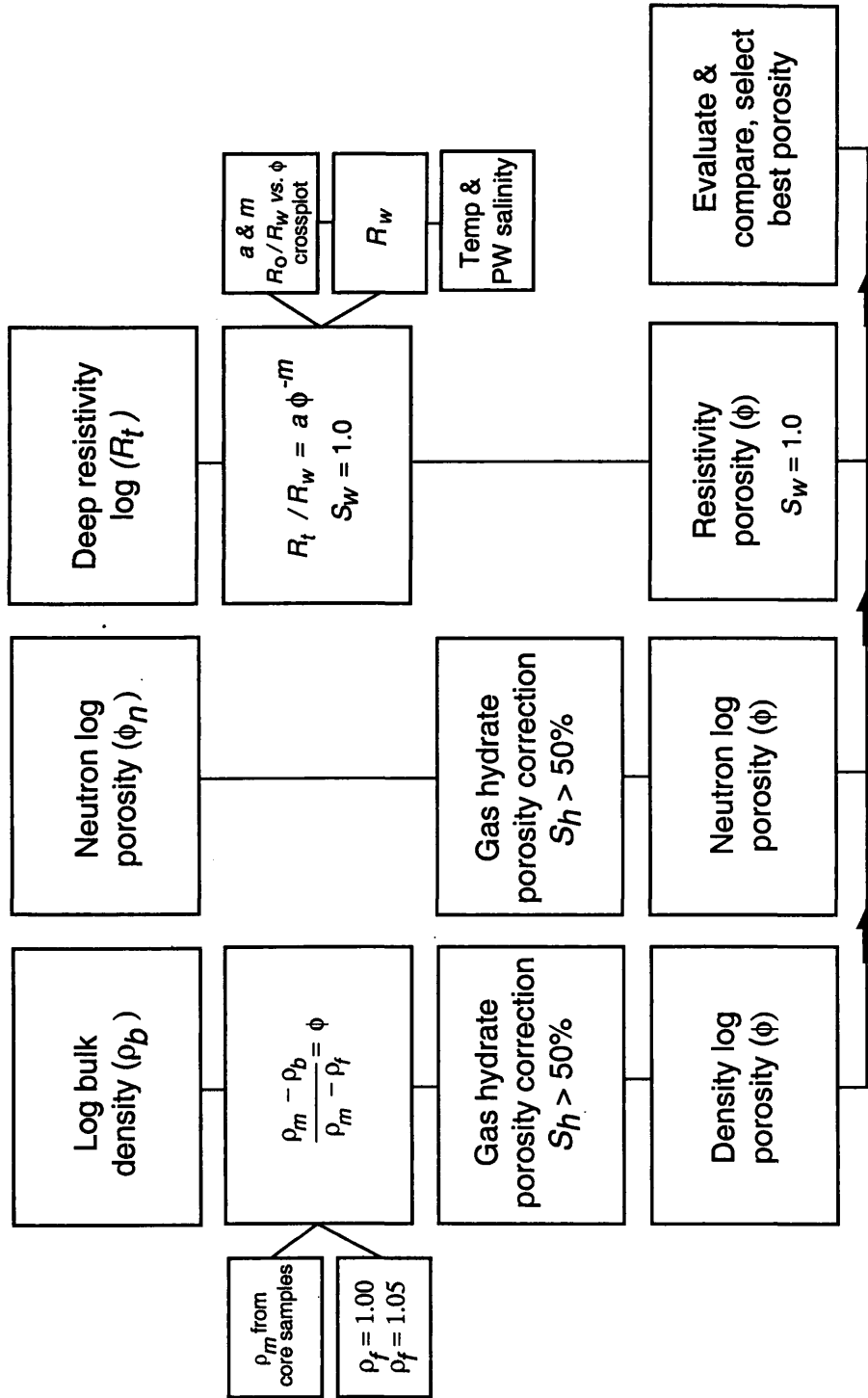
Figure 5.1a Well-log analysis procedures used in this thesis to calculate sediment porosities in gas-hydrate-bearing reservoirs.

**GAS HYDRATE LOG ANALYSIS FLOW CHART --
GAS-HYDRATE SATURATION -- RESISTIVITY
(shale-free reservoir)**
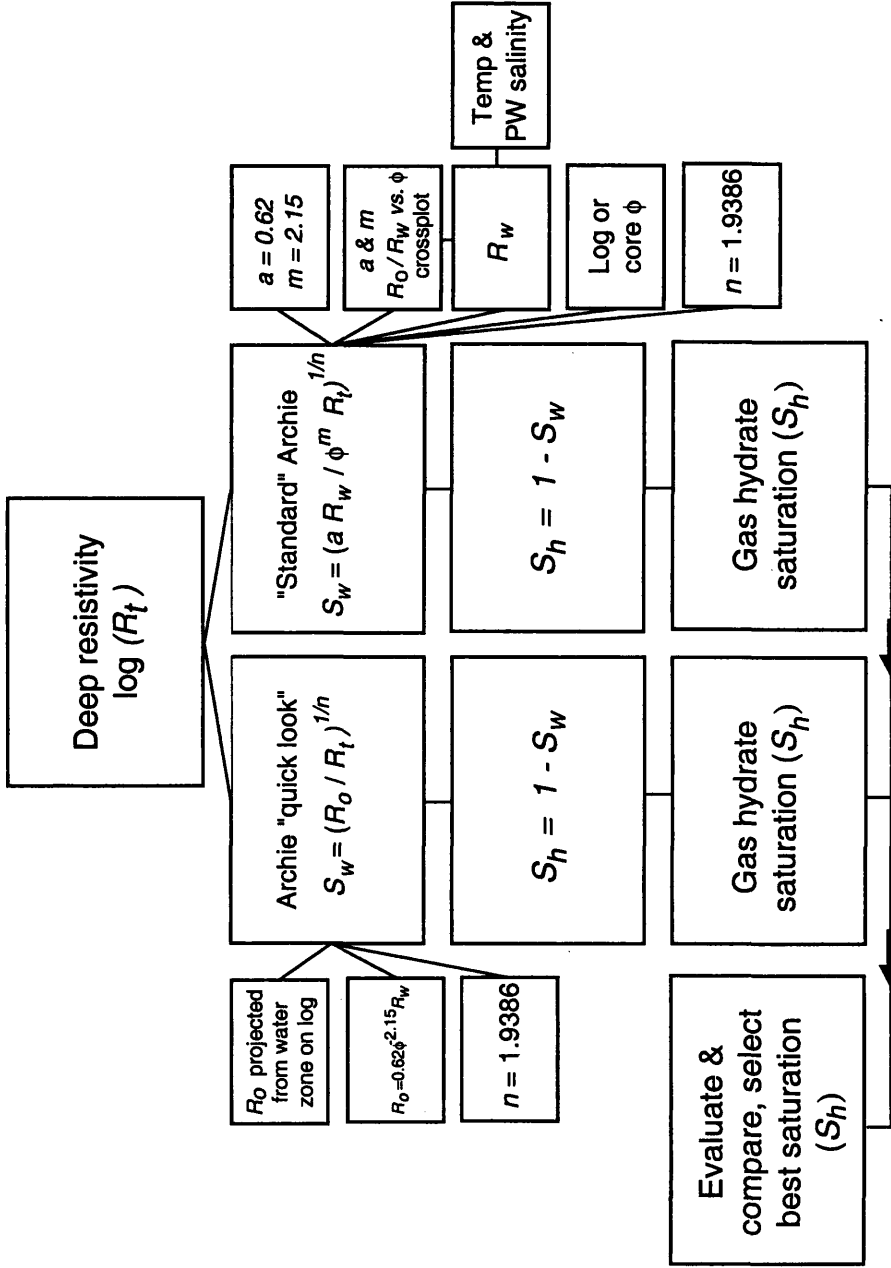
Figure 5.1b Electrical resistivity well-log analysis procedures used in this thesis to calculate gas-hydrate saturations in shale-free 34

GAS HYDRATE LOG ANALYSIS FLOW CHART :-
GAS-HYDRATE SATURATION – RESISTIVITY
(shale-bearing reservoir)

Formation conductivity (C_t) (from the deep resistivity log R_t)

Shaly sand Archie a^* m^* n^*

C_w

Temp & PW salinity

Sediment CEC data

Shale vol. (V_{sh})

Q_v (Eq. 3.13)

Shaly sand ϕ

Waxman-Smits model (Equation 3.12)

$S_h = 1 - S_w$

Gas hydrate saturation (S_h)

Indonesian model (Equation 3.11)

$S_h = 1 - S_w$

Gas hydrate saturation (S_h)

Shaly sand Archie a^* m^* n^*

C_w

Temp & PW salinity

Shale con. (C_{sh})

Shaly sand ϕ

Shale vol. (V_{sh})

Evaluate & compare, select best saturation (S_h)

Figure 5.1c Electrical resistivity well-log analysis procedures used in this thesis to calculate gas-hydrate saturations in shale-bearing reservoirs.

**GAS HYDRATE LOG ANALYSIS FLOW CHART –
GAS-HYDRATE SATURATION -- ACOUSTIC VELOCITY
(compressional-wave data)**

Log or core φ

W
Vp vs. φ crossplot

$r=1$

Evaluate & compare, select best saturation (S_h)

Log derived acoustic velocity (V_b) Vp only

Lee equation (Equation 3.16)

Lee Vp gas hydrate saturation (S_h)

Modified Wood equation (Equation 3.15)

Modified Wood gas hydrate saturation (S_h)

V_w V_h V_m Table 3.12

Log or core φ

ρ_w ρ_h ρ_m Table 3.12

ρ_b Equation 3.2

Timur equation (Equation 3.14)

Timur gas hydrate saturation (S_h)

Figure 5.1d Compressional-wave acoustic velocity well-log analysis procedures used in this thesis to calculate gas-hydrate saturations.

GAS HYDRATE LOG ANALYSIS FLOW CHART --
GAS-HYDRATE SATURATION -- ACOUSTIC VELOCITY
(compressional- and shear-wave data)

Log derived acoustic velocity (V_b) V_p & V_s data

ρ_b Equation 3.2

K G

$Km\ Gm$
$Km\ Gm$
Table 3.12

Kuster-Toksöz equations
(Eq. 3.18 & 3.19)

Grain contact (cementation) theory
Dvorkin et al. (1991)

Lee equation Vp results
(Equation 3.16)

Lee Vp - Vs relation
(Equation 3.17)

Timur Vp
(Eq. 3.14)

Wood Vp
(Eq. 3.15)

Log or core ϕ

α γ β

Kuster-Toksöz gas hydrate saturation (S_h)

Grain contact gas hydrate saturation (S_h)

Lee Vp - Vs gas hydrate saturation (S_h)

Evaluate & compare, select best saturation (S_h)

Figure 5.1e Combined compressional- and shear-wave acoustic velocity well-log analysis procedures used in this thesis to calculate gas-hydrate saturations.
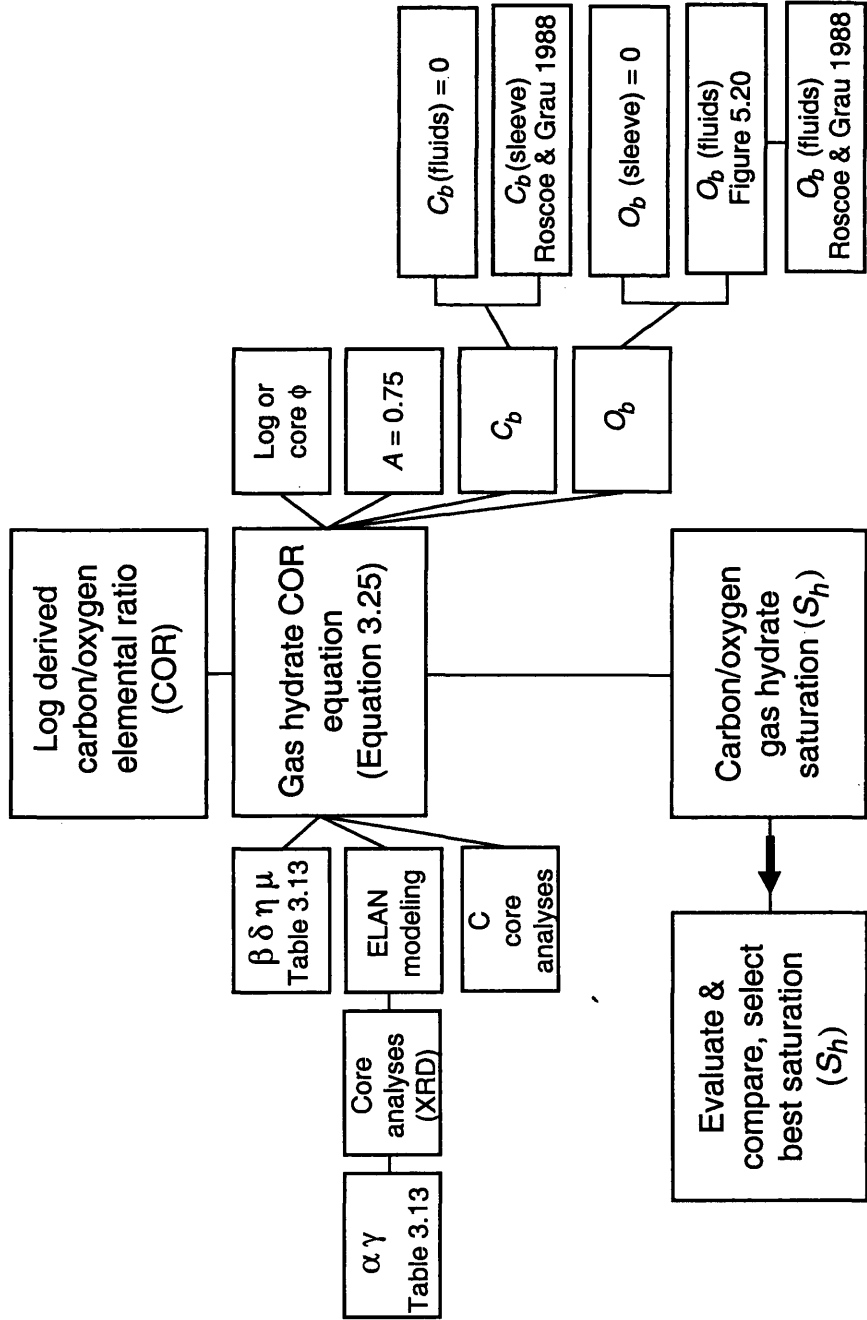
Figure 5.1f Well-log analysis procedures used in this study to calculate gas-hydrate saturations with log-derived carbon/oxygen elemental data.

rifting (Bally, 1981). During rifting of North America from North Africa and subsequent

subsidence, a thick wedge of Mesozoic and Cenozoic sediments built out onto the

subsiding continental margin. Major deltaic systems prograded across the continental

shelf, which occasionally were interrupted by more open marine conditions. Carbonate

reefs and micritic limestone buildups marked the shelf-slope break. The major

sedimentary basins along the Atlantic margin are generally elongated parallel to the

present-day coast and most contain more than 10,000 m of sediment. The major basins

include the Scotian, Georges Bank, Baltimore Canyon Trough, Carolina Trough, and

Blake Plateau. North of the Carolinas, the continental margin above 2,000-m

bathymetric depth is less than 150 km wide, whereas to the south, into the Florida-

Bahama region, the continental margin broadens to about 500 km. Beneath this broad

continental shelf region are located the Carolina Trough and Blake Plateau Basin, which

is bounded to the northeast by the Blake Outer Ridge (Figure 5.2).

Seismic profiles along the Atlantic margin (Figure 5.3) are often marked by large-

amplitude bottom simulating reflectors (BSRs) (Dillon et al., 1993; Lee et al., 1993),

which in this region are believed to be caused by large acoustic impedance contrast at the

base of the gas-hydrate stability zone that juxtaposes sediments containing gas hydrates

with sediments containing free gas. BSRs have been extensively mapped at two locations

off the east coast of the United States -- along the crest of the Blake Ridge and beneath

the upper continental rise of New Jersey and Delaware (Tucholke et al., 1977; Dillon et

al., 1993).
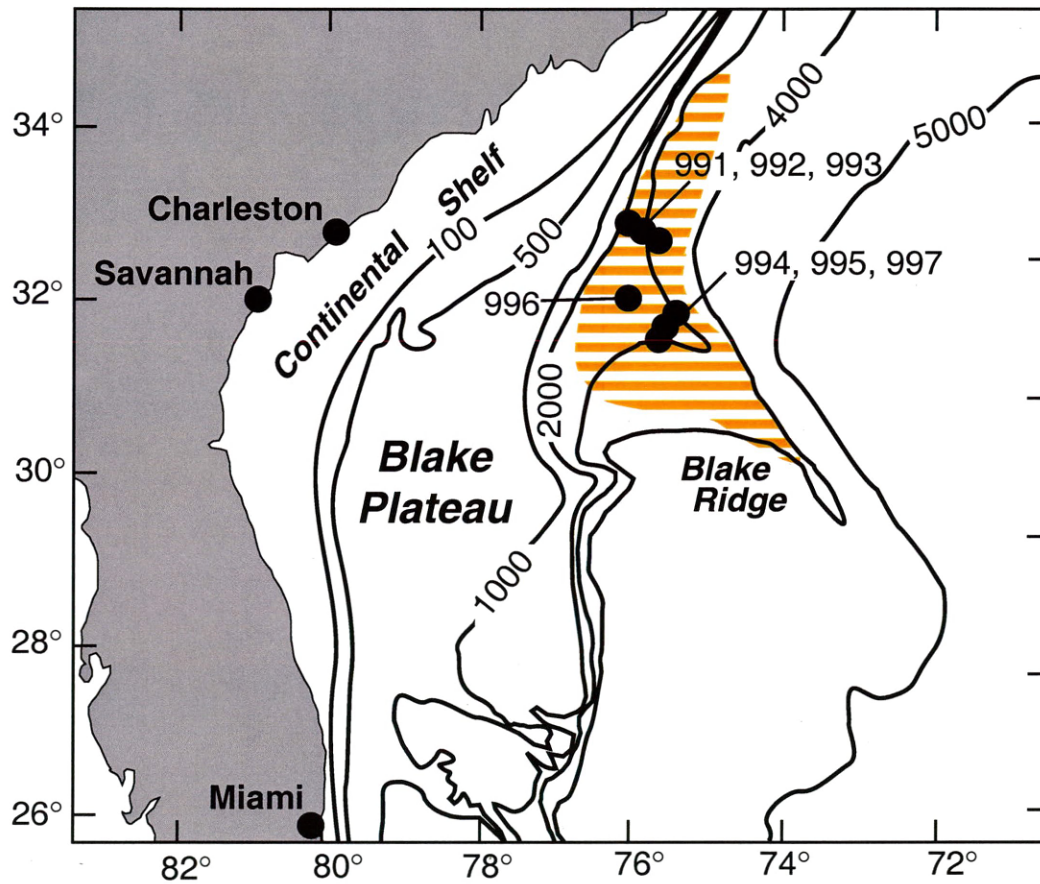
Figure 5.2 Physiographic map of the southeastern continental margin of North America. Location of ODP Leg 164 drill-sites are indicated. Also shown is the area (horizontally shaded area) where gas-hydrate occurrence has been mapped on the basis of bottom simulating reflectors (BSRs). Contours are in meters.
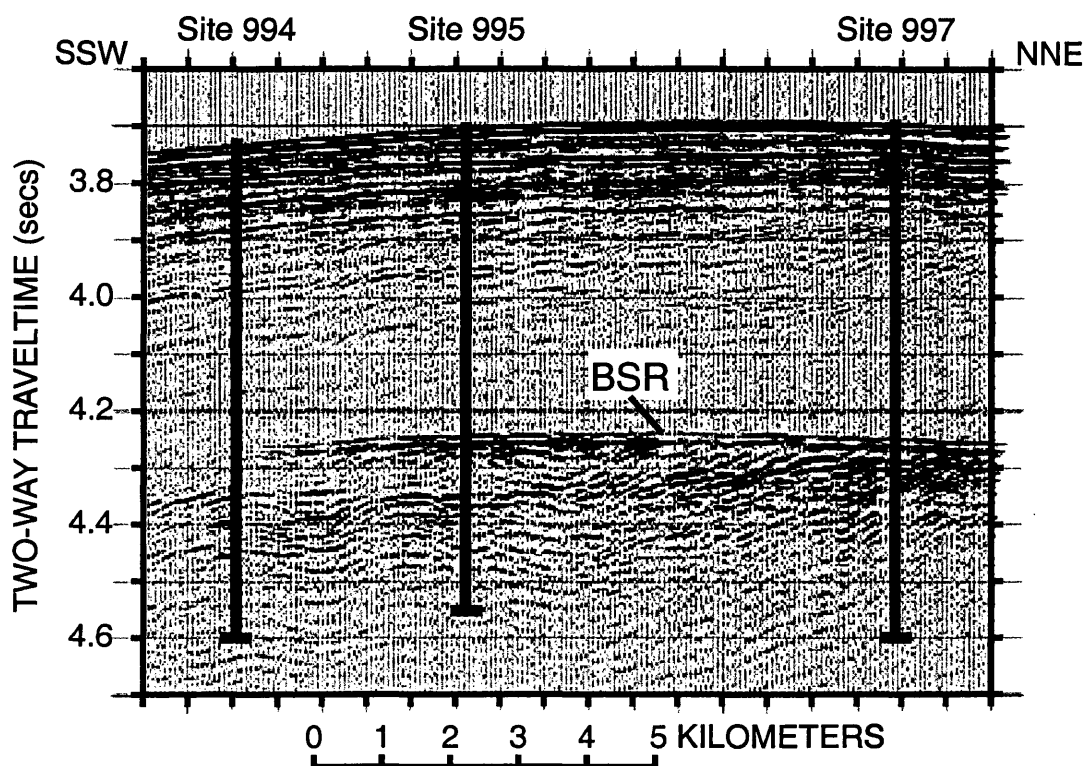
Figure 5.3 Seismic profile along which Sites 994, 995, and 997 are located. Note that Site 994 is not associated with a distinct BSR although a very strong BSR occurs at Sites 995 and 997.

The Blake Ridge is a positive topographic sedimentary feature on the continental slope and rise of the United States (Figure 5.2). The crest of the ridge extends approximately perpendicular to the general trend of the continental rise for more than 500 km to the southeast from water depths of 2,000 to 4,800 m. The upper ridge is referred to as the Blake Ridge, whereas the region below 3,000 m water depth is commonly called the Blake Outer Ridge (Tucholke et al., 1977). The Blake Ridge is thought to be a large sediment drift that was built upon transitional continental to oceanic crust by the complex accretion of marine sediments deposited by longitudinal drift currents (Tucholke et al., 1977). The Blake Ridge consists of Tertiary to Quaternary sediments of hemipelagic muds and silty clay (Shipboard Scientific Party, 1996). The thickness of the methane-hydrate stability zone in this region ranges from zero along the northwestern edge of the continental shelf to a maximum thickness of about 700 m along the eastern edge of the Blake Outer Ridge (Collett, 1995).

The first direct evidence that gas hydrate might be present along the Atlantic margin was found during deep-sea drilling on the Blake Outer Ridge in 1970 (Shipboard Scientific Party, 1972). Cores recovered from the Deep-Sea Drilling Project (DSDP) Sites 102, 103, and 104 contained large quantities of methane, which suggested the presence of gas hydrates. In addition, measured acoustic velocities (>2 km/sec.) within the suspected gas-hydrate-bearing section exceeded normal marine sediment velocities -- also suggesting the presence of gas hydrates. The occurrence of gas hydrates on the Blake Outer Ridge was confirmed during Leg 76 of the DSDP when a sample of gas

hydrate was recovered from a sub-bottom depth of 238 m at Site 533 (Shipboard

Scientific Party, 1980).

Leg 164 of the Ocean Drilling Program (Shipboard Scientific Party, 1996) was

designed to investigate the occurrence of gas hydrate in the sedimentary section beneath

the Blake Ridge (Figure 5.2). Sites 994, 995, and 997 comprise a transect of holes that

penetrate below the base of gas hydrate stability within the same stratigraphic interval

over a relatively short distance (9.6 km). This transect of holes on the southern flank of

the Blake Ridge extends from an area where a BSR is not detectable to an area where an

extremely well-developed and distinct BSR exists (Figure 5.3). A BSR is not observed at

Site 994, a modest BSR occurs at 995, and a strong BSR is seen at Site 997. The geology

and topography along this transect are relatively simple (Shipboard Scientific Party,

1996), which provides an opportunity to assess the basic properties of gas-hydrate-

bearing sediments and to understand lateral variations caused by local lithologic,

chemical, and hydrologic factors.

The Blake Ridge transect of Sites 994, 995, and 997 was also selected because it

is an area where seismic blanking is especially distinct (Figure 5.3) (Shipboard Scientific

Party, 1996). Because drilling at all three sites on the Blake Ridge penetrated below the

base of gas-hydrate stability, they provide critical information on the amounts of gas and

gas hydrate in the sediments as well as the nature of the BSR itself. Understanding the

causes of variations in sediment gas hydrate contents and BSR development was a major

objective of drilling during Leg 164. Since gas hydrates are unstable at surface pressure

and temperature conditions, a major emphasis was placed on the downhole-logging

program to determine the in-situ physical properties of the gas-hydrate-bearing

sediments.

5.2.2 Downhole-Logging Program

The Lamont-Doherty Borehole Research Group (LDEO-BRG) in conjunction

with the University of Leicester (Borehole Research-Leicester), the Institute

Méditerranéen de Technologie (IMT), and Schlumberger Well Logging Services,

conducted the downhole well-logging operations on the *JOIDES Resolution* during Leg

164.

Logging tool strings deployed on Leg 164 (Table 5.1, Figure 3.1) included the

Schlumberger quad- and split-combination (NGT, LSS-SDT, DITE, CNT-G, HLDT),

Formation MicroScanner (FMS), and the Geochemical Logging Tool (GLT). In addition

to the normal acquisition of capture-tau neutron geochemical data, a series of 41 inelastic

neutron geochemical measurements were made with the GLT. The split-combination

tool string consisted of separate runs of the seismic stratigraphic and lithoporosity

combinations discussed in Chapter 3 (Figure 3.1). To prepare for logging operations, the

completed boreholes were flushed of debris by circulating a "pill" of heavy viscous

drilling fluid (sepiolite mud with seawater) through the drill pipe to the mudline. The

bottom-hole assembly (BHA) was pulled up to about 60 to 100 mbsf, and it was then ran

down to the bottom of the hole again to condition the borehole for logging. Tool strings

comprised of one or more combinations of sensors were then lowered downhole by a 7-

conductor wireline cable during sequential runs. A wireline heave-motion compensator

Table 5.1 Ocean Drilling Program Leg 164 downhole-logging program.

Hole identification	Total hole penetration (mbsf)	Log run	Logging string	Interval logged (mbsf)
994C	703.5	1	DITE/SDT/HLDT/ CNT-G/NGT/LDEO-TLT	76.0-450.0
		2	GST(AACT/GST/NGT) (13 inelastic stations)	52.0-320.0
994D	670.0	1	DITE/LSS-SDT/HLDT/ NGT	114.0-618.0
		2	LDEO-SST	191.0-613.0
995B	700.0	1	DITE/LSS-SDT/NGT/ LDEO-TLT	134.0-639.0
		2	HLDT/CNT-G/NGT	134.0-639.0
		3	GST(AACT/GST/NGT) (18 inelastic stations)	135.0-634.5
		4	LDEO-SST	136.0-658.7
		5	FMS/GPIT/NGT (2)	145.0-658.7
997B	750.7	1	DITE/LSS-SDT/HLDT NGT/LDEO-TLT	113.0-715.0
		2	GST(AACT/GST/NGT) (13 inelastic stations)	115.0-683.0
		3	LDEO-SST	115.0-683.0
		4	FMS/GPIT/NGT (2)	115.0-681.0

(WHC) was employed to minimize the effect of ship's heave on the tool position in the borehole. The side-wall entry sub (SES) was inserted in the drill string when bad hole conditions were encountered. During each logging run, incoming data were acquired, archived and monitored in real time on the Maxis 500 logging computer. The Cyber Service Unit (CSU) computer was used for the geochemical logging string. After logging, data were transferred to a Sun workstation and a Macintosh computer for preliminary shipboard correlation and interpretation.

The quality of the log measurements on Leg 164 were moderately to severely degraded by the size and rugosity of the borehole. The caliper logs in Holes 994C, 994D, 995B, and 997B (Figure 5.4) show borehole diameters greater than the 46.9 cm maximum range of the caliper for a significant portion of the hole. The comparison of log data from Holes 994C and 994D (Shipboard Scientific Party, 1996), reveals that the log data from Hole 994D are of superior quality; therefore, the log analysis efforts at Site 994 have focused on the log data from Hole 994D.

The natural gamma-ray spectrometry (NGT), lithodensity (HLDT), and compensated neutron porosity (CNT-G) tools are particularly susceptible to adverse affects from large and irregular hole diameters. The natural gamma-ray (NGT) logs from Hole 995B were not significantly affected by the size of the borehole. However, the natural gamma-ray (NGT) logs from Holes 994D and 997B are highly degraded because of enlarged borehole sizes and the irregular (rugose) nature of the borehole. The lithodensity tool (HLDT), which is an excentered device, has a caliper arm that forces the tool against the wall of the borehole. If the hole is larger than the maximum reach (46.9
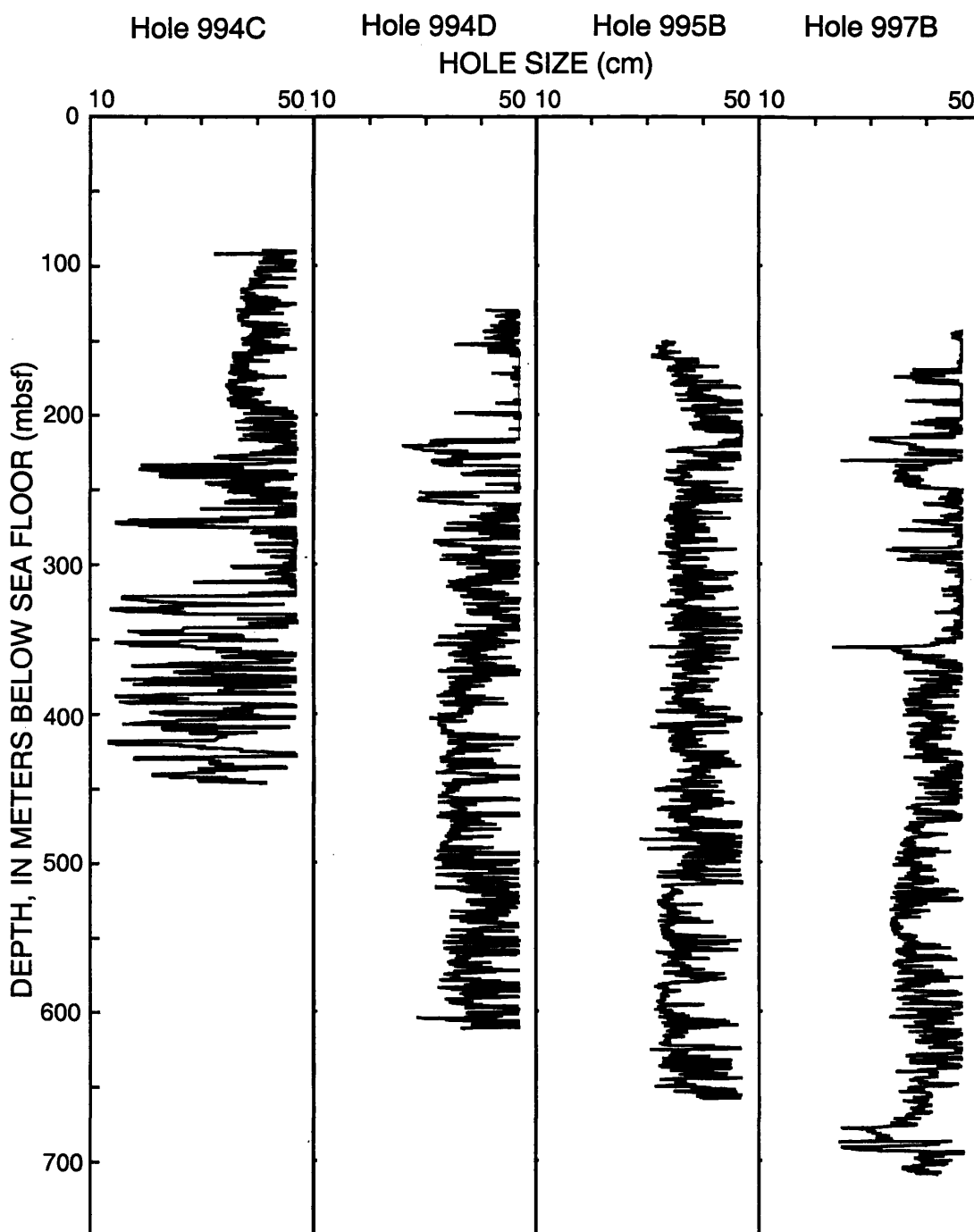
Figure 5.4 Caliper logs recorded from the lithodensity (HLDT) tool in Holes 994C, 994D, 995B, and 997B.

cm) of the caliper arm the density tool may lose contact with the formation. In general, the density log in all of the holes drilled on the Blake Ridge was degraded because of poor tool contact with the borehole wall. Data from the density logs have been used to calculate sediment porosities, however, the results of these calculations are unsatisfactory (see Section 5.2.5 of this thesis for additional information on density porosity calculations).

The compensated neutron porosity logs (CNTG) are severely affected by enlarged boreholes in all of the holes drilled on the Blake Ridge and all of the neutron porosity data from Leg 164 have been disregarded in this study (see Section 5.2.5 of this thesis for additional information on neutron porosity data). The acoustic velocity (LSS-SDT) and electrical resistivity (DITE) logs provided invaluable information on sediment porosities and gas-hydrate saturations in all of the Leg 164 Blake Ridge drill-sites. The geochemical tool string (GLT) also provided useful information; however, the GLT measurements have also been degraded by the enlarged borehole conditions, which required extensive shore-based processing to rectify (see Appendix 1 for information GLT data processing).

The absolute depths, relative to sea floor, for all of the logs were fixed by identifying the gamma-ray signal associated with the sea floor and depth-shifting the log data appropriately. The natural gamma-ray log pick for the sea floor in Holes 994D, 995B, and 997B where 2,809.0, 2,786.0 and 2,775.0 meters below the dual elevator stool (DES) on the drilling mask, which is located on the ship 11.4 m above sea level.

5.2.3 Logging Units

The description of the logged intervals in Holes 994D, 995B, and 997B are

divided into three "Logging Units" on the basis of obvious changes in the natural gamma-

ray (NGT), bulk-density (HLDT), acoustic velocity (LSS-SDT), and electrical resistivity

measurements (DITE) (Table 5.2, Figure 5.5a-c). The elemental yield data from the

geochemical log (GLT) have also been used to assess the mineralogy of the sediments in

the delineated Logging Units. A more detailed assessment of the GLT-derived

mineralogy at Sites 995 and 997 has been included in Section 5.2.6 of this thesis.

Log Unit 1 Logging Unit 1 is characterized by relatively low gamma ray, density,

velocity, and resistivity log values (Figure 5.5a-c). All of the recorded logs are affected

by enlarged borehole conditions which exceed the maximum recording size (46.9 cm) of

the caliper throughout most of Unit 1. In most cases, the gamma-ray log shows an abrupt

upward step in value at the boundary between Unit 1 and Unit 2. The caliper log (Figure

5.4) shows that the hole diameters are reduced across the boundary from Unit 1 to Unit 2.

The bulk-density and acoustic velocity ramp up gradually across the boundary between

Units 1 and 2. Within Unit 1, the weight percent of Potassium (K) and Aluminum (Al)

are relatively low and remain constant. Analyses of Potassium (K) and Thorium (Th)

elemental yields suggests that the clays in Unit 1 are predominately montmorillonites and

some illites.

Log Unit 2 Logging Unit 2 is characterized by increasing velocities (1.65 km/sec

at the top to over 2.0 km/sec at the bottom) with depth. The natural gamma-ray and bulk-

density logs are nearly constant throughout Unit 2. Both the acoustic velocity and

Table 5.2 Depth to the top and bottom of the downhole-log-identified Logging Units in Holes 994D, 995B, and 997B (Figure 5.5a-c).

Hole identification	Logging Unit	Depth to top of Logging Unit (mbsf)	Depth to bottom of Logging Unit (mbsf)
994D	1	Base of pipe (114.0)	212.0
	2	212.0	428.8
	3	428.8	End of log (618.0)
995B	1	Base of pipe (134.0)	193.0
	2	193.0	450.0
	3	450.0	End of log (658.7)
997B	1	Base of pipe (113.0)	186.4
	2	186.4	450.9
	3	450.9	End of log (715.0)
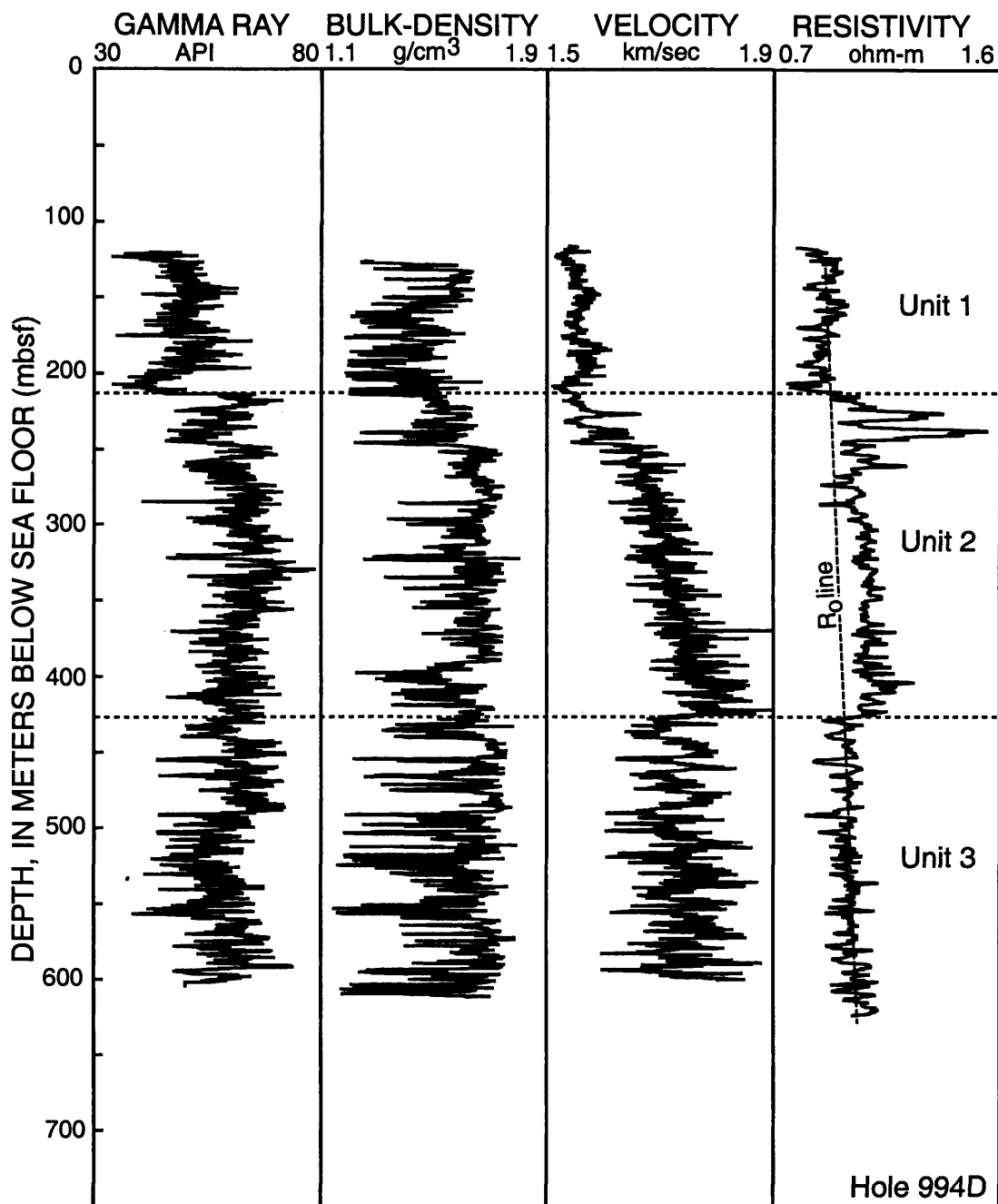
Figure 5.5a Downhole-log data from Hole 994D. Data shown include the natural gamma ray log from the NGT, bulk-density data from the HLDT, acoustic velocity data from the LSS-SDT, and deep-reading electrical resistivity data from the DITE. Also shown are the depths of Logging Unit 1, 2, and 3 (Table 5.2) and the projected R_O baseline.
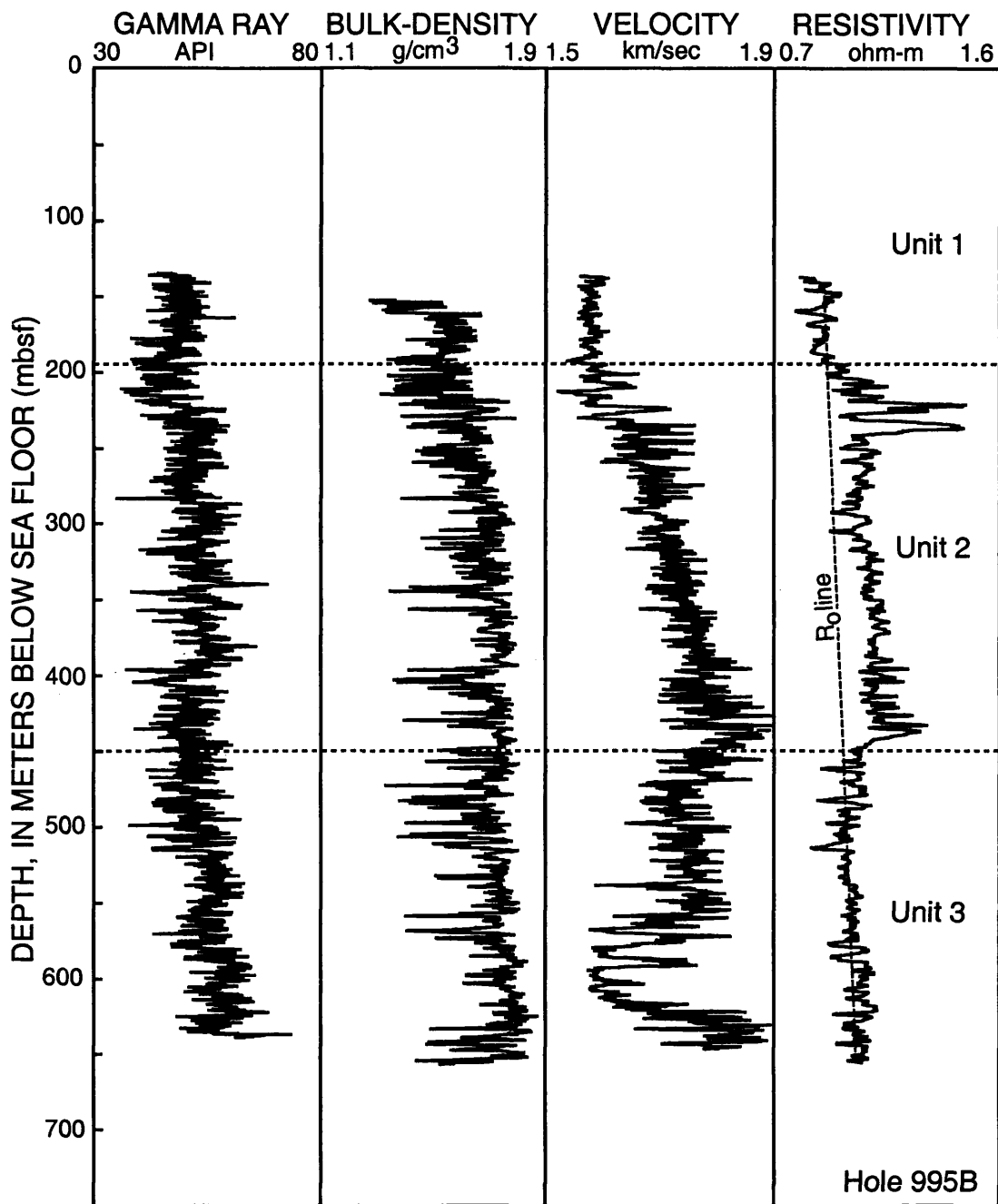
Figure 5.5b Downhole-log data from Hole 995B. Data shown include the
natural gamma ray log from the NGT, bulk-density data from the HLDT,
acoustic velocity data from the LSS-SDT, and deep-reading electrical resistivity
data from the DITE. Also shown are the depths of Logging Unit 1, 2, and 3
(Table 5.2) and the projected R_O baseline.
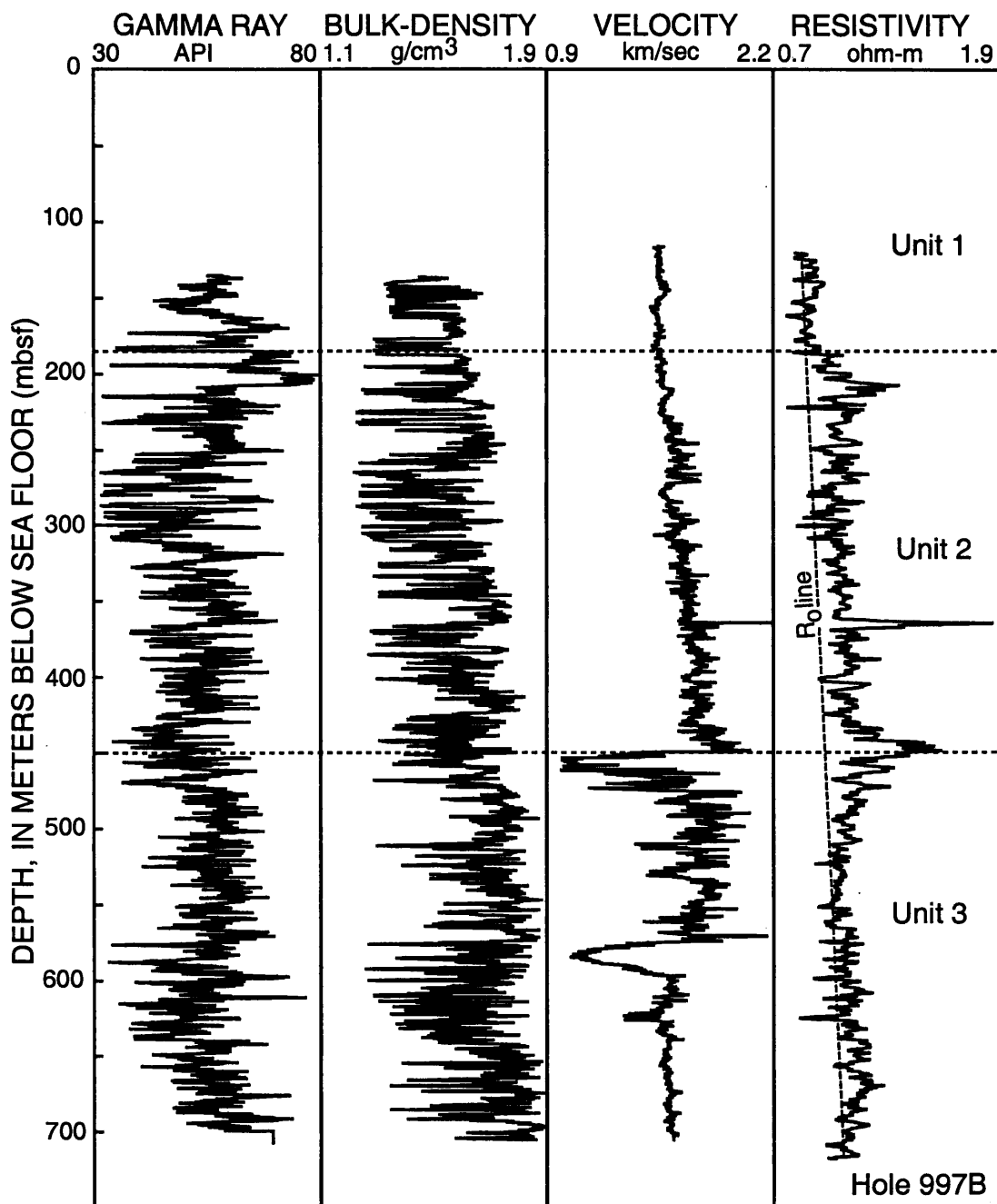
Figure 5.5c Downhole-log data from Hole 997B. Data shown include the natural gamma ray log from the NGT, bulk-density data from the HLDT, acoustic velocity data from the LSS-SDT, and deep-reading electrical resistivity data from the DITE. Also shown are the depths of Logging Unit 1, 2, and 3 (Table 5.2) and the projected R_O baseline.

resistivity logs are characterized by a distinct baseline shift to relatively higher values throughout Unit 2. The resistivity logs reveal several conspicuous high electrical resistivity intervals near the top of Unit 2 in all three coreholes. At the base of Unit 2, across the boundary into Unit 3, the acoustic velocity and resistivity logs step down to lower values. In Hole 997B (Figure 5.5c), the acoustic log (DTLF) has been used to precisely select a depth for the boundary between Units 2 and 3. This acoustic velocity (DTLF) boundary does not exactly match the apparent drop in resistivity observed near the base of Unit 2. This discrepancy of about eight meters is likely due to the presence of a significant amount of free-gas below the deepest downhole-log-inferred gas-hydrate occurrence. Analyses of Potassium (K) and Thorium (Th) elemental yields suggest that the clays in Logging Unit 2 are mostly montmorillonites.

Log Unit 3 Logging Unit 3 is characterized by consistently lower velocities and resistivities with respect to Unit 2. Anomalous low velocity intervals are seen in Unit 3; velocities within these anomalous intervals decrease to below 1.5 km/sec which suggests the presence of free-gas. The higher resistivities, near the boundary between Units 2 and 3 in Hole 997B, may be due to the presence of free-gas, which supports the acoustic-log observations. In Logging Unit 3, the natural gamma-ray, density, and electrical resistivity logs show slight increases with depth which are characteristics of a normal compacting sedimentary section.

5.2.4 Gas-Hydrate Occurrences

The presence of gas hydrates at Sites 994 and 997 was documented by direct

sampling; however, no gas hydrates were conclusively identified at Site 995 (Shipboard

Scientific Party, 1996). Although a BSR does not occur in the seismic reflection profiles

that cross Site 994, several pieces of gas hydrate were recovered from 259.90 mbsf in

Hole 994C and disseminated gas hydrate was observed at almost the same depth in Hole

994D. One large, solid piece (about 15 cm long) of gas hydrate was also recovered from

about 331 mbsf at Site 997 (Hole 997A). Despite these limited occurrences of gas

hydrates, it was inferred, based on geochemical core analyses and downhole-logging

data, that disseminated gas hydrates occur in Logging Unit 2 (which extends from a depth

of about 190 to 450 mbsf) of all the holes drilled on the Blake Ridge (Tables 5.2 and 5.3).

The presence of gas hydrates in Logging Unit 2 at Sites 994, 995, and 997 was inferred

on the basis of the following observations (Shipboard Scientific Party, 1996): (1) Cores

from all three sites were observed to evolve large amounts of gas, which is indicative of

the presence of gas hydrate. It is also speculated that gas evolution from decomposing

gas hydrate may have been a factor that contributed to the low core recovery at all the

Blake Ridge drill-sites. (2) Pressure-coring (PCS) data indicate that the sediments on the

Blake Ridge between about 200 and 450 mbsf contain methane concentrations that

exceed expected methane pore-water saturations. The only known source for this

methane is the decomposition of gas hydrate, thus it was concluded that gas hydrates

must occur within this interval of over-saturated gas. (3) Both the general trend of the

interstitial water chloride concentrations and the inter-sample variation in chloride

Table 5.3 Depth to the top and bottom of the interstitial-water-chloride- and well-log-inferred gas-hydrate occurrences at Sites 994, 995, and 997 (Figures 5.5 and 5.6).

Site	Top/Bottom	Gas hydrate - chloride anomaly depth (mbsf)	Log-inferred gas hydrate depth (mbsf)
994	Top	194.95-209.2	212.0
	Bottom	427.37-439.5	428.8
995	Top	190.25-195.35	193.0
	Bottom	438.0-465.12	450.0
997	Top	179.57-204.75	186.4
	Bottom	451.65-467.45	450.9

concentrations (chloride anomalies) between 190 and 450 mbsf (Table 5.3) suggest the

presence of gas hydrates throughout Logging Unit 2 (Figure 5.6). Gas hydrate

decomposition during core recovery releases water and methane into the interstitial pores,

resulting in a freshening of the pore-waters. (4) Temperatures of cores recovered on the

Blake Ridge transect were quite variable within Logging Unit 2. Because the

dissociation of gas hydrate is an endothermic reaction, the low temperature anomalies

within the recovered cores are interpreted as indicating areas where gas hydrate

decomposition has occurred during core recovery. (5) Data from downhole logs also

were interpreted as indicating the presence of gas hydrate in Logging Unit 2. The

downhole-log evidence for gas hydrates is discussed in more detail later in this section of

the thesis.

The depths to the top and the base of the zone of gas-hydrate occurrence at Sites

994, 995, and 997 were measured using interstitial water chloride concentrations and

downhole-log data (Tables 5.2 and 5.3). Interstitial water chloride concentrations were

used to establish whether gas hydrate occurred within a given core sample, which

establish the presence of gas hydrate in Logging Unit 2 (Figure 5.6). The observed

chloride concentrations also enable the amount of gas hydrate that occurs on the Blake

Ridge to be established by calculating the amount of interstitial water freshening that can

be attributed to gas hydrate dissociation. The estimated gas-hydrate saturations in the

recovered cores had a skewed distribution, ranging from a maximum of about 7% and

8.4% at Sites 994 and 995 to a maximum of about 13.6% at Site 997 (Figure 5.7).

However, these are minimum estimates because the baseline (undisturbed interstitial-
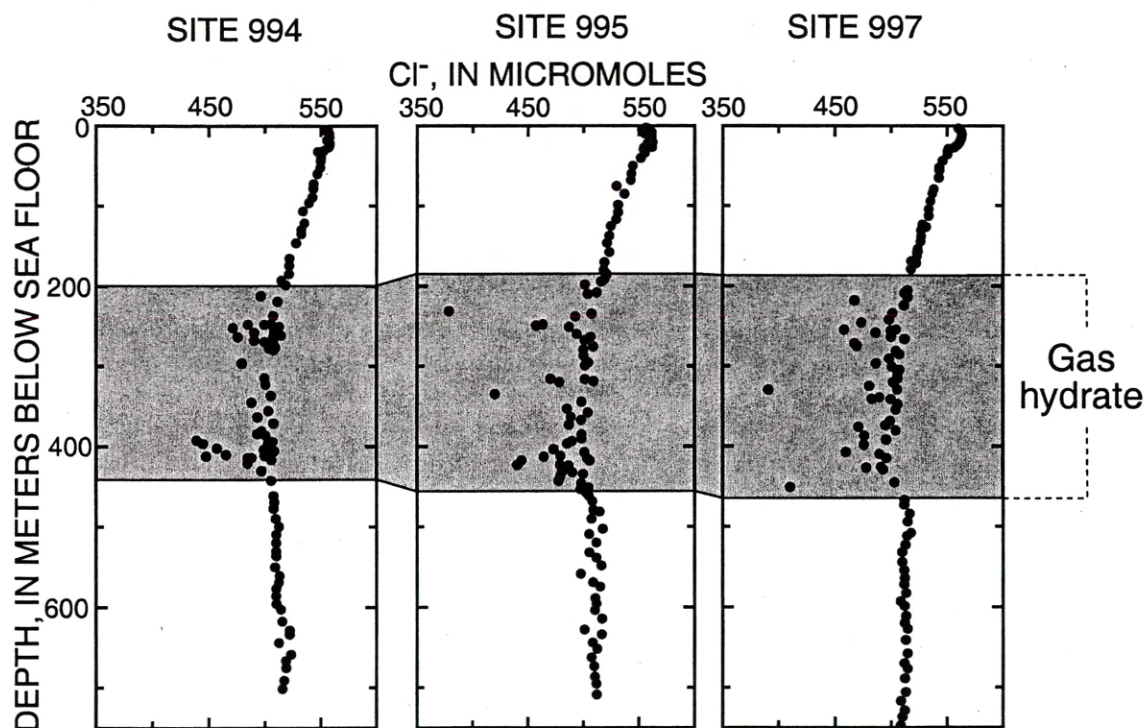
Figure 5.6 Chloride concentration profiles for interstitial waters collected from cores at Sites 994, 995, and 997. Also shown is the chloride-concentration-inferred gas-hydrate distribution (Table 5.3) (modified from Shipboard Scientific Party, 1996).
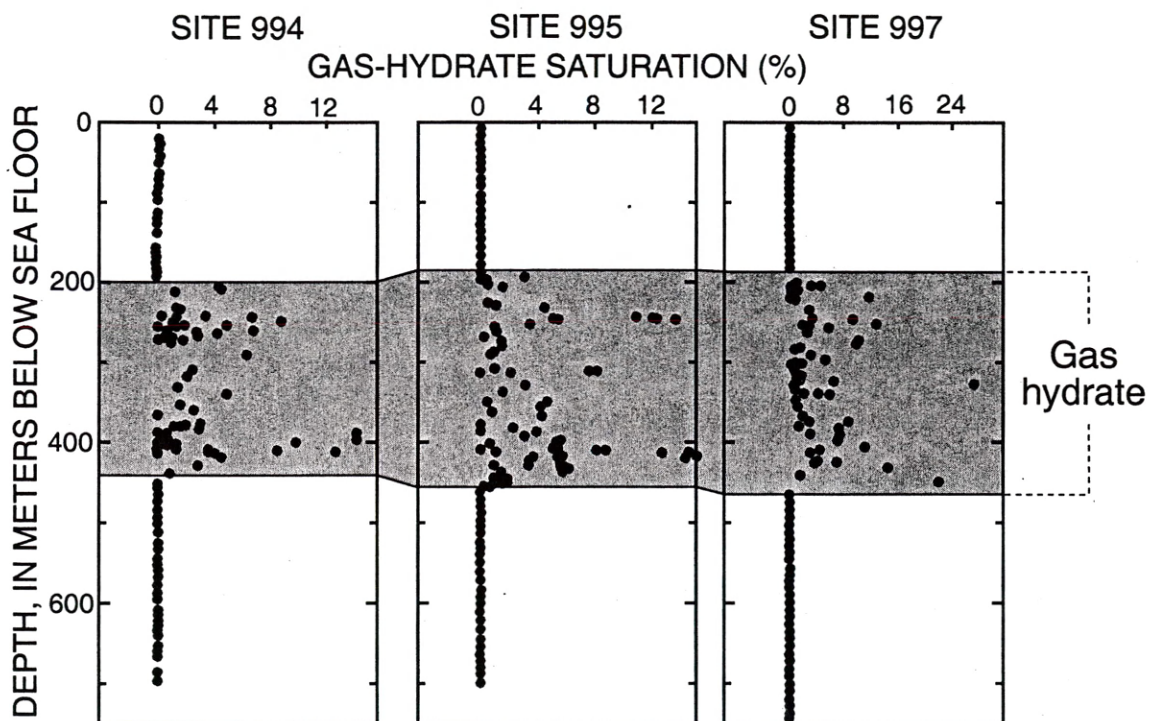
Figure 5.7 Plot of gas-hydrate saturations (percent of pore-space occupied by gas hydrate) calculated from interstitial water chlorinities, assuming that the chloride anomalies at each site (Sites 994, 995, and 997; Figure 5.6) are solely produced by gas hydrate decomposition during core recovery (modified from Shipboard Scientific Party, 1996).

water chlorinities) used to calculate these values may be lower than the actual in-situ interstitial-water salinities. For a more complete discussion on the chlorinity-calculated gas hydrate contents see Shipboard Scientific Party (1996).

As previously discussed in Chapter 1 of this thesis, natural gas-hydrate occurrences are generally characterized by the release of unusually large amounts of methane during drilling and an increase in log-measured acoustic velocities and electrical resistivities. The comparison of Logging Units 1, 2, and 3 in all three holes on the Blake Ridge (Holes 994D, 995B, and 997B), reveal that Logging Unit 2 is characterized by a distinct stepwise increase in both electrical resistivity (increase of about 0.1-0.3 ohm-m) and acoustic velocity (increase of about 0.1-0.2 km/sec) (Figure 5.5a-c). In addition, the deep reading resistivity device (RILD) reveals several high resistivity zones within the upper 100 m of Unit 2 at all three sites on the Blake Ridge (resistivities ranging from 1.4 to 1.5 ohm-m).

At Site 994, gas hydrates were recovered (depth 259.90 mbsf) from the same interval that exhibits high resistivities in the upper part of Unit 2. Further comparisons indicate that the high resistivity zones do not correlate with any apparent acoustic velocity anomalies at Sites 994 or 995. However, at Site 997 the high resistivity zones in the upper part of Unit 2 are characterized by an acoustic velocity increase of about 0.3 km/sec. The zone from which gas hydrates were recovered at Site 997 (depth of about 331 mbsf in Hole 997A) is also characterized by high resistivities and acoustic velocities. At Site 994, below the high resistivity zones at 216 and 264 mbsf, the resistivity-log values are almost constant throughout Logging Unit 2, while the acoustic velocities

increase with depth over the same interval. However, both electrical resistivities and acoustic velocities in Unit 2 increase with depth at Sites 995 and 997. Examination of the natural gamma-ray and bulk-density logs from all three sites (Figure 5.5a-c) reveals no apparent lithologic causes for the observed velocity and resistivity increases in Unit 2. The above observations are consistent with a material of increased resistivity and acoustic velocity, but similar density, partially replacing some of the pore-water in Unit 2. The depth of the boundary between Logging Units 2 and 3 on the Blake Ridge is in rough accord with the predicted base of the methane hydrate stability zone and it is near the lowest depth of the observed interstitial-water chlorinity anomaly (Table 5.3). It has been concluded that Logging Unit 2 at Sites 994, 995, and 997 contains some amount of gas hydrates.

5.2.5 Porosity Calculations

Sediment porosities can be determined from analyses of recovered cores and from numerous borehole measurements as discussed in Chapter 3 of this thesis. Data from the bulk-density (HLDT), neutron porosity (CNT-G), and electrical resistivity (DITE) logs have been used to calculate sediment porosities for Sites 994, 995, and 997. Core-derived physical property data, including porosities (Shipboard Scientific Party, 1996), have been used to both calibrate and evaluate the log-derived sediment porosities.

Core Porosities On Leg 164, water content, wet bulk-density, dry bulk-density, and grain density were routinely determined from recovered sediment cores. Other related physical property data, including sediment porosities, were calculated from these

"index properties" (Shipboard Scientific Party, 1996). The core-derived porosities

actually represent the measured total water content of the sediments, which include

interlayer-, bound- and free-water. Most downhole logs also measure the total water

content of the sediments; thus the core- and log-derived sediment porosities should be the

same. Sediment core porosities determined from Sites 994, 995, and 997 are shown in

Figure 5.8. In general, the core-derived sediment porosities decrease from about 80%

near the top of each hole to about 49% at the bottom.

Density-Log Porosities The density-log (HLDT) measurements of bulk-density in

Holes 994D, 995B, and 997B (Figure 5.5a-c) are highly variable and range from a

maximum of about 1.9 g/cm^3 to a very low value of about 1.2 g/cm^3. Other physical

property data from the Blake Ridge, including core-derived sediment wet bulk densities

and porosities (Figure 5.8) (Shipboard Scientific Party, 1996), are not consistent with the

density-log measurements. The core-derived bulk densities are relatively constant with

depth and are characterized by a relatively limited range of values. It is likely that the

density logs from all three sites have been severely degraded by both the rugosity and the

enlarged size of the boreholes. Before using the log-derived bulk-density data to

calculate sediment porosities, the apparent erroneous data from the recorded density logs

at Sites 994, 995, and 997 was removed. The detailed analysis of the recorded logs

indicates that the density log yields erroneous low values when the borehole exceeded a

diameter of about 36 cm, which is beyond the recommended hole size for the density tool

deployed on Leg 164. Therefore, the density-log data were systematically deleted from

the portion of Holes 994D, 995B, and 997B where the caliper log from the density tool
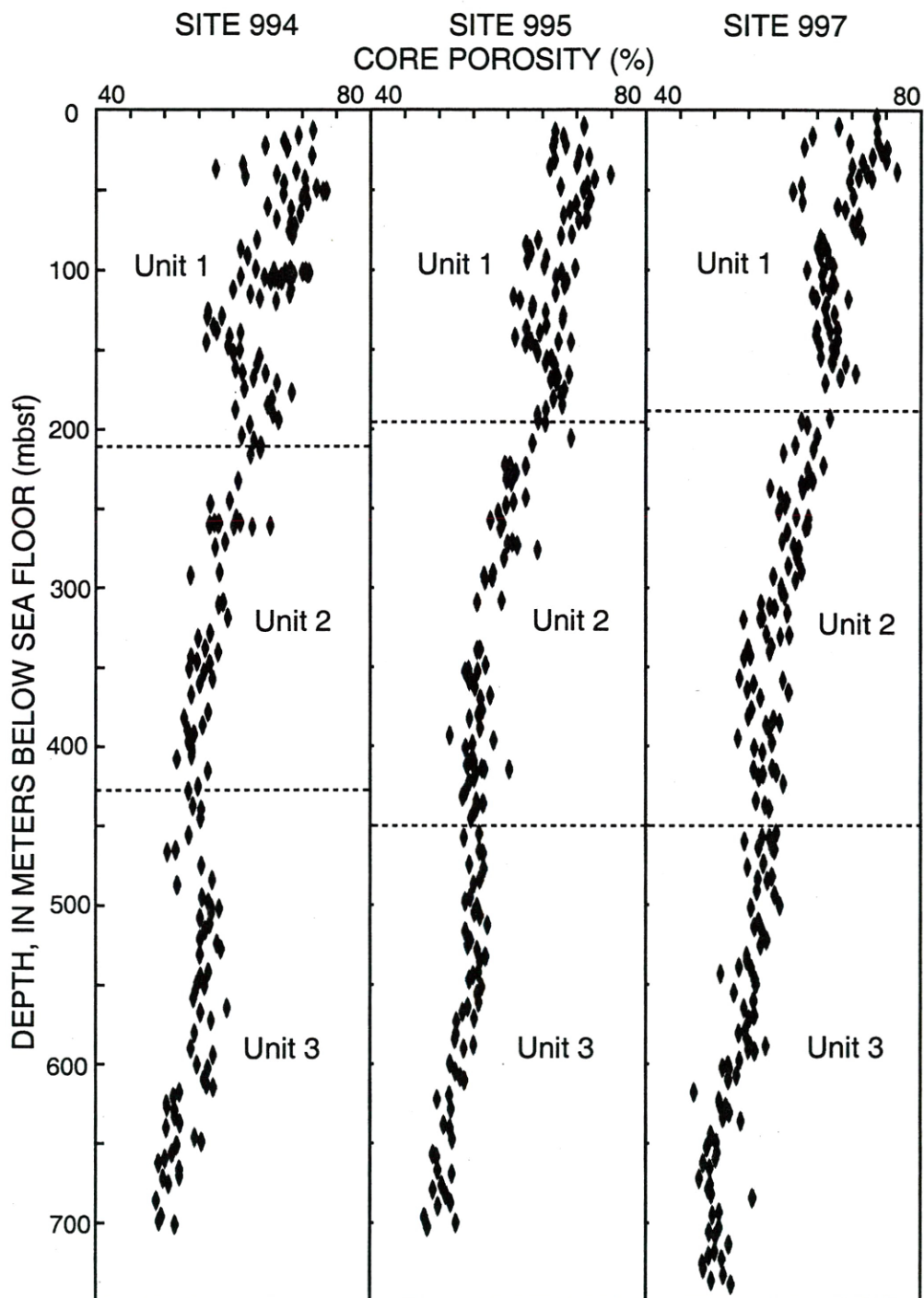
Figure 5.8 Core porosities derived from laboratory physical property data at Sites 994, 995, and 997 (modified from Shipboard Scientific Party, 1996).

indicates that the hole diameter is more than 36 cm. The edited density-log curve still

contained numerous unreasonably low density "spikes" which usually consisted of only

one or two data points. Therefore, any log-measured bulk-density of less than 1.6 g/cm^3,

which is significantly below the expected bulk-density for the sediments on the Blake

Ridge, were also deleted from the recorded log traces. The edited bulk-density-log (ρ_b)

measurements were then used to calculate sediment porosities ($\varnothing$) in Holes 994D, 995B,

and 997B using the standard density-porosity relation discussed in Chapter 3 of this

thesis: $\varnothing = \rho_m - \rho_b / \rho_m - \rho_w$ (Equation 3.1). Water densities (ρ_w) were assumed to be

constant and equal to 1.05 g/cm^3 for each hole, however, variable core-derived

grain/matrix densities (ρ_m) where assumed for each calculation. The core-derived grain

densities (ρ_m) in Holes 994C, 995A, and 997A range from an average value at the sea

floor of about 2.72 g/cm^3 to about 2.69 g/cm^3 at the bottom of each hole (Shipboard

Scientific Party, 1996). The density-log porosity calculations from all three sites yielded

values ranging from about 50 to near 70 percent (Figure 5.9). The density-log-derived

porosities are more variable and generally higher than the core-derived porosities also

shown in Figure 5.9. It appears that the density-log porosities overestimate both the

range and absolute porosities for the sediments on the Blake Ridge. It is likely that the

high clay-content and unlithified nature of the sediments on the Blake Ridge have

contributed to the inability of the density tool to make good contact with the borehole

wall. Further analysis of the density-log porosity plots in Figure 5.9 reveals that the left

side of the porosity-log curves (lower porosity values) appear to more closely match the
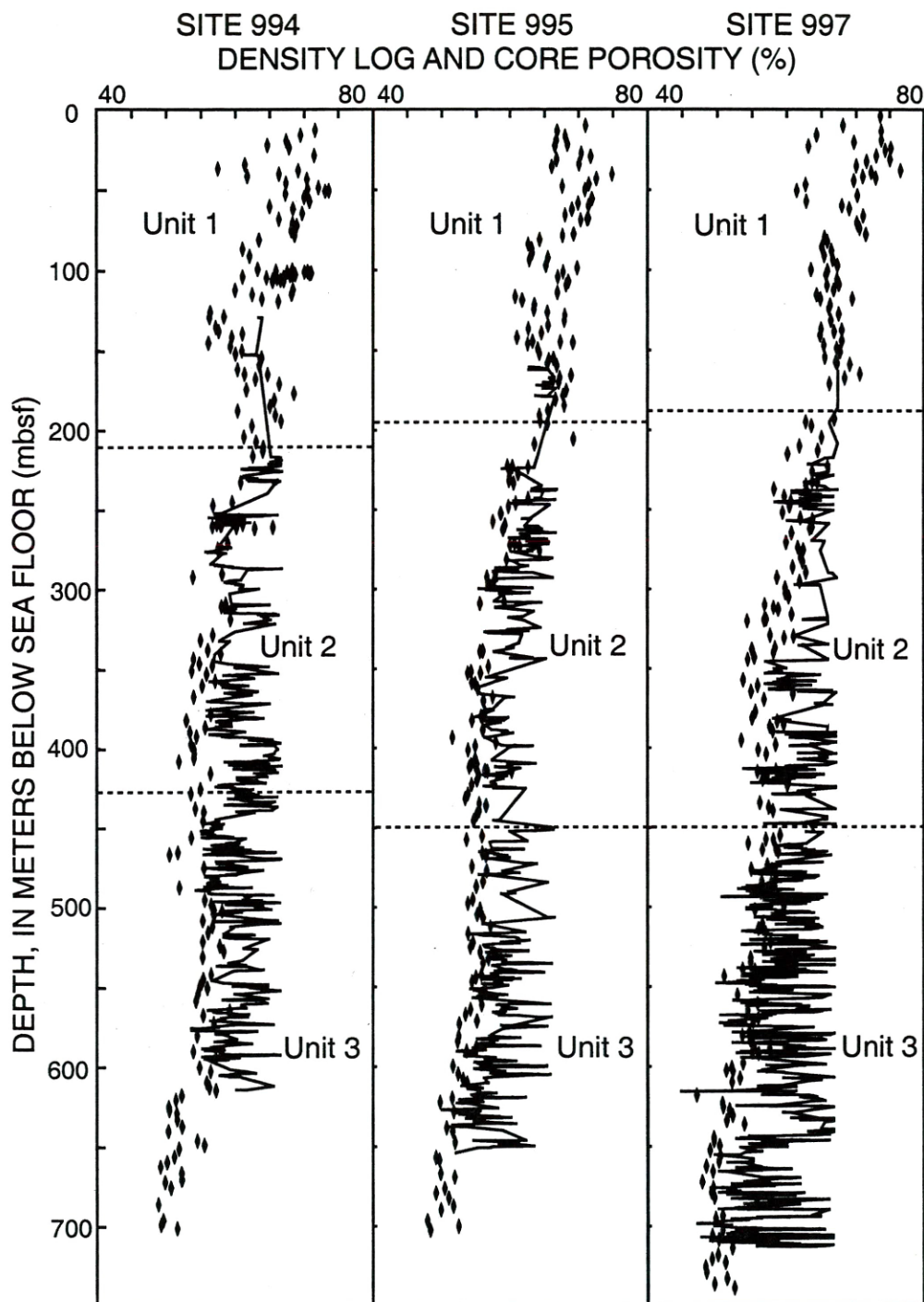
Figure 5.9 Sediment porosities (shown as continuous line plots) derived from downhole-density-log (HLDT) data at Sites 994, 995, and 997. Also shown (as discrete point measurements) are the core-derived porosities.

core-derived porosity values. It is possible that the lower porosity values on the density-log-derived porosity logs may contain accurate porosity estimates and that the log curves could be further edited to include only the lower density-log-derived porosity values that match the core results. This additional log interpretive step could improve the final density-log-derived porosity estimates, however, it does not contribute to our understanding of the affect of gas hydrates on log-derived sediment porosities. Further analysis of the density-log-derived porosity data from the Blake Ridge is beyond the scope of this study.

Data from the density logs in Holes 994D, 995B, and 997B can be used to assess general porosity trends but not for quantitative calculations; therefore, the proposed density-log gas hydrate corrections discussed in Chapter 3 of this thesis were not used to correct the Blake Ridge density-log data.

Neutron Porosity Log Because of poor hole conditions, the neutron porosity log (CNT-G) was deployed in only two holes (Holes 994C and 995B) on the Blake Ridge. As discussed in Chapter 3 of this thesis, the neutron-porosity-log (CNT-G) measures the amount of hydrogen within the pore-space of a sedimentary sequence, which is mostly controlled by the amount of water that is present. The CNT-G has two pairs of detectors that indirectly measure both epithermal (intermediate energy level) and thermal (low energy) neutrons, which provide two porosity measurements. The recorded neutron-porosity-log data from Holes 994C and 995B reveal an average thermal porosity of about 50% while the epithermal porosity averages about 100%. The thermal and epithermal porosity logs are calibrated to read 50% and 100%, respectively, in water (no sediment).

Therefore, the neutron porosity log in Holes 994C and 995B only detected the hydrogen in the borehole waters and the porosity data from the neutron log is of no value. In "standard" industry applications the CNT-G is ran with a bowspring which keeps the tool near the wall of the hole thus reducing the effects of an enlarged borehole. Due to the size limitation of running the logs through the drillpipe, it is impossible to use a bowspring on the CNT-G in ODP holes.

Resistivity-Log-Calculated Porosities One approach to obtaining sediment porosities from well logs is to use the electrical resistivity logs (Figure 5.5a-c) and Archie's relationship between the resistivity of the formation (R_t) and porosity $(\varnothing)$: $R_t/R_w = a \varnothing^{-m}$, where a and m are constants to be determined and R_w is the resistivity of the pore-waters (Archie, 1942).

The resistivity of pore-waters (R_w) is mainly a function of the temperature and the dissolved salt content (salinity) of the pore-waters. Pore-water salinity data from Sites 994, 995, and 997 are available from the analyses of interstitial water samples collected from recovered cores (Shipboard Scientific Party, 1996). The interstitial water salinity trends at all three core sites mimic the interstitial water chloride trends discussed in Section 5.2.4 of this thesis (Figure 5.6). In general, the core-derived interstitial water salinities decrease with depth from a maximum value of about 35 ppt near the sediment-water interface to about 31 ppt within the upper part of Logging Unit 2. The interstitial water salinities are also more variable within the inferred gas-hydrate-bearing sedimentary section (Logging Unit 2). Formation and seabed temperatures have been directly measured at all three core sites on the Blake Ridge as described in Shipboard

Scientific Party (1996). Listed in Table 5.4 are the measured seabed temperatures and

geothermal gradients for Sites 994, 995, and 997 (modified from Shipboard Scientific

Party, 1996). Arps formula (Hearst and Nelson, 1985) was used to calculate the pore-

water resistivity (R_W) at each site from the available core-derived interstitial water

salinities and measured formation temperatures (Table 5.4, Figure 5.10). In general, the

calculated pore-water resistivities (R_W) reach a maximum of about 0.34 ohm-m within

100 m of the sea floor and decrease with depth to a value below 0.20 ohm-m at the

bottom of each corehole. The "apparent" high water resistivities in Logging Unit 2,

depicted in Figure 5.10, are due to the presence of fresh water in the analyzed cores,

which was expelled from gas hydrates that had disassociated in the cores. To avoid

introducing errors into the subsequent resistivity porosity calculations, the gas-hydrate-

affected pore-water resistivities from Logging Unit 2 have been excluded and the pore-

water resistivities from Logging Units 1 and 3 have been used to statistically project

undisturbed pore-water resistivities (R_W) for Logging Unit 2 (Figure 5.10).

To determine the Archie constants a and m, a log analysis method described in

Section 3.4 of this thesis has been used along with the log-measured resistivities and

core-derived porosities (Shipboard Scientific Party, 1996) from each site drilled on the

Blake Ridge. The log-measured resistivity data from Logging Unit 2 in each hole has

been omitted from this calculation of the Archie constants to avoid introducing an error

caused by using resistivity-log measurements that have been affected by the occurrence

of in-situ gas hydrates. In addition, log-measured resistivities from expected free-gas

zones in Unit 3 of each hole have also been omitted from the determination of the Archie

Table 5.4 ODP Leg 164 formation temperature data and Archie constants (a and m) needed to calculate pore-water resistivities (R_W; Figure 5.10) and water saturations (S_W; Figure 5.12a-c) (temperature data from Shipboard Scientific Party, 1996).

Site	Seabed temperature (°C)	Geothermal gradient (°C/100m)	Archie constants	
			a	m
994	3.0	3.64	0.53 ?	3.68 ?
995	3.0	3.35	1.03	2.53
997	3.0	3.68	1.07	2.59
		Assumed constants --	1.05	2.56
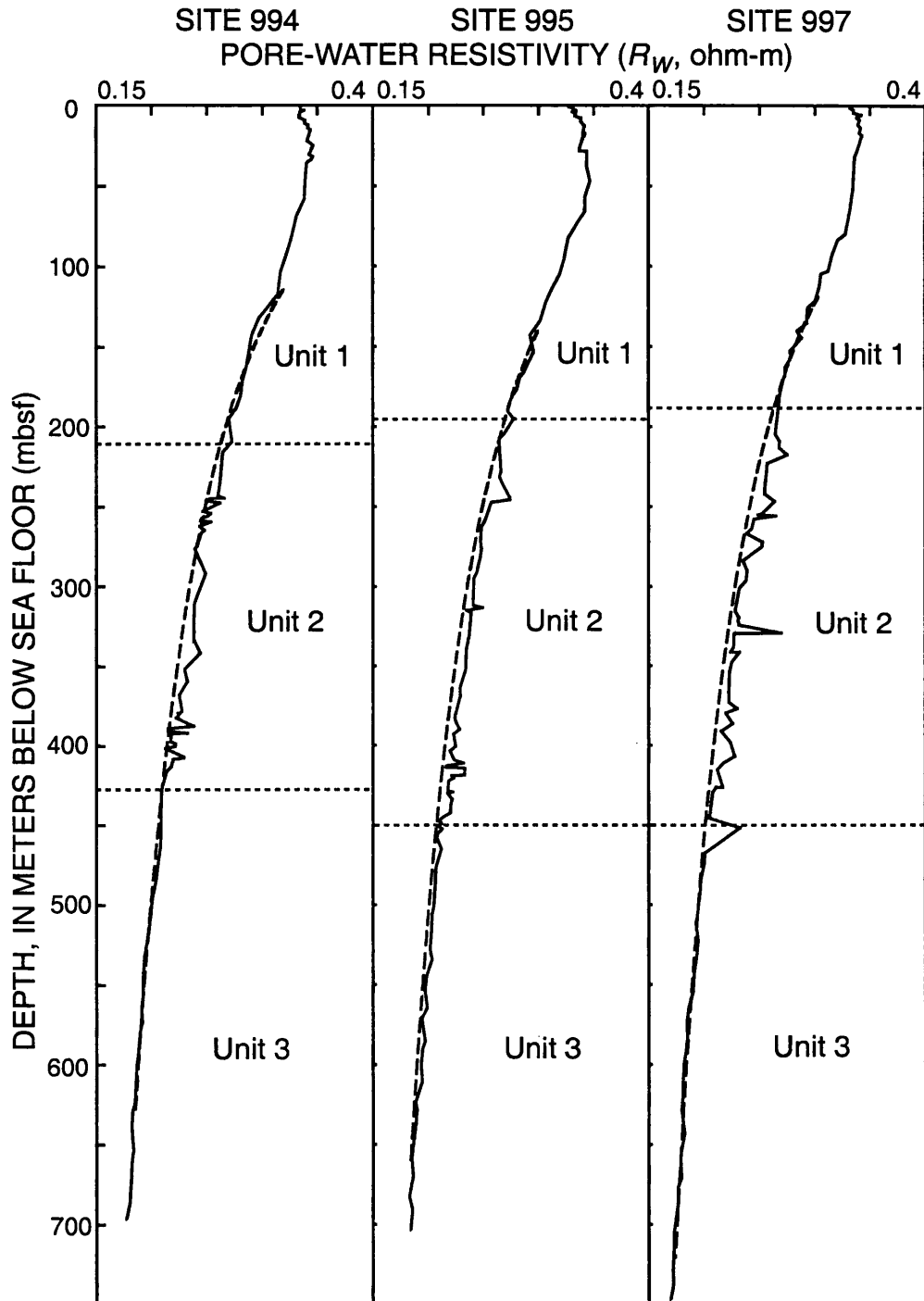
Figure 5.10 Pore-water resistivities (R_W) derived from interstitial water (core samples) salinities at Sites 994, 995, and 997. The dashed continuous line plots are the assumed undisturbed pore-water resistivities.

constants. Linear trends in resistivity-log and core-porosity data from Logging Units 1

and 3 (exclusive of Logging Unit 2) in each hole have been used to calculate

representative (100% water-saturated) formation resistivities (R_O) and porosities ($\emptyset$).

From these representative values, the slope, m, and the intercept, ln a, of the function ln

$(R_O/R_W) = -m$ ln $\emptyset$ + ln a were calculated for each of the logged coreholes. The

calculated a and m Archie constants for Holes 994D, 995B, and 997B have been listed in

Table 5.4. The Archie constants (a and m) calculated for Holes 995B and 997B are

similar and fall within the "normal" range of expected values (Serra, 1984). However,

the value of the a and m constants for Hole 994D falls outside of the "normal" range of

values. The cause of these anomalous Archie constants in Hole 994D is likely because of

poor hole conditions in Logging Unit 1, which has contributed to degraded resistivity-log

measurements. Since all three coreholes penetrated similar lithologic sections and

because they are located in relatively close proximity to each other, an average value

(calculated from Holes 995B and 997B) for the a and m Archie constants were used

throughout this study of the Blake Ridge (Table 5.4: a=1.05, m=2.56).

Given the Archie constants (a and m) and pore-water resistivities (R_W), it is

possible to calculate sediment porosities ($\emptyset$) from the resistivity log using Archie's

relation. The results of these calculations are the porosity logs shown in Figure 5.11.

The calculated resistivity porosities should be considered "apparent" porosity values

since the Archie relation assumes that all of the void space within the sediments is filled

with water (no gas hydrates), which is not true. In all three holes, the resistivity-derived

porosities decrease with depth (Figure 5.11). Relative to Units 1 and 3, Unit 2 exhibits a
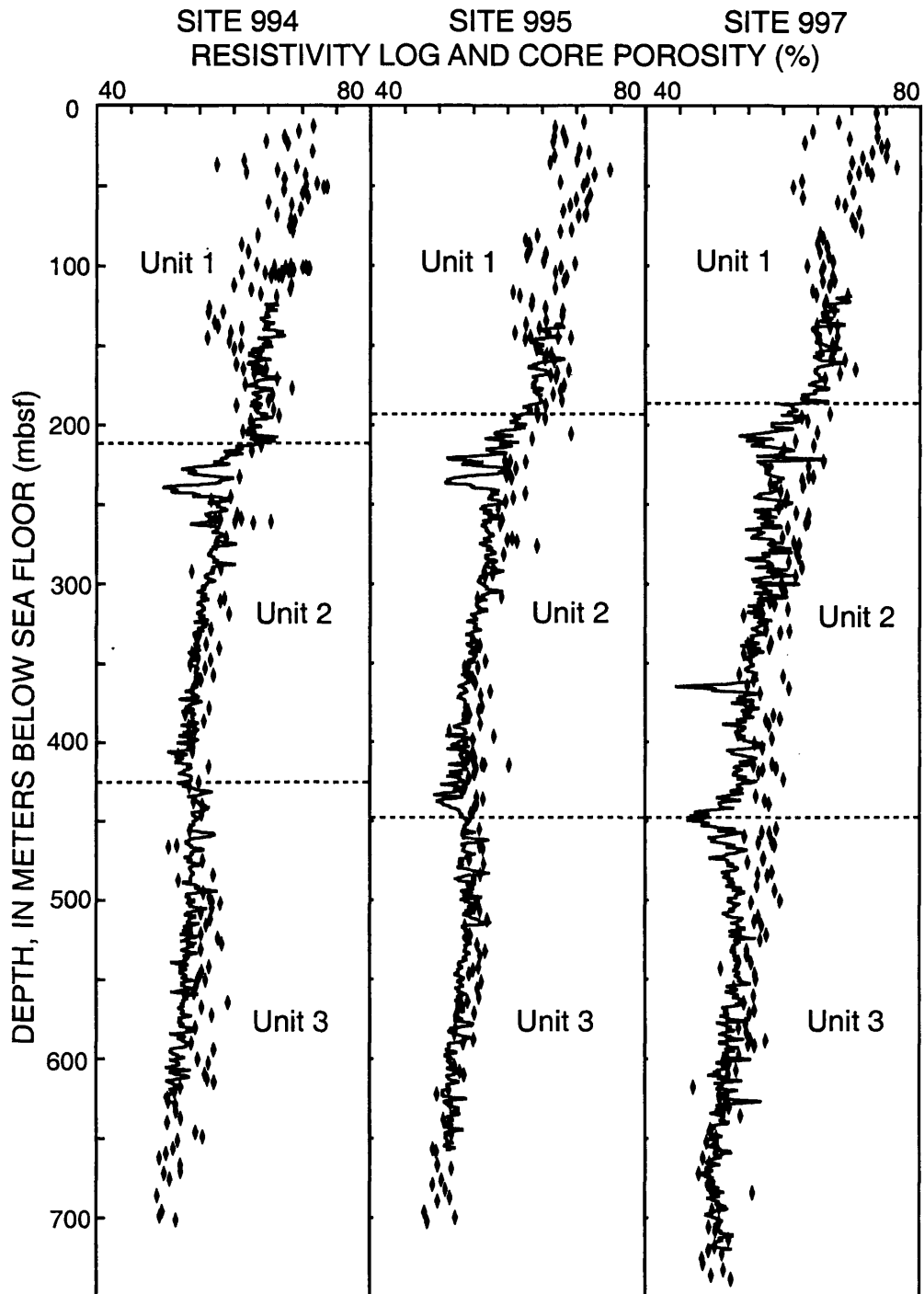
Figure 5.11 Sediment porosities (shown as continuous line plots) derived from downhole electrical resistivity logs (DITE) at Sites 994, 995, and 997. Also shown (as discrete point measurements) are the core-derived porosities.

baseline shift to higher resistivities and lower calculated resistivity porosities. The assumption that all of the pore-space within the sediments of Unit 2 is filled with only water is not valid. Some of the pore-space in Unit 2 is occupied by gas hydrates which exhibit very high electrical resistivities and would contribute to an "apparent" reduction in resistivity-derived porosities. It is possible that with an independent source of accurate porosity data, the difference between the Archie derived "apparent" porosities and the independent "true" porosities could be used to estimate the concentration (saturation) of gas hydrate in a sedimentary section.

Porosity Calculations -- Summary The comparison of core-derived and log-derived (density and resistivity) porosities in Figures 5.9 and 5.11, reveals that the resistivity-log-derived porosities are generally similar to the core porosities. However, the density-log-derived porosities are generally higher than the core porosities. It is likely that the density-log measurements have been degraded by poor borehole conditions. The resistivity-log-derived porosities in Figure 5.11 are the best downhole-derived porosity logs for all three holes on the Blake Ridge. However, because of gas hydrate induced resistivity effects in Logging Unit 2, the resistivity-derived porosity data from Leg 164 should be used with caution and the core-derived sediment porosities are the best available porosity data from the Blake Ridge.

5.2.6 Gas-Hydrate Distribution and Saturation

In the following section, data from the dual induction (DITE) and acoustic transit-time (LSS-SDT) logs in Holes 994D, 995B, and 997B have been used to quantify the

amount of gas hydrate in Logging Unit 2 (approximate depth interval of 185-450 mbsf) on the Blake Ridge. In addition, carbon/oxygen data from the geochemical logging tool (GLT) at all three sites on the Blake Ridge have been used to further assess gas-hydrate saturations.

Resistivity-Log-Calculated Gas-Hydrate Saturations For the purpose of discussion it is assumed that the anomalous high resistivities and velocities measured in Logging Unit 2 on the Blake Ridge are due to the presence of in-situ natural gas hydrates. An alternative hypothesis, however, suggests that interstitial water salinity changes could account for the electrical resistivity-log responses observed at Sites 994, 995, and 997. Geochemical analyses of cores from Logging Unit 2 at all three sites on the Blake Ridge have revealed the presence of pore-water with relatively low chloride concentrations (Figure 5.6) (Shipboard Scientific Party, 1996). This may indicate that Logging Unit 2 contains waters with relatively low salt concentrations that will contribute to an increase in the measured electrical resistivities. However, since the acoustic logs are not affected by changes in pore-water salinities it appears to refute the hypothesis that salinity changes are contributing to the anomalous acoustic velocity and resistivity properties of Logging Unit 2.

To evaluate the effect of pore-water salinity on the measured log values at Sites 994, 995, and 997, the observed changes in electrical resistivity in Logging Unit 2 have been compared to the pore-water salinity changes measured in the recovered cores. It was determined that to account for the high resistivities (as high as 1.50 ohm-m) observed in the upper part of Logging Unit 2 (Figure 5.5a-c), would require the pore-

waters to be diluted, relative to a sea water baseline of 32 ppt, by almost 72% (to about 9 ppt NaCl). A required pore-water salinity change of 72% is much greater than the maximum observed chlorinity changes measured in the recovered cores, which was determined to be about 15% (Shipboard Scientific Party, 1996). It is unlikely, therefore, that interstitial chlorinity differences could account for the observed resistivity-log trends.

To further evaluate the effect of variations in pore-water salinities on the log-measured formation resistivities, it is possible to compare the formation water resistivities (R_w) (Figure 5.10), calculated from the recovered core water samples at Sites 994, 995, and 997, with the log-measured formation resistivities (R_t). The log-measured formation resistivities in Logging Unit 2 on the Blake Ridge is characterized by a maximum resistivity range of 1.3 ohm-m (Figure 5.5a-c). However, the observed pore-water salinity variations in cores recovered from Logging Unit 2 correspond to a formation water resistivity range of only 0.05 ohm-m, which is less than 4% of the total formation resistivity range measured in Logging Unit 2. Therefore, the observed formation resistivities variations in Logging Unit 2 cannot be attributed to only changes in pore-water salinities, and the resistivity log in Logging Unit 2 is likely responding to the presence of in-situ gas hydrates.

Three variations of the Archie relation (Archie, 1942), discussed in Chapter 3 of this thesis, have been used to calculate water saturations (S_w) [gas-hydrate saturation (S_h) is equal to $(1.0\text{-}S_w)$] from the available electrical resistivity-log data (DITE) at Sites 994, 995, and 997. In the first computation, the "standard" Archie equation [Equation 3.8: $S_w = (a\,R_w\,/\varnothing^m\,R_t)^{1/n}$] has been used with two different sets of sediment porosity data to

calculate two comparable water saturations. Both sets of porosity data used in the

"standard" Archie equation were from the core-derived physical property data (Figure

5.8). In the first calculation, the absolute value (not statistically manipulated) of the core-

derived porosities were used and the sediment porosities between the core measurements

were linearly interpolated. However, in the second "standard" Archie calculation of

water saturation (S_W), the required sediment porosities were obtained from a regression

trendline (power function) projected through the core porosity data in each hole. The

formation water resistivities (R_W) (Figure 5.10) calculated from the recovered core water

samples in Logging Units 1 and 3 (discussed in Section 5.2.5 of this thesis), were used in

both "standard" Archie calculations along with the a and m Archie constants also

discussed in Section 5.2.5 of this thesis (a=1.05, m=2.56). The value of the empirical

constant n was assumed to be 1.9386 as determined by Pearson et al. (1983). In Figure

5.12a-c, the results of the two "standard" Archie calculations are shown as water

saturation (S_W) log traces for Holes 994D, 995B, and 997B.

In all three holes (Holes 994D, 995B, and 997B), the "standard" Archie relation

yielded water saturations (S_W) ranging from about 100% to a minimum of about 80%

(Figure 5.12a-c): The "standard" Archie calculation which used the non-statistically

manipulated core porosities (measured) resulted in the calculation of more highly

variable water saturations, while the "standard" Archie calculation which employed the

average core porosities yielded more consistent water saturations within each hole. The

zones in each hole characterized by water saturations exceeding 100%, which is

theoretically impossible, are likely caused by poor hole conditions which have degraded
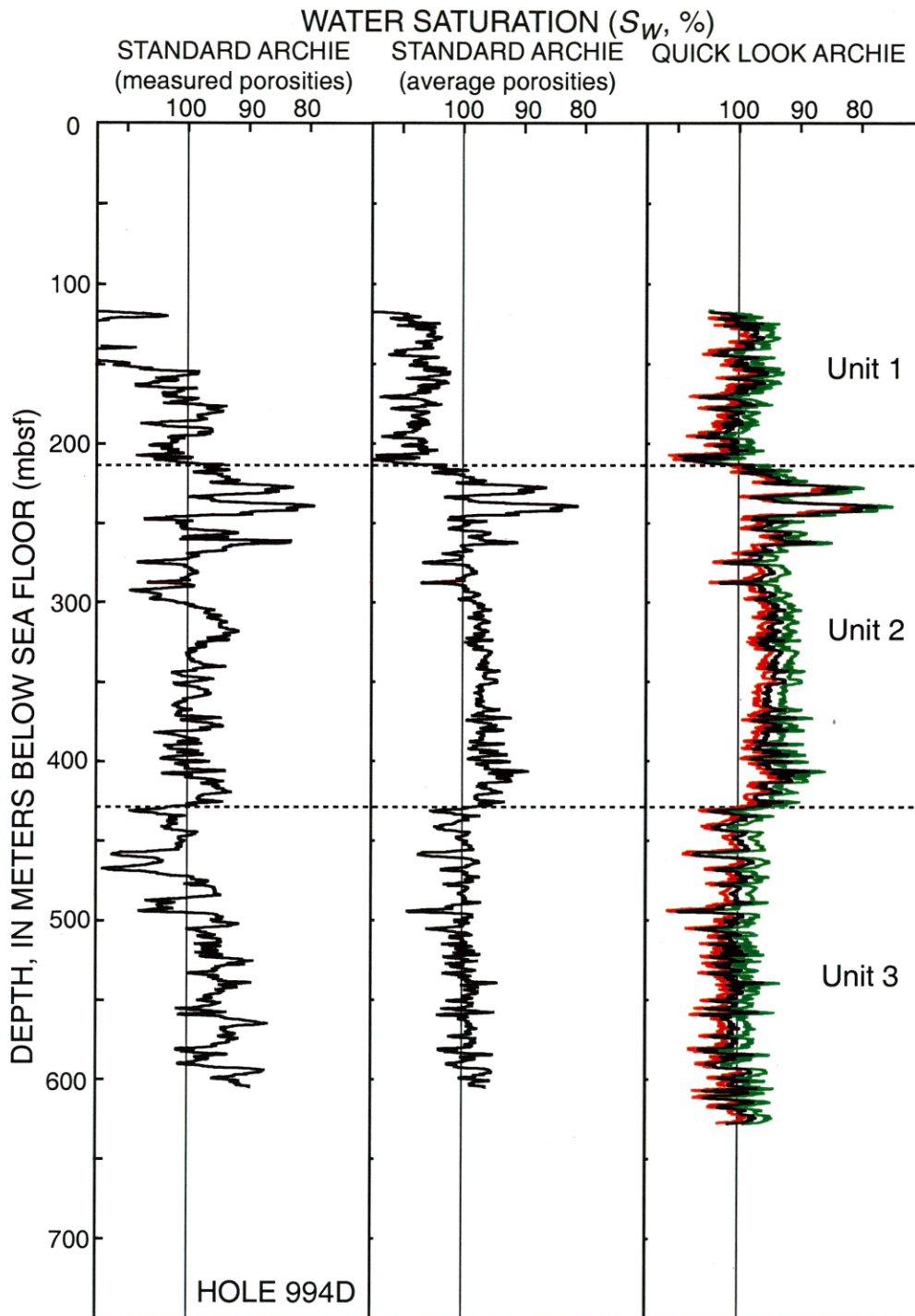
Figure 5.12a "Standard"- and "quick-look"-Archie-derived water saturations (S_w) calculated from the downhole electrical resistivity log at Hole 994D. The two "standard" Archie calculations assume different sediment porosities: (1) directly measured and (2) average core porosity trends. The three "quick-look"-derived saturation curves assume three different R_o values (i.e., maximum, median, and minimum).
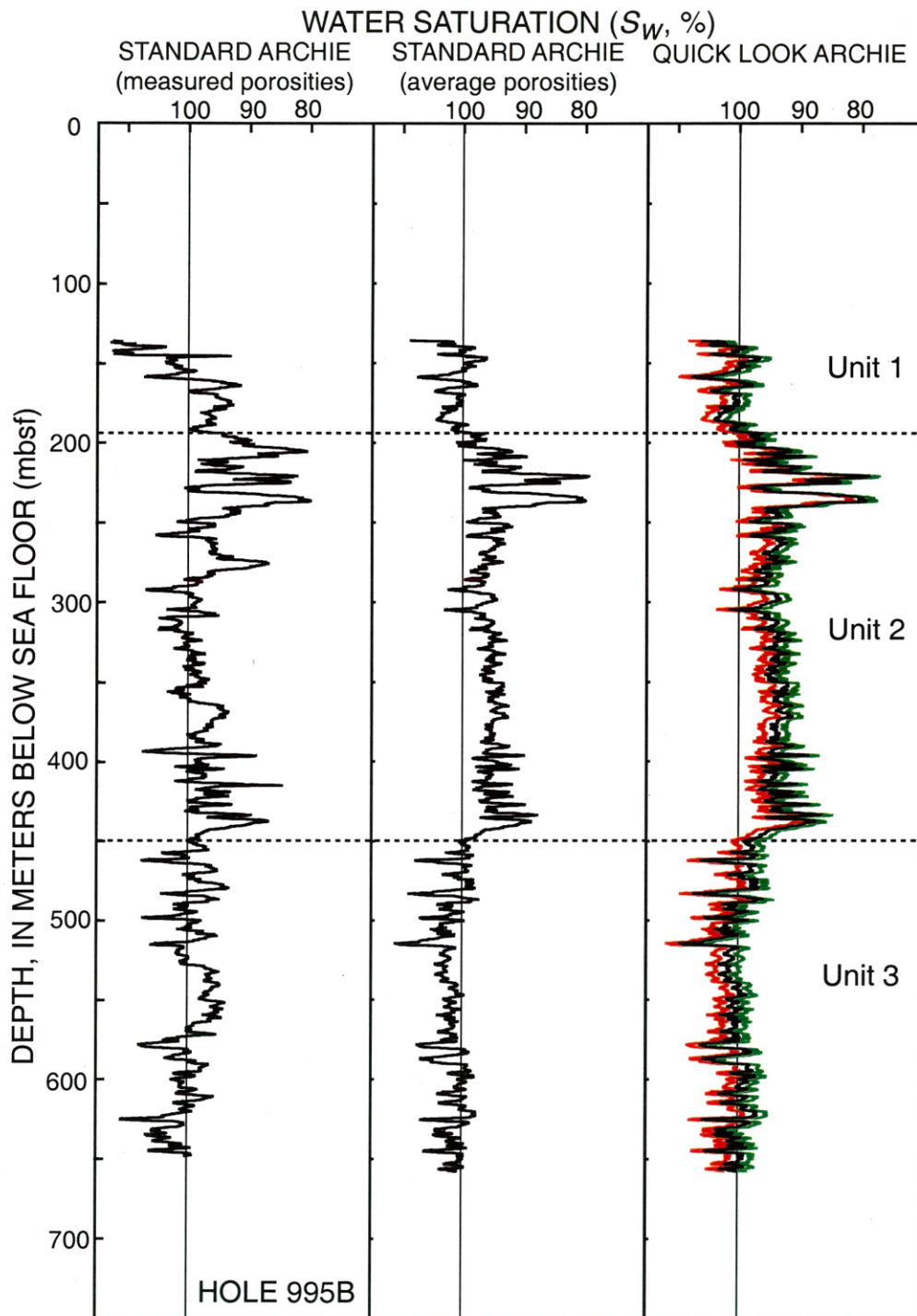
Figure 5.12b "Standard"- and "quick-look"-Archie-derived water saturations (S_w) calculated from the downhole electrical resistivity log at Hole 995B. The two "standard" Archie calculations assume different sediment porosities: (1) directly measured and (2) average core porosity trends. The three "quick-look"-derived saturation curves assume three different R_O values (i.e., maximum, median, and minimum).
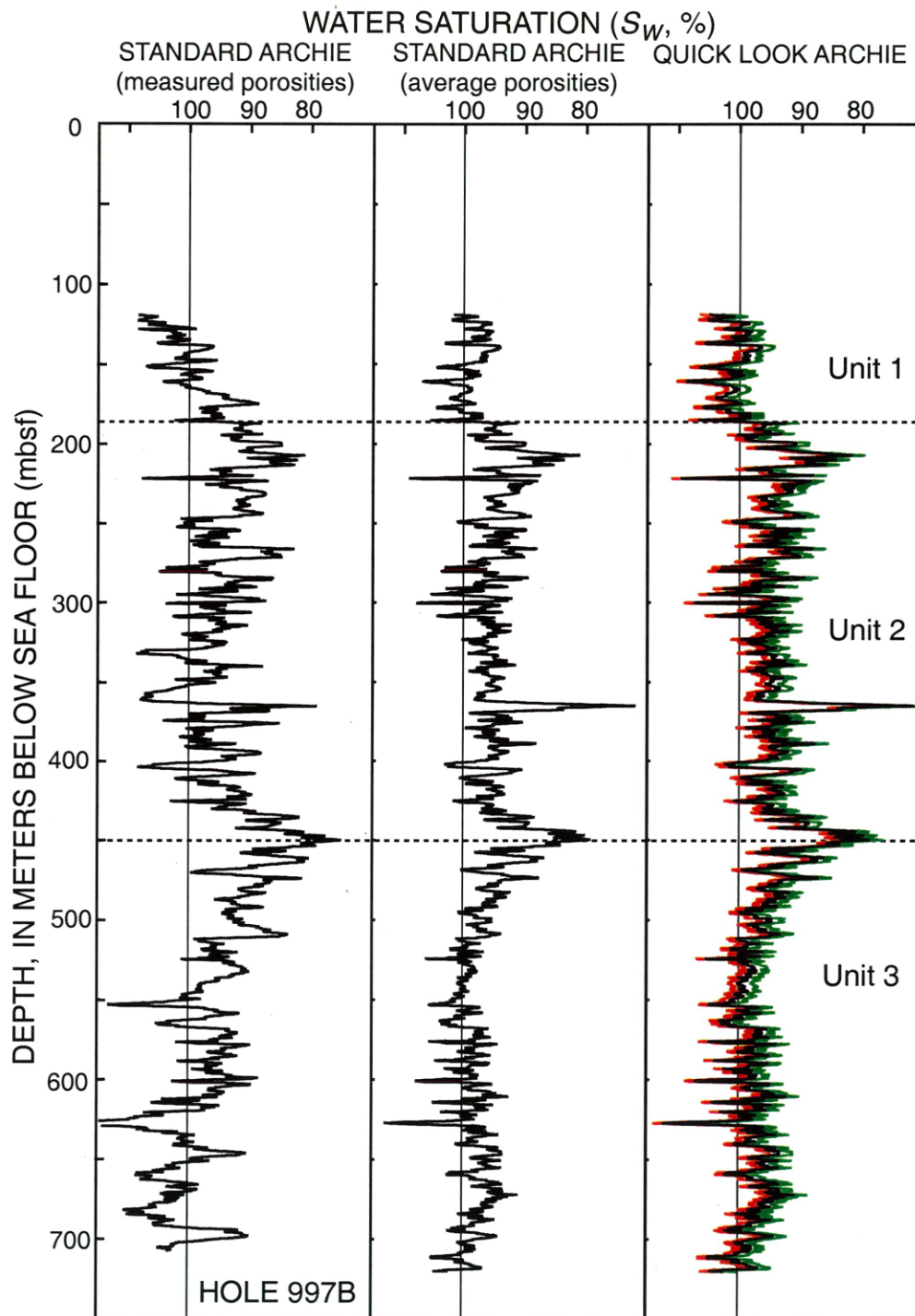
Figure 5.12c "Standard"- and "quick-look"-Archie-derived water saturations (S_w) calculated from the downhole electrical resistivity log at Hole 997B. The two "standard" Archie calculations assume different sediment porosities: (1) directly measured and (2) average core porosity trends. The three "quick-look"-derived saturation curves assume three different R_O values (i.e., maximum, median, and minimum).

the resistivity-log measurements. In an enlarged borehole, such as in Logging Unit 1 of

all three holes, the resistivity log will underestimate the true formation resistivity which

will correspond to an apparent increase in water saturations. The low water saturations in

Logging Unit 3 of all three holes, which is most pronounced in Hole 997B, are likely due

to the presence of free-gas as discussed in Section 5.2.3 of this thesis.

The next resistivity-log approach used to assess gas-hydrate saturations is based

on the modified "quick look" Archie log analysis technique (discussed in Chapter 3 of

this thesis) that compares the resistivity of water-saturated and hydrocarbon-bearing

sediments. Electrical-resistivity-log (R_t) measurements from Holes 994D, 995B, and

997B (Figure 5.5a-c) were used to calculate water saturations (S_w) using the following

modified Archie relationship: $S_w = (R_o/R_t)^{1/n}$ (Equation 3.10), where R_o is the resistivity

of the sedimentary section if it contained only water (S_w=1.0), R_t is the resistivity of the

gas-hydrate-bearing intervals (log values), and n is an empirically-derived constant. As

discussed in Chapter 3 of this thesis, this modified Archie relationship is based on the

following logic: If the pore-space of a sediment is 100% saturated with water, the deep

reading resistivity device will measure the resistivity of the 100% water-saturated

sedimentary section (R_o). This measured R_o value is considered to be a relative baseline

from which hydrocarbon saturations can be determined within nearby hydrocarbon-

bearing intervals. In order to determine R_o for Logging Unit 2 in all three holes, the

measured deep-resistivity-log data from the non-gas-bearing portions of Logging Units 1

and 3 (S_w=1.0) have been used to project R_o trend-lines for Unit 2 (Figure 5.5a-c).

Because of the sensitivity of the "quick look" calculations to the selection of an accurate

R_O trend-line, for each site assessed on the Blake Ridge three different R_O trend-lines

have been used that bracket (i.e., maximum, median, and minimum) the expected R_O

trend-line (best fit median trend-line) as shown in Figure 5.5a-c. Laboratory experiments

of different sediment types have yielded a pooled estimate for n of 1.9386 (reviewed by

Pearson et al., 1983). Now knowing R_t, R_O, and n it is possible to use the modified

"quick look" Archie relationship to estimate water saturations. Displayed in Figure

5.12a-c, along with the "standard"-Archie-derived water saturations, are the water

saturations calculated by the "quick look" Archie method. The "quick look"-calculated

water saturations are very similar to the water saturations calculated by the "standard"

Archie relation which employed average core porosities. However, the "quick look"-

derived water saturations (calculated from the best fit R_O trend-line) are 2 to 3 percent

higher, which is mostly controlled by the method used to select the R_O baseline. Figure

5.12a-c also shows that the "quick look"-derived water saturations are relatively

insensitive to the limited range of expected R_O values on the Blake Ridge.

The third derivation of the Archie relation used to calculate water saturations (S_W)

on the Blake Ridge was proposed by Pearson et al. (1983) as discussed in Chapter 3 of

this thesis. The Pearson et al. (1983) modified Archie relation (Equation 3.9: $R_f/R_O =$

$C^{-T} S_W^{1-n}$) assumes that water saturations can be calculated in a gas-hydrate-bearing

sedimentary section from a resistivity log if the resistivity of the "thawed" or 100%

water-saturated (R_O) (non-gas-hydrate-bearing) formation can be determined. The

modified Archie method proposed by Pearson et al. (1983) is very similar to the Archie

"quick look" method discussed above. The water-saturated formation resistivities (R_O, "thawed" non-gas-hydrate-bearing) calculated in Holes 994D, 995B and 997B for the "quick look" method have been used in the Pearson et al. (1983) modified Archie relation and the empirical parameters C and n have been given values of 1.057 and 1.9386, respectively (reviewed by Pearson et al., 1983). The required formation temperatures (Table 5.4) have been directly measured at all three core sites as described in Section 5.2.5 of this thesis.

The water saturations calculated from the modified Archie relation proposed by Pearson et al. (1983) are shown in Figure 5.13. In all three holes, the water saturations exponentially decrease with depth from values greater than 100% near the top of the holes to less than 20% at the bottom of each hole. It is obvious that the resistivity relation proposed by Pearson et al. (1983) does not yield accurate water saturations for reservoir temperatures above 0°C. When the temperature (T) variable is removed from the proposed Pearson et al. (1983) relation, the resultant water saturations are similar to the values calculated by the "standard" or "quick look" Archie methods. However, water saturations calculated by the Pearson et al. (1983) modified Archie relation are generally lower (10 to 20 percent lower) than those calculated by either the "standard" or "quick look" Archie relations. The low water saturations calculated by the Pearson et al. (1983) modified Archie relation are not likely valid. It is possible that in nature, the salts excluded during gas hydrate formation are not concentrated in the remaining "unfrozen" pore-waters and unfrozen brine inclusions do not control the flow of electrical current as proposed by Pearson et al. (1983). Geochemical core studies from Leg 164 revealed no
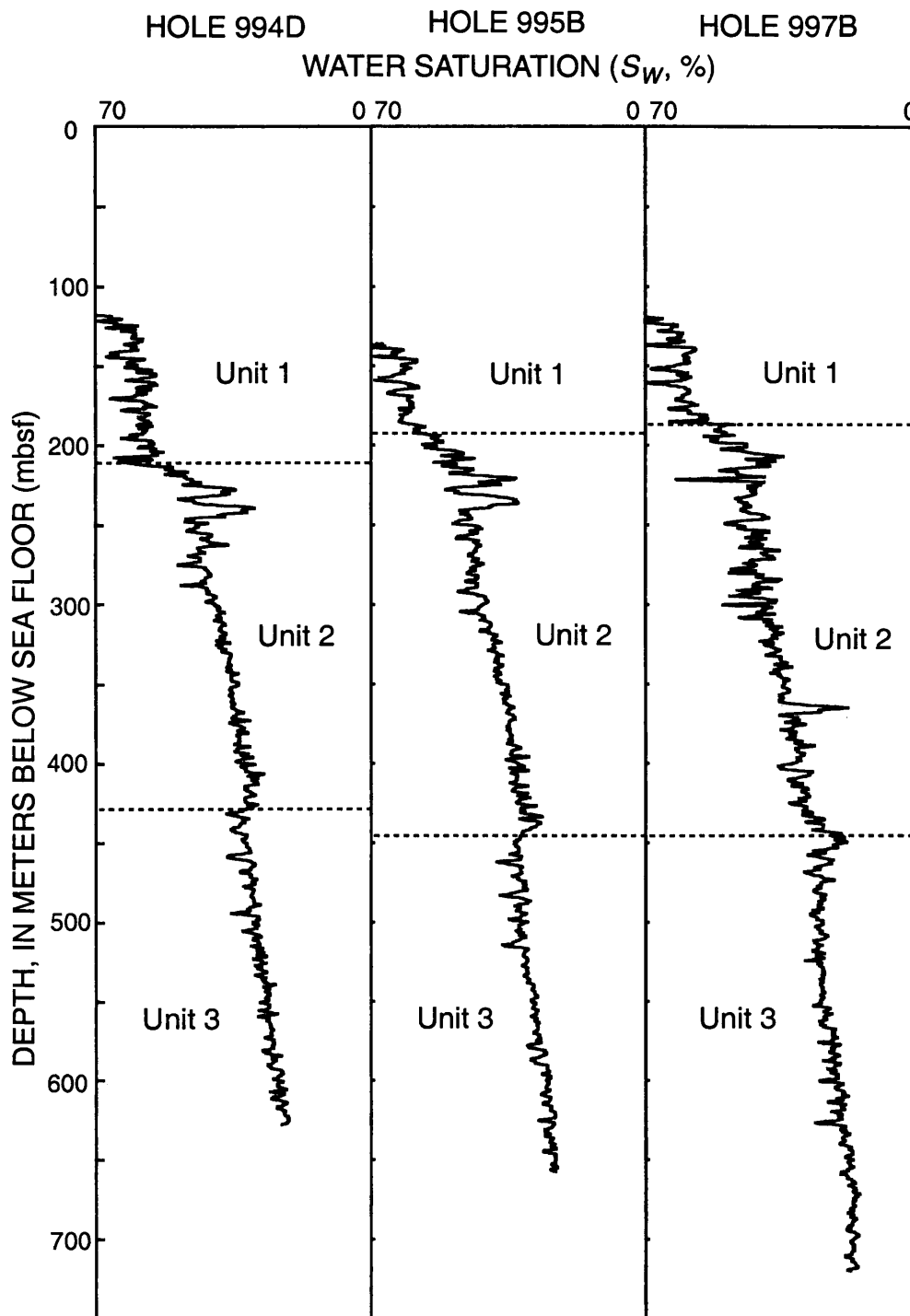
Figure 5.13 Water saturations (S_W) for Sites 994, 995, and 997 calculated from the modified Archie relation proposed by Pearson et al. (1983).

evidence of high pore-water salinities (excluded salt) associated with gas hydrates (Shipboard Scientific Party, 1996). It is possible that the salts excluded during gas hydrate formation have been redistributed in the stratigraphic section by chemical diffusion and/or gravity drainage.

As discussed in Chapter 3 of this thesis, the occurrence of shale (clay) in a sedimentary section can directly affect the electrical properties of the formation and lead to erroneous downhole-log-derived water saturations. Because of the relatively uniform lithologic nature of the sediments on the Blake Ridge and along the Cascadia margin, and because sediment cation exchange capacity (CEC) data was available from both locations, the Waxman-Smits saturation-resistivity relation for shaly formations was used to assess the affect of shales (clays) on resistivity-derived gas-hydrate saturations at Site 995 on the Blake Ridge and Site 889 on the Cascadia margin.

To simplify the assessment of the downhole-electrical-resistivity-log data from Site 995 on the Blake Ridge, the Waxman-Smits relation (Equation 3.12) used in this thesis was rewritten into terms of electrical resistivity (Waxman and Thomas, 1974). Many of the "conventional" variables required for the "standard" Archie relation (Equation 3.8; a, m, n, $\varnothing$, R_W, and R_t) need to be modified in the Waxman-Smits relation because of the affect of shales (clays) on the assumed clean (shale-free) sandstone Archie constants. The Waxman-Smits relation also contains several unique parameters (i.e., B = counterion activity, Q_V = cation exchange concentration) not found in the "standard" Archie relation. In this section of the thesis, the input variables needed for the Waxman-Smits shaly-sand assessment of the Site 995 downhole-log data have been determined.

One of the most critical input variables required by the Waxman-Smits relation is accurate laboratory analysis of sediment cation exchange capacities (CEC). For this study, 15 representative core samples from Hole 995A were selected for laboratory analysis of the CEC of the gas-hydrate-bearing sediments on the Blake Ridge (Table 5.5). The laboratory analysis of the Hole 995A sediment cores was performed by Huffman Laboratories Incorporated (Ronald L. Keil, Laboratory Director, Golden, Colorado). The laboratory procedures used to determine the CEC of the Site 995 sediment core samples was adapted from the "arid land soils" analytical technique which is designed to yield a total sediment CEC measurement, including the contribution of both the sedimentary organic carbon and carbonates (Polemio and Rhoades, 1977). Sample preparation consisted of vacuum drying each sediment sample at ambient temperatures for 48 hours and pulverizing the sample. The analytical procedure consisted of saturating the sediment sample with an ethanol-sodium chloride solution. The total concentration of exchangeable (sorbed) Na was subsequently determined from the composition of the excess saturating solution, which is equivalent to the CEC of the equilibrated sediment sample.

The laboratory-derived CECs for the sediment core samples from Hole 995A (Table 5.5) generally ranged from about 33 to 44 meq/100 grams of sample, with the exception of one relatively lower value of 26 meq/100 grams at a depth of 107.4 mbsf. Analysis of duplicate samples from Hole 995A revealed a probable uncertainty in the reported CEC measurements of ±2 meq/100 grams. Because of the relatively limited range in the laboratory-derived CEC measurements reported in Table 5.5, the required

Table 5.5 Laboratory-measured cation exchange capacity (CEC) of sediment core samples from Hole 995A.

Sample depth (mbsf)	Cation exchange capacity (CEC) (meq/100 grams)
107.4	26
121.4	36
163.9	44
220.0	37
257.0	36
263.1	36
290.9	37
373.9	34
397.9	37
407.5	32
425.7	38
446.5	36
494.7	36
554.8	35
574.5	33

meq=milliequivalents

Waxman-Smits CEC values for the non-sampled portions of Hole 995A were obtained

from a regression trendline projected through the laboratory-derived CEC values.

Before using the laboratory-derived CEC data in the Waxman-Smits relation, the

laboratory reported values were converted to sediment volumetric terms (Q_v) by

Equation 3.13 as described in Section 3.4 of this thesis. The resultant Waxman-Smits Q_v

values ranged from a near-surface value of about 0.5 meq/ml to about 0.8 meq/ml near

the bottom of Hole 995A. The relatively high Q_v values for Site 995 are of concern,

because the Waxman-Smits relation as described by Waxman and Thomas (1974) is

experimentally limited to reservoir rock conditions with Q_v values ranging from only

0.06 to 0.4 meq/ml.

The next variable unique to the Waxman-Smits relation is the counterion activity

variable or B, which relates formation water resistivities and temperatures. See Waxman

and Smits (1968) for the complete equation used to calculate the equivalent conductance

of conterions (B) for Site 995.

In the "standard" Archie assessment of water saturations at Site 995, the Archie a

and m (a=1.03, m=2.53) variables were directly calculated from available core porosity

and downhole-resistivity-log data. The Archie n variable was assumed to be equal to

1.9386 (Pearson et al., 1983). As previously noted, however, the Waxman-Smits relation

requires the Archie a, m, and n variables to be conceptually transformed from their

assumed clean sandstone equivalents to values for a shaly sandstone medium. The

calculation of shaly-sand a, m, and n equivalents can be problematic; therefore, it was

initially assumed that the "standard" Archie a and m values calculated from the

downhole-log and core data at Site 995 were correct (Table 5.4). It was also assumed,

that a n value of 1.9386 was also applicable for the shaly-sand assessment of water

saturations on the Blake Ridge. Similarly, the sediment porosity data needed for the

Waxman-Smits calculations were obtained from the regression trendline analysis of the

core porosity data discussed in the "standard" Archie assessment of Site 995. The pore-

water resistivity (R_w) trend-line (Figure 5.10) calculated for the Archie resistivity

porosity assessment of Site 995, was also used in the Waxman-Smits shaly-sand

assessment of Site 995.

The "standard" Archie and various Waxman-Smits-derived (assuming different

values for the Archie m variable, m=2.56, 2.80, 3.00, and 3.20) water saturations for the

drilled interval in Hole 995B on the Blake Ridge have been displayed in Figure 5.14. In

general, the Waxman-Smits calculations that assume the same a, m, and n constants as

the "standard" Archie relation, appear to significantly overestimate the amount of in-situ

gas hydrates at Site 995 (when compared to other independent calculations of gas-hydrate

concentrations). Subsequent sensitivity analysis have revealed that the Waxman-Smits

calculations at Site 995 to be relatively insensitive to changes in Archie a (ranging from

0.5 to 2.0) and n (ranging from 1.5 to 2.5) variables. As shown in Figure 5.14, however,

it was determined that the Waxman-Smits-derived water saturations were extremely

sensitive to changes in the Archie m variable (ranging from 2.56 to 3.20). However,

there is no geologic justification for using the higher values for the Archie m variables.

In general, it appears that the Waxman-Smits relation significantly underestimates

water saturations when relatively common Archie variables are considered. The likely
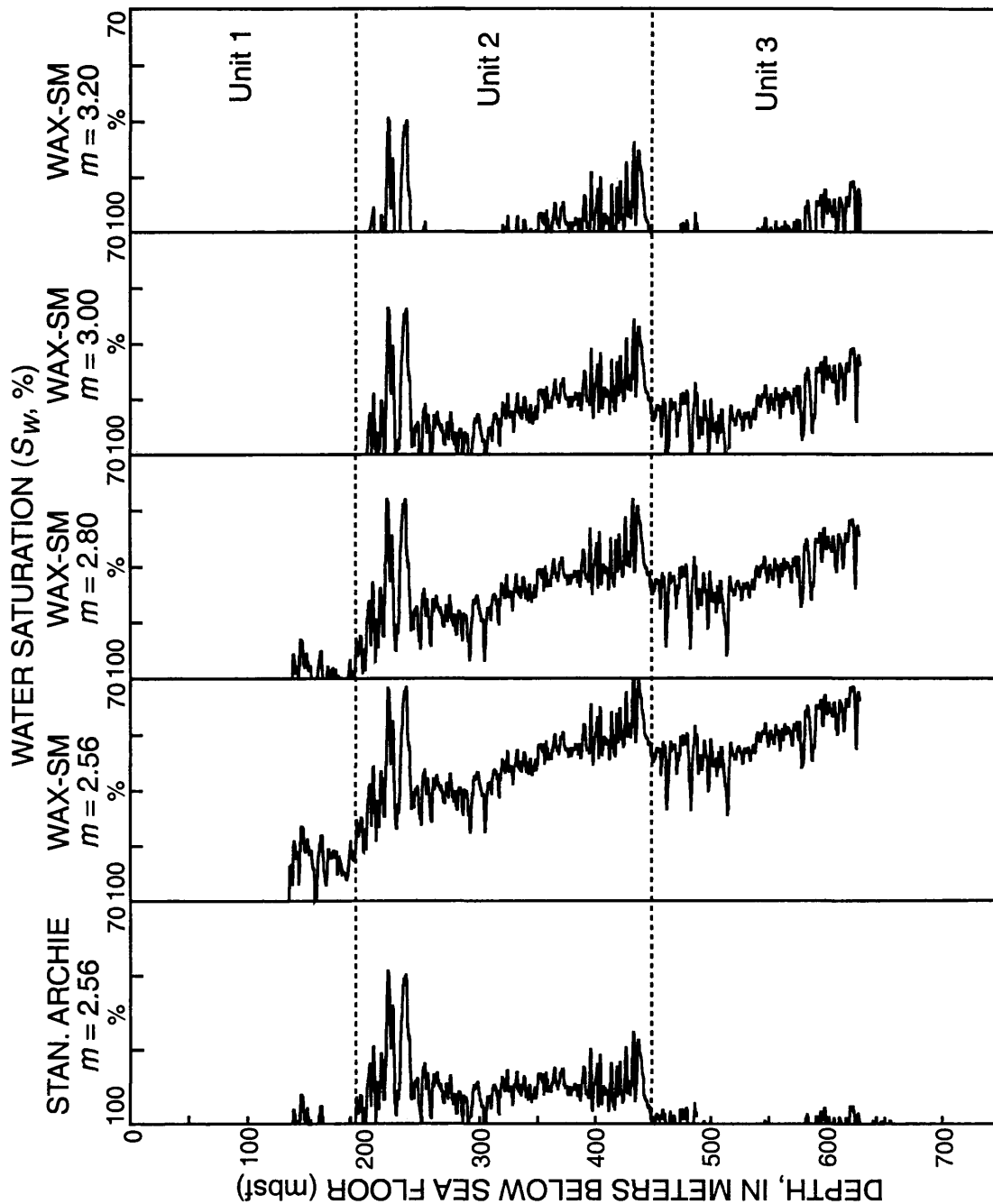
Figure 5.14 Water saturations (S_W) for Hole 995B calculated from the "Standard" Archie relation and the Waxman-Smits shaly-sand model (assuming various Archie m variables and average core porosities).

cause of this problem can be attributed to the high CEC nature (high clay contents) of the

sediments on the Blake Ridge, which yielded Q_v values outside of the experimental limits

of the Waxman-Smits relation as described by Waxman and Thomas (1974).

Acoustic-Log-Calculated Gas-Hydrate Saturations Described in Section 3.5 of

this thesis is a series of proposed equations that utilize both compressional- and shear-

wave acoustic well-log data to calculate gas-hydrate saturations [gas-hydrate saturation

(S_h) is equal to $(1.0-S_w)$]. In this section, compressional-wave acoustic-log data from

Sites 994, 995, and 997 will be used along with the Timur, modified Wood, and Lee

weighted average acoustic equations to calculate gas-hydrate saturations on the Blake

Ridge. As of this time, there are no shear-wave acoustic well-log data publicly available

from the Blake Ridge sites. Therefore, the combined compressional- and shear-wave

velocity gas-hydrate saturation equations proposed by Lee et al. (1996), Kuster-Toksöz

(Zimmerman and King, 1986), or Dvorkin et al. (1991, 1993) cannot be used to assess

gas-hydrate saturations along the Blake Ridge transect.

To facilitate the calculation of gas-hydrate saturations from the available acoustic

well logs, a computer program has been written to simultaneously calculate gas-hydrate

saturations with the Timur (Equation 3.14), Wood (Equation 3.15), and Lee (Equation

3.16) acoustic equations. In this acoustic calculation of gas-hydrate saturations at Sites

994, 995, and 997, two different sets of sediment porosity ($\emptyset$) data have been used,

similar to the electrical resistivity water saturation calculations discussed earlier in this

section of the thesis. Both sets of porosities are from the core-derived physical property

data (Figure 5.8). In the first set of calculations, the absolute value (not statistically

manipulated) of the core porosities was used and the sediment porosities between core

measurements were linearly interpolated. In the second set of acoustic gas-hydrate

saturation calculations (S_h), the sediment porosities were obtained from a regression

trendline (power function) projected through the core porosity data in each hole. The

remaining variables in the Timur and Wood equations have been assigned constant

values: With an assumed water velocity (V_w) of 1.5 km/sec, sediment matrix velocity

(V_m) of 4.37 km/sec, gas hydrate velocity (V_h) of 3.35 km/sec, water density (ρ_w) of 1.0

g/cm^3, sediment matrix density (ρ_m) of 2.7 g/cm^3, and a gas hydrate density (ρ_h) of 0.9

g/cm^3 (Table 3.12). In the Wood equation, the bulk-density (ρ_b) of the formation is

determined from the modified three-component density equation (Equation 3.2) discussed

in Section 3.2 of this thesis. The bulk compressional-wave velocity of the formation (V_b)

was obtained directly from the transit-time well logs. The final two variables needed

before conducting the acoustic gas-hydrate saturation calculations are the weight factor

(W) and the gas-hydrate cementation exponent (r) in the Lee weighted average equation.

As shown in Figure 3.20 and discussed in Section 3.5 of this thesis, a W of 1.1 best

characterizes the sediments on the Blake Ridge. A gas-hydrate cementation exponent (r)

of $r=1$ was selected, because the occurrence of gas hydrates has not significantly

contributed to the "cementation" of the unconsolidated sediments on the Blake Ridge

(Ecker et al., 1996). However, the acoustic velocities in Logging Unit 2 on the Blake

Ridge appear to be affected by relatively low gas-hydrate saturations (based on analysis

of electrical-resistivity-log data and interstitial water chloride freshening trends in

recovered cores); which suggests that at even low concentrations, gas hydrates contribute

to the mechanical strength of the host sediments. With increasing gas-hydrate saturations

(beyond 2 to 3 percent bulk volume), however, the acoustic well-log data from Leg 164

does not always exhibit corresponding acoustic velocity increases (Figure 5.5a-c). It is

possible that initial gas hydrate formation (below 2 to 3 percent bulk volume gas hydrate)

may occur at sediment grain contacts, but continued gas hydrate growth may occur away

from grain contacts suspended in the open pore-spaces (combination of Models 1 and 2;

Figure 2.6).

In Figure 5.15a-c, the results of the Wood and Lee acoustic velocity calculations

for both porosity conditions are shown as gas-hydrate saturation log traces for Logging

Unit 2 in Holes 994D, 995B, and 997D. The results of the Timur acoustic saturation

calculations have not been included in Figure 5.15a-c, because the Timur equation failed

to indicate the presence of gas hydrates in the Blake Ridge coreholes. As discussed in

Section 3.5 of this thesis, the Timur equation, which adequately predicts the acoustic

properties of gas hydrates in consolidated rock media, does not accurately predict the

acoustic properties of the unconsolidated sediments on the Blake Ridge. In all three

holes (Holes 994D, 995B, and 997B), the Wood equation yielded gas-hydrate saturations

(S_h) ranging from a minimum of about 20% to a maximum near 60%, which is

significantly higher than the gas-hydrate saturations calculated by other methods (i.e.,

interstitial water chloride freshening or electrical resistivity methods) on the Blake Ridge.

The Lee equation, however, yielded for the most part gas-hydrate saturations (S_h) ranging

from 0% to a maximum of about 20% (exclusive of several anomalous zones in Hole
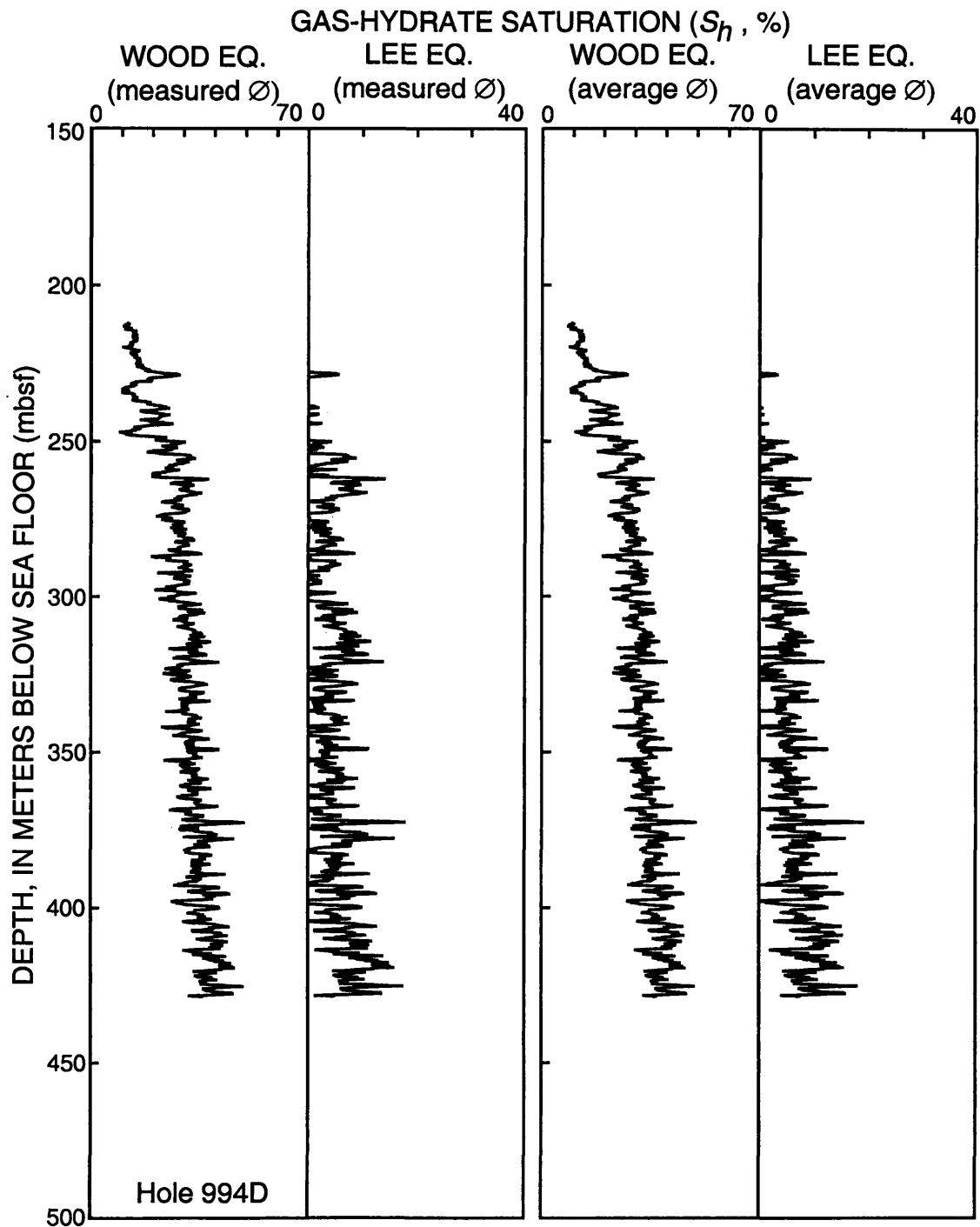
Figure 5.15a Gas-hydrate saturations (S_h) calculated from the downhole compressional-wave acoustic velocity log (LSS-SDT) at Site 994. The results of the modified Wood (Equation 3.15) and Lee (Equation 3.16) acoustic equations are shown assuming both directly measured and average core porosity trends.
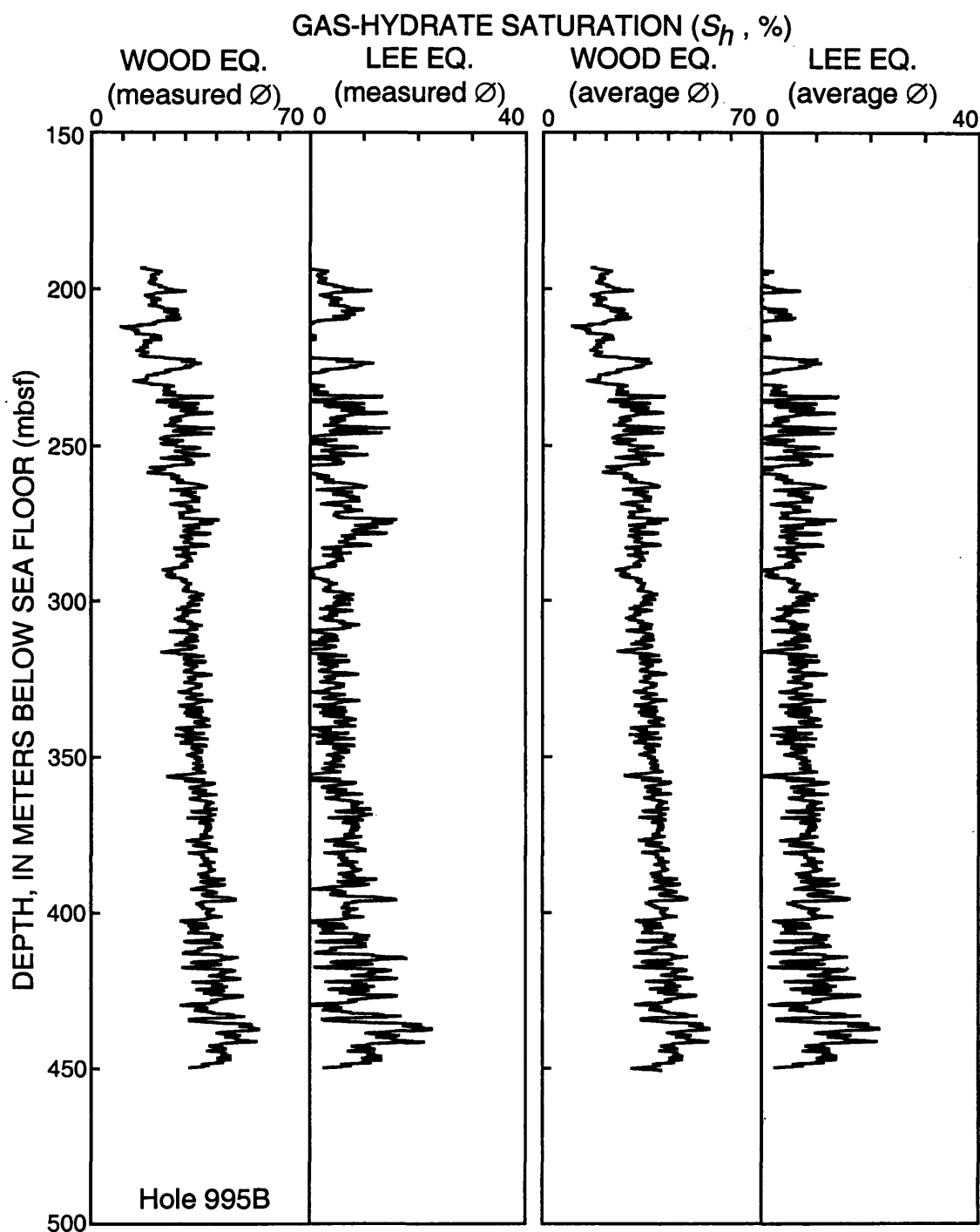
Figure 5.15b Gas-hydrate saturations (S_h) calculated from the downhole compressional-wave acoustic velocity log (LSS-SDT) at Site 995. The results of the modified Wood (Equation 3.15) and Lee (Equation 3.16) acoustic equations are shown assuming both directly measured and average core porosity trends.
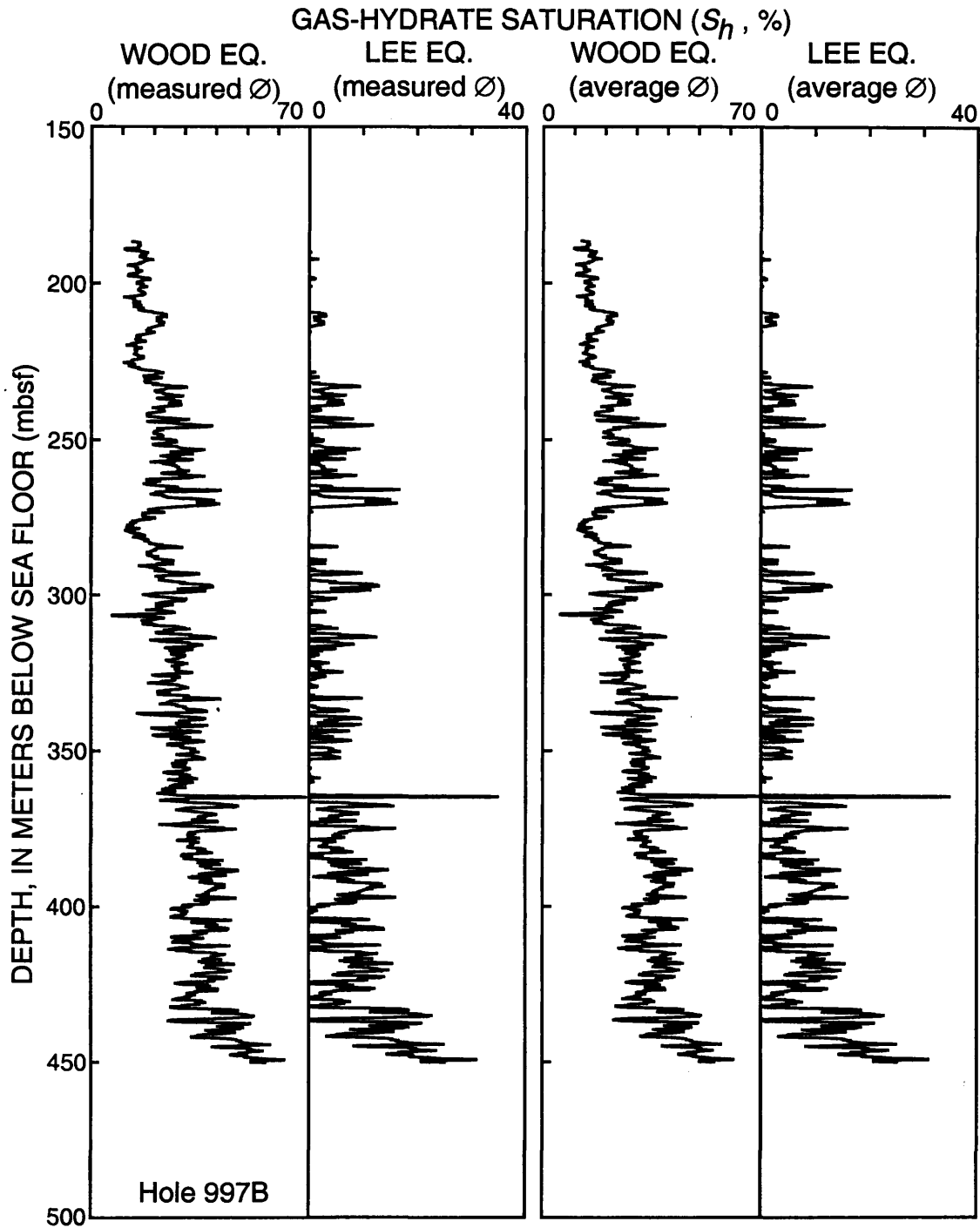
Figure 5.15c Gas-hydrate saturations (S_h) calculated from the downhole compressional-wave acoustic velocity log (LSS-SDT) at Site 997. The results of the modified Wood (Equation 3.15) and Lee (Equation 3.16) acoustic equations are shown assuming both directly measured and average core porosity trends.

997B), which are more compatible to the gas-hydrate saturations calculated from interstitial water chloride freshening trends and electrical-resistivity-log data (discussed earlier in this chapter of the thesis). In comparison, the Lee calculations which employed the non-statistically manipulated core porosities resulted in the calculation of more highly variable gas-hydrate saturations when compared to the Lee-calculated gas-hydrate saturations which used average core porosity data.

Neutron-Spectroscopy-Log-Calculated Gas-Hydrate Saturations By combining elemental yields from neutron spectroscopy logs, reservoir parameters including porosities, lithologies, formation fluid salinities, and hydrocarbon saturations (including gas hydrate) can be calculated, as previously discussed in Chapter 3 of this thesis. In this section, carbon/oxygen (C/O) elemental data from the geochemical logging tool (GLT) has been used to determine gas-hydrate saturations at all three sites (Sites 994, 995, and 997) drilled on the Blake Ridge during Leg 164.

As discussed in Section 5.2.2 of this thesis, Holes 994C, 995B, and 997B were logged with the geochemical combination tool (Figure 3.1, Tables 3.1 and 5.1). The geochemical-log data included both neutron capture and stationary inelastic neutron-log measurements. The inelastic neutron measurements consisted of 44 individual five minute duration stationary measurements. The shipboard-acquired capture and inelastic neutron geochemical measurements required a significant amount of post-field reprocessing to correct for the affects of enlarged and irregular boreholes, fluids in the borehole, logging speed variations, and neutron activation of various elements in the formation. The GLT data processing is performed with a set of log interpretation

computer programs developed by Schlumberger and the processing steps are described in Appendix 1 of this thesis.

The GLT logs from all three sites are significantly degraded by poor borehole conditions, but the neutron capture data from Holes 995B and 997B appear to yield useful information about the chemical composition of the formation. However, the neutron capture data from Hole 994C is severely degraded by the rugosity of the borehole, the effects of which could not be corrected. Therefore, the neutron capture data from Hole 994C has been disregarded in this study. Reprocessing of the GLT neutron capture and natural gamma radiation (NGT) data from Holes 995B and 997B yielded accurate estimates of the concentration of the following nine elements within the formation: calcium, iron, silicon, aluminum, potassium, uranium, thorium, gadolinium, and titanium. During reprocessing of the GLT neutron capture data, it was noted that sulfur occurred in concentrations below the resolution capability of the tool; thus, the GLT-derived sulfur concentrations were disregarded in this study. In addition, the configuration of the GLT as used in ODP does not allow the direct acquisition of hydrogen or chlorine concentrations. Therefore, the proposed hydrogen/oxygen compositional ratio method (see Section 3.6 of this thesis) could not be used to assess gas-hydrate saturations with the Leg 164 GLT-log data.

As previously noted, the inelastic neutron geochemical data also required post-field reprocessing. The reprocessing of the inelastic neutron data from Leg 164 was performed by Schlumberger-Doll Research (by Dr. Jim Grau, Schlumberger-Doll Research, Ridgefield, Connecticut). The relative elemental yields from the acquired

inelastic neutron data are calculated by comparing the recorded spectral data to a series of

standard spectra. The occurrence of both gadolinium and titanium was also considered

along with a spectral correction which accounts for the direct arrival of high energy

neutrons from the source. An activation standard (CACT) was also used in the analysis

of the inelastic neutron data, which deals with the neutron activation of mostly oxygen in

the formation. The shipboard-measured and reprocessed carbon and oxygen elemental

ratios for Holes 994C, 995B, and 997B are listed in Table 5.6. The data reprocessing

performed by Schlumberger-Doll Research revealed that the recorded spectra from nine

of the inelastic neutron measurement stations from Leg 164 did not yield statistically

accurate results and the reprocessed spectra were considered invalid and were not further

analyzed in this study (Table 5.6).

Described in Section 3.6 of this thesis are a series of proposed equations that

utilize GLT-derived elemental concentrations to determine in-situ gas-hydrate

saturations. Equation 3.25 is a modified version of a standard three-component

carbon/oxygen hydrocarbon saturation equation (Equation 3.23) which can be used to

calculate gas-hydrate saturations.

$$COR = A\frac{[\alpha(1-C)(1-\varnothing) + \eta[C(1-\varnothing)] + \beta\varnothing S_h + C_b]}{[\gamma(1-C)(1-\varnothing) + \delta\varnothing(1-S_h) + \mu\varnothing S_h + O_b]} \qquad (3.25)$$

COR = Log-measured carbon-oxygen ratio

A = Ratio of average carbon and oxygen fast neutron cross sections

$\varnothing$ = Porosity, fractional percent

Table 5.6 Unprocessed and processed (corrected) carbon/oxygen elemental ratios as measured with the GLT in Holes 994C, 995B, and 997B.

Hole identification and station depth (mbsf)	Unprocessed carbon/oxygen ratio	Processed carbon/oxygen ratio
Hole 994C		
228	0.017	0.025
233	0.042	0.052
238	0.017	0.026
243	0.028	0.034
248	0.019	0.026
253	0.005	Invalid data
258	0.027	0.034
263	0.012	0.018
268	0.025	0.032
273	0.017	Invalid data
278	0.025	0.032
283	0.022	Invalid data
288	0.014	Invalid data
Hole 995B		
221	0.022	0.029
226	0.025	0.031
235	0.037	0.041
339	0.022	0.029
349	0.031	0.038
414	0.036	0.043
439	0.037	0.044
449	0.042	0.049
454	0.043	0.050
464	0.020	0.028
489	0.033	0.039
514	0.031	0.038
524	0.036	0.044
534	0.022	Invalid data
594	0.038	0.046
599	0.025	Invalid data
604	0.040	0.048
614	0.029	0.037

Table 5.6-continued Unprocessed and processed (corrected) carbon/oxygen elemental ratios as measured with the GLT in Holes 994C, 995B, and 997B.

Hole identification and station depth (mbsf)	Unprocessed carbon/oxygen ratio	Processed carbon/oxygen ratio
Hole 997B		
210	0.025	0.034
215	0.018	Invalid data
361	0.037	0.051
366	0.038	0.047
425	0.039	Invalid data
440	0.031	0.039
445	0.026	0.033
455	0.024	0.028
465	0.041	0.049
475	0.034	0.043
580	0.042	0.051
585	0.041	0.048
590	0.029	Invalid data

S_h = Gas-hydrate saturation, fractional percent

C_b = Relative carbon concentration contribution from the borehole, variable units

O_b = Relative oxygen concentration contribution from the borehole, variable units

C = Organic carbon content of the sediments, volume fraction

α = Atomic concentration of carbon in the matrix, variable units

β = Atomic concentration of carbon in the formation fluid (gas hydrate), variable units

η = Atomic concentration of carbon in the dispersed organic carbon, variable units

γ = Atomic concentration of oxygen in the matrix, variable units

δ = Atomic concentration of oxygen in the formation fluid (water), variable units

μ = Atomic concentration of oxygen in a Structure-I methane hydrate, variable units

Equation 3.25 accounts for all of the carbon and oxygen atoms associated with the borehole in a gas-hydrate-bearing formation. As previously discussed in Section 3.6 of this thesis and as shown in Equation 3.25, the amount of carbon and oxygen in a formation is not only controlled by the chemistry of the pore-fluids. To use Equation 3.25 to calculate gas-hydrate saturations, the carbon and oxygen content of the sediment matrix (including the organic carbon content), borehole fluids, and the boron sleeve on the GLT must be determined.

In this section of the thesis, the shipboard sedimentologic data (Shipboard Scientific Party, 1996), the shore-based powder X-ray diffraction analysis of core samples from Hole 997B, and the GLT neutron capture data from Holes 995B and 997B have been used to generate a comprehensive mineralogic model for the sediments

(matrix) on the Blake Ridge and to assess the carbon and oxygen content of the

sediments. Shipboard sedimentologic data has also been used to assess the amount of

organic carbon within the sediments (matrix) on the Blake Ridge (Shipboard Scientific

Party, 1996). The borehole correction factors needed to assess the effect of oxygen and

carbon in the borehole fluids and within the boron sleeve on the GLT have also been

calculated. This section of the thesis concludes with a comprehensive analysis of the

carbon/oxygen-derived gas-hydrate saturations on the Blake Ridge.

Analyses of the recovered cores from Leg 164, indicate that the sediments on the

Blake Ridge consist of a very homogeneous upper Miocene through Holocene

hemipelagic accumulation of terrigeneous clays and nannofossils, with subordinate

amounts of diatoms and foraminifers. At Sites 994, 995, and 997, the sedimentary

section was divided into three lithologic units based on observed mineralogic

compositions (Shipboard Scientific Party, 1996). The upper two lithologic units

(Lithologic Units I and II; 0 to approximately 150 mbsf) are Pleistocene and latest

Pliocene in age and are characterized by alternating beds of dark greenish gray

nannofossil-rich clay and more carbonate-rich beds of lighter greenish gray nannofossil-

rich clay. Beds of coarse-grained foraminifer ooze and reddish brown terrigeneous muds

are rare but indicate contour-current activity. Lithologic Unit III (from a depth of

approximately 150 mbsf to the bottom of each hole at approximately 750 mbsf) is a

monotonous dark-greenish gray nannofossil-rich clay and claystone of late Pliocene to

late Miocene age that is moderately to intensively bioturbated.

Shipboard smear-slide and X-ray diffraction analyses reveal that the dominant mineral phases within the cored sediments of the Blake Ridge are clay minerals, calcite, and quartz. Feldspars, dolomite, and pyrite are minor components of the sedimentary section. The clay-size fraction is made up mostly of clay minerals and nannofossils. The silt-size fraction is dominated by quartz; the estimated quartz abundance based on shipboard X-ray diffraction data almost never exceeds 15 weight percent (Shipboard Scientific Party, 1996). Disseminated dolomite rhombs make up a few percent of the bulk mineralogy. The biogenic calcareous constituents consist of nannofossils and minor amounts of foraminifers. Siliceous fossils are present as diatoms and rare sponge spicules. Carbonate content is generally higher in Lithologic Units I and II (0-150 mbsf; 20-60 weight percent carbonate) than in Unit III (150-750 mbsf; 10-20 weight percent carbonate).

In general, the shipboard sedimentologic data from Leg 164 indicate that the cored sedimentary section on the Blake Ridge is characterized by relatively uniform mineralogic assemblage of clay minerals and quartz, and a more variable calcite content. The effect of the variable calcite content on the bulk composition of the sediment matrix must be accounted for in the carbon/oxygen elemental ratio calculation of gas-hydrate saturations. In addition, the composition of the clays must be further examined before proceeding with the proposed carbon/oxygen spectral analyses of gas-hydrate saturations.

To further evaluate the mineralogic composition of the sediments on the Blake Ridge, 21 core samples from Hole 997A were subjected to X-ray diffraction analysis (Table 5.7) at the X-ray Diffraction Laboratory in the Department of Geology and

Table 5.7 List of core samples from Hole 997A selected for X-ray diffraction analysis. Relative amount of illite and smectite in the mixed-layer clays from Hole 997A core samples are also listed.

Core sample depth (mbsf)	Illite (vol%)	Smectite (vol%)
203	45	55
205	50	50
208	55	45
210	55	45
354	55	45
366	50	50
370	45	55
424	50	50
425	55	45
427	50	50
443	50	50
448	50	50
450	50	50
472	50	50
475	55	45
482	50	50
570	55	45
573	55	45
579	45	55
582	50	50
589	55	45

Geological Engineering, Colorado School of Mines. The X-ray laboratory is equipped with an automated Scintag XDS-2000 X-ray generator and diffractrometer. The X-ray diffraction patterns were obtained with the following machine settings: X-ray generator = 40 kV and 40 mA; X-ray tube anode = copper; scatter slit width 1-2 mm; receiving slit width 0.3-0.5 mm (whole rock samples) and 0.1-0.3 mm (oriented clay samples); scan = continuous; scanning range = 2° to 60° 2θ (whole rock samples), 2° to 40° 2θ (oriented clay samples), 2° to 20° 2θ (glycolated and heat-treated oriented samples); scanning rate = 2° 2θ per minute; and the samples were rotated during analysis. Digital X-ray intensities were recorded and processed with Scintag's DMS X-ray diffraction processing program which operates under a Windows-NT operating system. The digital data has been processed by subtracting $CuK_{\alpha2}$ contributions and the position of each peak (2θ), d-spacing (Å), and intensity (counts per second above background) are calculated and displayed (Figure 5.16a-d). The X-ray diffractograms had a three-point smoothing function applied to them before generating graphical displays.

The 21 core samples from Hole 997A selected for X-ray diffraction analyses (XRD) are from near the depths at which the inelastic neutron measurements were made with the GLT in Hole 997B (Tables 5.6 and 5.7). Whole-rock samples and clay-sized separates were analyzed to identify the constituent minerals in the sediments. All of the core samples were air-dried and ground by hand to a uniform texture. Randomly oriented whole-rock subsamples of each core sample were prepared for X-ray diffraction analysis by packing the ground sediment samples into circular sample holders and sequentially X-raying the samples. The randomly oriented powders were not pretreated with any
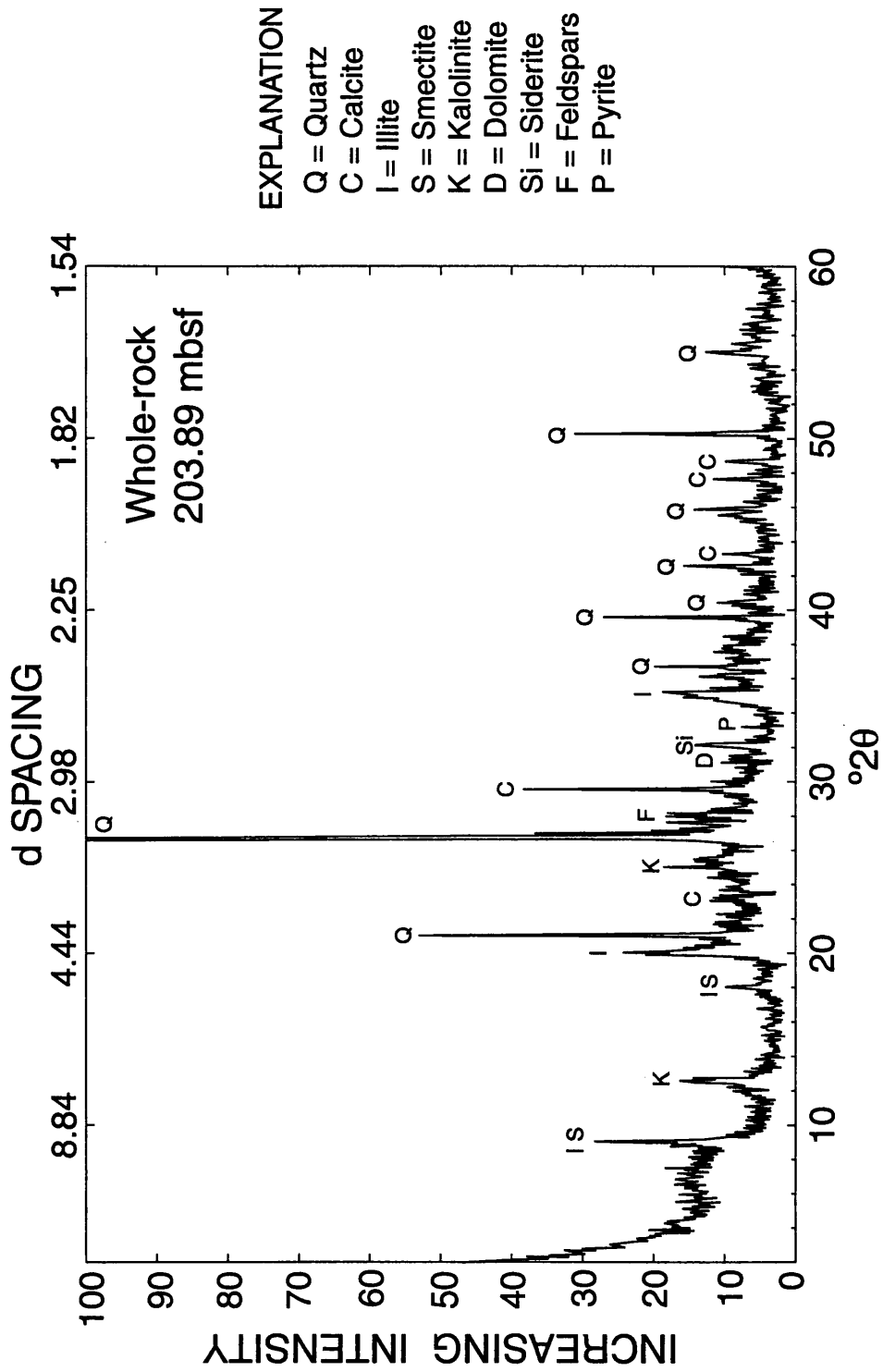
Figure 5.16a Whole-rock x-ray diffractogram of a sediment core sample from a depth of 203.89 mbsf in Hole 997A.
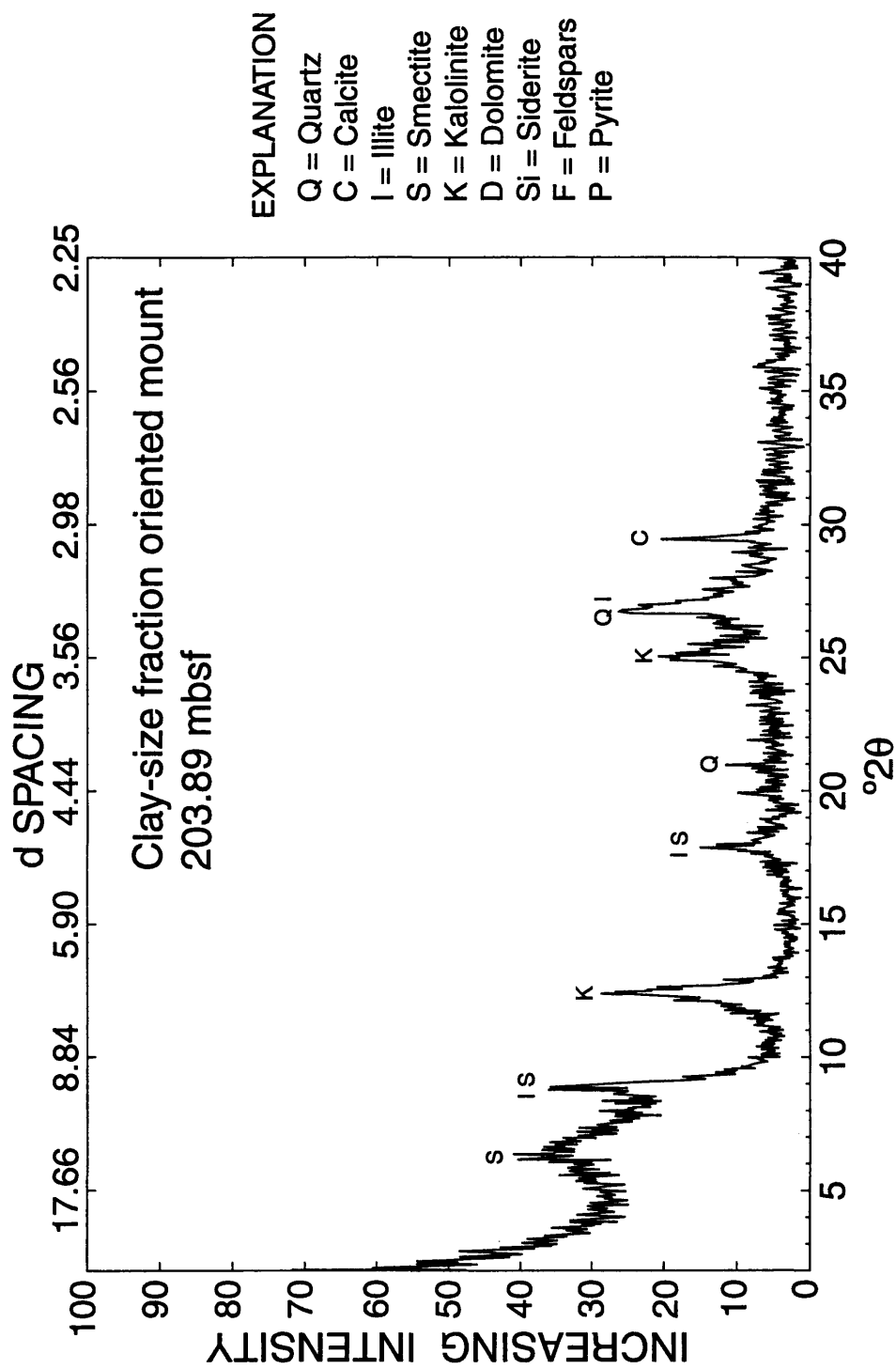
Figure 5.16b X-ray diffractogram of a untreated (air dried) oriented clay mount of the core sample from a depth of 203.89 mbsf in Hole 997A.
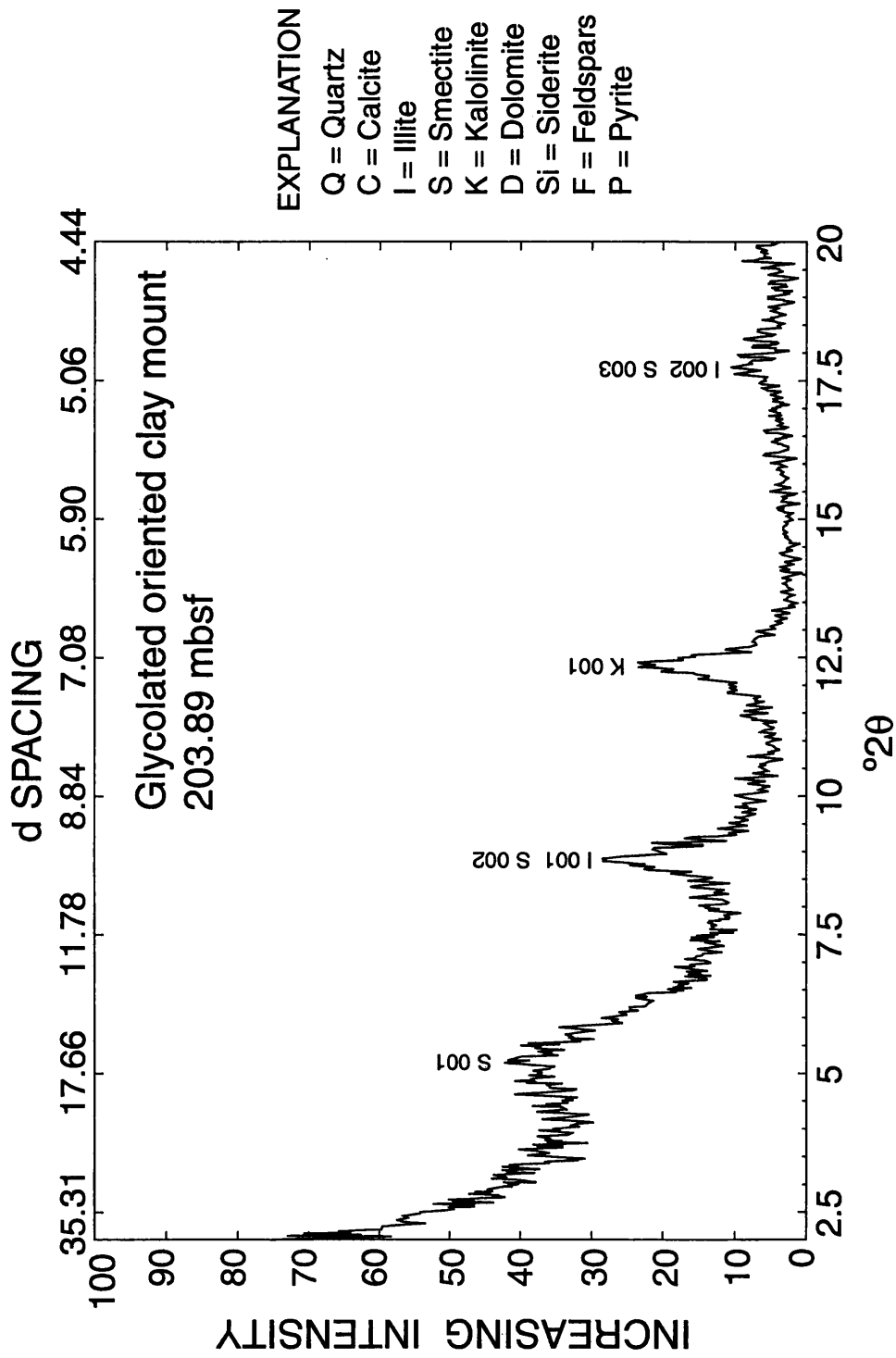
Figure 5.16c X-ray diffractogram of a glycol treated oriented clay mount of the core sample from a depth of 203.89 mbsf in Hole 997A.
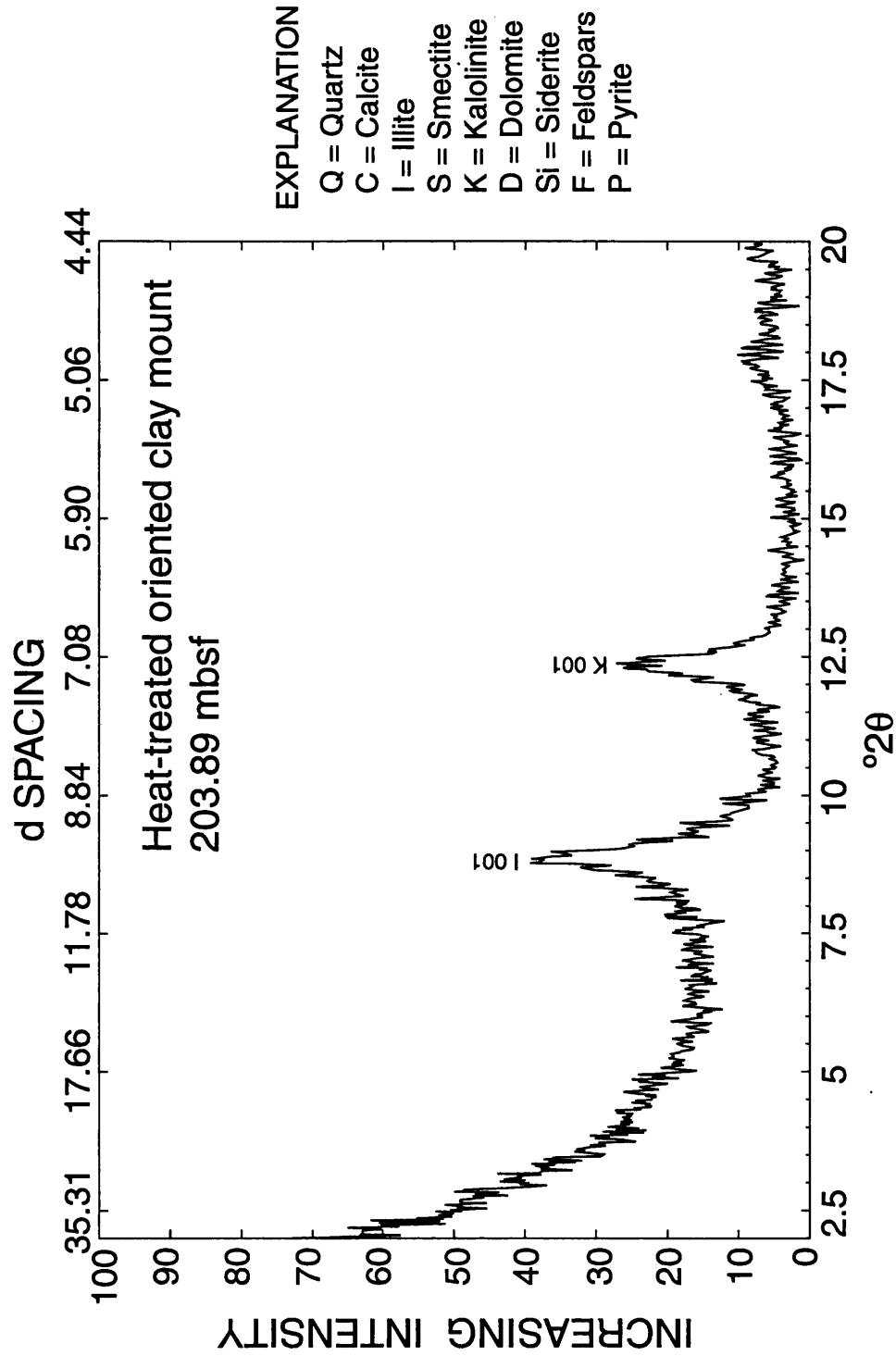
Figure 5.16d X-ray diffractogram of a heat-treated oriented clay mount of the core sample from a depth of 203.89 mbsf in Hole 997A.

chemicals. The X-ray diffractograms of the whole-rock samples were examined to identify the major minerals in the core samples; which included quartz, calcite, and clays. Occasionally, the samples contained detectable pyrite, dolomite, siderite, and feldspars (both plagioclase and alkali feldspars). An example whole-rock X-ray diffractogram (sample depth 203.89 mbsf) has been included in Figure 5.16a.

Additional X-ray diffraction analysis focused on semiquantitative identification of the type and amount of clays in the recovered core samples. Subsamples of each core sample were used to prepare oriented mounts of the clay-sized fraction. Using methods described in Moore and Reynolds (1989), mixtures of distilled water and crushed whole-rock core samples were centrifuged to separate the less than 2 μm fraction. Oriented mounts of the clay separates were prepared by a filter transfer method. X-ray diffractograms of the air-dried, glycolated (five days at 40°C), heat-treated (550°C for two hours) oriented clay mounts were examined to determine the proportion of illite and smectite in the clays (Table 5.7). The X-ray diffractograms of the untreated (air-dried) and treated (glycolated and heat-treated) oriented clay mounts for the core sample from 203.89 mbsf in Hole 997A have been included in Figure 5.16b-d for comparison purposes. Interpretation of clay mineralogy was based upon evaluating the spacing and relative intensity of the peaks on the X-ray diffractograms, which are controlled by the structure and composition of each mineral within the sample. Three clay minerals were identified within the core samples from the Blake Ridge: illite, smectite, and kaolinite. The method used to estimate the relative amount of illite and smectite (Table 5.7) in the mixed-layer clays was based on the work of Hower (1981). In this method, peak

positions and low-angle diffraction characteristics of the glycolated samples are compared to standard diffraction profiles published by Hower (1981). Characterization of chlorite and kaolinite is difficult because of peak overlaps and similarities in peak intensities in X-ray diffractograms of untreated samples. Standard heat treatment methods were used to identify the occurrence of chlorite and/or kaolinite in the core samples from Hole 997A. Heat treating chlorite changes the diffraction pattern, the intensity of the *001* reflection increases and shifts to about 6.3 °2θ; however, heat treating did not reveal any chlorite peaks within the X-ray diffraction patterns of the Site 997 core samples. In some cases, however, incomplete heating failed to fully collapse the kaolinite *001* reflection. The completed X-ray diffraction studies indicated that mixed-layer illite-smectite and kaolinite are the most abundant clay minerals in the sediments on the Blake Ridge.

In combination, the Leg 164 shipboard sedimentologic data and shore-based X-ray diffraction analysis of core samples from Hole 997A reveal that clay minerals (mixed-layer illite-smectite and kaolinite), calcite, and quartz are the major mineral components within the cored sedimentary section on the Blake Ridge. Pyrite, dolomite, siderite, and feldspars constitute minor components within the Blake Ridge sedimentary section.

To further evaluate the carbon and oxygen content of the sediments on the Blake Ridge, the results of the shipboard and shore-based sedimentologic studies (discussed above) were used along with GLT neutron capture data to construct detailed mineralogic models of the cored and logged sedimentary section in Holes 995B and 997B.

Schlumberger's ELAN-Plus (ELemental ANalysis) petrophysical program is a general-purpose inverse problem solving computer code which can be used to analyze GLT data (Quirein et al., 1986; Wendlandt and Bhuyan, 1990). With appropriate well-log data, including GLT measurements, ELAN-Plus can explicitly define 20 or more mineral components. The ELAN-Plus analyses of GLT elemental yields from Holes 995B and 997B are discussed in the following section.

ELAN-Plus uses available GLT elemental yields and inverse log-analysis procedures to simultaneously quantify various minerals in the formation (Quirein et al., 1986). In general, the ELAN-Plus computer program solves inverse problems, in which log measurements (GLT elemental yields) and expected response equations (mineral compositions) are used to compute volumetric formation components (volume percent of various mineral phases). ELAN-Plus solves an over-determined system of simultaneous linear response equations in which the number of equations exceeds or is equal to the number of unknowns (minerals).

As discussed earlier in this section, nine GLT elemental yields (calcium, iron, silicon, aluminum, potassium, uranium, thorium, gadolinium, and titanium) were considered while modeling the input response equations. Eventually, five GLT elemental yields (calcium, iron, silicon, aluminum, and potassium) were selected to construct the mineralogical models for the sediments at Sites 995 and 997. The elemental yields of uranium, thorium, gadolinium, and titanium were not used in this quantitative interpretation because it is not clear how these minor elemental constituents are associated with the different mineral phases in the sedimentary section being modeled.

Including trace elemental concentrations in the mineral response equations can have a significant affect on quantitative mineral calculations.

The ELAN-Plus program also requires the identification of the expected minerals (response equations) within the formation. When considering GLT data, the response equations consist of the chemical formula (composition) of the expected mineral phases. As previously discussed in this section of the thesis, Leg 164 shipboard sedimentologic data and shore-based X-ray diffraction analysis of core samples from Hole 997A have revealed the presence of eleven minerals within the sediments on the Blake Ridge: clay (illite, smectite, kaolinite), calcite, quartz, feldspars (albite, anorthite, and orthoclase), dolomite, siderite, and pyrite. Since the ELAN-Plus program can only solve over-determined systems, only six mineral phases can be quantified within a single ELAN-Plus model when only five GLT elemental yields are available. Therefore, a series of different (six mineral phases) ELAN-Plus models were constructed to quantitatively analyze all eleven mineral phases within the sediments on the Blake Ridge. Table 5.8 contains a list of the minerals and response equations (chemical composition of the minerals) that have been considered in the ELAN-Plus mineral modeling phase of this study. In addition, other log responses (including total gamma ray radiation, bulk-density, and neutron capture cross section) have been considered in the ELAN-Plus mineral modeling effort; however, the additional log measurements were of little value.

It was determined that the mineral assemblage that best achieved reasonable results (compared to core analyses results discussed later in this section of the thesis) consisted of smectite, illite, kaolinite, calcite, quartz, and pyrite. Given this mineral

Table 5.8 List of minerals and response equations (chemical compositions) used in the ELAN-Plus mineral interpretation models.

Mineral	Silicon (wt%)	Calcium (wt%)	Potassium (wt%)	Aluminum (wt%)	Iron (wt%)
Quartz	46.75	0	0	0	0
Illite-1	24	0.35	4	12	8
Illite-2	25.4	0.36	4.0	11.4	7.4
Illite-3	22.81	4.79	5.7	13.73	3.34
Smectite-1	22.76	0.658	0.658	11.84	1.316
Smectite-2	27.76	0.658	0.658	11.84	1.316
Smectite-3	21.1	0.2	0.5	8.5	0.5
Smectite-Na	30.61	0.658	0.658	12.28	1.316
Smectite-K	30.17	0.658	3.47	12.10	1.316
Smectite-Fe	26.73	0	0	12.84	7.30
Smectite-Fe	27.96	0	0	12.62	3.82
Kaolinite-1	22	0	0	19	0.8
Kaolinite-2	21.76	0	0	20.90	0
Feldspars					
Na-Feldspar	32.13	0	0	10.29	0
Ca-Feldspar	12.60	15.78	0	21.24	0
K-Feldspar-1	30.27	0	14.05	9.693	0
K-Feldspar-2	30.3	0	14.1	10.0	0
90Ab-10An	30.87	1.52	0	11.25	0
80Ab-10An-10Or	29.54	1.51	1.47	12.50	0
"Feldspar"	30	1	10	10	0
Calcite-1	0	40.06	0	0	0
Calcite-2	0	40.04	0	0	0.2
Dolomite	0	21.27	0	0	1.03
Siderite	0	0	0	0	48.20
Pyrite	0	0	0	0	46.55

assemblage (Table 5.9), compositions of quartz and pyrite are assumed to be independent

of solid solution. The compositions of the clay minerals were assumed to be nearly ideal

and were modified from the chemical analyses published by Herron and Herron (1988).

The assumed chemical formula for the smectite would be consistent with a

montmorillonite clay type. The Blake Ridge sedimentary section is characterized by a

complex carbonate mineral assemblage; principally calcite, siderite, with minor dolomite.

The presence of a single, hypothetical carbonate phase was assumed: an iron-bearing

calcite containing 40.04 weight percent calcium and 0.20 weight percent iron. As shown

in Table 5.8, various feldspars, including pure end-members and mixed end-members,

were considered in the ELAN-Plus modeling effort; however, the relative amount of

feldspar within the Blake Ridge sedimentary section never exceeded several (2-3 vol. %)

volume percent.

The ELAN-Plus-derived abundance of smectite (montmorillonite), illite,

kaolinite, calcite, quartz, and pyrite in the logged sedimentary sections of Holes 995B and

997B are shown in Figure 5.17a-b. In general, the mineralogy of the GLT-logged

sedimentary section in Hole 995B is relatively uniform with depth (Figure 5.17a). In

Hole 995B, clays (montmorillonite, illite, kaolinite) constitute about 60 to 80 percent of

the sedimentary section, with the amount of montmorillonite and illite being relatively

similar throughout the hole; however, kaolinite appears to be less abundant. Pyrite

occurs in Hole 995B as a widely disseminated minor component. The combined

abundance of calcite and quartz ranges from about 10 to 40 percent according to the

ELAN-Plus modeling estimates. In comparison, Hole 997B (Figure 5.17b) is

Table 5.9 List of minerals and response equations (chemical compositions) used to construct the ELAN-Plus mineral models for Holes 995B and 997B.

Mineral	Silicon (wt%)	Calcium (wt%)	Potassium (wt%)	Aluminum (wt%)	Iron (wt%)
Quartz	46.75	0	0	0	0
Illite	24	0.35	4	12	8
Smectite	22.76	0.658	0.658	11.84	1.316
Kaolinite	22	0	0	19	0.8
Calcite	0	40.04	0	0	0.2
Pyrite	0	0	0	0	46.55

294
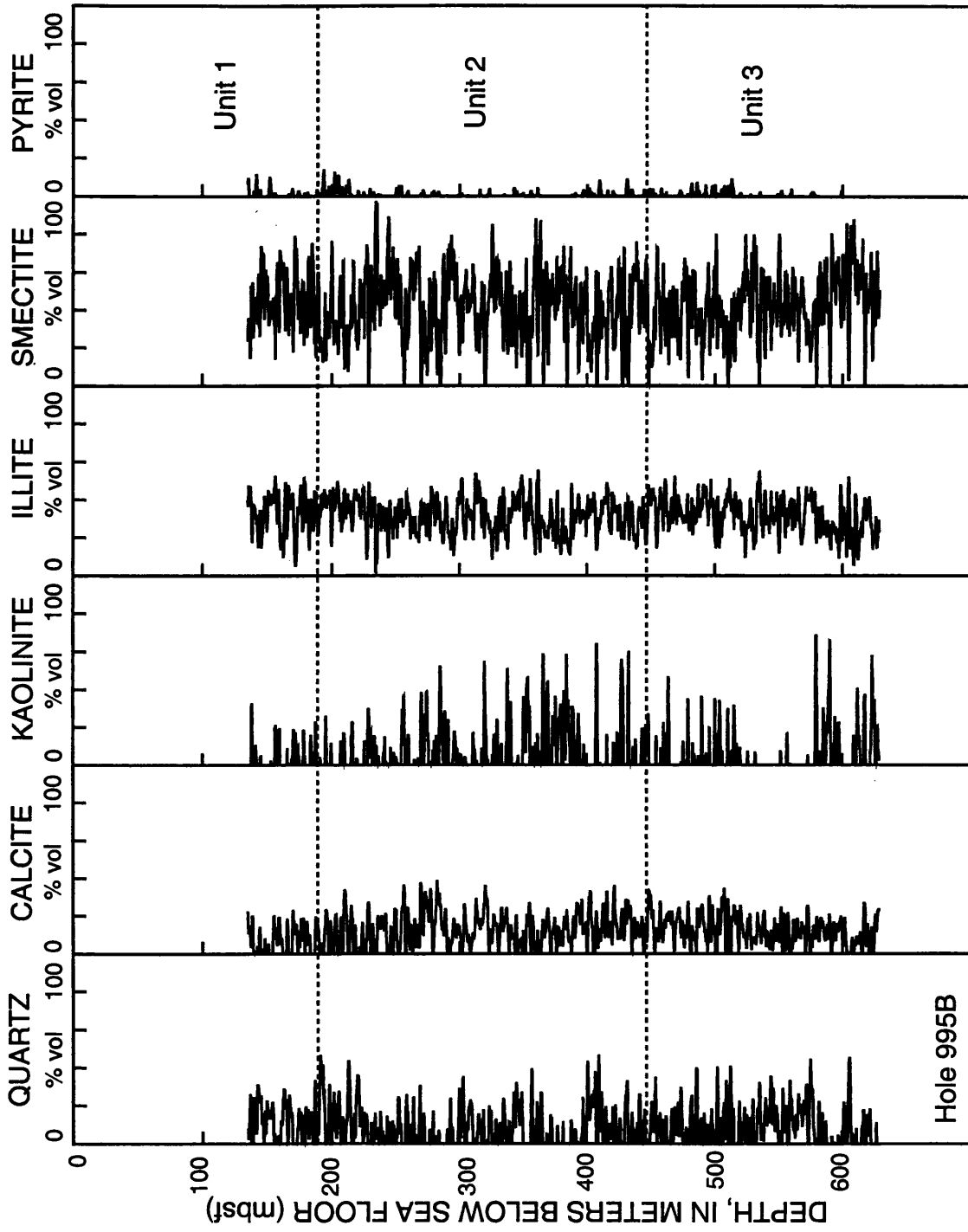
Figure 5.17a ELAN-Plus-derived mineral abundance in the GLT logged sedimentary section of Hole 995B.
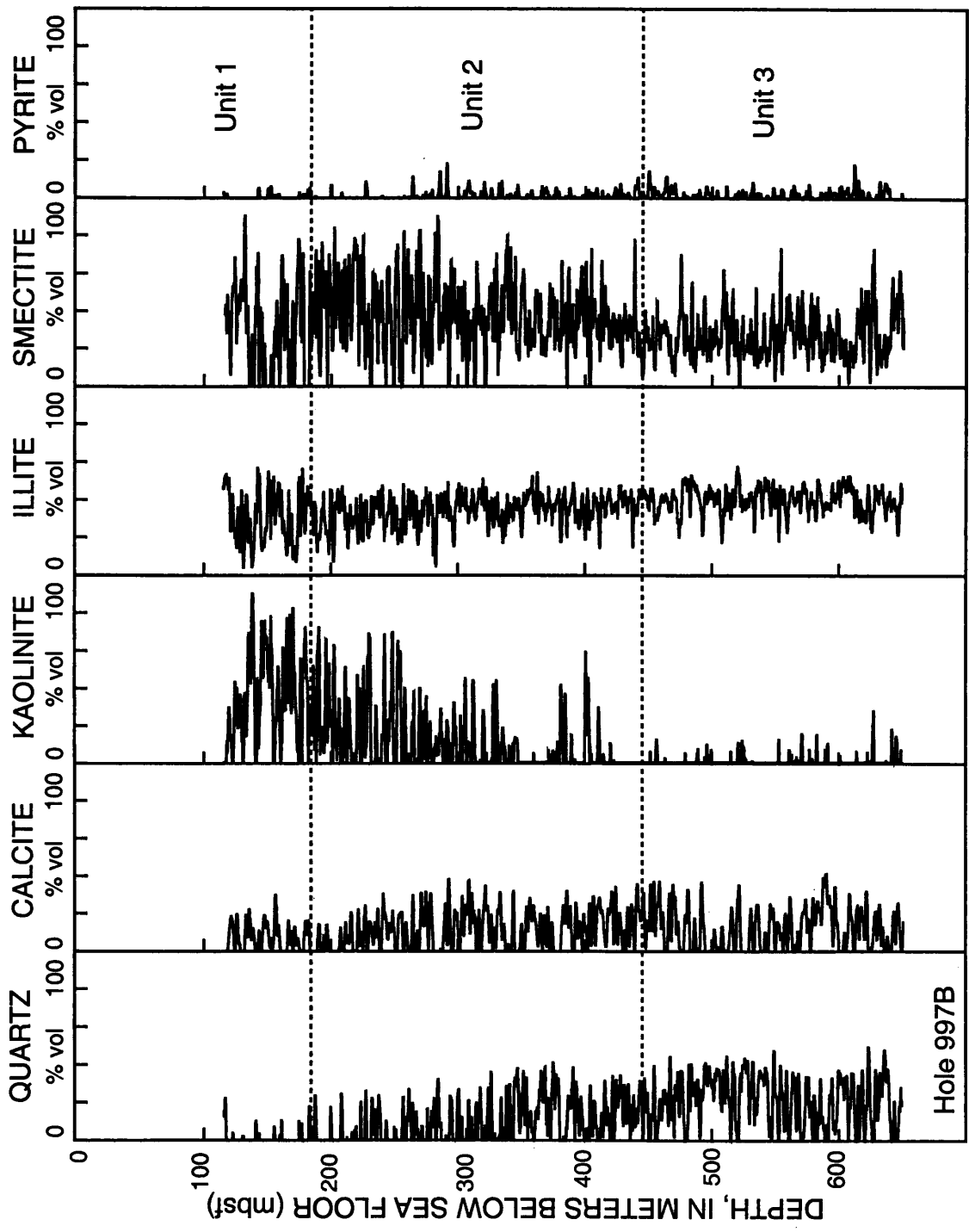
Figure 5.17b ELAN-Plus-derived mineral abundance in the GLT logged sedimentary section of Hole 997B.

characterized by a more variable sedimentologic section. ELAN-Plus analyses indicate

that clays comprise about 60 to 100 percent of the bulk sediments in Hole 997B. The

most notable mineralogic feature of Hole 997B is the obvious uphole increase in kaolinite

starting near 250 mbsf. In addition, the ELAN-Plus analyses from Hole 997B indicate a

downhole trend of increasing quartz which is not present in Hole 995B.

To evaluate the accuracy of the ELAN-Plus-derived mineralogic models, the

results of the ELAN-Plus modeling of the GLT data from Holes 995B and 997B have

been compared to mineralogic models from both shipboard and shore-based X-ray

diffraction analysis of core samples (Figure 5.18a-b and Figure 5.19). In Figure 5.18a-b

the ELAN-Plus-determined quartz and calcite abundance for Holes 995B and 997B have

been compared to shipboard X-ray diffraction analysis of core samples from Holes 995A

and 997A (Shipboard Scientific Party, 1996). In comparison, the relative abundance of

quartz in the sedimentary section at Sites 995 and 997 as determined by ELAN-Plus and

shipboard X-ray diffraction analysis are similar. The ELAN-Plus-interpreted downhole

trend of increasing quartz in Hole 997B was also observed in the shipboard X-ray

diffraction core analysis from Hole 997A. However, the ELAN-Plus-derived quartz

abundance in both Holes 995B and 997B is characterized by a high-frequency variation;

whether or not this variation is real is uncertain since the frequency of the GLT

measurements (every 0.1524 m) is much higher than the core sampling interval. The

relative abundance of calcite, as interpreted by ELAN-Plus and X-ray diffraction

analysis, at Sites 995 and 997 is also similar. The X-ray diffraction interpreted near-

surface (<100 mbsf) increase in calcite abundance is not observed in the ELAN-Plus
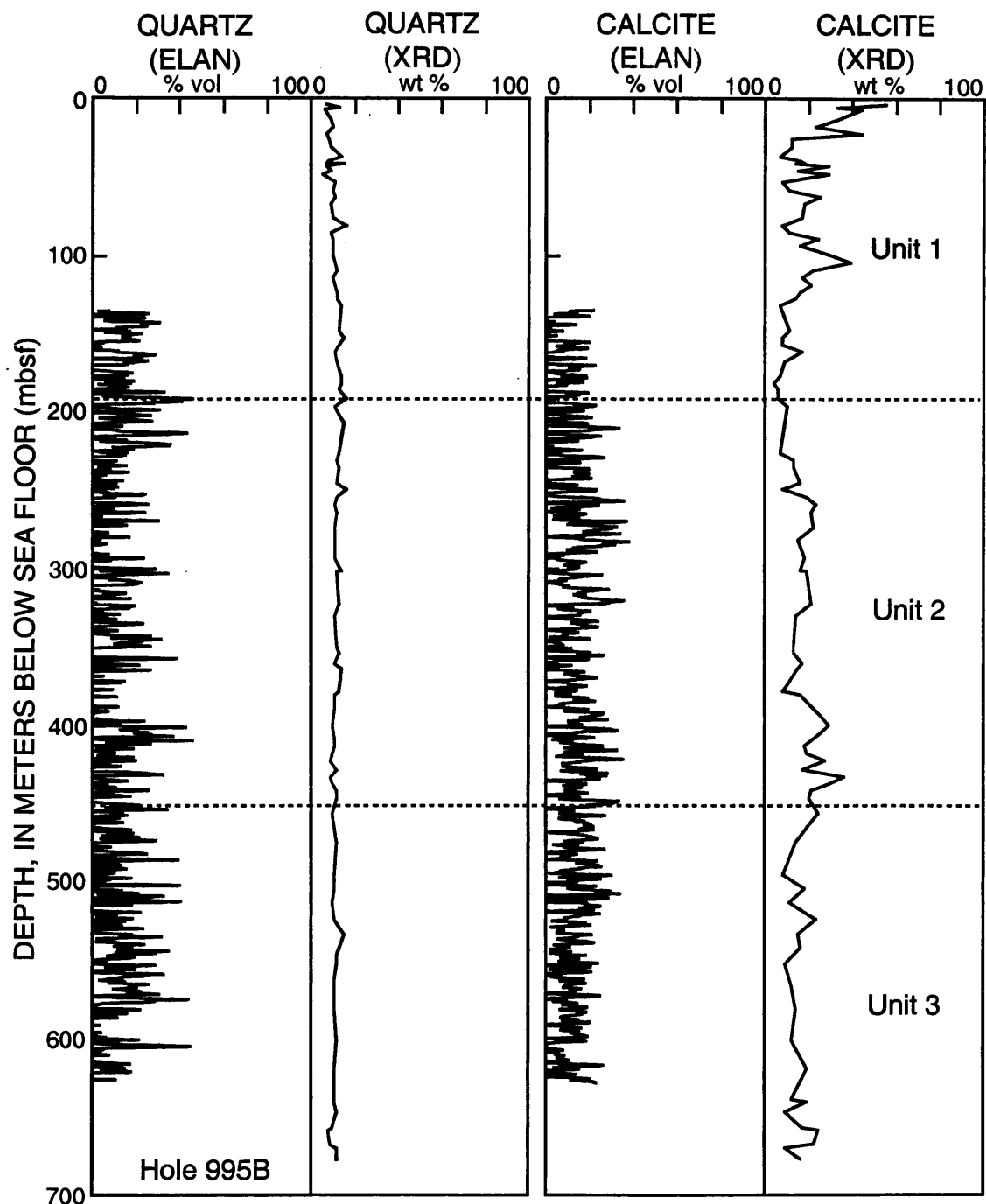
Figure 5.18a Comparison of ELAN-Plus and shipboard X-ray diffraction (Shipboard Scientific Party, 1996) analyses of quartz and calcite abundance in Hole 995B.
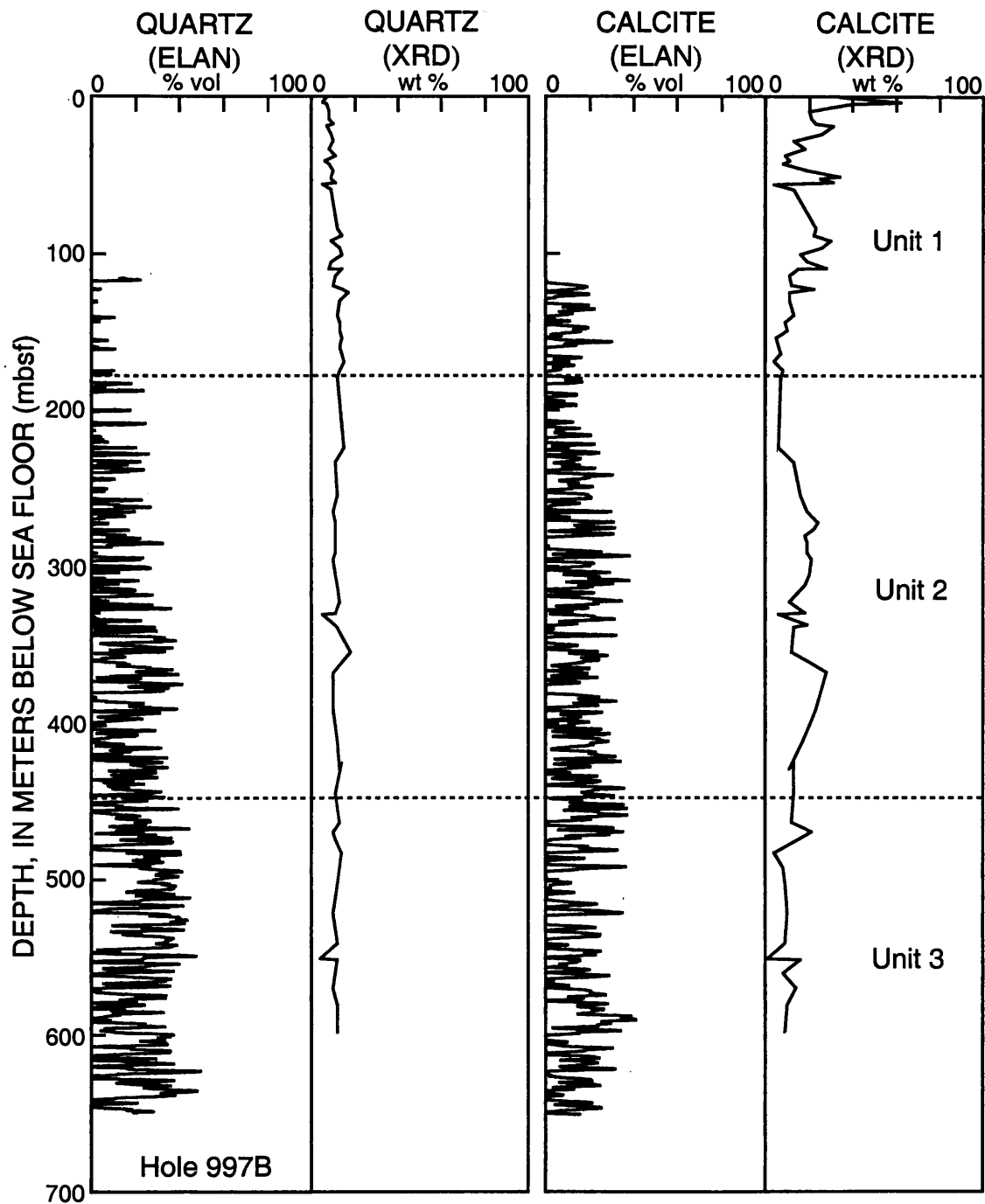
Figure 5.18b Comparison of ELAN-Plus and shipboard X-ray diffraction (Shipboard Scientific Party, 1996) analyses of quartz and calcite abundance in Hole 997B.
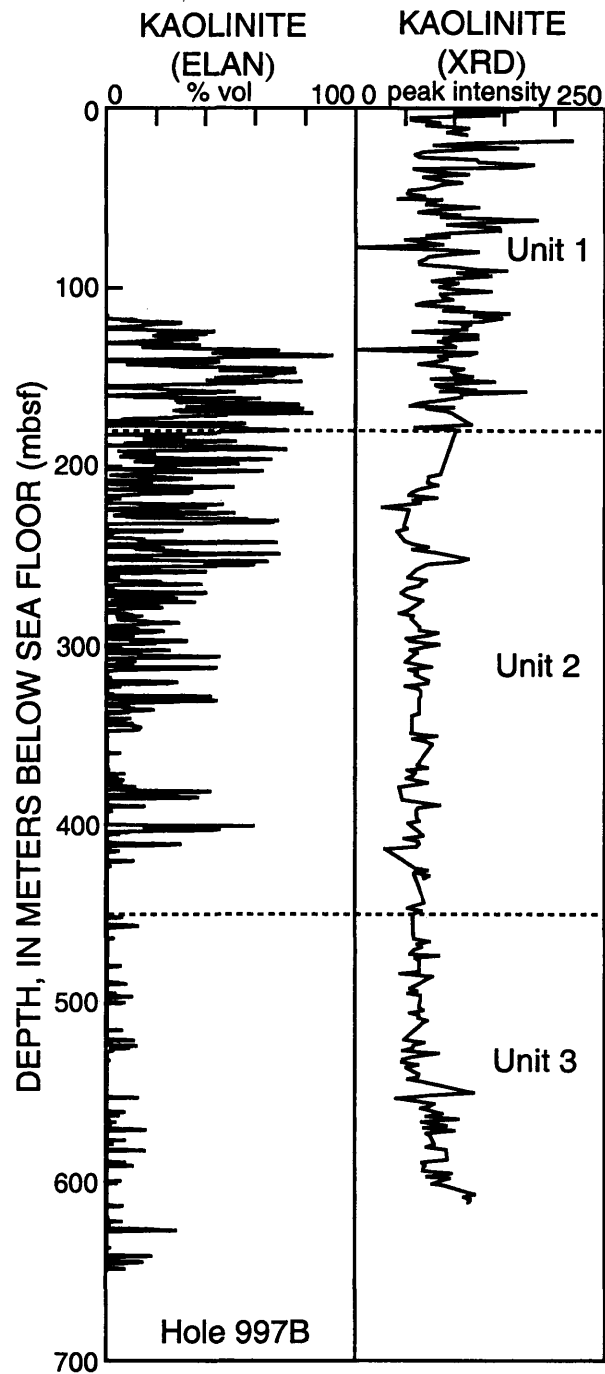
Figure 5.19 Comparison of ELAN-Plus and shorebased X-ray diffraction (Shipboard Scientific Party, 1996) analyses of kaolinite abundance in Hole 997B.

mineralogic models since the upper 100 m of both holes were not logged with the GLT.

However, both the ELAN-Plus and X-ray diffraction analysis do suggest a downhole

trend of increasing calcite abundance starting at a depth of about 200 mbsf. To further

evaluate the apparent uphole increase of kaolinite in Hole 997B, the ELAN-Plus

modeling results were compared with shore-based X-ray diffraction analyses of 300 core

samples from Hole 997A (Figure 5.19). The additional 300 X-ray diffraction analyses

from Hole 997A were provided by Dr. Ryo Matsumoto, University of Tokyo, Japan. As

shown in Figure 5.19 the relative abundance of kaolinite in Hole 997A as determined by

shore-based X-ray diffraction analysis of core samples is very similar to the kaolinite

concentrations predicted by the ELAN-Plus mineralogic modeling in Hole 997B. In

general, the mineralogic models for Sites 995 and 997, interpreted from available

shipboard and shore-based X-ray diffraction analysis of core samples, compare favorably

with the ELAN-Plus-derived mineralogic models for both drill-sites.

In this section of the thesis, the ELAN-Plus-derived mineralogic models for Holes

995B and 997B have been used to calculate the carbon and oxygen content of the

sediment matrix at the subsurface depths of the 35 inelastic neutron measurement stations

that were determined to have yielded valid carbon/oxygen elemental ratios in Holes

994C, 995B, and 997B (Table 5.10). The concentrations of carbon (α) and oxygen (γ) in

the sediment matrix were calculated by multiplying the carbon-oxygen elemental

concentration in each mineral assessed in Section 3.6 (Table 3.13) of this thesis by the

relative volumetric (volume percent) concentration of the ELAN-Plus-derived mineral

compositions in Holes 995B (Figure 5.17a) and 997B (Figure 5.17b). The ELAN-Plus

Table 5.10 Information needed to calculate gas-hydrate saturations with GLT-derived carbon/oxygen data.

Hole ID and station depth (mbsf)	Processed C/O ratio (COR)	Sediment porosity (Ø, %)	Sediment organic carbon content (C, vol %)	Sediment matrix carbon content (α, Avo)	Sediment matrix oxygen content (γ, Avo)	Borehole carbon correction factor (Cb, Avo)	Borehole oxygen correction factor (Ob, Avo)	Gas-hydrate saturation (Sh, %)
Hole 994C								
228	0.025	61	1.0	0.004	0.081	0.007	0.183	-4
233	0.052	61	0.9	0.005	0.081	0.007	0.068	+4
238	0.026	60	0.9	0.005	0.080	0.007	0.183	-6
243	0.034	60	0.9	0.005	0.080	0.007	0.160	+21
248*	0.026	57	0.9	0.005	0.080	0.007	0.210	0
258	0.034	58	1.0	0.004	0.081	0.007	0.135	0
263*	0.018	62	1.1	0.003	0.080	0.007	0.260	0
268	0.032	60	1.1	0.003	0.080	0.007	0.125	0
278	0.032	58	1.2	0.005	0.080	0.007	0.135	-16
Hole 995B								
221	0.029	60	1.0	0.003	0.082	0.007	0.182	+33
226	0.031	62	1.0	0.003	0.081	0.007	0.135	+8
235	0.041	61	1.0	0.004	0.079	0.007	0.110	+18
339	0.029	56	1.0	0.004	0.080	0.007	0.183	+12
349	0.038	57	1.0	0.003	0.081	0.007	0.110	+10
414	0.043	56	1.0	0.005	0.081	0.007	0.110	+11
439	0.044	56	1.0	0.005	0.080	0.007	0.110	+13
449	0.049	55	1.0	0.007	0.081	0.007	0.097	+7
454	0.050	56	1.0	0.003	0.082	0.007	0.068	+9
464*	0.028	55	1.0	0.007	0.081	0.007	0.210	0

Table 5.10-continued Information needed to calculate gas-hydrate saturations with GLT-derived carbon/oxygen data.

Hole ID and station depth (mbsf)	Processed C/O ratio (COR)	Sediment porosity (Ø, %)	Sediment organic carbon content (C, vol %)	Sediment matrix carbon content (α, Avo)	Sediment matrix oxygen content (γ, Avo)	Borehole carbon correction factor (Cb, Avo)	Borehole oxygen correction factor (Ob, Avo)	Gas-hydrate saturation (Sh, %)
489	0.039	55	1.0	0.005	0.081	0.007	0.110	-19
514	0.038	56	1.0	0.005	0.081	0.007	0.110	-16
524	0.044	54	1.0	0.004	0.080	0.007	0.097	0
594	0.046	53	1.0	0.005	0.080	0.007	0.097	0
604	0.048	52	1.0	0.003	0.080	0.007	0.068	-8
614	0.037	53	1.0	0.004	0.080	0.007	0.135	0
Hole 997B								
210	0.034	62	1.1	0.007	0.081	0.007	0.161	+18
361	0.051	52	1.4	0.007	0.081	0.007	0.097	+5
366	0.047	52	1.4	0.007	0.081	0.007	0.126	+22
440	0.039	56	1.6	0.008	0.081	0.007	0.161	+15
445	0.033	55	1.6	0.007	0.082	0.007	0.183	+8
455	0.028	57	1.6	0.007	0.082	0.007	0.183	-14
465	0.049	57	1.6	0.004	0.086	0.007	0.074	+1
475	0.043	57	1.7	0.003	0.082	0.007	0.097	+13
580	0.051	54	1.6	0.005	0.081	0.007	0.085	+3
585	0.048	53	1.6	0.005	0.081	0.007	0.097	+3

*Resistivity and acoustic transit-time log interpreted water-saturated (100%) zones. Avo=Avogadro Units

mineralogic model for Hole 995B was used to calculate the sediment matrix carbon-

oxygen elemental concentrations for the nine GLT inelastic neutron stations in Hole

994C.

The next variable needed before calculating gas-hydrate saturations with Equation

3.25 is the organic carbon content (C) of the sediments on the Blake Ridge. Fortunately,

standard Ocean Drilling Program core analysis includes the assessment of total organic

carbon content. On the Blake Ridge the total organic carbon content (TOC) of the

sediments cored at Sites 994, 995, and 997 ranged from about 0.5 to 2.0 weight percent

(Shipboard Scientific Party, 1996). Included in Table 5.10 are the shipboard-measured

total organic carbon content (C) of the sediments (converted to volume percent) at the

subsurface depths of the 35 "valid" GLT inelastic neutron stations at Sites 994, 995, and

997.

The last two variables needed to calculate gas-hydrate saturations with Equation

3.25 are the borehole correction factors for the presence of carbon and oxygen in the

borehole fluids and within the "boron sleeve" on the GLT. As discussed in Section 3.6 of

this thesis, each portion of the borehole (including the open-hole and tool sleeves) that

contribute to the carbon (C_b) and oxygen (O_b) borehole correction factors can be

individually quantified. Since Ocean Drilling Program boreholes are drilled with

seawater, the borehole carbon correction factor (C_b) relative to the carbon content of the

borehole fluids can be disregarded. However, since the GLT used on Leg 164 has a

boron sleeve, the volume of carbon within the sleeve needs to be determined. The

borehole carbon correction factor (C_b) for the boron sleeve was calculated by the method

described by Roscoe and Grau (1988) and reviewed in Section 3.6 of this thesis in which

the tool (GST) diameter (8.8265 cm) and sleeve thickness (0.6477 cm) are used to

calculate the volume of the boron sleeve (V_c) actually measured by the GST. Assuming

the carbon content of the boron sleeve is similar to the carbon content of oil (personal

communication, Dr. Jim Grau, Schlumberger-Doll Research, Ridgefield, Connecticut)

and by using the shipboard core-derived sediment porosities, it was possible to calculate

the required C_b correction factors for the boron sleeve of the GLT (Table 5.10). It is

worth noting that the carbon content of the boron sleeve is specially formulated to match

the carbon content of oil in a conventional hydrocarbon-bearing reservoirs.

The borehole oxygen correction factor (O_b) is assumed to be the product of the

drilling fluids (seawater) in the borehole. The volume of drilling fluids in the borehole is

dependent on the diameter of the logging tool and the size of the borehole. In

"conventional" boreholes, with diameters less than 30 cm, the borehole oxygen correction

factor (O_b) is calculated in the same manner as the boron sleeve carbon correction factor

(C_b) discussed above. In the borehole oxygen correction factor (O_b) calculations, the

GST tool diameter plus the boron sleeve thickness are used along with borehole caliper

logs to calculate the volume of water (V_o) within the borehole measured by the GLT.

Assuming a water oxygen content of 0.055509 Avogadro units (or 3.342758×10^{22} atoms

of oxygen per cubic centimeter of water; Table 3.13) and by using shipboard core-derived

porosities, it was possible to calculate the required oxygen correction factors (O_b) for the

drilling fluids in the portion of the boreholes that measured less than 30 cm in diameter

(Table 5.10). However, the calculation of borehole oxygen correction factors (O_b) for

boreholes exceeding 30 cm in diameter is more problematic due to the lack of GLT

calibration studies in severely enlarged boreholes. Since the diameter of the borehole

greatly exceeds 30 cm at the depth of most of the GLT inelastic neutron stations, a new

method of calculating the required borehole oxygen correction factors (O_b) was

developed. In this new method, GLT-measured carbon/oxygen ratios from three known

water-saturated (no hydrocarbons) zones in Holes 994C and 995B were used to calculate

borehole oxygen correction factors (O_b) for severely enlarged borehole conditions

(borehole diameters of 36, 38, and 46 cm). The three water-saturated GLT calibration

zones (Hole 994C: 248 and 263 mbsf; Hole 995B: 464 mbsf) were interpreted as 100%

water-saturated from available electrical resistivity and acoustic transit time borehole logs

discussed earlier in this section of the thesis. In Figure 5.20 the borehole oxygen

correction factors (O_b) calculated from the GLT-measured carbon/oxygen ratios in the

known water-saturated zones have been plotted along with the "standard" borehole

oxygen correction factors (O_b) calculated for smaller (<30 cm) "conventional" boreholes.

All of the borehole oxygen correction factors (O_b) in Figure 5.20 assume a sediment

porosity of 55%. In Figure 5.20, the power function regression trendline projected

through the "standard" and water zone calculated borehole oxygen correction factors (O_b)

has been used as a standard reference curve from which to calculate borehole oxygen

corrections within severely enlarged boreholes. Listed in Table 5.10 for each of the 35

"valid" GLT inelastic neutron stations in Holes 994C, 995B, and 997B are the borehole
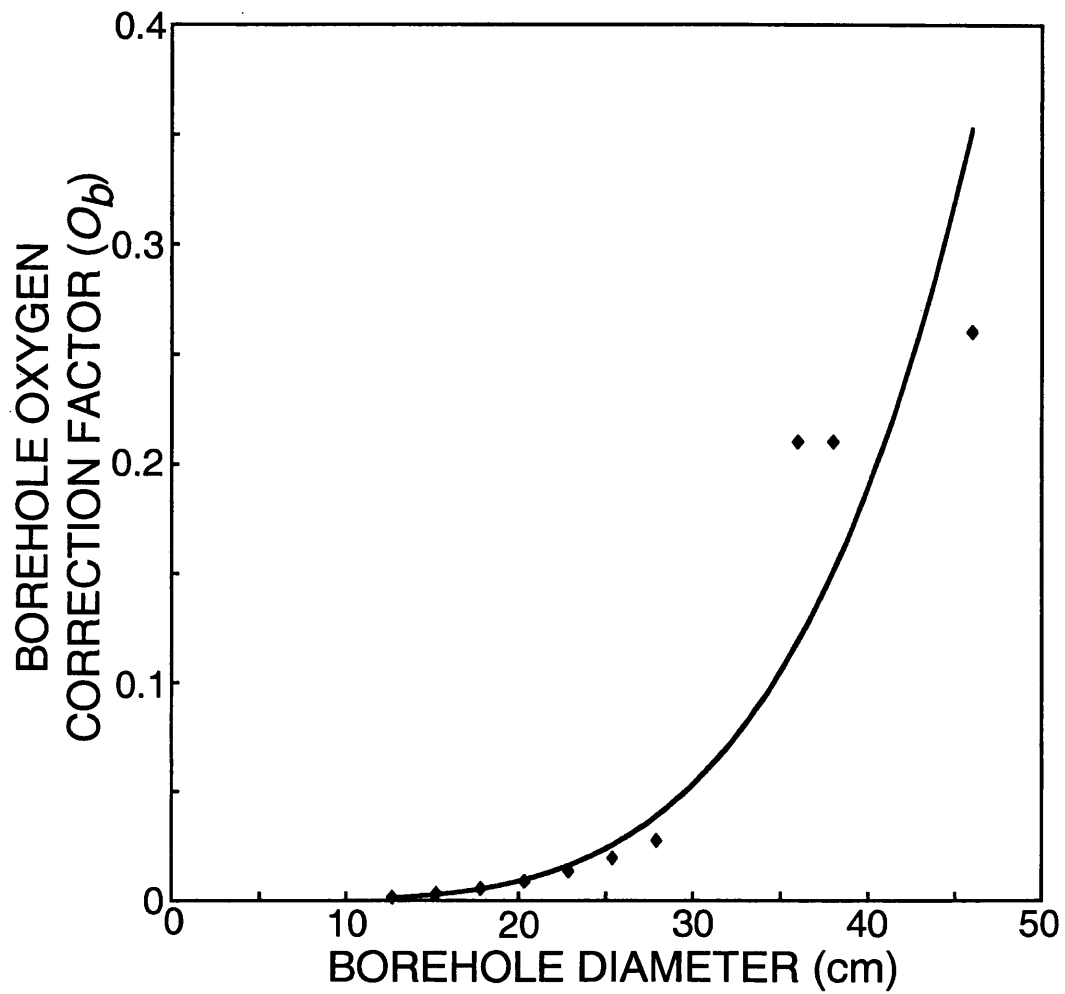
Figure 5.20 Borehole oxygen correction factors (O_b) for Holes 994C, 995B and 997B calculated from the published work of Roscoe and Grau (1988) and projected from known water-saturated zones in Holes 994C and 995B.

oxygen correction factors (O_b) as projected from the borehole oxygen correction

trendline in Figure 5.20.

The results of the carbon/oxygen-calculated gas-hydrate saturations from the 35

"valid" GLT inelastic neutron stations at Sites 994, 995, and 997 are listed in Table 5.10

and displayed in Figure 5.21a-c. The modified version of the standard three-component

carbon/oxygen hydrocarbon saturation equation (Equation 3.25) was used to calculate the

gas-hydrate saturations in Table 5.10 and Figure 5.21a-c. Table 5.10 also contains the

values for most of the required variables in Equation 3.25. Listed in Table 5.10 for each

of the GLT neutron stations (Holes 994C, 995B, and 997B) are the station depth,

reprocessed carbon/oxygen ratio (COR), core-derived sediment porosity ($\varnothing$), total

organic carbon content of the sediment (C), sediment matrix carbon (α) and oxygen

content (γ), borehole carbon (C_b) and oxygen (O_b) correction factors, and calculated gas-

hydrate saturations (S_h). The remaining variables in Equation 3.25 have been assigned

constant values: $A=0.75$, $\beta=0.007306$, $\eta=0.099908$, $\delta=0.055509$, and $\mu=0.044205$ (the

atomic concentrations for β, η, δ, and μ are listed in Avogadro units). The

carbon/oxygen-derived gas-hydrate saturations in Figure 5.21a-c are shown as discrete

values and have been plotted along with downhole-log traces of the resistivity-derived

"standard" Archie (average core porosity) calculated gas-hydrate saturations from Figure

5.12a-c. Each of the carbon/oxygen-derived gas-hydrate saturations in Figure 5.21a-c are

also depicted with an error bar of 10%, which is the likely minimum error associated with

the uncertainty in the calculated saturations. See Section 3.6 of this thesis for additional
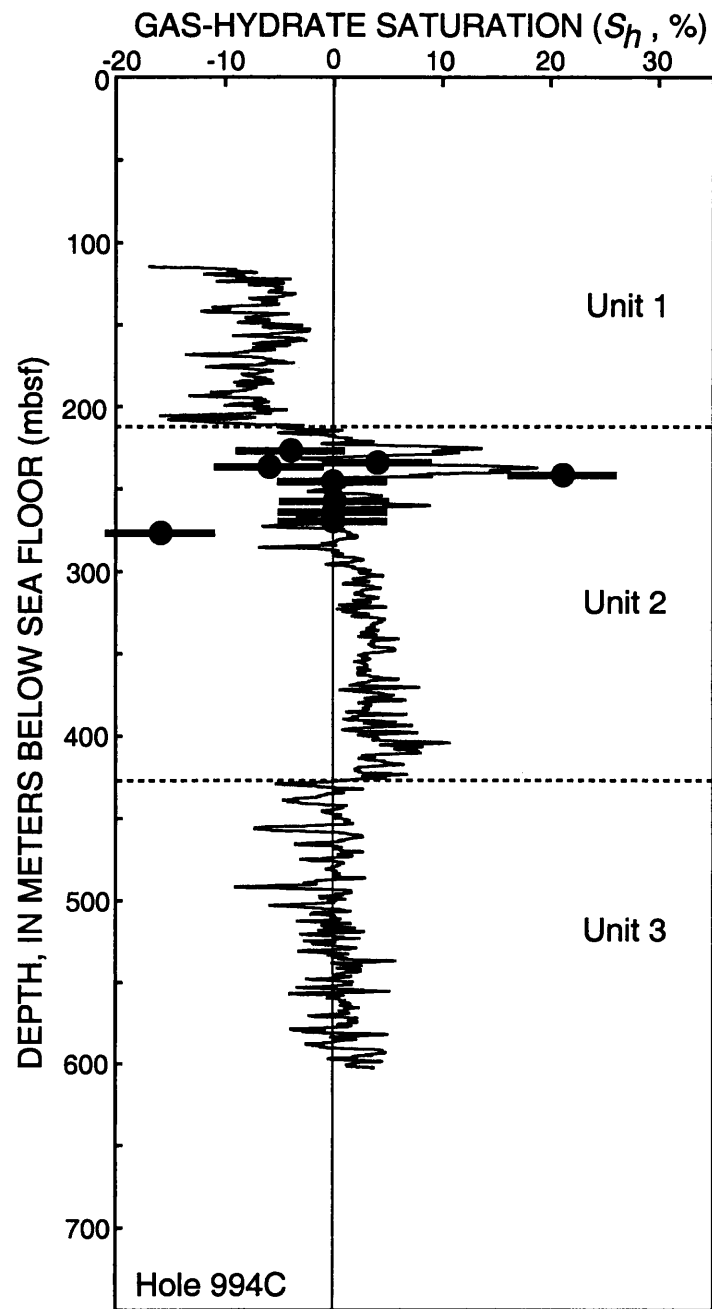
Figure 5.21a Carbon/oxygen-calculated (GST) gas-hydrate saturations (S_h) (shown as discrete point measurements with error bars) in Hole 994C. Also shown (as a continuous line plot) for comparison purposes are the gas-hydrate saturations calculated with the "standard" Archie electrical resistivity method in the same hole (Figure 5.12a).
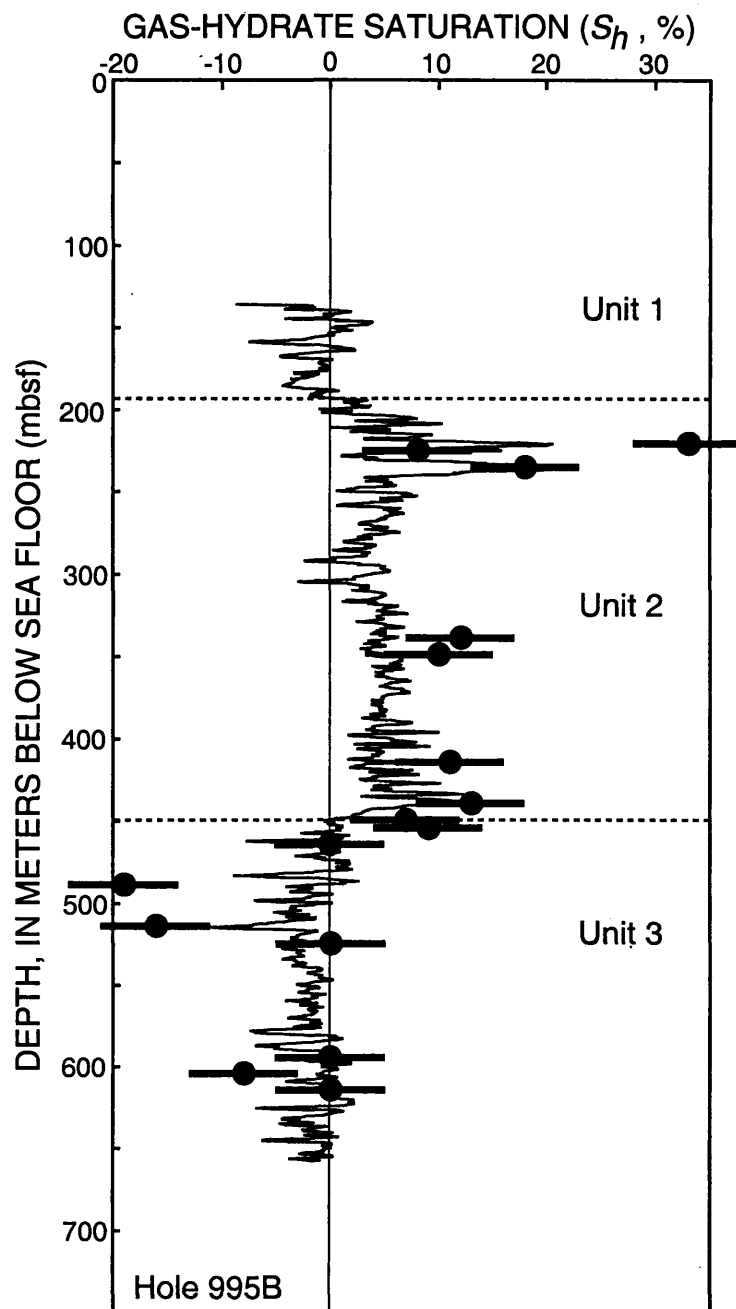
Figure 5.21b Carbon/oxygen-calculated (GST) gas-hydrate saturations (S_h) (shown as discrete point measurements with error bars) in Hole 995B. Also shown (as a continuous line plot) for comparison purposes are the gas-hydrate saturations calculated with the "standard" Archie electrical resistivity method in the same hole (Figure 5.12b).
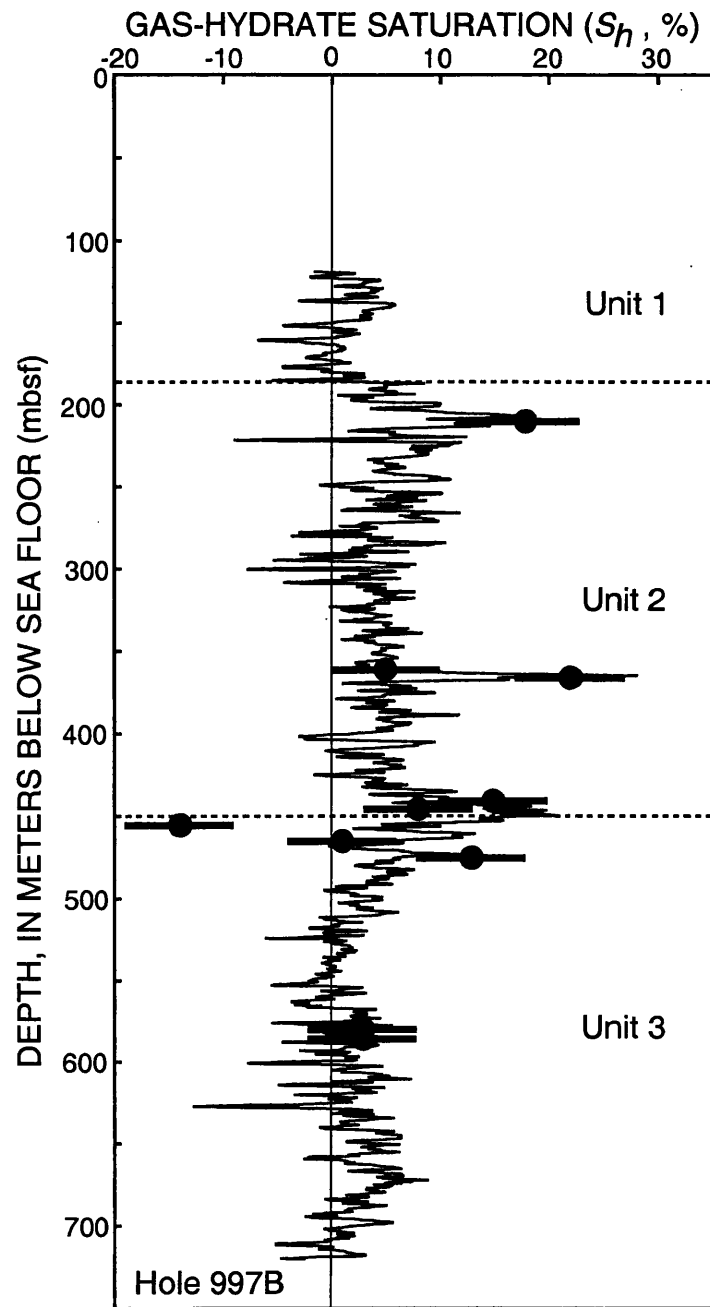
Figure 5.21c Carbon/oxygen-calculated (GST) gas-hydrate saturations (S_h) (shown as discrete point measurements with error bars) in Hole 997B. Also shown (as a continuous line plot) for comparison purposes are the gas-hydrate saturations calculated with the "standard" Archie electrical resistivity method in the same hole (Figure 5.12c).

information on the uncertainty associated with the carbon/oxygen gas-hydrate saturation

calculations.

The carbon/oxygen-derived gas-hydrate saturations in Hole 994C (Figure 5.21a),

Hole 995B (Figure 5.21b), and Hole 997B (Figure 5.21c) range from very low negative

values (less than -10%) to relatively high values near 30%. The carbon/oxygen-derived

gas-hydrate saturations that fall below 0% (or 100% water-saturated), which is

theoretically impossible, are likely caused by enlarged borehole conditions which have

degraded the inelastic neutron measurements that are not adequately corrected by the

procedures developed in this study. In comparison, the carbon/oxygen-derived gas-

hydrate saturations in Hole 995B (relative to Holes 994C and 997B) appear to more

closely match the resistivity-derived saturations; which further demonstrates the

dependence of the carbon/oxygen-derived gas-hydrate saturations on the size and

rugosity of the borehole, since Hole 995B was characterized by relatively good borehole

conditions. In general, the Leg 164 GLT measurements have been significantly degraded

by poor borehole conditions. However, within zones of relatively high quality GLT

measurements the carbon/oxygen-calculated gas-hydrate saturations from the Blake

Ridge compare favorably to the resistivity-derived gas-hydrate saturations (Figure 5.21a-

c).

Gas-Hydrate Saturation Calculations -- Summary In all three holes (Holes 994D,

995B, and 997B) on the Blake Ridge, the "standard" Archie relation (electrical resistivity

data) and the Lee weighted average acoustic equation (acoustic transit-time data) yielded,

for the most part, gas-hydrate saturations (S_h) ranging from 0% to a maximum near 20%

(Figures 5.12a-c and 5.15a-c); which are similar to the range of gas-hydrate saturations calculated from interstitial water chloride freshening trends (Figure 5.7). In comparison, the "standard" Archie relation and Lee calculations that employed the non-statistically manipulated core porosities resulted in the calculation of more highly variable gas-hydrate saturations than the saturation calculations that used average core porosities. The use of data from different sources (downhole logs and core data) and non-compatible downhole depths have likely contributed to the more variable nature of the gas-hydrate saturations calculated with the non-statistically manipulated core porosities. In comparison, however, the use of average porosity trends will mask localized porosity variations in complex geologic systems which could lead to erroneous gas-hydrate saturation calculations. Because of the uniform nature of the sedimentary section cored on Leg 164, the log analysis methods that use both the non-statistically manipulated and average core porosities yield similar results. Also because of the uniform nature of the sediments on the Blake Ridge, the "quick look" Archie method also yielded reasonable gas-hydrate saturations (Figure 5.12a-c). The Waxman-Smits shaly-sand analysis of Site 995 on the Blake Ridge appears to have yielded unreasonably high gas-hydrate saturations (Figure 5.14). In general, the modified Archie approach proposed by Pearson et al. (1983) and the Timur and modified Wood acoustic equations yielded erroneous gas-hydrate saturations which did not compare favorably with saturations calculated by other methods. The carbon/oxygen-calculated gas-hydrate saturations from all three sites on the Blake Ridge were degraded by enlarged and irregular borehole conditions; however,

in most cases the carbon/oxygen-calculated gas-hydrate saturations compare favorably

with saturations calculated by other methods.

5.2.7 Volume of Gas

Recent estimates of the volume of gas that may be contained in the gas hydrates

and free-gas beneath the gas hydrates on the Blake Ridge range from about 70 trillion

cubic meters of gas over an area of 26,000 km^2 (Dickens et al., 1997) to about 80 trillion

cubic meters of gas for an area of 100,000 km^2 (Holbrook et al., 1996). The difference

between these two estimates has been attributed to the observation that the amount of

free-gas directly measured within pressure-core samples (Dickens et al., 1997) from

beneath the gas hydrates is significantly larger than that estimated from borehole vertical

seismic profile data (Holbrook et al., 1996). Other published studies indicate that the gas

hydrates at the crest of the Blake Ridge alone (area of about 3,000 km) may contain more

than 18 trillion cubic meters of gas (Dillon and Paull, 1983). The broad range of these

estimates demonstrates the need for high-resolution measurements of the gas-hydrate and

associated free-gas volumes on the Blake Ridge. The log-interpreted gas-hydrate and

free-gas saturations from Sites 994, 995, and 997 in this thesis provide several of the

critical parameters needed to calculate the volume of gas on the Blake Ridge. The

volume of gas that may be contained in a gas-hydrate accumulation depends on five

"reservoir" parameters (modified from Collett, 1993b): (1) areal extent of the gas-hydrate

occurrence, (2) "reservoir" thickness, (3) sediment porosity, (4) degree of gas-hydrate

saturation, and (5) the hydrate gas yield volumetric parameter which defines how much

free-gas (at STP) is stored within a gas hydrate (also known as the hydrate number). In the following section, the five "reservoir" parameters (Table 5.11) needed to calculate the volume of gas associated with the gas hydrates on the Blake Ridge area assessed. In addition, the volume of free-gas trapped beneath the gas hydrates on the Blake Ridge is also assessed (Table 5.12).

The region in which seismic reflection profiling indicates the occurrence of gas hydrates on the Blake Ridge (shaded area on the map in Figure 5.2) extends over an area of approximately 26,000 km^2 (Dillon and Paull, 1983; Dickens et al., 1997). Despite the fact that the reflection seismic characteristics of the bottom simulating reflector (BSR) and inferred gas-hydrate occurrences are similar throughout the Blake Ridge it may be inappropriate to extrapolate gas hydrate and other geologic data from Sites 994, 995, and 997 to the entire 26,000 km^2 gas-hydrate accumulation. Most certainly there are local variations in the distribution of gas hydrates on the Blake Ridge which need to be further evaluated, however, this work is beyond the scope of this study. Therefore, the following "resource" assessment was conducted on a site-by-site basis; that is, for each site drilled on the Blake Ridge (Sites 994, 995, and 997) the volume of gas hydrate and associated free-gas within a one square kilometer area surrounding each drill-site was individually calculated (Tables 5.11 and 5.12).

For this "resource" assessment, the thickness of the gas-hydrate-bearing sedimentary section at all three drill-sites was defined to be the total thickness of Logging Unit 2, which ranges from about 217- to 265-meters-thick (Table 5.11). The core-derived sediment porosities (Figure 5.8) in Logging Unit 2 range from about 50 to 80 percent,

315

Table 5.11 Volume of natural gas within the downhole-log-inferred gas-hydrate occurrences at Sites 994, 995, and 997 on the Blake Ridge.

Site identification	Depth of Logging Unit 2 (mbsf)	Thickness of hydrate-bearing zone (m)	Sediment porosity (%)	Gas-hydrate saturation (%)	Volume of hydrate per square km (m^3)	Volume of gas within hydrate per square km (m^3)*
994	212.0-428.8	216.8	57.0	3.3	4,083,577	669,970,673
995	193.0-450.0	257.0	58.0	5.2	7,731,352	1,267,941,673
997	186.4-450.9	264.5	58.1	5.8	8,839,915	1,449,746,073

*Gas volume calculation assumes a hydrate number of 6.325 (90% gas filled clathrate), 1 m^3 of gas hydrate = 164 m^3 free-gas at STP.

Table 5.12 Volume of natural gas within the downhole-log-inferred free-gas occurrences at Sites 994, 995, and 997 on the Blake Ridge.

Site identification	Depth of identified free-gas zones (mbsf)	Thickness of free-gas-bearing zone (m)	Sediment porosity (%)	Free-gas saturation (%)	Volume of in-place gas per square km (m^3)*	Volume of gas within free-gas per square km at STP (m^3)
994	541-605	64	53.2	1.38	468,761	96,096,005
995	450-480	30	55.4	0.60	99,010	24,752,500
995	582-624	42	52.5	0.64	141,640	30,594,240
997	451-520	69	54.5	4.83	1,818,083	410,886,758
997	567-692	125	52.9	2.63	1,740,780	332,488,980

*Volume of in-place gas at in-situ pressure and temperature conditions. STP: pressure=101 kPa, temperature=15°C

and average approximately 58% (Table 5.11). Gas-hydrate saturations in Logging Unit 2 at all three drill-sites, calculated from the "standard" Archie relation (Figure 5.12a-c), range from an average value of about 3 to 6 percent (Table 5.11). The hydrate gas yield parameter or hydrate number is a factor that describes how much of the clathrate-cage structure is filled with gas. In this assessment a hydrate number of 6.325 (90% gas filled clathrate) was assumed, which corresponds to a gas yield of 164 m^3 of methane (at STP) for every cubic meters of gas hydrate (Collett, 1993b). In this study it was determined that the potential volume of gas within the log-inferred gas hydrates at each drill-site (Sites 994, 995, and 997) on the Blake Ridge ranges from 669,970,673 to 1,449,746,073 cubic meters of gas per square kilometer (Table 5.11).

For comparison purposes only, if it is assumed the geologic conditions and gas hydrate distribution at Site 997 (Table 5.11) is representative of the entire seismic delineated gas-hydrate accumulation (26,000 km^2) on the Blake Ridge it can be determined that there is about 37.7 trillion cubic meters of gas within the Blake Ridge gas-hydrate accumulation. One of the reasons that this estimate differs from that of Dickens et al. (1997) and Holbrook et al. (1996), is because both of these previous studies have included the volume of free-gas trapped beneath the gas hydrates in their total gas "resource" estimate. Therefore, the available log data from Sites 994, 995, and 997 were used in this study to calculate the volume of free-gas (Table 5.12) below the gas hydrates on the Blake Ridge.

The available acoustic- and resistivity-log data have been used to identify free-gas-bearing zones within Logging Unit 3 of Holes 994D, 995B, and 997B (Table 3.12).

At Site 994, one 64-m-thick free-gas zone has been identified, while at Sites 995 and 997, two laterally continuous free-gas-bearing zones have been delineated with combined total thicknesses of 72 and 194 meters, respectively (Table 5.12). The average porosity of the sediments within the free-gas-bearing zones at all three drill-sites on the Blake Ridge range from about 53 to 55 percent (Table 5.12). The free-gas-bearing zones at Sites 994 and 995 are characterized by free-gas saturations, calculated from the "standard" Archie relation (Figure 5.12a-c), of about 1% (Table 5.12). However, the free-gas saturations within the zone immediately below the base of the gas hydrates at Site 997 average about 5% (Table 5.12). In this study, it was determined that the potential volume of gas within the log-inferred free-gas-bearing zones at each drill-site (Sites 994, 995, and 997) on the Blake Ridge ranges from 743,375,738 cubic meters of gas (at STP) per square kilometer at Site 997 to only 55,346,740 cubic meters of gas (at STP) per square kilometer at Site 995 (Table 5.12). Following the calculations described in Dickens et al. (1997) and assuming that the volume of free-gas below the gas hydrates at Site 997 are representative of the free-gas volumes trapped below the gas hydrates throughout the Blake Ridge area (26,000 km^2) the total volume of gas occurring as free-gas on the Blake Ridge is about 19.3 trillion cubic meters (at STP). Thus, the combined volume of gas within the gas hydrate and underlying free-gas accumulations on the Blake Ridge would be about 57 trillion cubic meters of gas, which is near the volume (70 trillion cubic meters of gas) estimated by Dickens et al. (1997). It is unlikely, however, that the Site 997 downhole-log- or pressure-core-calculated gas-hydrate concentrations are representative for the entire Blake Ridge. It is known, for example, that the volume of

free-gas below the gas hydrates at Site 995 is much less than the volume of free-gas at

Site 997 (Table 5.12). More work is needed to assess the regional distribution and

variability of both the gas hydrate and associated free-gas accumulations on the Blake

Ridge before accurate resource estimates can be made.

5.3 Cascadia Continental Margin--Pacific Ocean

5.3.1 Introduction and Regional Geology

The structural development and depositional history of the Cascadia continental

margin (Figure 5.22) off the Pacific coast of Vancouver Island and the States of

Washington and Oregon has been mostly controlled by the motion of Pacific and North

American plates as reviewed by Atwater and Molnar (1973). Because of the active

tectonic history of the Cascadia continental margin, during which older basins were

destroyed and new ones created, rocks prospective for gas hydrates are limited mainly to

basins that formed during Cenozoic time. The Cascadia continental margin of the United

States and Canada, contains numerous small forearc basins composed of thick

sedimentary and volcanic rocks of Tertiary age. This region is stratigraphically complex

but only moderately folded and faulted; only several small accumulations of natural gas

have been reported within the region.

BSRs have been extensively mapped on the inner continental margin of northern

California (Field and Kvenvolden, 1985). These constitute a single, inferred, gas-hydrate

accumulation that covers an area of at least 3,000 km^2 on the Klamath Plateau and the

upper continental slope at water depths ranging from 800 to 1,200 m. Limited seismic
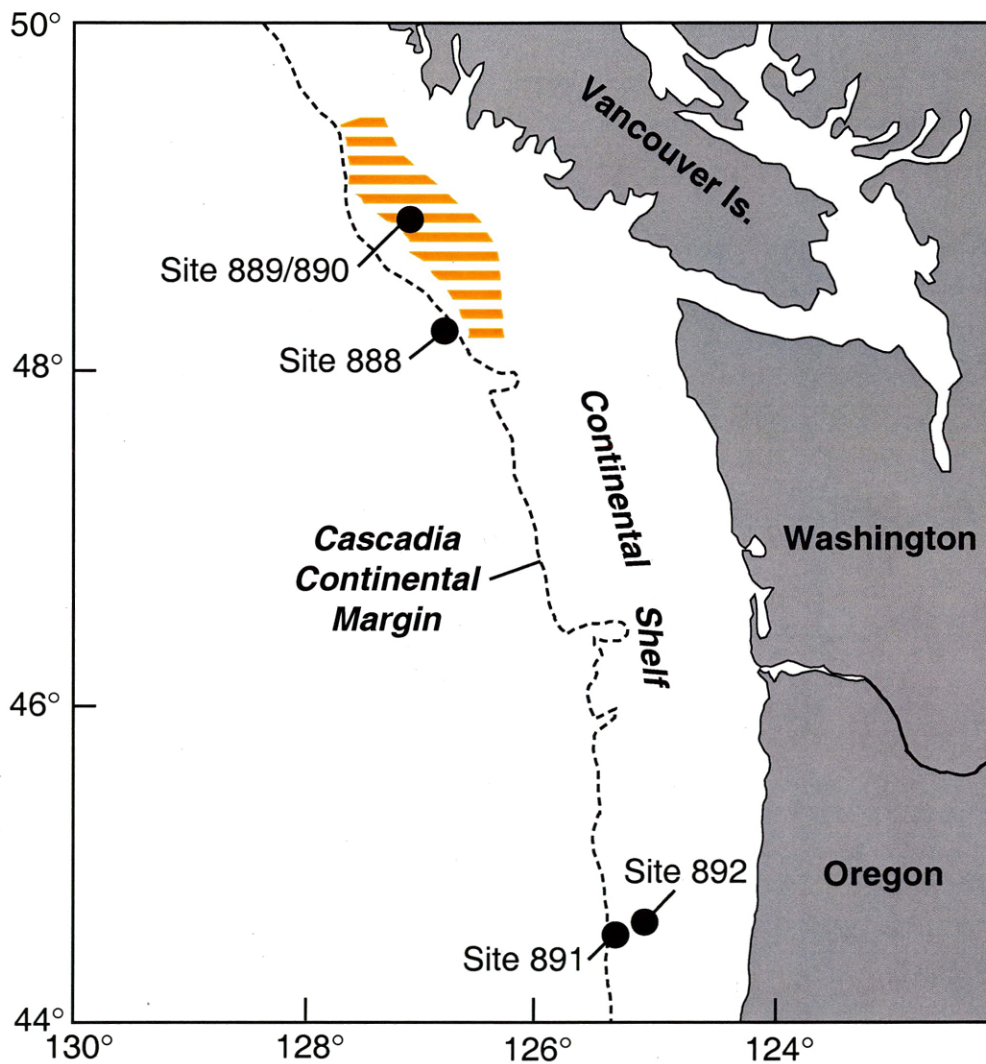
Figure 5.22 Physiographic map of the Cascadia continental margin of North America. Location of ODP Leg 146 drill-sites are indicated. Also shown is the area (horizontally shaded area) where gas-hydrate occurrence has been mapped on the basis of bottom simulating reflectors (modified from Hyndman et al., 1996).

data show that this regionally extensive inferred gas-hydrate occurrence extends

northward to offshore Canada (Hyndman et al., 1996) and seaward at least to the base of

the slope (3,000 m water depth). The occurrence of gas hydrates on the Pacific margin of

the United States was confirmed in 1989 when numerous gas-hydrate samples were

obtained during seabed (0-6 m) sediment coring operations (water depths ranging

between 510 and 642 m) in the Eel River Basin (Brooks et al., 1991). Recovered gas-

hydrate samples consisted of dispersed crystals, small nodules, and layered bands. The

location of these gas hydrates coincides nearly, but not exactly, with the area of BSR-

inferred gas hydrates described by Field and Kvenvolden (1985) along the northern

California coast. Gas hydrates have also been recovered along the Cascadia margin from

a relatively restricted zone within 17 m of the sea floor in three research coreholes drilled

during Leg 146 of the Ocean Drilling Program: Holes 892A, 892D, and 892E (Shipboard

Scientific Party, 1994). All of these coreholes are located on the Oregon continental

slope in about 675 m of water.

Leg 146 of the Ocean Drilling Program (Shipboard Scientific Party, 1994) was

designed to examine fluid movement in the Cascadia continental margin and to provide

well-constrained estimates of the volume of fluid associated with accretionary

sedimentary wedges. In addition, the presence of distinct BSRs on the Cascadia margin

also provided an opportunity to examine the potential interrelation between the

occurrence of natural gas hydrates and BSRs. Four locations were drilled off the west

coast of Vancouver Island and Oregon (Figure 5.22). As mentioned above, gas hydrate

crystals were recovered in the near-surface (2-17 mbsf) sediments at Site 892. Downhole

logs and a vertical seismic profile (VSP) at Site 892 established that locally the BSR is caused by free-gas below about 71 mbsf; however, the borehole surveys yielded relatively little useful gas hydrate data.

Site 889, located off the west coast of Vancouver Island, yielded a wealth of data pertaining to the in-situ nature of gas hydrates on the Cascadia margin. Massive accumulations of gas hydrate were not encountered at Site 889. Rather, indirect evidence from recovered cores and downhole geophysical surveys suggests that most of the gas hydrates at Site 889 occur as finely disseminated pore-filling substances. Temperature measurements of the recovered cores and the dilution of pore-water salts suggest that about 10 to 40 percent of the pore-space within the sediment is filled with gas hydrate at Site 889 (Shipboard Scientific Party, 1994). Despite the fact that gas hydrates were not physically observed in the cores from Site 889, indirect evidence of gas hydrates at this site appears to be irrefutable (Shipboard Scientific Party, 1994; Spence et al., 1995; Hyndman et al., 1996). In the following section of this thesis, therefore, the available downhole-log data from Site 889 is used to calculate sediment porosities and gas-hydrate saturations within the inferred gas-hydrate accumulation on the Cascadia continental margin. The available downhole-log data has also been used to estimate the volume of gas within the Cascadia gas-hydrate accumulation.

5.3.2 Downhole-Logging Program

The Schlumberger downhole tools deployed at Site 889 (Table 5.13) included the long-spaced sonic (LSS-SDT), natural gamma-ray tool (NGT), high-temperature

Table 5.13 Ocean Drilling Program Site 889 downhole-logging program.

Hole identification	Total hole penetration (mbsf)	Log run	Logging string	Interval logged (mbsf)
889A	345.8	1	DITE/LSS-SDT/ HLDT/CNT-G/NGT	65.0-250.0
		2	FMS/GPIT/NGT	73.0-240.0
889B	386.5	1	DITE/LSS-SDT/ CNT-G/NGT	60.0-234.0
		2	DITE/LSS-SDT/ CNT-G/NGT	213.0-259.0
		3	FMS/GPIT/NGT	110.0-240.0

lithodensity tool (HLDT), the compensated neutron porosity tool (CNT-G), the phasor

induction tool (DITE), and the formation microscanner (FMS). For Hole 889A, logs

were obtained from what was referred to in the Initial Reports volume for Leg 146

(Shipboard Scientific Party, 1994) as a "geophysical tool string" which appears to be the

same as a Schlumberger quad-combination (NGT, LSS-SDT, DITE, CNT-G, HLDT).

Hole 889A was logged with the "geophysical tool string" over the depth interval from 65

to 250 mbsf. Hole 889A was also logged with the formation microscanner within the

depth interval between 73 and 240 mbsf. Two runs of a modified "geophysical tool

string" (no HLDT density tool measurements) were conducted in Hole 889B: an initial

run from 60 to 234 mbsf and a deep run, made possible by using the side-entry sub

(SES), from 213 to 259 mbsf. Hole 889B was also logged with the formation

microscanner within the depth interval from 110 to 240 mbsf. Since most of the

published geophysical studies (Shipboard Scientific Party, 1994; Spence et al., 1995;

Hyndman et al., 1996) of Site 889 have dealt with data from only Hole 889B, the log

interpretive efforts at Site 889 in this study have also focused on the downhole-log data

from Hole 889B.

At Site 889, hole instabilities resulted in irregular borehole diameters, which

moderately to severely degraded the quality of the log measurements. The caliper from

the FMS log in Hole 889B (Figure 5.23) shows borehole diameters greater than the 37.9

cm maximum range of the caliper for a significant portion of the hole. Natural gamma-

ray, density, and neutron porosity tools are particularly susceptible to adverse effects

from large and irregular hole diameters. The bulk-density (HLDT) log (Figure 5.24) in
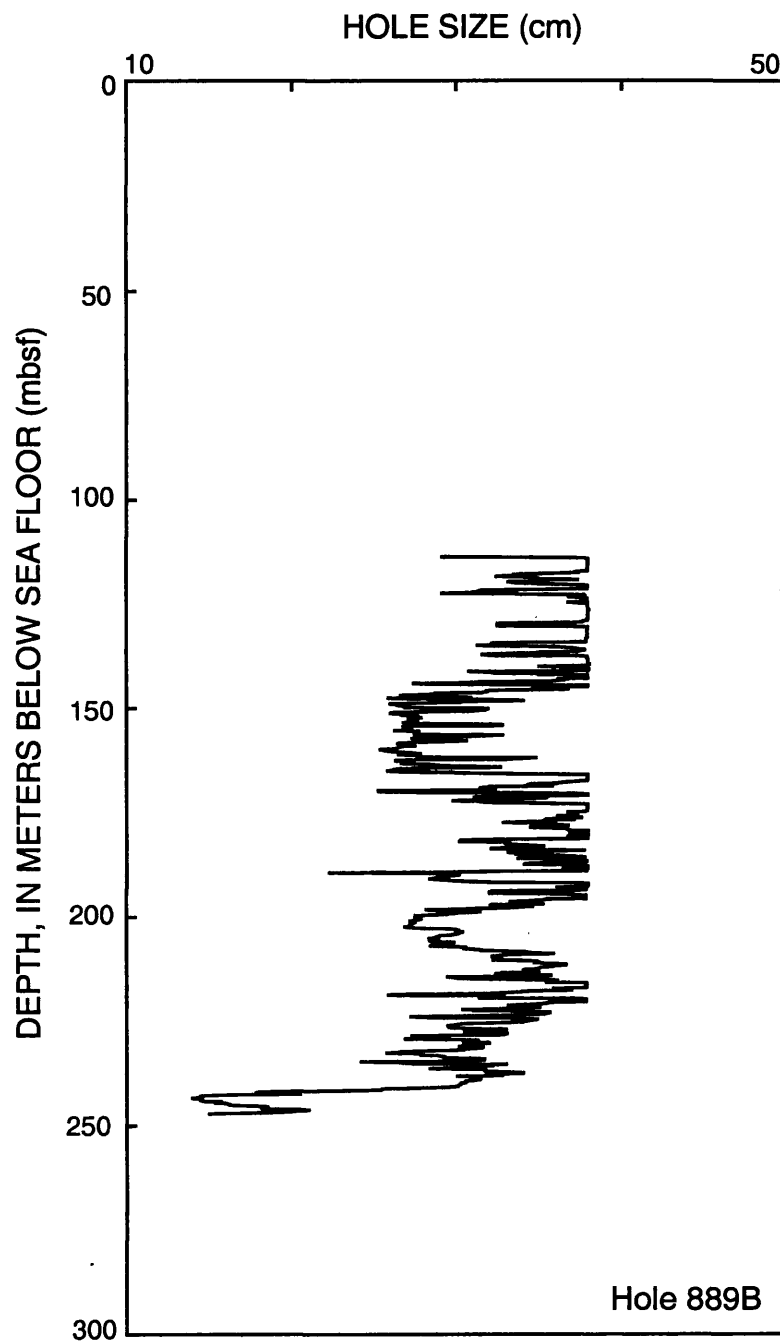
Figure 5.23 Caliper log recorded from the formation microscanner (FMS) tool in Hole 889B.
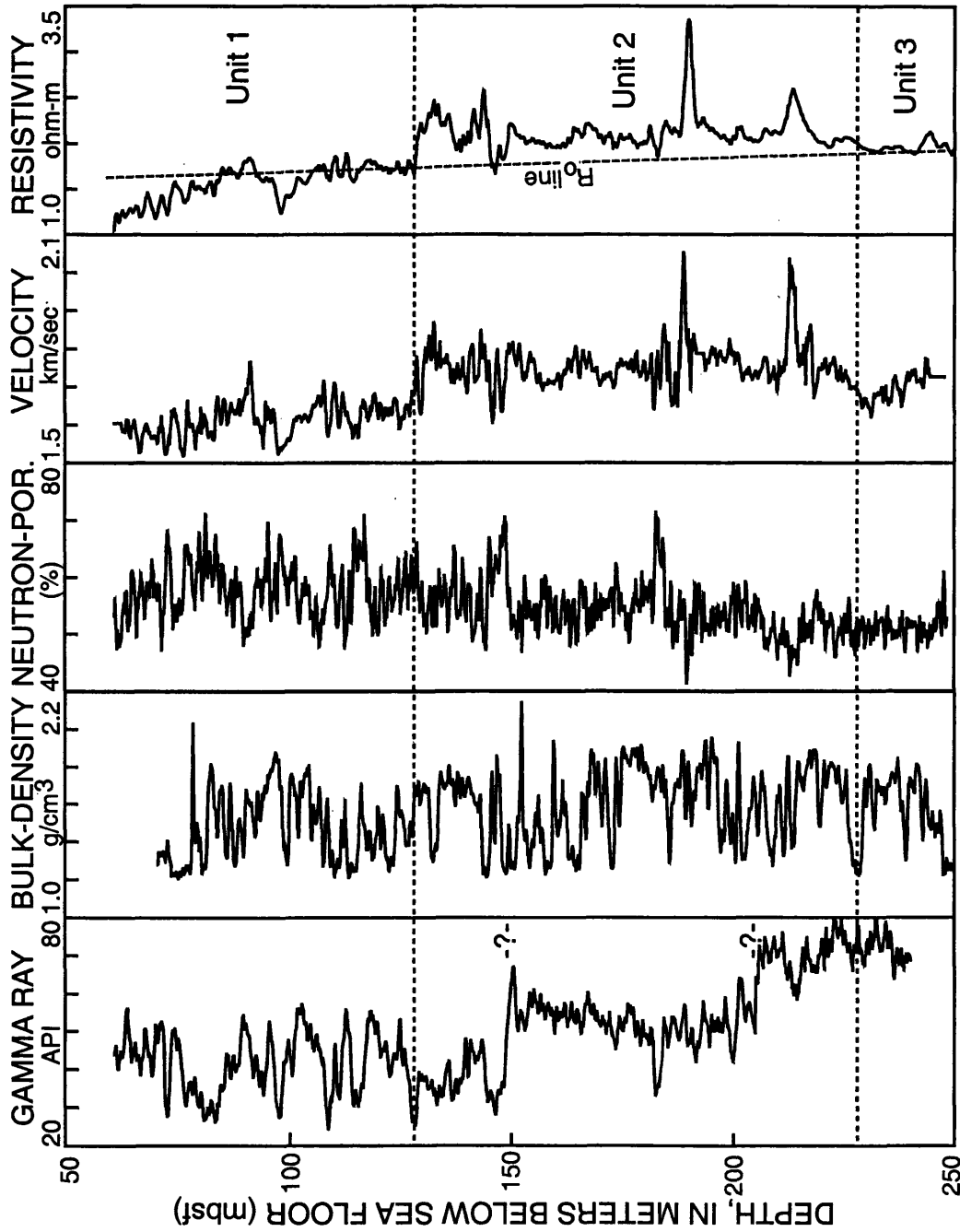
Figure 5.24 Downhole logs from Site 889. Data shown include the natural gamma ray log, bulk-density data, neutron porosity, acoustic velocity data, and deep-reading electrical resistivity data. Also shown are the depths of Logging Unit 1, 2, and 3 (Table 5.14) and the projected R_O baseline.

Hole 889A (not ran in Hole 889B) is characterized by many low-value spikes because of the inability of the tool's caliper to remain in contact with the borehole wall. The varying borehole diameter of Hole 889B has only moderately affected the quality of the neutron porosity (CNT-G) measurements (Figure 5.24). However, the gamma-ray log from Hole 889B is severely degraded with a pronounced shift to higher gamma-ray values at a depth of about 145 mbsf (Figure 5.24) which can be attributed in part to a significant change in the size of the borehole recorded on the caliper log (Figure 5.23). The acoustic velocity (LSS-SDT) and electrical resistivity (DITE) logs from Hole 889B (Figure 5.24) are only slightly degraded by poor borehole conditions. The FMS images from Hole 889B are degraded because of the large hole diameters, but some features can be interpreted.

The absolute depths, relative to sea floor, for all of the logs were fixed by identifying the gamma-ray signal associated with the sea floor and depth shifting the log data appropriately. The natural gamma-ray log pick for the sea floor in Holes 889A and 889B were 1,322.0 and 1,327.0 meters below the dual elevator stool (DES) on the drilling mask, which is located on the ship 10.8 m above sea level.

5.3.3 Logging Units

The description of the logged interval in Hole 889B is divided into three "Logging Units" on the basis of obvious changes in the acoustic velocity (LSS-SDT) and electrical resistivity measurements (DITE) (Table 5.14, Figure 5.24). Data from the analyses of recovered cores in Hole 889A have also been used to assess the sedimentology and

Table 5.14 Depth to the top and bottom of the downhole-log-identified Logging Units in Hole 889B (Figure 5.24).

Hole identification	Logging Unit	Depth to top of Logging Unit (mbsf)	Depth to bottom of Logging Unit (mbsf)
889B	1	Base of pipe (60.0)	127.6
	2	127.6	228.4
	3	228.4	End of log (255.7)

mineralogy of the sediments in the delineated Logging Units (Shipboard Scientific Party, 1994).

Log Unit 1 (base of pipe [60.0 mbsf] to 127.6 mbsf) This interval between the base of the pipe (60.0 mbsf) and 127.6 mbsf is characterized by relatively low gamma ray, density, velocity, and resistivity-log values (Figure 5.24). All of the recorded logs are affected by the enlarged borehole which exceeds the maximum recording size (37.9 cm) of the caliper throughout most of Unit 1 (Figure 5.23). The acoustic velocity and electrical resistivity logs show an abrupt upward step in value at the boundary between Units 1 and 2. Logging Unit 1 in Hole 889B correlates approximately with Lithostratigraphic Unit I (0-128.0 mbsf in Hole 889A; Shipboard Scientific Party, 1994). The sediments recovered in Lithostratigraphic Unit I consist of mostly homogeneous layers of silty clay and clayey silt laminated on a millimeter scale. The lower part of Lithostratigraphic Unit I (Subunit IB; 91.5-128.0 mbsf) was interpreted as a debris flow and/or slumped deposit.

Log Unit 2 (127.6 - 228.4 mbsf) Both the acoustic velocity and resistivity logs in Logging Unit 2 of Hole 889B are characterized by a distinct baseline shift to relatively higher values throughout Unit 2. At the base of Unit 2, across the boundary into Unit 3, the acoustic velocity and resistivity logs step down to lower values. The gamma-ray, neutron porosity, and density logs are characterized by more gradual or no changes at the upper and lower boundaries of Logging Unit 2. At a depth of about 145 mbsf the gamma-ray log shows an abrupt upward step in value, which is caused by a significant change in the diameter of the borehole (Figure 5.23). The measured neutron porosities in

Logging Unit 2 gradually decrease with depth from about 60% at the top to about 50% at

the bottom of the unit. The density-log values are significantly affected by enlarged

borehole conditions throughout Logging Unit 2. Logging Units 2 and 3 in Hole 889B

correlate with the upper part of Lithostratigraphic Unit II (120.0-301.5 mbsf in Hole

889A; Shipboard Scientific Party, 1994). Lithostratigraphic Unit II consists of firm

clayey silt of dark gray to dark olive gray color. No significant changes in mineralogical

composition were observed between Lithostratigraphic Unit I and II. Lithostratigraphic

Unit II differs from Unit I by its lower abundance of sand and the reduced thickness of

the sand layers. As a consequence, Lithostratigraphic Unit II is on average more fine

grained than Unit I.

Log Unit 3 (228.4-255.7 mbsf [end of log run]) Logging Unit 3 in Hole 889B is

characterized by consistently lower velocities and slightly lower resistivities with respect

to Logging Unit 2. An anomalous low velocity interval is seen from 228.4 to 236.0 mbsf;

which suggests the presence of free-gas. The natural gamma-ray, density, and neutron

porosity logs exhibit no conspicuous changes at the boundary between Logging Units 2

and 3.

5.3.4 Gas-Hydrate Occurrences

Gas hydrates were not conclusively identified at Site 889 (Shipboard Scientific

Party, 1994); however, it's presence was inferred, based on geochemical analyses of

cores and downhole geophysical surveys (VSPs) and borehole-logging data in Logging

Unit 2 (which extends from a depth of about 127.6 to 228.4 mbsf) and possibly in

Logging Unit 1 (which extends from the sea floor to a depth of 127.6 mbsf) (Tables 5.14

and 5.15). Similar to the observations from the Blake Ridge boreholes, the presence of

gas hydrates in Logging Unit 2 at Site 889 was inferred on the basis of gas-rich cores,

low interstitial water chloride concentrations, and low temperature measurements in the

recovered cores (Shipboard Scientific Party, 1994; Spence et al., 1995; Hyndman et al.,

1996). In addition, sediment velocity data from downhole VSP and ocean bottom

seismometer (OBS) surveys (Shipboard Scientific Party, 1994; Spence et al., 1995;

Hyndman et al., 1996) indicate that gas hydrates occur in the 50- to 80-m-thick interval

above the BSR (approximate depth of 230 mbsf) at Site 889. Data from downhole logs

also were interpreted as indicating the presence of gas hydrate in Logging Unit 2. The

downhole-log evidence for gas hydrates is discussed in more detail later in this section of

the thesis.

The depths to the top and the base of the zone of gas-hydrate occurrence at Site

889 was measured using interstitial water chloride anomalies and downhole-log data

(Tables 5.14 and 5.15). The observed chloride anomalies can be used to estimate the

amount of gas hydrate that occurs at Site 889 by calculating the amount of interstitial

water freshening that can be attributed to gas hydrate disassociation. The estimated

volume of sediment porosity occupied by gas hydrate (S_h) in the recovered cores had a

skewed distribution, ranging from a minimum of about 5% immediately below the sea

floor in Logging Unit 1 to a maximum of about 39% near the bottom of Logging Unit 2

(Hyndman et al., 1996). Unlike the interstitial water freshening calculated gas-hydrate

saturations from Leg 164 (Shipboard Scientific Party, 1996), these are likely maximum

Table 5.15 Depth to the top and bottom of the interstitial-water-chloride- and well-log-inferred gas hydrate occurrences at Site 889 (Figure 5.24).

Site	Top/Bottom	Gas hydrate - chloride anomaly depth (mbsf)	Log inferred gas hydrate depth (mbsf)
889	Top	130.0	127.6
	Bottom	?	228.4

values because the baseline (undisturbed interstitial water chlorinities) used to calculate these values may be higher than the actual in-situ interstitial water salinities. For a more complete discussion on the chlorinity-calculated gas-hydrate contents see Shipboard Scientific Party (1994, 1996).

As previously discussed in Chapter 1 of this thesis, natural gas-hydrate occurrences are generally characterized by the release of unusually large amounts of methane during drilling and an increase in log-measured acoustic velocities and electrical resistivities. The comparison of Logging Units 1, 2, and 3 at Site 889, reveals that Logging Unit 2 is characterized by a distinct stepwise increase in both electrical resistivity (increase of about 0.2-1.7 ohm-m) and acoustic velocity (increase of about 0.1-0.4 km/sec) (Figure 5.24). In addition, the deep reading resistivity device (RILD) reveals several high resistivity zones within the upper 20 m of Logging Unit 2 in Hole 889B (resistivities ranging from 2.5 to 2.8 ohm-m). Further comparisons indicate that the high resistivity zones in the upper part of Unit 2 are characterized by an acoustic velocity increase of about 0.2 km/sec. Below the high resistivity zones in the upper part of Logging Unit 2, the resistivity log reveals two conspicuous high resistivity zones at a depth of about 190 and 210 mbsf that also exhibit high acoustic velocities. Examination of the natural gamma-ray, neutron porosity, and bulk-density logs from Site 889 (Figure 5.24) reveals no apparent lithologic causes for the observed velocity and resistivity increases in Unit 2. The above observations are consistent with a gas-hydrate-bearing sedimentary section. The depth of the boundary between Logging Units 2 and 3 at Site 889 is in rough accord with the predicted base of the methane hydrate stability zone

(Shipboard Scientific Party, 1994). In this study it was assumed that Logging Unit 2 at

Site 889 contains some amount of gas hydrate. It should be noted, however, that in the

Downhole Logging section of the Initial Reports volume for Leg 146 the high acoustic

velocities and electrical resistivities in Logging Unit 2 of Hole 889B were attributed to

changes in lithology and reductions in porosities (Shipboard Scientific Party, 1994).

However, as previously discussed in this thesis, there is no evidence of significant

lithologic or sediment porosity differences between the three Logging Units surveyed at

Site 889.

5.3.5 Porosity Calculations

In this study, the bulk-density (HLDT) and neutron porosity (CNT-G) logs from

Site 889 were used to calculate sediment porosities. At Site 889 it was not necessary to

use the available electrical resistivity (DITE) log to calculate sediment porosities because

of the relatively high quality of the neutron-porosity-log data. Core-derived physical

property data, including porosities (Shipboard Scientific Party, 1996), have been used to

both calibrate and evaluate the log-derived sediment porosities at Site 889.

Core Porosities On Leg 146, water content, wet bulk-density, dry bulk-density,

and grain density were routinely determined from recovered sediment cores. Other

related physical property data, including sediment porosities, were calculated from these

"index properties" (Shipboard Scientific Party, 1994). The core-derived porosities

actually represent the measured total water content of the sediments, which include

interlayer-, bound- and free-water. Most downhole logs also measure the total water

content of the sediments; thus the core- and log-derived sediment porosities should be the same. Sediment core porosities determined from Site 889 are shown in Figure 5.25. In general, the core-derived sediment porosities decrease from about 65% near the top of Hole 889A to about 50% at the bottom.

Density-Log Porosities The density log (HLDT) measurements of bulk-density in Hole 889A (Figure 5.24) are highly variable and range from a maximum of about 2.1 g/cm^3 to a very low value of 1.2 g/cm^3. Other physical property data from Site 889, including core-derived sediment wet bulk densities and porosities (Figure 5.25) (Shipboard Scientific Party, 1994), are not consistent with the density-log measurements. It is likely that the density log from Hole 889A has been severely degraded by both the rugosity and the enlarged size of the borehole. Before using the log-derived bulk-density data to calculate sediment porosities, the density log editing technique described in Section 5.2.5 of this thesis was used to systematically remove the erroneous data from the recorded density log in Hole 889A. The edited bulk-density-log measurements were then used to calculate sediment porosities ($\emptyset$) in Hole 889A using the standard density-porosity relation discussed in Chapter 3 of this thesis (Equation 3.1). Water densities (ρ_w) were assumed to be constant and equal to 1.0 g/cm^3, however, variable core-derived grain/matrix densities (ρ_m) were assumed for each calculation. The core-derived grain densities (ρ_m) in Hole 889A range from an average value at the sea floor of about 2.71 g/cm^3 to about 2.61 g/cm^3 at the bottom of the hole (Shipboard Scientific Party, 1994). The density log porosity calculations from Site 889 yielded values ranging from about 47% to near 65% (Figure 5.26). The density-log-derived porosities are similar but
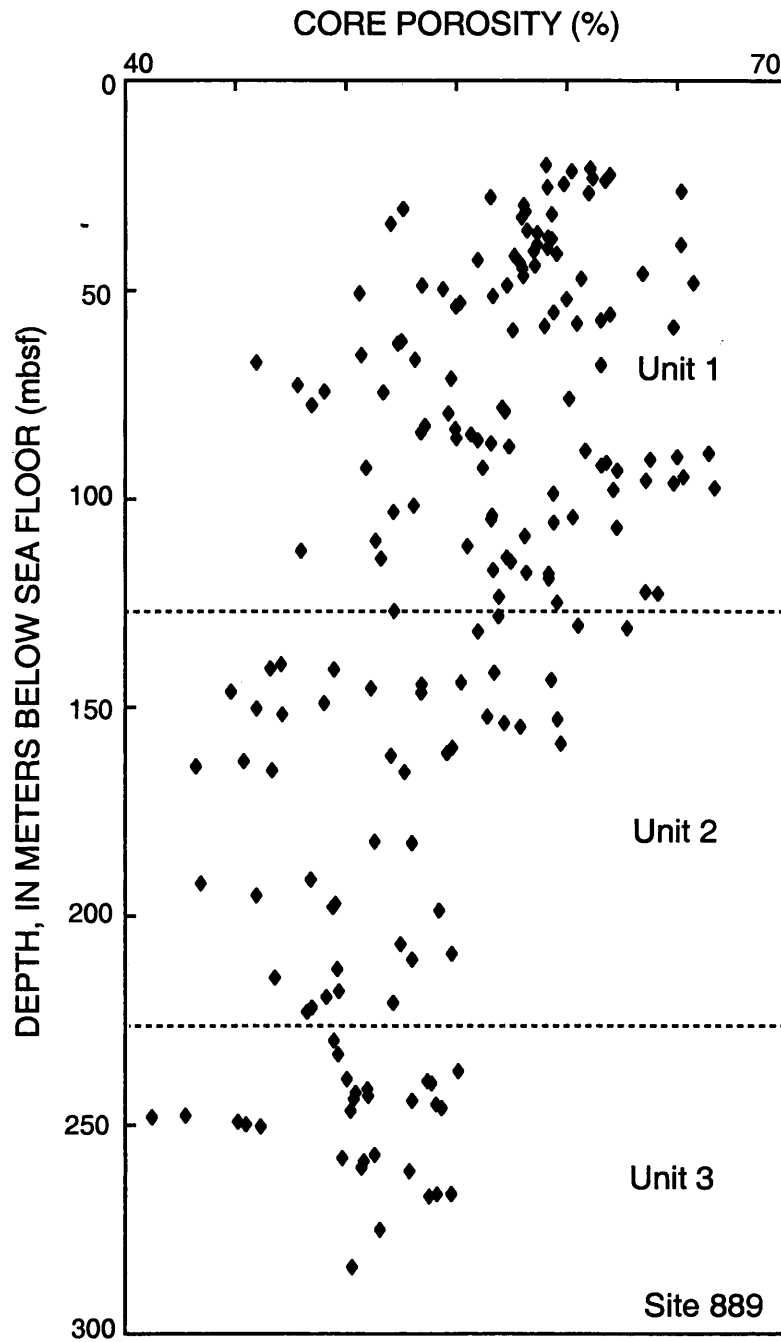
Figure 5.25 Core porosities derived from laboratory physical property data at Site 889 (modified from Shipboard Scientific Party, 1994).
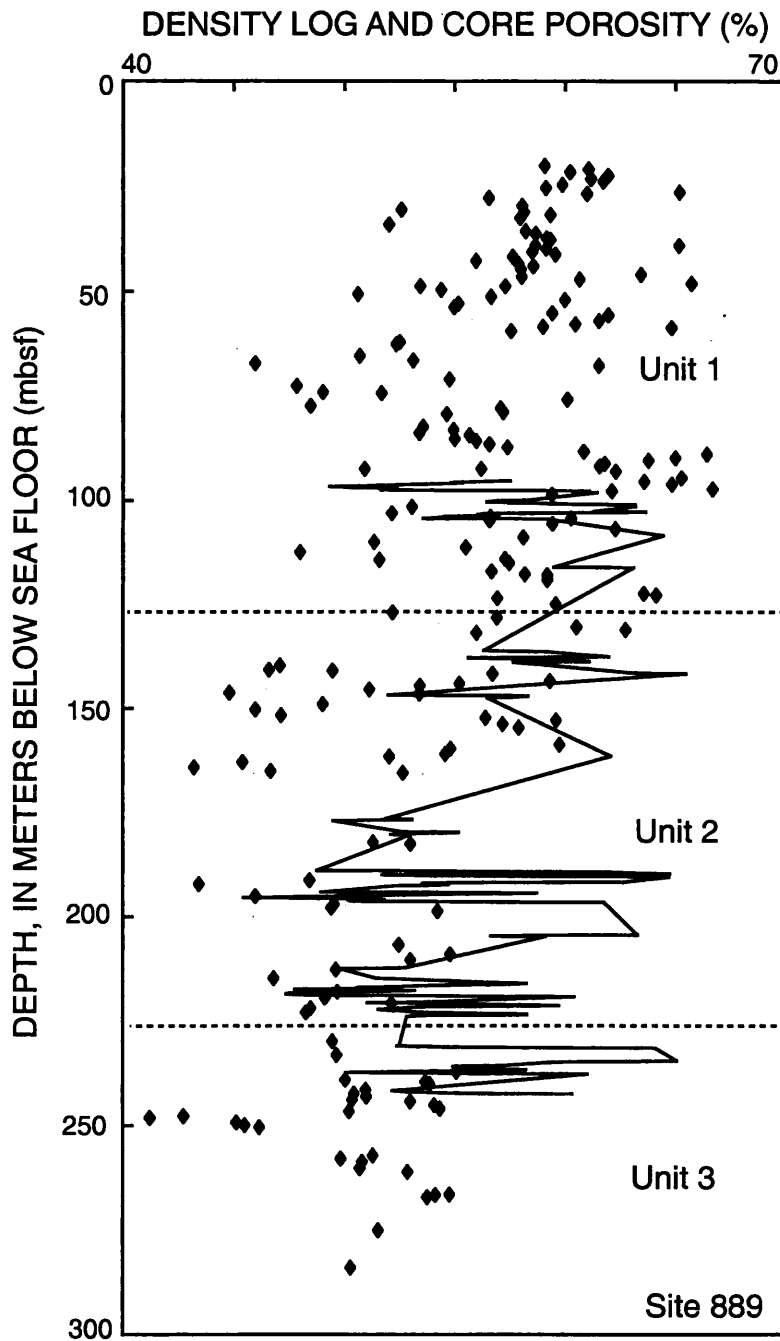
Figure 5.26 Sediment porosities (shown as continuous line plot) derived from downhole-density-log (HLDT) data at Site 889. Also shown (as discrete point measurements) for comparison purposes are the core-derived porosities (Figure 5.25).

generally higher than the core-derived porosities also shown in Figure 5.26. Similar to

the results from the Blake Ridge (Section 5.2.5 of this thesis), it appears that the density

log often overestimates porosities for the sediments at Site 889. Data from the density

log in Hole 889A can be used to assess general porosity trends but they are not useful for

quantitative calculations.

Neutron Porosity Log The thermal neutron porosity log from Hole 889B (Figure

5.27) yielded sediment porosities ranging from an average value at the top of the logged

section (about 60 mbsf) of about 59% to about 52% in Logging Unit 3 (about 255 mbsf).

As shown in Chapter 3 of this thesis, gas hydrate at relatively lower concentration

(S_h<50%) has relatively little affect on neutron porosity tool responses. Since the

maximum gas-hydrate saturations at Site 889 are far less than 50% (maximum log-

derived gas-hydrate saturation of about 30%) there is no need to correct the neutron

porosity measurements from Site 889 for the presence of in-situ gas hydrates (see

Hyndman et al., 1996 and the next section of this thesis for additional information on gas-

hydrate saturations at Site 889).

Porosity Calculations -- Summary The comparison of core- and log-derived

porosities in Figures 5.26 and 5.27, reveals that the neutron-log-derived porosities are

generally similar to the core porosities. The density-log-derived porosities, however, are

generally higher than the core porosities. It is likely that the density-log measurements

have been degraded by poor borehole conditions. The neutron-log-derived porosities in

Figure 5.27 are the best downhole-derived porosity logs from Site 889.
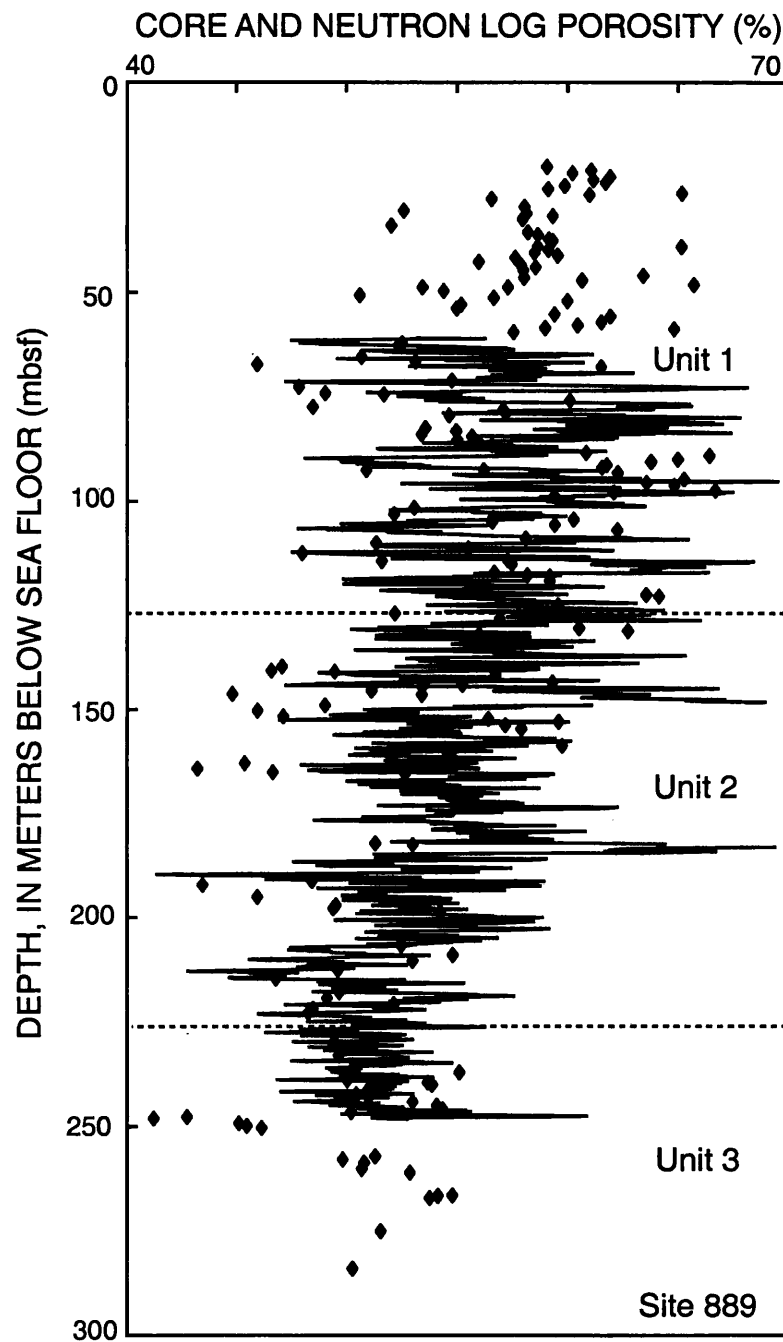
Figure 5.27 Sediment porosities (shown as continuous line plot) derived from downhole-neutron-porosity-log (CNT-G) data at Site 889. Also shown (as discrete point measurements) are the core-derived porosities (Figure 5.25).

5.3.6 Gas-Hydrate Distribution and Saturation

In the following section, the dual induction (DITE) and acoustic transit-time

(LSS-SDT) logs from Hole 889B have been used to quantify the amount of gas hydrate in

Logging Unit 2 (approximate depth interval of 128-228 mbsf) on the Cascadia

continental margin.

Resistivity-Log-Calculated Gas-Hydrate Saturations It is assumed that the

anomalous high resistivities and velocities measured in Logging Unit 2 at Site 889 are

due to the presence of in-situ natural gas hydrates. However, an alternative hypothesis

suggests that interstitial water "salinity" changes could account for the electrical-

resistivity-log responses observed at Site 889. Geochemical analyses of cores from

Logging Unit 2 at Site 889 have revealed the presence of pore-water with relatively low

salt concentrations which will contribute to an increase in the measured electrical

resistivities (Shipboard Scientific Party, 1994). Since the acoustic logs, however, are not

affected by changes in pore-water salinities it refutes the hypothesis that salinity changes

are significantly contributing to the anomalous acoustic velocities and resistivities in

Hole 889B. As demonstrated on the Blake Ridge (Section 5.2.6 of this thesis), it is also

possible to further evaluate the affect of variations in pore-water salinities on the log-

measured formation resistivities at Site 889 by comparing the formation water

resistivities (R_w) (Figure 5.28; discussed in more detail later in this section of the thesis)

calculated from the recovered core water samples in Hole 889A with the log-measured

formation resistivities (R_t) in Hole 889B. The log-measured formation resistivities (R_t)

in Logging Unit 2 at Site 889 are characterized by a maximum resistivity range of about
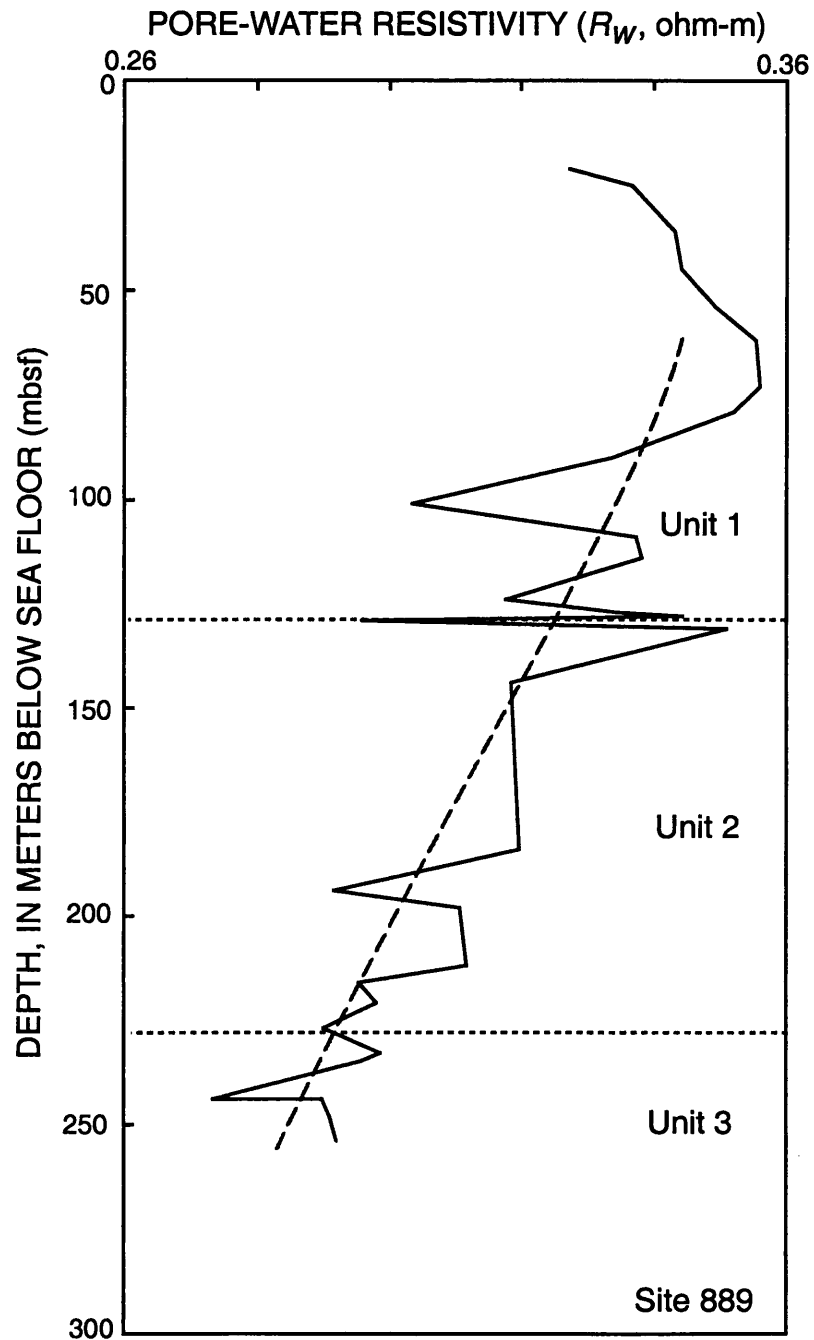
Figure 5.28 Pore-water resistivities (R_W) derived from interstitial water (core samples) salinities at Site 889. The dashed continuous line plot is the assumed undisturbed pore-water resistivities (R_W).

1.7 ohm-m (Figure 5.24). However, the observed pore-water salinity variations in cores

recovered from Logging Unit 2 correspond to a formation water resistivity (R_w) range of

only 0.05 ohm-m (Figure 5.28), which is less than 3% of the total formation resistivity

(R_t) range measured in Logging Unit 2. Therefore, the observed formation resistivity

(R_t) variations in Logging Unit 2 cannot be attributed to only changes in pore-water

salinities and the resistivity log in Logging Unit 2 is likely responding to the presence of

in-situ gas hydrates.

Two forms of the Archie relation (Archie, 1942), discussed in Chapter 3 of this

thesis, have been used to calculate water saturations (S_w) [gas-hydrate saturation (S_h) is

equal to (1.0-S_w)] from the available electrical-resistivity-log data (DITE) at Site 889

(Figure 5.24). The modified Archie relation proposed by Pearson et al. (1983) was not

used to calculate water saturations at Site 889 because of the problems encountered with

this approach in the Blake Ridge portion (Section 5.2.6) of this study. In the first

computation from Site 889, the "standard" Archie equation (Equation 3.8) was used with

two different sets of sediment porosity data to calculate two water saturations. The

porosity data used in the "standard" Archie equation were derived from the neutron

porosity log- and the core-derived physical property data (Figures 5.25 and 5.27). In the

first calculation, the downhole measured neutron-log-derived porosities were used

(Figure 5.27). Before calculating gas-hydrate saturations, however, the neutron-porosity-

log data was first smoothed with a five-point moving average algorithm in order to obtain

a neutron porosity log with a spatial frequency content close to that of the induction log.

In the second "standard" Archie calculation of water saturation (S_w), the required

sediment porosities where obtained from a regression trendline (power function)

projected through the core porosity data from Hole 889A (Figure 5.25). The two

different sets of porosity data (i.e., neutron-porosity-log data and the statistically

manipulated core-derived porosities) were used in the "standard" Archie calculations to

evaluate the affect of various porosity data sources on the resultant gas-hydrate saturation

calculations.

In addition to porosity, the "standard" Archie relation also requires as input the

value of the empirical Archie constants (a, m, and n), the resistivity of the in-situ pore-

waters (R_w), and the resistivity of the formation (R_t) which is obtained from the deep-

resistivity-log measurements in Hole 889B (Figure 5.24). In the following paragraphs,

the resistivity of the "undisturbed" pore-waters (R_w) and the Archie constants a, m, and n

for Site 889 have been determined.

The resistivity of pore-waters (R_w) is mainly a function of the temperature and the

dissolved salt content (salinity) of the pore-waters. In general, the core-derived

interstitial water salinities from Hole 889A decrease with depth from a maximum value

of about 32 ppt near the sediment-water interface to about 21 ppt within the lower part of

Logging Unit 2 (Shipboard Scientific Party, 1994). Formation and seabed temperatures

have been directly measured at Site 889 as described in Shipboard Scientific Party

(1994). Listed in Table 5.16 are the measured seabed temperature and geothermal

gradient for Site 889. Arps formula (Hearst and Nelson, 1985) was used to calculate the

pore-water resistivities (R_w) at Site 889 from the available core-derived interstitial water

salinities and measured formation temperatures (Table 5.16, Figure 5.28). The calculated

Table 5.16 ODP Site 889 formation temperature data and Archie constants (a and m) needed to calculate pore-water resistivities (R_W; Figure 5.28) and water saturations (S_W; Figure 5.29) (temperature data from Shipboard Scientific Party, 1994).

Site	Seabed temperature (°C)	Geothermal gradient (°C/100m)	Archie constants	
			a	m
889	2.6	5.26	0.97	2.81

pore-water resistivities (R_w) reach a maximum of about 0.35 ohm-m near the sea floor

and decrease with depth to a value below 0.28 ohm-m in Logging Unit 3. In the

subsequent resistivity gas-hydrate saturation calculations, the gas-hydrate-affected pore-

water resistivities from Logging Unit 2 have been excluded and the pore-water

resistivities from Logging Units 1 and 3 have been used to statistically project

undisturbed pore-water resistivities for Logging Unit 2 (Figure 5.28).

The method used to calculate the Archie constants a and m is described in Section

3.4 of this thesis. The log-measured resistivity data from Logging Unit 2 has been

omitted from this calculation of the Archie constants to avoid introducing an error caused

by using resistivity-log measurements that have been affected by the occurrence of in-situ

gas hydrates. In addition, log-measured resistivities from above 105 mbsf in Hole 889B

have also been omitted from the determination of the Archie constants because of several

anomalous resistivity-log measurements in the upper part of Logging Unit 1. Linear

trends in resistivity-log and core-porosity data from Logging Units 1 and 3 (exclusive of

Logging Unit 2 and the upper part of logging Unit 1) have been used to calculate

representative (100% water-saturated) formation resistivities (R_O) and porosities $(\varnothing)$.

From these representative values the slope, m, and the intercept, $\ln a$, of the function $\ln$

$(R_O/R_W) = -m \ln \varnothing + \ln a$ were calculated. The a and m Archie constants for Hole 899B

have been calculated to be 0.97 and 2.81, respectively; which are similar to the values

calculated for the Blake Ridge (Section 5.2.6 of this thesis) and fall within the "normal"

range of expected values (Serra, 1984). The value of the empirical constant n was

assumed to be 1.9386 as determined by Pearson et al. (1983).

Given the Archie constants (a, m, and n) and pore-water resistivities (R_W), it is possible to calculate water saturations (S_W) from the resistivity log using the "standard" Archie's relation. In Figure 5.29, the results of the two "standard" Archie calculations are shown as water saturation (S_W) log traces for Hole 889B. In Hole 889B, the "standard" Archie relation yielded water saturations (S_W) ranging from about 100% to a minimum of about 70% (Figure 5.29). In comparison to the "standard" Archie saturation calculation, which employed average core porosities, the "standard" Archie calculation which used the neutron-log-derived porosities resulted in the calculation of more highly variable water saturations. The slightly depressed water saturations in Logging Unit 3 are likely due to the presence of free-gas.

The next log analysis method used to assess gas-hydrate saturations in Hole 889B was based on the modified "quick look" Archie log analysis technique (Equation 3.10, discussed in Chapter 3 of this thesis). For the modified "quick look" Archie log technique, the measured deep resistivities from all of Logging Unit 3 and the lower 22 m of Logging Unit 1 were used to project a best fit R_O trend-line for Unit 2 in Hole 889B (Figure 5.24). Similar to the "quick look" analysis performed with the Blake Ridge downhole-resistivity-log data, for Site 889 three different R_O trend-lines were used to bracket (i.e., maximum, median, and minimum R_O trend-lines) the expected R_O best fit trend line. The Archie constant n was set at 1.9386 (reviewed by Pearson et al., 1983). Now knowing R_t, R_O, and n it is possible to use the modified "quick look" Archie relationship to estimate water saturations. Displayed in Figure 5.29 are both the "standard"- and "quick look"-Archie-derived water saturations. The "quick look"-
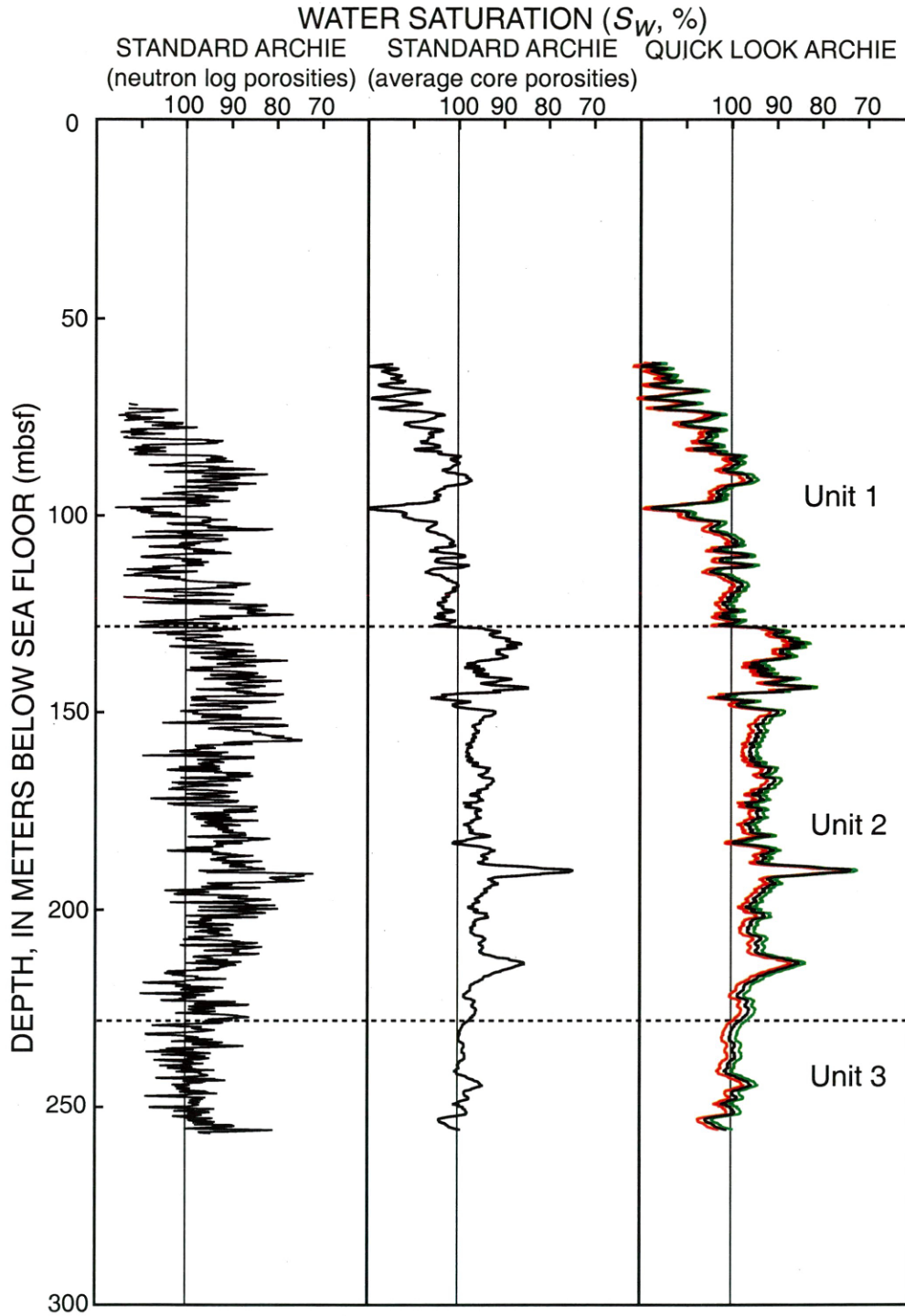
Figure 5.29 "Standard"- and "quick-look"-Archie-derived water saturations (S_W) calculated from the downhole electrical resistivity log at Hole 889B. The "standard" Archie calculations assume different sediment porosities: (1) neutron porosity log measurements and (2) average core porosity trends. The three "quick-look"-derived saturation curves assume three different R_O values (i.e., maximum, median, and minimum).

calculated water-saturations are very similar to the water saturations calculated by the

"standard" Archie relation which employed average core porosities. However, the

"quick-look"-derived water saturations are 2 to 3 percent higher, which is mostly

controlled by the method used to select the R_O baseline. But the "quick-look"-derived

water saturations are relatively insensitive to the limited range of expected R_O values at

Site 889. In general, both the "standard" and "quick look" Archie relations appear to

yield reasonable hydrocarbon (gas-hydrate and free-gas) saturations on the Cascadia

continental margin.

As introduced in the Blake Ridge gas-hydrate saturation assessment section of

this thesis, the Waxman-Smits saturation-resistivity relation for shaly formations was also

used assess the affect of shales (clays) on resistivity-derived gas-hydrate saturations at

Site 889 on the Cascadia margin. As discussed in Section 5.2.6 of this thesis, the

Waxman-Smits relation (Equation 3.12) used in this thesis was rewritten into terms of

electrical resistivity (Waxman and Thomas, 1974), and the input variables (a, m, n, $\varnothing$,

R_W, R_t, B, and Q_V) needed for the Waxman-Smits shaly-sand assessment of Site 899 have

been determined in the following section.

A total of 15 representative core samples from Hole 889A were selected for

laboratory analysis of the CEC of the gas-hydrate-bearing sediments along the Cascadia

margin (Table 5.17). The laboratory analysis of the Hole 889A sediment cores were also

performed by Huffman Laboratories Incorporated (Ronald L. Keil, Laboratory Director,

Golden, Colorado). The laboratory procedures used to determine the CECs of the Site

889 sediment core samples were identical to the methods used to analyze the Site 995

Table 5.17 Laboratory-measured cation exchange capacity (CEC) of sediment core samples from Hole 889A.

Sample depth (mbsf)	Cation exchange capacity (CEC) (meq/100 grams)
88.5	40
98.4	31
108.6	40
114.1	28
123.0	43
140.3	48
151.3	34
160.6	36
180.3	27
189.9	27
209.1	33
219.4	37
229.8	44
237.9	40
259.2	33

meq=milliequivalents

samples from the Blake Ridge. The laboratory-derived CECs for the sediment core samples from Hole 889A (Table 5.17), relative to the samples from Site 995, are more variable with values ranging from about 27 to 48 meq/100 grams of sample (assumed CEC measurement error of ±2 meq/100 grams). Because of the highly variable laboratory-derived CEC measurements reported in Table 5.17, the Waxman-Smits CEC values within the non-sampled portions of Hole 889A were linearly interpolated between the analyzed core samples. The laboratory reported CEC values were converted to sediment volumetric terms (Q_v) by Equation 3.13, the resultant Waxman-Smits Q_v values ranged from about 0.4 meq/ml to about 1.2 meq/ml. Similar to the Blake Ridge results, the relatively high Q_v values for Site 889 are of concern, because the Waxman-Smits relation is experimentally limited to reservoir rock conditions with Q_v values of less than 0.4 meq/ml.

In the "standard" Archie assessment of Site 889, the Archie a and m (a=0.97, m=2.81) variables were directly calculated from available downhole-log data. The Archie n variable was assumed to be equal to 1.9386 (Pearson et al., 1983). Because of problems associated with calculating shaly-sand a, m, and n equivalents, it was initially assumed that the "standard" Archie a and m values calculated from the downhole-log data at Site 889 were correct (Table 5.16). It was also assumed, that an n value of 1.9386 was applicable for the Site 889 shaly-sand assessment. The sediment porosity data needed for the Waxman-Smits calculations were also obtained from the regression trendline analysis of the available core porosity data at Site 889. The pore-water resistivity (R_w) trend-line

(Figure 5.28) calculated for the "standard" Archie assessment of Site 889, was also used in the Waxman-Smits shaly-sand assessment of Site 889.

The "standard" Archie and various Waxman-Smits-derived (assuming different values for the Archie m variable, m=2.81, 3.00, 3.20 and 3.40) water-saturations for Site 889 on the Cascadia margin have been displayed in Figure 5.30. Similar to the results from the Blake Ridge, the Waxman-Smits calculations that assume the same a, m, and n constants as the "standard" Archie relation appear to significantly overestimate the amount of in-situ gas hydrates at Site 889. As shown in Figure 5.30, the Waxman-Smits-derived water-saturations were extremely sensitive to changes in the Archie m variable; however, there is no geologic justification for using the higher values for the Archie m variables.

At Site 889, the Waxman-Smits relation appears to have underestimated water saturations. The likely cause of this problem can be again attributed to the high clay content of the marine sediments on the Cascadia margin.

Acoustic-Log-Calculated Gas-Hydrate Saturations In this section, compressional-wave acoustic-log data from Site 889 has been used along with the Timur, modified Wood, and Lee weighted average acoustic equations (discussed in Section 3.5 of this thesis) to calculate gas-hydrate saturations at Site 889. Because of the lack of downhole shear-wave acoustic-log data, the Lee et al. (1996), Kuster-Toksöz (Zimmerman and King, 1986), or Dvorkin et al. (1991, 1993) combined compressional- and shear-wave velocity gas-hydrate saturation equations (discussed in Section 3.5 of this thesis) could not be used to assess gas-hydrate saturations at Site 889.

352
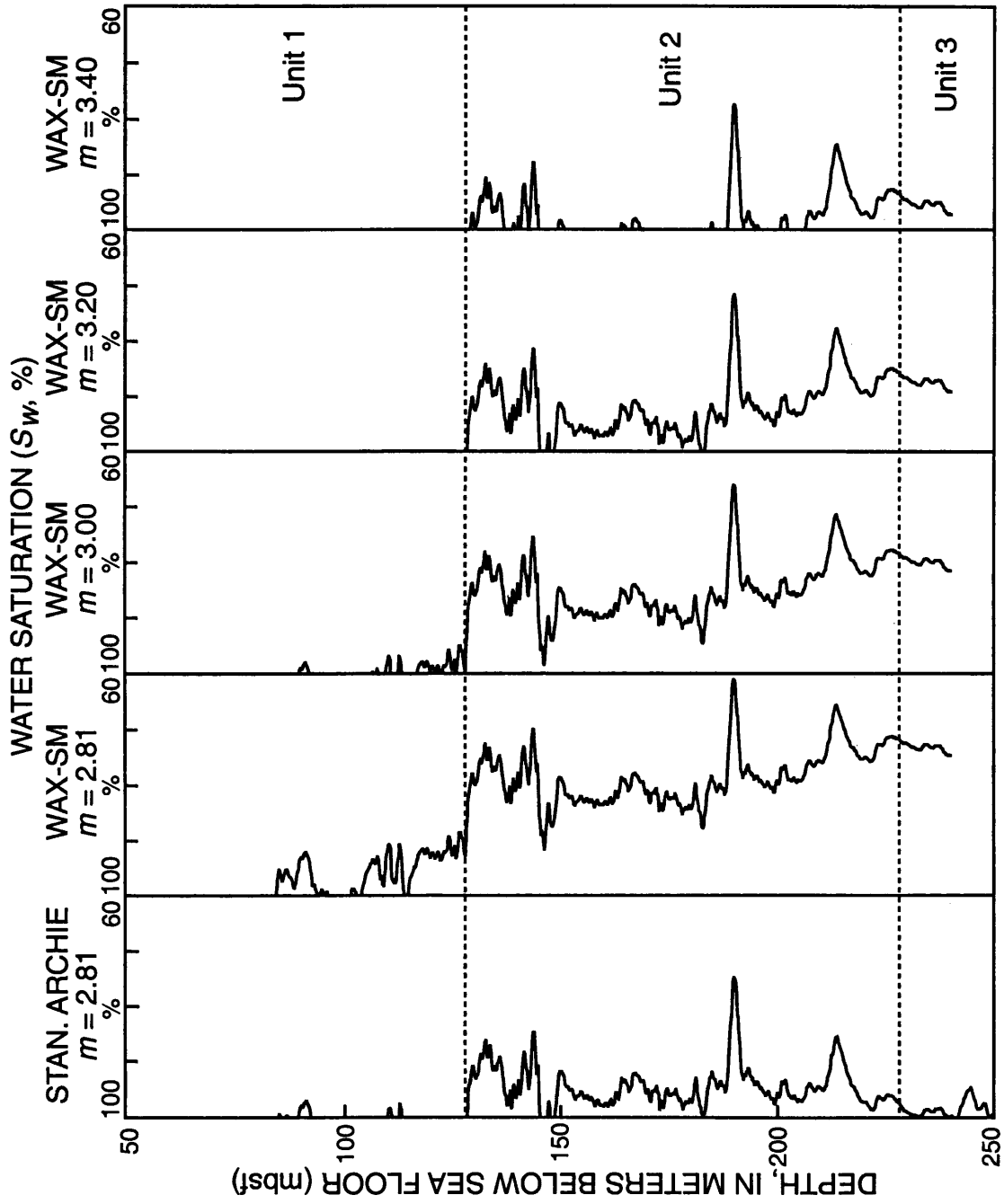
Figure 5.30 Water saturations (S_w) for Hole 889B calculated from the "Standard" Archie relation and the Waxman-Smits shaly-sand model (assuming various Archie m variables and average core porosity trends).

As previously discussed in Section 5.2.6 of this thesis, a computer program was constructed which simultaneously calculates gas-hydrate saturations with the Timur (Equation 3.14), Wood (Equation 3.15), and Lee (Equation 3.16) acoustic equations. In this calculation of gas-hydrate saturations at Site 889, two different sets of sediment porosity ($\emptyset$) data were used, similar to the electrical resistivity water saturation calculations discussed earlier in this section of the thesis. The porosity data used in the acoustic gas-hydrate saturation equations were derived from the neutron porosity log and the core-derived physical property data (Figure 5.25 and 5.27). In the first set of calculations, the absolute value (not statistically manipulated) of the neutron-log-derived porosities was used (Figure 5.27). In the second set of acoustic gas-hydrate saturation calculations (S_h), the sediment porosities where obtained from a regression trendline (power function) projected through the core porosity data from Hole 889A (Figure 5.25). The remaining variables in the Timur and Wood equations have been assigned constant values: with an assumed water velocity (V_w) of 1.5 km/sec, sediment matrix velocity (V_m) of 4.37 km/sec, gas hydrate velocity (V_h) of 3.35 km/sec, water density (ρ_w) of 1.05 g/cm^3, sediment matrix density (ρ_m) of 2.7 g/cm^3, and a gas hydrate density (ρ_h) of 0.9 g/cm^3 (Table 3.12). In the Wood equation, the bulk-density (ρ_b) of the formation was determined from the modified three-component density equation (Equation 3.2). The bulk compressional-wave velocity of the formation (V_b) was obtained directly from the transit-time well logs.

The next two variables needed for the acoustic gas-hydrate saturation calculations are the weight factor (W) and the gas-hydrate cementation exponent (r) in the Lee weighted average equation. As shown in Section 3.5 of this thesis, the Lee equation weight factor, W, can be estimated from field velocity-porosity data for sediments which contain no gas hydrate. In Figure 5.31, neutron-log-derived porosities and log-derived compressional velocity data from the water-saturated (no hydrate) portion of Hole 889B (Logging Unit 3 and the lower 22 m of Logging Unit 1) have been plotted along with various curves calculated from the Lee equation (assumed W values of 0.7, 1.0, and 1.2). The selection of an accurate weight factor, W, at Site 889 is made difficult because of the apparent presence of free-gas below the base of the well-log inferred gas hydrate occurrence on the Cascadia continental margin. As shown in Figure 5.31, the compressional-wave velocities and porosity measurements from Unit 3 plot below the Lee derived model curves, indicating the presence of free-gas. As discussed in Section 3.5 of this thesis, the best fit Lee equation derived porosity-velocity model curve (for a specific W value) is selected such that the plotted porosity and velocity data for expected water-saturated zones at Site 889 fall on or below the best fit Lee model curve (Figure 5.31). In Figure 5.31 it appears that a weight factor, W, of 1.2 best characterizes the sediments from Site 889, with most of the water-saturated zones falling on or below the Lee equation (W=1.2) water baseline. A gas-hydrate cementation exponent (r) of r=1 was selected, because the occurrence of gas hydrates has not significantly contributed to the "cementation" of the unconsolidated sediments on the Cascadia continental margin (Spence et al., 1995).
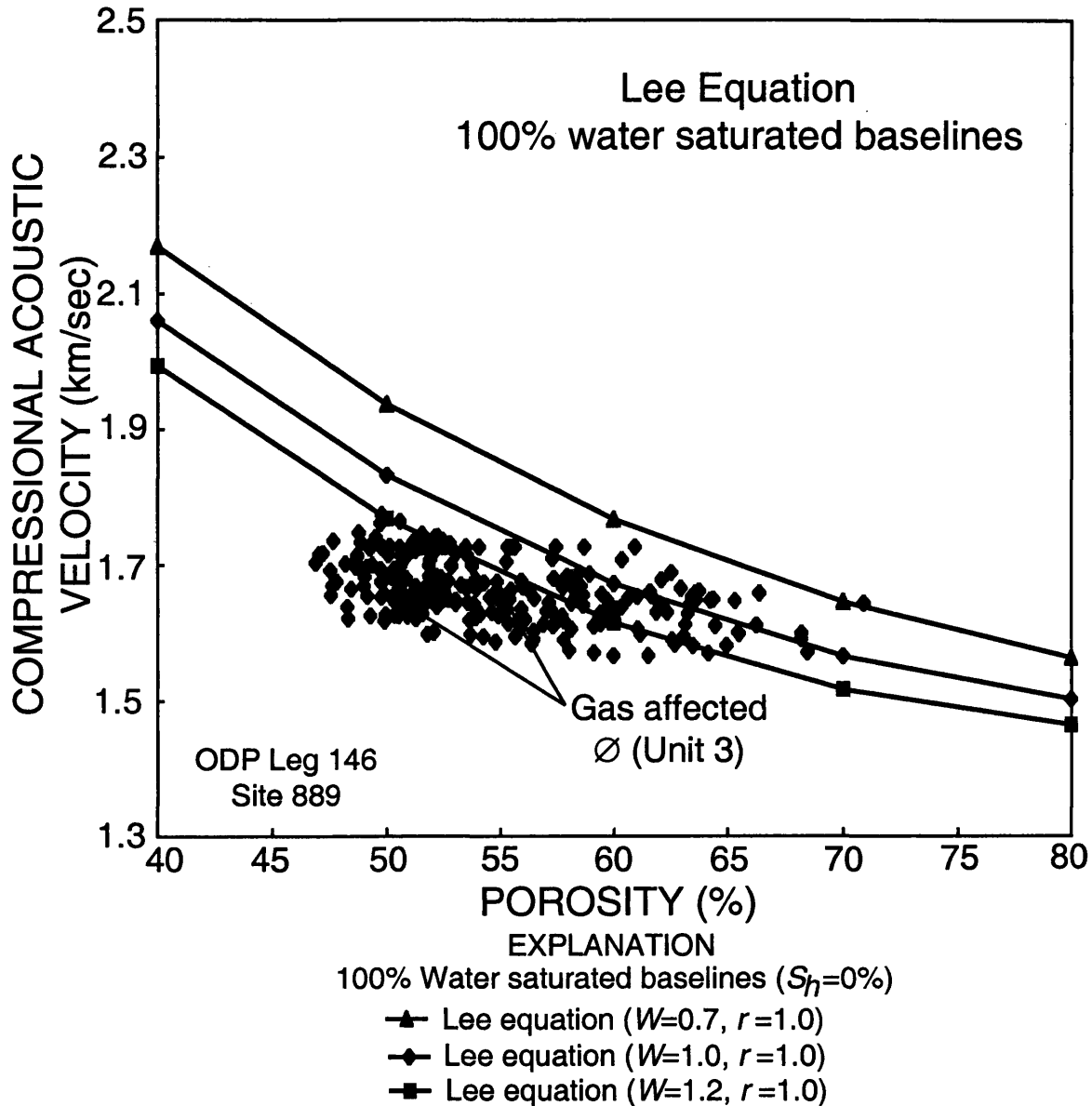
Figure 5.31 Graph showing downhole-log-derived compressional-wave velocities (V_p) and neutron-log-derived porosities for water-saturated sediments (no hydrocarbons) at Site 889. Also shown are several 100% water-saturated porosity-velocity curves predicted from a series of Lee (Equation 3.16) compressional-wave (V_p) acoustic equations that assume different Lee weight factors (W).

In Figure 5.32, the results of the Wood and Lee acoustic velocity calculations, for both porosity conditions, are shown as gas-hydrate saturation log traces for Hole 889B. The results of the Timur acoustic saturation calculations have not been included in Figure 5.32, because the Timur equation failed to indicate the presence of gas hydrates at Site 889. Similar to the results from the Blake Ridge (Section 5.2.6), the Timur equation did not accurately predict the acoustic properties of the unconsolidated sediments on the Cascadia continental margin. In Logging Unit 2 of Hole 889B, the Wood equation yielded gas-hydrate saturations (S_h) ranging from a minimum of about 20% to a maximum near 60%, which is significantly higher than the gas-hydrate saturations calculated by other methods (i.e., interstitial water chloride freshening or electrical resistivity methods) at Site 889. The Lee equation, however, yielded for the most part gas-hydrate saturations (S_h) in Logging Unit 2 of Hole 889B ranging from 0% to a maximum of about 30%, which are more compatible to the gas-hydrate saturations calculated from the electrical-resistivity-log data (discussed earlier in this section of the thesis). In comparison, the Lee calculations which employed the neutron-log-derived porosities resulted in the calculation of more highly variable gas-hydrate saturations when compared to the Lee-calculated gas-hydrate saturations which used the average core porosity data.

Gas-Hydrate Saturation Calculations -- Summary In Logging Unit 2 (approximate depth of 128 to 228 mbsf) of Hole 889B on the Cascadia continental margin, the "standard" Archie relation (electrical resistivity data) and the Lee weighted average acoustic equation (acoustic transit-time data) yielded for the most part gas-
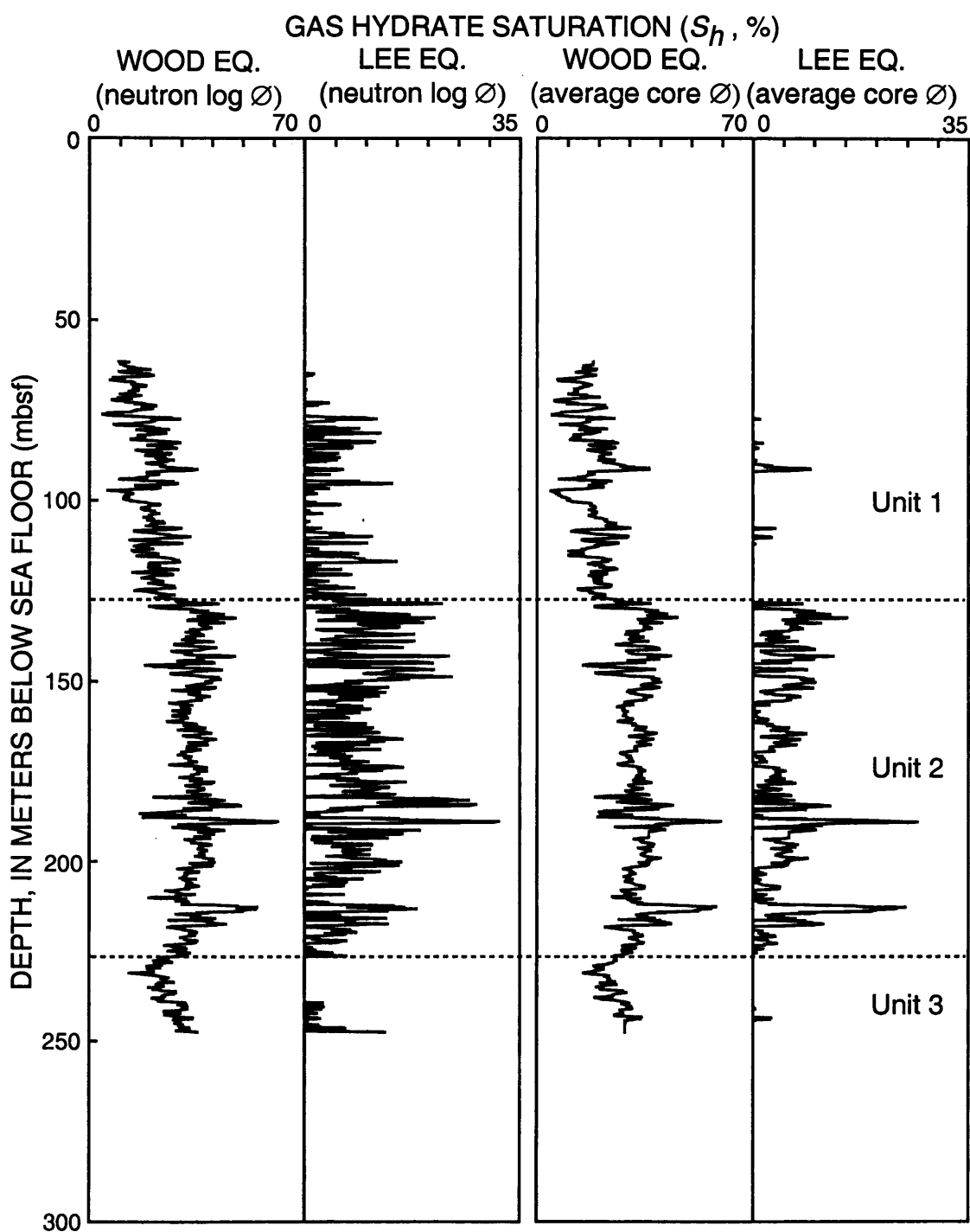
Figure 5.32 Gas-hydrate saturations (S_h) calculated from the downhole compressional-wave acoustic velocity log at Site 889. The results of the modified Wood (Equation 3.15) and Lee (Equation 3.16) acoustic equations are shown assuming both neutron-log-derived porosities and average core porosity trends.

hydrate saturations (S_h) ranging from 0% to a maximum near 30% (Figures 5.29 and 5.32); which are similar to the range of gas-hydrate saturations calculated from interstitial water chloride freshening trends (Shipboard Scientific Party, 1994; Hyndman et al., 1996). The Waxman-Smits shaly-sand relation, however, yielded erroneous gas-hydrate saturations (Figure 5.30) that did not compare favorably with saturations calculated by other methods for Site 889.

In comparison, the "standard" Archie relation and Lee calculations that employed the neutron-log-derived porosities resulted in the calculation of more highly variable gas-hydrate saturations than those calculated with average core porosities. In addition, both the "standard" Archie relation and Lee calculations that used neutron-log porosities yielded relatively higher gas-hydrate saturations in both Logging Units 1 and 2. In comparison to the Blake Ridge, the sedimentary section cored at Site 889 is relatively more complex with highly variable porosity conditions. Thus, the use of average core porosity trends may mask porosity variations within the sedimentary section which may have led to the calculation of erroneous gas-hydrate saturations at Site 889. Therefore, it is possible that the "standard" Archie relation and Lee calculations that use neutron log porosities yield more accurate gas-hydrate saturations on the Cascadia continental margin. However, because of inherent problems with depth matching of downhole-log data from various log runs in ODP boreholes, the more conservative gas-hydrate saturations calculated with the average core porosity data were used in the next section of this thesis to estimate the volume of gas hydrate on the Cascadia continental margin. The "quick look" Archie method also yielded reasonable gas-hydrate saturations (Figure

5.29). In general, the Timur and modified Wood acoustic equations yielded gas-hydrate

saturations which did not compare favorably with saturations calculated by other

methods.

5.3.7 Volume of Gas

The volume of gas that may be contained in the gas hydrates on the Cascadia

continental margin west of Vancouver Island has been estimated from available seismic

data at about 10 trillion cubic meters of gas over an area of 6,000 km^2 (Hyndman et al.,

1996). The log-interpreted gas-hydrate saturations calculated for Site 889 in this thesis

can also be used to estimate the volume of gas that may be contained in the gas hydrates

on the Cascadia continental margin. It is assumed that the volume of gas that may be

contained in a gas-hydrate accumulation depends on five "reservoir" parameters as

discussed in Section 5.2.7 of this thesis (modified from Collett, 1993b). In the following

section, the five "reservoir" parameters (Table 5.18) needed to calculate the volume of

gas associated with the gas hydrates on the Cascadia continental margin are assessed.

The following "resource" assessment has been conducted with data from a single

drill-site; that is, for Site 889 the volume of gas hydrate and associated free-gas within a

one square kilometer area surrounding Hole 889B was calculated (Tables 5.18). For this

"resource" assessment, the thickness of the gas-hydrate-bearing sedimentary section at

Site 889 was defined to be the total thickness of Logging Unit 2, which is 100.8-meters-

thick (Table 5.18). The core-derived sediment porosities (Figure 5.25) in Logging Unit 2

average 51.8% (Table 5.18). Gas-hydrate saturations in Logging Unit 2, calculated from

Table 5.18 Volume of natural gas within the downhole-log-inferred gas hydrate occurrence at Site 889.

Site identification	Depth of Logging Unit 2 (mbsf)	Thickness of hydrate-bearing zone (m)	Sediment porosity (%)	Gas-hydrate saturation (%)	Volume of hydrate per square km (m^3)	Volume of gas within hydrate per square km (m^3)*
889	127.6-228.4	100.8	51.8	5.4	2,845,340	466,635,705

*Gas volume calculation assumes a hydrate number of 6.325 (90% gas filled clathrate), 1 m^3 of gas hydrate = 164 m^3 free-gas at STP.

the "standard" Archie relation (Figure 5.29), average about 5.4%. (Table 5.18). In this assessment a hydrate number of 6.325 (90% gas filled clathrate) was assumed, which corresponds to a gas yield of 164 m^3 of methane (at STP) for every cubic meter of gas hydrate (Collett, 1993b). In this study it was determined that the potential volume of gas within the log-inferred gas hydrates at Site 889 on the Cascadia continental margin is about 466,635,705 cubic meters of gas per square kilometer (Table 5.18).

If it is assumed that the geologic conditions and gas hydrate distribution at Site 889 (Table 5.18) are representative of the entire seismic delineated gas-hydrate accumulation (6,000 km^2) on the Cascadia continental margin, it can be estimated that there is about 2.8 trillion cubic meters of gas within the Cascadia gas-hydrate accumulation; which is about one-quarter of the amount estimated by Hyndman et al. (1996). One of the reasons that this estimate differs from that of Hyndman et al. (1996), is because they also included in their estimate significant gas-hydrate accumulations from Logging Unit 1, which were not included in this assessment. In addition, the gas-hydrate saturations in Logging Unit 2 calculated by Hyndman et al. (1996) are slightly higher than those calculated from the available downhole-log data.

Because of the limited logging depths at Site 889, no attempt was made to calculate the volume of free-gas below the gas hydrates on the Cascadia continental margin. However, the available acoustic and resistivity downhole logs have been used to identify a 7.6-m-thick free-gas zone (228.4-236.0 mbsf) immediately below the base of the deepest gas hydrate at Site 889. This log delineated free-gas-bearing zone is

characterized by an average gas-saturation, calculated from the "standard" Archie relation (Figure 5.29), of 0.77% or about 1%.

5.4 Middle America Trench--Pacific Ocean

5.4.1 Introduction and Regional Geology

A discussed in Section 1.4.2 of this thesis, a massive gas hydrate sample was recovered from Site 570 (Leg 84 of the Deep Sea Drilling Project) in 1982 during research coring operations off the southwest coast of Guatemala (Kvenvolden and McDonald, 1985). At Site 570 (Figure 5.33), a 1.05-m-long section of massive gas hydrate was unexpectedly cored in an area where none of the usual signs of gas hydrate in seismic records were present. The sedimentologic section from which the massive gas hydrate was recovered was analyzed using the following downhole logging tools: electrical resistivity, acoustic velocity, spontaneous potential, bulk-density, neutron porosity, natural gamma-ray, temperature, and a caliper (Figure 1.6). The acoustic velocity, electrical resistivity, and density logs (Figure 5.34) defined a 15-m-thick gas-hydrate-bearing zone (240.5-255.5 mbsf) within which a 4-m-thick interval (247.4-251.4 mbsf) of "nearly pure" gas hydrate section appears to occur (Kvenvolden and McDonald, 1985; Mathews, 1986). The "nearly pure" gas hydrate zone is clearly defined by the high apparent electrical resistivities (about 155 ohm-m) and acoustic velocities (about 3.6 km/sec), and the low apparent bulk-density measurements (about 1.05 g/cm^3). The cored massive gas hydrate sample was from the same depth as the downhole-log-inferred 4-m-thick "nearly pure" gas hydrate interval (247.4-251.4 mbsf).
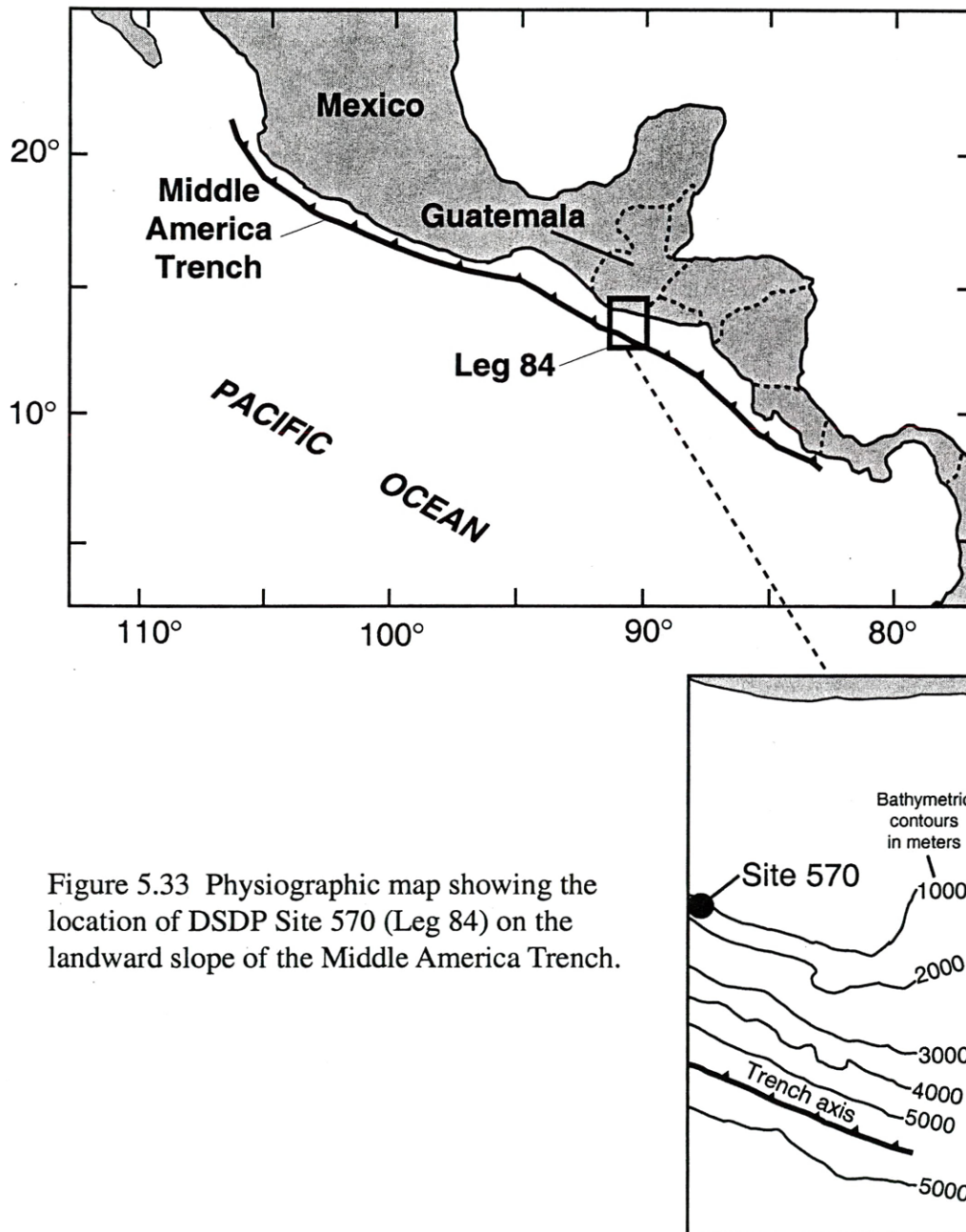
Figure 5.33 Physiographic map showing the location of DSDP Site 570 (Leg 84) on the landward slope of the Middle America Trench.
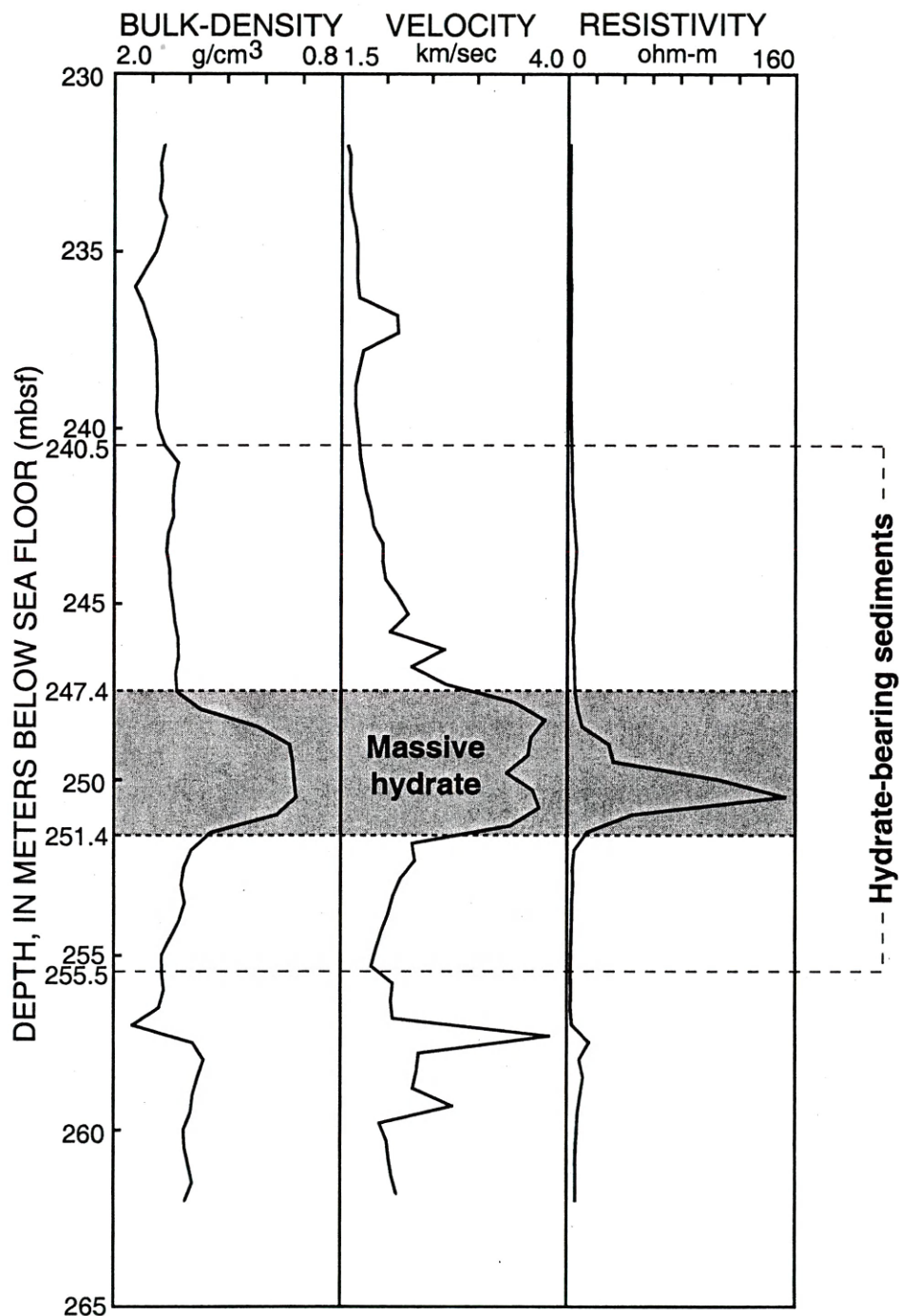
Figure 5.34 Downhole bulk-density, acoustic velocity, and deep-reading electrical resistivity logs that define the massive gas hydrate zone (247.4-251.4 mbsf) and the gas-hydrate-bearing sediment section (240.5-255.5 mbsf) in the DSDP Site 570 corehole.

Site 570 is located on the edge of a small bench in the upper slope of the Middle America Trench, at a water depth of 1,718 m (Figure 5.33). The drill-site is 40 km north of the Trench axis, 25 km south of the edge of the shelf, and 70 km south of the coast of Guatemala. Bathymetric mapping and high-resolution seismic data reveal a major fault adjacent to the drill-site. Drilling at Site 570 may have penetrated through this fault, which may have provided the space within the clay-rich sedimentary section for the accumulation of the cored massive gas hydrate. Seismic records show no BSR or other evidence of gas hydrates at Site 570 (Shipboard Scientific Party, 1985). The calculated base of the methane hydrate stability zone at Site 570 occurs at a depth of approximately 700 mbsf, which is about 300 meters below the deepest penetration of Hole 570.

As discussed in Chapter 2 of this thesis, massive gas-hydrate occurrences, such as the one encountered at Site 570, are not conducive to conventional well-log interpretation procedures. However, a naturally occurring massive gas hydrate may prove useful for calibrating the in-situ well responses to a pure gas hydrate. Therefore, this study of Site 570 has focused on the cored massive gas hydrate zone within the depth interval from 247.4 to 251.4 mbsf (Figure 5.34). In the following section of this thesis, the available downhole-log data have been used to calculate sediment "porosities" and gas-hydrate "saturations" within the massive gas hydrate zone at Site 570. The available downhole-log data was also used to estimate the volume of gas within the massive gas-hydrate accumulation at Site 570.

5.4.2 Downhole-Logging Program

Hole 570 was cored to a total depth of 398.9 mbsf. In preparation for downhole logging, the borehole was flushed and filled with a heavy-weight drilling mud. Downhole logging at Site 570 consisted of four individual logging runs: Run-1 consisted of the compensated density, caliper, compensated thermal neutron, and natural gamma-ray tools; Run-2 included the deep and shallow laterolog, spontaneous-potential, and natural gamma-ray tools; Run-3 consisted of the acoustic transit-time and natural gamma-ray tools; and Run-4 consisted of only a temperature survey.

The quality of all the downhole logs from Hole 570 is very good to excellent. The entire corehole shows some evidence of enlargement on the caliper from the compensated density log (Figure 1.6). Because the borehole diameter variation was small, the borehole corrections, which would be minor for most of the logs from Hole 570, were neglected in this study.

The absolute depths, relative to sea floor, for all of the logs were fixed by identifying the gamma-ray signal associated with the sea floor and depth shifting the log data appropriately. The natural gamma-ray log pick for the sea floor in Hole 570 was at 1,718.0 meters below the rig floor. To determine DSDP sub-bottom depths, subtract 1,718.0 m from the downhole-measured log depths.

5.4.3 Logging Units

No attempt was made to divide the logged interval in Hole 570 into Logging Units. Core studies reveal that the sediments overlying the basement at Site 570 can be

divided into four Lithostratigraphic Units on the basis of lithology and biostratigraphy (Shipboard Scientific Party, 1985). The massive gas hydrate zone at Site 570 occurs within Lithostratigraphic Unit II, which is comprised of olive gray to moderate olive brown mudstones of early to late Pliocene age. The base of Lithostratigraphic Unit II is marked by a highly fractured and indurated dolomite. Some of the fractures in the dolomite were filled with solid gas hydrate, including the massive gas-hydrate occurrence at a depth of 247.4-251.4 mbsf. Solid gas hydrates were also recovered from zones immediately above the dolomite at the base of Lithostratigraphic Unit II (Table 1.4).

5.4.4 Gas-Hydrate Occurrences

At Site 570, the first visual evidence of gas hydrate (Table 1.4) was obtained in a core from a depth of 192 mbsf in the form of gas-hydrate-bearing ash lamina. At a sub-bottom depth of 246 m, gas hydrate was observed filling fractures in mudstones. Core 570-27 (249.1-258.8 mbsf) contained the 1.05-m-thick massive gas hydrate (Figure 5.34) which is the focus of this downhole log evaluation study. Additional, pieces of gas hydrate were also recovered from fractures in mudstones and within volcanic ash lamina and sand lenses in the depth interval from 258.8 to 354.8 mbsf.

5.4.5 Porosity Calculations

At Site 570, bulk-density and neutron porosity logs have been used to calculate sediment porosities. Core-derived physical property data, including porosities

(Shipboard Scientific Party, 1985), have been used to calibrate the log-derived sediment porosities.

Core Porosities In general, the core-derived (gravimetric) sediment porosities decrease from about 70% near the top of Hole 570 to about 50% at a depth of about 388 mbsf. The core-derived sediment porosities immediately above and below the massive gas hydrate zone (247.4-251.4 mbsf) at Site 570 average about 61%.

Density-Log Porosities The log-measured bulk-density of the massive gas hydrate zone (247.4-251.4 mbsf) in Hole 570 is about 1.0 g/cm^3, which is near the calculated density of pure methane hydrate (0.9 g/cm^3; Table 1.1). If the massive gas hydrate zone in Hole 570 is assumed to have a bulk-density of 1.0 g/cm^3, the standard density-porosity relation discussed in Chapter 3 of this thesis (Equation 3.1) can be used along with an assumed formation water density (ρ_w =1.05 g/cm3) and a core-derived grain/matrix density (ρ_m=2.65 g/cm^3) to calculate a sediment "porosity" of the massive gas hydrate zone. The density-log-derived porosities for the massive gas hydrate zone (247.4-251.4 mbsf) in Hole 570 average about 100% (Figure 5.35), which suggests that the entire zone is filled with only gas hydrate (no sediment). At high gas-hydrate saturations, however, the density-log-derived sediment porosities need to be corrected as discussed in Section 3.2 of this thesis. Figure 5.36, which is a modified version of Figure 3.2, can be used to correct "apparent" density porosities within gas-hydrate-bearing sediments. As shown in Figure 5.36, the corrected density porosity for the massive gas hydrate zone (247.4-251.4 mbsf) in Hole 570 is 92%, which indicates that this zone actually contains a small amount of sediment. Photographs of the massive gas hydrate
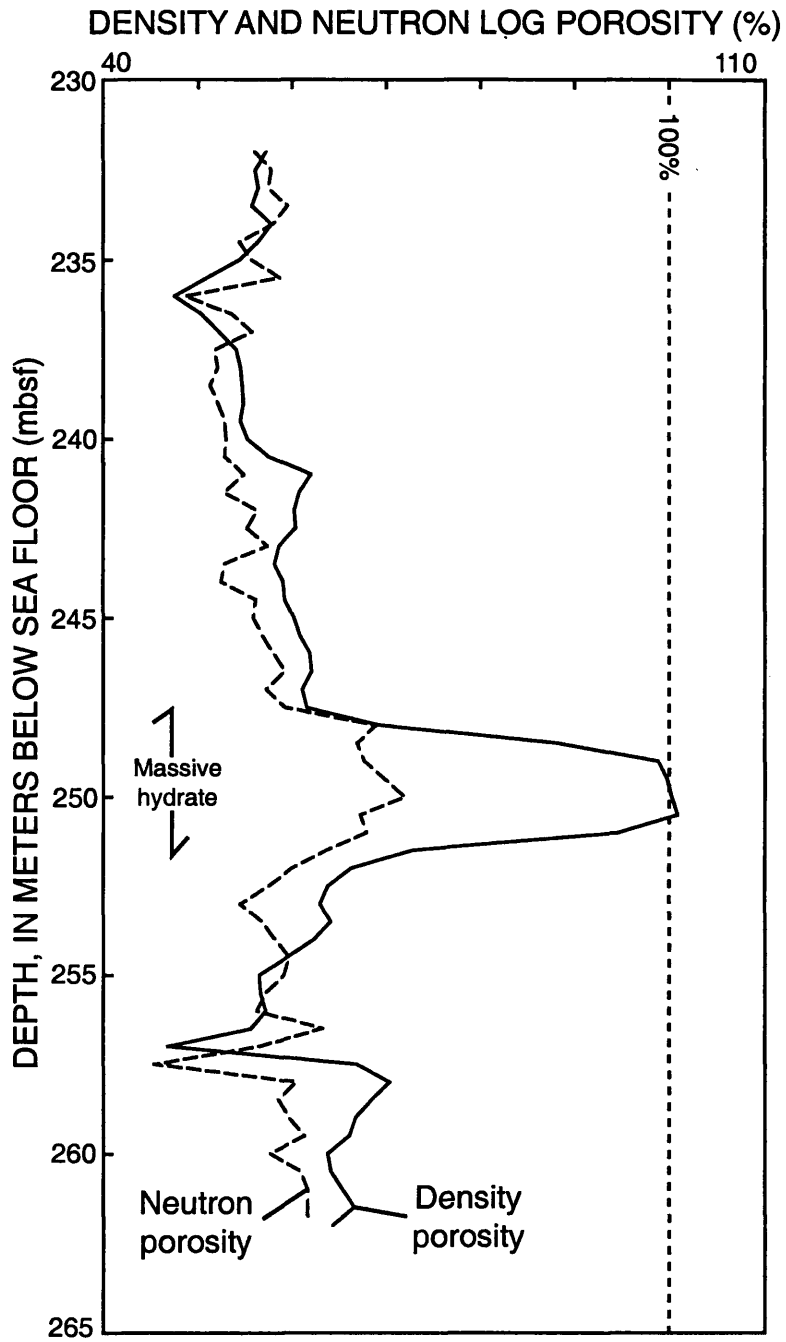
Figure 5.35 Sediment porosities derived from downhole density and neutron porosity logs at Site 570.
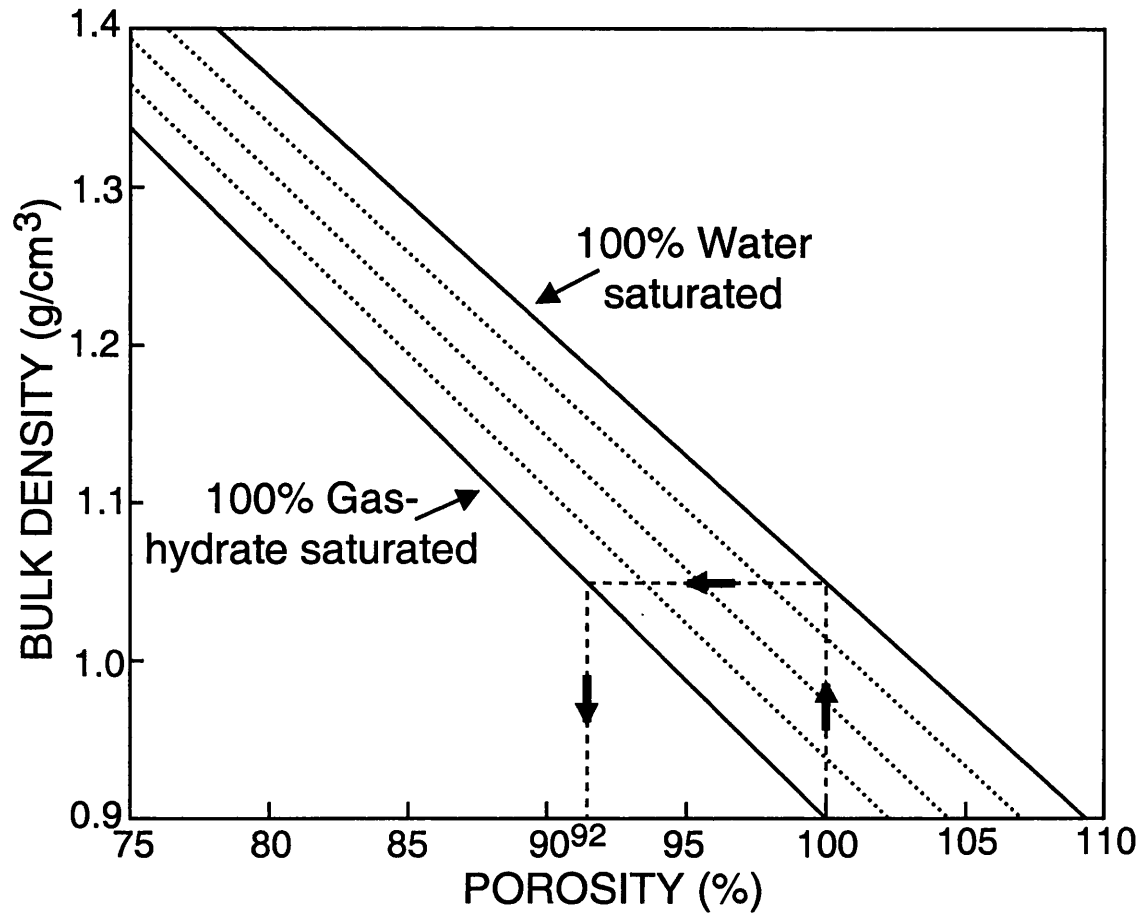
Figure 5.36 Plot of the density porosity gas hydrate correction nomograph for Site 570 (modified from Figure 3.2 in this thesis).

core in the Leg 84 Initial Reports volume (Shipboard Scientific Party, 1985) reveal the presence of a considerable amount of suspended sediment throughout the gas hydrate cemented matrix.

It should be noted that Mathews (1986) calculated a true bulk-density for the massive gas hydrate zone (247.4-251.4 mbsf) at Site 570 of 0.92 g/cm^3, which would result in a calculated density porosity of nearly 100% (no sediment). However, the equation Mathews (1986) used to convert log-derived apparent densities to true bulk densities assumed an electron density of a free-gas-bearing sedimentary section. As shown in Section 3.2 of this thesis, the electron density of natural gas is significantly different then that of a methane hydrate. Therefore, Mathews (1986) underestimated the actual true bulk-density of the massive gas hydrate zone (247.4-251.4 mbsf) at Site 570.

Neutron Porosity Log The thermal neutron porosity log from Hole 570 (Figure 5.35) yielded a sediment porosity for the massive gas hydrate zone (247.4-251.4 mbsf) of about 68%. As shown in Chapter 3 of this thesis, gas hydrate at relatively lower concentration (S_h<50%) has relatively little effect on neutron porosity tool responses; however, at high gas-hydrate concentrations neutron-derived porosities need to be corrected. Similar to the density porosity corrections depicted in Figure 5.36, Figure 5.37 (which is a modified version of Figure 3.4) can be used to correct neutron-log-derived porosities for the presence of gas hydrates. As shown in Figure 5.37, the corrected neutron-derived porosity for the massive gas hydrate zone (247.4-251.4 mbsf) in Hole 570 is about 64%.
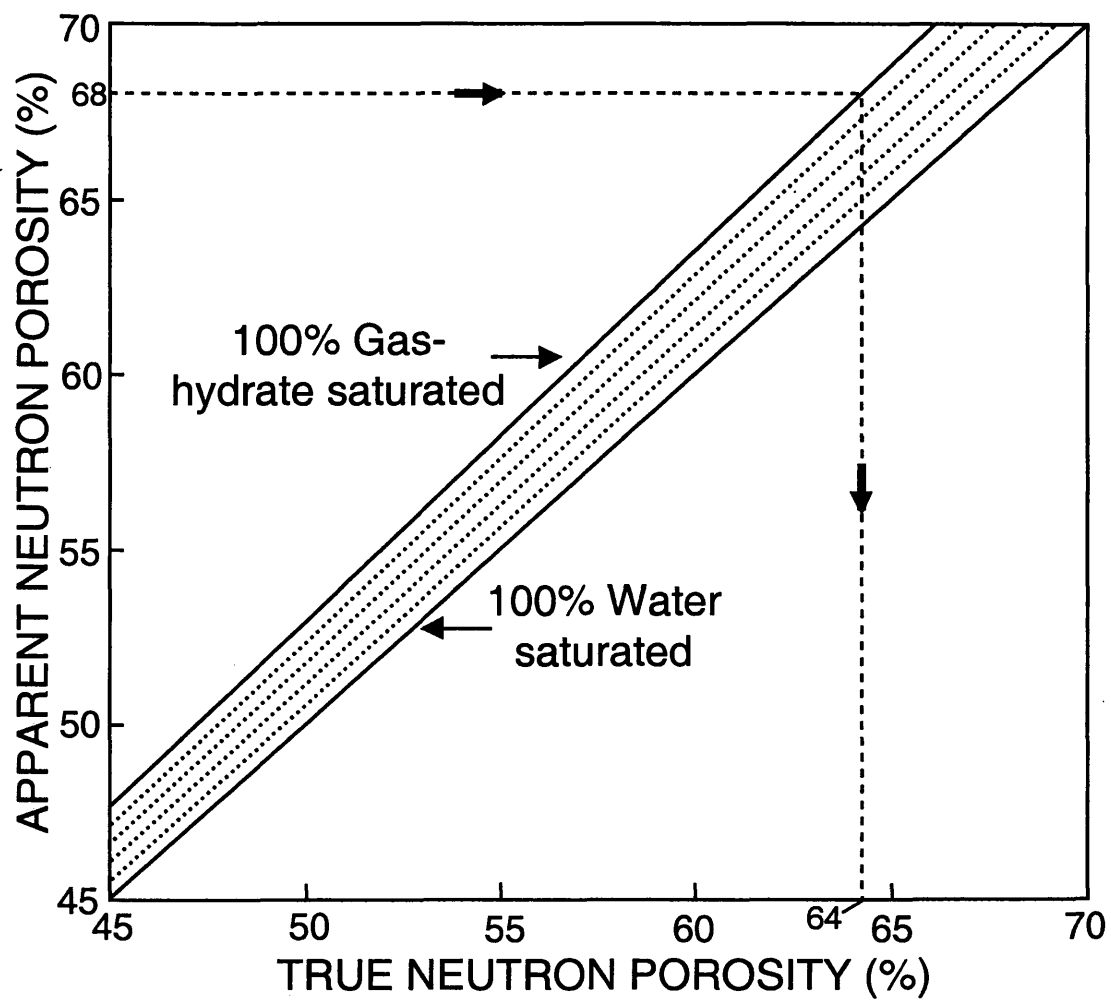
Figure 5.37 Plot of the neutron porosity gas hydrate correction nomograph for Site 570 (modified from Figure 3.4 in this thesis).

Porosity Calculations -- Summary The comparison of the corrected (Figures 5.36

and 5.37) downhole-log porosities from Hole 570 reveals that the neutron-derived

porosity (corrected neutron porosity = 64%) for the massive gas hydrate zone is

considerably lower than the density-derived porosity (corrected density porosity = 92%).

The high density-derived porosity is more compatible with the physical description of the

cores within the massive gas hydrate zone. The neutron-derived porosity for this zone,

however, is very similar to the core-derived porosities for the sediments immediately

above and below the massive gas hydrate zone (247.4-251.4 mbsf) in Hole 570.

The reason for the difference in the corrected neutron and density-log-derived

porosities from the massive gas hydrate zone (247.4-251.4 mbsf) at Site 570 is unknown.

It is possible, however, that because of different vertical resolution capabilities, the

neutron porosity log responded more to the sediments surrounding the massive gas

hydrate, while the density log more accurately measured the physical properties of just

the massive gas hydrate zone. Based on the physical description of the cores and

photographs of the massive gas hydrate core in the Leg 84 Initial Reports volume

(Shipboard Scientific Party, 1985), the corrected density-log-derived porosity (92%) is

assumed to best represent the actual in-situ porosity of the massive gas hydrate zone

(247.4-251.4 mbsf) at Site 570.

5.4.6 Gas-Hydrate Distribution and Saturation

In the following section, data from the electrical resistivity and acoustic transit-time logs have been used to quantify the amount of gas hydrate within the cored and logged "massive" gas-hydrate occurrence at Site 570.

Resistivity-Log-Calculated Gas-Hydrate Saturations It was assumed that the high resistivities and velocities measured in the log-inferred massive gas hydrate zone (247.4-251.4 mbsf) at Site 570 are due to the presence of in-situ natural gas hydrates. Two unique forms of the Archie relation (Archie, 1942), discussed in Chapter 3 of this thesis, have been used to calculate water saturations (S_w) [gas-hydrate saturation (S_h) is equal to $(1.0-S_w)$] from the available electrical-resistivity-log data at Site 570. The modified Archie relation proposed by Pearson et al. (1983) was not used to calculate water saturations at Site 570 because of the problems with this approach encountered in the Blake Ridge portion (Section 5.2.6) of this study.

The first resistivity log approach used to assess gas-hydrate saturations at Site 570 is based on the modified "quick look" Archie log analysis technique (Equation 3.10, discussed in Chapter 3 of this thesis). In order to calculate the R_O baseline for the massive gas hydrate zone (247.4-251.4 mbsf) at Site 570, the log-measured deep resistivities from a relatively thin zone (255-257 mbsf) located immediately below the massive gas hydrate was used, which yielded an R_O of 2.8 ohm-m. The resistivity-log data from above the massive gas hydrate zone (0-247.4 mbsf) was not used to calculate the R_O baseline because the resistivity of the overlying sediment is generally lower than the resistivity of the sediments below the massive gas hydrate zone. Because of the

limited range of expected R_O values at Site 570, no further attempts were made to test the sensitivity of the "quick look" method to variations in R_O values. The Archie constant n was set to 1.9386 (reviewed by Pearson et al., 1983). In Figure 5.38, the results of the "quick look" Archie calculations are shown as a water saturation (S_W) log trace for Hole 570. The "quick look" Archie approach yielded a water saturation (S_W) for the massive gas hydrate zone (247.4-251.4 mbsf) at Site 570 of about 13%.

The next resistivity approach used to assess gas-hydrate saturations at Site 570 is based on the "standard" Archie equation (Equation 3.8). At Site 570, the porosity data needed for the "standard" Archie equation were derived from the available downhole-density log and corrected for the presence of gas hydrates. In this section of the thesis, the Archie constants a, m, and n and the resistivity of the pore-waters (R_W) for Site 570 have been determined.

Because of the limited range of sediment porosities within the log-inferred gas-hydrate-bearing zone (240.5-255.5 mbsf) at Site 570, reasonable values for the empirical Archie constants (a and m) could not be calculated. Therefore, the so-called "Humble" values were used for the a (0.62) and m (2.15) Archie constants which are considered applicable for granular matrix systems. The value of the empirical constant n was assumed to be 1.9386 as determined by Pearson et al. (1983). The resistivity of pore-waters (R_W) are mainly a function of the temperature and the dissolved salt content (salinity) of the pore-waters. Pore-water salinity data from Hole 570 are available from the analyses of interstitial water samples collected from recovered cores (Shipboard Scientific Party, 1985). In general, the core-derived interstitial water salinities decrease
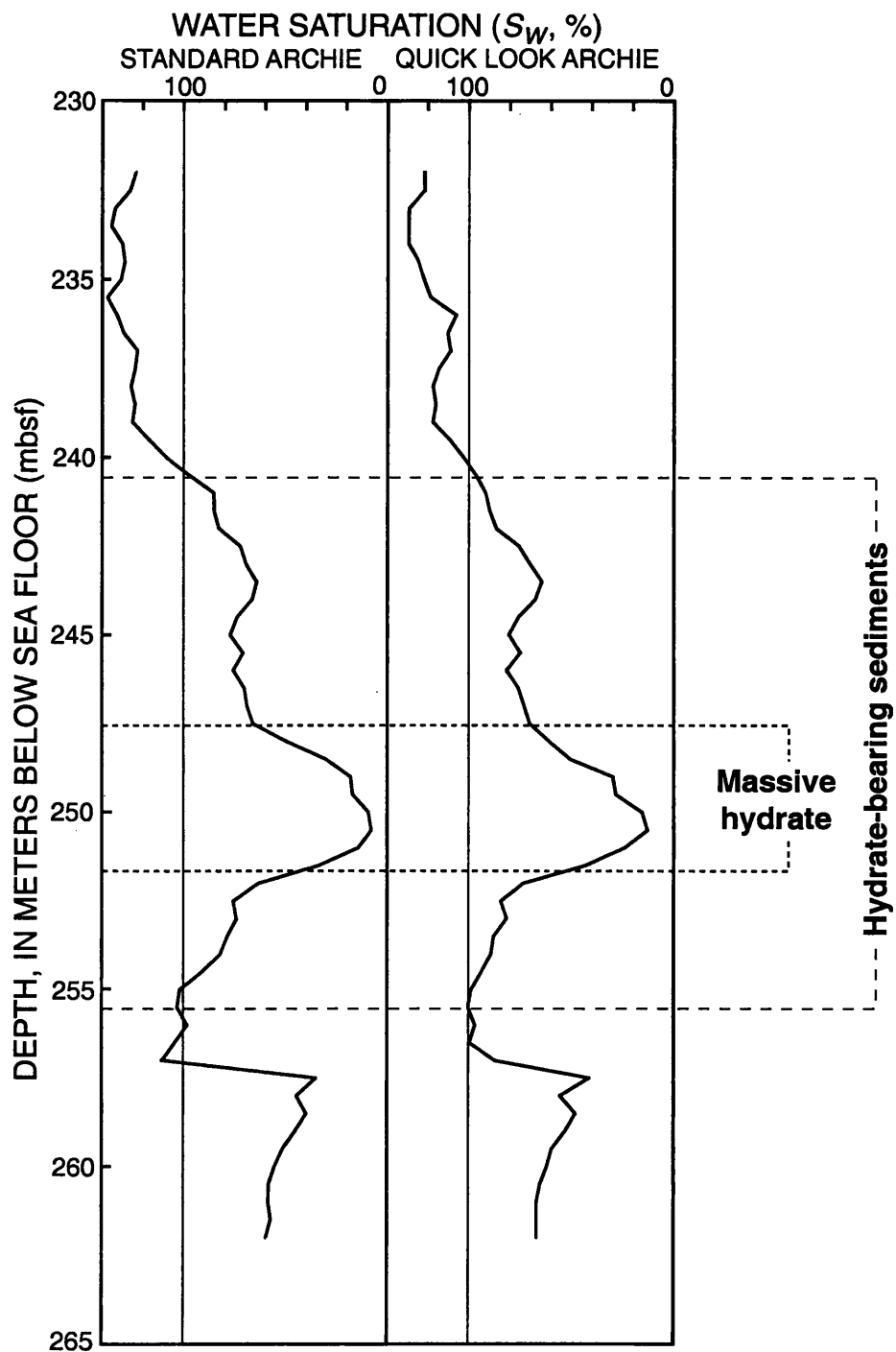
Figure 5.38 "Standard"- and "quick-look"-Archie-derived water saturations (S_W) calculated from the downhole electrical resistivity log at Site 570.

with depth from a maximum value of about 34 ppt near the sediment-water interface to

about 16 ppt near the bottom of the hole. Formation and seabed temperature

measurements at Site 570 have yielded a geothermal gradient of 2.5°C/100m and a

seabed temperature of 4°C. Arps formula (Hearst and Nelson, 1985) was used to

calculate the pore-water resistivity (R_w) at Site 570 from the available core-derived

interstitial water salinities and measured formation temperatures. The calculated pore-

water resistivities (R_w) within the sediments near the depth of the massive gas hydrate

zone (247.4-251.4 mbsf) reach a maximum of about 0.32 ohm-m. Subsequent

calculations, however, revealed that a R_w of 0.32 ohm-m significantly over estimates gas-

hydrate saturations at Site 570. Therefore, the log-calculated R_o of 2.8 ohm-m (discussed

earlier in this section of the thesis) was used to directly calculate the resistivity of the

formation waters within the massive gas hydrate zone. By using the following modified

form of the Humble relation $[R_o = 0.62 \, \varnothing^{-2.15} \, R_w]$ and sediment porosities derived from

the density log it was possible to calculate a pore-water resistivity (R_w) of 1.4 ohm-m for

the thin water-saturated zone (255-257 mbsf) located immediately below the massive gas

hydrate at Site 570 (calculated pore-water salinity of 7 ppt). Given the Archie constants

$(a, m,$ and $n)$ and pore-water resistivities (R_w), it was possible to calculate water

saturations (S_w) from the resistivity log using the "standard" Archie relation. In Figure

5.38, the results of the "standard" Archie calculation are shown as a water saturation (S_w)

log trace along with the results of the "quick look" Archie method for Hole 570. The

"standard" Archie relation at Site 570 yielded an average water saturation (S_w) for the

massive gas hydrate zone (247.4-251.4 mbsf) of about 8%. In general, the "standard"-Archie-calculated water saturations for Site 570 compare favorably with the results of the "quick look" Archie method. No attempt was made to account for the affect of shales (clays) on the Archie-derived water saturations at Site 570.

Acoustic-Log-Calculated Gas-Hydrate Saturations In this section, compressional-wave acoustic-log data from Site 570 have been used along with the Timur (Equation 3.14), modified Wood (Equation 3.15), and Lee (Equation 3.16) weighted average acoustic equations (discussed in Section 3.5 of this thesis) to calculate in-situ gas-hydrate saturations. Because of the lack of shear-wave acoustic downhole-log data, it was not possible to utilize the combined compressional- and shear-wave acoustic relations proposed by Lee et al. (1996), Kuster-Toksöz (Zimmerman and King, 1986), or Dvorkin et al. (1991, 1993) to assess gas-hydrate saturations at Site 570.

The porosity data used in the acoustic gas-hydrate saturation equations were derived from the available downhole density log and corrected for the presence of gas hydrates. The remaining variables in the Timur and Wood equations have been assigned constant values: with a water velocity (V_w) of 1.5 km/sec, sediment matrix velocity (V_m) of 4.37 km/sec, gas hydrate velocity (V_h) of 3.35 km/sec, water density (ρ_w) of 1.05 g/cm^3, sediment matrix density (ρ_m) of 2.65 g/cm^3, and a gas hydrate density (ρ_h) of 0.9 g/cm^3 (Table 3.12). In the Wood equation, the bulk-density (ρ_b) of the formation is determined from the modified three component density equation (Equation 3.2). The bulk compressional-wave velocity of the formation (V_b) is obtained directly from the transit-time well logs.

The final two variables needed before conducting the acoustic gas-hydrate

saturation calculations are the weight factor (W) and the gas-hydrate cementation

exponent (r) in the Lee weighted average equation. In Figure 5.39, corrected density-log-

derived porosities and log-derived compressional velocity data from both within and

surrounding the massive gas hydrate zone at Site 570 have been plotted along with

various curves calculated from the Lee equation (assumed W values of 0.7, 1.0, and 1.2).

In Figure 5.39, it appears that a weight factor, W, of 1.0 best characterizes the sediments

from Site 570, with most of the water-saturated zones falling on or below the Lee

equation (W=1.0) water baseline. A gas-hydrate cementation exponent (r) of r=1 was

selected for Site 570. In Figure 5.40, the results of the Timur, Wood, and Lee acoustic

velocity calculations are shown as gas-hydrate saturation log traces for Hole 570. As

shown in Figure 5.40, both the Timur and Lee equations yielded average gas-hydrate

saturations (S_h) for the Site 570 massive gas hydrate zone (247.4-251.4 mbsf) of about

97%. Further comparisons of the Lee- and Timur-derived gas-hydrate saturations,

however, reveal that the Timur equation more accurately predicts the occurrence of the

expected water-saturated zones both above and below the massive gas hydrate zone

(247.4-251.4 mbsf) at Site 570. The Wood equation yielded for the most part

unreasonable gas-hydrate saturations (S_h).

Gas-Hydrate Saturation Calculations -- Summary In general, the "quick look"

and "standard" Archie electrical resistivity methods yielded gas-hydrate saturations (S_h)

for the massive gas hydrate zone (247.4-251.4 mbsf) at Site 570 ranging from about 87 to

92 percent. The Lee and Timur acoustic equations generally yielded gas-hydrate
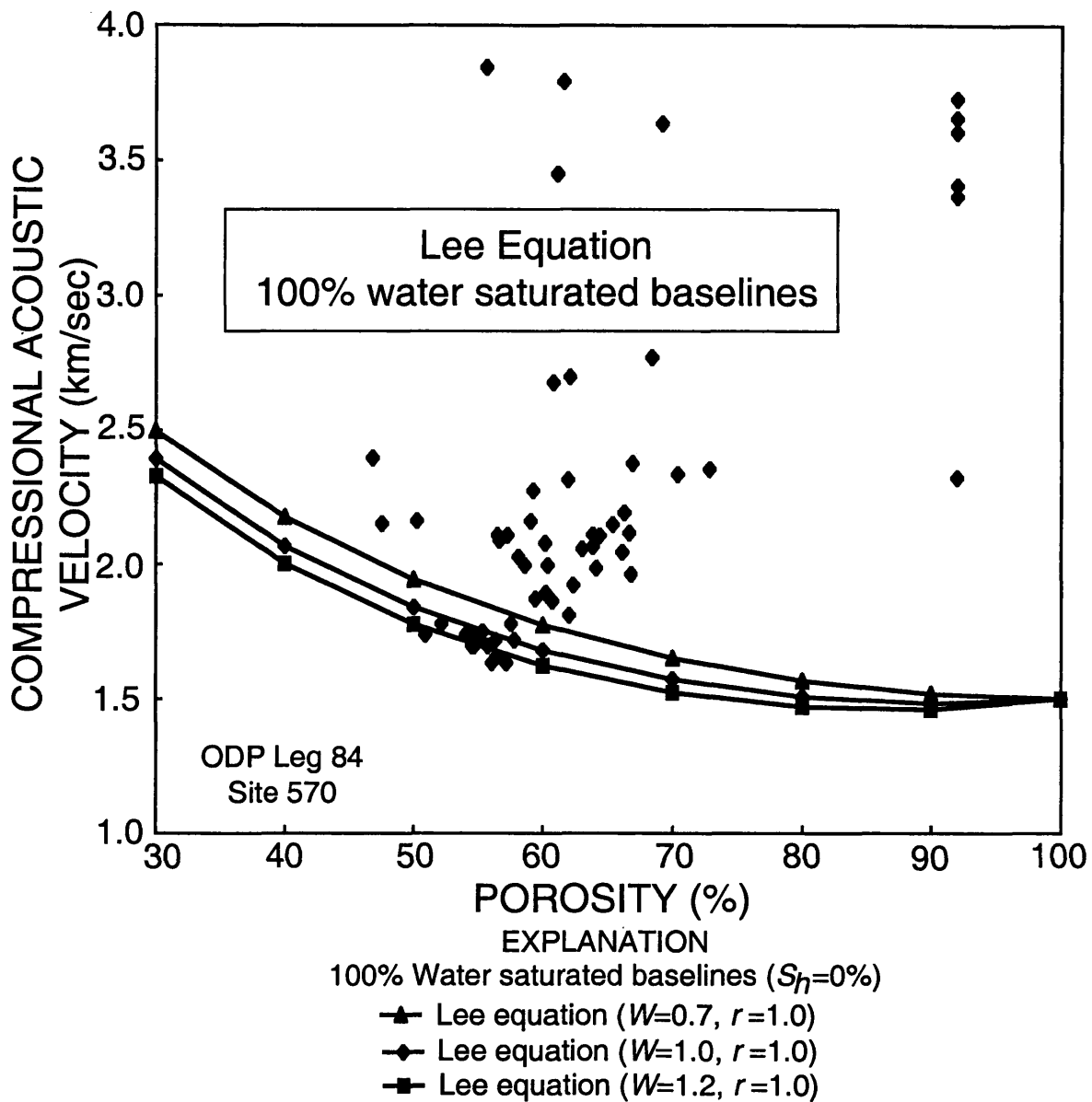
Figure 5.39 Graph showing downhole-log-derived compressional-wave velocities (V_p) and density-derived porosities for both gas-hydrate and water-saturated sediments at Site 570. Also shown are several 100% water-saturated porosity-velocity curves predicted from a series of Lee (Equation 3.16) compressional-wave (V_p) acoustic equations that assume different Lee weight factors (W).
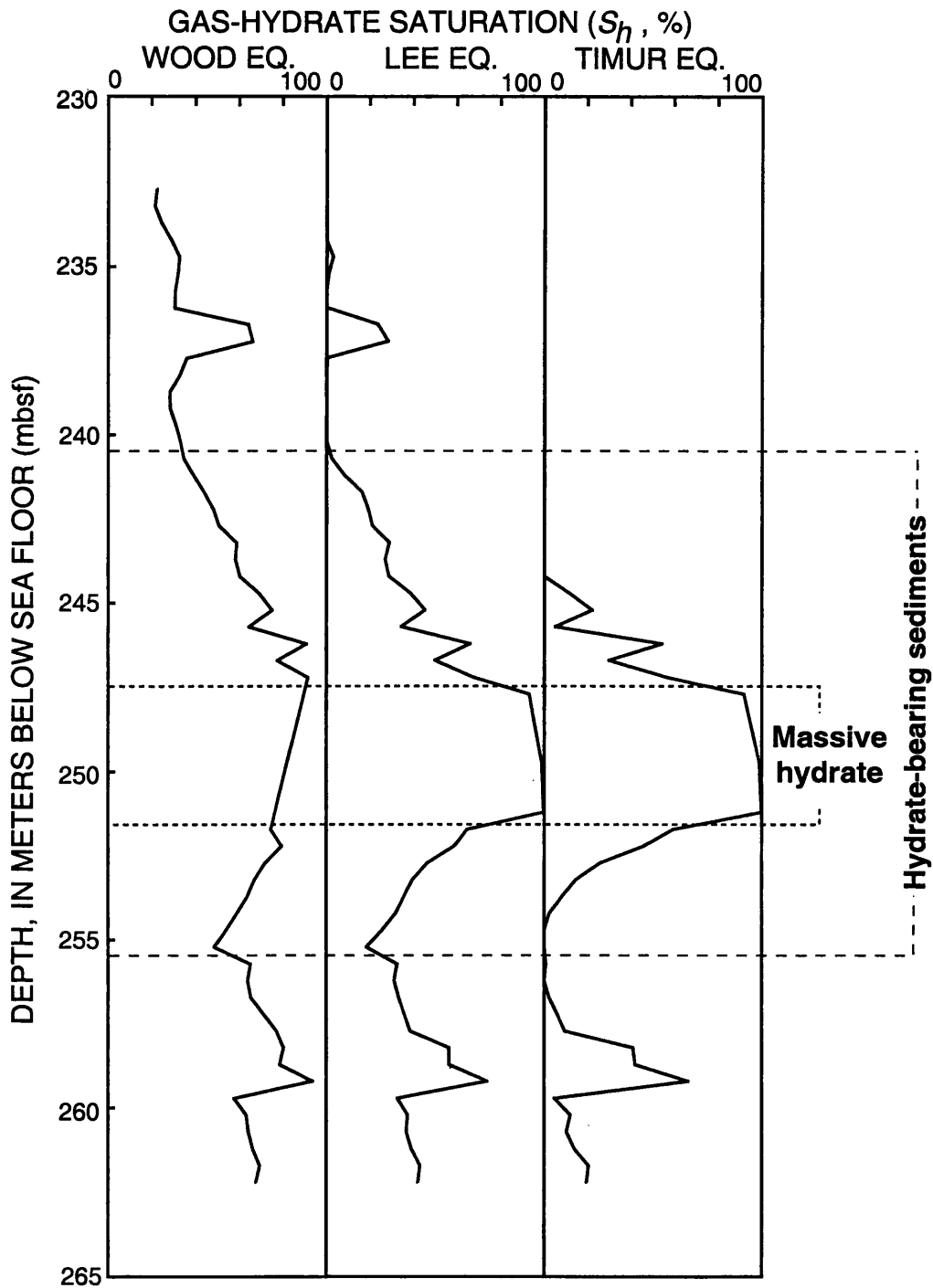
Figure 5.40 Gas-hydrate saturations (S_h) calculated from the downhole compressional-wave acoustic velocity log at Site 570. The results of the modified Wood (Equation 3.15), Lee (Equation 3.16), and Timur (Equation 3.14) acoustic equations are shown.

saturations (S_h) slightly greater than those calculated from the electrical-resistivity-log data; with the Lee and Timur acoustic log-derived gas-hydrate saturations averaging about 97%. The modified Wood acoustic equation yielded erroneous gas-hydrate saturations which did not compare favorably with saturations calculated by other methods.

5.4.7 Volume of Gas

In this section, five "reservoir" parameters (Table 5.19) needed to calculate the volume of gas associated with the massive gas hydrate zone (247.4-251.4 mbsf) at Site 570 are assessed. The lateral extent of the massive gas hydrate zone at Site 570 is unknown; therefore, the following "resource" assessment deals with calculating only the volume of gas hydrate and associated free-gas within a one square kilometer area surrounding Hole 570 (Table 5.19). For this "resource" assessment, the thickness of the gas-hydrate-bearing sedimentary section at Site 570 was defined to be the total thickness of the downhole-log-inferred massive gas hydrate zone, which is 4-meters-thick (Table 5.19). The corrected density-log-derived sediment porosities in the massive gas hydrate zone average 92% (Table 5.19). Gas-hydrate saturations in the massive gas hydrate zone, calculated from the "standard" Archie relation (Figure 5.38), average 92% (Table 5.19). In this assessment, a hydrate number of 6.325 (90% gas filled clathrate) was assumed, which corresponds to a gas yield of 164 m^3 of methane (at STP) for every cubic meter of gas hydrate (Collett, 1993b). The above calculations indicate that the potential volume of gas within the massive gas hydrate zone (247.4-251.4 mbsf) at Site 570 is about

Table 5.19 Volume of natural gas within the downhole-log-inferred gas-hydrate occurrence at Site 570.

Site identification	Depth of massive gas hydrate zone (mbsf)	Thickness of massive gas hydrate zone (m)	"Sediment" porosity (%)	Gas-hydrate saturation (%)	Volume of hydrate per square km (m^3)	Volume of gas within hydrate per square km (m^3)*
570	247.4-251.4	4	92	92	3,385,600	555,238,400

*Gas volume calculation assumes a hydrate number of 6.325 (90% gas filled clathrate), 1 m^3 of gas hydrate = 164 m^3 free-gas at STP.

555,238,400 cubic meters of gas per square kilometer (Table 5.19). For comparison

purposes, Mathews (1986) determined that the log-inferred massive gas hydrate zone

(assuming a thickness of 3.44 m) at Site 570 contains about 627,000,000 cubic meters of

gas per square kilometer, which is relatively near the value calculated in this study.

5.5 North Slope--Alaska

5.5.1 Introduction and Regional Geology

As discussed in Section 1.4.1 of this thesis, the occurrence of natural gas hydrate

on the North Slope of Alaska was confirmed in 1972 with data from the Northwest Eileen

State-2 well located in the northwest part of the Prudhoe Bay Oil Field. Studies of

pressurized core samples, downhole logs, and the results of formation production testing

have confirmed the occurrence of three gas-hydrate-bearing stratigraphic units in the

Northwest Eileen State-2 well (reviewed by Collett, 1993b). Gas hydrates are also

inferred to occur in an additional 50 exploratory and production wells in northern Alaska

based on downhole-log responses calibrated to the known gas-hydrate occurrences in the

Northwest Eileen State-2 well. Many of these wells have multiple gas-hydrate-bearing

units, with individual occurrences ranging from 3- to 30-m-thick. Most of these well-log-

inferred gas hydrates occur in six laterally continuous sandstone and conglomerate units;

all these gas hydrates are geographically restricted to the area overlying the eastern part

of the Kuparuk River Oil Field and the western part of the Prudhoe Bay Oil Field

(Figures 5.41 and 5.42). The six gas-hydrate-bearing sedimentary units have each been

assigned a reference letter (Units A through F); Unit A is stratigraphically the deepest
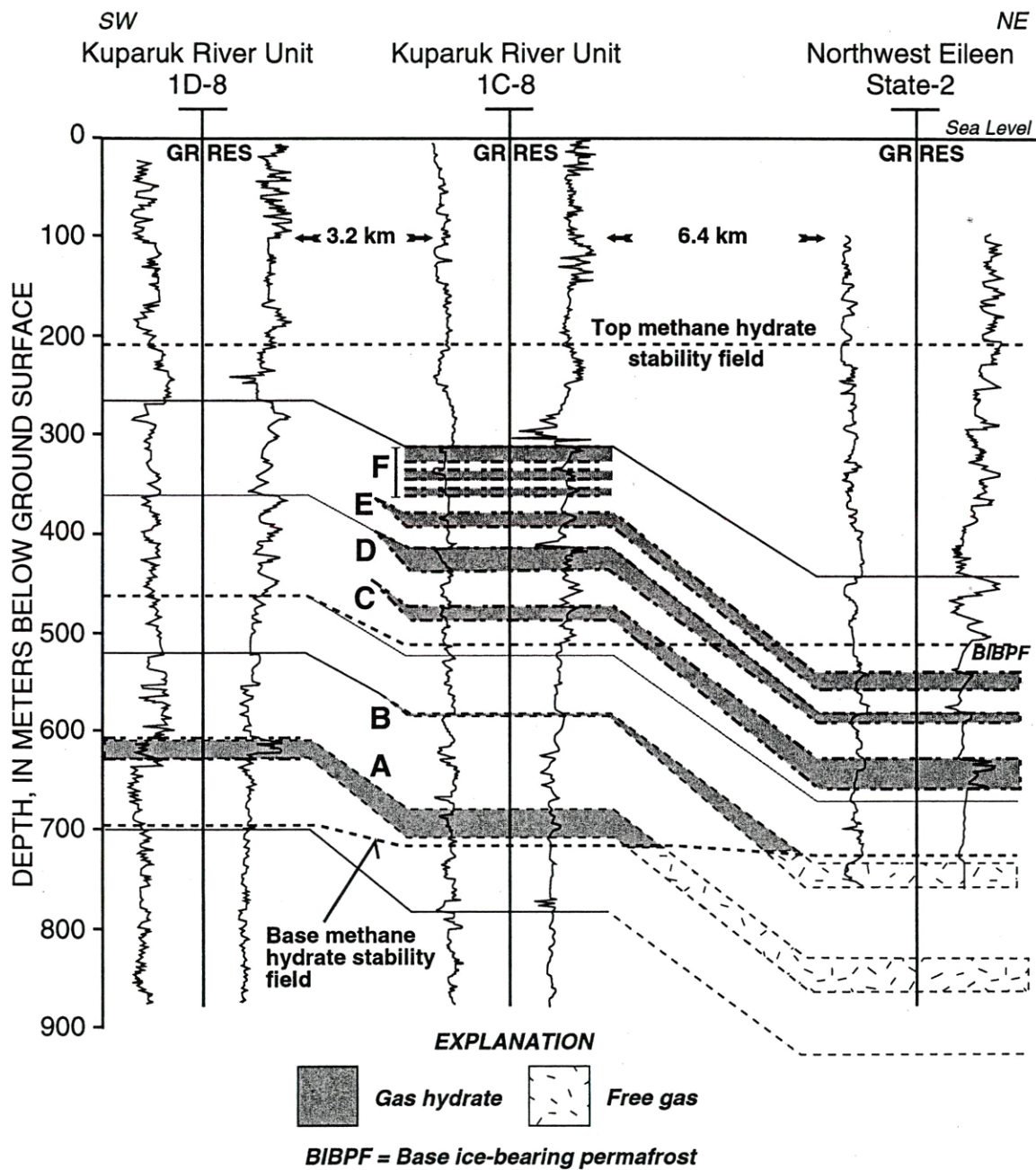
Figure 5.41 Cross section showing the lateral and vertical extent of gas hydrates and underlying free-gas occurrences in the Prudhoe Bay-Kuparuk River area in northern Alaska. See Figure 5.42 for location of cross section. The gas-hydrate-bearing units are identified with the reference letters A through F (modified from Collett, 1993b).
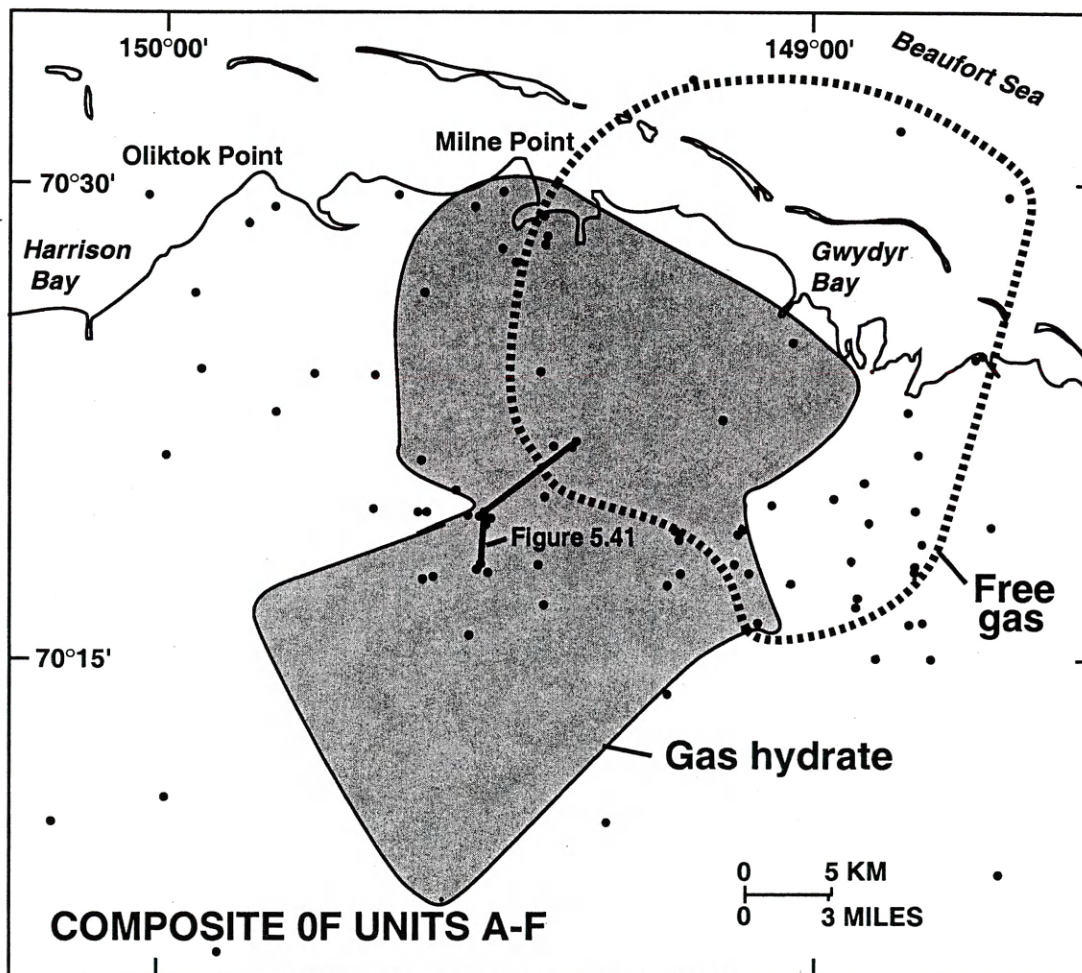
Figure 5.42 Composite map of all six gas-hydrate/free-gas units (Units A-F) from the Prudhoe Bay-Kuparuk River area in northern Alaska. Also shown is the location of the cross section in Figure 5.41.

(Figure 5.41). Three-dimensional seismic surveys and downhole logs from wells in the western part of the Prudhoe Bay Oil Field indicate the presence of several large free-gas accumulations trapped stratigraphically downdip below four of the log-inferred gas hydrate units (Figures 5.41 and 5.42; Units A through D). The total mapped area of all six gas-hydrate occurrences is about 1,643 km^2; the areal extent of the individual units range from 3 to 404 km^2. The volume of gas within the gas hydrates of the Prudhoe Bay-Kuparuk River area is estimated to be about 1.0 to 1.2 trillion cubic meters, or about twice the volume of conventional gas in the Prudhoe Bay Field (Collett, 1993b).

Previous North Slope studies (Collett, 1983; Collett et al., 1988; Collett, 1993b) indicate that the Prudhoe Bay-Kuparuk River gas-hydrate accumulation is restricted to Tertiary age sediments of the Sagavanirktok Formation. The Sagavanirktok Formation consists of shallow-marine shelf and delta-plain deposits composed of sandstone, shale, and conglomerate whose provenance is the Brooks Range, to the south. In the Prudhoe Bay area, the Sagavanirktok Formation thickens from southwest (about 1,000 m) to northeast (about 2,000 m), and conformably overlies marine shale of the Canning Formation. The regional structure of the Sagavanirktok Formation in the Prudhoe Bay area is a gentle (1°-2°) northeasterly-dipping monocline. The Sagavanirktok Formation includes the informally named West Sak and Ugnu sands. These oil-bearing horizons have been extensively described by Werner (1987) and are estimated to contain more than approximately 6 million metric tons of in-place oil.

As discussed in Section 1.4.1 of this thesis, the confirmed gas-hydrate-bearing stratigraphic units (Units C, D, and E) in the Northwest Eileen State-2 well are an ideal

starting point for the development of gas hydrate well-log evaluation techniques and have been the focus of numerous well-log related studies (Collett, 1983; Mathews, 1986; Collett et al., 1988; Collett, 1993b). The completed well-log studies from the Northwest Eileen State-2 well, however, are mostly qualitative in nature and are based on untested petroleum industry evaluation procedures as described in Section 1.4.3 of this thesis. In this study, therefore, the focus of the interpretative efforts was on conducting a detailed quantitative well-log study of the three gas-hydrate-bearing units (Units C, D, and E) in the Northwest Eileen State-2 well.

In the following section, the available downhole-log data has been used to calculate sediment porosities and gas-hydrate saturations within the three gas-hydrate-bearing units delineated by the Northwest Eileen State-2 well. The available downhole data have also been used to re-calculate the volume of gas within a portion of the Prudhoe Bay-Kuparuk River gas-hydrate accumulation.

5.5.2 Downhole-Logging Program

Northwest Eileen State-2 was drilled to a total depth of 916.7 m. After setting the permafrost casing to a depth of 511 m, the deeper gas-hydrate-bearing stratigraphic section was drilled and cored (21.6 cm diameter drill bit) with chilled (-5 to +1 °C) Invermul mud to prevent gas hydrate decomposition. The sub-permafrost, gas-hydrate-bearing stratigraphic section in the Northwest Eileen State-2 well was surveyed with three individual downhole logging runs (Table 5.20): Run-1 consisted of the dual induction-laterolog (DIL) and gamma-ray (GR) tools; Run-2 included the borehole

Table 5.20 Downhole-logging program within the sub-permafrost portion of the Northwest Eileen State-2 well.

Total hole penetration (m)	Log run	Logging string	Interval logged (m)
916.7	1	DIL/GR	510.4-915.1
	2	BHC/GR	508.6-913.0
	3	FDC/CALI/SNP/ GR	508.6-915.8

compensated acoustic transit-time (BHC) and gamma-ray (GR) tools; and Run-3

consisted of the compensated formation density (FDC), caliper (CALI), sidewall neutron

porosity (SNP), and gamma-ray (GR) tools.

The quality of all the downhole logs from the Northwest Eileen State-2 well is

excellent. The entire borehole shows minor evidence of enlargement on the caliper from

the compensated formation density log (Figure 5.43); because the borehole diameter

variation is small, the borehole corrections for the logs from the Northwest Eileen State-2

well were neglected in this study.

The absolute depths, relative to ground level, for all of the logs from the

Northwest Eileen State-2 well were fixed by subtracting 7.44 m (height above ground

level of the Kelley Bushing on the drilling rig) from the downhole-measured log depths.

The ground surface at the location of the Northwest Eileen State-2 well is 11.9 m above

sea level.

5.5.3 Logging Units and Gas-Hydrate Occurrences

The Northwest Eileen State-2 well actually drilled five (Units B-F) of the six

Prudhoe Bay-Kuparuk River gas-hydrate-bearing stratigraphic units described in Collett

(1993b). As previously discussed in this thesis, Units C, D, and E were determined to

contain gas hydrates in the Northwest Eileen State-2 well, while Unit B was determined

to contain both water and free-gas (no gas hydrates), and Unit F is saturated with only

water and ice (no gas hydrates). During drilling of the Northwest Eileen State-2 well,

Unit B was cored and subjected to a drill-stem test which yielded critical reservoir data
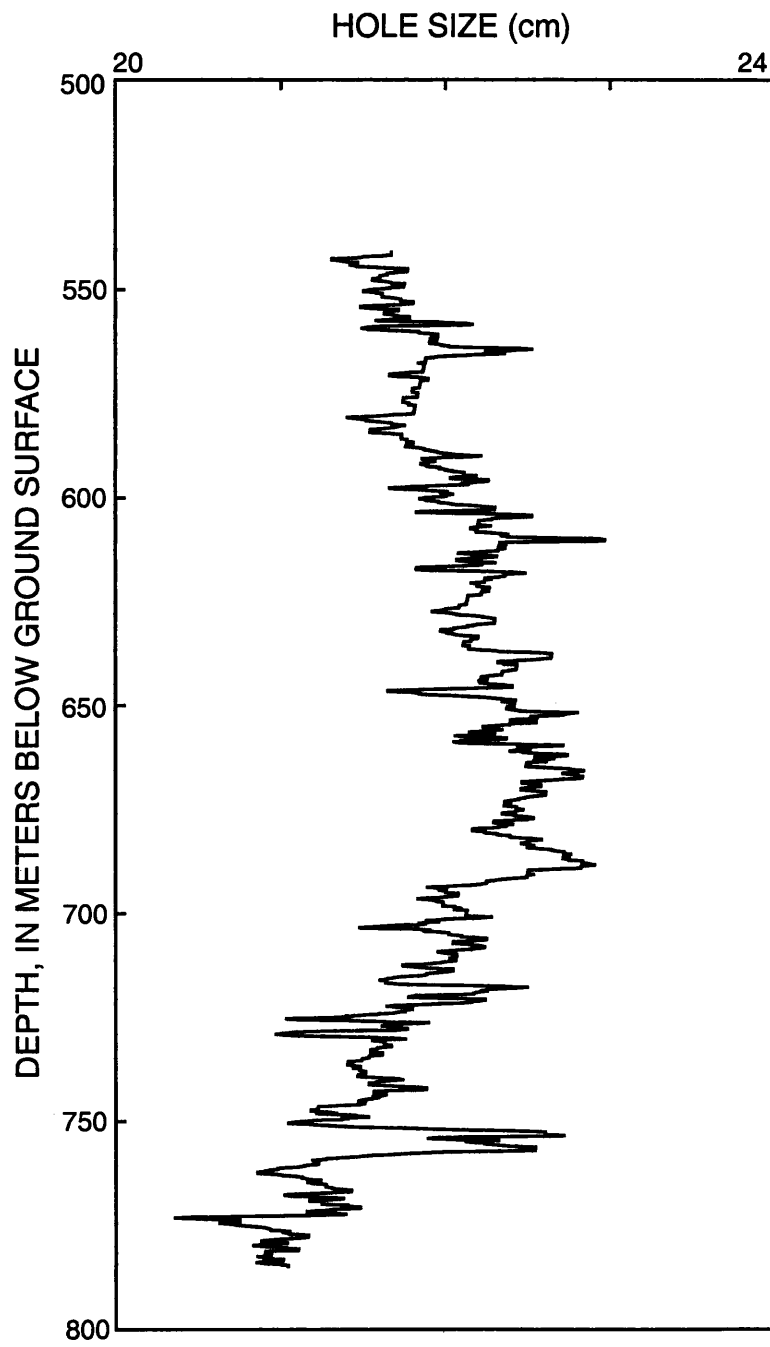
Figure 5.43 Caliper log recorded from the compensated formation density (FDC) tool in the Northwest Eileen State-2 well.

from a non-gas-hydrate-bearing sedimentary unit in close proximity to the three overlying gas-hydrate-bearing units (Units C, D, and E). Therefore, the following description of the logged gas hydrate Units in the Northwest Eileen State-2 well also includes a description of the non-gas-hydrate-bearing Unit B (Table 5.21, Figure 5.44). In the following logging unit descriptions, data from coring, downhole logging, and production testing in the Northwest Eileen State-2 well have been used to assess the local occurrence and distribution of gas hydrates.

Unit E (564.0-580.8 m) The first evidence of gas hydrates in the Northwest Eileen State-2 well was encountered while attempting to take the first core (Core-1) in Unit E. The first core attempt in Unit E failed to recover any sediments, which was attributed to "solid" gas hydrate severely damaging the "unconsolidated" core catchers used on the first coring run. Positive confirmation of gas hydrates in Unit E was made with Core-2 (second core run in Unit E) which exhibited classic gas hydrate pressure responses when tested at the surface (see Section 1.4.1 of this thesis for a description of the Northwest Eileen State-2 gas hydrate pressure core experiments). It was determined that Core-2 contained about 1.5 m of very-fine grained sandstone in a mudstone matrix. Unit E is characterized by relatively high electrical resistivities (ranging from 20 to 70 ohm-m) and acoustic velocities (ranging from 2.0 to 2.8 km/sec), while the gamma-ray, formation density, and neutron porosity measurements in Unit E are indicative of a sandstone reservoir. Unit E was not subjected to formation production testing.

Unit D (602.7-609.4 m) Unit D was cored over the depth interval from 606.7 to 609.8 m (Core-3). A total of only 1.2 m of core was recovered, the lithology of which

Table 5.21 Depth to the top and bottom of the downhole-log-identified Logging Units in the Northwest Eileen State-2 well (Figure 5.44).

Logging Unit	Depth to top of Logging Unit (m)	Depth to bottom of Logging Unit (m)
B	752.1	773.7
C	651.5	680.5
D	602.7	609.4
E	564.0	580.8
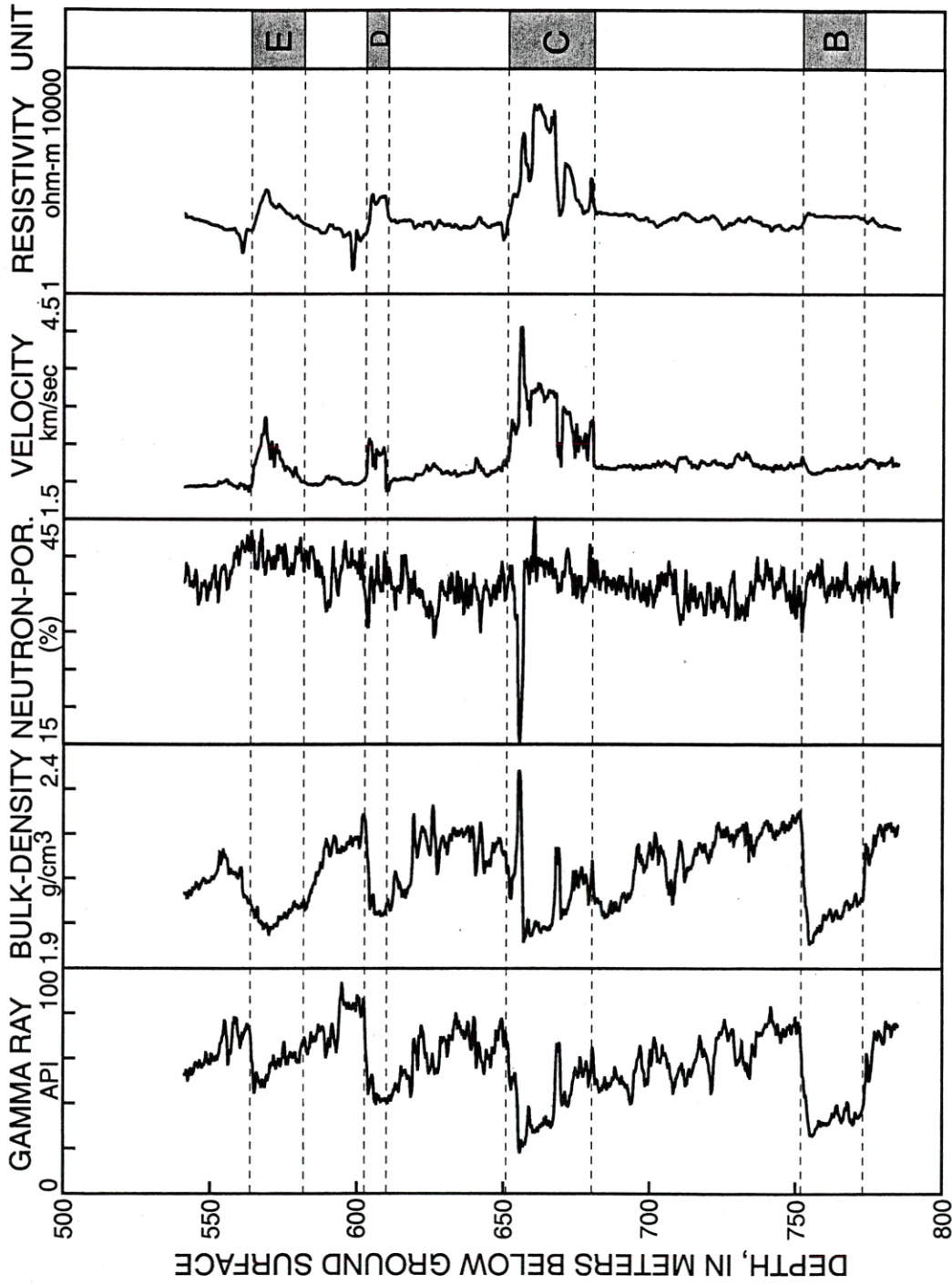
Figure 5.44 Downhole logs from the Northwest Eileen State-2 well. Data shown include the natural gamma ray log, bulk-density, neutron porosity, acoustic velocity, and electrical resistivity data. Also shown are the depths of Units B, C, D, and E (Table 5.21).

was described as an unconsolidated very-fine grained sandstone. Coring in Unit D failed

to yield any direct information on the occurrence of gas hydrates. Similar to Unit E, Unit

D is characterized by both high electrical resistivities (ranging from 20 to 60 ohm-m) and

acoustic velocities (ranging from 2.0 to 2.6 km/sec). The gamma-ray, formation density,

and neutron porosity measurements from Unit D, however, reveal slightly better reservoir

conditions in comparison to Unit E. Unit D was not subjected to formation production

testing.

Unit C (651.5-680.5 m) Two attempts were made to core Unit C. The second

core attempt (Core-5) failed; however, the first core taken from Unit C, Core-4, has been

the focus of numerous gas hydrate studies (Collett, 1983; Mathews, 1986; Collett et al.,

1988; Collett, 1993b). The results of the pressure test on Core-4 (Figure 1.4), described

in Section 1.4.1 of this thesis, is often used as an example of how a gas-hydrate-bearing

sediment core should behave. Upon further examination, it was determined that Core-4

consisted of a 1.7-m-long core of a very-fine grained sandstone. The downhole-log

responses in Unit C have also been the focus of numerous gas hydrate studies. Included

in Section 1.4.1 of this thesis is a detailed review of the downhole-log responses within

Unit C. Of note, however, is the conspicuous low neutron porosity and high formation

density zone (654.6-656.7 m) within the upper part of Unit C, which is likely due to the

presence of a "hard" well cemented zone (Figure 5.44). After completing the Northwest

Eileen State-2 well, Unit C was perforated and tested. A drill-stem test of the perforated

interval from 655 to 663 m flowed and swabbed gas at a maximum rate of 112 m^3/day.

Unit B (752.1-773.7 m) Two attempts were made to core Unit B, which resulted

in the recovery of slightly over 5.9 m of core. Subsequent tests of the recovered cores

yielded evidence of only free-gas and water (no gas hydrates). The lithology of the cores

recovered from Unit B was similar to the lithology of sediments in Units C and D, with

most of the core described as a very-fine grained sandstone. Unit B is characterized by

low electrical resistivities (ranging from 20 to 25 ohm-m) and acoustic velocities

(averaging about 2.2 km/sec) indicative of water- and gas-saturated sediments (no

downhole-log evidence of gas hydrate). After well completion, Unit B was also

perforated and drill-stem tested, however, only a small amount of formation water was

recovered.

5.5.4 Porosity Calculations

In the Northwest Eileen State-2 well, the compensated formation density and

neutron porosity logs were used to calculate sediment porosities. Because of the high

quality of the downhole logs from the Northwest Eileen State-2 well, it was also possible

to use standard crossplotting techniques to combine and compare the results of the

density- and neutron-log porosity calculations. No core-derived physical property or

porosity data are available from the Northwest Eileen State-2 well.

Density-Log Porosities As previously discussed, the caliper log (Figure 5.43)

from the compensated formation density tool in the Northwest Eileen State-2 well reveals

an almost constant borehole diameter throughout all three gas-hydrate-bearing

stratigraphic units (Units C, D, and E), which has yielded high quality formation density

measurements. The compensated-formation-density-log measurements of bulk-density in the sub-permafrost (below a depth of about 500 m) part of the Northwest Eileen State-2 well (Figure 5.44) are relatively consistent with depth. The three gas-hydrate-bearing stratigraphic units (Units C, D, and E) are characterized by a limited range of measured densities, ranging from about 2.0 to 2.1 g/cm^3.

The unedited bulk-density-log (ρ_b) measurements were used to calculate sediment porosities ($\varnothing$) in the Northwest Eileen State-2 well using the standard density-porosity relation (Equation 3.1) discussed in Chapter 3 of this thesis. Within Equation 3.1, the density of the formation waters (ρ_w) was assumed to be constant and equal to 1.00 g/cm^3 and the grain/matrix densities (ρ_m) were assumed to equal 2.65 g/cm^3. The density-log-calculated porosities for Units B-E in the Northwest Eileen State-2 well average about 37% (Figure 5.45).

Neutron Porosity Log The sidewall (epithermal) neutron porosity log from the Northwest Eileen State-2 well (Figure 5.46) yielded sediment porosities for the most part ranging from an average value in Unit B (at a depth of about 763 m) of about 36% to about 40% in Unit E (at a depth of about 572 m). The neutron-log-derived porosities will be further discussed and compared to the density-log-derived porosities in the following section of this thesis.

Comparison of Log-Derived Porosities In conventional well-log studies it is common to combine and compare porosity data from different sources in order to determine accurate porosities and infer lithologies in complex geologic systems. Crossplots of porosities from various sources, including neutron porosity and density
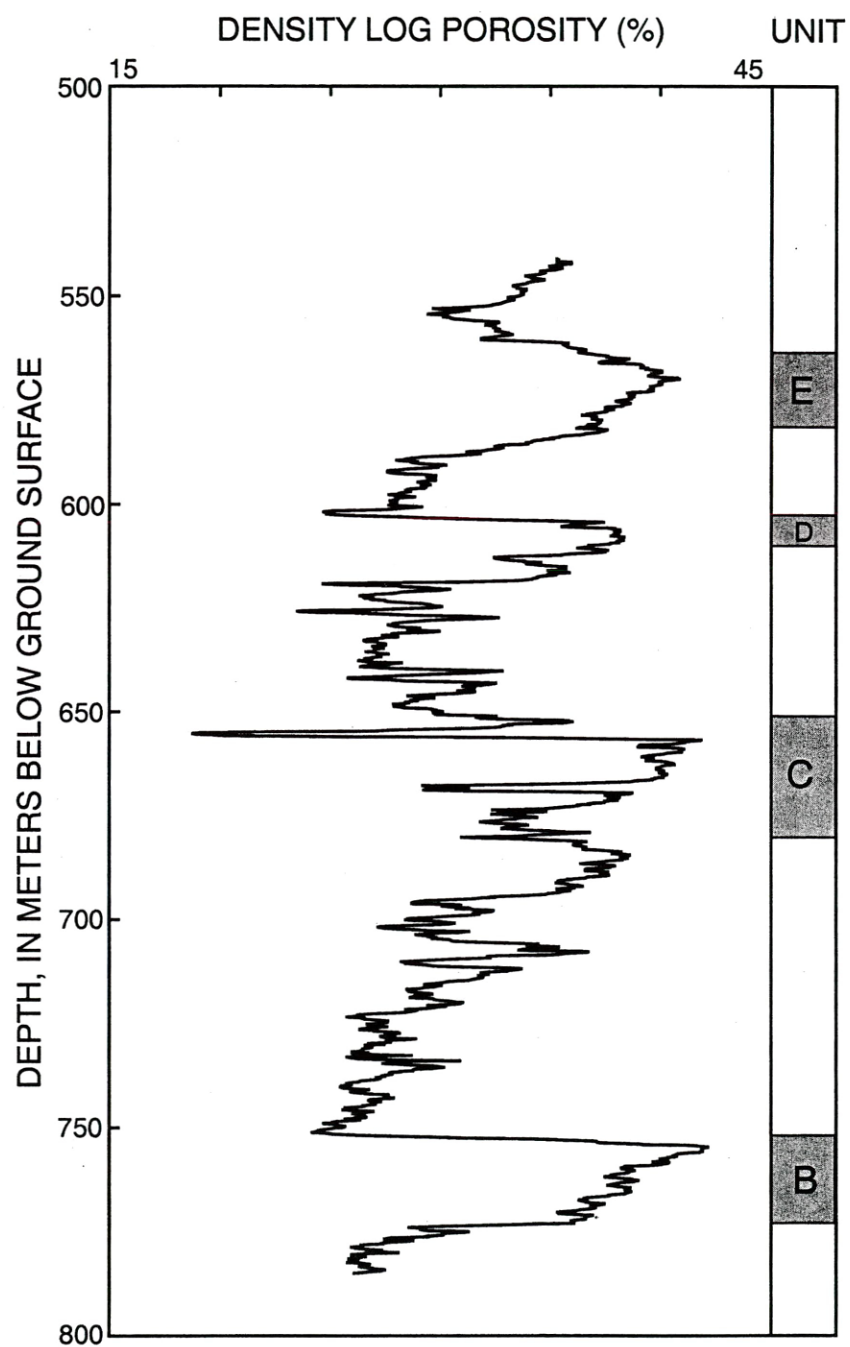
Figure 5.45 Sediment porosities derived from the downhole density log (FDC) in the Northwest Eileen State-2 well.
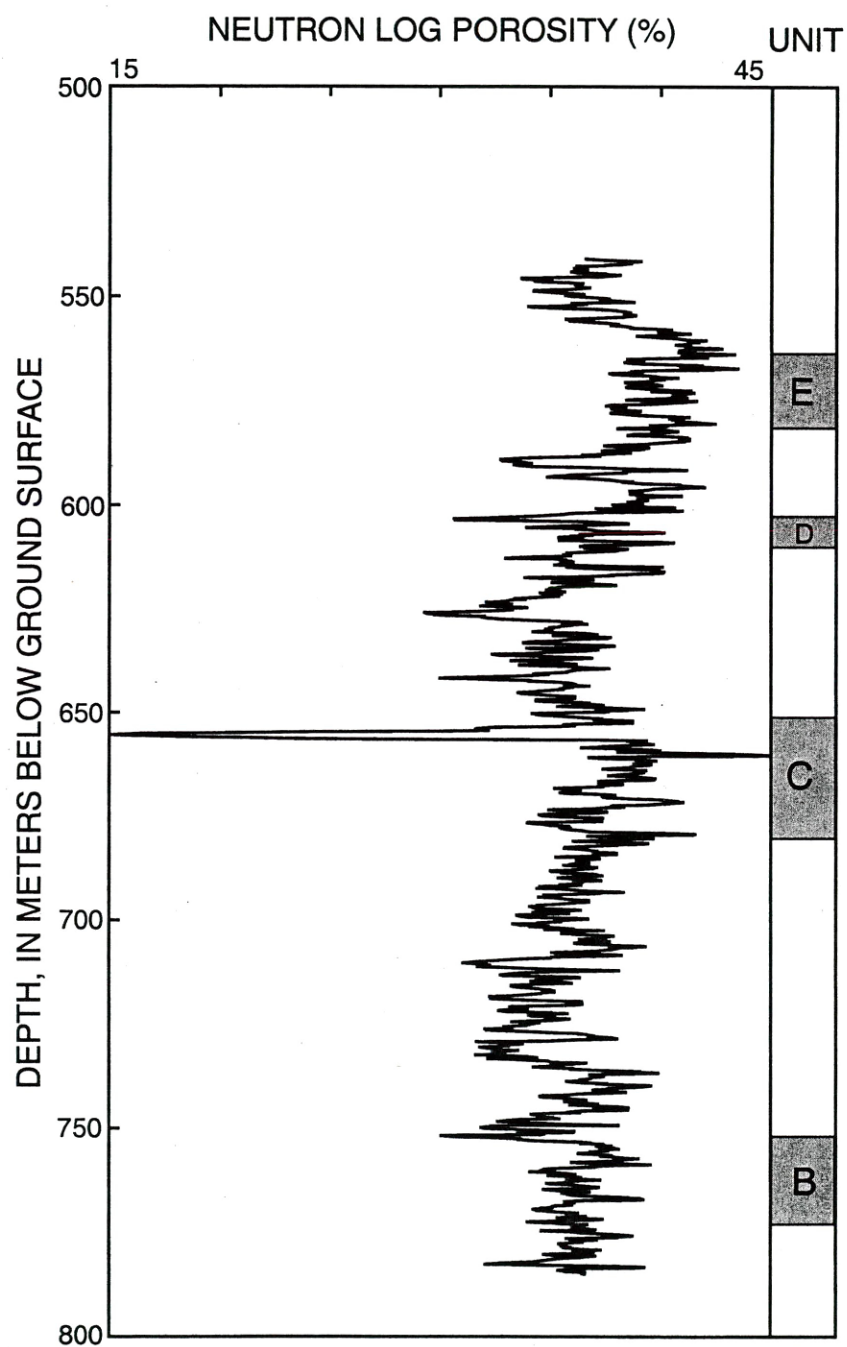
Figure 5.46 Sediment porosities derived from the downhole neutron porosity log (SNP) in the Northwest Eileen State-2 well.

logs, can be used to identify and quantify the affects of shale (clay), free-gas, and gas

hydrates on well-log-calculated porosities. In Figure 5.47a-d, crossplots of the neutron-

and density-log-derived porosities for the three gas-hydrate-bearing (Units C, D, and E)

and the one free-gas-bearing (Unit B) stratigraphic units in the Northwest Eileen State-2

well have been individually depicted. Neutron- and density-log-calculated porosities for

a 100% water-saturated "clean" (shale/clay free) sandstone reservoir should yield the

same results and plot along the "clean water-bearing matrix line" in a neutron-density

porosity crossplot.

A review of the neutron-density porosity crossplots in Figure 5.47a-d, however,

reveals several significant departures in the plotted porosity data from the "clean water-

bearing matrix line". The cause of the observed discrepancies in the plotted neutron-

density-log-derived porosities in Figure 5.47a-d can be individually evaluated. For

example, the occurrence of shale (clay) in an otherwise clean water-bearing sandstone

reservoir would cause an apparent reduction in the density-derived porosities and an

increase in neutron-derived porosities. The effect of free-gas on the neutron and density-

log measurements are opposite to that of the shale (clay) effect. As discussed in Chapter

3 of this thesis, the occurrence of gas hydrate at relatively high concentrations ($S_h > 50\%$)

will result in minor but measurable shifts to higher neutron- and density-derived apparent

porosities. In the neutron-density porosity crossplot for Unit E (Figure 5.47a), a large

number of the plotted porosities fall below the clean water-bearing matrix line, which is

likely due to the presence of a small amount of clay within the mudstone matrix as

described in the recovered core (Core-2). The gamma-ray log, which can be used to
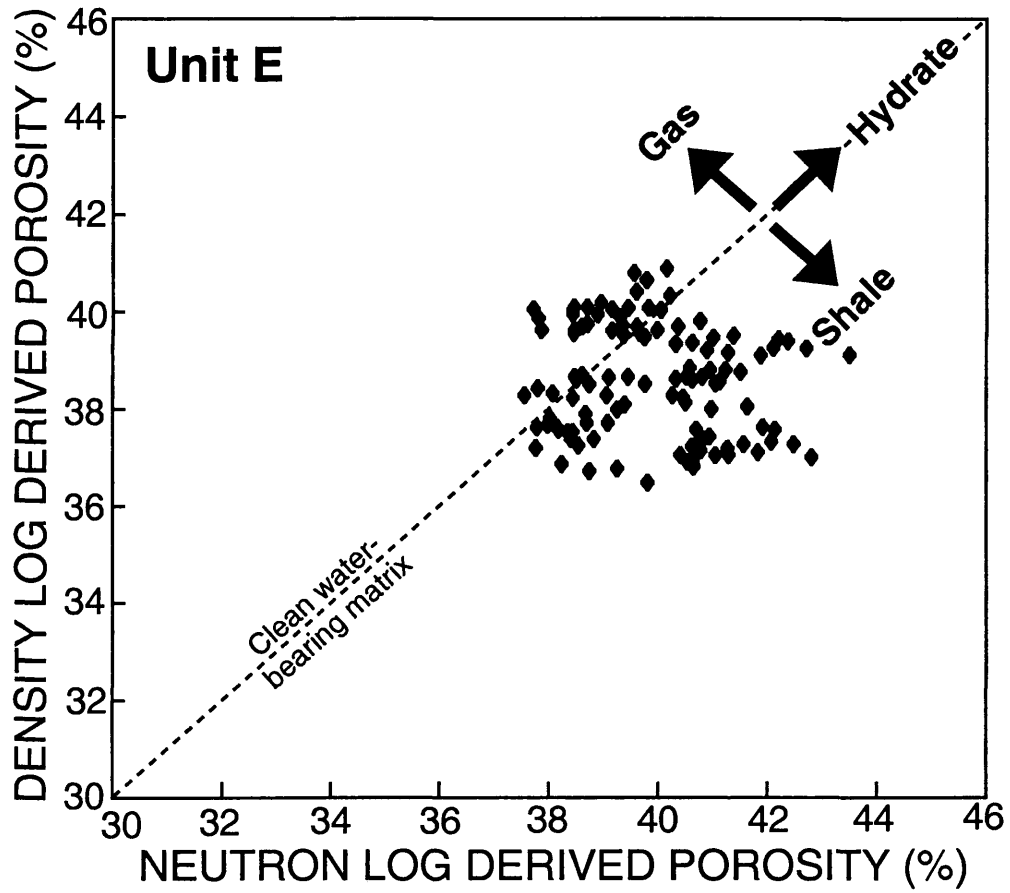
Figure 5.47a Crossplot of the neutron- and density-log-derived sediment porosities for Unit E in the Northwest Eileen State-2 well.
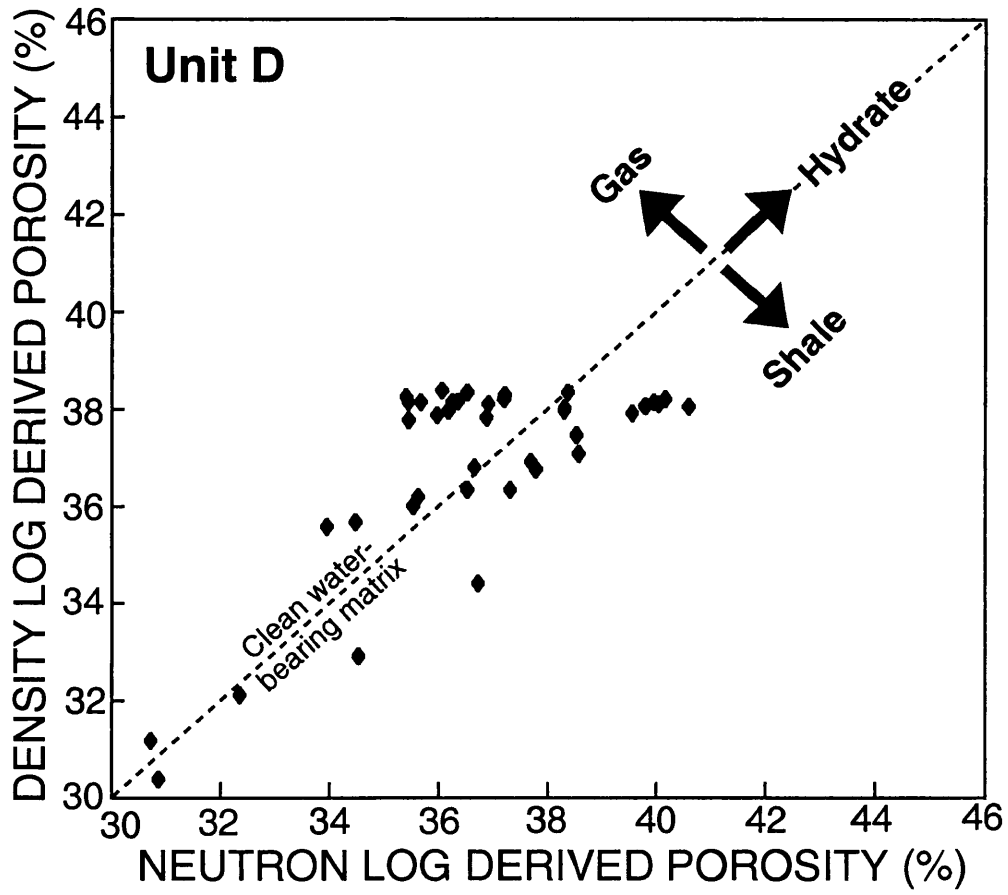
Figure 5.47b Crossplot of the neutron- and density-log-derived sediment porosities for Unit D in the Northwest Eileen State-2 well.
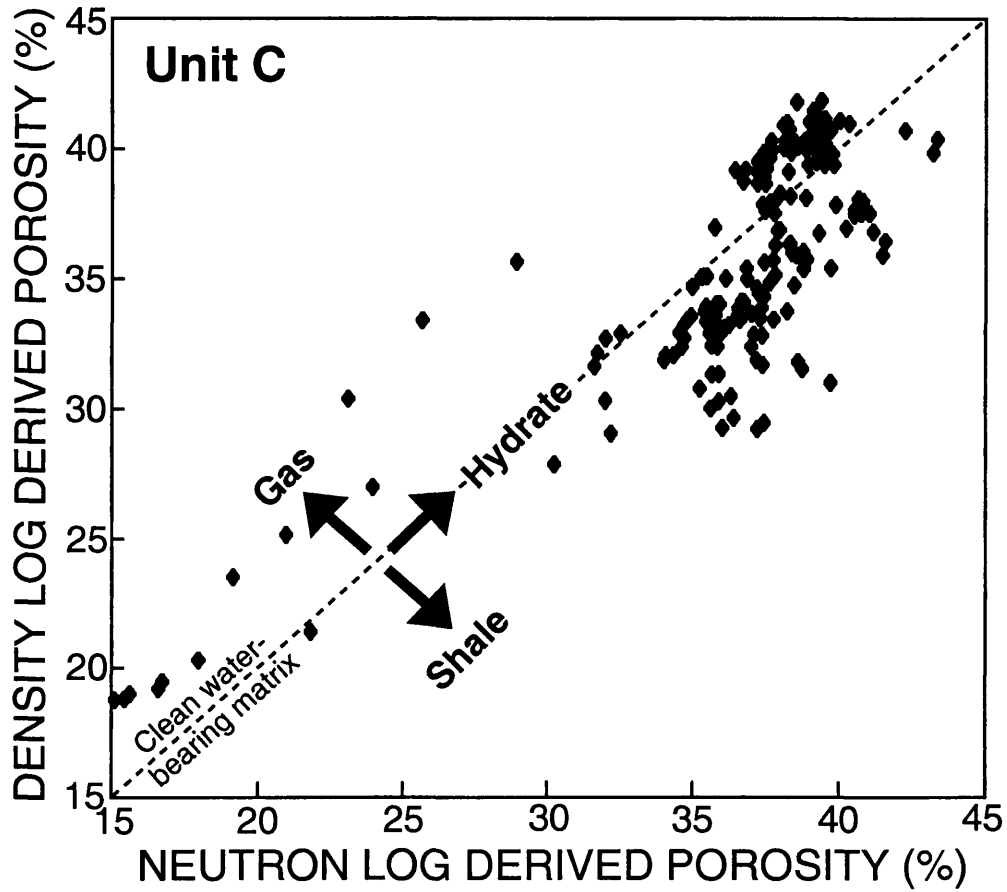
Figure 5.47c Crossplot of the neutron- and density-log-derived sediment porosities for Unit C in the Northwest Eileen State-2 well.
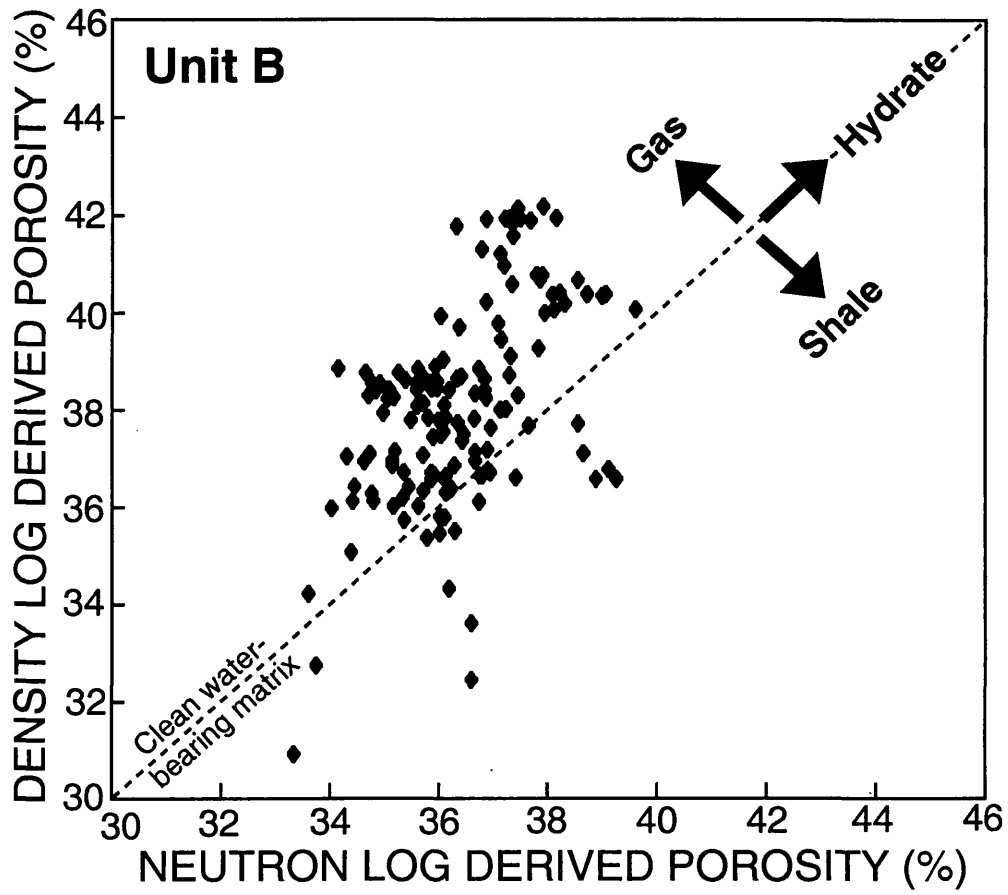
Figure 5.47d Crossplot of the neutron- and density-log-derived sediment porosities for Unit B in the Northwest Eileen State-2 well.

assess the shale (clay) content of a sedimentary section, indicates that Unit E contains relatively more clay than the other gas-hydrate-bearing stratigraphic units (Units C and D). The neutron- and density-log-derived porosities for Unit D generally fall along the clean water-bearing matrix line in the neutron-density porosity crossplot in Figure 5.47b. In Figure 5.47c, however, the neutron- and density-log-derived porosities for Unit C are relatively inconsistent and plot over a considerable range of values. The low porosity values (<25%) depicted in Figure 5.47c are associated with the "hard", well cemented zone in the upper part of Unit C (654.6-656.7 m). The remaining cluster of porosities ranging from about 30 to 45 percent in Figure 5.47c have been affected by both the presence of shale (clay) and gas hydrates, which will be dealt with in greater detail later in this section of the thesis. In the neutron-density porosity crossplot for Unit B (Figure 5.47d) a large number of the plotted porosities fall above the clean water-bearing matrix line which indicates the presence of free-gas in Unit B, which has been confirmed from the analyses of other well logs and the recovered cores.

To further investigate the apparent differences in the downhole-log-derived porosities from Unit C in the Northwest Eileen State-2 well (Figure 5.47c), the uncorrected neutron- and density-log-derived porosities from Unit C have been displayed in Figure 5.48 as individual well-log curves. The "hard" (well cemented) zone near the top of Unit C is easily identified in Figure 5.48 by the low log-derived porosities within the depth interval from 654.6 to 656.7 m. Further examination of Figure 5.48, reveals that the density-log-derived porosities are generally higher (about 2%) than the neutron-log-derived porosities in a 10.3-m-thick interval in Unit C from immediately below the
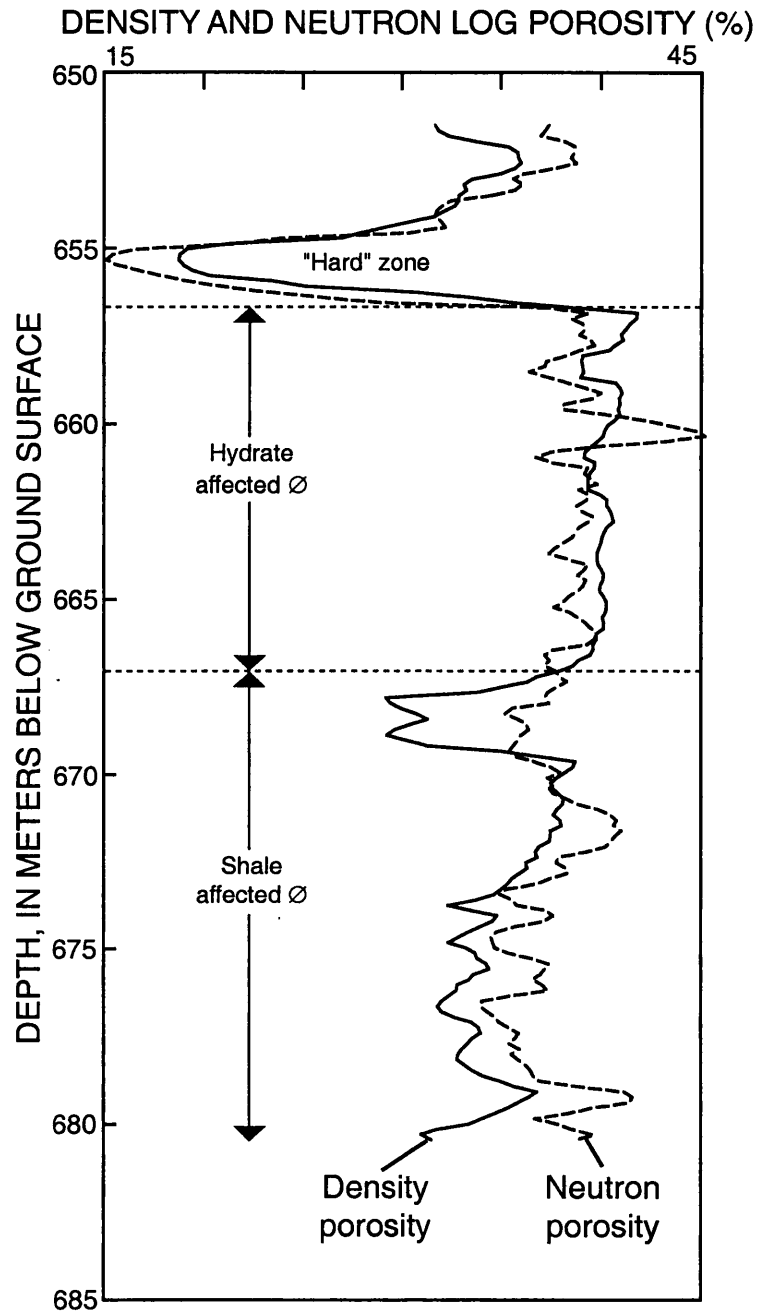
Figure 5.48 Well log plot of the neutron- and density-log-derived porosities for Unit C in the Northwest Eileen State-2 well.

"hard" zone to a depth of 667.0 m. In the lower part of Unit C (667.0-680.5 m), depicted in Figure 5.48, the neutron-log-derived porosities are generally higher than the density-log-derived porosities. The gamma-ray log reveals that the lower part of Unit C is characterized by a relatively high shale (clay) content, which has contributed to an apparent increase in neutron-log-derived porosities and a decrease in the density-log-derived porosities.

The upper part of Unit C (656.7-667.0 m), characterized by relatively higher density-log-derived porosities, is interpreted to be relatively shale (clay) free; however, this interval is believed to contain a considerable amount of gas hydrate. Analysis of the electrical-resistivity-log data from the upper part of Unit C (656.7-667.0 m) yield gas-hydrate saturations (S_h) as high as 93% (discussed in the next section of this thesis), which would have a significant affect on the neutron porosity and formation density tools. Modified versions of the density and neutron porosity gas hydrate correction nomographs in Figures 3.3 and 3.5 were used to calculate correction factors for the log-calculated porosities in the upper part (656.7-667.0 m) of Unit C. The porosity nomographs (Figures 3.3 and 3.5), modified for the reservoir conditions in Unit C of the Northwest Eileen State-2 well, yield a neutron porosity correction of -2% and a density porosity correction of -3%. Crossplotted in Figure 5.49a are the uncorrected neutron- and density-log-derived porosities for the upper part (656.7-667.0 m) of Unit C. The neutron-density porosity crossplot in Figure 5.49b depicts the log-derived porosities from the upper part (656.7-667.0 m) of Unit C after the neutron-density gas hydrate porosity corrections have been applied to the log-measured porosities. Except for one small
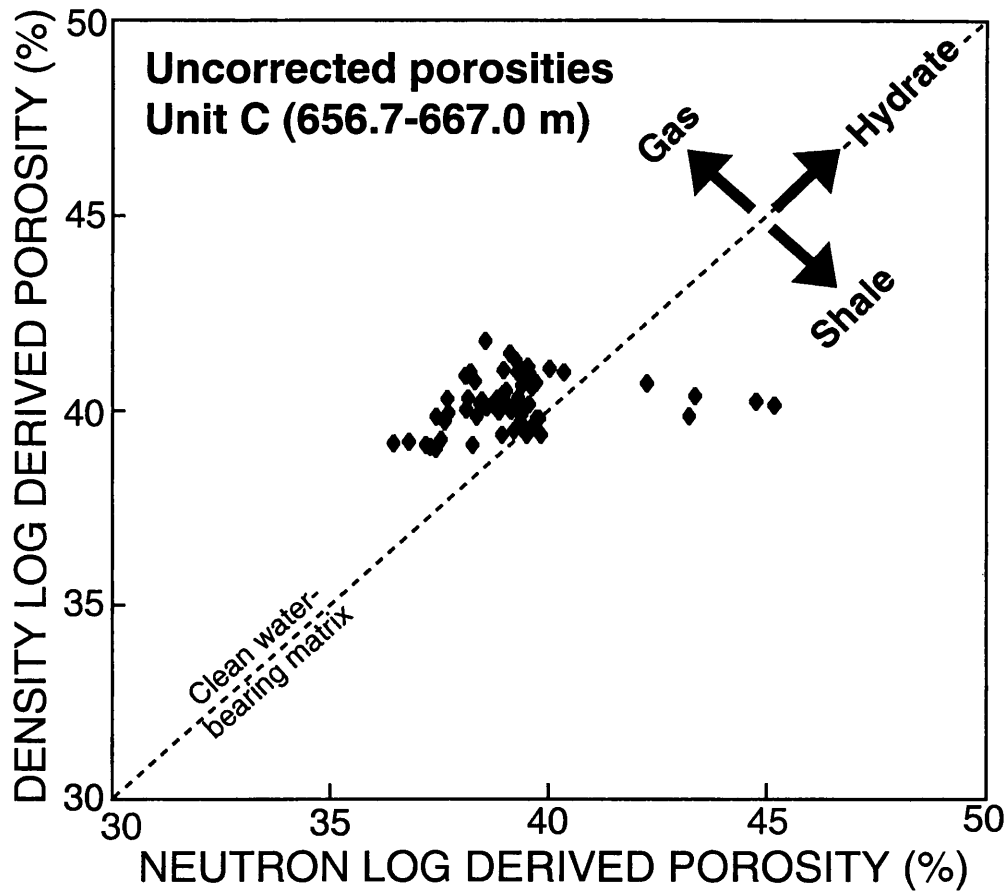
Figure 5.49a Crossplot of the uncorrected (no "hydrate correction")
neutron- and density-log-derived porosities for the upper part of Unit C
(656.7-667.0 m) in the Northwest Eileen State-2 well.
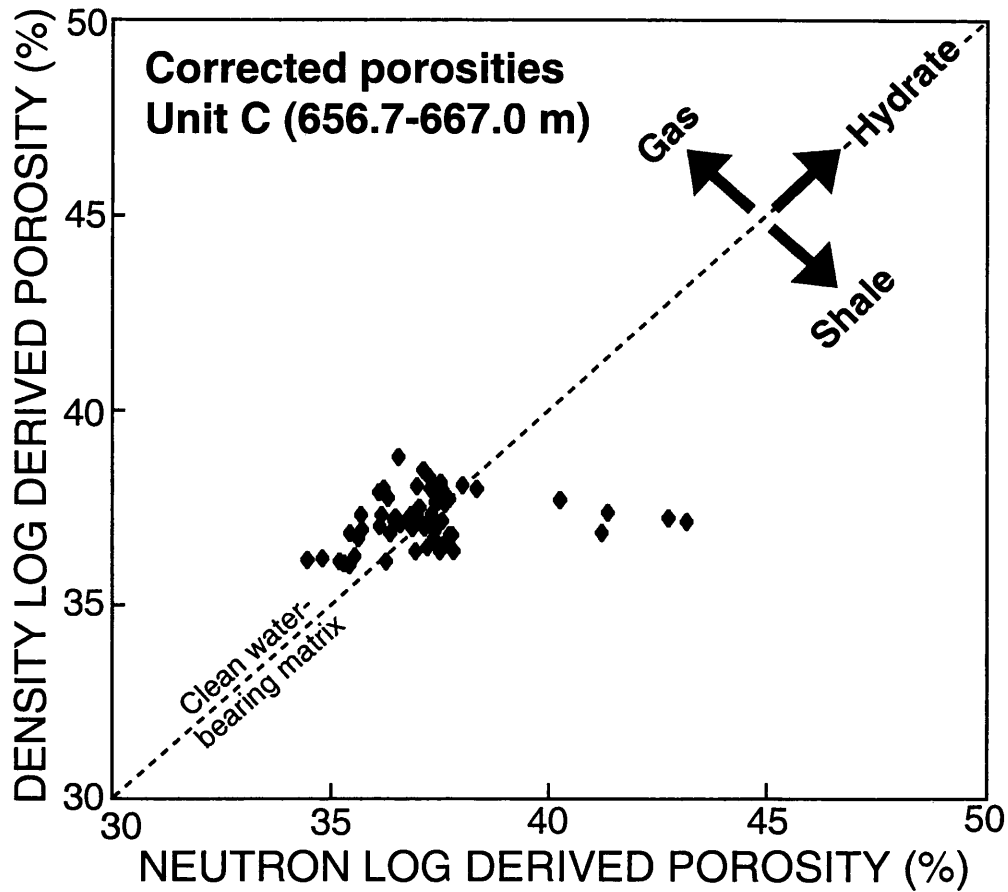
Figure 5.49b Crossplot of the "hydrate-corrected" neutron- and density-log-derived porosities for the upper part of Unit C (656.7-667.0 m) in the Northwest Eileen State-2 well.

cluster of data points, most of the gas-hydrate corrected neutron- and density-log

porosities in Figure 5.49b fall along the clean water-bearing matrix line. Because of

relatively low gas-hydrate saturations (S_h generally less than 50%), no attempt has been

made to correct the log-derived porosities in Units D and E for the presence of gas

hydrate. In the next section of this thesis, in which porosity data is needed to calculate

gas-hydrate saturations, the density-log-derived porosities are used that have been

corrected (upper part of Unit C only) for the presence of gas hydrate.

5.5.5 Gas-Hydrate Distribution and Saturation

In the following section, downhole data from the dual induction and acoustic

transit-time logs in Northwest Eileen State-2 well have been used to quantify the amount

of gas hydrates within the cored and tested gas-hydrate accumulations in the western

portion of the Prudhoe Bay Oil Field.

<u>Resistivity-Log-Calculated Gas-Hydrate Saturations</u> It is assumed that the high

resistivities and acoustic velocities measured in Units C, D, and E of the Northwest

Eileen State-2 well are due to the presence of in-situ natural gas hydrates. The first

resistivity log approach used to assess gas-hydrate saturations in the Northwest Eileen

State-2 well is based on the modified "quick look" Archie log analysis technique

(Equation 3.10, discussed in Chapter 3 of this thesis). In order to calculate the R_O

baseline for the "quick look" Archie analysis of the Northwest Eileen State-2 well, the

log-measured deep resistivities from Unit B (752.1-773.7 m) were used, which yielded an

"apparent" R_O of 24 ohm-m. This "apparent" R_O is not likely valid because Unit B is

interpreted to contain not only water but an undetermined amount of free-gas, which directly affects the log-measured resistivity of this unit. However, the "apparent" R_O from Unit B was used in this "quick look" Archie analysis because all of the sub-permafrost reservoir quality rocks drilled and logged in the Northwest Eileen State-2 well are interpreted to contain either gas hydrate or free-gas. Unit B was selected as one source of the R_O baseline because it exhibits the lowest resistivity of all the reservoir quality rocks drilled in the Northwest Eileen State-2 well. In an attempt to select a more appropriate R_O for the "quick look" Archie analysis of the Northwest Eileen State-2 well, formation pore-water salinity data and log-derived porsoity data were used to calculate an "accurate" value for R_O. As discussed later in this section of the thesis, pore-water salinities derived from the analysis of waters collected during formation testing in the Northwest Eileen State-2 well range from 0.9 to 4.0 ppt. Under the reservoir conditions exhibited in the Northwest Eileen State-2 well, pore-water salinities of 0.9 to 4.0 ppt would correspond to R_O values 55 and 15 ohm-m respectively; which bracket the well-log-derived R_O value of 24 ohm-m from Unit B. As discussed later in this section of the thesis, the lower pore-water salinity of 0.9 ppt is not considered representative of the undisturbed pore-water conditions in the Northwest Eileen State-2 well; however, the relatively higher measured value of 4.0 ppt is believed to represent the undisturbed in-situ pore-water salinities. Therefore, for the "quick look" analysis of water saturations in the Northwest Eileen State-2 well, both the log-derived R_O value of 24 ohm-m and the pore-water salinity derived R_O value of 15 ohm-m were used. The value of the empirical Archie constant n was assumed to be 1.9386 (reviewed by Pearson et al., 1983). In

Figure 5.50, the results of the "quick look" Archie calculations are shown as two water

saturation (S_W) log traces for the sub-permafrost portion of the Northwest Eileen State-2

well. The "quick look" Archie approach, that assumed an R_O value of 24 ohm-m, yielded

average water saturations (S_W) for the three gas-hydrate-bearing stratigraphic units (Units

C, D, and E) in the Northwest Eileen State-2 well ranging from 47% to 88%. While the

"quick look" Archie calculations, that assumed an R_O value of 15 ohm-m, yielded slightly

lower water saturations (S_W).

The next resistivity approach used to assess gas-hydrate saturations in Northwest

Eileen State-2 well is based on the "standard" Archie equation (Equation 3.8). In the

Northwest Eileen State-2 well, the porosity data needed for the "standard" Archie

equation was derived from the available downhole density log and corrected for the

presence of gas hydrates. In the following section, the Archie constants a, m, and n and

the resistivity of the pore-waters (R_W) within the sediments drilled by the Northwest

Eileen State-2 well have been determined.

Because of the limited range of sediment porosities within the reservoir quality

rocks in the Northwest Eileen State-2 well and since most of the delineated reservoirs

also contain ice (permafrost) and gas hydrate, which directly affect the electrical

resistivity of the formation, it was not possible to calculate reasonable values for the

empirical Archie constants (a and m) from the available porosity and resistivity-log data.

Therefore, the so-called "Humble" values were used for the a (0.62) and m (2.15) Archie

constants. The value of the empirical constant n was assumed to be 1.9386 as determined

by Pearson et al. (1983). The resistivity of pore-waters (R_W) are mainly a function of the
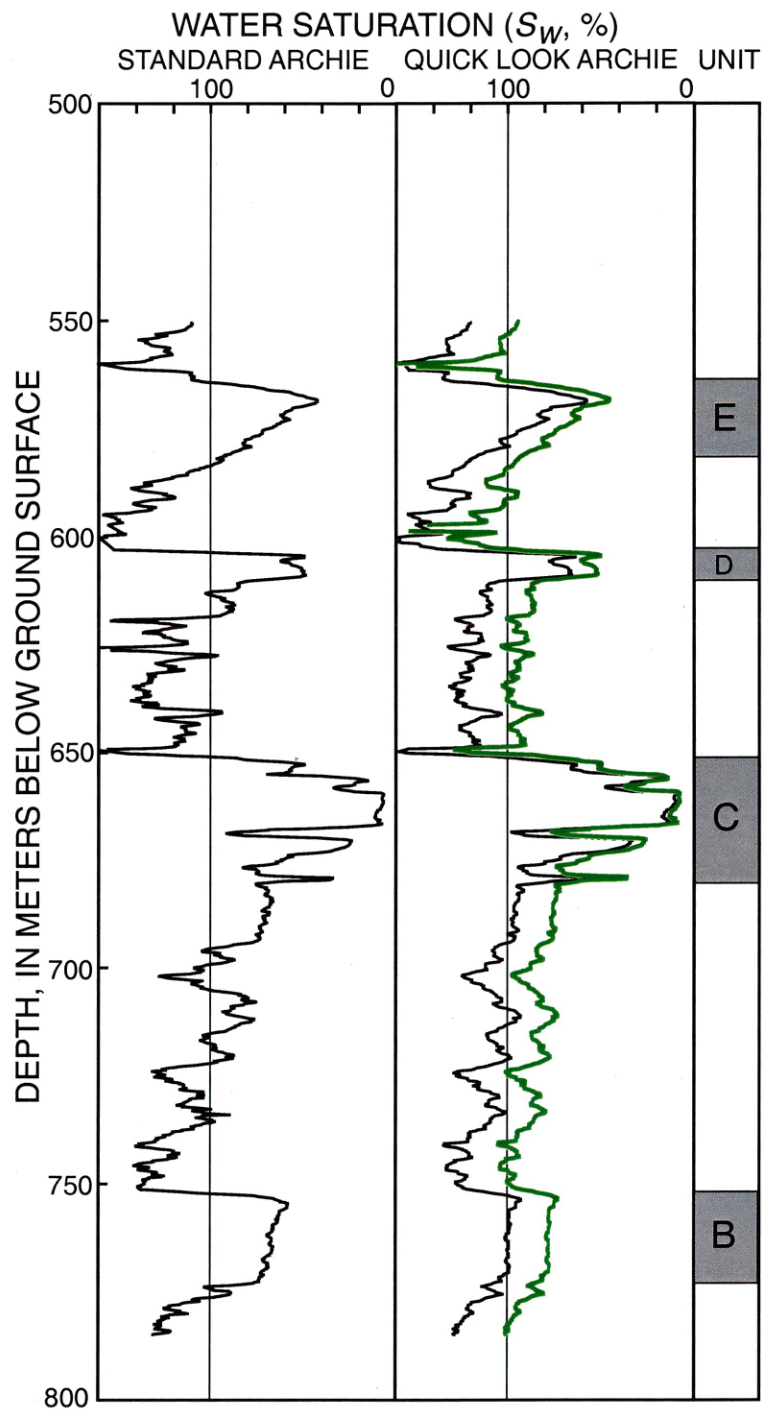
Figure 5.50 "Standard"- and "quick-look"-Archie-derived water saturations (S_W) calculated from the electrical resistivity log in the Northwest Eileen State-2 well. The two "quick-look"-derived saturation curves assume two different R_O values (R_O = 24 ohm-m and R_O =15 ohm-m)

temperature and the dissolved salt content (salinity) of the pore-waters. Pore-water

salinity data from the Northwest Eileen State-2 well are available from the analyses of

interstitial water samples collected from a series of drill-stem production tests in Units B

and C. The salinity of the water samples from the production test in the gas-hydrate-

bearing Unit C is very low, averaging about 0.9 ppt. The salinity of the waters sampled

from the production test in Unit B averaged about 4.0 ppt. It is likely, the low water

salinities calculated from Unit C are the result of pore-water freshening caused by gas

hydrate disassociation during the production test. Therefore, the higher pore-water

salinities of 4.0 ppt from the non-gas-hydrate-bearing Unit B likely represent the actual

in-situ salinity of the undisturbed pore-waters in the Northwest Eileen State-2 well. It is

worth noting, that the pore-water salinities in the gas-hydrate-bearing units may be higher

because of gas hydrate salute exclusion; however, since there is no evidence of elevated

pore-water salinities in the gas-hydrate-bearing stratigraphic units on the North Slope, the

maximum observed pore-water salinity of 4.0 ppt was assumed for the Archie calculated

gas-hydrate saturations in the Northwest Eileen State-2 well.

Formation temperature data in the Northwest Eileen State-2 well are available

from downhole temperature surveys in nearby wells which yield a sub-permafrost

geothermal gradient of 3.25 °C/100m and a base of ice-bearing permafrost (541.2 m)

temperature of -1.0°C. Arps formula (Hearst and Nelson, 1985) was used to calculate the

pore-water resistivities (R_W) in the Northwest Eileen State-2 well from the assumed

interstitial water salinity of 4.0 ppt and the measured formation temperatures. The

calculated pore-water resistivities (R_W) within the sub-permafrost sedimentary section of

the Northwest Eileen State-2 well ranges from about 2.23 to 3.08 ohm-m. Given the

Archie constants (a, m, and n) and pore-water resistivities (R_W), it was possible to

calculate water saturations (S_W) from the resistivity log using the "standard" Archie

relation. In Figure 5.50, the results of the "standard" Archie calculation are shown as a

water saturation (S_W) log trace along with the results of the "quick look" Archie method.

The average water saturations (S_W) calculated with the "standard" Archie relation within

the three gas-hydrate-bearing units (Units C, D, and E) in the Northwest Eileen State-2

well range from about 39% to 67%. In comparison, the "standard" Archie relation

yielded similar, but slightly lower, water saturations than the "quick look" Archie method

that assumed a R_O value of 24 ohm-m (Figure 5.50). In addition, the "standard" Archie

relation yielded an average free-gas saturation (1.0-S_W) for Unit B of about 32%. The

"quick look" Archie approach that assumed a R_O value of 24 ohm-m failed to measure the

concentration of free-gas in Unit B since this "quick look" analysis assumed Unit B was

100% water-saturated (no hydrocarbons). However, the "quick look" Archie method that

assumed a R_O value of 15 ohm-m yielded an average free-gas saturation (1.0-S_W) for Unit

B of about 20%.

The modified Archie approach proposed by Pearson et al. (1983), discussed in

Chapter 3 of this thesis, failed to yield reasonable estimates of gas-hydrate saturations

with the downhole-log data from the Northwest Eileen State-2 well.

In two of the field case studies presented previously in this Chapter (Section 5.2.6

for the Blake Ridge and Section 5.3.6 for the Cascadia margin) the Waxman-Smits

saturation-resistivity relation was used to assess the affect of shales (clays) on resistivity-

derived gas-hydrate saturations. For the Northwest Eileen State-2 well, however, the well-log-inferred gas hydrates occur within a series of interbedded sedimentary units with highly variable shale (clay) concentrations; thus, limiting the usefulness of the Waxman-Smits model in the Alaskan example. Therefore, the empirical Indonesian model (Equation 3.11), which takes into account differences in shale (clay) concentrations, was used to calculate "shaly-sand"-corrected water saturations in the gas-hydrate-bearing reservoirs of the Northwest Eileen State-2 well (Poupon and Leveaux, 1971).

In addition to the normal variables required for the "standard" Archie relation (Equation 3.8; a, m, n, $\varnothing$, R_w, and R_t), the Indonesian model (Equation 3.11) also requires values for the conductivity of the shale (clay) in the formation (C_{sh}), volume of shale (clay) in the formation (V_{sh}), and sediment porosities corrected for the presence of shale ($\varnothing_{sc}$). In this section of the thesis, the above list of input variables for the "Indonesian model" assessment of the Northwest Eileen State-2 gas-hydrate accumulation have been determined.

The Indonesian model (Equation 3.11) is usually expressed in terms of electrical conductivity. To simplify the calculations, however, the Indonesian model as used in this thesis was rewritten into terms of electrical resistivity. It is known that the presence of shale in a formation can directly affect the values for the "standard" Archie a, m, and n variables. As previously discussed in Section 5.5.5 of this thesis, it was not possible to directly calculate reasonable values for the empirical Archie variables with the available data from the Northwest Eileen State-2 well. Therefore, the "Humble" values for the a (0.62) and m (2.15) variables were used in the Indonesian model assessment of the

Northwest Eileen State-2 well along with a n value of 1.9386 (reviewed by Pearson et al.,

1983). The pore-water resistivities (R_w) calculated for the "standard" Archie assessment

of the Northwest Eileen State-2 well have also been used in the Indonesian model

assessment of the downhole-log data from the this drill-site. The resistivity of the

formation (R_t) was obtained from the deep reading resistivity log in the Northwest Eileen

State-2 well (Figure 5.44).

Gamma ray logs are often used to detect and quantify shales in sedimentary rocks.

In this assessment of the Northwest Eileen State-2 well, the so-called Tertiary gamma ray

model was used to determine the volume of shale (V_{sh}) in the well-log-inferred gas-

hydrate-bearing sedimentary units. The Tertiary gamma ray model (reviewed by Serra,

1984), is an empirical relationship between shale volume and the relative gamma-ray-log

response in which the gamma-ray-log response in the formation is (linearly) normalized

between the gamma ray responses in a clean (shale-free) sand and in a pure shale to

calculate the volume of shale (V_{sh}). In the Northwest Eileen State-2 well, the gamma ray

value for the clean sand was set at 20 API and the pure shale was given a value of 90

API. The gamma-ray-log-derived shale volumes (V_{sh}) in the Northwest Eileen State-2

well (Figure 5.51) range from near 0% in Unit C to over 90% at a depth of about 600 m.

In this study, various methods were used to correct the log-derived porosity data

for the presence of shale. The shale-porosity correction method that yielded the most

consistent results relied on correcting density-log-derived porosities with gamma-ray-log-

determined shale volumes (Figure 5.51) and known in-situ shale densities (ρ_{sh} = 2.25

g/cm^3 for the Northwest Eileen State-2 well). For the Northwest Eileen State-2 well the
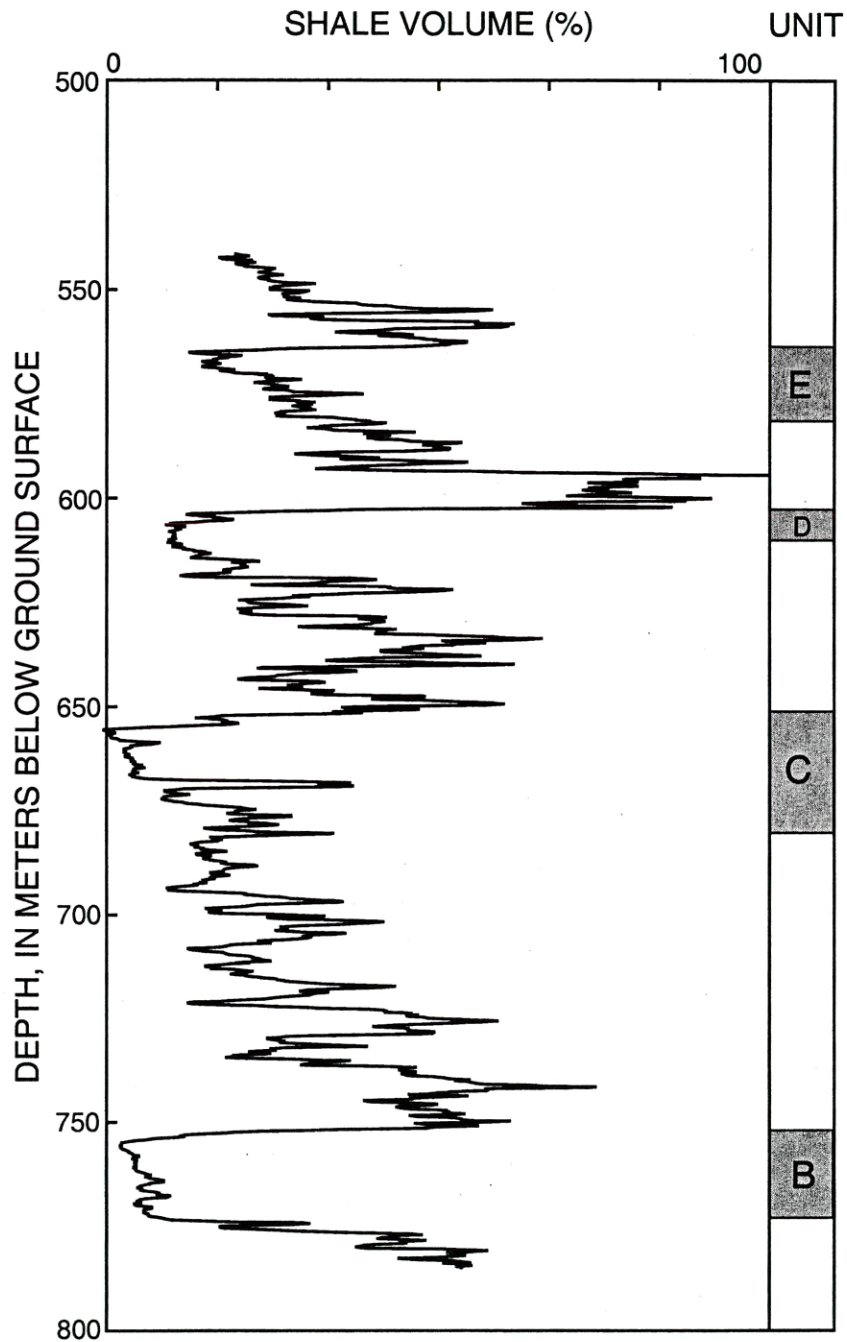
SHALE VOLUME (%) UNIT

Figure 5.51 Sediment shale volumes (V_{sh}) calculated from the downhole natural gamma ray log in the Northwest Eileen State-2 well.

shale corrections for the log-derived density porosities was done with the following equation:

$$\varnothing_{sc} = \varnothing_{den} - V_{sh}\left(\frac{\rho_m - \rho_{sh}}{\rho_m - \rho_w}\right) \tag{5.1}$$

$\varnothing_{sc}$ = Shale-corrected porosity, fractional %

$\varnothing_{den}$ = Uncorrected density porosity, fractional %

V_{sh} = Shale volume, fractional %

ρ_m = Matrix density, g/cm^3

ρ_{sh} = Shale density, g/cm^3

ρ_w = Water density, g/cm^3

The plot of the uncorrected and shale-corrected density porosities in Figure 5.52, reveals relatively little difference in the density-log porosities calculated in the clean gas-hydrate-bearing sandstone units; however, the shale-corrected porosities in the shale-rich horizons are considerably lower than the uncorrected density-log-derived values.

The last variable needed before proceeding with the Indonesian assessment of the gas-hydrate-bearing units in the Northwest Eileen State-2 well is the resistivity of the shale (clay) in the formation. A shale resistivity value (R_{sh}) of 15 ohm-m was selected from the gamma-ray-log-inferred shale zone at a depth of about 600 m in the Northwest Eileen State-2 well (Figure 5.44).
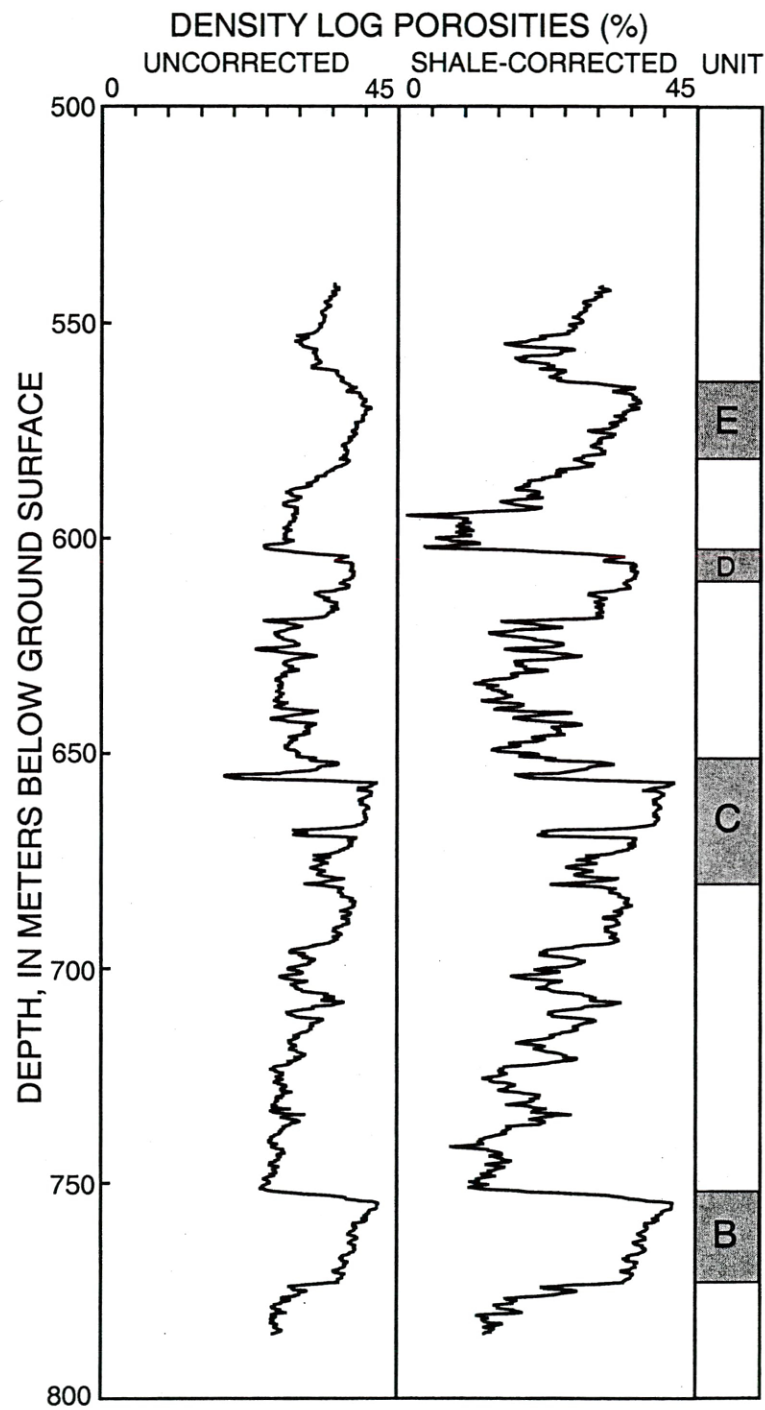
Figure 5.52 Well log plots of the "uncorrected" and "shale-corrected" density-log-derived porosities in the Northwest Eileen State-2 well.

The Indonesian-model-derived water saturations for the gas-hydrate-bearing units in the Northwest Eileen State-2 well have been displayed in Figure 5.53 along with the water saturations derived from the "standard" (clean sand) Archie relation (Equation 3.8; Figure 5.50). In general, the presence of shale appears to have little affect on the Archie-derived water saturations in the shale-free gas-hydrate-bearing sandstone reservoirs. Within the gamma-ray-log-inferred shaly-sand reservoirs, however, the shale-corrected water saturations are significantly lower.

Acoustic-Log-Calculated Gas-Hydrate Saturations   In this section of the thesis, compressional-wave acoustic-log data from the Northwest Eileen State-2 well have been used along with the Timur (Equation 3.14), modified Wood (Equation 3.15), and Lee weighted average (Equation 3.16) acoustic equations (discussed in Section 3.5 of this thesis) to calculate gas-hydrate saturations. There are no shear-wave acoustic well-log data available from the Northwest Eileen State-2 well; therefore, the combined compressional- and shear-wave velocity gas-hydrate saturation equations proposed by Lee et al. (1996), Kuster-Toksöz (Zimmerman and King, 1986), and Dvorkin et al. (1991, 1993) (discussed in Section 3.5 of this thesis) can not be used to assess gas-hydrate saturations at this drill-site.

The porosity data used in the acoustic gas-hydrate saturation equations were derived from the available downhole density log and corrected for the presence of gas hydrates. The remaining variables in the Timur and Wood equations have been assigned constant values: with an assumed water velocity (V_w) of 1.5 km/sec, sediment matrix velocity (V_m) of 4.65 km/sec, gas hydrate velocity (V_h) of 3.35 km/sec, water density
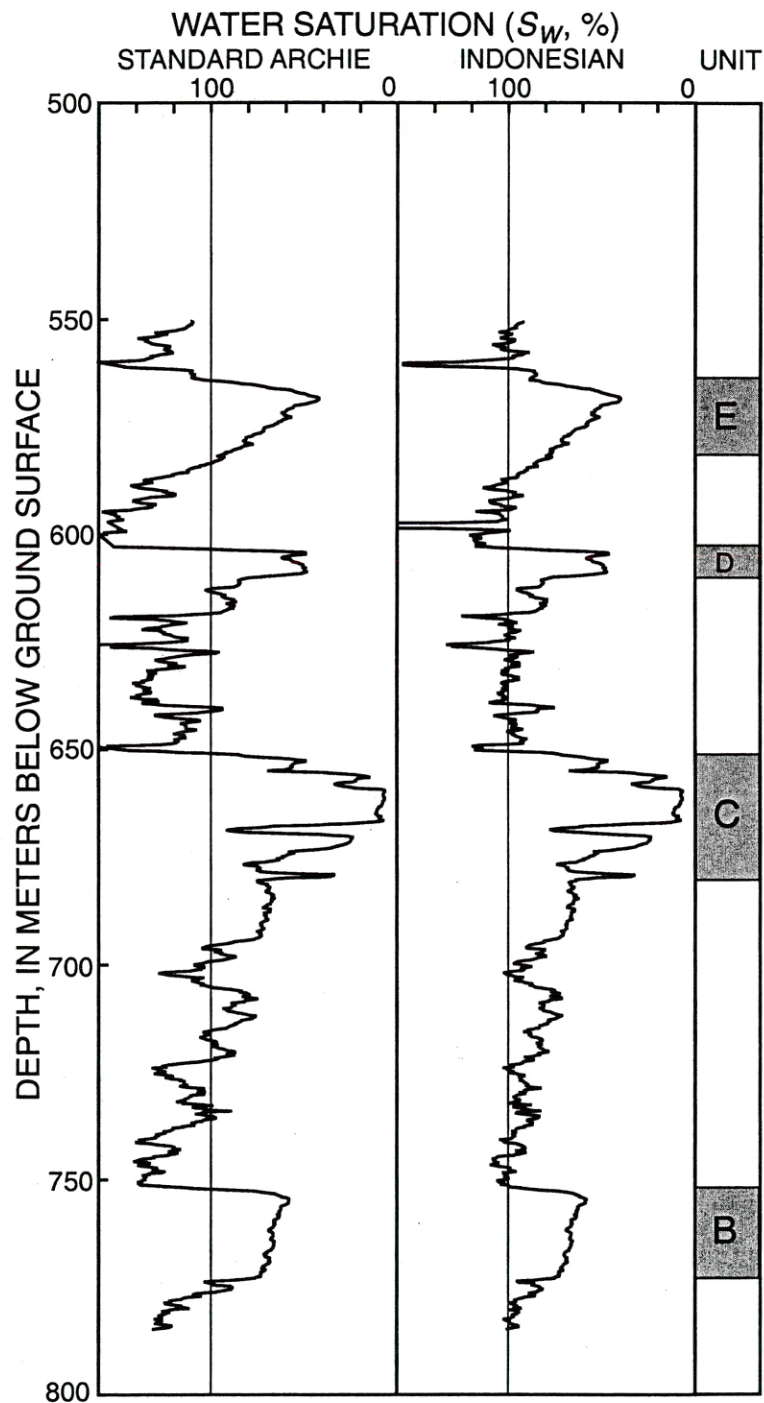
Figure 5.53 Water saturation (S_W) log plots for the
Northwest Eileen State-2 well calculated from the
"Standard" Archie relation and the Indonesian model.

(ρ_w) of 1.00 g/cm^3, sediment matrix density (ρ_m) of 2.65 g/cm^3, and a gas hydrate

density (ρ_h) of 0.9 g/cm^3 (Table 3.12). In the Wood equation, the bulk-density (ρ_b) of

the formation is determined from the modified three component density equation

(Equation 3.2). The bulk compressional-wave velocity of the formation (V_b) is obtained

directly from the transit-time well logs.

The final two variables needed before conducting the acoustic gas-hydrate

saturation calculations are the weight factor (W) and the gas-hydrate cementation

exponent (r) in the Lee weighted average equation. In Figure 5.54, corrected density-log-

derived porosities and log-derived compressional velocity data from the entire

stratigraphic interval below Unit C (including Unit B) have been plotted along with

various curves calculated from the Lee equation (assumed W values of 0.8, 1.0, and 1.2).

The selection of an appropriate Lee equation weight factor, W, is hampered by the fact

that all of the sub-permafrost reservoir quality rocks drilled and logged in the Northwest

Eileen State-2 well are interpreted to contain either gas hydrate or free-gas. In Figure

5.54, therefore, only the acoustic-log data from below Unit C was considered; however,

Unit B is interpreted to contain not only water but a considerable amount of free-gas. But

the occurrence of free-gas in Unit B has only slightly depressed the well-log-measured

velocities. In Figure 5.54 it appears that a weight factor, W, of 0.8 best characterizes the

sediments in the Northwest Eileen State-2 well, with most of the water- and free-gas-

bearing zones falling on or below the Lee equation $(W=0.8)$ water baseline. A gas-

hydrate cementation exponent (r) of $r=1$ was selected for the Northwest Eileen State-2
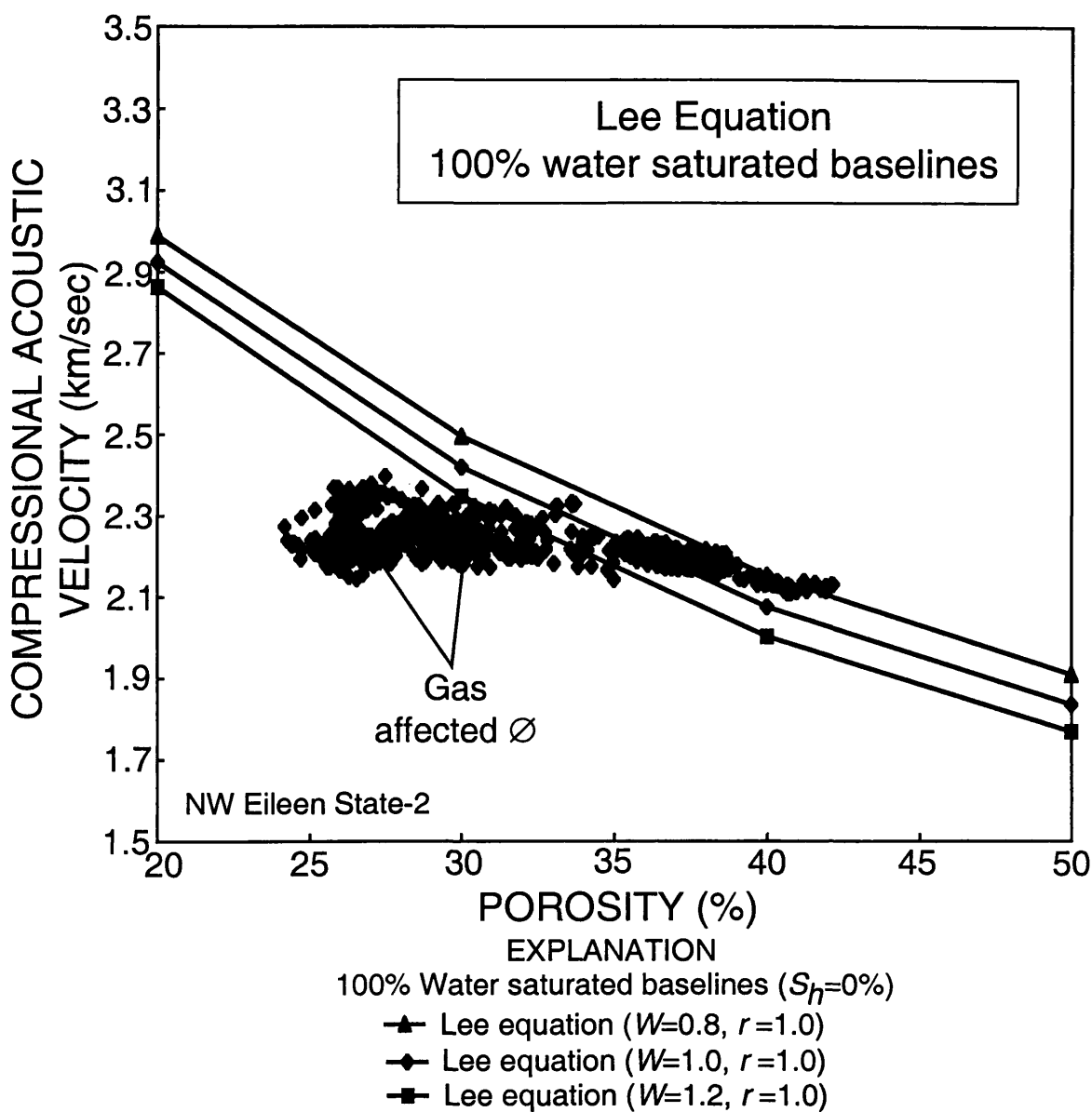
well.

Figure 5.54 Graph showing the downhole-log-derived compressional-wave velocities (V_p) and density-log-derived porosities for the entire stratigraphic section below Unit C in the Northwest Eileen State-2 well. Also shown are several 100% water-saturated porosity-velocity curves predicted from a series of Lee (Equation 3.16) compressional-wave (V_p) acoustic equations that assume different Lee weight factors (W).

In Figure 5.55, the results of the Timur, Wood, and Lee acoustic velocity

calculations are shown as gas-hydrate saturation log traces for the Northwest Eileen

State-2 well. As shown in Figure 5.55, the Timur equation yielded relatively low gas-

hydrate saturations (S_h) for most of the gas-hydrate-bearing stratigraphic units (Units C,

D, and E) in the Northwest Eileen State-2 well. The Lee equation yielded for the most

part average gas-hydrate saturations (S_h) within the three gas-hydrate-bearing

stratigraphic units (Units C, D, and E) ranging from 10% to about 40%, which are

compatible but slightly lower than the gas-hydrate saturations ($1-S_w$) calculated from the

electrical-resistivity-log data (discussed earlier in this section of the thesis) in the

Northwest Eileen State-2 well. The Wood equation yielded for the most part

unreasonable gas-hydrate saturations (S_h).

Gas-Hydrate Saturation Calculations -- Summary The "quick look" and

"standard" Archie electrical resistivity methods yielded for the most part average gas-

hydrate saturations ($1-S_w$) for the three gas-hydrate-bearing stratigraphic units (Units C,

D, and E) in the Northwest Eileen State-2 well ranging from about 12% to 61%. The

Indonesian-derived (shaly-sand) water saturations for the gas-hydrate-bearing units in the

Northwest Eileen State-2 well were similar, but slightly lower, than the "standard" (clean

sand) Archie-derived water saturations.

The Lee and Timur acoustic equations, generally yielded gas-hydrate saturations

(S_h) less than those calculated from the electrical-resistivity-log data. The modified

Wood acoustic equation yielded erroneous gas-hydrate saturations which did not compare
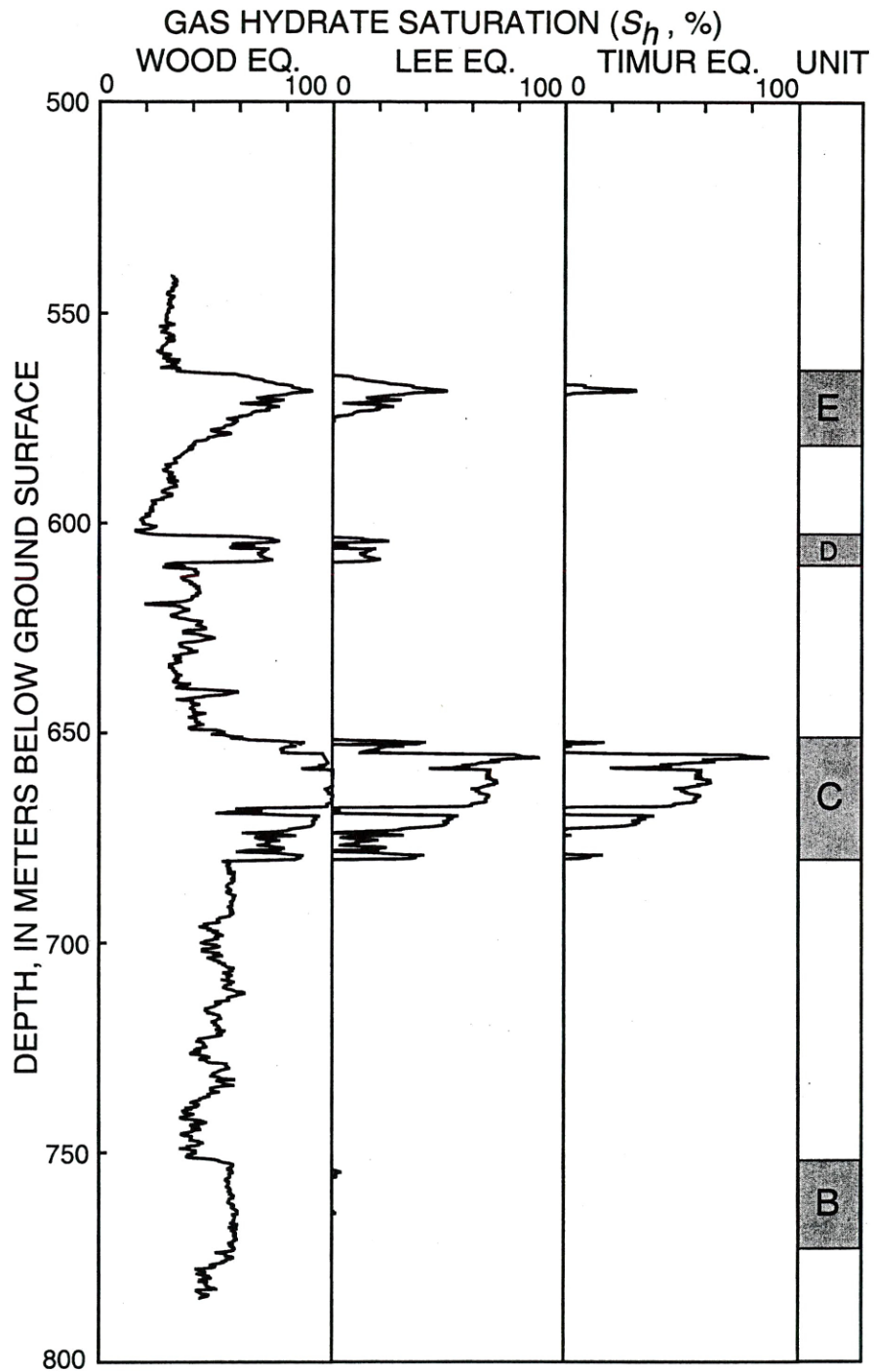
Figure 5.55 Gas-hydrate saturations (S_h) calculated from the compressional-wave acoustic log in the Northwest Eileen State-2 well. The results of the modified Wood (Equation 3.15), Lee (Equation 3.16), and Timur (Equation 3.14) equations are shown.

favorably with saturations calculated by other methods. Only the "standard" Archie

electrical resistivity method yielded reasonable free-gas saturations $(1-S_w)$ for Unit B.

5.5.6 Volume of Gas

In Collett (1993b), it was determined that the well-log-inferred gas-hydrate

accumulation of the Prudhoe Bay-Kuparuk River area may contain between 1.0 and 1.2

trillion cubic meters of gas (at STP). As discussed in Section 1.4.3 of this thesis,

Mathews (1986) also determined that the gas hydrates within a portion (665.5-674.6 m)

of Unit C in the Northwest Eileen State-2 well, as defined in Collett (1993b), contains

between 191.6 to 412.4 million cubic meters of gas per square kilometer. The log-

interpreted sediment porosities, gas-hydrate and free-gas saturations from the Northwest

Eileen State-2 well calculated within this study provide several of the critical parameters

needed to verify the existing estimates of the volume of gas within the Prudhoe Bay-

Kuparuk River gas-hydrate accumulation. In this section, five "reservoir" parameters

(Table 5.22) needed to calculate the volume of gas associated with the gas hydrates in the

Northwest Eileen State-2 well are assessed. In addition, the volume of free-gas within

Unit B at the location of the Northwest Eileen State-2 well is also assessed (Table 5.23).

In this "resource" assessment the volume of gas hydrate and associated free-gas

within a one square kilometer area surrounding the Northwest Eileen State-2 well has

been determined (Tables 5.22 and 5.23). For this "resource" assessment, the thickness of

the gas-hydrate-bearing sedimentary section was defined as the total thickness of Units C,

D, and E, which yields a total thickness of 52.5 m (Table 5.22). The gas-hydrate-

Table 5.22 Volume of natural gas within the downhole-log-inferred gas-hydrate-bearing logging Units of the Northwest Eileen State-2 well.

Logging unit	Depth of Logging Unit (m)	Thickness of hydrate-bearing unit (m)	Sediment porosity (%)	Gas-hydrate saturation (%)	Volume of hydrate per square km (m^3)	Volume of gas within hydrate per square km (m^3)*
C	651.5-680.5	29.0	35.6	60.9	6,286,005	1,030,904,796
D	602.7-609.4	6.7	35.8	33.9	813,308	133,382,462
E	564.0-580.8	16.8	38.6	32.6	2,115,420	346,928,811
					Total --	1,511,216,069

*Gas volume calculation assumes a hydrate number of 6.325 (90% gas filled clathrate), 1 m^3 of gas hydrate = 164 m^3 free-gas at STP.

Table 5.23 Volume of natural gas within the downhole-log-inferred free-gas-bearing logging unit (Unit B) of the Northwest Eileen State-2 well.

Logging unit	Depth of identified free-gas unit (m)	Thickness of free-gas-bearing unit (m)	Sediment porosity (%)	Free-gas saturation (%)	Volume of in-place gas per square km (m³)*	Volume of gas within free-gas per square km at STP (m³)
B	752.1-773.7	21.6	37.9	31.8	2,603,493	412,653,641

*Volume of in-place gas at in-situ pressure and temperature conditions. STP: pressure=101 kPa, temperature=15°C

corrected density-log-derived sedimentary porosities for the three gas-hydrate-bearing

units (Units C, D, and E) range from an average value of about 36 to 39 percent (Table

5.22). Gas-hydrate saturations (S_h) in all three gas-hydrate-bearing units (Units C, D,

and E) in the Northwest Eileen State-2 well, calculated from the "standard" Archie

relation (Figure 5.50), range from an average value of about 33 to 61 percent. (Table

5.22). A hydrate number of 6.325 (90% gas filled clathrate) was assumed, which

corresponds to a gas yield of 164 m^3 of methane (at STP) for every cubic meter of gas

hydrate (Collett, 1993b). Cumulatively all three log-inferred gas-hydrate-bearing

stratigraphic units (Units C, D, and E) drilled and cored in the Northwest Eileen State-2

well may contain 1,511,216,069 cubic meters of gas in the one square kilometer area

surrounding this drill-site (Table 5.22).

In this study, it was determined that within the one square kilometer area

surrounding the Northwest Eileen State-2 well, the gas hydrates in Unit C contain

1,030,904,796 m^3 of gas (Table 5.22), which is considerably higher than the range of gas

volumes calculated for Unit C (191,600,000-412,400,000 m^3 of gas) by Mathews (1986).

Mathews (1986), however, assumed a total thickness of only 9.1 m for the gas-hydrate-

bearing portion of Unit C, which is almost 20 m less then the actual thickness of 29 m. If

Mathews (1996) assumed a thickness of 29 m for Unit C, the calculated range of gas

volumes would be near the value determined for Unit C in this thesis. It is also possible

to compare the results of this study with those of Collett (1993b). For comparison

purposes only, if it is assumed that the areal extent of Units C, D, and E calculated in

Collett (1993b) are correct (Unit C = 363 km^2, Unit D = 357 km^2, Unit E = 404 km^2)

and it is further assumed that the geologic conditions and gas hydrate distribution in the

Northwest Eileen State-2 well (Table 5.22) are representative of the entire well-log-

inferred gas-hydrate accumulations in Units C, D, and E; it can be determined that there

is about 562 billion cubic meters of gas within the gas hydrates of Units C, D, and E of

the Prudhoe Bay-Kuparuk River area. In Collett (1993b), however, it was determined

that the same units (Units C, D, and E) contain about 787 billion cubic meters of gas.

One reason for the difference in these two estimates is because the gas-hydrate

saturations calculated within this study of the Northwest Eileen State-2 well are

considerably lower than those calculated in Collett (1993b).

In Collett (1993b), composite Pickett crossplots were used to calculate gas-

hydrate saturations (as discussed in Section 1.4.3 of this thesis) assuming a formation

water resistivity (R_W) of 0.4 ohm-m, which is significantly lower than the R_W values

calculated in this study from the Northwest Eileen State-2 well. The use of an incorrect

low formation water resistivity (R_W) would result in an over estimation of gas-hydrate

saturations. In Collett (1993b), the selection of a low formation water resistivity (R_W)

was based on the analyses of water salinities in pore-water samples collected from

numerous cores within the ice- and gas-hydrate-bearing sediments of the Prudhoe Bay-

Kuparuk River area (not just the Northwest Eileen State-2 well). Regionally, the

salinities of the pore-waters in the gas-hydrate-bearing sedimentary section are higher

(ranging from 9 to 15 ppt) than those measured in the water samples collected from the

cores and drill-stem tests in the Northwest Eileen State-2 well, which ranged from 0.9 to

4 ppt. It is possible that the pore-water resistivities (R_W) calculated for the Northwest

Eileen State-2 well are not representative of the pore-water resistivities (R_w) throughout

the entire Prudhoe Bay-Kuparuk River gas-hydrate accumulation. This discrepancy in

the measured pore-water salinities, identifies the need to systematically re-evaluate all of

the wells from the area of the Prudhoe Bay-Kuparuk River gas-hydrate accumulation and

if possible collect new downhole-log, core, and production test data; all of which are

beyond the scope of this study.

The available log data from the Northwest Eileen State-2 well were also used to

calculate the volume of free-gas within Unit B (Table 5.23). In the Northwest Eileen

State-2 well, the free-gas-bearing portion of Unit B has been determined to be about 21.6-

m-thick (Table 5.23). The average porosity of the sediments within Unit B is about

37.9% (Table 5.23). The downhole-log-derived free-gas saturations within Unit B

average 31.8% (Table 5.23). The potential volume of gas within the log-inferred free-gas

portion of Unit B in the Northwest Eileen State-2 well is about 412,653,641 cubic meters

of gas (at STP) per square kilometer (Table 5.23). The lateral extent of the free-gas-

bearing portion of Unit B is unknown, therefore no attempt has been made to assess the

regional "resource" potential of the free-gas accumulation in Unit B.

5.6 Mackenzie River Delta-- Canada

5.6.1 Introduction and Regional Geology

The JAPEX/JNOC/GSC Mallik 2L-38 gas hydrate research well was designed to

investigate the occurrence of in-situ natural gas hydrates in the Mallik area of the

Mackenzie River Delta of Canada (Figure 5.56) (Dallimore et al., 1999). A major

EXPLANATION

✳ **Well with gas hydrate**   • **Well**

- - - - - **Contours of base of methane hydrate (m)**
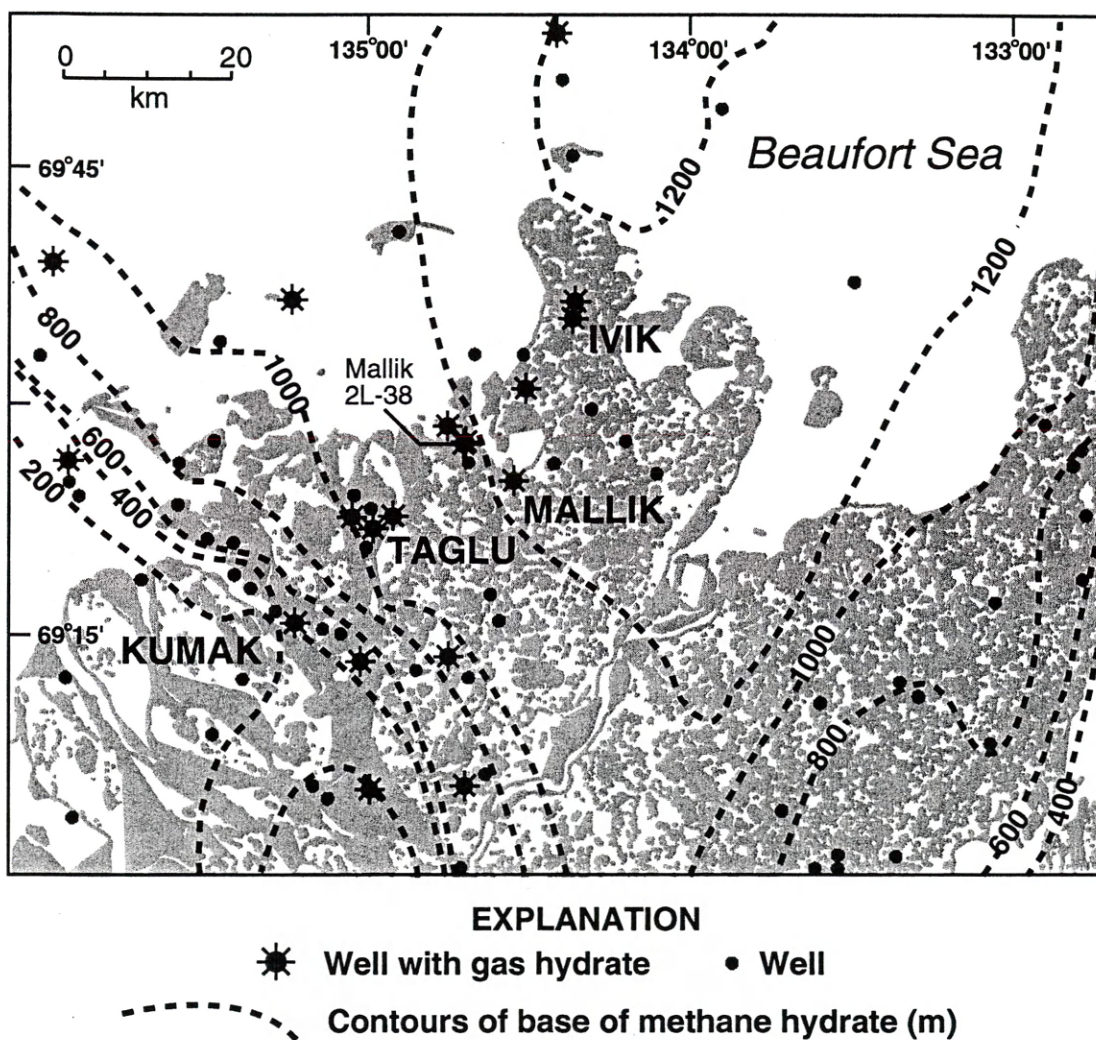
Figure 5.56 Map of part of the Mackenzie Delta region showing the calculated depth to the base of the methane hydrate stability zone (modified from Dallimore et al., 1999). Wells with downhole-log-inferred gas-hydrate occurrences are also shown.

component of the Mallik research program was to refine and assess available downhole wireline logging tools as applied to an actual gas-hydrate occurrence.

The Mallik 2L-38 gas hydrate research well was drilled near the site of the existing Mallik L-38 well, which was drilled by Imperial Oil in 1972 (Bily and Dick, 1974). As described in Collett and Dallimore (1998), the Mallik L-38 well is believed to have encountered at least 10 significant gas-hydrate-bearing stratigraphic units within the depth interval from 810.1 to 1,102.3 m. Bily and Dick (1974) concluded that each of the gas-hydrate-bearing units in the Mallik L-38 well contained substantial amounts of gas hydrate. However, no attempt was made to quantify the amount of gas hydrate or associated free gas that may have been trapped within the log-inferred gas-hydrate occurrences.

The geology of the Mackenzie Delta-Beaufort Sea region has been described in numerous publications with extensive regional overviews given in Dixon et al., (1992). Surficial sediments of the Mackenzie Delta are composed in part of modern deltaic sediments and of older fluvial and glacial deposits of Richards Island and the Tuktoyaktuk Peninsula (Figure 5.56). At depth, the area is underlain by deltaic sandstones and shales of Mesozoic and Cenozoic age that thicken to more than 12 km over a short distance seaward from the present shoreline. This sedimentary section overlies faulted Paleozoic rocks stepping down steeply beneath the Mesozoic and Cenozoic section.

The post Paleozoic sedimentary rocks of the Beaufort Sea continental shelf are subdivided into two major sections: pre-Upper Cretaceous and Upper Cretaceous to

Holocene strata. A major regional unconformity marks the boundary between the Upper

Cretaceous and older strata. Above this regional unconformity, sedimentation was

dominated by deltaic processes, resulting in a series of thick, generally northward

prograding delta-complexes, to which lithostratigrahic terminology can be applied

(reviewed by Dixon et al., 1992).

Assessments of gas-hydrate occurrences in the Mackenzie Delta-Beaufort Sea

area have been made mainly on the basis of data obtained during the course of

hydrocarbon exploration conducted over the past three decades (reviewed by Judge et al.,

1994). A data base presented by Smith and Judge (1993) summarizes a series of

unpublished consultant studies that investigated well-log data from 146 exploration wells

in the Mackenzie Delta area. In total, 25 wells (17%) were identified as containing

possible or probable gas hydrates (Figure 5.56). All of these inferred gas hydrates occur

in clastic sedimentary rocks of the Kugmallit, Mackenzie Bay, and Iperk sequences

(Dixon et al., 1992). Two of the occurrences were associated with ice-bearing permafrost

while the remainder were beneath the permafrost interval. The frequency of gas-hydrate

occurrence in offshore wells was greater, with possible or probable gas hydrates

identified in 35 out of 55 wells (63%).

In this section of the thesis, available downhole physical property data from cores,

density-log data, and neutron-porosity-log data have been used to calculate porosities

within the gas-hydrate-bearing sediments drilled by the Mallik 2L-38 well. Available

downhole resistivity and acoustic transit-time (both compressional- and shear-wave

measurements) data have also been used to calculate gas-hydrate saturations in the Mallik

2L-38 well. In addition, the core- and well-log-derived sediment porosities and gas-

hydrate saturations have been used to calculate the volume of gas within the "Mallik"

gas-hydrate accumulation in the Mackenzie River Delta.

5.6.2 Downhole-Logging Program

Within wells drilled in the Arctic, the permafrost interval is usually drilled and

cased before drilling to greater depths. The Mallik 2L-38 well was drilled in similar

fashion, with all of the log-inferred gas-hydrate-bearing zones occurring below the base

of the ice-bearing permafrost estimated from the log data in the Mallik L-38 well at a

depth of 640 m (Collett and Dallimore, 1998). Before running the "permafrost casing",

the upper 580 m of the Mallik 2L-38 well was surveyed with a Schlumberger Platform

Express logging array which contained a high resolution laterolog (HALS-PLATFORM

EXPRESS). The "permafrost" logging program also included a Dipole Shear Sonic Imager

(DSI-GR-AMS) log run. After running and cementing the permafrost casing to 669 m,

the sub-permafrost gas-hydrate-bearing units were drilled and cored to a total depth of

1,142 m. The sub-permafrost section of Mallik 2L-38 was surveyed with the

Schlumberger [RUN-1] Array Induction Imager Tool (AIT-EMS-GR-SP), [RUN-2]

Platform Express (HALS-PLATFORM EXPRESS), [RUN-3] Dipole Shear Sonic Imager

(DSI-GR-AMS), and [RUN-4] Fullbore Formation MicroImager (FMI-HNGS) well-

logging arrays (Table 5.24).

The quality of the well logs in the gas-hydrate-bearing portion of the Mallik 2L-

38 well is excellent with a near-gauge hole throughout the gas hydrate interval (Figure

Table 5.24 Downhole-logging program within the sub-permafrost portion of the Mallik 2L-38 well.

Total hole penetration (m)	Log run	Logging string	Interval logged (m)
1,142	1	AIT/EMS/GR/SP	668.1-1,136.3
	2	HALS	668.1-1,137.3
	3	DSI/GR/AMS	531.6-1,132.6
	4	FMI/HNGS	766.7-1,116.6
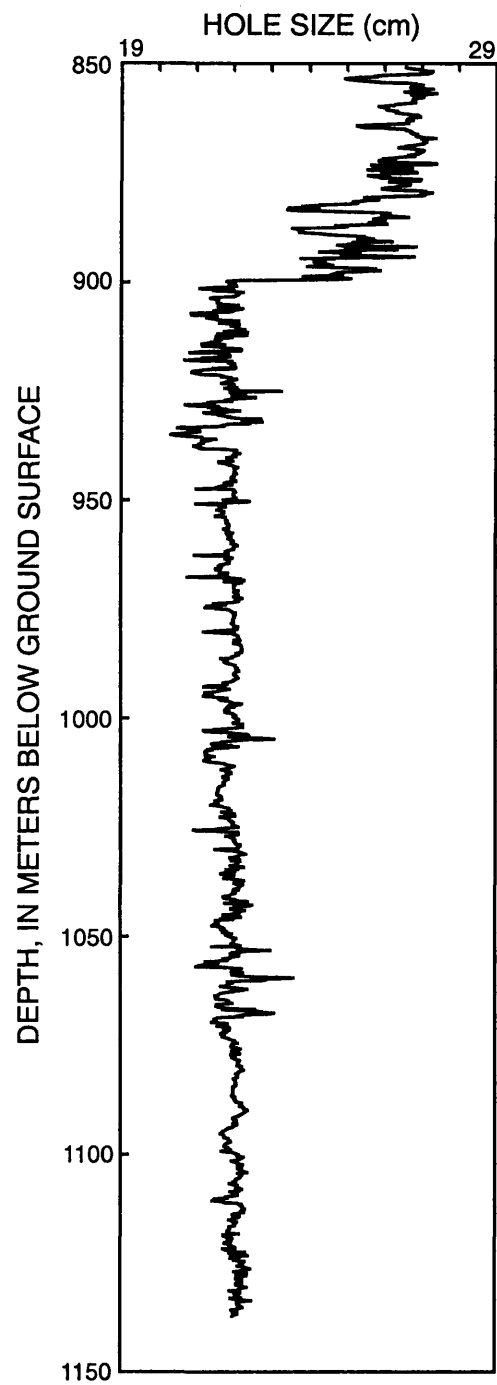
Figure 5.57 Caliper log (CAL) from the Mallik 2L-38 well.

5.57). The post-field processing of the log data from the Mallik 2L-38 well consisted of (1) depth adjusting all logs to common gamma ray measurements, (2) corrections specific to certain tools for the composition (high barite content) of the drilling mud, (3) special post-field processing of the Dipole Shear Sonic Imager (DSI) log, (4) processing and interpretation of the Fullbore Formation MicroImager (FMI), and (5) the evaluation and rejection of unrealistic log values. The depth adjustment procedure is based on an interactive graphical depth-match computer program that allows the processor to correlate and match the gamma ray responses from each log run. Specific tool corrections were performed on the gamma-ray, density, photoelectric, spectral gamma, and neutron porosity data to account for the composition of the drilling fluids. The Dipole Shear Sonic Imager (DSI) post-field processing consisted of interactively extracting compressional- and shear-wave travel-times directly from the field recorded DSI wave-forms. The interactively picked DSI travel-times were then used to calibrate the full DSI signal array. Well-log data quality control consisted of evaluating anomalous and unrealistic values, which resulted in the recognition of several coal and "hard" zones in the logged gas-hydrate-bearing interval.

The subsurface depths used in this thesis for the Mallik 2L-38 well were adjusted to the depth below ground level by subtracting 8.41 m (height above ground level of the Kelly Bushing on the drilling rig) from the downhole-measured log depths. The ground surface at this site is at an elevation of 1.36 m.

5.6.3 Logging Units and Gas-Hydrate Occurrences

In most of the previous descriptions of gas-hydrate-bearing reservoirs (Sections 5.2.3, 5.3.3, and 5.5.3), the sedimentary section has been divided into various "Logging Units". Because of the complex geologic nature of the gas-hydrate occurrences in the Mallik area, no attempt has been made to divide the sedimentary section penetrated by the Mallik 2L-38 well into Logging Units. The well-log-inferred gas-hydrate occurrence in the Mallik 2L-38 well occupies the depth interval between 888.84 and 1,101.09 m (Figure 5.58a-b); however, not all of this interval is occupied by gas hydrate.

While drilling the Mallik 2L-38 well, a major emphasis was placed on coring the log-inferred gas hydrate intervals identified in the Mallik L-38 well. A total of 13 coring runs were attempted with a variety of coring systems. Approximately 37 m of core was recovered from the gas hydrate interval (878-944 m) in the Mallik 2L-38 well (Dallimore et al., 1999). Pore-space gas hydrate and several forms of visible gas hydrate were observed in a variety of sediment types.

Data from downhole logging in both the Mallik L-38 and 2L-38 wells and formation production testing in the Mallik L-38 well have been used to assess local geology, permafrost, and gas hydrate conditions. In the upper 1,500 m, three stratigraphic sequences have been identified using reflection seismic records and well data (Jenner et al., 1999): These include the Iperk Sequence (0-337.6 m), the Mackenzie Bay Sequence (337.6-918.1 m), and the Kugmallit Sequence (918.1 m-bottom of hole). The Iperk Sequence appears to be composed almost entirely of coarse grained sandy sediments. Previous coring experience (Dallimore and Matthews, 1997) indicate that the
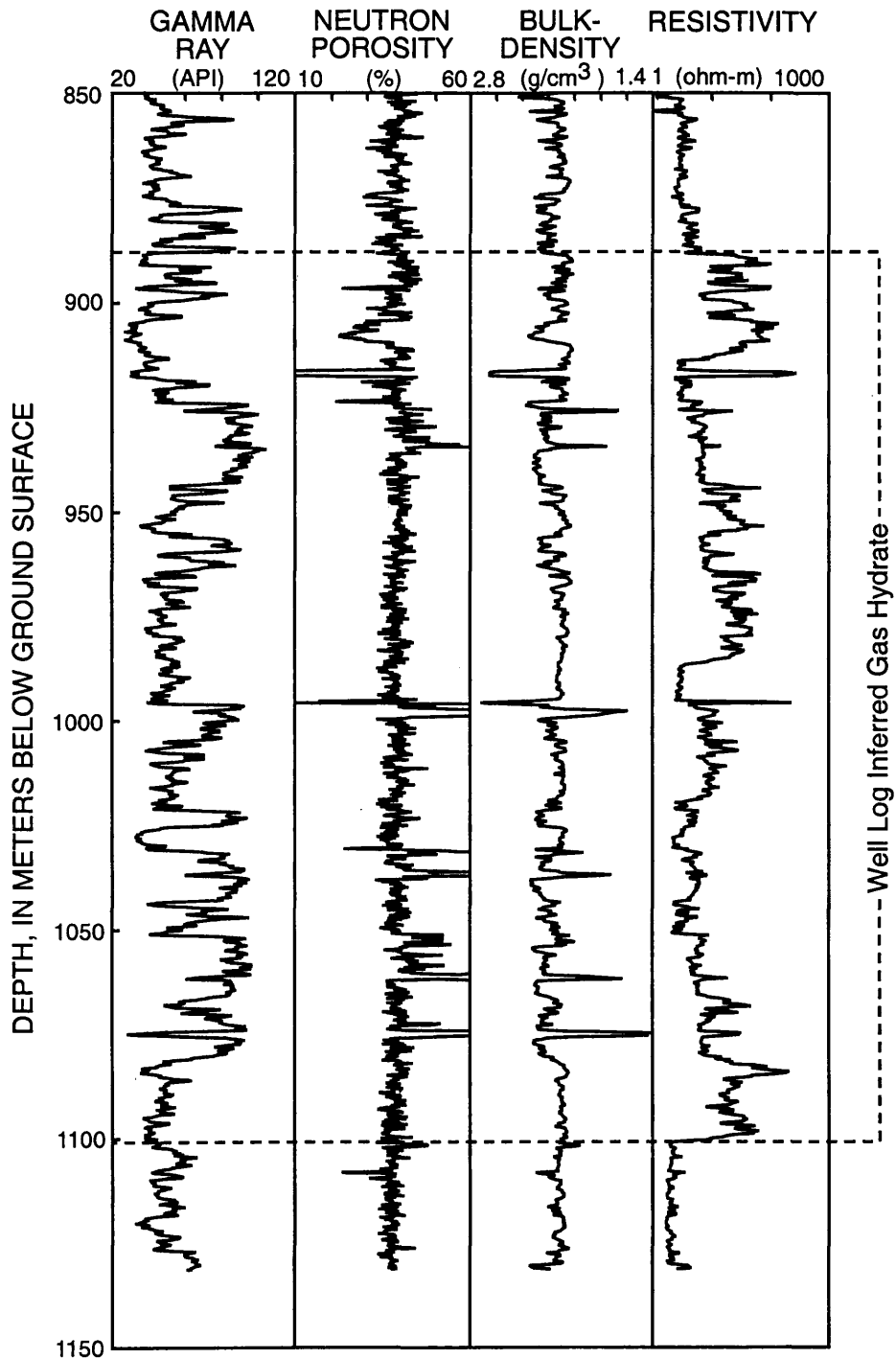
Figure 5.58a Downhole logs from the Mallik 2L-38 well (Table 5.24). Also shown are the depths of the log-inferred gas-hydrate-bearing interval.
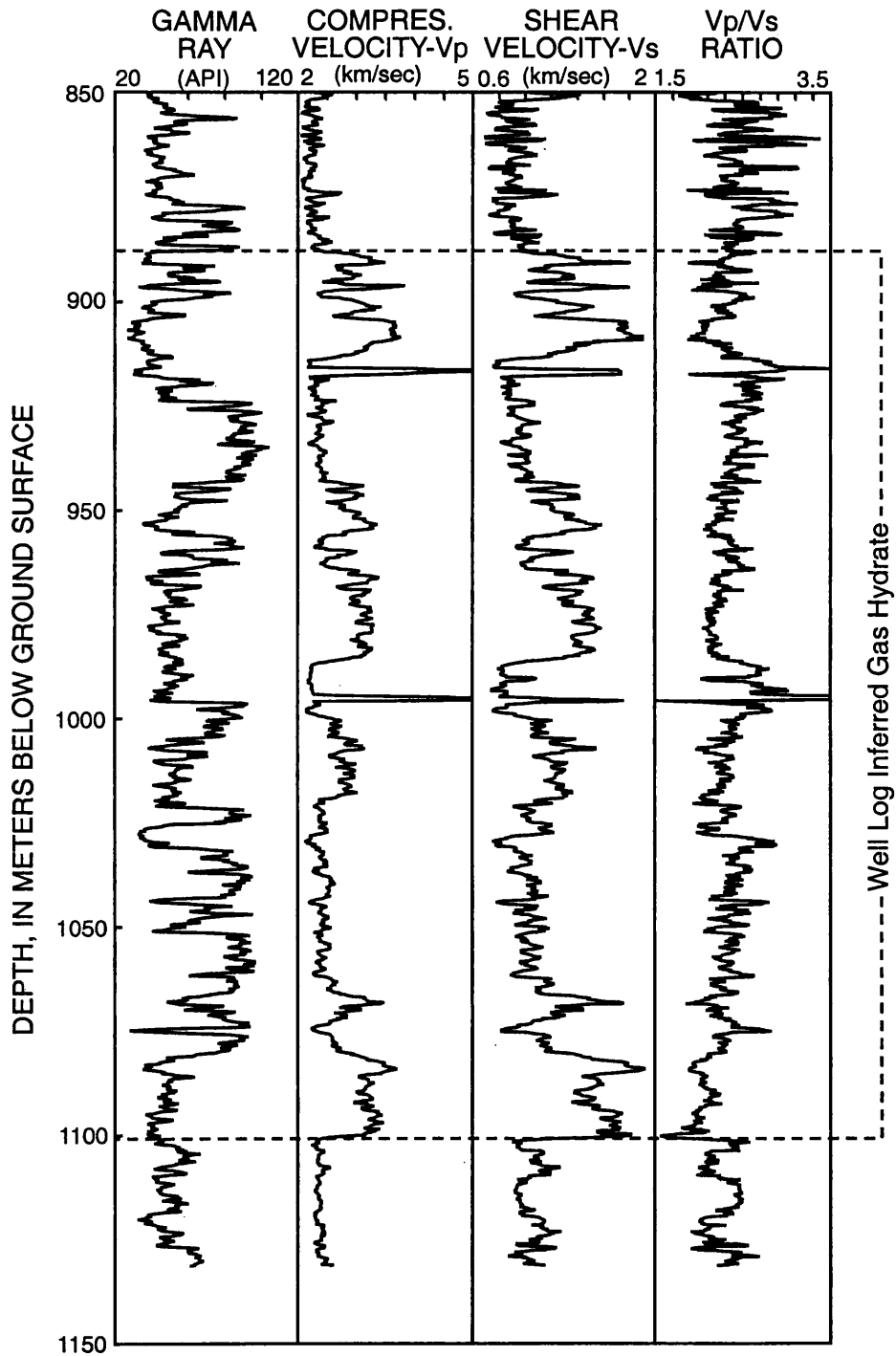
Figure 5.58b Downhole logs from the Mallik 2L-38 well (Table 5.24).
Also shown are the depths of the log-inferred gas-hydrate-bearing
interval.

Iperk sediments are unconsolidated. The Mackenzie Bay sequence is also sand dominated with a distinct fining upward section near its upper contact with the Iperk Sequence. The Kugmallit sequence (>918 m) consists of interbedded sandstone and siltstone. Chip samples and drilling records suggest that the grain cementation in the Mackenzie Bay and Kugmallit Sequences is quite variable. The base of ice-bearing permafrost in the Mallik 2L-38 well is estimated at about 640 m on the basis of available well-log information.

The cored and logged gas-hydrate occurrences in the Mallik 2L-38 well (Figure 5.58a-b) exhibit deep electrical resistivity measurements (HALS-PLATFORM EXPRESS) ranging from 10 to 100 ohm-m and compressional-wave acoustic velocities (V_p) ranging from 2.5 to 3.6 km/sec. In addition, the measured shear-wave acoustic velocities (V_S) of the confirmed gas-hydrate-bearing units in the Mallik 2L-38 well range from 1.1 to 2.0 km/sec. The Fullbore Formation MicroImager (FMI) log in the gas-hydrate-bearing stratigraphic section of the Mallik 2L-38 well is characterized by light (high resistivity) to dark (low resistivity) bands, which represent distinct stratigraphic units with thicknesses ranging between 20 to 50 cm (Figure 2.5). It is likely that the light colored stratigraphic beds in the FMI display contain gas hydrates that have been directly measured by the logging tool (as discussed in Section 2.3 of this thesis). As described above, the consolidation state of the gas-hydrate-bearing Mackenzie Bay and Kugmallit sediments in the Mallik 2L-38 well is highly variable ranging from relatively unconsolidated to well cemented.

Bily and Dick (1974) originally interpreted the presence of free-gas in contact with gas hydrate on the basis of spontaneous-potential well-log responses within several intervals of the Mallik L-38 well. They also speculated that rapid pressure responses during a production test (Production Test-1: 1,098-1,101 m) within a suspected free-gas unit are evidence of highly permeable free-gas-bearing sediments. Acoustic transit-time log data from the Mallik 2L-38 well, confirmed the occurrence of a relatively thin free-gas zone (1,100.0-1,101.9 m) at the base of the deepest downhole-log-inferred gas-hydrate. As shown in Figure 5.58b, the log-measured compressional-shear-wave velocity ratios (V_p / V_s) below 1.8 are indicative of a free-gas-bearing sediment.

5.6.4 Porosity Calculations

In the Mallik 2L-38 well, the density and neutron porosity devices ran on the Platform Express [RUN-2] array were used to calculate sediment porosities. Core-derived physical property data, including porosities, have been used to calibrate the log-derived porosities.

Core Porosities Sediment porosities (index porosities) as determined from the analysis of the water content and the mass of the solids in 75 rock samples collected from the cored interval (878-944 m) in the Mallik 2L-38 well (Winters et al., 1999) are shown as discrete samples in Figures 5.59 and 5.60. In general, the core-derived porosities in the Mallik 2L-38 well range from about 30 to 45 percent.

Density Log Porosities The downhole log-measured bulk densities in the sub-permafrost part of the Mallik 2L-38 well (Figure 5.58a) are variable with depth. The
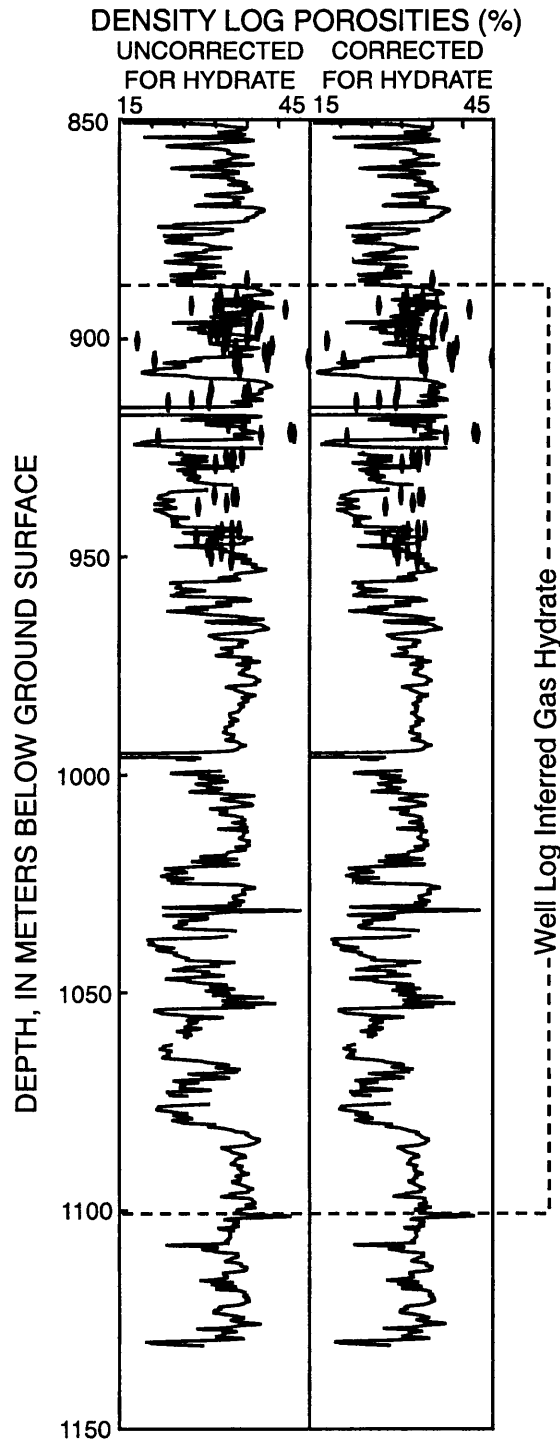
Figure 5.59 "Uncorrected" and "gas-hydrate-corrected" sediment porosities (shown as log traces) derived from the density log in the Mallik 2L-38 well. Also shown (as discrete point measurements) are the core-derived porosities.
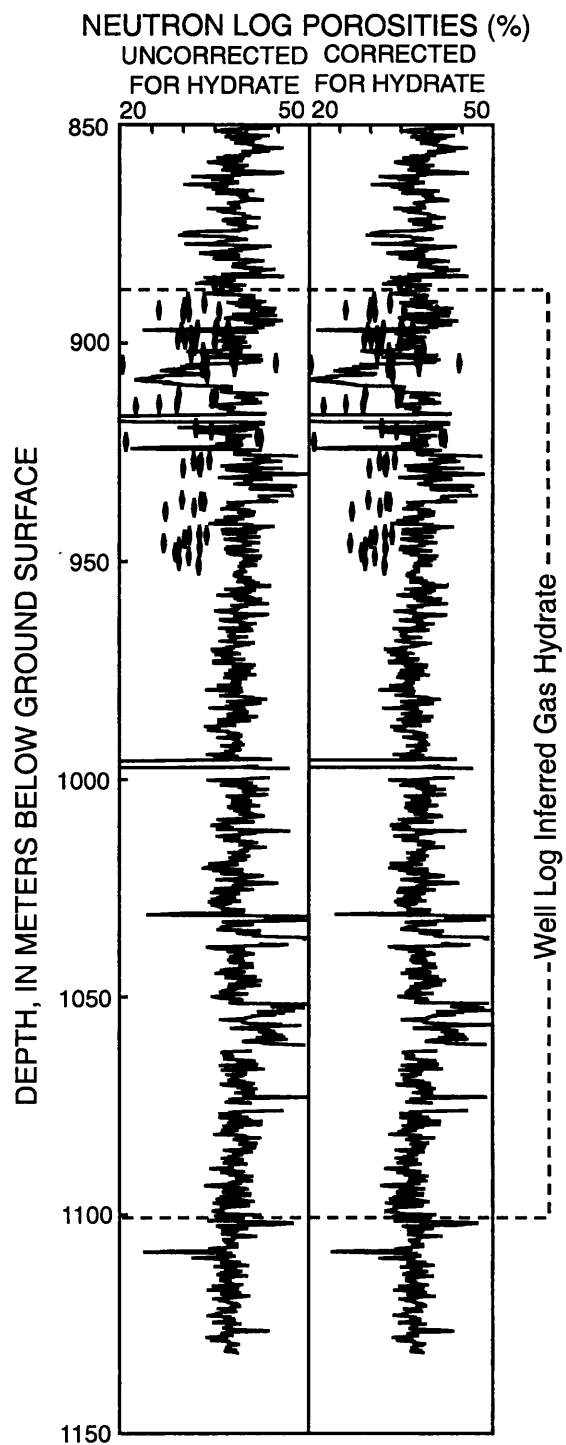
Figure 5.60 "Uncorrected" and "gas-hydrate-corrected" sediment porosities (shown as log traces) derived from the neutron porosity log in the Mallik 2L-38 well. Also shown (as discrete point measurements) are the core-derived porosities.

density log is characterized by numerous thin low density zones, ranging in thickness

from 2 to 4 meters. Sedimentary and physical property analyses of the recovered cores

from the Mallik 2L-38 well confirm that these low density zones, with measured bulk

densities of 1.9 g/cm^3 and lower, contain organic rich "coals" (Jenner et al., 1999;

Winters et al., 1999). Also shown in Figure 5.58a, are two high density "hard" zones at a

depth of 916.5-918.2 m and 995.8-996.7 m, which appear to be dolomite-cemented

sandstones (Jenner et al., 1999).

The bulk-density-log (ρ_b) measurements were used to calculate sediment

porosities ($\emptyset$) in the Mallik 2L-38 well using both the standard density-porosity relation

(Equation 3.1) and the modified density equation (Equation 3.2) that was developed for a

three component system (water, hydrate, matrix). In both density-porosity relations, the

formation water densities (ρ_w) were assumed to be constant and equal to 1.00 g/cm^3 and

the grain/matrix densities (ρ_m) were assumed to equal 2.65 g/cm^3 (which was obtained

from the analysis of the recovered cores, see Winters et al., 1999). In Equation 3.2, the

density of gas hydrate (ρ_h) was assumed to be 0.9 g/cm^3 and gas-hydrate saturations (S_h)

were determine from the Archie "quick look" method which will be discussed in the next

section of this Chapter. The density-log porosities in the gas-hydrate-bearing interval of

the Mallik 2L-38 well derived from the standard density-porosity relation (Equation 3.1)

averaged about 30.1% (Figure 5.59). However, the density-log porosities in the gas-

hydrate-bearing interval of the Mallik 2L-38 well, calculated using the modified three

component density relation (Equation 3.2), averaged about 29.3% (Figure 5.59).

Neutron Porosity Log Thermal-neutron-derived sediment porosities (assuming

sandstone matrix and corrected for borehole fluids) as measured by the Platform Express

[RUN-2] are shown as a log plot in Figure 5.60. The neutron porosity log is

characterized by numerous apparent high porosity zones which correlate with the density-

log-identified organic rich coal zones. The neutron log also reveals the two low porosity

hard zones detected by the density log. Also shown in Figure 5.60 is the "hydrate-

corrected" neutron porosity log plot. As discussed in Chapter 3 of this thesis, the

occurrence of gas hydrate at high concentrations in a reservoir can directly affect the

accuracy of the neutron-log-derived sediment porosities. A modified version of the

neutron porosity gas hydrate correction nomograph in Figure 3.5 was used to calculate

the required neutron porosity correction factors (ranging from 0% to 3%) for the full

range of "quick look"-derived gas-hydrate saturations (S_h ranging from 0% to near 90%)

observed in the Mallik 2L-38 well.

Comparison of Log-Derived Porosities In comparison, neutron porosity and

density logs have unique responses to porosity, lithology, and hydrocarbons. They can be

used together in simultaneous equation fashion and in crossplots to derive accurate

sediment porosities, infer lithologies and identify hydrocarbon-bearing intervals.

Crossplotted in Figure 5.61 are the "hydrate-corrected" neutron porosities (Figure 5.60)

and "hydrate-corrected" density-log-derived sediment porosities (Figure 5.59) from the

Mallik 2L-38 well. In the neutron-density porosity crossplot in Figure 5.61, most of the

plotted porosities fall below the clean water-bearing matrix line, which is likely due to

the occurrence of various amounts of shale (clay) in the sediment matrix.
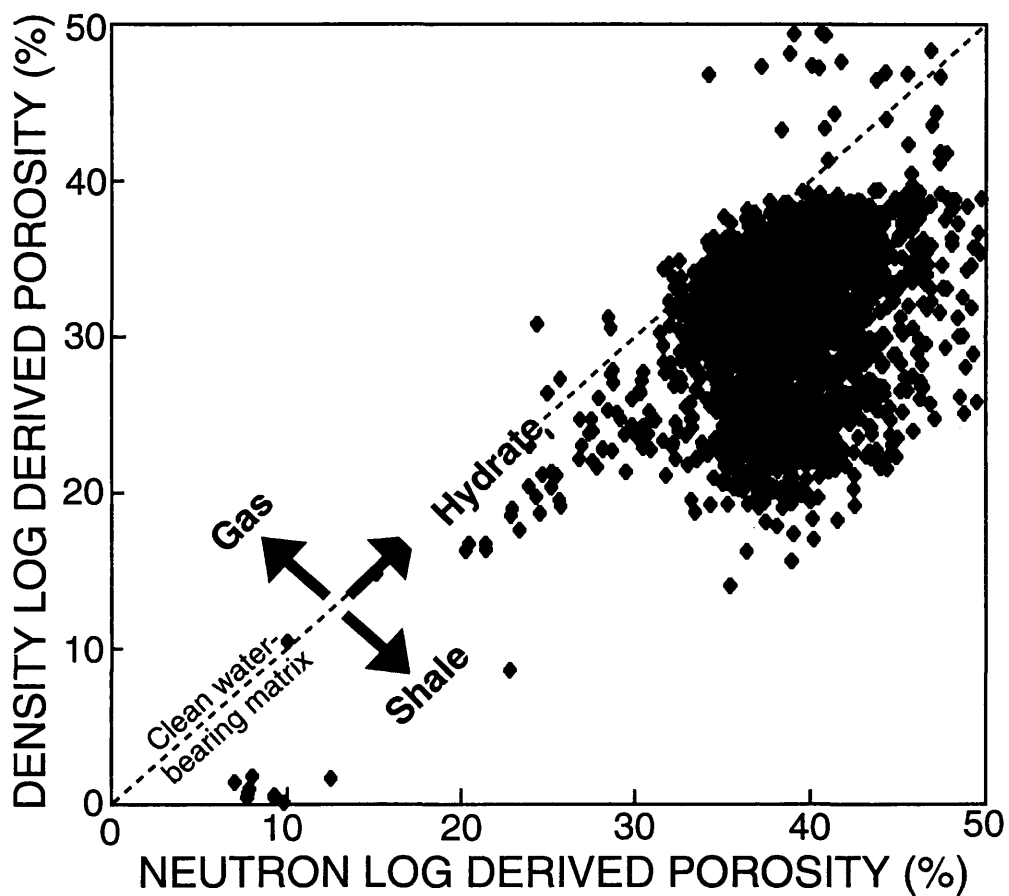
Figure 5.61 Crossplot of the neutron- and density-log-derived sediment porosities for the sub-permafrost portion of the Mallik 2L-38 well.

Before using the available downhole-log-derived neutron or density porosities to calculate gas-hydrate saturations in the next section of this thesis, the density and neutron porosity logs were corrected for the presence of "shale" by using two standard log analyses techniques: (1) the shale density correction method and (2) the crossplot method. The first method (Equation 5.1) relies on correcting density porosities with gamma ray log determined formation shale volumes and in-situ shale densities as described in Section 5.5.5 of this thesis. In the crossplot method, the log analyses program (Schlumberger GeoFrame Log Analyses Program) used to process and analyze the Mallik 2L-38 well-log data allows the log analyst to solve a series of simultaneous equations that compare the neutron-porosity- and density-log responses. This cross comparison of neutron-porosity- and density-log data results in the generation of a porosity log which is corrected for changes in matrix lithologies (clay/shale content) and the occurrence of hydrocarbons (free gas) and coal.

In both of the methods used to correct the log-derived reservoir porosities for the presence of shale in the sediments, it was necessary to determine the volume of shale (clay) in the matrix of the formation. The Tertiary gamma ray model (as described in Section 5.5.5 of this thesis) was used to calculate the volume of shale in the sediments drilled by the Mallik 2L-38 well. At Mallik, the gamma ray value for clean sand was set at 30 API and the pure shale end-member was given a value of 100 API. The gamma-ray-log-derived shale volumes (V_{sh}) in the Mallik 2L-38 well (Figure 5.62) range from near 0% in the gas-hydrate-bearing sandstone reservoirs to over 90% within shale-rich siltstone intervals.
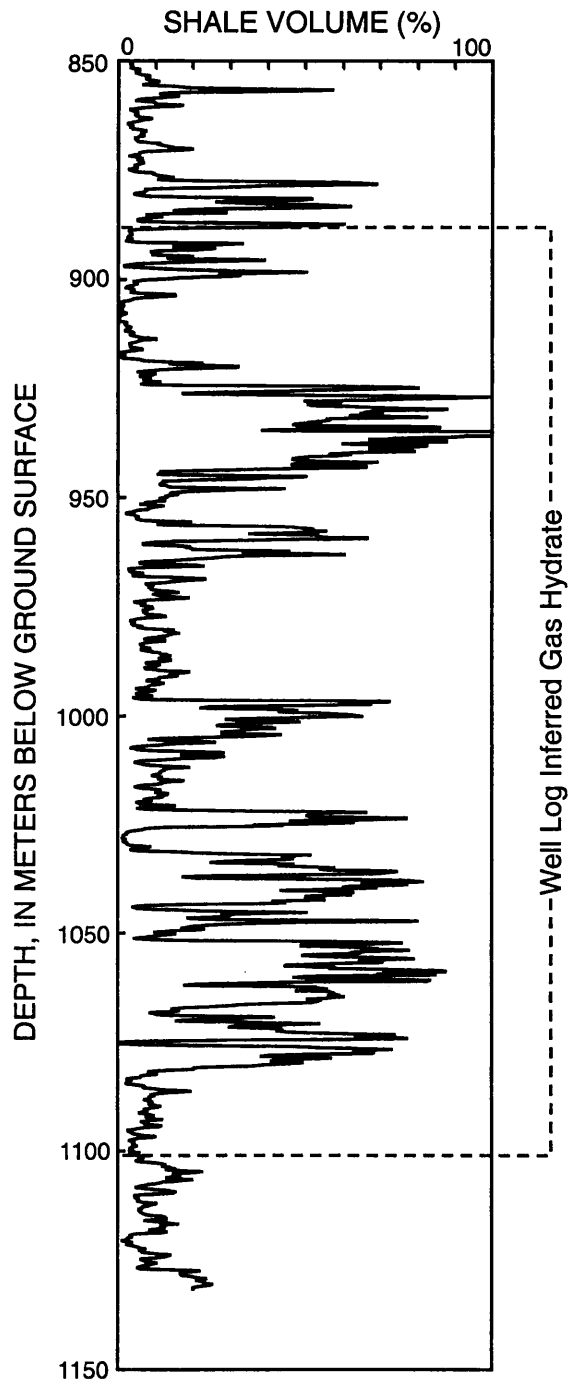
Figure 5.62 Sediment shale volumes (V_{sh}) calculated from the downhole natural gamma ray log in the Mallik 2L-38 well.

The comparison of core-derived porosities with the shale-corrected (1) density porosities and the (2) neutron-density crossplot corrected porosities in Figure 5.63, reveal that the shale-corrected density porosities more closely match the core-derived porosities; while, the neutron-density crossplot corrected porosities are considerably lower than the core-derived porosities.

5.6.5 Gas-Hydrate Distribution and Saturation

In this section of the thesis, the electrical resistivity data from the Azimuthal Resistivity Imager (ARI) on the Platform Express tool and acoustic transit-time data (both compressional- and shear-wave measurements) from the Dipole Shear Sonic Imager (DSI) device have been used to quantify the concentration (gas-hydrate saturation) of gas hydrate within the log-inferred gas-hydrate-bearing interval (888.84-1,101.9 m) in the Mallik 2L-38 well.

Resistivity-Log-Calculated Gas-Hydrate Saturations Two unique forms of the Archie relation (Archie, 1942) have been used to calculate water saturations (S_w) [gas-hydrate saturation (S_h) is equal to ($1.0-S_w$)] from the available electrical-resistivity-log data in the Mallik 2L-38 well. At the end of this section, the empirical Indonesian shaly-sand model has also been used calculate gas-hydrate saturations in the Mallik 2L-38 well. The modified Archie relation proposed by Pearson et al. (1983) was not used to assess the "Mallik" gas-hydrate accumulation.

The first resistivity-log approach used to assess gas-hydrate saturations (S_h) in the Mallik 2L-38 well was based on the modified "quick look" Archie log analysis technique
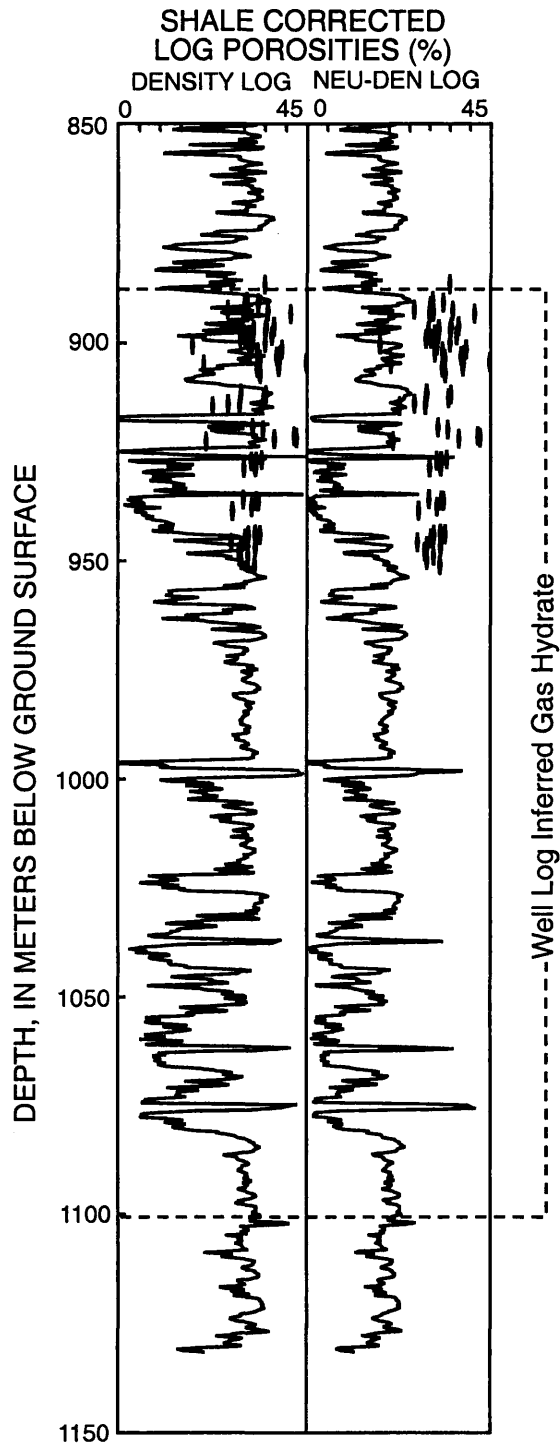
Figure 5.63 Plots of the "shale-corrected" density log and combined neutron/density-log-derived porosities in the Mallik 2L-38 well. Also shown (as discrete point measurements) are the core-derived porosities.

(Equation 3.10). The modified "quick look" Archie relationship requires as input the resistivity of the 100% water-saturated sedimentary section (R_O) in the well. In order to calculate R_O for the gas-hydrate-bearing stratigraphic units in the Mallik 2L-38 (888.84-1,101.9 m), the log-measured deep resistivities from a series of apparent water-saturated units above the log-inferred gas-hydrate-bearing units were used, which yielded a R_O of 3.5 ohm-m. To test the sensitivity of the "quick look" Archie log analysis of the Mallik well, two additional "quick look" calculations were conducted assuming R_O values that bracket the best fit 3.5 ohm-m R_O value (assumed minimum and maximum R_O values of 2.5 and 4.5 ohm-m). For the Mallik 2L-38 well, the Archie constant n was assumed to be equal to 1.9386 (reviewed by Pearson et al., 1983). Knowing R_t, R_O, and n, it is possible to use the modified "quick look" Archie relationship to estimate water saturations. In Figure 5.64, the results of the "quick look" Archie calculations are shown as water saturation (S_w) log traces for the sub-permafrost portion of the Mallik 2L-38 well. The "quick look" Archie approach, that assumed a best fit R_O value of 3.5 ohm-m, yielded an average water saturation (S_w) for the gas-hydrate-bearing stratigraphic interval (888.84-1,101.9 m) in the Mallik 2L-38 well of 52.5%.

The next resistivity approach used to assess gas-hydrate saturations in Mallik 2L-38 well was based on the "standard" Archie relation (Equation 3.8). In the Mallik 2L-38 well, the porosity data needed for the "standard" Archie equation was derived from the available downhole-density-log data and the modified three-component density porosity equation (Equation 3.2) (no shale correction). In addition to porosity, the "standard"
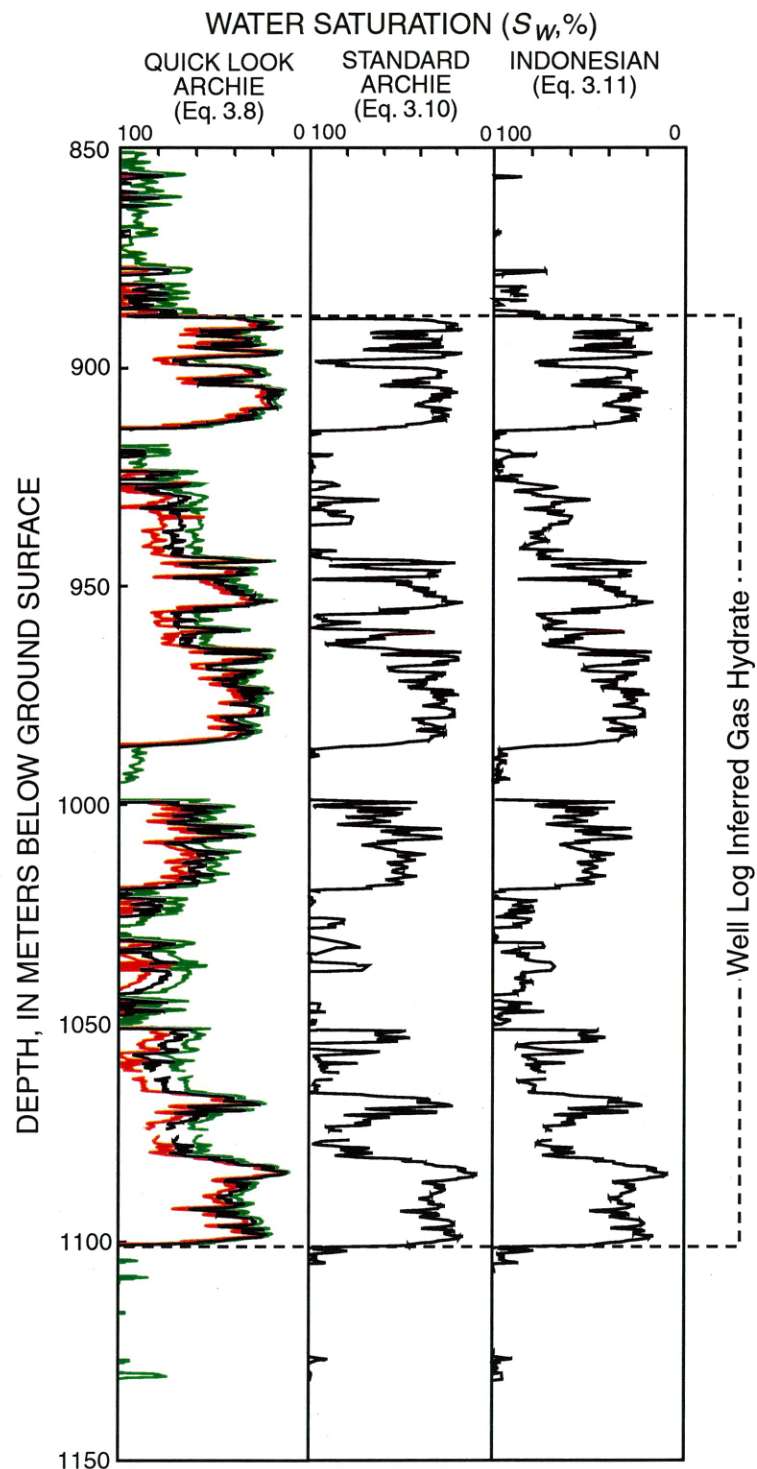
Figure 5.64 Water saturation (S_W) log plots for the Mallik 2L-38 well calculated from the "quick look" and "standard" Archie relation and the Indonesian model. The three "quick-look"-derived saturation curves assume three different R_O values (R_O = 2.5 ohm-m, R_O = 3.5 ohm-m, and R_O = 4.5 ohm-m).

Archie relation also requires as input the values for the empirical Archie constants (a, m, and n), the resistivity of the in-situ pore-waters (R_w), and the resistivity of the formation (R_t) which is obtained from the deep reading resistivity log (Figure 5.58a).

In this analysis of the Mallik 2L-38 well, the "Humble" values were used for the a (0.62) and m (2.15) Archie constants and the value of the empirical constant n was assumed to be 1.9386 as determined by Pearson et al., (1983). The resistivity of pore-waters (R_w) is mainly a function of the temperature and the dissolved salt content of the pore-waters. For the Mallik 2L-38 well, a geothermal gradient of 3.28°C/100m and a ice-bearing permafrost depth of 640 m (at a temperature of -1°C) were assumed. It has been determined that the pore-water salinity of the formation water in the Mackenzie Delta-Beaufort Sea region, within the depth range from 200 to 2,000 m, is approximately 10 ppt (Collett and Dallimore, 1998). However, pore-water salinity data from the recovered cores in the Mallik 2L-38 well (Cranston, 1999) and the analyses of interstitial water samples collected from formation production tests in the gas-hydrate-bearing section of the Mallik L-38 well yielded highly variable pore-water salinities ranging from near 1 ppt to values over 25 ppt. It is possible that solute exclusion during gas hydrate formation has locally enriched the pore-water salinities within the gas-hydrate-bearing units of the Mallik area. Therefore, a formation water resistivity (R_w) based on a single assumed pore-water salinity value for the Mallik 2L-38 well would have lead to the calculation of erroneous gas-hydrate saturations. To overcome this problem, the resistivity-log data from a series of log-inferred water-saturated zones in the Mallik 2L-38 well have been

used to estimate a pore-water resistivity trend line for the gas-hydrate-bearing interval in the Mallik area.

The well log plot of pore-water resistivity (R_W) in Figure 5.65 was derived from the deep reading resistivity log in the Mallik 2L-38 well and the "standard" Archie relation (Equation 3.8) (assuming a=0.62, m=2.15, n=1.9386, and S_W=100%). The porosity data needed for the "standard" Archie equation were derived from the density-log data (discussed in Section 5.6.4 of this thesis). The pore-water resistivity log in Figure 5.65 is actually an "apparent" pore-water resistivity (R_{wa}) log and it is considered accurate in only water-saturated (no hydrocarbons) clean (shale-free) reservoir type rocks. Therefore, the apparent pore-water resistivities within the log-inferred gas-hydrate-bearing zones are not considered accurate where the conditions above are not met. However, the apparent pore-water resistivities in a series of resistivity-log-inferred water zones at about 842-885 m, 915-942 m, 987-1,002 m, 1,022-1,065 m, and 1,102-1,122 m appear to be correct. To obtain the in-situ pore-water resistivity trend line used to calculate the "standard"-Archie-derived gas-hydrate saturations (Figure 5.65), a water resistivity trend line was projected through the log-derived apparent water resistivities (R_{wa}) in the log-inferred water-bearing zones in Mallik 2L-38. In general, the log-derived pore-water resistivities (Figure 5.65) match the core-derived pore-water resistivities (from Cranston, 1999) in the well-log-inferred water-saturated zones.

Given the Archie constants (a, m, and n), sediment porosities, and pore-water resistivities (R_W), it was possible to calculate water saturations (S_W) from the resistivity log in the Mallik 2L-38 well using the "standard" Archie relation (Equation 3.8). In
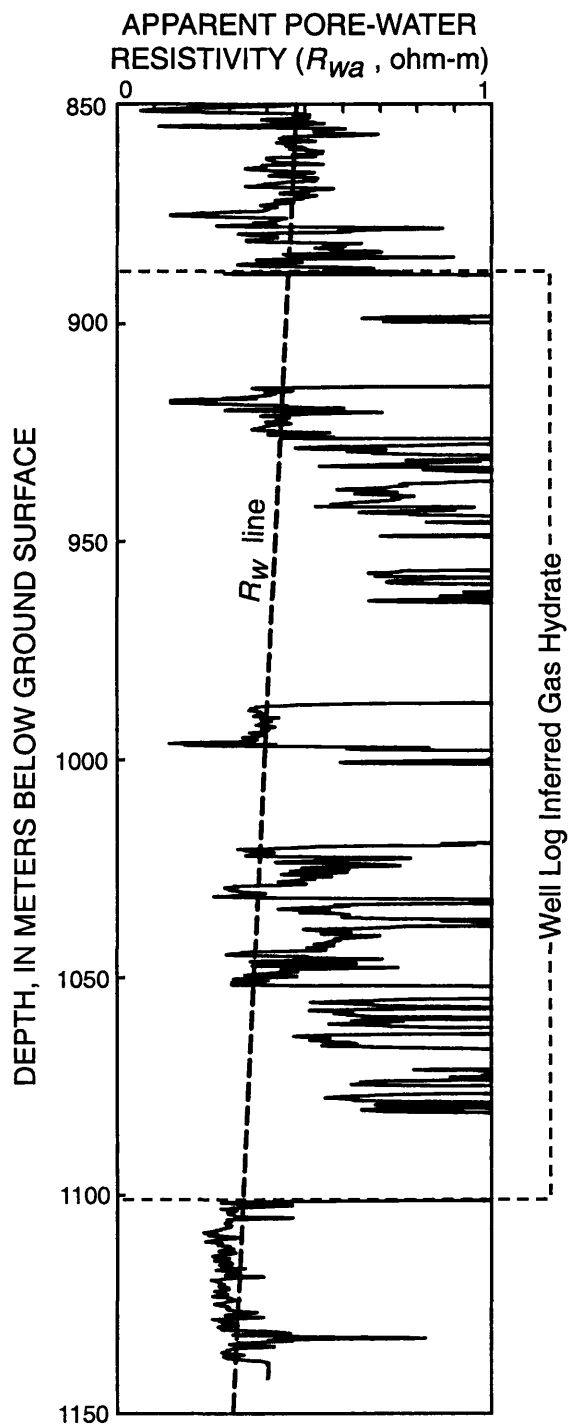
Figure 5.65 Plot of apparent pore-water resistivities (R_{wa}) as derived from the resistivity log in the Mallik 2L-38 well. The dashed continuous line represents the assumed pore-water resistivities (R_w).

Figure 5.64, the results of the "standard" Archie calculation is shown as a water

saturation (S_w) log trace along with the results of the "quick look" Archie method. The

water saturations (S_w) calculated with the "standard" Archie relation within the gas-

hydrate-bearing interval (888.84-1,101.9 m) of the Mallik 2L-38 well average 53.0%,

which is almost identical to the average water saturation determined by the "quick look"

Archie method (Figure 5.64).

The well-log-inferred gas hydrates in the Mallik 2L-38 occur within a complex

series of interbedded sedimentary units with highly variable shale (clay) concentrations.

Therefore, the empirical Indonesian shaly-sand model (Equation 3.11) was used to

calculate shale-corrected (clay) water saturations in the gas-hydrate-bearing reservoirs of

the Mallik 2L-38 well.

In addition to the usual Archie variables (Equation 3.8: a, m, n, R_w, and R_t), the

Indonesian model (Equation 3.11) also requires values for the resistivity of the shale

(clay) in the formation (R_{sh}), volume of shale (clay) in the formation (V_{sh}), and sediment

porosities corrected for the presence of shale ($\varnothing_{sc}$) (as discussed in Sections 3.4 and

5.5.5 of this thesis). The resistivity of the formation (R_t) was obtained directly from the

deep reading laterolog tool on the Platform Express (HALS-PLATFORM EXPRESS) log

run (Figure 5.58a). For the Indonesian shaly-sand assessment of the Mallik 2L-38 well

the "Humble" values for the a (0.62) and m (2.15) variables were used along with a n

value of 1.9386 (reviewed by Pearson et al., 1983). The pore-water resistivity (R_w)

trend-line calculated for the "standard" Archie assessment of the Mallik 2L-38 well

(Figure 5.65), was also used in the Indonesian shaly-sand assessment of the Mallik well.

Previously in this chapter of the thesis (Section 5.6.4), the required shale (clay) volume

(V_{sh}) estimates and shale-corrected density porosities ($\emptyset_{sc}$) were calculated. The last

variable needed for the Indonesian shaly-sand assessment of the Mallik 2L-38 gas-

hydrate occurrence, is the resistivity of the shale (clay) in the formation. A shale

resistivity (R_{sh}) of 4 ohm-m was selected for the Indonesian shaly-assessment of the

Mallik 2L-38 well.

As shown in Figure 5.64, the Indonesian-derived (shaly-sand) water saturations in

the shale-free gas-hydrate-bearing sandstone reservoirs are similar to the water

saturations calculated by either the "standard" or "quick look" Archie relations. Within

the shaly-sand reservoirs, however, the Indonesian model often yielded significantly

lower water saturations.

Acoustic-Log-Calculated Gas-Hydrate Saturations Described in Section 3.5 of

this thesis are a series of equations that utilize both compressional- and shear-wave

acoustic well-log data to calculate gas-hydrate saturations. Until the successful

completion and downhole logging of the Mallik 2L-38 well, no gas-hydrate occurrence

had been surveyed with an acoustic device that could accurately measure shear-wave

transit-times. The high quality of the both compressional- and shear-wave acoustic well-

log data from the Mallik 2L-38 has allowed the testing of all of the acoustic gas-hydrate

saturation equations presented in Section 3.5 of this thesis. The first set of equations used

in this section of the thesis employ compressional-wave acoustic log data to calculate

gas-hydrate saturations (the Timur [Equation 3.14], modified Wood [Equation 3.15], and

Lee [Equation 3.16] equations). The last set of acoustic equations used in this section,

utilize both compressional- and shear-wave acoustic well-log data to calculate gas-

hydrate saturations (the Lee shear-wave [Equation 3.17] and the Kuster-Toksöz

[Equations 3.18, 3.19, 3.20, and 3.21] equations). The gas-hydrate cementation theory,

proposed by Dvorkin et al. (1991, 1993), was also assessed in this section of the thesis

with the available downhole-log data from the Mallik 2L-38 well.

As introduced above, compressional-wave acoustic-log data from the Mallik 2L-38

well has been used along with the Timur (Equation 3.14), modified Wood (Equation

3.15), and Lee (Equation 3.16) weighted average acoustic equations to calculate gas-

hydrate saturations at the site of the Mallik well. The porosity data (Figure 5.59) used in

the acoustic gas-hydrate saturation equations were derived from the modified three

component density relation (Equation 3.2), which is described in Sections 3.2 and 5.6.4

of this thesis. The remaining variables in the Timur, Wood, and Lee equations have been

assigned constant values; with an assumed water velocity (V_w) of 1.5 km/sec, sediment

matrix velocity (V_m) of 4.65 km/sec, gas hydrate velocity (V_h) of 3.35 km/sec, water

density (ρ_w) of 1.0 g/cm^3, sediment matrix density (ρ_m) of 2.65 g/cm^3, and a gas hydrate

density (ρ_h) of 0.9 g/cm^3. In the Wood equation, the bulk-density (ρ_b) of the formation

was determined from the modified three component density equation (Equation 3.2). The

bulk compressional-wave velocity of the formation (V_b) is obtained directly from the

transit-time well logs. In the crossplot (Figure 5.66) of downhole-log-measured density

porosities and compressional-wave velocities from two water-saturated zones (800-885 m

and 1,102-1,131 m) in the Mallik 2L-38 well, it appears that a weight factor, W, of 1.3

best characterizes the sediments from the Mallik drill-site. A gas-hydrate cementation
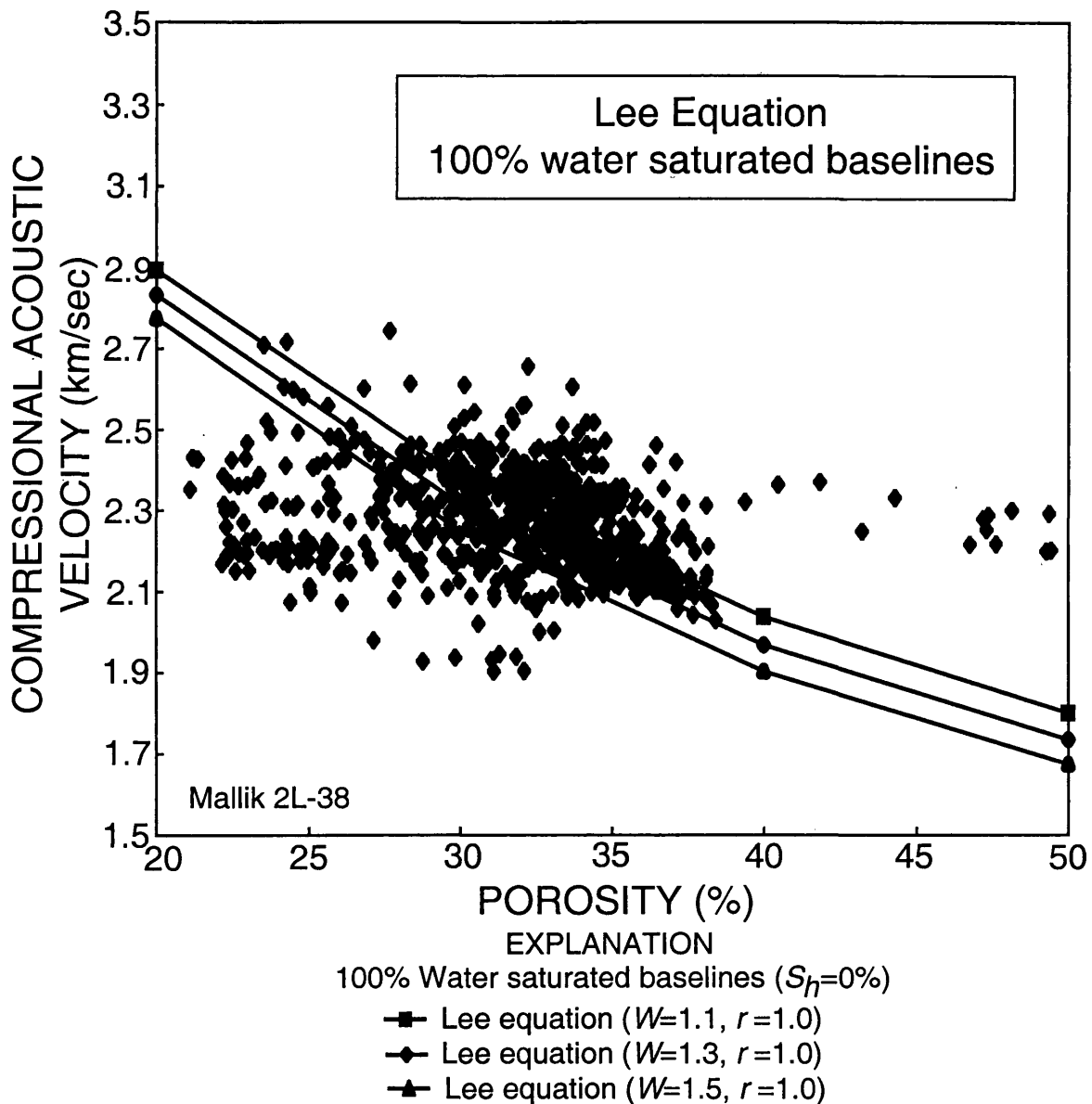
Figure 5.66 Graph showing the downhole-log-derived compressional-wave velocities (Vp) and density-log-derived porosities for a portion of the stratigraphic section both above (800-885 m) and below (1,102-1,131 m) the well-log-inferred gas-hydrate-bearing interval in the Mallik 2L-38 well. Also shown are several 100% water-saturated porosity-velocity curves predicted from a series of Lee (Equation 3.16) compressional-wave (Vp) acoustic equations that assume different Lee weight factors (W).

exponent (r) of $r=1$ was selected for the Mallik 2L-38 well, because there is no evidence that the occurrence of gas hydrates has any significant affect on the "cementation" of sediments in either marine (Ecker et al., 1996) or permafrost settings.

In Figure 5.67, the results of the Timur, Wood and Lee acoustic velocity (compressional-wave) calculations are shown as gas-hydrate saturation log traces for the Mallik 2L-38 well. In the Mallik 2L-38 well, the Timur (Equation 3.14) and Lee (Equation 3.16) acoustic equations yielded gas-hydrate saturations (S_h) ranging from 0% to a maximum near 80%, which are slightly lower than the gas-hydrate saturations calculated by the electrical resistivity methods discussed earlier in this section of the thesis. For the most part, the Wood equation (Equation 3.15) yielded unreasonable results.

As discussed above, the deployment of the Schlumberger Dipole Shear Sonic Imager (DSI) tool in the Mallik 2L-38 well provided the first data set for accurately estimating the amount of in-situ gas hydrate using both compressional- and shear-wave velocity data. In this section of the thesis, the empirical Lee relationship (Equation 3.16) was extended to include shear-wave velocity data as shown in Equation 3.17 (discussed in Section 3.5 of this thesis). In the combined compressional- and shear-wave acoustic relation proposed by Lee (Equation 3.17) most of the input variables are the same as those required for the Lee compression-wave relation (Equation 3.16) discussed previously in this section of the thesis (i.e., $V_{p\text{-}water}$, $V_{p\text{-}matrix}$, $V_{p\text{-}hydrate}$, ρ_w, ρ_m, ρ_h, ρ_b, $\varnothing$, W, and r). As can be seen from Equation 3.17, the parameter α can be estimated from assumed matrix compressional- and shear-wave velocities or can be directly
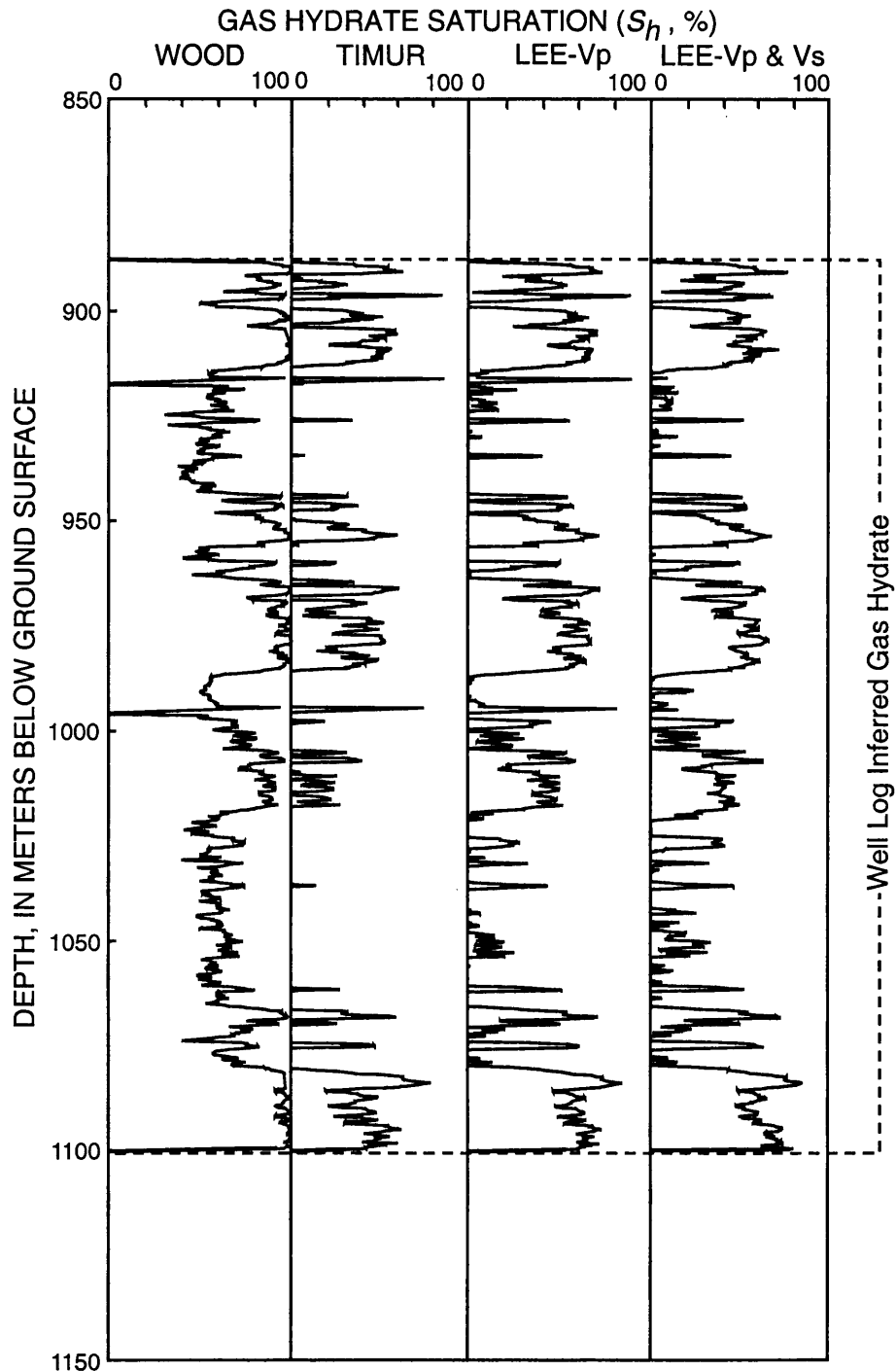
Figure 5.67 Gas-hydrate saturations (S_h) calculated from the compressional-wave (V_p) acoustic velocity log in the Mallik 2L-38 well. The results of the modified Wood (Equation 3.15), Timur (Equation 3.14), and Lee (Equation 3.16) acoustic equations are shown. Also shown are the gas-hydrate saturations (S_h) derived from the compressional- and shear-wave (V_p-V_s) Lee acoustic relation (Equation 3.17).

determined from downhole-measured compressional- and shear-wave velocities in non-gas-hydrate-bearing sediments. The parameter β can be calculated from laboratory-measured compressional- and shear-wave velocities of pure gas hydrate samples (Tables 1.1 and 3.11). The last term in Equation 3.17 (γ) can be dropped, since fluids cannot sustain shear-waves. In this study, the parameter β was taken from the V_s/V_p ratio for a Structure-I methane hydrate given in Table 1.1 ($\beta = V_{s\text{-}hydrate}/V_{p\text{-}hydrate} = 0.51$). The parameter α was estimated from the measured compressional- and shear-wave velocities of non-gas-hydrate-bearing sediments overlying the log-inferred gas-hydrate occurrences in Figure 5.58b ($\alpha = V_{s\text{-}matrix}/V_{p\text{-}matrix} = 0.558$).

In Figure 5.67, the results of the combined compressional- and shear-wave Lee acoustic relation (Equation 3.17) assessment of the Mallik 2L-38 well have been included with the results of the Timur, Wood and Lee compressional-wave acoustic velocity calculations. In the Mallik 2L-38 well, the combined compressional- and shear-wave Lee acoustic relation (Equation 3.17) yielded similar but slightly lower gas-hydrate saturations than the Lee compressional-wave acoustic velocity calculations (Equation 3.16).

As previously noted, this section of the thesis also includes the assessment of the multiphase wave scattering theory of Kuster and Toksöz (1974), which has been modified to assess the acoustic properties of gas-hydrate-bearing sediments (Zimmerman and King, 1986; Lee et al., 1996). An alternative gas hydrate acoustic model proposed in Dvorkin et al. (1991) and Dvorkin and Nur (1993, 1996), which is based on estimating acoustic properties of cemented gas-hydrate-bearing sediments from grain contact theory,

has also been tested in this section of the thesis. In order to test the wave scattering

theory of Kuster and Toksöz and the cementation theory of Dvorkin, the downhole-log-

measured density porosities and compressional-wave velocities from two water-saturated

zones (800-885 m and 1,102-1,131 m) in the Mallik 2L-38 well have been crossplotted in

Figure 5.68 along with series of model-derived water-saturated matrix curves calculated

for the gas-hydrate reservoir conditions at the site of the Mallik well. The water-

saturated matrix curves (100% water filled pore-space, no gas hydrate) displayed in

Figure 5.68 are derived from the Timur (Equation 3.14), Wood (Equation 3.15), and Lee

(Equation 3.16) (W=1.3) compressional-wave acoustic velocity relations, and the

combined compressional- and shear-wave acoustic relations proposed by Kuster-Toksöz

(wave scattering theory; Equations 3.18, 3.19, 3.20, and 3.21) and Dvorkin (cementation

theory). In the crossplot of the density porosities and compressional-wave velocities of

the water-saturated zones from the Mallik 2L-38 well (Figure 5.68), it appears that most

of the water-saturated zones fall far above the water-saturated baselines predicted by the

Wood compressional-wave acoustic relation (Equation 3.15) and the combined

compressional- and shear-wave acoustic relations proposed by Kuster-Toksöz (wave

scattering theory) and Dvorkin (cementation theory). Therefore, both the wave scattering

theory of Kuster-Toksöz and the cementation theory of Dvorkin would overestimate gas-

hydrate saturations in the Mallik 2L-38 well, similar to the Wood equation

overestimation of gas-hydrate saturations in all five case studies previously reviewed in

this Chapter of the thesis. Further examination of Figure 5.68 indicates that the Lee

acoustic equation (Equation 3.16) yielded a relatively accurate water-saturated baseline,
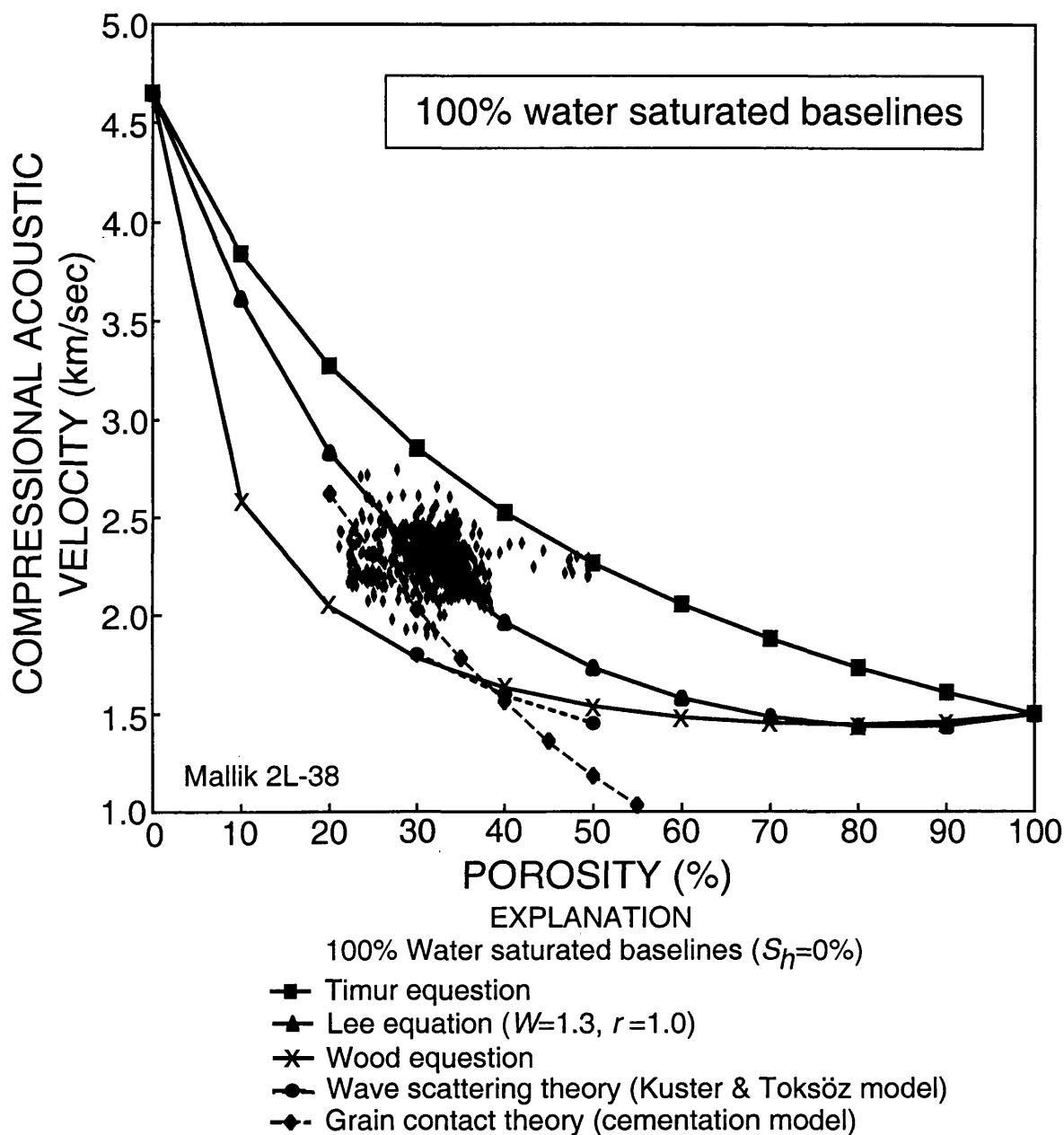
Figure 5.68 Graph showing a series of 100% water-saturated porosity-velocity curves predicted from the Wood (Equation 3.15), Timur (Equation 3.14), and Lee (Equation 3.16) compressional-wave (V_p) equations. This graph also includes water-saturated porosity-velocity curves calculated from the wave scattering (Kuster-Toksöz model) and grain contact (cementation model) theories. Also shown are the log-derived compressional-wave velocities (V_p) and density-log-derived porosities from the water-saturated portions of the stratigraphic section both above (800-885 m) and below (1,102-1,131 m) the well-log-inferred gas-hydrate-bearing interval in Mallik 2L-38.

with most of the water-saturated zones in the Mallik well plotting on or near the Lee water-saturated baseline, which should result in the calculation of accurate gas-hydrates saturations (as discussed earlier in this section).

To further evaluate the combined compressional- and shear-wave acoustic relations proposed by Kuster-Toksöz (wave scattering theory) and Dvorkin (cementation theory), in Figures 5.69 and 5.70 the downhole-log-measured density porosities have been crossplotted against the ratio of the compressional- and shear-wave velocities for two water-saturated zones (800-885 m and 1,102-1,131 m) in the Mallik 2L-38 well. Also shown in Figures 5.69 and 5.70 are the acoustic-model-derived water-saturated matrix curves and a series of gas-hydrate saturation matrix curves calculated for the reservoir conditions at the site of the Mallik well. The water-saturated matrix and gas-hydrate saturation curves displayed in Figure 5.69 were derived from the Kuster-Toksöz wave scattering theory (Equations 3.18, 3.19, 3.20, and 3.21). On the other hand, the water-saturated matrix and gas-hydrate saturation curves displayed in Figure 5.70 were derived from the cementation theory as proposed in Dvorkin et al. (1991) and Dvorkin and Nur (1993, 1996). In both Figure 5.69 and 5.70, most of the water-saturated zones from the Mallik 2L-38 well fall far above and below the water-saturated matrix curves, respectively; which again indicates that the Kuster-Toksöz wave scattering theory and the Dvorkin cementation theory overestimate gas-hydrate saturations in the Mallik 2L-38 well.

Gas-Hydrate Saturation Calculations -- Summary The "standard" Archie and "quick-look" Archie electrical resistivity methods yielded for the most part gas-hydrate
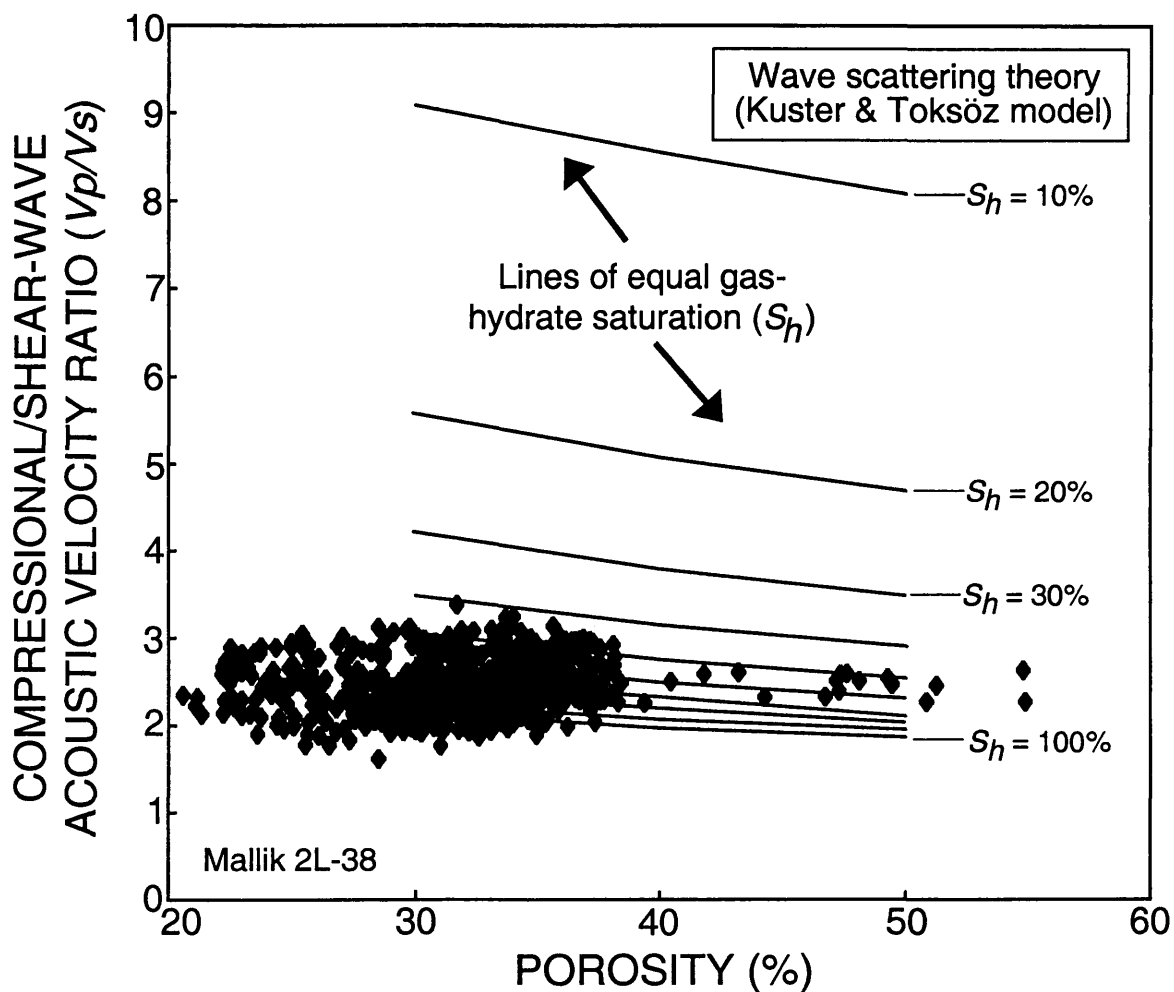
Figure 5.69 Graph showing a series of gas-hydrate saturation curves (S_h ranging from 10 to 100%) as calculated from the wave scattering theory (Kuster-Toksöz model). Also shown are the downhole-log-derived compressional-shear-wave acoustic velocity ratios (V_p/V_s) and density-log-derived porosities from the water-saturated portions of the stratigraphic section both above (800-885 m) and below (1,102-1,131 m) the well-log-inferred gas-hydrate-bearing interval in the Mallik 2L-38 well.
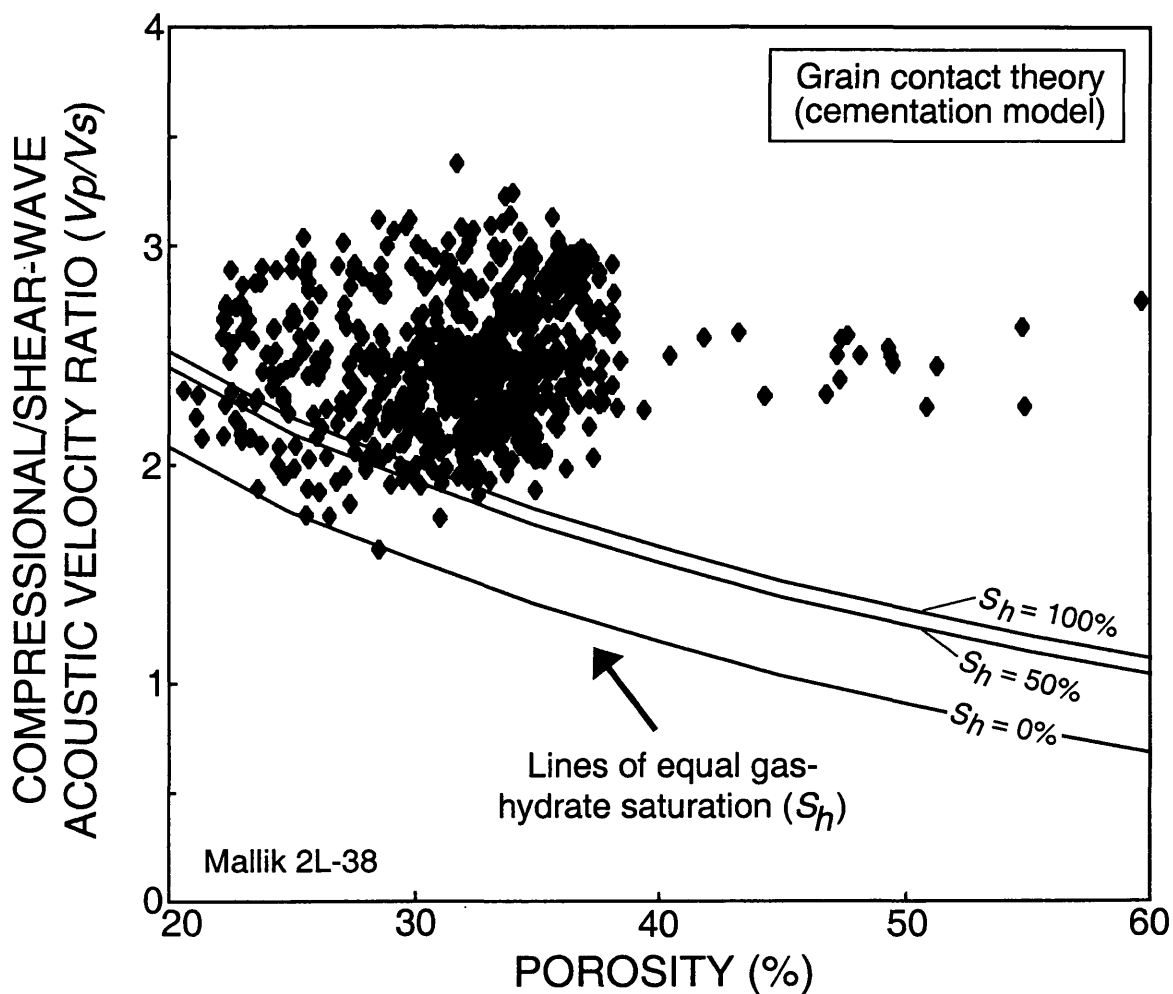
Figure 5.70 Graph showing a series of gas-hydrate saturation curves (S_h ranging from 0 to 100%) as calculated from the grain contact theory (cementation model). Also shown are the downhole-log-derived compressional-shear-wave acoustic velocity ratios (V_p/V_s) and density-log-derived porosities from the water-saturated portions of the stratigraphic section both above (800-885 m) and below (1,102-1,131 m) the well-log-inferred gas-hydrate-bearing interval in the Mallik 2L-38 well.

saturations (1-S_w) for the log-inferred gas-hydrate-bearing interval in the Mallik 2L-38

well ranging from zero to about 90 percent. The Indonesian-derived (shaly-sand) gas-

hydrate saturations were similar to the "standard"- and "quick-look"-Archie-derived gas-

hydrate saturations in clean (shale-free) gas-hydrate-bearing sandstone reservoirs.

However, in some of the relatively more shale-rich intervals, the Indonesian shaly-sand

relation revealed significantly higher gas-hydrate saturations. The Lee (compressional-

and shear-wave relations) and Timur acoustic equations, however, generally yielded gas-

hydrate saturations (S_h) less than those calculated from the electrical-resistivity-log data.

The apparent discrepancy between the resistivity- and acoustic-derived gas-hydrate

saturations is not easily explained. It is possible that the assumed pore-water resistivities

(R_w) calculated for the water zones in the Mallik 2L-38 well may not be representative of .

the pore-water resistivities (R_w) in the gas-hydrate-bearing zones. It is also possible that

the selection of certain critical constants in the acoustic transit-time calculations could be

in error. Most recently there has even been concern expressed about the assumed

acoustic velocity of pure gas hydrate (Helgerud et al., 1999). Most certainly more

laboratory and field studies are required to quantitatively assess the electrical resistivity

and acoustic properties of gas-hydrate-bearing sediments. For this study, however,

comparisons of independent observations and measurements of gas hydrate content in the

recovered cores from the Mallik 2L-38 well agree more closely with the resistivity-

derived gas-hydrate saturations (Wright et al., 1999; Cranston, 1999). In general, the

combined compressional- and shear-wave acoustic relations proposed by Kuster-Toksöz

(wave scattering theory; Equations 3.18, 3.19, 3.20, and 3.21) and Dvorkin (cementation

theory) overestimate gas-hydrate saturations in the Mallik 2L-38 well. Therefore, it is

assumed that the "standard"-Archie-derived gas-hydrate saturations are the best

downhole-log-derived gas-hydrate saturations from the Mallik 2L-38 well.

5.6.6. Volume of Gas

The volume of gas that may be contained in a gas-hydrate accumulation depends

on five "reservoir" parameters as discussed in Sections 5.2.7, 5.3.7, 5.4.7, and 5.5.6 of

this thesis. In the assessment of the gas resources associated with the Mallik gas-hydrate

accumulation, the following "resource" assessment is based on the calculation of the

volume of gas hydrate within a one square kilometer area surrounding the Mallik 2L-38

well. Because of the discrepancy in the resistivity and acoustic-derived gas-hydrate

saturations (Figures 5.64 and 5.67), two unique gas hydrate "resource" assessments of the

Mallik 2L-38 well were conducted: (1) one assessment assuming the "standard" Archie

gas-hydrate saturations are correct, and (2) second assessment assuming the

"compressional-wave" gas-hydrate saturations are correct. For this "resource"

assessment, the thickness of the gas-hydrate occurrence was defined as the total thickness

of the well-log-inferred gas-hydrate interval (888.84-1,101.9 m) in the Mallik 2L-38 well

(Figure 5.58a-b). The porosity data needed for this "resource" assessment was derived

from the modified three-component density porosity equation (Equation 3.2) (no shale

correction) and the downhole-measured density-log data from the Mallik 2L-38 well. In

this assessment a hydrate number of 6.325 (90% gas filled clathrate) was assumed, which

corresponds to a gas yield of 164 m^3 of methane (at STP) for every cubic meter of gas

hydrate. Based on these assumptions, is was determined that the log-inferred gas-hydrate-bearing stratigraphic interval drilled in the Mallik 2L-38 well contains about 4,800,000,000 cubic meters of gas in the one square kilometer area surrounding the drill-site, assuming the "standard" Archie gas-hydrate saturations are correct (Table 5.25). However, if the Lee (compressional-wave) gas-hydrate saturations are assumed to be correct, the log-inferred gas-hydrate-bearing stratigraphic interval drilled in the Mallik 2L-38 well contains about 2,930,000,000 cubic meters of gas in the one square kilometer area surrounding the drill-site. As previously discussed in this thesis, however, the "standard"-Archie-derived gas-hydrate saturations compare more favorably with other independent measurements of gas hydrate concentration. Both calculations assume that there is no lateral variability in the thickness of the gas hydrate section, porosity, or gas-hydrate saturation.

Table 5.25 Volume of natural gas within the downhole-log-inferred gas-hydrate-bearing interval in the Mallik 2L-38 well.

Depth of log inferred gas hydrates (m)	Thickness of hydrate-bearing unit (m)	Sediment porosity (%)	Gas-hydrate saturation (%)*	Volume of hydrate per square km (m³)	Volume of gas within hydrate per square km (m³)**
888.8-1,101.9	213.1	29.3	47.0	29,346,001	4,812,744,164

*"Standard" Archie derived gas-hydrate saturation.

**Gas volume calculation assumes a hydrate number of 6.325 (90% gas filled clathrate), 1 m³ of gas hydrate = 164 m³ free-gas at STP.

CHAPTER 6

REVIEW OF WELL-LOG METHODS

FOR GAS HYDRATE RESERVOIR EVALUATION

In Chapter 3 of this thesis, the known and modeled responses of the gamma-gamma density, neutron porosity, electrical resistivity, acoustic transit-time, nuclear magnetic resonance, and neutron spectroscopy well-logging devices to the presence of gas hydrate were examined. Chapter 3 also contains descriptions of existing and newly proposed well-log evaluation techniques used to characterize sediment porosities ($\emptyset$) and water saturations (S_w) [gas-hydrate saturation (S_h) is equal to (1.0-S_w)] in gas-hydrate-bearing reservoirs. In Chapter 5 of this thesis, most of the quantitative gas hydrate well-log evaluation techniques introduced in Chapter 3, were tested and utilized to calculate reservoir porosities and the degree of gas-hydrate saturation within five known gas-hydrate accumulations: (1) Blake Ridge, (2) Cascadia continental margin, (3) Middle-America Trench, (4) North Slope of Alaska, and (5) Mackenzie River Delta. This chapter (Chapter 6) includes a systematic review of the gas hydrate well-log evaluation techniques proposed in Chapter 3 and an assessment of their performance in the field verification portion (Chapter 5) of this study. This chapter begins with a review of the well-log analysis methods used to determine sediment porosities in gas-hydrate-bearing

reservoirs, which is followed by a review of the log analysis methods used to calculate

gas-hydrate saturations.

6.1 Porosity Calculations

As discussed in Chapter 3 of this thesis, sediment porosities can be determined

from numerous downhole measurements. In Chapter 5 of this thesis, electrical resistivity,

bulk-density, and neutron porosity logs were used to calculate sediment porosities. As

shown with log data from the coreholes on the Blake Ridge (Section 5.2.5), electrical

resistivity logs can be used to calculate sediment porosities using the Archie relation

(Equation 3.7). The calculated resistivity-log porosities from Sites 994, 995, and 997

(Figure 5.11) on the Blake Ridge are generally similar to the available core porosities.

The occurrence of gas hydrate in the sedimentary section beneath the Blake Ridge,

however, results in an "apparent" reduction in the resistivity-derived porosities and limits

the utility of this well-log analysis method in gas-hydrate-bearing reservoirs.

In Section 3.2 of this thesis, the standard density-porosity relation (Equation 3.1)

and a modified three-component (water, hydrate, matrix) density-porosity equation

(Equation 3.2) have been presented and used to assess the affect of gas hydrate on the

density-log-derived sediment porosities. As shown in Figures 3.2 and 3.3, at relatively

low gas-hydrate saturations (S_h<50%) and "normal" sediment porosity conditions

($\varnothing$<40%) the standard density-porosity relation (Equation 3.1) yields relatively accurate

results. At higher sediment porosities and gas-hydrate saturations, however, the

downhole-log-derived bulk-density porosities need to be corrected. Modified versions of

the proposed gas hydrate density correction nomograph in Figure 3.3 and the three

component density-porosity equation (Equation 3.2) have been successfully used to

correct the "apparent" density porosities within the gas-hydrate-bearing sediments at Site

570 (Figure 5.36) and in both the Northwest Eileen State-2 and the Mallik 2L-38 (Figure

5.59) wells. Because of relatively low gas-hydrate saturations (S_h<30%) and the poor

quality of the density-log data from ODP Leg 146 and 164, no attempt was made to

correct the "apparent" density porosities within the gas-hydrate-bearing sediments or to

use the density porosities for any quantitative calculations at Sites 889, 994, 995, or 997.

Simple chemical modeling of hydrogen concentrations in gas-hydrate-bearing

sediments and complex computer well-log response modeling, as described in Section 3.3

of this thesis, reveal that gas hydrate has little affect on neutron-porosity log responses at

relatively low gas-hydrate saturations (S_h<50%) and within "normal" sediment porosity

conditions ($\varnothing$<40%). At relatively high gas-hydrate saturations, however, the neutron

porosity log will significantly over estimate porosities (Figures 3.4 and 3.6). Modified

versions of the proposed gas hydrate neutron porosity correction nomographs (Figures

3.5 and 3.7) have been used to correct the "apparent" neutron-log-derived porosities at

Site 570 (Figure 5.37) and in both the Northwest Eileen State-2 and Mallik 2L-38 (Figure

5.60) wells. The "hydrate-corrected" density- and neutron-log-derived porosities from

the Northwest Eileen State-2 well compare favorably. The "hydrate-corrected" density-

and neutron-log-derived porosities in the Mallik 2L-38 well are similar within the shale-

free gas-hydrate-bearing sandstone reservoirs; however, in relatively shale-rich intervals

the density- and neutron-log-derived porosities differ considerably. The "hydrate-

corrected" density- and neutron-log-derived porosities from the massive gas hydrate zone in Hole 570 differ by almost 30%. The reason for this difference is unknown (as discussed in Section 5.4.5 of this thesis); however, because of different vertical resolution capabilities, the density tool may have more accurately measured the physical properties of the massive gas hydrate zone at Site 570. Because of relatively low gas-hydrate saturations (S_h<30%), the neutron-porosity-log data from Site 889 was used without any further gas hydrate corrections. Because of poor borehole conditions, the neutron-porosity-log data from the three sites (Sites 994, 995, and 977) drilled on the Blake Ridge was disregarded.

The affect of shales (clay) on both density- and neutron-log derived sediment porosities are well established in published assessments of conventional oil and gas reservoirs. The shale porosity corrections used in this thesis generally followed standard log analysis schemes as discussed in each of the case studies presented in Chapter 5. In situations where core-derived sediment grain (matrix) densities were available, the density log yielded the most accurate porosities within lithologic complex reservoirs.

In summary, assuming good borehole conditions, the density and neutron porosity logs should yield accurate sediment porosities within most gas-hydrate-bearing reservoirs (with appropriate corrections in shale-rich sedimentary sections). However, at relatively high gas-hydrate saturations, density- and neutron-log-derived porosities need to be corrected for the presence of gas hydrate.

6.2 Gas-Hydrate Saturations

As discussed in Chapter 3 of this thesis, electrical resistivity, acoustic transit-time, and neutron spectroscopy downhole-log data can be used to quantify the amount of gas hydrate in a sedimentary section. Three unique forms of the Archie relation (Archie, 1942) have been used to calculate water saturations (S_w) [gas-hydrate saturation (S_h) is equal to ($1.0-S_w$)] from the available electrical-resistivity-log data at all five gas-hydrate accumulations assessed in Chapter 5 of this thesis (Figures 5.12a-c, 5.13, 5.29, 5.38, 5.50, and 5.64). The "standard" Archie relation (Equation 3.8) and "quick look" Archie method (Equation 3.10) yielded, for the most part, gas-hydrate saturations that compare favorably with gas-hydrate concentrations calculated by other means. The modified Archie approach proposed by Pearson et al. (1983) (Equation 3.9) yielded erroneous gas-hydrate saturations.

In most cases, the values of the empirical parameters (a, m, and n) in the various modified forms of the Archie relation used in this study have been directly calculated from available downhole-log and core data. In several cases, however, the empirical Archie parameters were assigned constant values that have been developed for "conventional" well-log analysis procedures. When possible, formation water resistivities (R_w) and water-saturated sediment resistivity (R_o) baselines have been calculated from the analyses of recovered formation waters and projected from available downhole-resistivity-log surveys.

At Site 570 and in the Northwest Eileen State-2 and Mallik 2L-38 wells, sediment porosity data from the density and neutron porosity logs have been used in the various

forms of the electrical resistivity and acoustic velocity gas-hydrate saturation equations to calculate accurate gas-hydrate saturations. For the Blake Ridge and Cascadia continental margin drill-sites, however, both statistically manipulated and unmanipulated porosity data from downhole-log surveys and core studies have been used to assess the in-situ gas-hydrate saturations. For the most part, the gas-hydrate saturation calculations that employed average core porosities yielded more consistent saturation values. While the resistivity and acoustic velocity methods that employed non-statistically manipulated core and log porosities resulted in the calculation of more highly variable gas-hydrate saturations. The use of data from different sources (downhole-logs and core data) and non-compatible downhole depths (mismatched log depth data) have contributed to the more variable nature of the gas-hydrate saturations calculated with the non-statistically manipulated core and log porosities. However, the use of average core porosity trends may mask porosity variations within the sedimentary section which can lead to the calculation of erroneous gas-hydrate saturations. Therefore, in complex geologic settings, such as at Site 889 on the Cascadia continental margin, the use of average core or log porosity trends in the resistivity and acoustic velocity gas-hydrate saturation equations may yield erroneous results.

As discussed in Chapter 3 and demonstrated in Sections 5.2.6, 5.3.6, 5.5.5, and 5.6.5 of this thesis, the occurrence of shale (clay) in the sediment matrix of a reservoir can affect the calculation of hydrocarbon saturations with downhole-resistivity-log data. In this thesis, the Waxman-Smits (Waxman and Smits, 1968) and Indonesian (Poupon and Leveaux, 1971) shaly-sand resistivity models have been used to evaluate the affect of

shales (clay) on the resistivity-log-derived gas-hydrate saturations in four of the gas-hydrate accumulations assessed in Chapter 5. Due to the availability of sediment cation exchange capacity (CEC) data, the Blake Ridge and Cascadia margin gas-hydrate occurrences were assessed with the Waxman-Smits model. While the Northwest Eileen State-2 and Mallik 2L-38 gas-hydrate occurrences were assessed with the Indonesian model, which generally works well in lithologically complex reservoirs.

The Indonesian-derived (shaly-sand) gas-hydrate saturations in the relatively clean (shale-free) gas-hydrate-bearing sandstone reservoirs in the Northwest Eileen State-2 and Mallik 2L-38 wells (Figures 5.53 and 5.64) compared favorably with the "standard"-Archie-derived (clean-sand) gas-hydrate saturations. Within relatively clay-rich intervals, however, the Indonesian-derived gas-hydrate saturations were often significantly higher than the "standard"-Archie-derived saturations.

The Waxman-Smits-derived gas-hydrate saturations for Site 995 (Figure 5.14) on the Blake Ridge and Site 889 (Figure 5.30) on the Cascadia margin were significantly higher than the "standard"-Archie-derived (clean-sand) gas-hydrate saturations for the same sites (Figures 5.12a-c and 5.29). It appears that the high clay content of the sediments on the Blake Ridge and along the Cascadia margin has yielded sediment cation exchange capacities (CECs) beyond the operational limits of the Waxman-Smits relation as defined by Waxman and Thomas (1974). However, it still appears that the "standard" (clean-sand) Archie relation yielded gas-hydrate saturations that compare favorably to gas-hydrate saturations calculated from available downhole-acoustic-log data and core-derived chlorinity profiles. The apparent lack of a shale induced error in the "standard"

Archie saturation calculations on the Blake Ridge and the Cascadia margin is possibly due to (1) the techniques used to determine the constants within the "standard" Archie relation and/or (2) the relative resistivity of the formation waters.

In the "standard" Archie assessment of both Sites 997 and 889, the a and m Archie constants were directly calculated with downhole-measured resistivity and porosity data from each site. Therefore, the directly calculated Archie constants (a and m) are unique values calculated for the specific lithologic (shale content) and reservoir conditions on the Blake Ridge and the Cascadia margin, respectively. Thus, the unique values for the a and m Archie constants take into account the shale content of the formation. Field and laboratory studies (reviewed by Hearst and Nelson, 1985) have also revealed that in shale-rich sandstone (shaly-sand) reservoirs with pore-water resistivities (R_w) ranging from 0.10 to 0.50 ohm-m, shale has relatively little affect on the Archie-derived water saturations; which is significant because the pore-water resistivities in the gas-hydrate-bearing intervals on the Blake Ridge and the Cascadia margin range from about 0.20 to 0.35 ohm-m as described in Sections 5.2.5 and 5.3.6 of this thesis. In "conventional" log studies a clay can be modeled as consisting of two-components: electrically inert dry clay and bound water. The electrical conductivity of a clay-rich rock is modeled as being derived solely from the clay-bound- and free-water. In both of these case studies, it appears that the "standard" Archie relation accounts for the electrical properties of both the clay-bound- and free-water; assuming the electrical conductivity of the clay-bound- and free-water are similar, which is likely true in these low salinity pore-water systems.

As described in Chapter 5 of this thesis, compressional-wave acoustic-log data have been used along with the Timur (Equation 3.14), modified Wood (Equation 3.15) and Lee weighted average (Equation 3.16) acoustic equations to calculate gas-hydrate saturations (S_h) in all five of the gas-hydrate accumulations assessed in this study (Figures 5.15a-c, 5.32, 5.40, 5.55, and 5.67). For the most part, the Lee weighted average acoustic equation (Equation 3.16), that utilizes compressional-wave acoustic-log data, yielded gas-hydrate saturations (S_h) that compared favorably to saturations calculated by other means. However, the Timur equation (Equation 3.14), which adequately predicts the acoustic properties of gas hydrates in consolidated rock media, yielded reasonable gas-hydrate saturations (S_h) with the acoustic data from only Site 570 and the Northwest Eileen State-2 and Mallik 2L-38 wells. While the Wood equation (Equation 3.15) yielded unreasonable gas-hydrate saturations (S_h) in all five gas-hydrate accumulations assessed.

Within the laboratory phase of this study (Chapter 4), acoustic velocity measurements of tetrahydrofuran-hydrate-bearing synthetic rock cores have also revealed that the Timur (Equation 3.14) and Lee (Equation 3.16) acoustic equations should yield accurate gas-hydrate saturations, particularly within well consolidated "rigid" rock media and at relatively high gas-hydrate saturations ($S_h > 70\%$).

The selection of accurate weight factors (W) and gas hydrate cementation exponents (r) for the Lee weighted average equation (Equation 3.16) remains problematic. As shown in Chapters 3 and 5 of this thesis, the Lee equation weight factor (W) can be determined from available downhole-log porosity and acoustic-velocity data

(Figures 3.20, 5.31, 5.39, 5.54 and 5.66); however, the occurrence of in-situ

hydrocarbons (gas-hydrate or free-gas) and highly variable lithostratigrahic conditions

can greatly complicate the selection of accurate Lee equation weight factors (W). In all

cases within this study, a value of 1.0 has been assigned to the Lee equation gas hydrate

cementation exponent (r), which means that no special allowance for the "cementation"

properties of gas hydrates were needed to calculate accurate gas-hydrate saturations. It

should be noted, however, that without additional field and laboratory studies of the

acoustic properties of gas-hydrate-bearing sediments, the relative affect of gas-hydrate on

the mechanical properties of sediments, including cementation, cannot be fully assessed.

As discussed in Section 5.6.5 of this thesis, the Mallik 2L-38 well has provided

the first accurate downhole measurements of compressional- and shear-wave velocities of

a gas-hydrate-bearing sedimentary section. In general, the combined compressional- and

shear-wave Lee acoustic relation (Equation 3.17) yielded gas-hydrate saturations (Figure

5.67) almost identical to the Lee compressional-wave relation (Equation 3.16). However,

the multiphase wave scattering theory of Kuster-Toksöz (Equations 3.18, 3.19, 3.20, and

3.21) and the cementation model proposed by Dvorkin et al. (1991) and Dvorkin and Nur

(1993, 1996) overestimated gas-hydrate saturations in the Mallik 2L-38 well (similar to

the results of the Wood relation, Equation 3.15).

As proposed in Chapter 3 of this thesis, carbon/oxygen and hydrogen/carbon

elemental data from downhole neutron spectroscopy logs can also be used to determine

gas-hydrate saturations. The proposed hydrogen/carbon gas-hydrate saturation

assessment approach remains untested; however, carbon/oxygen elemental data from the

geochemical logging tool (GLT) has been used to determine gas-hydrate saturations at all three sites (Sites 994, 995, and 997) drilled on the Blake Ridge during Leg 164. In some cases the carbon/oxygen-calculated gas-hydrate saturations (Figure 5.21a-c) from the Blake Ridge drill-sites compare favorably with the gas-hydrate concentrations calculated by other methods, however, in general the results of the carbon/oxygen calculations were significantly degraded by pore borehole conditions.

In summary, the "standard" Archie relation (Equation 3.8) and the Lee weighted average acoustic equation (Equation 3.16) yielded, for the most part, gas-hydrate saturations that compare favorably with gas hydrate concentrations calculated by other means. For consistency, the gas-hydrate saturations derived from the "standard" Archie relation have been used to determine the volume of gas hydrate and associated free-gas within each of the gas-hydrate accumulations assessed in this study.

6.3 Gas Hydrate Volumetric Estimates

The calculation of critical reservoir parameters in this thesis for five of the best known gas-hydrate accumulations in the world has yielded the necessary data to validate and further refine existing estimates of the volume of gas associated with the world's gas-hydrate accumulations. The downhole-log-derived reservoir data, especially gas-hydrate saturations, have also yielded critical information about the in-situ nature of gas hydrates. In this section of the thesis, the downhole-log-derived reservoir parameters described in Chapter 5 have been used to further assess the in-situ nature of gas-hydrate occurrences and evaluate existing gas hydrate volumetric estimates.

As shown in Chapter 5 of this thesis, the volume of gas that may be contained in a gas-hydrate accumulation depends on five primary "reservoir" parameters: (1) areal extent of the gas-hydrate occurrence, (2) "reservoir" thickness, (3) sediment porosity, (4) degree of gas-hydrate saturation, and (5) the hydrate gas yield volumetric parameter (in this thesis one cubic meter of gas hydrate was assumed to yield 164 cubic meters of gas at STP). In Chapter 5, downhole-well-log data has been used to calculate sediment porosities, gas-hydrate saturations, and the thickness of individual gas-hydrate accumulations at each of the drill-sites examined in this study. In several cases, the areal extent of the well penetrated and downhole-logged gas-hydrate accumulations, as inferred from studies of seismic reflection data and log data from additional wells, have been used to estimate the volume of gas within the entire gas-hydrate accumulation. Table 6.1 contains a compilation of data dealing with the depth, thickness, sediment porosity, gas-hydrate saturation and volume of gas (as measured within a one square kilometer area surrounding each drill-site) as determined from the interpretation of the available downhole-log data from the five gas-hydrate accumulations assessed in Chapter 5 of this thesis.

With the exception of the massive gas-hydrate occurrence at Site 570, the remaining gas-hydrate accumulations listed in Table 6.1 are characterized as disseminated gas-hydrate occurrences with the gas hydrate occurring as pore-filling constituents in either shale (clay) dominated or relatively "clean" sandstone reservoirs. Within the shale-rich (clay) sediments of the Blake Ridge (Sites 994, 995, and 997) and the Cascadia continental margin (Site 889), the downhole-log-derived gas-hydrate

Table 6.1 Volume of natural gas within the downhole-log-inferred gas-hydrate occurrences at DSDP Site 570, ODP Sites 889, 994, 995, and 997, and in the Northwest Eileen State-2 and Mallik 2L-38 wells. The average gas-hydrate saturations listed in this table were calculated by the "standard" Archie method.

Site/Well identification	Depth of log inferred gas hydrates (m)	Thickness of hydrate-bearing zone (m)	Sediment porosity (%)	Average gas-hydrate saturation (%)	Volume of gas within hydrate per square km (m^3)*
Ocean Drilling Program Drill-Sites:					
Site 570	247.4-251.4	4	92	92	555,238,400
Site 889	127.6-228.4	100.8	51.8	5.4	466,635,705
Site 994	212.0-428.8	216.8	57.0	3.3	669,970,673
Site 995	193.0-450.0	257.0	58.0	5.2	1,267,941,673
Site 997	186.4-450.9	264.5	58.1	5.8	1,449,746,073
Northwest Eileen State-2 Drill-Site:					
Unit C	651.5-680.5	29.0	35.6	60.9	1,030,904,796
Unit D	602.7-609.4	6.7	35.8	33.9	133,382,462
Unit E	564.0-580.8	16.8	38.6	32.6	346,928,811
				Total --	1,511,216,069
Mallik 2L-38 Drill-Site:					
Hydrate Unit	888.8-1,101.9	213.1	29.3	47.0	4,812,744,164

*In this assessment a hydrate number of 6.325 (90% gas filled clathrate) was assumed, which corresponds to a gas yield of 164 m^3 of methane (at STP) for every cubic meter of gas hydrate.

saturations are very low, ranging from an average value of about 3 to 6 percent (Table 6.1). However, within the clean (shale-free) sandstone reservoirs of the Northwest Eileen State-2 and Mallik 2L-38 wells, gas-hydrate saturations calculated from available downhole-log data are relatively high, ranging from about 33 to 61 percent (Table 6.1). Thus, the gas-hydrate saturation calculations in this thesis suggest that the mineralogy and lithology of the reservoir sediments may have a direct affect on the concentration of gas hydrate in a reservoir. Other researchers, including the laboratory studies of gas-hydrate-bearing cores by Wright et al. (1999), have suggested that the gas hydrate carrying capacity of course-grained sandstone cores is much greater than that exhibited by shale-rich rock cores. However, the gas-hydrate saturations calculated in this thesis have provided the first direct field evidence for a mineralogic/lithologic control on the occurrence of gas hydrates in nature.

The low concentration of gas hydrate in most of the world's marine gas-hydrate occurrences raises a concern over the production technology required to produce gas from highly disseminated gas-hydrate accumulations. In addition, the host-sediments also represent a significant technical challenge to potential gas hydrate production. In most cases, marine gas hydrates have been found in clay-rich unconsolidated sedimentary sections that exhibit little or no permeability. Most of the existing gas hydrate production models (reviewed by Sloan, 1998) require the establishment of reliable flow paths within the formation to allow the movement of produced gas to the wellbore and injected fluids into the gas-hydrate-bearing sediments. It is unlikely, however, that most marine sediments possess the mechanical strength to allow the

generation of significant flow paths. It is possible that in basins with significant input of coarse-grained clastic sediments, such as the Gulf of Mexico or along the eastern margin of India, gas hydrates may occur at high concentrations in conventional clastic reservoirs; which is more analogous to the nature of gas-hydrate occurrences in onshore permafrost environments examined in this study.

Within several of the gas-hydrate accumulations assessed in Chapter 5 of this thesis, well-log-derived gas hydrate reservoir data have been used along with estimates of the areal extent of the individual gas-hydrate occurrences to calculate the volume of gas trapped as gas hydrate within the entire gas-hydrate accumulation. In this study, it was determined that the Blake Ridge may contain as much as 37.7 trillion cubic meters of gas trapped as gas hydrates (with an additional 19.3 trillion cubic meters of free gas trapped beneath the Blake Ridge gas-hydrate accumulation). It was also determined that the gas-hydrate accumulation on the Cascadia continental shelf may contain about 2.8 trillion cubic meters of gas, while three of the six gas-hydrate-bearing stratigraphic units in the Northwest Eileen area of northern Alaska may contain about 562 billion cubic meters of gas. The gas hydrate volumetric calculations in this thesis generally yielded gas volume estimates slightly lower than those reported in other published studies (reviewed in Chapter 5). In most cases, however, the gas hydrate volumetric estimates derived in this thesis are close enough to the previous published estimates to discount the differences as not significant. Therefore, the existing estimates of the amount of natural gas within the gas hydrate deposits of the world, as reviewed in Chapter 1 of this thesis, should be considered valid; and the current consensus estimates of the amount of gas in the world's

gas-hydrate accumulations, as reviewed by Kvenvolden (1993) at 20,000 trillion cubic meters gas, should also be considered valid. Despite the fact that relatively little is still known about the world accumulation of natural gas hydrates, it is certain that gas hydrates are a vast storehouse of natural gas.

6.4 Future Research Recommendations

Based on the results of this study, it is possible to make several recommendations regarding the future development of gas hydrate related quantitative well-log evaluation techniques. The recommendations described in this section of the thesis can be generally grouped into two categories: (1) The acquisition of additional high-quality downhole well logs from known gas-hydrate accumulations, and (2) The development of an integrated gas hydrate laboratory research program designed to characterize various well-log properties of in-situ natural gas-hydrate occurrences.

As discussed in Chapter 1 of this thesis, only a limited number of marine and permafrost-associated gas-hydrate accumulations have been logged with modern downhole tools and only a few of these logged boreholes also have core-derived physical property data with which to calibrate and evaluate the gas hydrate interpreted well-log responses. In addition, most of the downhole logs from the gas-hydrate accumulations assessed in Chapter 5 were also moderately to severely degraded by poor borehole conditions. Thus, the acquisition of new, high-quality, downhole well-log data and core-derived physical property data from various geologic environments is needed to further develop and field test the growing number of proposed gas hydrate well-log evaluation

techniques. Future gas-hydrate related downhole well-logging programs should focus on the acquisition of highly integrated well-log suites with a particular focus on electrical resistivity, both compressional- and shear-wave acoustic velocity, and nuclear magnetic resonance measurements. The results of the Mallik 2L-38 well-logging program, in which high quality well logs were obtained, demonstrates the value of adopting specialized drilling procedures designed to prevent the disassociation of gas hydrates in the borehole.

The physical properties of gas-hydrate-bearing sediments are still poorly characterized, mainly because of the lack of well constrained laboratory studies of gas hydrates under simulated natural conditions. What is most needed for the continued development of quantitative gas hydrate well-log evaluation techniques is the establishment of an integrated gas hydrate laboratory research program designed to characterize various well-log properties of in-situ natural gas-hydrate occurrences under controlled conditions. Two of the most critical well-log measurements that need to be studied in much greater detail are the electrical resistivity and acoustic properties (both compressional- and shear-wave acoustic properties) of gas-hydrate-bearing sediments.

As demonstrated in this thesis, the selection of appropriate acoustic models for sediments with various lithologies and compaction characteristics can be problematic. The development of a comprehensive acoustic petrophysical model for the occurrence of gas hydrates would greatly simplify the acoustic log assessment of gas-hydrate-bearing sediments. The question therefore is, can a series of laboratory experiments be designed to rigorously assess the acoustic properties of gas-hydrate-bearing sediments under well-

constrained simulated natural conditions? Similar problems and concerns have been

expressed in this thesis regarding the electrical resistivity properties of gas-hydrate-

bearing sediments. Again, can laboratory experiments be adequately designed to fully

investigate the electrical resistivity properties of sediments under simulated natural

conditions? The short, controversial answer to both of these questions is that it may be

theoretically possible to conduct the required electrical resistivity or acoustic

experiments, but no research group has successfully achieved the daunting goal of

obtaining the necessary well-constrained and repeatable laboratory results.

One area of recommended focused research should deal with the affects of shales

(clays) on Archie-derived gas-hydrate saturations under conditions of relatively low pore-

water salinities and very high shale contents. As demonstrated in the field application

section of this thesis, the "standard" Archie relation generally yielded reasonable gas-

hydrate saturations in clay-rich marine rocks, while the Waxman-Smits relation failed to

yield reasonable results. Several potential explanations were presented in this thesis to

explain the apparent difference between the "standard" Archie and Waxman-Smits

results; however, the conclusions presented here are still less than fully satisfactory.

Laboratory studies are also needed to characterize the expected nuclear magnetic

resonance well-log response to gas hydrate in various sediment types. At this time, no

field or laboratory studies have been published dealing with nuclear magnetic resonance

characteristics of gas-hydrate-bearing sediments. It is speculated in Chapter 3 of this

thesis, that modern downhole nuclear magnetic resonance tools used in conjunction with

density and/or neutron porosity tools may yield detailed information on gas-hydrate

saturations. However, the lack of field or laboratory data severely limits the development of the nuclear magnetic resonance well-logging device as a quantitative gas hydrate research tool.

Over the last several years, interest in downhole-log measurements as quantitative gas hydrate research tools has significantly grown; and it is almost certain that the use of well logs in gas hydrate studies will continue to expand into the future.

CHAPTER 7

SUMMARY AND CONCLUSIONS

The major achievements and conclusions of this study are listed below:

1.   Descriptions of recovered gas hydrate samples and analysis of downhole-log data
     from areas of known gas-hydrate occurrences (including formation imaging logs
     from ODP Hole 995B and the Mallik 2L-38 well) have revealed that gas hydrates
     are usually disseminated within sediments as pore-filling constituents and that in
     most cases "standard" well-log evaluation techniques that assume adherence to
     mixing rules can be used to assess gas-hydrate-bearing reservoirs.

2.   In this study, well-log response modeling has revealed that under most conditions,
     the bulk-density of a water-bearing sedimentary section is almost identical to the
     bulk-density of a gas-hydrate-bearing sedimentary section as measured by a
     gamma-gamma density logging tool. At relatively high porosities ($\emptyset > 40\%$) and
     gas-hydrate saturations ($S_h > 50\%$), however, the downhole-log-derived bulk-density
     porosities need to be corrected for the presence of gas hydrate. Within this study,
     density porosity nomographs have been developed with which it is possible to
     correct for the affect of high gas-hydrate saturations on the density-log-derived

porosities. In the field verification phase of this study, downhole-density-log data, corrected for the presence of gas hydrates (in some cases corrected for the presence of shale in the sediment matrix), have yielded porosities consistent with those from other sources in the gas-hydrate-bearing sedimentary section of the DSDP Site 570 corehole and in both the Northwest Eileen State-2 and Mallik 2L-38 wells. The density-log data from the holes drilled on ODP Leg 146 and 164 were severely degraded by poor borehole conditions and were not used for quantitative calculations.

3. Elemental calculations in the neutron porosity response modeling phase of this study have yielded a hydrogen index (HI) value for pure Structure-I methane hydrate of 1.059 which is near the hydrogen index of water (HI for water is 1.0). Complex neutron well-log response computer simulators, SNUPAR and MCNP-4, have also been used to calculate nuclear transport and capture parameters for various reservoir constituents, including gas hydrate. The calculated thermal neutron capture cross section of various hypothetical gas-hydrate-bearing reservoirs indicates that Structure-I methane hydrate has little affect on neutron porosity measurements within "normal" reservoir conditions ($\varnothing<40\%$) and low gas-hydrate saturations ($S_h<50\%$). The thermal neutron capture cross section modeling effort and the hydrogen index (HI) calculations have yielded neutron porosity nomographs that can be used to correct neutron-log-derived porosities within reservoirs that exhibit high gas-hydrate saturations. In the field verification phase

of this study, downhole-neutron-porosity-log data (in some cases corrected for the presence of gas hydrate and shale in the sediment matrix) have yielded porosities consistent with those calculated from other sources for the gas-hydrate-bearing sedimentary section in the ODP Site 889 corehole and in both the Northwest Eileen State-2 and Mallik 2L-38 wells.

4. In general, the "standard" and "quick look" Archie relations yielded gas-hydrate and free-gas saturations that compared favorably with saturations calculated by other methods in all of the gas-hydrate accumulations assessed in the field verification phase of this study. However, the modified Archie approach proposed by Pearson et al. (1983) and Waxman-Smits shaly-sand relation yielded erroneous gas-hydrate saturations. When compared to gas-hydrate saturations calculated by other techniques, it was determined that the "standard" and "quick look" Archie relations yield similar gas-hydrate saturations in marine sediments without any consideration for the presence of clay (shale). It is suggested that the electrical resistivity properties of the clay-bound- and free-water in these relatively low pore-water salinity systems (R_w ranging from 0.10 to 0.50 ohm-m) are nearly the same.

5. Laboratory compressional-wave acoustic velocity measurements of consolidated synthetic rock cores containing stoichiometric and non-stoichiometric hydrate mixtures of tetrahydrofuran and water were used in this study to test the accuracy of gas-hydrate saturations calculated from a series of compressional-wave acoustic

velocity gas-hydrate saturation equations introduced and described in the well-log response modeling phase of this study (Chapter 3). The laboratory analysis of tetrahydrofuran-hydrate-bearing rock cores have shown that the Timur time-average equation (Equation 3.14) and the Lee weighted average equation (Equation 3.16) yielded tetrahydrofuran-hydrate saturations that compared favorably with the "known" tetrahydrofuran-hydrate saturations. However, the Wood equation (Equation 3.15) yielded unreasonable tetrahydrofuran-hydrate saturations in the laboratory phase of this study.

6. Compressional-wave acoustic-log data have been used along with the Timur (Equation 3.14), modified Wood (Equation 3.15), and the Lee weighted average (Equation 3.16) acoustic equations to calculate gas-hydrate saturations in all five gas-hydrate accumulations assessed in this study. The Lee weighted average equation (Equation 3.16) generally yielded gas-hydrate saturations that compared favorably with saturations calculated by other methods within all of the gas-hydrate accumulations assessed. However, the Timur equation (Equation 3.14) yielded compatible gas-hydrate saturations in only the DSDP Site 570 corehole and in the Northwest Eileen State-2 and Mallik 2L-38 wells. The Wood equation (Equation 3.15) failed to yield reasonable gas-hydrate saturations.

7. Also introduced in the log-response modeling phase of this study is a series of combined compressional- and shear-wave acoustic velocity relations proposed by

Lee et al. (1986) (Equation 3.17), Kuster-Toksöz (Equations 3.18, 3.19, 3.20, and 3.21) and Dvorkin et al. (1991) and Dvorkin and Nur (1993, 1996) that can be used to assess gas-hydrate saturations with downhole-log-measured compressional- and shear-wave acoustic velocity data. In the Mallik 2L-38 well, the combined compressional- and shear-wave Lee acoustic relation (Equation 3.17) yielded gas-hydrate saturations similar to those calculated by other methods. However, the wave scattering theory of Kuster-Toksöz and the cementation theory of Dvorkin overestimated gas-hydrate saturations in the Mallik 2L-38 well.

8. Examination of downhole-acoustic-log data in this study indicates that no special allowance for the "cementation" properties of gas hydrates is needed to accurately calculate gas-hydrate saturations in sediments; suggesting that gas hydrates do not contribute to the "stiffness" of the sediment frame and gas hydrate growth occurs away from grain contacts in the "bulk" pore-volume of the sediments.

9. The calculation of gas-hydrate saturations with the downhole electrical resistivity, acoustic transit-time, and porosity-log data from the holes drilled on ODP Leg 146 and 164 have demonstrated the problem with the integration of data from different downhole logging runs and data sources (downhole-logs and core data). Non-compatible downhole depths (mismatched log depths) of data used for the quantitative analysis of the log data from ODP Leg 146 and 164 have contributed to the more variable nature of the gas-hydrate saturations calculated with the non-

statistically manipulated core and log porosities. However, the analysis of the downhole-log data from Site 889 (ODP Leg 146), suggests that the use of "average" or "smoothed" log trends may mask local geologic variations that may adversely affect the resultant well-log calculations.

10. In the log response modeling phase of this study, elemental analyses of hypothetical gas-hydrate accumulations suggest that neutron-spectroscopy-log-derived carbon/oxygen and hydrogen/carbon ratios can be used to calculate gas-hydrate saturations in complex reservoir systems. In order to use downhole-log-derived carbon/oxygen data to calculate gas-hydrate saturations in complex reservoirs, a "conventional" carbon/oxygen hydrocarbon saturation equation (Equation 3.23) was modified into a new equation (Equation 3.25) that accounts for the unique carbon and oxygen composition of gas hydrate and also for the presence of clay and organic carbon in the sediment matrix. The modified carbon/oxygen gas-hydrate saturation equation (Equation 3.25) was used to determine gas-hydrate saturations at all three Blake Ridge drill-sites (Sites 994, 995, and 997). The carbon/oxygen elemental data from the GLT on the Blake Ridge was severely degraded by poor borehole conditions. In zones of relatively high quality log data, however, the carbon/oxygen elemental data yielded gas-hydrate saturations that compared favorably with saturations calculated by other methods.

11. The downhole-log-derived gas-hydrate saturations, as calculated in this thesis, indicate that the potential volume of gas within the log-inferred gas hydrates at each drill-site (Sites 994, 995, and 997) on the Blake Ridge ranges from 669,970,673 to 1,449,746,073 cubic meters of gas per square kilometer. Well-log calculations from the Blake Ridge also indicate that the potential volume of gas within the log-inferred free-gas zones at each drill-site (Sites 994, 995, and 997) range from 743,375,738 cubic meters of gas (at STP) per square kilometer at Site 997 to 55,346,740 cubic meters of gas (at STP) per square kilometer at Site 995. Collectively, the volume of gas within the gas-hydrate and free-gas accumulations on the Blake Ridge may be about 57 trillion cubic meters of gas. Similarly, the downhole-log-derived sediment porosities and gas-hydrate saturations calculated in this thesis at Site 889, indicate that the potential volume of gas within the log-inferred gas hydrates on the Cascadia margin is about 466,635,705 cubic meters of gas per square kilometer. If the distribution of gas hydrate at Site 889 is representative of the entire seismic delineated gas-hydrate accumulation on the Cascadia continental margin, it can be concluded that there is about 2.8 trillion cubic meters of gas within the Cascadia gas-hydrate accumulation as defined within this study. Downhole-log-derived reservoir data indicate that the massive gas hydrate zone at DSDP Site 570 on the upper slope of the Middle America Trench contains 555,238,400 cubic meters of gas per square kilometer. While the analysis of downhole logs has determined that within the one square kilometer area surrounding the Northwest Eileen State-2 well on the North Slope of Alaska, all three gas-hydrate-bearing stratigraphic units (Units C, D, and E) drilled and cored by the Eileen well collectively contain 1,511,216,069 cubic meters of gas in the one

square kilometer area surrounding the well. It was also determined in this thesis that the 213 m thick gas-hydrate occurrence penetrated by the Mallik 2L-38 well in the Mackenzie Delta of Canada contains about 4,812,744,164 cubic meters of gas in the one square kilometer area surrounding the Mallik drill-site.

12. The gas hydrate volumetric calculations in this thesis generally yielded gas volume estimates similar to those reported in other published studies; therefore, the assessment methods used to derive the consensus estimate of the amount of gas in the world's gas-hydrate accumulations of 20,000 trillion cubic meters appear to be valid.

CHAPTER 8

REFERENCES CITED

Albayrak, C., and Zeider, M.D. 1987. Interactions of water in ionic and nonionic hydrates, Springer Publishers, Berlin, Germany, 131 p.

Archie, G.E. 1942. The electrical resistivity log as an aid in determining some reservoir characteristics. Journal of Petroleum Technology, v. 5, p. 1-8.

Atwater, T., and Molnar, P. 1973. Relative motion of the Pacific and North American plates deduced from sea-floor spreading in the Atlantic, Indian, and South Pacific Oceans. Stanford University Publications, Geologic Publications, Geologic Science, v. 13, p. 136-148.

Bally, A.W. 1981. Atlantic type margins. *in* Bally, A.W., ed., Geology of Passive Continental Margins -- History, structure, and sedimentologic record. American Association of Petroleum Geologists Education Course Note Series 19, p. 1-1 to 1-48.

Bathe, M., Vagle, S., Saunders, G.A., and Lambson, E.F. 1984. Ultrasonic wave velocities in the structure II clathrate hydrate THF-17H_2O. Journal of Materials Science Letter, v. 3, no. 10, p. 904-906.

Bily, C., and Dick, J.W.L. 1974. Natural occurring gas hydrates in the Mackenzie Delta,

Northwest Territories. Bulletin of Canadian Petroleum Geology, v. 22, p. 340-

352.

Booth, J.S., Rowe, M.M., and Fischer, K.M. 1996. Offshore gas hydrate sample database

with an overview and preliminary analysis. U.S. Geological Survey Open-File

Report 96-272, 17 p.

Brooks, J.M., Cox, B.H., Bryant, W.R., Kennicutt, M.C., Mann, R.G., McDonald, T.J.

1986. Association of gas hydrates and oil seepage in the Gulf of Mexico. Organic

Geochemistry, v. 10, p. 221-234.

Brooks, J.M., Field, M.E., and Kennicutt, M.C. 1991. Observations of gas hydrates in

marine sediments, offshore northern California. Marine Geology, v. 96, p. 103-

109.

Castagna, J.P., Batzle, M.L., and Eastwood, R.L. 1985. Relationship between

compressional-wave and shear-wave velocities in clastic silicate rocks.

Geophysics, v. 50, p. 571-581.

Cherskiy, N.V., Tsarev, V.P., and Nikitin, S.P. 1985. Investigation and prediction of

conditions of accumulation of gas resources in gas-hydrate pools. Petroleum

Geology, v. 21, p. 65-89.

Collett, T.S. 1983. Detection and evaluation of natural gas hydrates from well logs,

Prudhoe Bay, Alaska. Proceedings of the Fourth International Conference on

Permafrost, July 17-22, Fairbanks, Alaska, National Academy of Sciences

Publishers, Washington D.C., p. 169-174.

_____. 1993a. Natural gas production from Arctic gas hydrates. *in* Howell, D.G., ed., The Future of Energy Gases. U.S. Geological Survey Professional Paper 1570, p. 299-312.

_____. 1993b. Natural gas hydrates of the Prudhoe Bay and Kuparuk River area, North Slope, Alaska: American Association of Petroleum Geologists Bulletin, v. 77, no. 5, p. 793-812.

_____. 1995. Gas hydrate resources of the United States. *in* Gautier, D.L., Dolton, G.L., Takahashi, K.I., and Varnes, K.L., eds., 1995 National assessment of United States oil and gas resources on CD-ROM. U.S. Geological Survey Digital Data Series 30.

Collett, T.S., Bird, K.J., Kvenvolden, K.A., and Magoon, L.B. 1988. Geologic interrelations relative to gas hydrates within the North Slope of Alaska. U.S. Geological Survey Open-File Report 88-389, 150 p.

Collett, T.S., and Dallimore, S.R. 1998. Quantitative assessment of gas hydrates in the Mallik L-38 well, Mackenzie Delta, N.W.T., Canada: Proceedings of the Eight International Conference on Permafrost, June 23-27, 1998, Yellowknife, N.W.T., Canada, p. 189-194.

Collett, T.S., and Ginsburg, G.D. 1998. Gas hydrates in the Messoyakha gas field of the West Siberian Basin -- a re-examination of the geologic evidence: International Journal of Offshore and Polar Engineering, v. 8, no. 1, p. 22-29.

Collett, T.S., Godbole, S.P., and Economides, C.E. 1984. Quantification of in-situ gas

hydrates with well logs. Proceedings of the 35th Annual Technical Meeting of the

Petroleum Society of CIM, June 10-13, Calgary, Canada, p. 571-582.

Cranston, R.E. 1999. Pore-water geochemistry, JAPEX/JNOC/GSC Mallik 2L-38 gas

hydrate research well. *in* Dallimore, S.R., Uchida, T., and Collett, T.S. eds.,

Scientific Results from JAPEX/JNOC/GSC Mallik 2L-38 Gas Hydrate Research

Well, Mackenzie Delta, Northwest Territories, Canada. Geological Survey of

Canada Bulletin 544, p. 165-175.

Dallimore, S.R., and Collett, T.S. 1995. Intrapermafrost gas hydrates from a deep core

hole in the Mackenzie Delta, Northwest Territories, Canada. Geology, v. 23, no.

6, p. 527-530.

Dallimore, S.R., and Matthews, J.V. 1997. The Mackenzie Delta Borehole Project.

Environmental Studies Research Funds Report 135, 1 CD-ROM.

Dallimore, S.R., Uchida, T., and Collett, T.S. 1999. Summary. *in* Dallimore, S.R.,

Uchida, T., and Collett, T.S. eds., Scientific Results from JAPEX/JNOC/GSC

Mallik 2L-38 Gas Hydrate Research Well, Mackenzie Delta, Northwest

Territories, Canada. Geological Survey of Canada Bulletin 544, p. 1-10.

Davidson, D.W., Garg, S.K., Gough, S.R., Handa, Y.P., Ratcliffe, C.I., Ripmeester, J.A.,

Tse, J.S., and Lawson, W.F. 1986. Laboratory analysis of a naturally occurring

gas hydrate from sediment of the Gulf of Mexico. Geochemica et Cosmochimica

Acta, v. 50, p. 619-623.

Davidson, D.W., and Ripmeester, J.A. 1984. NMR, NQR and dielectric properties of clathrates: *in* Atwood, J.L., Davies, J.E.D., and MacNichol, D.D., eds., Inclusion Compounds, v. 3, Chapter 3, p. 69-127.

Dickens, G.R., Paull, C.K., Wallace, P., and the ODP Leg 164 Scientific Party. 1997. Direct measurement of in situ methane quantities in a large gas-hydrate reservoir. Nature, v. 385, p. 426-428.

Dillon, W.P., Lee, M.W., Fehlhaber, K., and Coleman, D.F. 1993. Gas hydrates on the Atlantic continental margin of the United States -- Controls on concentration. *in* Howell, D.G., ed., The Future of Energy Gases. U.S. Geological Survey Professional Paper 1570, p. 313-330.

Dillon, W.P., and Paull, C.K. 1983. Marine gas hydrates, II. Geophysical evidence. *in* Cox, J.S., ed., Natural Gas Hydrates: Properties, Occurrences, and Recovery. Butterworth Publishing, London, England, p. 73-90.

Dixon, J., Dietrich, J.R. and McNeil, D.H. 1992. Upper Cretaceous to Pleistocene Sequence Stratigraphy of the Beaufort-Mackenzie and Banks Island Areas, Northwest Canada. Geological Survey of Canada Bulletin 407, p. 1-90.

Dobrynin, V.M., Korotajev, Yu. P., and Plyuschev, D.V. 1981. Gas hydrates--A possible energy resource. *in* Meyer, R.F., and Olson, J.C., eds., Long-Term Energy Resources. Pitman Publishing, Boston, Massachusetts, p. 727-729.

Dupree, R.G., and Noel, S.D. 1988. Monte Carlo simulations of an epithermal neutron logging tool. The Log Analyst, v. 29, no. 2, p. 95-102.

Dvorkin, J., Mavko, G., and Nur, A. 1991. The effect of cementation on the elastic properties of granular material. Mechanical Materials, v. 12, p. 207-217.

Dvorkin, J., and Nur, A. 1993. Rock physics for characterization of gas hydrates, *in* Howell, D.G., ed., The Future of Energy Gases. U.S. Geological Survey Professional Paper 1570, p. 293-311.

_____. 1996. Elasticity of high-porosity sandstones: theory for two North Sea data sets. Geophysics, v. 61, p. 1,363-1,370.

Dyadin, Y., Kuznetzov, P.N., Yakovlov, I.I., and Pyrinova, A.V. 1973. Doklady Academy of Sciences U.S.S.R., Chemistry Section, v. 208, no. 9.

Ecker, C., Lumley, D., Dvorkin, J., and Nur, A. 1996. Structure of hydrate sediment from seismic and rock physics. Proceedings of the Second International Conference on Natural Gas Hydrates, June 2-6, Toulouse, France, p. 491-498.

Ekstrom, M.P., Dahan, C.A., Chen, M.-Y., Loyd, P.M., and Rossi, D.J. 1986. Formation imaging with microelectrical scanning arrays. Transactions of the Society of Professional Well Log Analysts 27th Annual Logging Symposium, Paper BB.

Ellis, D.V., Ullo, J., and Sherman, H. 1981. Comparison of calculated and measured responses of a dual-detector epithermal neutron porosity device. Proceedings of the 56th Annual Technical Conference and Exhibition of the Society of Petroleum Engineers of AIME, October 4-7, San Antonio, Texas, Paper Number SPE 10294, 8 p.

Field, M.E., and Kvenvolden, K.A. 1985. Gas hydrates on the northern California continental margin. Geology, v. 13, p. 517-520.

Friend, D.G., Ely, J.F., and Ingham, H. 1989. Tables for the thermophysical properties of methane. National Institute of Standards and Technology Technical Note 1325, 478 p.

Gassmann, F. 1951. Elasticity of porous media: uber die elastizitat poroser medien. Vierteljahrsschrift der Naturforschenden Gesselschaft in Zurich, Heft 1.

Gautier, D.L., Dolton, G.L., Takahashi, K.I., and Varnes, K.L. 1995. National assessment of United States oil and gas resources on CD-ROM. U.S. Geological Survey Digital Data Series 30.

Ginsburg, G.D., Guseinov, R.A., Dadashev, A.A., Ivanova, G.A., Kazantsev, S.A., Soloviev, V.A., Telepnev, Ye.V., Askery-Nasirov, R.E., Yesikov, A.D., Mal'tseva, V.I., Mashirov, Yu.G., and Shabayeva, I.Yu. 1992. Gas hydrates in the southern Caspian Sea. Izvestiya Akademii Nauk Serya Geologisheskaya, v. 7, p. 5-20.

Ginsburg, G.D., Soloviev, V.A., Cranston, R.E., Lorenson, T.D., and Kvenvolden, K.A. 1993. Gas hydrates from the continental slope, offshore from Sakhalin Island, Okhotsk Sea. Geo-Marine Letters, v. 13, p. 41-48.

Grau, J.A., and Schweitzer, J.S. 1989. Elemental concentrations from thermal neutron capture gamma-ray spectra in geological formations. Nuclear Geophysics, v. 3, p. 1-9.

Grau, J.A., Schweitzer, J.S., and Hertzog, R.C. 1990. Statistical uncertainties of elemental concentrations extracted from neutron-induced gamma-ray measurements. IEEE Transactions in Nuclear Science, v. 37, p. 2,175-2,178.

Hearst, J.R., and Nelson, P.H. 1985. Well logging for physical properties. McGraw-Hill

Book Company, New York, 571 p.

Helgerud, M.B., Waite, W.F., Nur, A., Pinkston, J., Stern, L.A., Kirby, S.H., and

Durham, W.B. 1999. Laboratory measurement of compressional and shear wave

speeds through methane hydrate. Proceedings of the Spring Meeting of the

American Geophysical Union, June 1-4, Boston, Massachusetts, Abstract T51A-

03.

Herron, M.M., and Herron, S.L. 1988. Geological applications of geochemical well

logging. Transactions of the International Spectroscopy and Geochemistry

Symposium, September 28-30, Ridgefield, Connecticut, Schlumberger-Doll

Research, Paper A.

Hertzog, R.C. 1978. Laboratory and field evaluation of an inelastic neutron scattering and

capture gamma ray spectroscopy tool. Proceedings of the 53th Annual Technical

Conference and Exhibition of the Society of Petroleum Engineers of AIME,

October 1-4, Houston, Texas, Paper Number SPE 7430, 8 p.

Hertzog, R.C., Colson, J.L., Seeman, B., O'Brien, M.S., Scott, H.D., McKeon, D.C.,

Wraight, P.D., Grau, J.A., Ellis, D.V., Schweitzer, J.S., and Herron, M.M. 1987.

Geochemical logging with spectrometry tools. Society of Petroleum Engineers

Paper 16792, 9 p.

Hertzog, R.C., Colson, J.L., Seeman, B., O'Brien, M.S., Scott, H.D., McKeon, D.C.,

Wraight, P.D., Grau, J.A., Ellis, D.V., Schweitzer, J.S., and Herron, M.M. 1989.

Geochemical logging with spectrometry tools. Society of Petroleum Engineers,
Journal of Formation Evaluation, v. 4, p. 153-162.

Hill, A.D. 1990. Production logging--theoretical and interpretive elements, Chapter 12.
Other Logs to Measure Behind Casing. Society of Petroleum Engineers
Publishers, Richardson, Texas, p. 141-145.

Holbrook, W.S., Hoskins, H., Wood, W.T., Stephen, R.A., and the ODP Leg 164
Scientific Party. 1996. Methane hydrate, bottom-simulating reflectors, and gas
bubbles: results of vertical seismic profiles on the Blake Ridge. Science, v. 273, p.
1,840-1,843.

Hower, J. 1981. X-ray diffraction identification of mixed-layer clay minerals. in
Longstaffe, F.J., ed., Clays and the Resource Geologist. Short Course Handbook,
Mineralogical Association of Canada, p. 39-80.

Hoyer, W.A., Simmons, S.O., Spann, M.M., and Watson, A.T. 1975. Evaluation of
permafrost with logs. Transactions of the Society of Professional Well Log
Analysts 16th Annual Logging Symposium, Paper 15.

Hunt, J.M. 1979. Petroleum geology and geochemistry. W.H. Freeman and Company
Publishers, San Francisco, California, 716 p.

Hyndman, R., Spence, G., Yuan, T., and Desmons, B. 1996. Gas hydrate on the
continental slope off Vancouver Island. Proceedings of the Second International
Conference on Natural Gas Hydrates, June 2-6, Toulouse, France, p. 485-489.

Jenner, K.A., Dallimore, S.R., Clark, I.D., Pare, D., and Medioli, B.E. 1999.
Sedimentology of gas hydrate host strata from the JAPEX/JNOC/GSC Mallik 2L-

38 gas hydrate research well. *in* Dallimore, S.R., Uchida, T., and Collett, T.S. eds., Scientific Results from JAPEX/JNOC/GSC Mallik 2L-38 Gas Hydrate Research Well, Mackenzie Delta, Northwest Territories, Canada. Geological Survey of Canada Bulletin 544, p. 57-68.

Judge, A.S. 1988. Mapping the distribution and properties of natural gas hydrates in Canada. Proceedings of the American Chemical Society Third Chemical Congress of the North American Continent, June 6-7, Toronto, Ontario, Abstract no. 29.

Judge, A.S., and Majorowicz, J.A. 1992. Geothermal conditions for gas hydrate stability in the Beaufort-Mackenzie area: the global change aspect. Global and Planetary Change, v. 98, no. 2/3, p. 251-263.

Judge, A.S., Smith, S.L., and Majorowicz, J. 1994. The current distribution and thermal stability of natural gas hydrates in the Canadian Polar Regions. Proceedings of the Fourth International Offshore and Polar Engineering Conference, Osaka, Japan, p 307-313.

Kiefte, H., Clouter, M.J., and Gagnon, R.E. 1985. Determination of acoustic velocities of clathrate hydrates by brillouin spectroscopy. Journal of Physical Chemistry, v. 89, p. 3,103-3,108.

King, M.S. 1984. The influence of clay-sized particles on seismic velocity for Canadian Arctic permafrost. Canadian Journal of Earth Science, v. 14, p. 1004-1013.

Kleinberg, R.L. 1996. Well logging. *in* Encylopedia of Nuclear Magnetic Resonance. John Wiley and Sons Publishers, Chichester, v. 8, p. 4,960-4,969.

Kreft, A. 1974. Calculation of the neutron slowing down length in rocks and soils. Nukleonika, v. 19, p. 59-70.

Kuster, G.T., and Toksöz, M.N. 1974. Velocity and attenuation of seismic waves in two-phase media, 1, theoretical formulation. Geophysics, v. 39, p. 587-606.

Kuustraa, V.A., and Hammershaimb, E.C. 1983. Handbook of gas hydrate properties and occurrence. U.S. Department of Energy, Morgantown Energy Technology Center, Morgantown, West Virginia, Contract Number DE-AC21-82MC19239, 234 p.

Kvenvolden, K.A. 1988. Methane hydrate--A major reservoir of carbon in the shallow geosphere? Chemical Geology, v. 71, p. 41-51.

_____. 1993. Gas hydrates as a potential energy resource -- a review of their methane content. in Howell, D.G., ed., The Future of Energy Gases. U.S. Geological Survey Professional Paper 1570, p. 555-561.

Kvenvolden, K.A., and Barnard, L.A. 1983. Hydrates of natural gas in continental margins. in Watkins, J.S., and Drake, C.L., eds., Studies in Continental Margin Geology. American Association of Petroleum Geologists Memoir 34, p. 631-641.

Kvenvolden, K.A., and Claypool, G.E. 1988. Gas hydrates in oceanic sediment. U.S. Geological Survey Open-File Report 88-216, 50 p.

Kvenvolden, K.A., and Kastner, M. 1990. Gas hydrates of the Peruvian outer continental margin. in Suess, E., von Huene, R., et al., Proceedings, Ocean Drilling Program, Scientific Results, College Station, Texas, v. 112, p. 517-526.

Kvenvolden, K.A., and McDonald, T.J. 1985. Gas hydrates of the Middle America Trench, Deep Sea Drilling Project Leg 84. in von Huene, R., Aubouin, J., et al.,

Initial Reports Deep Sea Drilling Project, Washington, D.C., U.S. Government

Printing Office, v. 84, p. 667- 682.

Lee, M.W., and Collett, T.S. 1999. Amount of gas hydrate estimated from compressional-

and shear-wave velocities at the JAPEX/JNOC/GSC Mallik 2L-38 gas hydrate

research well. *in* Dallimore, S.R., Uchida, T., and Collett, T.S. eds., Scientific

Results from JAPEX/JNOC/GSC Mallik 2L-38 Gas Hydrate Research Well,

Mackenzie Delta, Northwest Territories, Canada. Geological Survey of Canada

Bulletin 544, p. 313-322.

Lee, M.W., Hutchinson, D.R., Collett, T.S., and Dillon, W.P. 1996. Seismic velocities for

hydrate-bearing sediments using weighted equation. Journal of Geophysical

Research, v. 101, no. B9, p. 20,347-20,358.

Lee, M.W., Hutchinson, D.R., Dillon, W.P., Miller, J.J., Agena, W.F., and Swift, B.A.

1993. Method of estimating the amount of in situ gas hydrates in deep marine

sediments. Marine and Petroleum Geology, v. 10, p. 493-506.

Lichtenstein, H., Cohen, M.O., Steinberg, H.A., Troubetzkoy, E.S., and Beer, M. 1979.

The SAM-CE Monte Carlo system for radiation transport and criticality

calculations in complex configurations. EPRI Computer Code Manual CCM-8,

Research Project 972.

Lock, G.A., and Hoyer, W.A. 1971. Natural gamma-ray spectral logging. Log Analyst, v.

12, p. 3-9.

Los Alamos Monte Carlo Group. 1991. MCNP--Monte Carlo Neutron and Photon

Transport Code System, RISC Computer Code Collection (Version 3A). Los

Alamos National Laboratory Report CCC-200A/B, 639 p.

MacDonald, G.T. 1990. The future of methane as an energy resource. Annual Review of

Energy, v. 15, p. 53-83.

Makogon, Y.F. 1981. Hydrates of natural gas. Penn Well Publishing Company, Tulsa,

Oklahoma, 237 p.

Makogon, Y.F., Trebin, F.A., Trofimuk, A.A., Tsarev, V.P., and Cherskiy, N.V. 1972.

Detection of a pool of natural gas in a solid (hydrate gas) state. Doklady Academy

of Sciences U.S.S.R., Earth Science Section, v. 196, p. 197-200.

Masters, C.D., Root, D.H., and Attanasi, E.D. 1991. Resource constraints in petroleum

production potential. Science, v. 253, p. 146-152.

Mathews, M. 1986. Logging characteristics of methane hydrate. The Log Analyst, v. 27,

no. 3, p. 26-63.

McIver, R.D. 1981. Gas hydrates. in Meyer, R.F., and Olson, J.C., eds., Long-Term

Energy Resources. Pitman Publishing, Boston, Massachusetts, p. 713-726.

McKeon, D.C., and Scott, H.D. 1988. SNUPAR--a nuclear parameter code for nuclear

geophysics applications. Nuclear Geophysics, v. 2, no. 4, p. 215-230.

Meyer, R.F. 1981. Speculations on oil and gas resources in small fields and

unconventional deposits. in Meyer, R.F., and Olson, J.C., eds., Long-Term

Energy Resources. Pitman Publishing, Boston, Massachusetts, p. 49-72.

Moore, D.M., and Reynolds, R.C., Jr. 1989. X-ray diffraction and the identification and analysis of clay minerals. Oxford University Press, New York, New York, p. 179-201.

Nobes, D.C., Villinger, H., Davis, F.F., and Law, L.K. 1986. Estimation of marine sediment bulk physical properties at depth from sea floor geophysical measurements. Journal of Geophysical Research, v. 91, no. B14, p. 14,033-14,043.

Pandit, B.I., and King, M.S. 1979. A study of the effects of pore-water salinity on some physical properties of sedimentary rocks at permafrost temperature. Canadian Journal of Earth Sciences, v. 16, p. 1,566-1,580.

Pandit, B.I., and King, M.S. 1982. Elastic wave propagation in propane gas hydrates. Proceedings of the Fourth Canadian Permafrost Conference, March 2-6, 1981, Calgary, Alberta, National Research Council of Canada Publishers, p. 335-342.

Pearson, C.F., Halleck, P.M., McGuire, P.L., Hermes, R., and Mathews, M. 1983. Natural gas hydrate deposit: a review of in-situ properties. Journal of Physical Chemistry, v. 87, p. 4,180-4,185.

Pearson, C.F., Murphy, J., and Hermes, R. 1986. Acoustic and resistivity measurements on rock samples containing tetrahydrofuran hydrates: laboratory analogs to natural gas hydrate deposits. Journal of Geophysical Research, v. 91, no. B14, p. 14,132-14,138.

Polemio, M., and Rhoades, J.D. 1977. Determining cation exchange capacity: a new procedure for calcareous and gypsiferous soils. Journal of the Soil Science Society of America, v. 41, p. 524-528.

Poupon, A., and Leveaux, J. 1971. Evaluation of water saturation in shaly formation. Transactions of the Society of Professional Well Log Analysts 11th Annual Logging Symposium, Paper O.

Quirein, J., Kimminau, S., LaVigne, J., Singer, J., and Wendel, F. 1986. A coherent framework for developing and applying multiple formation evaluation models. Transactions of the Society of Professional Well Log Analysts 27th Annual Logging Symposium, Paper DD.

Ratcliffe, C.I., and Ripmeester. 1986. ^{1}H and ^{13}C NMR studies on carbon dioxide hydrate. Journal of Physical Chemistry, v. 90, p. 1,259-1,263.

Ripmeester, J.A., and Ratcliffe, C.I. 1989. Solid-state NMR studies if inclusion compounds. National Research Council Canada, Division of Chemistry, Report Number C1181-89S, 87 p.

Ripmeester, J.A., Tse, J.S., Ratcliffe, C.I., and Powell, B.M. 1987. A new clathrate hydrate structure. Nature, v. 325, p. 135.

Rodin, V.V., Arkhangelskii, A.N., Isangalin, F.Sh., and Volkov, V.Ya. 1984. Kriobiol Kriomed, v. 14, 8 p.

Roscoe, B.A., and Grau, J.A. 1988. Response of the carbon/oxygen measurement for an inelastic gamma ray spectroscopy tool. Society of Petroleum Engineers, Formation Evaluation, v. 3, no. 1, p. 76-80.

Ruckebusch, G. 1983. A Kalman filtering approach to natural gamma ray spectroscopy in

   well logging. IEEE Transactions Automatic Control, AC-28, p. 372-380.

Saki, A. 1999. Velocity analysis of vertical seismic profile (VSP) survey at

   JAPEX/JNOC/GSC Mallik 2L-38 gas hydrate research well, and related problems

   for estimating gas hydrate concentration. in Dallimore, S.R., Uchida, T., and

   Collett, T.S. eds., Scientific Results from JAPEX/JNOC/GSC Mallik 2L-38 Gas

   Hydrate Research Well, Mackenzie Delta, Northwest Territories, Canada.

   Geological Survey of Canada Bulletin 544, p. 323-340.

Schlumberger Educational Services. 1989. Log Interpretation Principles/Applications.

   Schlumberger Educational Services Publishers, Houston, Texas, 247 p.

Schweitzer, J.S., Grau, J.A., and Hertzog, R.C. 1988. Precision and accuracy of short-

   lived activation measurements for in situ geological analyses. Journal of Trace

   Microprobe Techniques, v. 6, p. 437-451.

Scott, H.D., and Smith, M.P. 1973. The aluminum activation log. Log Analyst, v. 14, p.

   3-12.

Serra, O. 1984. Fundamentals of well-log interpretation. Developments in Petroleum

   Science, v. 1, Elesevier Publishing, Amsterdam, The Netherlands.

Serra, O. 1989. Formation microscanner image interpretation. Schlumberger Educational

   Services Publisher, Houston, Texas.

Shipboard Scientific Party. 1972. Sites 102, 103, 104 (Leg 11). in Hollister, C.D., et al.,

   Proceedings, Deep Sea Drilling Project, Initial Reports, Washington D.C., U.S.

   Government Printing Office, v. 11, p. 135-218.

_____. 1980. Site 533 and 534 (Leg 76). *in* Sheridan, R.E., et al., Proceedings, Deep Sea Drilling Project, Initial Reports, Washington D.C., U.S. Government Printing Office, v. 76, p. 35-80.

_____. 1985. Site 570 (Leg 84). *in* von Huene, R., et al., Proceedings, Deep Sea Drilling Project, Initial Reports, Washington D.C., U.S. Government Printing Office, v. 67, p. 283-336.

_____. 1986. Sites 614-624 (Leg 96). *in* Bouma, A.H., et al., Proceedings, Deep Sea Drilling Project, Initial Reports, Washington D.C., U.S. Government Printing Office, v. 96, p. 3-424.

_____. 1990. Site 796 (Leg 127). *in* Tamake, K., et al., Proceedings, Ocean Drilling Program, Initial Reports, College Station, Texas, v. 127, p. 247-322.

_____. 1991. Site 808 (Leg 128). *in* Taira, A., et al., Proceedings, Ocean Drilling Program, Initial Reports, College Station, Texas, v. 131, p. 71-269.

_____. 1994. Sites 892 and 889 (Leg 146). *in* Westbrook, G.K., et al., Proceedings, Ocean Drilling Program, Initial Reports, College Station, Texas, v. 146, p. 301-396.

_____. 1996. Sites 994, 995, and 997 (Leg 164). *in* Paull, C.K., et al., Proceedings, Ocean Drilling Program, Initial Reports, College Station, Texas, v. 164, p. 99-623.

Shipley, T.H., and Didyk, B.M. 1982. Occurrence of methane hydrates offshore Mexico. *in* Watkins , J.S., Moore, J.C., et al., Initial Reports, Deep Sea Drilling Project: Washington D.C., U.S. Government Printing Office, v. 66, p. 547-555.

Sloan, E.D. 1998. Clathrate hydrates of natural gases. Second Edition, Marcel Dekker
Inc. Publishers, New York, New York 705 p.

Smith, S.L., and Judge, A.S. 1993. Gas hydrate database for Canadian Arctic and selected
east coast wells. Geological Survey of Canada Open File Report 2746, p. 1-7.

Smith, H.D., Jr., Wyatt, D.F., Jr., and Arnold, D.M. 1989. Obtaining intrinsic formation
capture cross sections with pulsed neutron capture logging tools. The Log
Analyst, v. 30, no. 3, p. 178-195.

Spence, G.D., Minshull, T.A., and Fink, C. 1995. Seismic studies of methane gas hydrate,
offshore Vancouver Island. in Carson, B., Westbrook, G.K., Musgrave, R.J., and
Suess, E., eds., Proceedings of the Ocean Drilling Program, Scientific Results, v.
146, pt. 1, p. 163-174.

Timur, A. 1968. Velocity of compressional waves in porous media at permafrost
temperature. Geophysics, v. 33, p. 584-595.

Timur, A., and Toksöz, M.N. 1985. Downhole geophysical logging. Annual Reviews of
Earth and Planetary Sciences, v. 13, p. 315-344.

Toksöz, M.N, Cheng, C.H., and Timur, A. 1976. Velocity of seismic waves in porous
rocks. Geophysics, v. 41, p. 621-645.

Tosaya, C., and Nur, A. 1982. Effects of diagenesis and clays on compressional velocities
in rock. Geophysical Research Letters, v. 9, p. 5-8.

Trofimuk, A.A., Cherskiy, N.V., and Tsarev, V.P. 1977. The role of continental
glaciation and hydrate formation on petroleum occurrences. in Meyer, R.F., ed.,

Future Supply of Nature-Made Petroleum and Gas. Pergamon Press, New York, New York, p. 919-926.

Tucholke, B.E., Bryan, G.M., and Ewing, J.I. 1977. Gas-hydrate horizons detected in seismic-profiler data from the western North Atlantic. American Association of Petroleum Geologists Bulletin, v. 61, no. 5, p. 698-707.

Waxman, M.H., and Smits, L.J.M. 1968. Electrical conductivities in oil-bearing shaly sands. Society of Petroleum Engineers Journal, v. 243, no. 7, p. 107-122.

Waxman, M.H., and Thomas, E.C. 1974. Electrical conductivities in shaly sands, I. The relation between hydrocarbon saturation and resistivity index, II. The temperature coefficient of electrical conductivity. Journal of Petroleum Technology, February, p. 213-225.

Wendlandt, R.F., and Bhuyan, K. 1990. Estimation of mineralogy and lithology from geochemical log measurements. American Association of Petroleum Geologists Bulletin, v. 74, no. 6, p. 837-856.

Werner, M.R. 1987. Tertiary and Upper Cretaceous heavy oil sands, Kuparuk River area, Alaskan North Slope. in Tailleur, I.L., and Weimer, Paul, eds., Alaskan North Slope Geology. Jointly published by the Pacific Section, Society of Economic Paleontologists and Mineralogists and the Alaska Geological Society, Book 50, v. 1, p. 109-118.

Whalley, E. 1980. Speed of longitudinal sound in clathrate hydrates. Journal of Geophysical Research, v. 85, no. B5, p. 2,539-2,542.

Whiffen, B.L., Kiefte, H., and Clouter, M.J. 1982. Determination of acoustic velocities in

xenon and methane hydrates by brillouin spectroscopy. Geophysical Research

Letters, v. 9, no. 6, p. 645-648.

Wiley, R., and Patchett, J.G. 1990. CNL neutron porosity modeling--a step forward. The

Log Analyst, v. 31, no. 3, p. 133-149.

Winters, W.J., Dallimore, S.R., Collett, T.S., Katsube, T.J., Jenner, K.A., Cranston, R.E.,

Wright, J.F., Nixon, F.M., and Uchida, T. 1999. Physical properties of sediments

from the JAPEX/JNOC/GSC Mallik 2L-38 gas hydrate research well. in

Dallimore, S.R., Uchida, T., and Collett, T.S. eds., Scientific Results from

JAPEX/JNOC/GSC Mallik 2L-38 Gas Hydrate Research Well, Mackenzie Delta,

Northwest Territories, Canada. Geological Survey of Canada Bulletin 544, p. 95-

100.

Wood, A.B. 1941. A text book of sound. MacMillan Publishing, New York, New York,

578 p.

Woodhouse, R., and Kerr, S.A. 1992. The evaluation of oil saturation through casing

using carbon/oxygen logs. The Log Analyst, v. 33, no. 1, p. 1-11.

Wright, J.F., Taylor, A.E., Dallimore, S.R., and Nixon, F.M. 1999. Estimating in situ gas

hydrate saturation from core temperature observations, JAPEX/JNOC/GSC

Mallik 2L-38 gas hydrate research well. in Dallimore, S.R., Uchida, T., and

Collett, T.S. eds., Scientific Results from JAPEX/JNOC/GSC Mallik 2L-38 Gas

Hydrate Research Well, Mackenzie Delta, Northwest Territories, Canada.

Geological Survey of Canada Bulletin 544, p. 101-108.

Yakushev, V.S., and Collett, T.S. 1992. Gas hydrates in Arctic regions: risk to drilling and production. Proceedings of the Second International Offshore and Polar Engineering Conference, June 14-19, San Francisco, California, p. 669-673.

Yefremova, A.G., and Zhizhchenko, B.P. 1974. Occurrence of crystal hydrates of gas in sediments of modern marine basins. Doklady Akademii Nauk SSSR, v. 214, p. 1,179-1,181.

Zimmerman, R.W., and King, M.S. 1986. The effect of the extent of freezing on seismic velocities in unconsolidated permafrost. Geophysics, v. 51, no. 6, p. 1,285-1,290.

APPENDIX 1

OCEAN DRILLING PROGRAM (ODP)

SHORE-BASED LOG-DATA PROCESSING

The following description of the shore-based processing of the log data from ODP Leg 146 and 164 has been extracted from the ODP Leg 146 and 164 Initial Reports Volumes (Shipboard Scientific Party, 1994, 1996). Shore-based log processing was performed on all of the downhole-log data collected during ODP Leg 146 and 164 by the Lamont-Doherty Borehole Research Group (LDEO-BRG), University of Leicester (Borehole Research-Leicester), and the Institute Méditerranéen de Technologie (IMT), using Schlumberger "Logos" software and additional programs developed by members of LDEO-BRG. Shore-based processing of data from each hole consisted of (1) depth adjustments of all logs to a common measurement below the sea floor, (2) corrections specific to certain tools, and (3) quality control and rejection of unrealistic values. The depth-shifting procedure is based on an interactive, graphical depth-match program that allows the processor to visually correlate logs and define appropriate shifts. The reference log and the log to be adjusted in depth are displayed side-by-side on a screen, and vectors connect the two logs at positions chosen by the user. The total gamma-ray curve (SGR) from the NGT tool on each logging string was used, in most cases, to correlate the logging runs. In general, the reference curve was chosen on the basis of low

recorded cable tensions and high cable speeds. Other factors, however, such as the length

of the logged interval, presence of the bottom-hole assembly, and the statistical quality of

the collected data (better statistics are obtained at lower logging speeds) were also

considered in the selection. Specific tool corrections were performed on the gamma-ray

data to account for changes in borehole size and for the composition of the drilling fluid;

however, borehole size induced errors often persist. Processing techniques unique to the

AACT and GST tools of the geochemical logging string (GLT) are described in detail

below.

Quality control is performed by cross-correlation of all logging data. If the data

processor concluded that individual log measurements represented unrealistic values, the

choices were to either discard the data or identify a specific depth interval containing

suspect values that must be used with caution. Quality control of the acoustic data was

based on discarding any of the four independent transit time measurements that were

negative or that fell outside a range of reasonable values selected by the processor. In

addition to the standard 15.2 cm sampling rate, bulk-density (HLDT) and neutron (CNT-

G) data on Leg 146 and 164 were recorded at a sampling rate of 2.5 and 5.1 cm,

respectively. The enhanced bulk-density curve is the result of a Schlumberger enhanced

processing technique performed onboard. Whereas in normal processing, short-spacing

data is smoothed to match the long-spacing data, in enhanced processing this is reversed.

In a situation where there is good contact between the HLDT tool and the borehole wall

the results are improved because the short-spacing data have better vertical resolution.

Locally, some HLDT- and CNT-G-log data appeared unreliable (usually because of poor

hole conditions) and were not processed beyond what had been done on board the ship. In general, a large (>30.5 cm) and/or irregular borehole affects most log measurements, particularly those that require eccentralization (HLDT) and a good contact with the borehole wall.

Geochemical-logging data (GLT) from all three sites logged on Leg 164 (Sites 994, 995, and 997) was also extensively reprocessed. The geochemical logging tool string (Figure 3.1) consists of four logging tools: the NGT, the CNT-G, the AACT, and the GST. The natural gamma-ray tool (NGT) is located at the top of the tool string, so that it can measure the naturally occurring radionuclides, Th, U, and K, before the formation is irradiated by the nuclear sources contained in the other tools. The compensated neutron tool (CNT-G), located below the natural gamma-ray tool, carries low-energy Californium-252 (^{252}Cf) to activate the Al atoms in the formation. The aluminum activation clay tool (AACT), a modified NGT, is located below the ^{252}Cf source and measures the activated gamma rays in the formation. By combining the AACT measurement with the NGT measurement, the background radiation is subtracted and a reading of formation Al is obtained (Scott and Smith, 1973). The gamma-ray spectrometry tool (GST), at the base of the string, carries a pulsed neutron generator to bombard the formation and an NaI(Tl) scintillation detector, which measures the spectrum of gamma rays generated by neutron interactions. Because each of the elements in the formation is characterized by a unique spectral signature, it is possible to derive the contribution (or yield) of each of the major elements silicon (Si), iron (Fe), calcium (Ca), titanium (Ti), sulfur (S), gadolinium (Gd), and potassium (K) to the measured spectrum

and, in turn, to estimate its abundance in the formation. The GST can also measure the hydrogen (H) and chlorine (Cl) in the borehole and formation, but the signal for these elements is almost entirely because of seawater in the borehole, and they are, hence, of little value. The only major rock-forming elements not measured by the geochemical tool string are magnesium (Mg) and sodium (Na); the neutron-capture cross sections of these elements are too small relative to their typical abundances for the tool string to detect them.

Processing of the GLT spectrometry data is required to transform the relative elemental yields into oxide weight fractions. The processing is performed with a set of log interpretation programs written by Schlumberger that have been slightly modified to account for the lithologies and hole conditions encountered in ODP holes. The processing steps are summarized below:

Step 1: Reconstruction of Relative Elemental Yields from Recorded Spectral Data

The first processing step uses a weighted least-squares method to compare the measured spectra from the geochemical spectrometry tool with a series of standard spectra to determine the relative contribution (or yield) of each element. Whereas six elemental standards (Si, Fe, Ca, S, Cl, and H) are used to produce the shipboard yields, three additional standards (Ti, Gd, and K) can be included in the shore-based processing to improve the fit of the spectral standards to the measured spectra (Grau and Schweitzer, 1989). Although these additional elements often appear in the formation in very low concentrations, they can make a large contribution to the measured spectra because they

have large neutron capture cross sections. For example, the capture cross section of Gd is 49,000 barns; that of Si is 0.16 barns (Hertzog et al., 1987). Gd is, therefore, included in the calculation of a best fit between the measured and the standard spectra. This best fit analysis was done for the elements in each of the logged holes to include spectral standards for Si, Ca, Fe, Ti, Gd, H, and Cl. During the processing of Holes 995B and 997B the spectral standards for K and S were not used because these two elements existed in concentrations below the resolution of the tool and including them would significantly increase error associated with the other elemental yields. A nine-point smoothing filter was applied to the yields to reduce noise in the data.

Step 2: Depth-Shifting

The second processing step is to depth shift the logging runs to a chosen reference run. A total gamma-ray curve (from the NGT) is usually chosen as a reference curve. For Hole 994C, the reference NGT run was taken from the Quad-combination (DITE/SDT-C/HLDT/CNT-G/NGT) run. For Hole 995B, the NGT curve on the geochemical logging tool itself was used as the reference curve, so no depth shifting was necessary. For Hole 997B, the reference NGT run was taken from the second (repeat) FMS run. The latter was the most appropriate run because of its greater speed and depth coverage.

Step 3: Calculation of Total Radioactivity and Th, U, and K Concentrations

The third processing routine calculates the total natural gamma radiation in the formation as well as concentrations of Th, U, and K, using the counts in five spectral windows from the natural gamma-ray tool (Lock and Hoyer, 1971). This resembles shipboard processing, except that corrections for hole-size changes are made in the shore-based processing of these curves. A Kalman filter (Ruckebusch, 1983) was applied to minimize the statistical uncertainties in the logs, which would otherwise create erroneous negative readings and anti-correlations (especially between Th and U). At each depth level, calculations and corrections also were performed for K contained in the mud. This K correction is particularly useful where KCl is routinely added to the hole; however, because of dispersion it is difficult to know exactly how much K is in the borehole. This program outputs K (wet weight percentage), U (parts per thousand), and Th (parts per thousand), along with a total gamma-ray curve and a computed gamma-ray curve (total gamma ray minus U contribution).

Step 4: Calculation of Al Concentration

The fourth processing routine calculates Al concentrations using four energy windows while concurrently correcting for natural activity, borehole fluid neutron-capture cross section, formation neutron-capture cross section, formation slowing-down length, and borehole size. Porosity and density logs are needed in this routine to convert the wet weight percentage K and Al curves to dry weight percentage. For Hole 997B, because of the very poor hole conditions, log density data were not used. Instead, a

working porosity curve was constructed from the core-derived physical properties data of bulk- and grain-density and substituted as a log curve. A correction is also made for Si interference with Al; the ^{252}Cf source activates the Si, producing the aluminum isotope, ^{28}Al (Hertzog et al., 1987). The program uses the Si yield from the gamma-ray spectrometry tool to determine the Si background correction. The program outputs dry weight percentages of Al and K, which are used in the calculation and normalization of the remaining elements.

Step 5: Normalization of Elemental Yields from the GST to Calculate the Elemental Weight Fractions

This routine combines the dry weight percentages of Al and K with the reconstructed yields to obtain dry weight percentages of the GST elements using the relationship: $W_i = FY_i/S_i$, where W_i = dry weight percentage of the i-th element, F = normalization factor determined at each depth interval, Y_i = relative elemental yield for the i-th element, and S_i = relative weight percentage (spectral) sensitivity of the i-th element. The normalization factor, F, is a calibration factor determined at each depth from a closure argument to account for the number of neutrons captured by a specific concentration of rock elements. Because the sum of oxides in a rock is 100%, F is given by the following equation: $F(\sum X_iY_i/S_i) + X_KW_K + X_{Al}W_{Al} = 100.0$, where X_i= factor for the element to oxide (or carbonate) conversion, X_K = factor for the conversion of K to K_2O (1.205), X_{Al} = factor for the conversion of Al to Al_2O_3 (1.899), W_K= dry weight

percentage of K determined from natural activity, and W_{Al} = dry weight percentage of Al

determined from the activation measurement. The sensitivity factor, S_i, is a tool constant

measured in the laboratory, which depends on the capture cross section, gamma ray

production, and detection probabilities of each element measured by the GST (Hertzog et

al., 1987). The factors X_i are simply element to oxide conversion coefficients and

effectively include the O, C, or S bound with each element. In processing the GLT data,

the correct choice of X_i is important in the closure algorithm described above and

requires some geological input. In most lithologies, the elements measured by the tool

occur in silicates in which the compositions can be expressed completely as oxides. The

only choice here concerns the degree of oxidation: Should iron be expressed as FeO or

Fe_2O_3? With carbonate or carbonate-rich lithologies, the measured calcium is more

likely to be present as $CaCO_3$ (X_{Ca}: 2.497) than as the oxide (CaO; X_{Ca}: 1.399). A

good indication of the choice of calcium conversion factors can often be gained from

shipboard XRD and $CaCO_3$ measurements, which estimate acid-liberated $CaCO_3$. In the

absence of suitable shipboard data, a rough rule of thumb was used such that if elemental

Ca was below 6% then all Ca was assumed to be in silicate, above 12%, in carbonate. Ca

concentrations between these values were converted using linear interpolation. During

Leg 164, XRD and $CaCO_3$ data were available for processing the geochemical logs from

Holes 995B and 997B. Although Ca is low over most of the logged section, there are no

calcium-bearing silicates present in significant proportions, and the calcium is assumed to

be tied up as carbonate. For this reason, a carbonate factor of 2.497 ($CaCO_3$) was used

for Holes 995B and 997B. A variable carbonate oxide factor was chosen, however, for Hole 994C (see Table A1.1). With the variable oxide factor, a factor of 1.399 is used if Ca is less than or equal to 6% by weight, a factor of 2.497 is used if Ca is greater than 12%, and the oxide factor is linearly interpolated if Ca is between 6% and 12%.

Step 6: Calculation of Oxide Percentages

This routine converts the elemental weight percentages into oxide percentages by multiplying each by its associated oxide factor, as shown in Table A1.1.

Step 7: Calculation of Error Logs

The seventh and final step in processing is the calculation of the statistical uncertainty of each element, using methods described by Grau et al. (1990) and Schweitzer et al. (1988). This error is strongly related to the normalization factor, F, which is calculated at each depth level. A lower normalization factor represents better counting statistics and, therefore, higher quality data. Overall, the logs in all three holes are degraded by poor hole conditions (particularly the size and rugosity of the boreholes), but some general trends in chemical variation are apparent that need to be considered in any geological interpretation of the borehole.

Table A1.1 Leg 164 GST oxide factors used to normalize elements to 100% and converting elements to oxides (modified from Shipboard Scientific Party, 1996).

| Element	Oxide/carbonate	Conversion factor
Si	SiO_2	2.139
Ca	$CaCO_3$	2.497 (Holes 995B, 997B)
Ca	CaO-$CaCO_3$	1.399-2.497 (Hole 994C)
Fe	FeO	1.358
K	K_2O	1.205
Ti	TiO_2	1.668
Al	Al_2O_3	1.889

APPENDIX 2

NEUTRON TRANSPORT THEORY

The following discussion dealing with neutron transport theory has been largely extracted from Hearst and Nelson (1985). The neutron is a neutral atomic particle of approximately the same mass as a proton. The neutron sources used in most modern logging tools emit "fast" neutrons with an average energy of about 4.5 million electronvolts (MeV). Because it is rare for neutrons to be absorbed until they have lost most of their energy, each neutron will often have many interactions with other particles in the process of losing its energy. During the life of a neutron it may undergo three basic types of interactions: (1) inelastic scatter, (2) elastic scatter, and (3) radioactive capture; which are discussed in more detail in the following section.
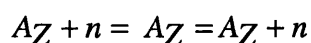
1. Inelastic Scatter

Inelastic scatter can only take place while the neutron is highly energetic. During an inelastic scattering event the neutron (n) interacts with a nucleus of a atom with an atomic number Z and a mass A and forms a compound with a mass number of $A+1$. This compound nucleus is in an excited state, which decays very rapidly to the ground state while emitting a gamma-ray, and then emits a neutron. The reaction is written as (* signifies an excited state):

$$A_Z + n = {}^{A+1}A_Z{}^* = A_Z + n + \gamma$$
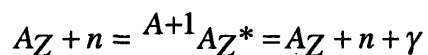
Inelastic scattering cannot take place unless the energy of the incident neutron is large enough to create an excited state of the compound nucleus. The gamma-rays that are produced have a unique energy level that can be used to identify chemical composition of the compound (target) nucleus.

2. Elastic Scatter

Perhaps the most common neutron interaction is elastic, or billiard ball, scattering. In an elastic scattering event the neutron (n) collides with a nucleus of an atom (A_Z), but no potential energy is internally transferred to the nucleus. The only energy transferred is the kinetic energy given the struck nucleus. The reaction is written as:

$$A_Z + n = A_Z = A_Z + n$$

An elastic scattering analogy has often been made using the collision between a marble and a billiard ball. The marble (neutron) bounces off the billiard ball (nucleus) transferring only a small amount of its energy in the process. A notable exception to this analogy is the element hydrogen because it has a mass approximately equal to the mass of the incident neutron. For neutron-hydrogen elastic collisions, a more reasonable analogy would be the collision of two marbles. When hydrogen is the struck nucleus, the

maximum energy loss is 100%. On average, however, neutrons will lose about 50% of their energy in each elastic scatter with hydrogen. Once neutrons pass below the energy threshold for inelastic scatter, the presence of hydrogen dominates the neutron slowing process.

3. Radioactive Capture

The life of a neutron ends with the third type of reaction involving neutron removal or capture. As a result of inelastic and elastic scatter, the neutrons are eventually slowed to an average energy at which they coexist in thermal equilibrium with the formation nuclei. By this time most have undergone many collisions and have been reduced to about one millionth of one percent of their original energy. The thermal neutrons continue to elasticity scatter with the formation nuclei and diffuse through the formation, with as many neutrons gaining kinetic energy from the thermally agitated formation nuclei as those losing energy to these nuclei. Eventually each neutron is captured by one of the nuclei, leaving the nucleus in an excited state. The excited nucleus, in most cases, instantaneously emits "capture" gamma radiation, the energy of which is indicative of the capturing nucleus. The reaction is written as:

$$A_Z + n = {}^{A+1}A_Z{}^* = {}^{A+1}A_Z + \gamma$$
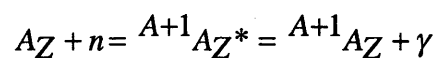
The cross section for thermal neutron capture, unlike those for inelastic and elastic scatter, are very strongly dependent on the nucleus involved.